Notes on Numerical Fluid Mechanics
and Multidisciplinary Design 124

Andreas Dillmann · Gerd Heller
Ewald Krämer · Hans-Peter Kreplin
Wolfgang Nitsche · Ulrich Rist *Editors*

New Results in Numerical and Experimental Fluid Mechanics IX

Contributions to the 18th STAB/DGLR Symposium, Stuttgart, Germany, 2012

Springer

Notes on Numerical Fluid Mechanics and Multidisciplinary Design

Volume 124

About this Series

Notes on Numerical Fluid Mechanics and Multidisciplinary Design publishes state-of-art methods (including high performance methods) for numerical fluid mechanics, numerical simulation and multidisciplinary design optimization. The series includes proceedings of specialized conferences and workshops, as well as relevant project reports and monographs.

Andreas Dillmann · Gerd Heller
Ewald Krämer · Hans-Peter Kreplin
Wolfgang Nitsche · Ulrich Rist
Editors

New Results in Numerical and Experimental Fluid Mechanics IX

Contributions to the 18th STAB/DGLR Symposium, Stuttgart, Germany, 2012

Springer

Editors
Andreas Dillmann
Hans-Peter Kreplin
Deutsches Zentrum für Luft- und Raumfahrt (DLR)
Institut für Aerodynamik und Strömungstechnik
Göttingen
Germany

Gerd Heller
Airbus Deutschland
Bremen
Germany

Ewald Krämer
Ulrich Rist
Institut für Aerodynamik und Gasdynamik
University of Stuttgart
Stuttgart
Germany

Wolfgang Nitsche
Institut für Luft- und Raumfahrt
TU Berlin
Berlin
Germany

ISSN 1612-2909 ISSN 1860-0824 (electronic)
ISBN 978-3-319-03157-6 ISBN 978-3-319-03158-3 (eBook)
DOI 10.1007/978-3-319-03158-3
Springer Cham Heidelberg New York Dordrecht London

Library of Congress Control Number: 2013957123

Printed on acid-free paper

Springer is part of Springer Science+Business Media (www.springer.com)

Preface

This volume contains the papers presented at the 18th DGLR/STAB-Symposium held in Stuttgart, Germany, in November, 6–7, 2012 and organized by the Institute of Aerodynamics and Gas Dynamics of Stuttgart University. STAB is the German Aerospace Aerodynamics Association, founded toward the end of the 1970s, whereas DGLR is the German Society for Aeronautics and Astronautics (Deutsche Gesellschaft für Luft- und Raumfahrt—Lilienthal Oberth e.V.).

The mission of STAB is to foster development and acceptance of the discipline "Aerodynamics" in Germany. One of its general guidelines is to concentrate resources and know-how in the involved institutions and to avoid duplication in research work as much as possible. Nowadays, this is more necessary than ever. The experience made in the past makes it easier now, to obtain new knowledge for solving today's and tomorrow's problems. STAB unites German scientists and engineers from universities, research-establishments, and industry doing research and project work in numerical and experimental fluid mechanics and aerodynamics for aerospace and other applications. This has always been the basis of numerous common research activities sponsored by different funding agencies.

Since 1986 the symposium has taken place at different locations in Germany every 2 years. In between STAB workshops regularly take place at the DLR in Göttingen. The changing meeting places were established as focal points in Germany's Aerospace Fluid Mechanics Community for a continuous exchange of scientific results and their discussion. Moreover, they are a forum where new research activities can be presented, often resulting in new commonly organized research and technology projects.

It is the ninth time now that the contributions to the Symposium are published after being subjected to a peer review. The material highlights the key items of integrated research and development based on fruitful collaboration of industry, research establishments, and universities. The research areas include airplane aerodynamics, multidisciplinary optimization and new configurations, turbulence research and modeling, laminar flow control and transition, rotorcraft

aerodynamics, aeroelasticity and structural dynamics, numerical simulation, experimental simulation and test techniques, aeroacoustics as well as the rather new fields of biomedical flows, convective flows as well as aerodynamics and acoustics of ground vehicles.

From some 90 lectures presented at the Symposium 68 are included in this book.

The Review Board, partly identical with the Program Committee, consisted of J. Arnold (Göttingen), K. Becker (Bremen), S. Becker (Erlangen), M. Behr (Aachen), H. Bieler (Bremen), P. Birken (Kassel), J. Bosbach (Göttingen), C. Breitsamter (Garching), G. Brenner (Clausthal), M. Buschmann (Dresden), C. Cierpka (Neubiberg), K. Ehrenfried (Göttingen), J. Fassbender (Bremen), D. Fiala (Stuttgart), H. Foysi (Siegen), A. Friedl (Neubiberg), J. Fröhlich (Dresden), A. Gardner (Göttingen), N. Gauger (Aachen), K. Geurts (Aachen), C. Gmelin (Berlin), P. Gnemmi (St. Louis), C. Grabe (Göttingen), S. Grundmann (Darmstadt), S. Guerin (Berlin), H. Hansen (Bremen), R. Hartmann (Braunschweig), A. Hartmann (Aachen), M. Haupt (Braunschweig), S. Hein (Göttingen), R. Heinrich (Braunschweig), M. Hepperle (Braunschweig), H. Herwig (Hamburg), S. Hickel (Garching), R. Höld (Unterschleißheim), R. Hörnschemeyer (Aachen), S. Illi (Stuttgart), T. Indinger (Garching), S. Jakirlic (Darmstadt), L. Jehring (Cottbus), J. Jovanovic (Erlangen), C. Kandzia (Aachen), M. Keßler (Stuttgart), T. Kier (Oberpfaffenhofen), M. Klaas (Aachen), A. Klein (München), I. Klioutchnikov (Aachen), M. Kloker (Stuttgart), J. Kokavecz (Göttingen), M. Konstantinov (Göttingen), E. Krämer (Stuttgart), H.-P. Kreplin (Göttingen), M. Kriegel (Berlin), A. Krumbein (Göttingen), M. Kruse (Braunschweig), F.-O. Lehmann (Rostock), T. Lerche (Hamburg), T. Lutz (Stuttgart), H. Mai (Göttingen), M. Meinke (Aachen), F. Menter (Otterfing), R. Meyer (Berlin), C. Mockett (Berlin), T. Möller (Braunschweig), D. Müller (Aachen), B. Müller (Berlin), C.-D. Munz (Stuttgart), A. Nemili (Aachen), W. Nitsche (Berlin), F. Obermeier (Freiberg), H. Olivier (Aachen), C. Othmer (Wolfsburg), I. Peltzer (Berlin), J. Raddatz (Braunschweig), R. Radespiel (Braunschweig), L. Reimer (Braunschweig), M. Rein (Göttingen), B. Reinartz (Aachen), C. Resagk (Ilmenau), S. Reuss (Göttingen), K. Richter (Göttingen), U. Rist (Stuttgart), M. Ritter (Göttingen), H. Rosemann (Göttingen), T. Rösgen (Zürich), C.-C. Rossow (Braunschweig), F. Rüdiger (Dresden), M. Rütten (Göttingen), E. Sarradj (Cottbus), M. Schmidt (Aachen), G. Schmitz (Hamburg), P. Scholz (Braunschweig), N. Schönwald (Berlin), W. Schröder (Aachen), E. Schülein (Göttingen), V. Schulz (Trier), J. Schumacher (Ilmenau), D. Schwamborn (Göttingen), T. Schwarz (Braunschweig), A. Seitz (Braunschweig), W. Send (Göttingen), M. Siebenborn (Trier), C. Stemmer (Garching), A. Stück (Braunschweig), A. Stuermer (Braunschweig), E. Stumpf (Aachen), F. Thiele (Berlin), C. Tropea (Darmstadt), C. Weckmüller (Berlin), W. Wegner (Göttingen), K. Weinman (Göttingen), M. Widhalm (Braunschweig), J. Wild (Braunschweig), C. Willert (Köln), and W. Würz (Stuttgart).

Nevertheless, the authors sign responsible for the contents of their contributions.

The editors are grateful to Prof. Dr. W. Schröder as the General Editor of the "Notes on Numerical Fluid Mechanics and Multidisciplinary Design" and to the Springer-Verlag for the opportunity to publish the results of the Symposium.

June 2013

A. Dillmann
G. Heller
E. Krämer
H.-P. Kreplin
U. Rist

Contents

Part XII Biofluid Mechanics

Part I
Airplane Aerodynamics

Influence of Meshing on Flow Simulation in the Wing-Body Junction of Transport Aircraft

Philipp Peter Gansel, Patriz Dürr, Markus Baumann, Thorsten Lutz and Ewald Krämer

Abstract A common problem in the field of CFD simulations of aircraft is the construction of hybrid grids at concave geometry corners. The challenge is to generate boundary layer meshes normal to both intersecting walls, while none of the grid cells collide with each other. Boundary layer interaction combined with pressure gradients and three-dimensional effects causes very complex flows which demand a high mesh quality. An unstructured and three different hybrid grids of a generic aircraft geometry are compared to each other. The analysis focuses on the results in the wing-body junction. With the smallest meshing effort the unstructured grid simulation yields good agreement of surface pressure and boundary layers with the hybrid meshes. The strong impact of the boundary layer grid edge on the velocity profiles emphasizes the need of sufficiently high boundary layer grids on all surface parts.

1 Introduction

Continuous progress is achieved in CFD simulations of industry-relevant aircraft configurations by the availability of new numerical methods and modeling as well as increasing computational capabilities. However the spatial discretization in terms of computational mesh is disregarded often. Especially when meshing entire

P. P. Gansel (✉) · P. Dürr · M. Baumann · T. Lutz · E. Krämer
Institute of Aerodynamics and Gas Dynamics, University of Stuttgart, Pfaffenwaldring 21, 70569 Stuttgart, Germany
e-mail: gansel@iag.unistuttgart.de|
http://www.iag.uni-stuttgart.de/

T. Lutz
e-mail: lutz@iag.uni-stuttgart.de

E. Krämer
e-mail: Kraemer@iag.uni-stuttgart.de

A. Dillmann et al. (eds.), *New Results in Numerical and Experimental Fluid Mechanics IX*, Notes on Numerical Fluid Mechanics and Multidisciplinary Design 124,
DOI: 10.1007/978-3-319-03158-3_1,

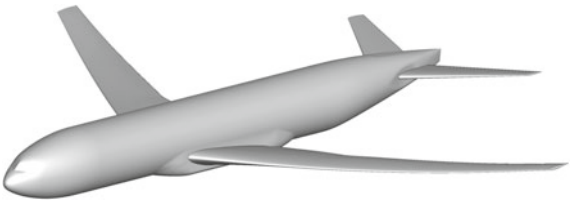

Fig. 1 NASA CRM including wing, body, belly fairing and horizontal tail plane

aircraft geometries with a variety of components and corners for viscous simulations problems occur with most grid generators using hybrid grids. The most frequent challenge in the vicinity of concave corners is to generate a boundary layer mesh normal to both intersecting walls, without having the grid cells collide with each other, which often leads to grids of locally poor quality. Actually the interaction of both boundary layers in combination with strong pressure gradients and three-dimensional effects causes very complex flows. Their simulation claims a high quality mesh and is challenging today's turbulence models.

Basic experimental and numerical investigations of the horseshoe vortex system developing at a wing-body junction have been conducted. The flow regime is also present in wind tunnel testing at the junction of the airfoil with the test section side walls. An overview of different measured and simulated geometries can be found in [1]. In simulations of the Reynolds-Averaged Navier-Stokes (RANS) equations the grid and turbulence model dependency of the corner separation is a known problem which presumably arises from the deficiency of eddy-viscosity models to represent the anisotropy of the Reynolds stresses (see e.g. [2]).

In the present study particularly the influence of the meshing strategy on the simulation of the junction flow is investigated to highlight the effects separately.

2 Simulation Setup

2.1 Test Case

The NASA Common Research Model (CRM), a representative commercial transport aircraft configuration (see [3]), is used as test case in this study. The generic geometry consists of a fuselage, a transonic wing, a belly fairing and a horizontal tail plane. The considered configuration in Fig. 1 omits the nacelle and pylon to provide a clean wing. The CRM has been subject to the Drag Prediction Workshops (DPW) IV and V, where different numerical results and comparisons of grid generators and flow solvers could be achieved (see [4]). Experimental wind tunnel results were published by NASA amongst others in [5].

The CFD model has a reference wing area of 383.690 m^2 and a mean aerodynamic chord of 7.005 m. The wing has a span of 58.763 m, an aspect ratio of 9.0 and a taper ratio of 0.275. The quarter chord line is swept back by 35°. The considered freestream

Table 1 Grid points and cell element counts of the used CFD meshes

Grid	Points	Tets	Prisms	Pyras	Hexas	Cells
GG aniso tets	13,530,358	80,375,105	–	–	–	80,375,105
GG recomb prisms	13,530,484	64,378,306	5,332,464	–	–	69,710,770
PW recomb prisms	13,530,358	19,164,798	20,389,639	20,695	–	39,575,132
GG hexa and prisms	10,189,056	11,495,105	5,520,872	70,186	5,357,947	22,444,110

conditions $Ma = 0.85$, $Re = 5 \cdot 10^6$ and $c_l = 0.5$ represent the CRM design point despite a lower Reynolds number ($Re_{\text{design}} = 40 \cdot 10^6$).

2.2 Grids

Basically there are three different meshing topologies: structured, unstructured and hybrid grids. Although structured grids have the big advantages of structured calculation schemes and proper resolution of corner flow boundary layers, the disadvantages of high generation effort and point numbers—unless methods like hanging nodes or overset grids are used—limit their applicability for complex geometries. One unstructured grid consisting of tetrahedra only and three different hybrid meshes are investigated in the present study. The total grid point and cell element counts are displayed in Table 1.

Unstructured Grid "GG Aniso Tets" Production, refinement and adaption of unstructured grids are very simple. Usually they consist of nearly isotropic tetrahedra, which mostly restricts possible applications to Euler or other simulations with no need of a boundary layer resolution. Such a RANS mesh would have an exhaustively high surface and near wall resolution caused by having the same cell size in tangential and wall normal direction. The grid generator used for the considered meshes Gridgen V15.18 [6] provides anisotropic tetrahedral elements to solve this problem. In the meshing process points of an unstructured surface mesh are extruded from the walls. The resulting prisms are divided into three tetrahedral each. This allows an adequately resolved boundary layer using element aspect ratios up to three orders of magnitude. After completing a prescribed amount of anisotropic element layers (in this case 35) the remaining flow domain is filled up with ordinary tetrahedra. Figure 2 illustrates the boundary layer resolution in the wing-body junction and near the wing leading edge of this mesh referenced as "GG aniso tets". In order to avoid grid cells to collapse or overlap with others the grid extrusion process is stopped in concave corner regions before it reaches the designated boundary layer mesh height. Another specific problem of this kind of unstructured mesh is an increased numerical error introduced by the extremely skewed tetrahedra. If a cell vertex scheme is used, the angles of some faces of the median dual grid, the fluxes are evaluated on, to the corresponding edge deviate extremely from the 90° optimum (see [7]).

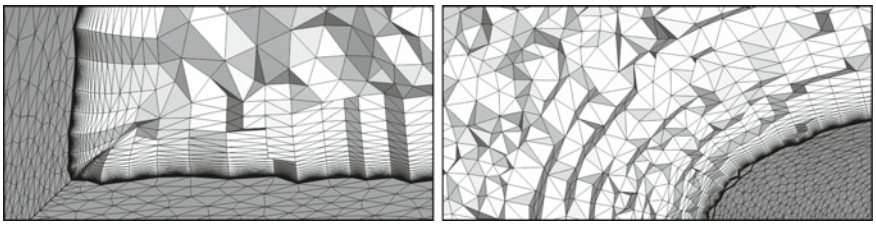

Fig. 2 Details of the "GG aniso tets" grid in the wing-body junction and near the wing leading edge

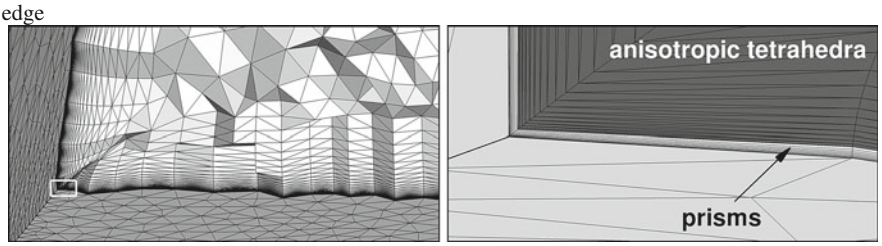

Fig. 3 Details of the "GG recomb prisms" grid in the wing-body junction

Hybrid Grid "GG Recomb Prisms" To prevent the accuracy issue of anisotropic unstructured elements Gridgen provides the possibility to recombine prisms of three anisotropic tetrahedra at a time in the boundary layer part of the grid. The required connectivity information is present in the mesh data from the cell extrusion process. The unstructured grid is divided in two blocks—one tetrahedral and one prismatic—which can be edited further individually. A strong constrain is that the new built prism block must consist of complete element layers. Because of the described chopping of extrusion layers in the vicinity of corners only few prisms layers can be constructed in this way. The grid "GG recomb prisms" which is derived from "GG aniso tets" using this functionality achieves 9 layers of prisms at the walls. They cover only a very thin part of the boundary layer mesh (see Fig. 3) which also explains the relatively small decrease of element count compared to the "GG aniso tets" mesh in Table 1.

Hybrid Grid "PW Recomb Prisms" The Gridgen succeeding meshing software Pointwise [8] provides another approach where all anisotropically extruded tetrahedra are used for prism recombination (up to 35 prism layers in this case). This can only be done at the very end of mesh generation with no further editing. In the current version V17.0R2 it is embedded in the export process of finished grids to the simulation software. To obtain a mesh suitable for the used CFD code TAU an appropriate export plugin for Pointwise had to be developed first. It outputs a TAU readable NetCDF mesh and includes the prisms recombination. The resulting grid is referenced as "PW recomb prisms". Figure 4 shows detailed views of the wing-body junction and the wing leading edge. Note that—originating from the same unstructured grid—"GG aniso tets", "GG recomb prisms" and "PW recomb prisms"

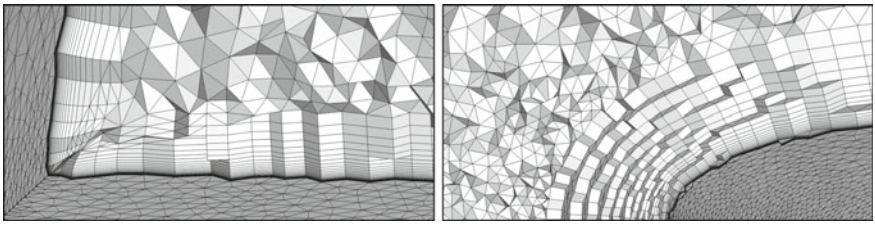

Fig. 4 Details of the "PW recomb prisms" grid in the wing-body junction and near the wing leading edge

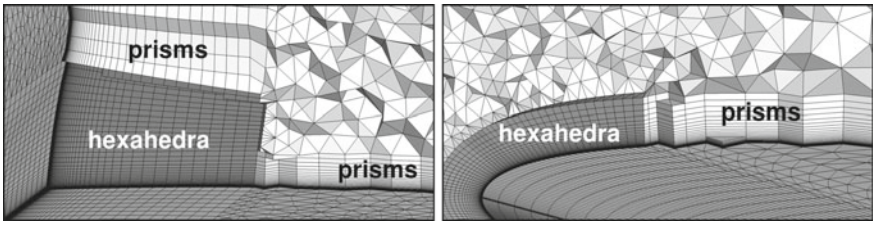

Fig. 5 Details of the "GG hexa and prisms" grid in the wing-body junction and near the wing leading edge

have identical surface meshes, outer region unstructured meshes and volume grid points.

Hybrid Grid "GG Hexa and Prisms" As any other hybrid grids where the boundary layer mesh is extruded from the surface the three grids described above suffer from deficient boundary layer resolution in two ways. Because of the chopping near geometry corners the boundary layer mesh there is too thin and the outer part of the boundary layer cannot be resolved by the outer isotropic tetrahedral mesh. The second aspect is the near wall resolution which close to the corner is defined by the surface mesh of the respectively other wall. This usually leads to a wall distance of the first point orders of magnitudes higher than desired. One possible solution to these problems is to adopt some aspects of structured meshing. By inserting volume blocks of hexahedral elements in the corners the boundary resolution normal to both walls can be ensured and adjusted independently. Such combinations of structured and hybrid meshing was already investigated mostly using chimera technique e.g. in [9] and [10]. In the present study the hexahedral and prismatic grid parts are connected to each other directly, which can be seen in Fig. 5. The hexahedral blocks are wrapped around the wing-body junction in an O-type topology. The leading/trailing edge and wingtip regions are meshed with hexahedra, too. This enables independent resolution in chord- and spanwise dierection, but does not affect the considered junction region. The remaining surface parts are filled up with prisms. The same is applied to the horizontal tail plane.

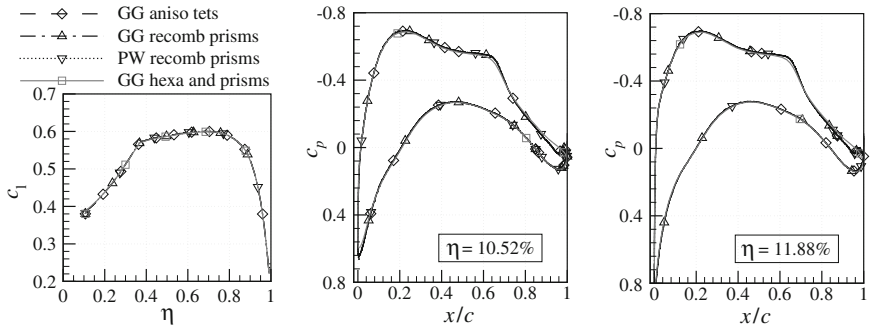

Fig. 6 Spanwise lift distribution on the different meshes (*left*) and streamwise pressure distribution at $\eta = 10.52\,\%$ (*middle*) and $11.88\,\%$ (*right*).

2.3 Numerics

The simulations are conducted using the unstructured finite volume code TAU (DLR) [11] in the versions 2011.2.0 and 2012.1.0. Central discretization scheme with artificial matrix dissipation is applied. Residual smoothing and a 3w+ multigrid cycle are used for convergence acceleration. To enable the usage of identical and low-dissipation parameters on all grids the one-equation turbulence model of Spalart and Allmaras [12] was applied due to its stability advantages over Reynolds stress models which also account for the turbulence anisotropy.

3 Results and Discussion

Despite the varying grid types the integral forces on all meshes agree very well. Differences in the spanwise c_l distribution (Fig. 6, left) are within one line width.

Remarkable differences of pressure distribution can be found in the area of the wing-body junction. While the results on the unstructured grid and the two derived hybrid grids yield the same c_p close to the corner in Fig. 6 (middle and right), the solution on the "GG hexa and prisms" grid shows slightly lower pressure close to the leading edge and a less pronounced separation at the trailing edge. The deviation in the area of the shock is due to an insufficient refinement of "GG hexa and prisms" on the wing upper surface. The wall normal velocity profiles of the boundary layer at $\eta = 10.52\,\%$ are plotted in Fig. 7 (upper row) for three streamwise positions. Due to the chopping of anisotropic or prismatic elements all grids except "GG hexa and prisms" show characteristic kinks in the velocity profiles at the border to the outer flow grid's isotropic tetrahedra at $20\,\%$ and $40\,\%$ chord length. "GG hexa and prisms" produces a smooth velocity profile and reaches the outer boundary layer edge velocity at a higher wall distance. At $98\,\%$ a much smaller separation is evident on the hexahedral cells. In the lower row of Fig. 7 there are only small differences

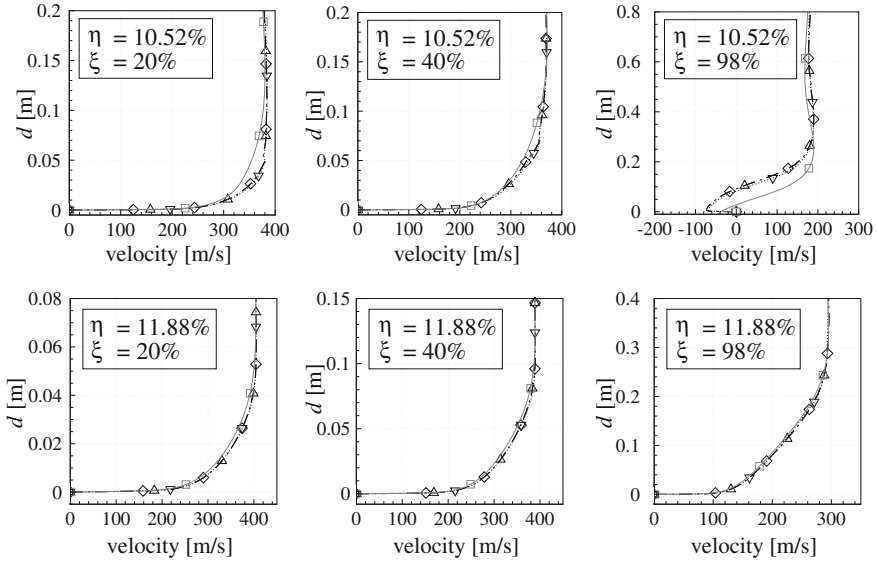

Fig. 7 Boundary layer velocity profiles at two spanwise and three streamwise positions. The same line legend applies as in Fig. 6

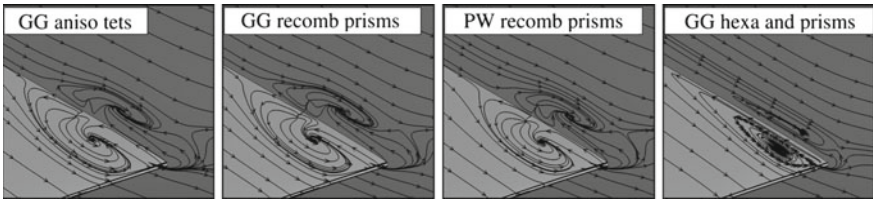

Fig. 8 Wall shear stress lines at the trailing edge of the wing-body junction

in the velocity profiles at $\eta = 11.88\,\%$, although small kinks on the first three meshes remain visible. No trailing edge separation is predicted at this spanwise location.

Looking closer at the corner separation at the trailing edge of the wing-body junction in Fig. 8 all grids based on the "GG aniso tets" grid predict the same shape and dimensions (6.5 % chord streamwise and 1.0 % half span spanwise). On the "GG hexa and prisms" grid the separation is longer (9.3 %), slightly narrower (0.8 %) and also lower as indicated by the flatter streamline swirl on the fuselage. The appearance of the corner separation is under discussion and already found in previous numerical simulations of the CRM (e.g. in [4]).

Also the pressure differences at the leading edge of "GG hexa and prisms" grid can be explained by the better boundary layer discretization using hexahedral cells. Figure 9 shows the differences in resulting flow topologies on "PW recomb prisms" and "GG hexa and prisms". On the prismatic mesh the streamlines just follow the

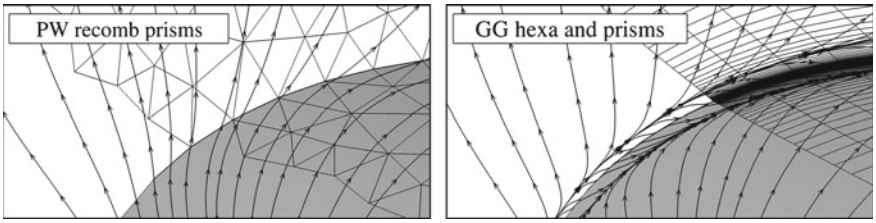

Fig. 9 Wall shear stress lines at the leading edge of the wing-body junction

induction of the developing horseshoe vortex and run from the wing over the corner to the fuselage surface. The higher resolution of the hexahedral grid in contrast can reproduce their separation close to the corner and reattachment at the fuselage. Thus a counter-rotating secondary vortex is formed in the wing-body junction. Even with refined surface triangles the prismatic volume mesh would still suffer from an even stronger reduction of the boundary layer grid height and the consequential kinks in the velocity profiles.

4 Conclusions

The all tetrahedral unstructured mesh—which is the way fastest to generate—yields results comparable to the usual prismatic hybrid grids in terms of integral forces, pressure distribution and boundary layer data including separation prediction. However all of these meshes show a strong effect on the boundary layer profile when the border of anisotropic or prismatic cells is shifted towards the surface inside the boundary layer. This is the case at the wing-body junction, where only the grid with hexahedral cells in the corner can resolve the complete boundary layer. This also results in another secondary flow topology very close to the corner and differences in the prediction of trailing edge separation.

References

1. Gand, F., Deck, S., Brunet, V., Sagaut, P.: Flow dynamics past a simplified wing body junction. Phys. Fluids **22**, 115111 (2010)
2. Klein, A., Illi, S., Nübler, K., Lutz, T., Krämer, E.: Wall Effects and Corner Separations for Subsonic and Transonic Flow Regimes. In: Kroener, D.B., Resch, M.M. (eds.) High Performance Computing in Science and Engineering '11, pp. 393–407. Springer, Berlin (2011)
3. Vassberg, J.C., DeHaan, M.A., Rivers, S.M., Wahls, R.A.: Development of a Common Research Model for Applied CFD Validation, Studies. AIAA-2008-6919 (2008)
4. Vassberg, J.C., Tinoco, E.N., Mani, M., Rider, B.: Summary of the Fourth AIAA CFD Drag Prediction Workshop. AIAA 2010–4547 (2010)
5. Rivers, M.B., Dittberner, A.: Experimental Investigations of the NASA Common Research Model in the NASA Langley National Transonic Facility and NASA Ames 11-Ft Transonic Wind Tunnel. AIAA 2011–1126 (2011)

6. Pointwise, Inc.: Gridgen Version 15. User Manual, Fort Worth (2012)
7. Aftonis, M., Gaitonde, D., Tavares, T.S.: Behaviour of linear reconstruction techniques on unstructured meshes. AIAA J. **33**(11), 2038–2049 (1995)
8. Pointwise, Inc.: Pointwise User Manual, Fort Worth (2012)
9. Doerffer, P., Szulc, O.: High-lift behaviour of half-models at flight reynolds numbers. Task Quart. **10**(2), 191–206 (2006)
10. Crippa, S.: Application of novel hybrid mesh generation methodologies for improved unstructured CFD simulations. AIAA 2010–4672 (2010)
11. Schwamborn, D., Gerhold, T., Heinrich, R.: The DLR TAU-code: recent applications in research and industry. In: ECCOMAS, Egmond a.Z., (2006)
12. Spalart, P.R., Allmaras, S.R.: A one-equation turbulence model for aerodynamic flows. AIAA-92-0439 (1992)

Numerical Approach Aspects for the Investigation of the Longitudinal Static Stability of a Transport Aircraft with Circulation Control

Dennis Keller

Abstract The aim of the investigation is to gain more certainty about the approach to evaluate the longitudinal stability and controllability of a high-lift configuration of a transport aircraft with circulation control. Since the work was carried out with a CFD RANS approach, a comprehensive meshing study was performed in advance.

1 Introduction

In compliance with the vision *Flightpath 2050*, the German research project *SFB 880* is investigating a STOL aircraft configuration, which possibly allows to reduce emissions and travel time by utilizing existing aerospace infrastructure more efficiently. In order to achieve short runway usage, an active high-lift system in terms of circulation control (CC) is employed. The potential of such systems is already well known (see [5, 8]) and is further assessed within the research project by M. Burnazzi [2]. However, the technology raises new questions, which are not adequately addressed so far. One of those is how CC will impact the handling qualities of a transport aircraft. For example, it is expected that the high flap loading and the low dynamic pressure during take off and landing will pose challenges to the flight control systems. This paper gives an aerodynamic view of the longitudinal static stability issue by investigating the flight mechanical properties of a circulation controlled wing itself, its influence on the HTP and eventually of the whole aircraft. Prior to the analysis, a meshing study was performed on a simplified 2D geometry in order to derive an efficient and accurate meshing strategy for the 3D configuration.

D. Keller (✉)
Institute of Aerodynamics and Flow Technology, German Aerospace Center,
38108 Braunschweig, Germany
e-mail: Dennis.Keller@dlr.de

A. Dillmann et al. (eds.), *New Results in Numerical and Experimental Fluid Mechanics IX*,
Notes on Numerical Fluid Mechanics and Multidisciplinary Design 124,
DOI: 10.1007/978-3-319-03158-3_2,

Table 1 Number of grid points

	Coarse	Medium	Fine
Structured	128454	524558	2119854
Hybrid_PW	–	284918	–
Hybrid	84856	181714	337342

2 Flow Solver

The calculations are performed with the *DLR TAU* code [6], which is based on an unstructured finite volume approach for solving the Reynolds-averaged Navier Stokes equations. For this investigation, the implicit LUSGS scheme is used for time stepping and a central scheme for the spatial discretization of the convective fluxes. The turbulence effects are modeled with the original Spalart-Allmaras formulation (SA) [12] with vortical and rotational flow correction based on the Spalart-Shur correction [13].

3 Test Configurations

3.1 2D Configuration

The 2D geometry represents a cut through the wing of the reference aircraft at the location of its mean aerodynamic chord. In order to investigate discretization influences especially near the active flow outlet, several cell size settings as well as different meshing methods were utilized (Table 1). Hybrid meshes were created with Pointwise [10] (Hybrid_PW) and Centaur [3] (Hybrid), whereas structured meshes were solely built with the former (Structured) (Fig. 1). The edge lengths along the surface were kept almost equal within the refinement levels. However, small adaptions had to be introduced on the Centaur meshes in order to achieve an optimal boundary layer discretization. Furthermore, in contrast to the structured meshes, the wall distances of the quad layers were kept constant on these meshes.

3.2 3D Configuration

At the beginning of the *SFB 880* research project, an aircraft with a capacity of 100 passengers was designed with the preliminary aircraft design tool *PrADO* [7]. The wing's span measures 28.8 m with an aspect ratio of 9 and a leading edge sweep of 10°. The HTP's span equals 10.4 m, resulting in a relative tail volume of 1.235. The underlying 3D geometry (Fig. 5) represents the landing configuration of this design,

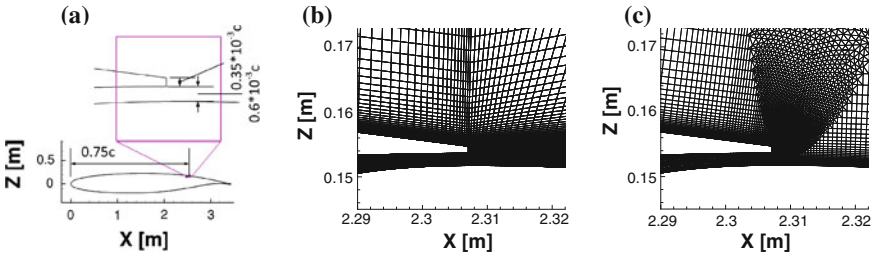

Fig. 1 Slot region. **a** Geometry. **b** Structured mesh. **c** Hybrid mesh

which has no leading edge device but a circulation controlled plain flap and aileron with 65° deflection and 45° droop, respectively. Hybrid meshes were built for the tail-off configuration and for the whole aircraft based on the experiences from the 2D investigations. The wing wake was refined with either tetrahedra or with a structured hexahedron box. A modular mesh approach was chosen in order to trim the aircraft with the smallest possible meshing influence.

4 Computational Results

4.1 Preliminary 2D Studies

Grid Convergence Study When working with complex geometries, semi automated hybrid mesh generators often seem to be the best choice as they offer a good compromise between work effort and quality of results. However, the quality may become unacceptable low when the automated mesh topology does not reflect the flow topology. Typical examples for this are free shear layers. With the investigation of wake interaction and CC in general, these types of flow phenomena are of particular importance. Therefore, the main purpose of the meshing study was to evaluate the feasibility of using a semi automated hybrid mesh generator for these kind of problems. Furthermore, a grid convergence study was carried out for both the structured as well as the hybrid mesh approach.

Figure 2 shows the influence of the grid resolution on the global coefficients for both mesh families. While the coefficients of the structured mesh show a clear trend, the hybrid meshes have a change in gradients at the medium size mesh. However, when considering the difference in grid sizes, the hybrid meshes deliver good results. Following G. de Vahl Davis [4] and applying the Richardson Extrapolation on the structured mesh family, the *exact* coefficients and the deviations of the medium sized meshes can be derived [11]. With far less than one per cent in deviation from the *exact* lift and moment coefficients, both medium size meshes show excellent results (Table 2). The comparably high difference in drag is probably coming from small

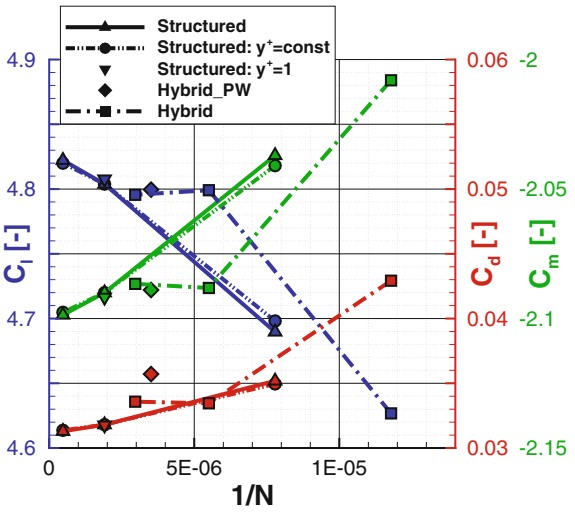

Fig. 2 Grid dependence of global coefficients

Table 2 Error estimates for global coefficients

	Coarse		Medium			Fine	
	Structured	Hybrid	Structured	Hybrid_PW	Hybrid	Structured	Hybrid
$\frac{c_l - c_{l,R.ex.}}{c_{l,R.ex.}}$ [%]	2.82	4.12	0.455	0.54	0.56	0.073	0.625
$\frac{c_d - c_{d,R.ex.}}{c_{d,R.ex.}}$ [%]	12.77	37.58	1.93	14.46	7.12	0.31	7.63
$\frac{c_m - c_{m,R.ex.}}{c_{m,R.ex.}}$ [%]	3.01	4.39	0.488	0.54	0.57	0.079	0.65

pressure differences on the flap, which have a large influence on the drag coefficient due to its order of magnitude.

The pressure distribution supports this assumption (Fig. 3). While showing only slight differences in most parts, the suction peak on the coanda surface indicates a bigger impact by the discretization level. It also reflects the change in gradients of the global coefficients of the hybrid mesh family, with the peak being stronger on the medium hybrid mesh than the one on the fine hybrid mesh.

The velocity profiles within the boundary layer show a fairly good agreement for the medium and fine meshes in all investigated cuts except at the slot exit (Fig. 4). Here, the velocity within the slot seems to be overestimated on all hybrid Centaur meshes. Furthermore, the velocity distributions on the coarse and the medium hybrid mesh show a peak towards the upper wing surface. Comparison to experimental investigations of circulation controlled airfoils [1, 9] lead to the assumption, that these peaks are unphysical and arise due to the O-type topology at the wing trailing edge. In contrast, the velocity profiles on all structured meshes show a homogeneous distribution. However, the higher velocities at the slot exit on the hybrid meshes do not seem to have a big influence on the general flow topology, since this difference cannot be detected in the velocity distributions further downstream anymore.

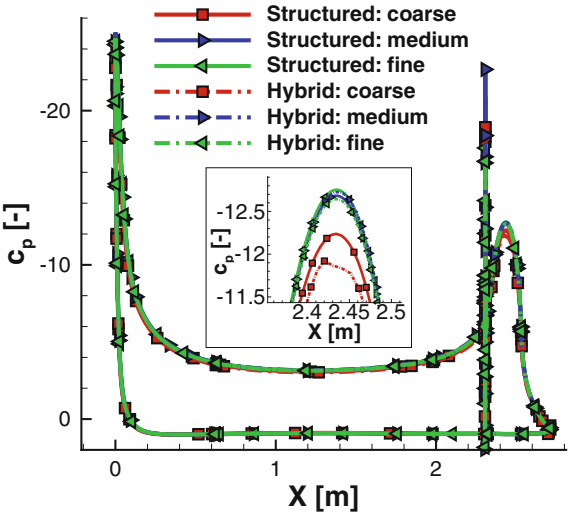

Fig. 3 Pressure distribution

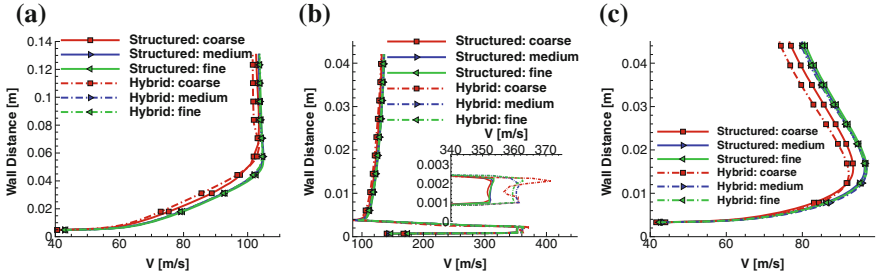

Fig. 4 Velocity profiles in boundary layer along the upper surface. **a** x/c = 0.45. **b** x/c = 0.75. **c** x/c = 0.84

4.2 3D Configuration

Wake Meshing Influence For the investigation of the longitudinal handling qualities, the HTP's efficiency is of particular importance. It is driven by downwash effects and altered dynamic pressure due to the wake of the main wing. The former is visualized for a cutting plane through the basic mesh at the leading edge of the HTP's mean aerodynamic chord (Fig. 5) in Fig. 6. The velocity vectors confirm the existence of an inboard flap vortex and a wing tip vortex. Between these vortices, the vertical velocity reaches about 30 % of the free stream velocity. When enhancing the wake resolution by halving the edge length of the tetrahedra, the contour of the vortices sharpens. Besides the increased strength of the vortical flow around the vortex cores, the delta plot of the local angle of attack also reveals two merging vortex cores in the outboard region instead of one (Fig. 7a).

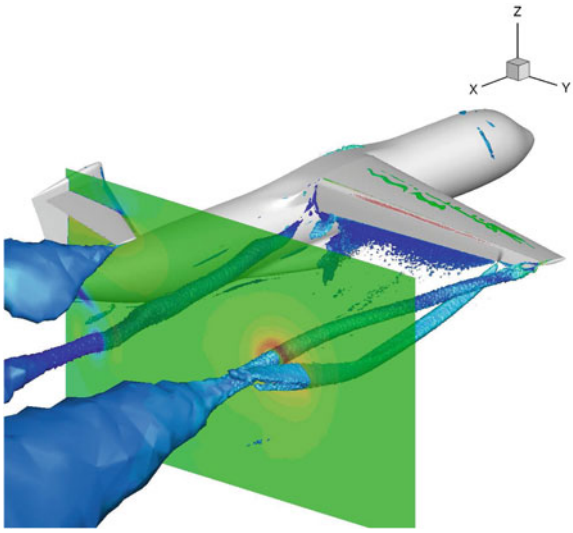

Fig. 5 Vortex visualization and position of cutting plane on the tetrahedral refined mesh

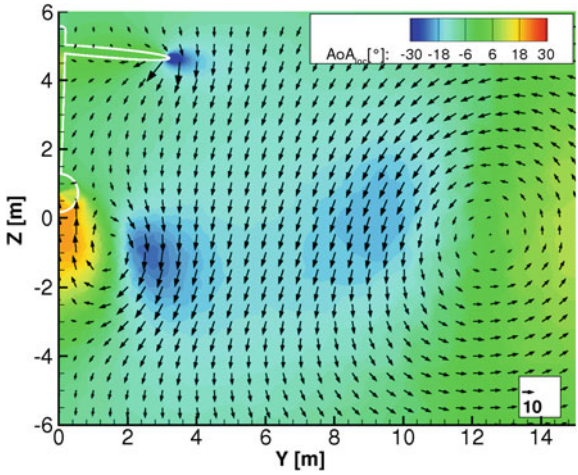

Fig. 6 Flow characteristics on basic mesh in x-plane at x = 29.4 m

Regarding the outboard vortex system, the trend is even more visible on the mesh with hexahedral wake refinement (Fig. 7b). However, the plot shows a rather clustered picture of the inboard flap vortex, which leads to the assumption that the transition between structured and unstructured elements behind the origin of the inboard flap vortex is negatively affecting the vortex resolution.

Downwash Investigation When employing CC on a flap, one can distinguish between two different operating modes. For comparably low blowing coefficients, the flow on the flaps is not completely attached and the energization regulates the amount of separation. This utilization is called boundary layer control and is the

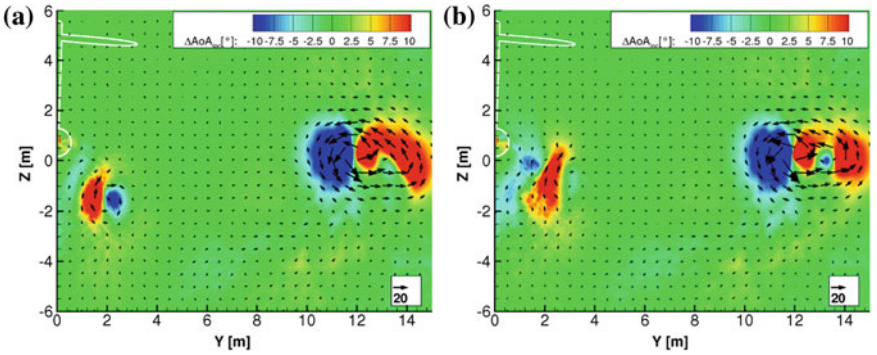

Fig. 7 Delta of local angle of attack in x-plane at x = 29.4 m. **a** Difference plot between tetrahedral refinement and basic mesh. **b** Difference plot between hexahedral refinement and basic mesh

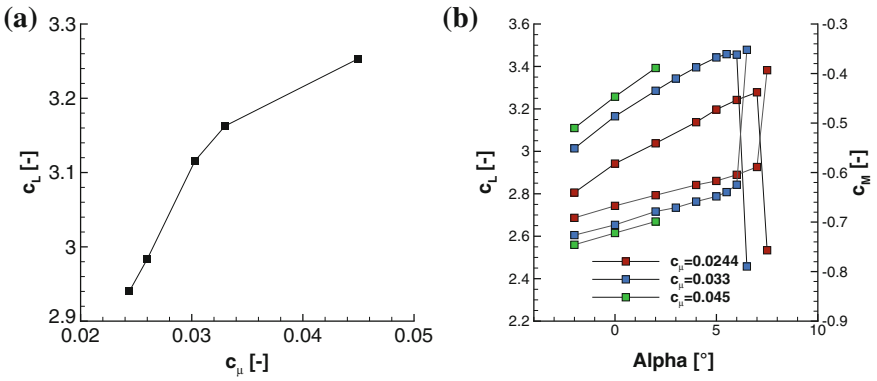

Fig. 8 Lift coefficients of wing-body configuration. **a** Lift coefficients at $\alpha = 0°$ for differenct blowing coefficients c_μ. **b** Lift and pitching moment at the aerodynamics center over α

most effective way to use CC. After reaching fully attached flaps, additional blowing leads to so-called super-circulation, which is less effective. For landing cases, the threshold between these two utilization ranges is interesting, as it gives the maximum lift at good effectiveness. The investigation was conducted at three global blowing coefficients which reflect these characteristics (Fig. 8). These coefficients result from an optimized pressure setting in each of six different plena along the span (Fig. 10b). Figure 9a shows the downwash along the position of the quarter chord line of the HTP for the chosen blowing settings at $\alpha = 0°$. As expected, the downwash increases with increasing blowing coefficient. Furthermore, the local angle of attack dips in spanwise direction. The slightly different gradient at the lowest blowing ratio is due to an altered wing loading. Figure 9b compares the change of downwash due to a change in lift caused by an altered angle of attack on the one hand and a modified blowing coefficient on the other. It shows that the values of the gradients are lower and constant for lift increases due to changed blowing. The gradients for constant

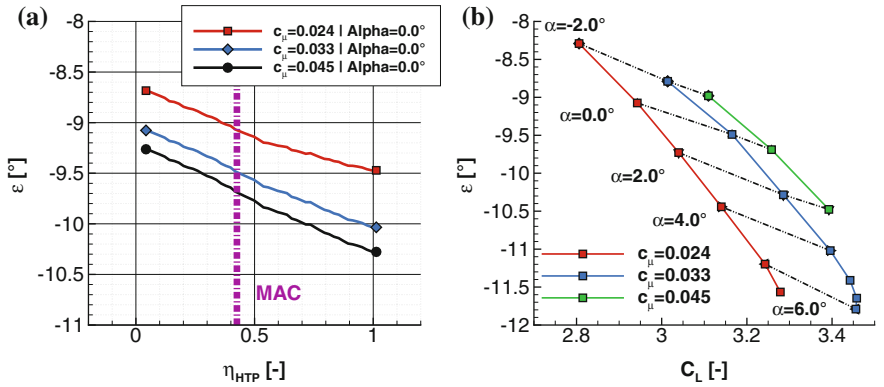

Fig. 9 Downwash at the horizontal tail plane position. **a** Downwash at $\alpha = 0°$ along HTP span. **b** Change of downwash due to change in lift coefficient

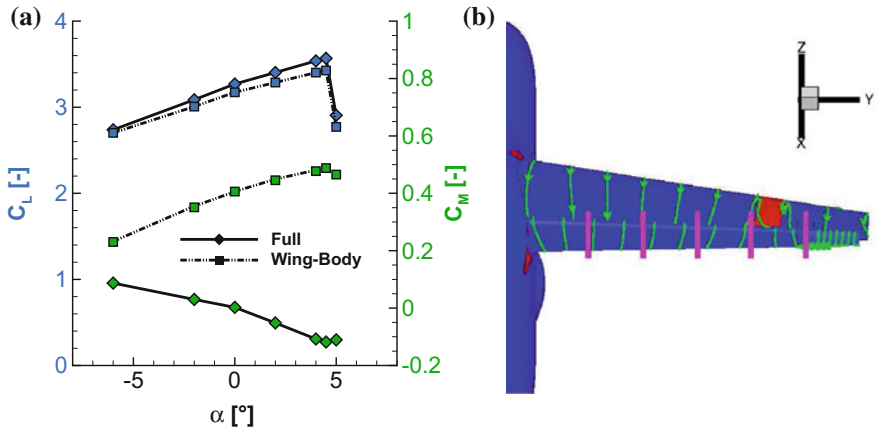

Fig. 10 Aerodynamic characteristics of trimmed landing configuration. **a** Global coefficients over angle of attack α for $i_{\mathrm{HTP}} = 16.13°$. **b** Separation behavior and plena positions

blowing get slightly steeper towards higher angle of attacks due to the reduced distance between the main wing wake and the HTP position. The break down near $\alpha_{\max}$ is associated with a shift in the main wing loading and a resulting change in downwash distribution.

Static Stability Investigation The preliminary aircraft design led to a maximum rearward position of the center of gravity, which has to be confirmed. The CFD simulations of the landing configuration show the aerodynamical feasibility, even though the maximum trim angle of the horizontal stabilizer from the preliminary design is exceeded by around 8°. Figure 10a shows that with a trim angle of $i_{\mathrm{HTP}} = 16.13°$ the configuration is still controllable at an angle of attack of $\alpha = 0.0°$. Below $\alpha_{\max}$ it is also stable while satisfying the stability reserve requirement with

$\Delta x_{S25}/l_\mu \approx -0.15$. However, there is a high risk, that the configuration is not stable during stall due to its outboard stall mechanism (Fig. 10b) and the resulting additional downwash at the HTP. In this context it is worth mentioning that the wing itself has a nose down tendency after α_{max}.

5 Summary

The preliminary 2D studies justify the meshing approach, especially the usage of hybrid meshes, for the 3D calculations. Even though embedding a structured hex box into an unstructured mesh region most likely leads to a more efficient way to resolve wake characteristics, the interface regions between these two cell types can lead to higher discretization errors resulting in unexpected vortex distortions. The high lift values obtained by circulation controlled configurations lead to a strong downwash behind the main wing, which is dependant not only on the lift coefficient itself but also on the way the lift is created. Even though the CFD results confirm the feasibility of the most rearward position of the center of gravity from the preliminary design, the necessary HTP trim angles are exceptionally high due to the downwash. Furthermore the results of the post stall simulation, which have to be treated with caution, lead to the assumption that the wing design and its associated stall mechanism are unfavorable regarding the longitudinal handling qualities and result in unstable flight conditions.

References

1. Allan, B.G., Jones, G.S., Lin, J.C.: Reynolds-averaged navier-stokes simulation of a 2D circulation control wind tunnel experiment. AIAA Paper 2011-25 (2011)
2. Burnazzi, M., Radespiel, R., Keller, D.: Numerical simulation of a 3D aircraft model equipped with active Coanda high-lift devices. 18. DGLR-Fach-Symposium der STAB, Stuttgart, Germany (2012).
3. CentaurSoft: http://www.centaursoft.com (2012). Accessed on June 2012
4. de Vahl Davis, G.: Natural convection of air in a square cavity: a benchmark numerical solution. Int. J. Numer. Meth. Fluids. **3**(3), 249–264 (1983)
5. Englar, R.J., Blaylock, G.M., Gaeta, R.J.: Recent experimental development of circulation control airfoils and pneumatic powered-lift systems. AIAA Paper 2010–345 (2010)
6. Gerhold, T.: Overview of the Hybrid RANS Code TAU. Notes on Numerical Fluid Mechanics and Multidisciplinary Design, vol. 89, pp. 81–92 (2005)
7. Heinze, W.; Österheld, C.M., Horst, P.: Multidisziplinäres Flugzeugentwurfsverfahren PrADO - Programmentwurf und Anwendung im Rahmen von Flugzeug-Konzeptstudien. Vortrag DGLR-2001-194, DLR-Jahrestagung 2001 in Hamburg, erschienen im DGLR-Jahrbuch 2001, Band 3, S.1701-1712, DGLR, Bonn (2001)
8. Korbacher, G.K.: Aerodynamics of powered high-lift systems. Annu. Rev. Fluid Mech. **6**, 319–358 (1974)
9. Pfingsten, K.-C., Jensch, C., Körber, K.W., Radespiel, R.: Numerical Simulation of the Flow around Circulation Control Airfoils. First CEAS European Air and Space Conference, Berlin, Germany (2007)

10. Pointwise: http://www.pointwise.com (2012). Accessed on June 2012
11. Roache, P.J.: Quantification of uncertainty in computational fluid dynamics. Annu. Rev. Fluid Mech. **29**, 123–160 (1997)
12. Spalart, P.R., Allmaras, S.R.: A one-equation turbulence model for aerodynamic-flows. AIAA Paper 92–0439 (1992)
13. Spalart, P.R., Shur, M.: On the sensitization of turbulence models to rotation and curvature. Aerosp. Sci. Technol. **1**(5), 297–302 (1997)

Numerical Investigation of the Influence of Shock Control Bumps on the Buffet Characteristics of a Transonic Airfoil

Steffen Bogdanski, Klemens Nübler, Thorsten Lutz and Ewald Krämer

Abstract This article presents a numerical investigation on the influence of three-dimensional shock control bumps (SCB) on the effect of transonic buffet. Three different types of SCBs are generated by an optimization for low drag in steady flow conditions at a medium lift coefficient. The impact of these SCB types is then investigated for two different Mach numbers with steady and unsteady RANS methods. It will be shown that all SCBs worsen buffet in terms of buffet onset and buffet amplitudes and shift the shock upstream. The impact is largely independent of the Mach number. Vortex strength and amount of separation in steady conditions are only poor indicators for the buffet inhibition potential of the bumps.

1 Introduction

Two and three-dimensional shock control bumps (SCBs) have been investigated and optimized for numerous years at IAG. These SCBs expand the compression shock to a lambda-shock and reduce wave drag [1]. The main focus of the recent work has been on a robust bump design, i.e. a performance gain over a large range of lift coefficients, without performance deterioration in the design point of the baseline airfoil.

There are only few attempts to use SCBs to reduce the shock motion in transonic buffet [2]. All these attempts used steady computations for the design and evaluation of these "buffet bumps" and the criterion for the determination of the buffet onset has been the extend and shape of the separated flow rather than the unsteady behaviour [3].

It is the aim of this investigation to utilize steady and unsteady RANS methods to evaluate the impact of SCBs which are optimized for drag reduction on the buffet characteristics of a transonic airfoil. The investigation is conducted for two different Mach numbers: the design Mach number of the bumps and a smaller Mach number

S. Bogdanski (✉) · K. Nübler · T. Lutz · E. Krämer
Institute of Aerodynamics and Gas Dynamics, University of Stuttgart, 70569 Stuttgart, Germany
e-mail: bogdanski@iag.uni-stuttgart.de; http://www.iag.uni-stuttgart.de

A. Dillmann et al. (eds.), *New Results in Numerical and Experimental Fluid Mechanics IX*,
Notes on Numerical Fluid Mechanics and Multidisciplinary Design 124,
DOI: 10.1007/978-3-319-03158-3_3,

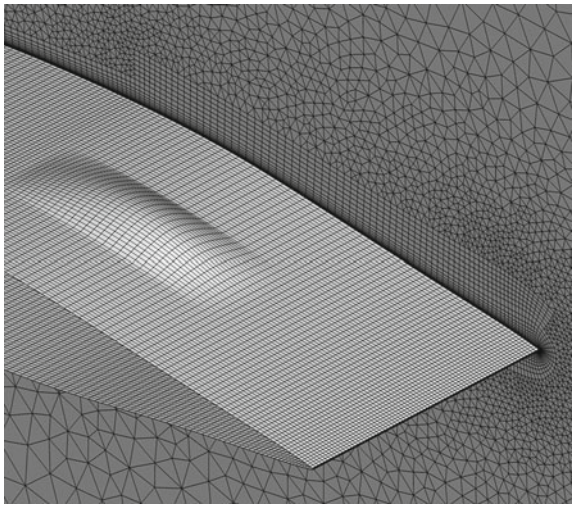

Fig. 1 Surface grid and periodic boundary, coarse mesh

where the bumps are effective at a higher angle of attack, closer to the buffet onset. It can be supposed that bump design conditions closer to the buffet onset boundary will have a positive effect on the buffet characteristics.

2 Numerical Methods

The simulations presented in this chapter have been conducted with the unstructured CFD code "TAU" developed by the German Aerospace center (DLR) [4]. The code solves the Euler-, Navier-Stokes- or RANS-equations on grids with unstructured cells. It can be used for steady computations with various acceleration techniques as well as for unsteady computations with a second order dual time-stepping scheme. Several one-equation, two-equation and Reynolds stress turbulence models are implemented. All simulations in this chapter have been carried out with the "Menter SST" model with the "scale-adaptive simulation" modification (SST-SAS) [5].

The time step δt was chosen to $\frac{1}{40}\frac{c}{u_{inf}}$, with c as the chord length and u_{inf} as the free stream velocity. This leads to approximately 500 time steps per buffet period and has been proven to guarantee a time step independent solution [6]. Every fifth time step, a solution is preserved and used for post processing.

An implicit backward euler scheme has been used for the inner iterations with multi grid and residual smoothing. The flux discretization was realized with the second order Jameson, Schmidt, Turkel scheme.

For post processing purposes a python tool was written which extracts slices of the unsteady surface solution. The data of each slice and time step is then processed separately and values like lift, drag, shock position and extent of the separated area are

Table 1 Properties of the three grid levels (*Panel A*) and SCB positions x/c (*Panel B*)

Panel A: three grid levels			
	Fine	Medium	Coarse
Grid points	$4 \cdot 10^6$	$2 \cdot 10^6$	$1 \cdot 10^6$
Spanwise	121	96	76
Circumference	452	360	284
No. hexahedral layers	50	40	31
Extra prisms	10	8	6
Panel B: SCB positions			
	HSCB	Wedge	Extended
Begin	0.47	0.50	0.47
Crest	0.63	0.63	0.60
End	0.77	0.80	1.00

determined. These values are then integrated and time averaged. All post processing has been done with 25 slices equally spaced in spanwise direction and the tool has been verified against the results of the TAU solver.

2.1 Grids

Hybrid grids with structured hexahedral blocks for the boundary layer treatment and unstructured tetrahedral blocks for the treatment of the inviscid regions have been created with the commercially available software "Gridgen". An additional structured block was created over the rear part of the airfoil to account for the thickened/separated boundary layer behind the shock. All grids have a spanwise extent of 0.3 c and use periodic boundary conditions since these impose the least amount of artificial constraints on the flow solution Fig. 1.

Three different grid levels have been created to investigate the grid dependancy of the solutions. The cell size was scaled with $\sqrt[3]{2}$ so as the overall amount of points doubles with each level. Table 1 (Panel A) shows the properties of each grid level and Fig. 1 shows the surface grid and one periodic boundary of the coarsest grid. The computations with the baseline airfoil have been carried out with both 2D and 3D grids, yet only minor differences occur in the solutions.

3 Results

3.1 Baseline Airfoil

The baseline airfoil originates from the Pathfinder transonic laminar wing [7] and has a thickness of 12.2 %. The airfoil has been investigated for the two Mach numbers

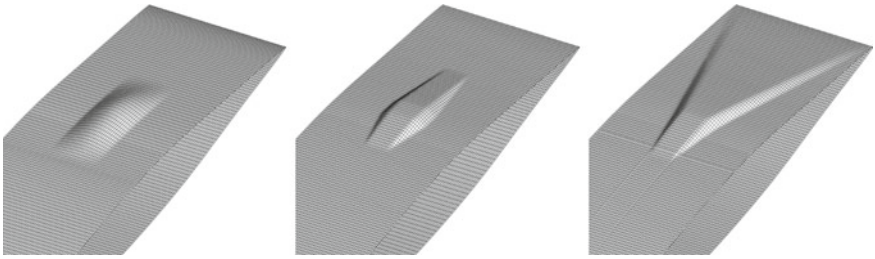

Fig. 2 Shape of the three bumps: HSCB, wedge and extended

$Ma = 0.74$ and $Ma = 0.76$ at a constant Reynolds number of $Re = 20 \cdot 10^6$. The transition was fixed at 10 % of the chord length by limiting the production of turbulence in the laminar region. This leads to a boundary layer thickness near the shock comparable to that of wind tunnel test conducted in Cambridge. Steady solutions exist for all angles of attack with $\alpha \leq 4°$ for $Ma = 0.76$ and $\alpha \leq 3°$ for $Ma = 0.76$. Above these values transonic buffet occurs, with higher Mach number showing the smaller amplitudes.

With increasing angle of attack and shock strength the baseline airfoil develops a separation bubble at the location of the shock which is growing in streamwise direction. Once it reaches the trailing edge buffet occurs. This behaviour corresponds to "model A" according to the buffet classification of Pearcey [8].

3.2 Grid Dependency

The grid dependency has been investigated for all geometries at the higher Mach number of $Ma = 0.76$. Though the differences between the different levels are small for conditions with attached flow, large differences occurred in the buffet regime. In general the finer grids reduced the buffet amplitudes but shifted the buffet onset to smaller angles of attack. The largest differences for the lift amplitudes of about a factor of 4 occurred between the coarse and medium gird, it is therefore mandatory that fine grids are used for reliable results.

3.3 Bump Generation

Three different bumps have been created for the Pathfinder airfoil: a smooth—hill shaped—one (HSCB), a wedge shaped one and an extended bump (see Fig. 2). An lift coefficient of $c_l = 0.417$ and a Mach number of $Ma = 0.76$ has been chosen as design point for all bumps.

The bumps have been optimized with a downhill simplex algorithm for minimal drag by variation of the two parameters height and position. The length of the smooth

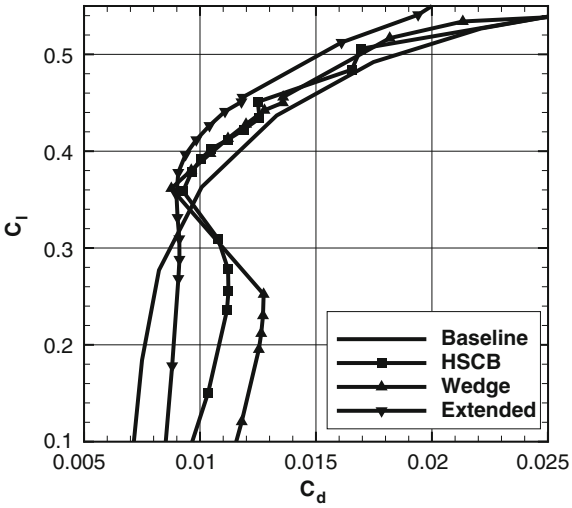

Fig. 3 Drag polar for the three bumps, $Ma = 0.76$

and the wedge bump have been fixed at $l = 0.3\,\mathrm{c}$, whereas the extended bump varies in length and reaches the trailing edge for all designs. The spanwise extent of the wedge, the smooth and the front ramp of the extended bump have been fixed at $0.1\,\mathrm{c}$. When the performance of the three bumps is compared (see Fig. 3) it is evident, that the extended bumps shows the best performance at the design point. At off design conditions at lower lift coefficients the extended bump is superior to the two other bumps, too.

3.4 Impact of SCBs on Buffet at Ma = 0.76

Buffet Onset and Shock Motion All SCBs lower the buffet onset by an angle of attack of about 0.5° (see Fig. 4 left) and show larger buffet amplitudes inside the buffet regime than the baseline airfoil. However, it is not possible to determine the bump with the best/worst buffet behaviour since the buffet amplitudes vary with angle of attack.

The smooth and the extended bump shift the shock upstream, whereas the wedge bump shifts the shock downstream with regard to the baseline airfoil. During the buffet cycle the (spanwise averaged) shock positions stay above the front flank of the bumps, i.e. the bumps should influence the shock even in the buffet regime (compare Fig. 4 right with Table 1 Panel B).

Separation The HSCB and the wedge bump exhibit separated flow below the design point in contrast to the extended bump as shown in Fig. 5. This seems to be the reason for the better performance of the extended bump at lower lift coefficients. At design conditions almost no separation is apparent for all bumps. The amount of

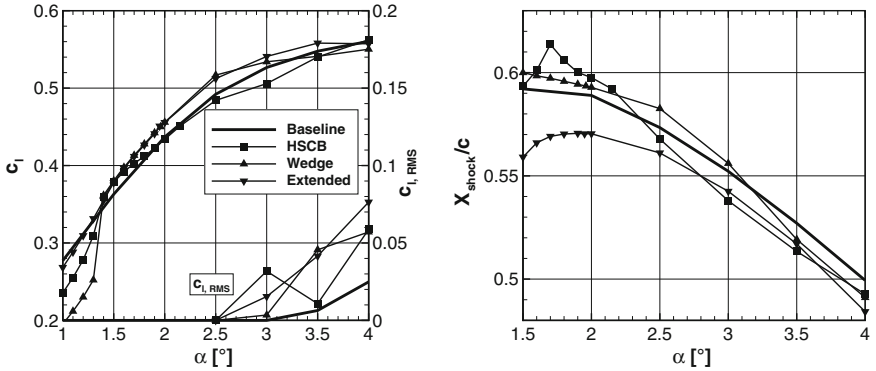

Fig. 4 Lift polar (*left*) and spanwise and temporally averaged shock position (*right*) for the three SCBs, $Ma = 0.76$

Fig. 5 Separated area over angle of attack for the three SCBs, $Ma = 0.76$

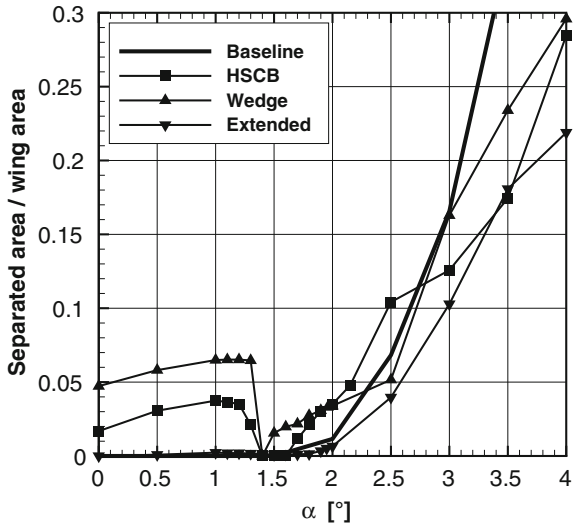

separation grows with increasing angle of attack for all bumps but it's not directly correlated with the amount of lift variation. Hence, the amount of separated flow at or above design conditions is not a good indication for determining buffet inhibition capabilities.

Vortex generation Figure 6 shows the vortex generation and the surface streamlines for the three bumps at design conditions. The slices show the x-component of the rotation $curl(v)$. At the end of the rear flank the wedge bump shows the largest values and thus creates the strongest vortices of all bumps. This is due to the separation at the rear flank and causes the vortices of the wedge bump to rotate in the opposite direction than the vortices on the other bumps. The HSCB and the extended bump

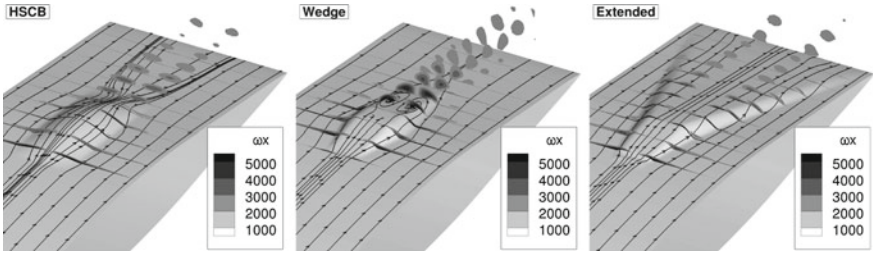

Fig. 6 Vortex generation for the three SCBs, $Ma = 0.76$, $\alpha = 1.5°$

have similar peak values at this position, though the vortices of the extended bump are considerably flatter than those of the HSCB.

Since the SCBs show a similar buffet behaviour in terms of buffet onset and amplitudes it can be concluded, that the peak vorticity of the streamwise vortices is not correlated with the ability of the bump to inhibit buffet.

3.5 Impact of SCBs on Buffet at Ma = 0.74

When the freestream Mach number is lowered the shock moves upstream and likewise SCBs optimized for performance have to move in the same direction. The aforementioned bumps, optimized for the higher Mach number, are thus located too far downstream for good performance at medium lift coefficients. Their operating area is shifted towards higher lift coefficients, where the shock moves downstream to its original location. RANS computations showed that the new operation area is at a lift coefficient of $c_l \approx 0.6$. It can be presumed that bumps, which are effective in the vicinity of the buffet boundary, are more likely to enhance the buffet boundary. Since the wedge bump exhibited the worst off-design performance only the smooth and the extended bump are investigated at the lower Mach number.

Buffet onset and shock motion Figure 7 (left) shows that the smooth as well as the extended bump both deteriorate the buffet behaviour for the lower Mach number. The angle of attack for buffet onset is lowered about $\alpha = 0.5°$ and the lift variations are considerably higher than those of the baseline airfoil. At least the maximum lift coefficient of the HSCB is slightly higher than that of the baseline airfoil, yet this point is already inside the buffet regime.

Figure 7 (right) shows the spanwise averaged shock positions. It can be seen that the shock is more upstream with regard to the bumps than for the higher Mach number. Thus a greater part of the bumps is located in the area with separated flow behind the shock and obviously less effective.

Separation At the lower Mach number separation starts before buffet onset (Fig. 8). The two bumps show a very similar development with the HSCB exhibiting approx.

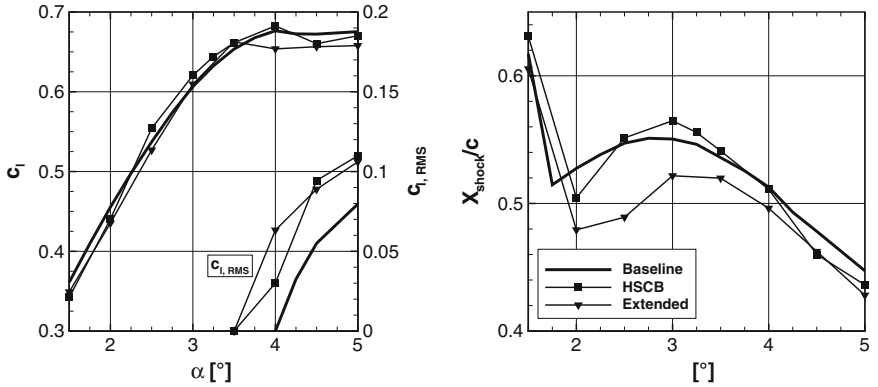

Fig. 7 Lift polar (*left*) and spanwise and temporally averaged shock postion (*right*) at $Ma = 0.74$

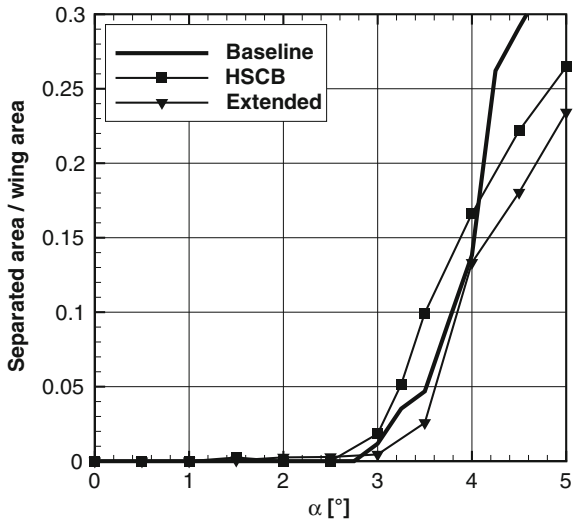

Fig. 8 Separated area over angle of attack at $Ma = 0.74$

5 % larger values, which is almost constant for higher angles of attack. Yet, inside the buffet regime the HSCB shows more separation than the baseline airfoil and the extended bump shows less than the baseline airfoil but both exhibit a similar buffet behaviour. For lower angles of attack almost no separation is visible for all configurations.

Vortex generation The vortices pictured in Fig. 9 are created at an angle of attack of $\alpha = 3.5°$, which yields the last steady solution for both bumps. The HSCB generates a pair of considerably larger vortices than the Extended bump, though both exhibit almost the same buffet characteristics. When the surface streamlines of the HSCB are regarded first signs of asymmetry can be seen.

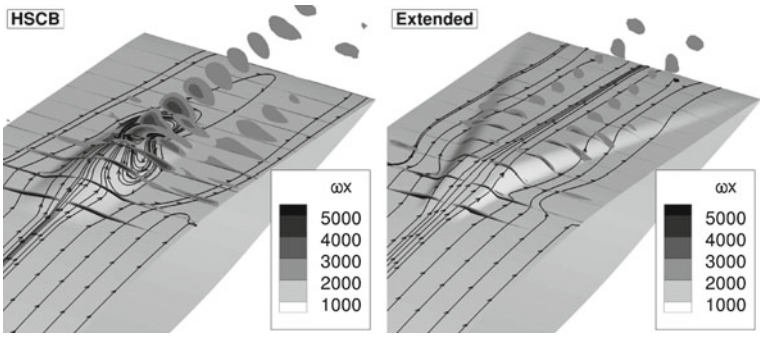

Fig. 9 Vortex generation for the three SCBs, $Ma = 0.74$, $\alpha = 3.5°$

4 Conclusions

The buffet characteristics of three bumps have been investigated with URANS methods in the transonic flow regime. It has been shown, that fine grids are mandatory to keep the grid influence small. At the design Mach number all bumps deteriorate the buffet behaviour: they lower the angle of attack for buffet onset and lead to higher buffet amplitudes inside the buffet regime. The amount of separated flow and the vortex strength at steady conditions give only limited evidence of the buffet inhibition potential of a bump. The assumption, that a lower Mach number will be beneficial for the buffet characteristics of the bumps has been proven wrong. This behaviour is due to the fact that the bumps shift the shock upstream and thus lie in the area of separated flow behind the oscillating shock.

Notes and Comments.

The research leading to these results has received funding from the European Union's Seventh Framework Programme (FP7/2007-2013) for the Clean Sky Joint Technology Initiative under grant agreement no. 271843.

References

1. Pätzold, M.: Auslegungsstudien zu 3D Shock-Control-Bumps mittels numerischer Optimierung. University of Stuttgart, Dissertation (2008)
2. Corre, C., et al.: Transonic flow control using a NS-solver and a multi-objective genetic algorithm. Mech. Appl. **73**, 297–302 (2003)
3. Eastwood, J., Jarett, J.: Towards designing with 3-D bumps for Wing Drag reduction. AIAA 2011–1168 (2011)
4. Gerhold, T.: Overview of the Hybrid RANS Code TAU. In: Kroll, N., Fassbender, J.K. (eds.) Notes on Numerical Fluid Mechanics and Multidisciplinary Design, Vol. 89, pp. 81–92. Springer, Heidelberg (2005)
5. Menter, F., Egorov, Y.: A scale-adaptive simulation model using two-equation models. AIAA 2005–1095 (2005)

6. Soda, A.: Numerical Investigation of Unsteady transonic Shock/boundary-Layer Interaction for Aeronautical Applications. Dissertation, RWTH Aachen (2006)
7. Streit, T., Horstmann, K.-H., Schrauf, G., Hein, S., Fey, U., Egami, Y., Perraud, J., El Din, I., Cella, U., Quest, J.: Complementary numerical and experimental data analysis of the ETW Telfona Pathfinder wing transition tests. 49th AIAA Aerospace Sciences Meeting, Orlando, AIAA Paper 2011–881 (2011)
8. Pearcey, H., Osborne, J.: The Interaction between Local Effects at the Shock and Rear Separation a Source of Significant Scale Effects in Wind-Tunnel Tests on Airfoils and Wings. AGARD, CP35 (1968)

Numerical Investigation of the Flutter Behaviour of a Laminar Supercritical Airfoil

A. C. L. M. van Rooij and W. Wegner

Abstract Nowadays laminar airfoils are considered in aircraft design in order to achieve laminar flow, thereby reducing the drag. Laminar flow should however not lead to a performance reduction of the aircraft. One of the constraints of the flight envelope is the flutter boundary. The influence of (partly) laminar flow on this boundary is however still unclear. Therefore numerical simulations have been performed. These show that the flutter behaviour of a laminar supercritical airfoil is more critical at transonic conditions in case of (partly) laminar flow.

1 Introduction

Today laminar flow has regained new interest, because of the drag reduction. Laminar flow may, however, not degrade the performance of aircraft. Flutter is one of the most important constraints of the flight envelope of an aircraft. The flutter boundary should never be surpassed in flight. Laminar flow might significantly influence the aerodynamic forces and moments. Therefore, it is important to consider this type of flow when determining the flutter behaviour. Especially in the transonic flow regime where the flutter boundary exhibits a minimum, the so-called transonic dip.

Numerous flutter behaviour studies have been performed (e.g. [1–4]). However, these have only considered fully turbulent flow or inviscid flow. Although no experimental results are available for validation of transitional flow at transonic flow conditions, a first step was taken to investigate the effect of boundary layer

A. C. L. M. van Rooij (✉) · W. Wegner
German Aerospace Center, Institute of Aeroelasticity, Göttingen, Germany
e-mail: Anouk.vanRooij@dlr.de

W. Wegner
e-mail: Wolfgang.Wegner@dlr.de

A. C. L. M. van Rooij
Delft University of Technology, Delft, Netherlands

A. Dillmann et al. (eds.), *New Results in Numerical and Experimental Fluid Mechanics IX*,
Notes on Numerical Fluid Mechanics and Multidisciplinary Design 124,
DOI: 10.1007/978-3-319-03158-3_4, © Springer International Publishing Switzerland 2014

transition on the flutter behaviour of a two-dimensional laminar supercritical airfoil, the CAST-10 airfoil [5].

Steady and unsteady CFD simulations with a fully turbulent boundary layer as well as with free boundary layer transition have been performed with the DLR TAU code [6] as well as with ANSYS CFX [7]. The resulting aerodynamic loads, were then used to compute the flutter behaviour via the k-method.

In this paper the numerical models used are presented first. Then the numerical set-up is discussed. After which the results of the steady, quasi-steady and unsteady flow simulations are depicted and described. Finally, the flutter behaviour of the CAST-10 airfoil is shown and discussed.

2 Numerical Models

To determine the flutter behaviour the aerodynamic loads are needed. These were computed using Computational Fluid Dynamics (CFD).

2.1 Computational Fluid Dynamics

In both TAU and CFX the Reynolds-Averaged Navier-Stokes equations are solved using the Menter SST turbulence model [8]. The prediction of boundary layer transition is performed by two different methods; the e^N-method [9, 10] in TAU and the γ-Re_θ transition model [11] in CFX. Both CFD codes are vertex-based finite-volume solvers. For the unsteady flow computations Jameson's dual-time stepping [12] is used. The 2nd order BDF scheme is used to integrate in physical time. For spatial discretisation 2nd order flux-upwinding is used in TAU, where the upwind fluxes are determined by AUSMDV [13]. CFX uses a so-called high resolution scheme (2nd order scheme) [7]. In both CFD codes the transport equations of the turbulence model (and transition model in CFX) are also solved with 2nd order accuracy.

2.2 Flutter Boundary Determination

In order to determine the flutter boundary of an airfoil, the equations of motion of the airfoil need to be solved. The airfoil has two coupled degrees of freedom (pitch α and plunge h). Figure 1 shows the structural model used.

The airfoil is elastically mounted at the quarter chord point. K_h is the stiffness of the vertical spring and K_α that of the torsional spring. The distance between the center of gravity and the elastic axis is $x_\alpha = S_\alpha / m$ in Fig. 1, where S_α is the static mass moment.The equations of motion of this system are [14]:

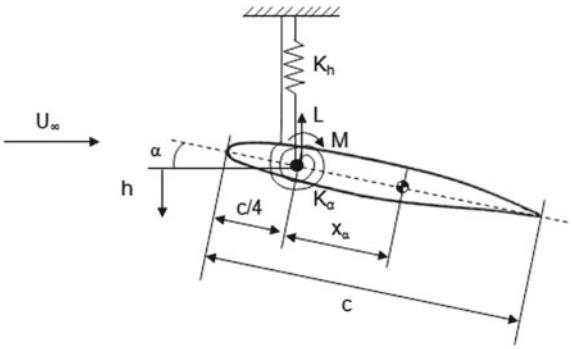

Fig. 1 Sketch of the model with two degrees of freedom

$$\begin{bmatrix} m & S_\alpha \\ S_\alpha & I_\alpha \end{bmatrix} \begin{bmatrix} \ddot{h} \\ \ddot{\alpha} \end{bmatrix} + \left(\begin{bmatrix} K_h & 0 \\ 0 & K_\alpha \end{bmatrix} - qS \begin{bmatrix} -c_{l_h} & -c_{l_\alpha} \\ c_{m_{y_h}} c & c_{m_{y_\alpha}} c \end{bmatrix} \right) \begin{bmatrix} h \\ \alpha \end{bmatrix} = \mathbf{0},$$

where m is the mass, I_α the mass moment of Inertia, q the dynamic pressure, S the surface area and c the chord length. A harmonic solution of the form: $[h(t), \alpha(t)]^T = [\hat{h}, \hat{\alpha}]^T e^{i\omega t}$ is assumed and the aerodynamic derivatives (c_{l_h}, c_{l_α}, $c_{m_{y_h}}$ and $c_{m_{y_\alpha}}$) are computed in the time domain using forced pitch and plunge motions and then transferred to the frequency domain. After which the k-method [14] is used iteratively to solve the resulting eigenvalue problem (k is the reduced frequency, made non-dimensional by c and the velocity U_∞). The so-called non-dimensional flutter index $Fi = 2v_\infty / \left(\sqrt{\mu} c \omega_\alpha\right)$ is often used in the flutter diagram. Here μ the mass ratio $\left(\mu = m / \left(0.25\pi \rho_\infty c^2\right)\right)$ and ω_α is the uncoupled natural torsional frequency ($\omega_\alpha = \sqrt{K_\alpha / I_\alpha}$).

3 Numerical Set-up

The airfoil used for this investigation is the CAST-10 airfoil ($c = 0.3$ m). The CFD simulations were performed on a hybrid mesh with 110194 nodes. For the unsteady flow simulations the timestep size Δt was $2.5 \cdot 10^{-4}$ s. A previous grid- and timestep study showed that the CFD results are grid- and timestep-independent [15]. This study addressed both fully turbulent as well as transitional flow for the TAU code. For CFX no mesh-independency study was performed. The Reynolds number for the flow simulations was $2 \cdot 10^6$. The turbulence intensity level was set to 0.05 % for the transitional flow simulations. The Mach number varied from 0.5 to 0.8 and the (mean) angle of attack was 0°.

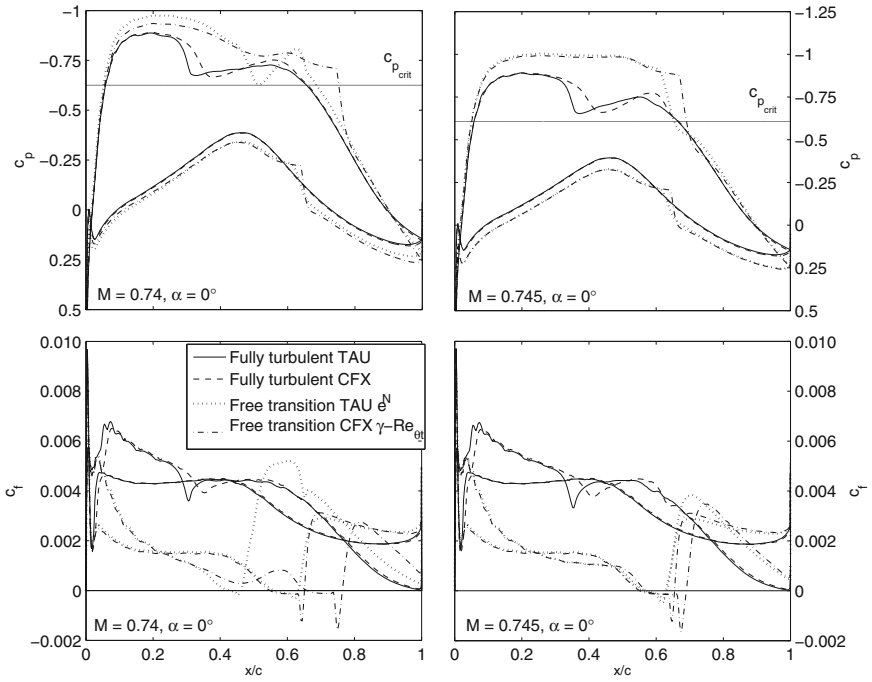

Fig. 2 Pressure- and skin friction distributions on the CAST-10 airfoil

4 Results and Discussion

In this section the results of steady, quasi-steady and unsteady CFD simulations as well as the computed flutter boundary are shown and discussed.

4.1 Steady Flow Simulations

The pressure- and skin friction distributions at $\alpha = 0°$ and two Mach numbers for both fully turbulent flow as well as in case of free boundary layer transition are shown in Fig. 2.

From Fig. 2 it is seen that when the flow is fully turbulent there is one strong shock for both Mach numbers and CFD codes. In case of free transition TAU predicts a double shock-system at $M = 0.74$, whereas CFX predicts a single strong shock. The shock(s) are located further downstream in comparison to fully turbulent flow. From the skin friction distribution it is seen that both codes predict transition via a separation bubble near the location of the shock. For TAU this is at about $x/c = 0.45$ at $M = 0.74$ at the upper surface, whereas for CFX transition is predicted at 75 % of

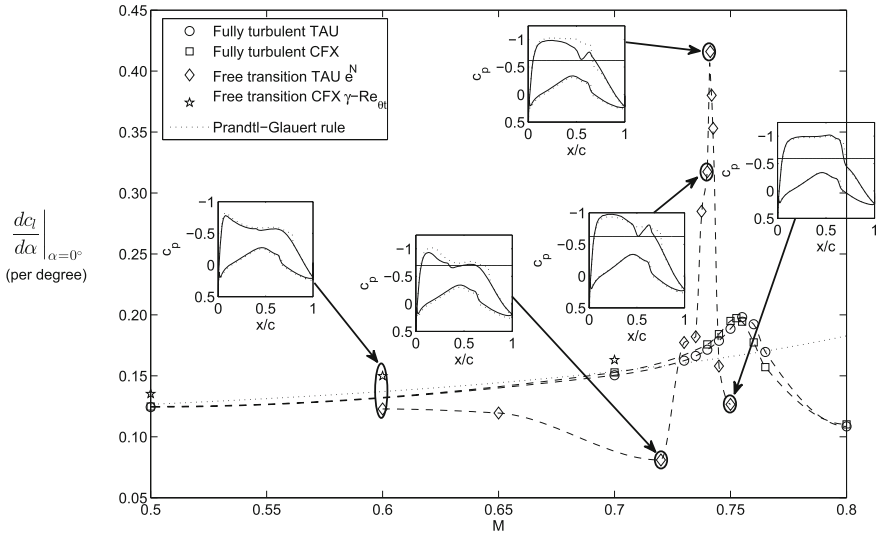

Fig. 3 Quasi-steady lift-polar slope versus Mach number

the chord length on the upper surface. These differences are attributed to the different transition models used. At the $M = 0.745$ the difference in predicted transition location is only 5 % on the upper surface. On the lower surface the transition locations are at around $x/c = 0.65$ for both Mach numbers and CFD codes. In case of fully turbulent flow small differences in the c_p- and c_f-distributions are observed as well, which might be caused by the differences in production of turbulent kinetic energy. Furthermore, the contour of the CAST-10 airfoil is very sensitive to small changes in the flow.

4.2 Quasi-steady Flow Simulations

The Mach number at which $dc_l/d\alpha|_{\alpha=0^\circ}$ has a maximum is a good indicator of the location of the transonic dip in the flutter boundary [4]. Figure 3 shows the lift-polar slope at $\alpha = 0^\circ$ versus Mach number for fully turbulent as well as for transitional flow. Pressure distributions in case of free transition at $\alpha = 0^\circ$ are also shown (solid lines TAU, dashed lines CFX). It should be noted that in case of free transition highly non-linear behaviour of the lift polar was observed around 0°. Therefore for some Mach numbers forward differences have been used to construct $dc_l/d\alpha|_{\alpha=0^\circ}$ from TAU. From CFX no $dc_l/d\alpha|_{\alpha=0^\circ}$ could be derived for transonic Mach numbers, because the lift curve was so non-linear around $\alpha = 0^\circ$ that taking finite differences did not make sense (see [15]). This non-linearity, caused by a shift in transition

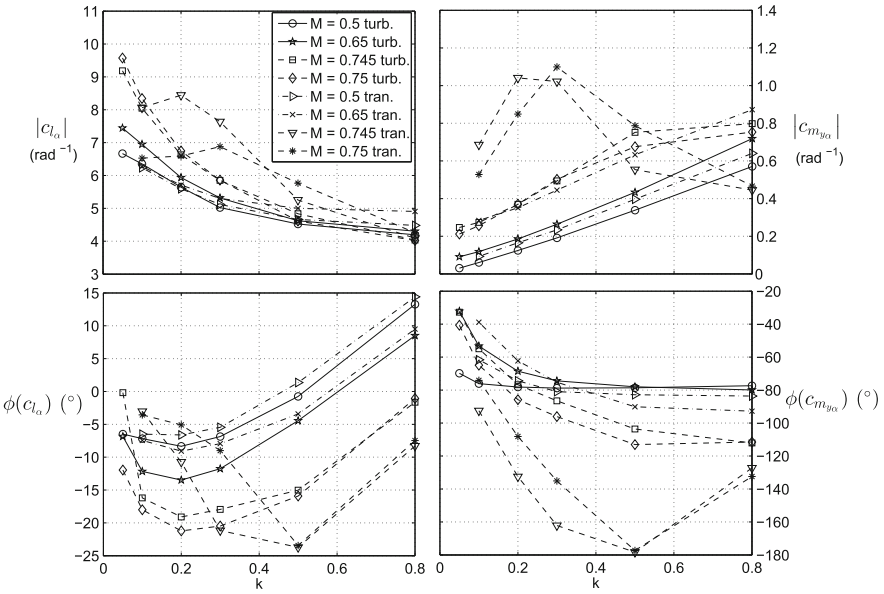

Fig. 4 Magnitude and phase angle of c_l and c_{m_y} versus k (pitch)

location, is probably a reason for the difficulty in obtaining converged solutions at transonic Mach numbers.

From Fig. 3 it is observed that in the fully turbulent case good agreement between both CFD codes is obtained. In case of free boundary layer transition the maximum $dc_l/d\alpha|_{\alpha=0^\circ}$ obtained from TAU is located at $M = 0.74$. Furthermore its value is more than twice as high compared to the fully turbulent case (0.42 versus 0.20). The lift-curve slope as obtained from CFX in case of free transition has an offset from that obtained with TAU for the subsonic Mach numbers shown. This is attributed to the large differences in transition location at the upper surface (see [15]). Furthermore, near $M = 0.7$ convergence problems were encountered in TAU. Therefore, the decrease in $dc_l/d\alpha|_{\alpha=0^\circ}$ might not represent the correct trend.

4.3 Unsteady Flow Simulations

Unsteady forced pitch and plunge simulations have only been performed with TAU. Figure 4 shows the first harmonic components for forced pitch for fully turbulent flow as well as for free transition. The mean angle of attack used was 0° and the amplitude was 0.05°. Figure 4 shows that at $M = 0.5$ and $M = 0.65$ the differences between fully turbulent flow and free transition are small for all harmonic components. At $M = 0.745$ and $M = 0.75$ significant differences occur. In case of free transition a

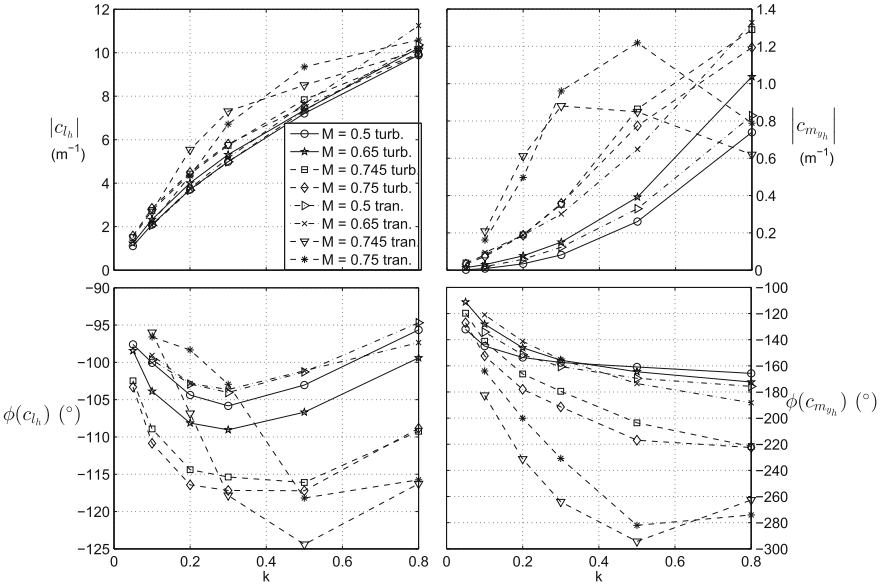

Fig. 5 Magnitude and phase angle of c_l and c_{m_y} versus k (plunge)

maximum or minimum suddenly occurs or is shifted with respect to the fully turbulent case (for $\phi(c_{l_\alpha})$).

The harmonic components of the forced plunge motion are depicted in Fig. 5. The mean position is 0 m and the amplitude is $0.001c/k$. Figure 5 shows similar behaviour as observed for the pitching motion. Magnitude and phase angle of both lift and moment coefficient are close together for the fully turbulent flow and free transition case when the flow is subsonic and large differences are observed when the flow becomes transonic.

4.4 Flutter Behaviour

The flutter boundary has been computed on the basis of the unsteady TAU results. Figure 6 shows the flutter boundary at $\alpha = 0°$ as well as the lift-polar slope at $\alpha = 0°$ versus Mach number, both for fully turbulent flow and in case of free transition.

From Fig. 6 it is clear that, in case of free transition, the minimum in the flutter boundary is lower (0.08 versus 0.13) and occurs at a lower Mach number (0.74 versus 0.755) than for fully turbulent flow. The reduced frequency at flutter is about 0.24 at transonic Mach numbers. At subsonic Mach numbers it varies between 0.4 ($M = 0.5$) and 0.27 ($M = 0.7$). Furthermore, it is observed that the location of the maximum $dc_l/d\alpha|_{\alpha=0°}$ coincides with the location of the transonic dip minimum in the flutter boundary. Upon comparing the results with those obtained by Dietz et al. [3] (from

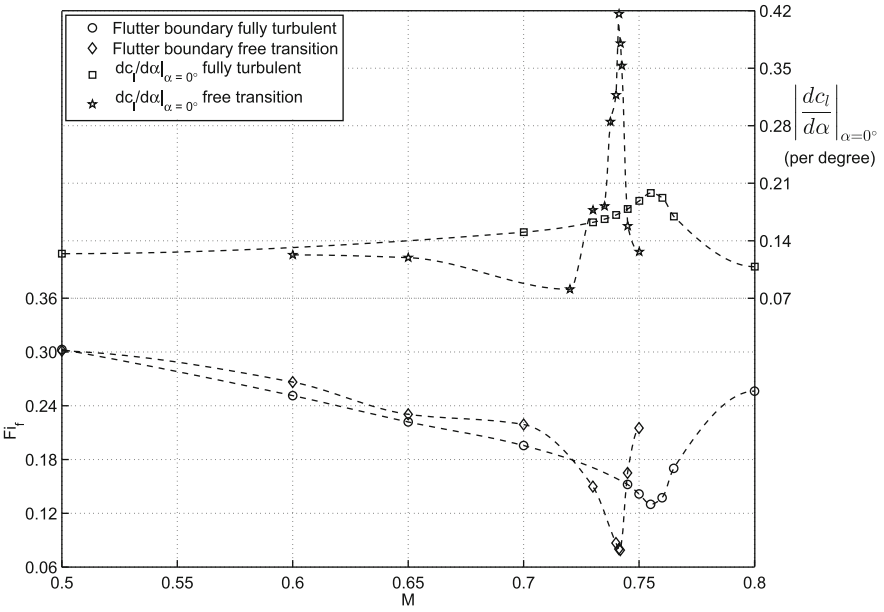

Fig. 6 Flutter boundary and quasi-steady lift-polar slope versus Mach number

which the structural parameters were taken) it is clear that the TAU code is in principle able to predict the correct flutter indices range. In case of free transition, for some Mach numbers ($M = 0.72$ and $M > 0.75$) no convergence of the CFD simulations was obtained. Therefore those could not be used to compute the flutter boundary. Furthermore, the accuracy of the prediction of unsteady shock-wave/boundary-layer interaction might have an influence on the flutter behaviour. This remains to be investigated however.

5 Conclusions

The influence of laminar to turbulent boundary layer transition on the flutter behaviour of a laminar supercritical airfoil (CAST-10) has been investigated. Numerical flow simulations were performed and used to determine the airfoil's flutter behaviour. The steady, quasi-steady and unsteady flow simulations showed a clear influence of (partly) laminar flow, especially at transonic Mach numbers. The flutter behaviour of the CAST-10 airfoil was found to differ significantly when the flow is partly laminar. The transonic dip is much deeper when boundary layer transition is free. Furthermore, its location is shifted to a lower Mach number. However, since this is only a first investigation these conclusions are drawn with caution. They indicate however that transition should be considered in the flutter analysis.

Acknowledgments The results presented in this paper have been generated during the first author's master thesis [15] and were also was part of the DLR-project "IGREEN" [16].

References

1. Goura, G., Badcock, K., Woodgate, M., Richards, B.: Implicit method for the time marching analysis of flutter. Aeronaut. J. (Paper No. 2548), 199–214 (2001)
2. Voß, R., Hippe, C.: Computation of the Flutter Boundary of the NLR 7301 Airfoil in the Transonic Range. In: New Results in Numerical and Experimental Fluid Mechanics V. Volume 92 of Notes on Numerical Fluid Mechanics and Multidisciplinary Design (NNFM), pp. 338–347 (2006)
3. Dietz, G., Schewe, G., Mai, H.: Experiments on heave/pitch limit-cycle oscillations of a supercritical airfoil close to the transonic dip. J. Fluids Struct. **19**, 1–16 (2004)
4. Bendiksen, O.: Review of unsteady transonic aerodynamics: theory and applications. Prog. Aerosp. Sci. **47**(2), 135–167 (2011)
5. Kühl, P., Zimmer, H.: The design of airfoil profiles for commercial aircraft with improved high speed flight characteristics. Technical report 74/16 B, Dornier GmbH (1974)
6. Gerhold, T., Galle, M.: Calculation of complex three-dimensional configurations employing the DLR TAU-code. AIAA Paper 97–0167 (1997)
7. ANSYS Inc.: Ansys cfx-solver theory guide (November 2010) Release 13.0
8. Menter, F.: Two-equation eddy-viscosity turbulence models for engineering applications. AIAA J. **32**(8), 1598–1605 (1994)
9. van Ingen, J.: A suggested semi-emprical method for the calculation of the boundary layer transition region. Technical Report V.T.H.-74, Delft University of Technology, Aerospace Engineering (1956)
10. Smith, A., Gamberoni, N.: Transition, pressure gradient and stability theory. Technical Report ES-26388, Douglas Aircraft (1956)
11. Menter, F., Langtry, R., Voelker, S.: Transition modelling for general purpose cfd codes. Flow Turbul. Combust. **77**, 277–303 (2006)
12. Jameson, A.: Time dependent calculations using multigrid, with applications to unsteady flows past airfoils and wings. In: AIAA 10th Computational, Fluid Dynamics Conference, AIAA Paper 91–1596, 24–26 June 1991)
13. Wada, Y., Liou, M.: An accurate and robust flux splitting scheme for shock and contact discontinuities. SIAM J. Sci. Comput. **18**, 633–648 (1997)
14. Hodges, D.H. Pierce, G.A.: Introduction to Structural Dynamics and Aeroelasticity. Cambridge University Press, New York (2002)
15. van Rooij, A.C.L.M.: Flutter behaviour of laminar supercritical airfoil. Master's thesis, Delft University of Technology, Delft, The Netherlands (2012)
16. Wegner, W., Voß, G., van Rooij, A.C.L.M.: Instationäre Transition und Flatterverhalten eines transsonischen Laminarprofils. IGREEN Abschlusskolloquium, DLR Göttingen, Institut für Aeroelastik (February 2012)

Part II
Optimization

Aero-Elastic Multipoint Optimization Using the Coupled Adjoint Approach

Mohammad Abu-Zurayk and Joël Brezillon

Abstract In the aircraft design process, several flight conditions that cover the flight envelop have to be considered, where the wing's structure behaves differently at these different flight conditions. Considering the structural behavior during the design optimization is computationally expensive, therefore an efficient approach is required when optimizing aero-structural systems. The coupled adjoint approach which is efficiently employed in gradient-based optimizations was previously developed at DLR and successfully applied for optimizing coupled aero-structural systems with high-fidelity flow and structure solvers. This new study employs the coupled adjoint approach to perform a proof-of-concept multipoint aero-elastic optimization. The optimized design is then compared to another design resulting from a single point optimization and proved to have a better overall performance.

1 Introduction

During the flight, the wing is exposed to gravitational as well as aerodynamic loads. These loads deform the wing into its so-called *flight shape*. This aeroelastic deformation depends on the wing's structural properties (elasticity) and varies with the fuel consumption and the flight conditions. Hence, a different flight condition results in a different wing deformation which affects the flow over the wing, especially in transonic flow regimes [1]. For this reason, it was conventional to limit the effects of aero-elasticity by designing stiffer wings. However, this results in increasing the wing's structural weight [2], which by default decreases the aircraft's efficiency.

M. Abu-Zurayk (✉) · J. Brezillon
DLR-AS, Lilienthalplatz 7, 38108 Braunschweig, Germany
e-mail: Mohammad.abu-zurayk@dlr.de

J. Brezillon
e-mail: Joel.brezillon@dlr.de

A. Dillmann et al. (eds.), *New Results in Numerical and Experimental Fluid Mechanics IX*,
Notes on Numerical Fluid Mechanics and Multidisciplinary Design 124,
DOI: 10.1007/978-3-319-03158-3_5,

Another technique consists in designing the wings structure so that it deforms into its optimum shape in cruise flight [3]. In this approach, the optimum shape is obtained by a pure aerodynamic optimization, and then the jig-shape, i.e. the wing shape when its not subjects to any loads, is obtained by subtracting the wing deflection under cruise load from the optimum flight shape. Several couplings between the structure optimisation and the deformation are mandatory to retrieve the desired cruise shape. This procedure however converges due to the linear model used for the aerodynamic and the structure.

The main advantage of this technique is the ability to decouple the complex aero-elastic optimisation into separate aerodynamic and structural problems. However, there is no guarantee to converge to the optimal aeroelastic design [4] and such approach is not likely to work for multi-point designs with drastic variation of aeroelastic deformations. A good example mentioned in Vazquez's study [5], is the multi-point optimization of a supersonic jet where the aeroelastic behaviour is different in supersonic and subsonic flow regimes.

The third approach to deal with the wing's aero-elasticity is to consider the flow and the structure simultaneously. Here the flight shape is computationally evaluated from the jig-shape, by coupling the flow solver with the structure solver. This implies that additional effort is needed for coupling the solvers and computing the flight shape. However, this approach allows multi-point design.

Employing this approach to get the flight shape is costly, while it is an iterative process that includes several couplings between the flow and the structure solvers. Therefore, an efficient optimization algorithm is required. The gradient-based algorithms are efficient optimization techniques, nonetheless, the cost of computing the gradients with the conventional finite differences approach (FD) scales linearly with the number of design parameters at which the gradients need to be computed. This means that FD is computationally prohibitive if the number of design parameters is high, as in modern high-fidelity design optimizations problems. The adjoint approach on the other hand can provide the gradients efficiently and independently of the number of design variables. This approach was previously developed and validated at DLR for high-fidelity aero-elastic systems [6].

In the design process, several flight conditions (design points) that cover the flight envelope, from start to end of cruise, need to be considered. While different flight conditions result in different structure behaviours and while the structure's elasticity plays a significant roll in predicting the correct aerodynamic properties of the wing, this study aims at employing the efficient coupled aero-elastic adjoint approach to perform a proof-of-concept multi-point aero-elastic optimization. Here, the design point in addition to several off-design points will be taken into consideration. The objective of this optimization is to enhance the performance of the aircraft at different flight conditions that are around the main design point.

2 The Coupled Aero-Structure Adjoint Approach

In a previous study [6], the adjoint approach was developed for high-fidelity aero-elastic models. The aero-structural system is defined by the residual of the RANS equations (Ra) governing the flow and the residual of the linear elasticity equation (Rs) governing the structure (1).

$$R = \begin{bmatrix} Ra \\ Rs \end{bmatrix} \tag{1}$$

The state and design variables are defined as follows respectively:

$$W = \begin{bmatrix} w \\ u \end{bmatrix} \tag{2}$$

$$D = \begin{bmatrix} A \\ T \end{bmatrix} \tag{3}$$

where (w) is the flow state variables vector and (u) is the structure state variables vector which represents the structural deformation. The design variables vector (D) includes the aerodynamic shape design variables (A) and the structure design variables (T) like the structure thickness.

The cost function to be minimized (I) and the residuals (R) are functions of the state variables vector (W) and the design variables vector (D). Taking these dependencies into account, the gradients of the cost function and the residuals w.r.t. the design variables vector become

$$\frac{dI}{dD} = \frac{\partial I}{\partial D} + \begin{bmatrix} \frac{\partial I}{\partial w} & \frac{\partial I}{\partial u} \end{bmatrix} \begin{bmatrix} \frac{\partial w}{\partial A} & \frac{\partial w}{\partial T} \\ \frac{\partial u}{\partial A} & \frac{\partial u}{\partial T} \end{bmatrix} \tag{4}$$

$$\frac{dR}{dD} = \frac{\partial R}{\partial D} + \begin{bmatrix} \frac{\partial R}{\partial w} & \frac{\partial R}{\partial u} \end{bmatrix} \begin{bmatrix} \frac{\partial w}{\partial A} & \frac{\partial w}{\partial T} \\ \frac{\partial u}{\partial A} & \frac{\partial u}{\partial T} \end{bmatrix} \tag{5}$$

respectively.

To formulate the coupled adjoint equations, the Lagrange approach is employed by defining:

$$L = I + \Psi^T R \tag{6}$$

where (Ψ) is the Lagrange multiplier which is also called the adjoint field. In an aero-structural coupled system

$$\Psi = \begin{bmatrix} \psi a \\ \psi s \end{bmatrix} \tag{7}$$

where (ψa) is the aerodynamic adjoint field and (ψs) is the structure adjoint field.

Since the residual (R) is zero, the gradient of the Lagrangian with respect to the design variables is equal to the gradient of the cost function with respect to the design variables, which is the gradient required by the optimizer. Considering all the presented dependencies, the gradient of the Lagrangian after rearranging the terms is:

$$\frac{dI}{dD} = \frac{dL}{dD} = \left(\begin{bmatrix} \frac{\partial I}{\partial A} \\ \frac{\partial I}{\partial T} \end{bmatrix}^T + \begin{bmatrix} \frac{\partial I}{\partial w} \\ \frac{\partial I}{\partial u} \end{bmatrix}^T \begin{bmatrix} \frac{\partial w}{\partial A} & \frac{\partial w}{\partial T} \\ \frac{\partial u}{\partial A} & \frac{\partial u}{\partial T} \end{bmatrix} \right) + \begin{bmatrix} \psi a \\ \psi s \end{bmatrix}^T \left(\begin{bmatrix} \frac{\partial Ra}{\partial A} & \frac{\partial Ra}{\partial T} \\ \frac{\partial Rs}{\partial A} & \frac{\partial Rs}{\partial T} \end{bmatrix} + \begin{bmatrix} \frac{\partial Ra}{\partial w} & \frac{\partial Ra}{\partial u} \\ \frac{\partial Rs}{\partial w} & \frac{\partial Rs}{\partial u} \end{bmatrix} \begin{bmatrix} \frac{\partial w}{\partial A} & \frac{\partial w}{\partial T} \\ \frac{\partial u}{\partial A} & \frac{\partial u}{\partial T} \end{bmatrix} \right) \tag{8}$$

In this Eq. (8), the very last matrix which contains the sensitivities of the state variables w.r.t the design variables is computationally expensive for a high number of design variables, since it requires computing one converged flow-structure coupling for each design variable. To eliminate this term, the adjoint field vector (Ψ) is found so that:

$$\begin{bmatrix} \frac{\partial I}{\partial w} \\ \frac{\partial I}{\partial u} \end{bmatrix}^T + \begin{bmatrix} \psi a \\ \psi s \end{bmatrix}^T \begin{bmatrix} \frac{\partial Ra}{\partial w} & \frac{\partial Ra}{\partial u} \\ \frac{\partial Rs}{\partial w} & \frac{\partial Rs}{\partial u} \end{bmatrix} = 0 \tag{9}$$

which is the coupled aero-structure adjoint equation. This equation is not dependant on the number of design variables, but on the number of cost functions and constraints. Therefore, it should be solved only one time for each cost function or constraint. After solving this system of equations for the adjoint field vector (Ψ), it is used to compute the gradients:

$$\frac{dI}{dD} = \frac{dL}{dD} = \left(\begin{bmatrix} \frac{\partial I}{\partial A} \\ \frac{\partial I}{\partial T} \end{bmatrix}^T + \begin{bmatrix} \psi a \\ \psi s \end{bmatrix}^T \begin{bmatrix} \frac{\partial Ra}{\partial A} & \frac{\partial Ra}{\partial T} \\ \frac{\partial Rs}{\partial A} & \frac{\partial Rs}{\partial T} \end{bmatrix} \right) \tag{10}$$

3 Results

In this section the performance of the designs resulting from single and multi-point optimizations will be evaluated and compared. The test case used in these optimizations is a wing-body configuration based on the Dornier-728 geometry. The optimization algorithm is the gradient-based nonlinear Conjugate Gradient (CG) algorithm. The coupled adjoint approach, which is employed to compute the gradients efficiently, is based on the DLR-TAU [7] flow solver coupled with the ANSYS [8] structure solver. The multi-point flight conditions are taken around the cruise flight condition (the design point) which is at Ma = 0.8 and $C_L = 0.417$, as presented in Table 1. On the other hand, the single-point optimization is performed

Table 1 Definition of points in multi-point optimization

point	Mach number	Lift coefficient
Point 1	0.780	0.417
Point 2	0.800	0.340
Point 3 (cruise)	0.800	0.417
Point 4	0.800	0.500
Point 5	0.820	0.417

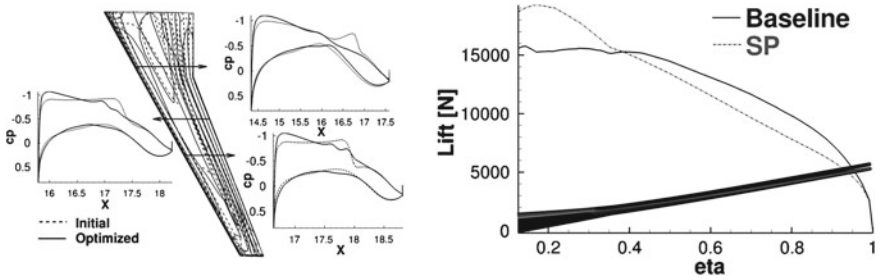

Fig. 1 Single-point (SP) optimization; chordwise cp and spanwise lift distributions of baseline and optimized configurations

at the cruise condition. The flow in both optimization scenarios was computed for $\mathrm{Re} = 21 * 10^6$.

The CFD mesh is a structured O-type mesh that contains 1.2 million grid nodes. The structure CSM model (4000 nodes) contains 27 ribs and 2 spars covered with upper and lower skins. It is modeled using rectangular shell elements that allow 6 degrees of freedom, three translational and three rotational. This means that the wing can hold translation as well as bending.

The objective of the optimization is to reduce the drag at constant lift and wing thickness. To control the geometry shape, 75 design parameters governed by the free-form deformation technique [9], are employed in such a way to keep the wing's thickness constant. They are distributed over 15 spanwise sections; each section contains 5 parameters. It is important here to mention that performing a multi-point (or even a single point) optimization with such a large number of design variables would not have been computationally affordable without the coupled adjoint approach. This approach saves indeed around 85 % of the time needed to compute the gradients when compared to the central finite differences approach.

The single-point optimization reduced the drag by 14 counts at constant lift and thickness. Figure 1 presents on the left hand side the chordwise pressure distribution for the initial and the optimized configurations. As illustrated the shock is reduced. The figure also presents (on the right hand side) the spanwise lift distribution for the baseline and the optimized configurations. As illustrated, the optimized wing shows a more elliptic loading, which is beneficial to lower the induced drag.

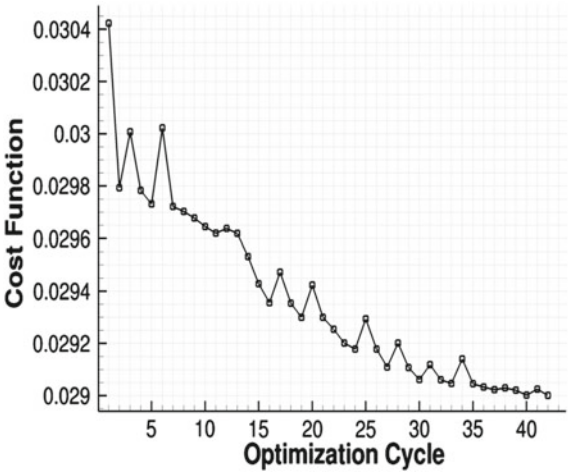

Fig. 2 Multi-point optimization convergence

Table 2 Drag reduction (in drag counts) of each point in multi-point optimization

point	Mach number	Lift coefficient	Reduced C_D(counts)
Point 1	0.780	0.417	−5
Point 2	0.800	0.340	−7
Point 3 (cruise)	0.800	0.417	−8
Point 4	0.800	0.500	−19
Point 5	0.820	0.417	−30

In the multi-point optimization, the five points were weighted equally:

$$\text{Cost Function} = \sum_{\text{i=1}}^{5} 0.2 * \text{CD}_\text{i} \tag{11}$$

Figure 2 presents the convergence history of the multi-point optimization.

Having equal weighting factors, means that the highest drag reduction will occur at the points with the highest gradients, i.e. at the fourth and fifth design points. This is confirmed by the drag reductions observed on the optimal shape, as shown in Table 2.

Figure 3 shows the LoD (lift to drag ratio) trend on the left side and the drag rise on the right side for the baseline, the single-point and the multi-point resulting designs. The single-point optimization permits a valuable increase in the LoD ratio at the design point. However, the overall LoD trend shows that the single-point design performs worse at higher lift values. On the other hand, the multipoint optimization showed better LoD and drag-rise trends for the different flight conditions.

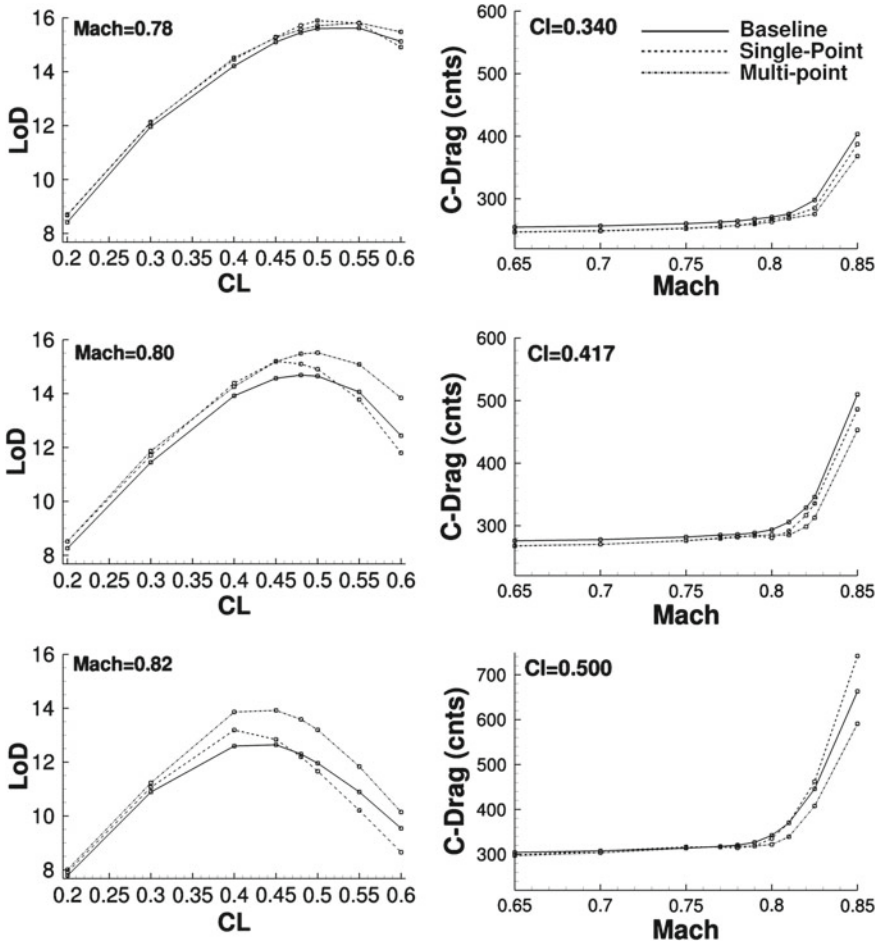

Fig. 3 The LoD and the Drag-rise trends, comparison between single- and multi-point optimizations

4 Conclusions

The coupled aero-elastic adjoint approach was employed here to perform single-point and multi-point aero-elastic gradient-based optimizations. Performing such high-fidelity without the coupled adjoint approach would not have been computationally reasonable. Even though the single-point brought valuable enhancement at the design point, the multi-point optimization showed better LoD and Drag trends for the different flight conditions.

References

1. Elsholz, E.: Fluid-structure coupling, simplified structural model on complex configurations, MEGADESIGN. Notes Numer. Fluid Mech. Multi. Des. **107**, 169–178 (2009)
2. Flick, P., Love, M., Zink, P.: The Impact of Active Aeroelastic Wing Technology on Conceptual Aircraft Design. RTO AVT Specialists' Meeting, Canada (1999)
3. Röhl, P., Mavris, D., Schrage, D.: Combined Aerodynamic and Structural Optimization of a high-speed civil transport wing, AIAA paper-95-1222 (1995)
4. Maute, K., Allen, M.: Conceptual design of aeroelastic structures by topology optimization. Struct. Multi. optim. **27**(1–2), 27–42 (2004)
5. Vázquez, M., Dervieux, A., Koobus, B.: A methodology for the shape optimization of flexible wings. Eng. Computat. **23**)(4), 344–367 (2006)
6. Abu-Zurayk, M., Brezillon, J.: Shape optimization using the aero-structural coupled adjoint approach for viscous flows, evolutionary and deterministic methods for design. In: Optimization and Control. Conference proceedings, Capua, Italy (2011)
7. Gerhold, T: Overview of the hybrid RANS code TAU. In: Kroll, N., Fassbender, JK (eds.) Notes on Numerical Fluid Mechanics and Multi-disciplinary Design, vol. 89, pp. 81–92. Springer, Heidelberg (2005)
8. http://www.ansys.com
9. Ronzheimer, A.: Shape parameterization using freeform deformation. In: MEGAFLOW-Numerical Flow Simulation for Aircraft Design, ISBN 3-540-24383-6 (2005)

Efficient Global Optimization of a Natural Laminar Airfoil Based on Surrogate Modeling

Chunna Li, Joël Brezillon and Stefan Görtz

Abstract Surrogate-based optimization and efficient global optimization in particular, is considered for aerodynamic design and analysis to deal with some of the drawbacks of classical direct optimization methods. Design of Experiment methods, optimization algorithms, various surrogate modeling methodologies, adaptive sample refinement strategies, multiple criteria for terminating the refinement procedure and several other techniques, are developed and integrated into a practical optimization framework. To search the design space globally and efficiently, several adaptive sample refinement strategies are studied and compared. Two test cases, minimizing the drag of a NLF0416 airfoil with ten design variables and optimizing the performance of a laminar profile with 26 design variables at two design points, are performed. The results indicate that the developed optimization methodology in combination with the adaptive sample refinement strategies features a good balance between global exploration and local exploitation. Additionally, the effect of different design points on the objective function can be automatically considered in the refinement procedure.

1 Introduction

Aerodynamic optimization usually deals with problems with multiple design variables and/or multiple objectives. Thus, the objective function may show highly nonlinear behavior and/or have multiple optima. It is a challenge to find the global optimum for such problems efficiently. Classical direct optimization methods, such as gradient-based methods, are efficient in searching the design space but search locally, while evolutionary algorithms are capable of finding the global optimum at

C. Li (✉) · J. Brezillon · S. Görtz
DLR Institut für Aerodynamik und Strömungstechnik, Lilienthalplatz 7,
38108 Braunschweig, Germany
e-mail: chunna.li@dlr.de

A. Dillmann et al. (eds.), *New Results in Numerical and Experimental Fluid Mechanics IX*,
Notes on Numerical Fluid Mechanics and Multidisciplinary Design 124,
DOI: 10.1007/978-3-319-03158-3_6,

the expense of a considerable amount of expensive CFD computations. Surrogate-Based Optimization (SBO) [1], on the other hand, and the Efficient Global Optimization (EGO) [2] method in particular, provides an alternative to overcome some of the drawbacks of the other optimization methods, but relies on additional techniques.

At DLR, a surrogate-based optimization framework has been developed in Python based on an existing framework for classical optimization, called Pyranha [3]. Different enabling techniques, such as DoE methods, sample refinement strategies and criteria for terminating the refinement have been developed and integrated into the framework together with several other modules, including the DLR toolbox for surrogate modeling [4], the in-house tools GenGeo and MegaCADs [5] for geometry parameterization, and the DLR TAU code [6] for flow simulation.

Two test cases, minimizing the drag of a NLF0416 airfoil with ten design variables at constant lift and optimizing the performance of a laminar profile at two design points, were carried out to evaluate and compare different refinement strategies with respect to efficiency and accuracy.

2 Surrogate-based Optimization

As was stated above, surrogate-based optimization depends on several enabling techniques, which are briefly introduced in the following.

2.1 Design of Experiment Methods

Modern Design of Experiment (DoE) methods use certain mathematical algorithms to generate samples within the design space in an optimal way to gain as much information of the objective function as possible from a given number of samples. A certain number of samples are required for constructing an initial surrogate model. The choice of the samples has an obvious effect on the efficiency and accuracy of the surrogate-based optimization chain, because sparsely or badly distributed samples may lead to a surrogate model that is not globally accurate or depicts a fake landscape of the design space, which could result in premature convergence to the region with a local optimum or a huge amount of expensive high-fidelity computations in the sample refinement procedure. The Random Latin Hypercube Sampling [7] (RLHS), the Optimized Latin Hypercube Sampling [8] (OLHS) and the Transport Propagation Latin Hypercube Sampling [9] (TPLHS) were integrated into the framework, because the number of samples is independent of the number of variables, and the random samples can be taken one each time.

2.2 Optimization Algorithms

The optimization methods in the framework consist of gradient-free methods (Simplex/Subplex), three gradient-based optimizers (Conjugate Gradient method (CG), Steepest Descent method (SD), the Newton method), and the Differential Evolution algorithm (DE). Out of those methods, only the DE is a global optimizer.

For classical direct optimization, i.e. by directly evaluating the objective function using a high-fidelity flow solver, gradient-based optimizers are usually the best choice because of their high efficiency, but they search locally. In comparison, the DE is favored for its global search characteristics at the expense of a considerable amount of CFD computations. SBO is a good alternative to overcome some drawbacks of the other optimization methods, because it is much cheaper to approximate the objective(s) on the constructed surrogate model, provided that the surrogate model is accurate enough. The classical optimization methods are also used to select infill samples in order to improve the accuracy of the surrogate model both locally and globally.

2.3 Surrogate Modeling

Surrogate modeling is a mathematical approach to approximate the objective at an unobserved location using observations nearby, or to analyze the trend of the objective function, or to evaluate the correlation between the objective function and the design variables. In SBO, it is used to predict the objective function instead of the high-fidelity solver. Here, the DLR surrogate modeling toolbox was integrated into the framework for SBO, including different Kriging models: Simple Kriging, Ordinary Kriging, Universal Kriging, Regression Kriging and Gradient-Enhanced Kriging. A detailed description of Kriging can be found in the reference [10].

2.4 Sample Refinement Strategies

Adaptive sample refinement is the key technique in SBO due to its decisive effect on the efficiency of SBO and the local and global accuracy of the surrogate model. The EGO algorithm adaptively refines the design space by maximizing the (constrained) Expected Improvement Function (EIF). It evaluates the potential improvement of the objective function on the surrogate model by balancing the probability that the objective at any location in the design space will fall below the current minimum and the model error there. However, in the developed optimization framework, the objective function on the surrogate model, as well as the Kriging error, were also optimized to select infill samples to improve the accuracy of the surrogate model. These are standard sample refinement strategies, called EI-based, Cost-based and KE-based refinement respectively. Besides, different combinations of the three standard refinement strategies were developed to enhance the accuracy of the surrogate model both locally and globally. In addition, multiple infill samples can be selected in each

Fig. 1 Flowchart of SBO

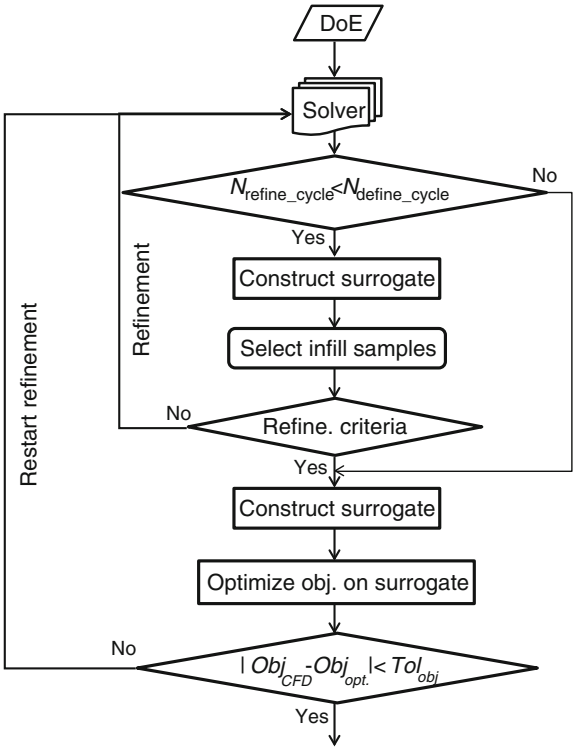

refinement cycle, e.g. by running a local optimizer in turn with different starting points when maximizing the EIF. The computation of multiple infill samples per refinement cycle with the flow solver can be performed in parallel to improve the efficiency of the optimization chain.

In case the geometry of an infill sample is infeasible or the CFD computation fails due to convergence, the objective of the infill sample is approximated by interpolating the objective on surrogate model plus considering model error. Thus, the refinement becomes robust, because the surrogate model can always be updated.

To deal with problems with multiple design variables or with multiple optima, for which the convergence of the refinement procedure to the optimum may slow down and the local accuracy of the surrogate model is difficult to be guaranteed, the range of the design space can be decreased after a given number of refinement cycles. This tends to enhance the surrogate model locally in a region where the global optimum may exist and saves computational time by reducing the number of samples used to construct surrogate models. The refinement procedure can be controlled and terminated based on different criteria, e.g. by specifying the maximum number of refinement cycles or a tolerance for the maximum expected improvement on the surrogate model. Properly tuned criteria can guarantee an effective refinement of the design space and a better optimum as well. The flowchart of the efficient global optimization method is shown in Fig. 1.

Table 1 Settings of the refinement strategies

Cases	DoE (RLHS)	Settings of the refinements (The number stands for refinement cycles)	Optimizers for refinement		
			EI	KE	Cost
Pure EI	20	(EI) (0 ∼ 100)	DE		
Hybrid	20	(EI + KE) (0 ∼ 50) + (EI + Cost) (51 ∼ 100)	DE + CG	DE	CG
Enhanced	20	(EI + KE) (0 ∼ 20) + (EI + Cost) (21 ∼ 30) + Start shrinking design space + (EI+Cost)(31 ∼ 35) + (Cost) (36 ∼ 50)	DE + CG (2 start. pts.)	DE	CG (2 start. pts.)

3 Test Cases

3.1 Optimization of a NLF0416 Airfoil with 10 Design Variables

The first test case was performed to evaluate the behavior of different sample refinement strategies. The geometry to be optimized is the NLF0416 airfoil. The flow conditions were a Mach number of 0.1 and a Reynolds number of 2.0e6. The DLR TAU RANS solver combined with the Spalart-Allmaras turbulence model was used and the transition points were predicted using the e^N-method ($N = 8$). The geometry was parameterized with 10 Hicks-Henne bump functions using the in-house parameterization tool GenGeo. During optimization, and hybrid unstructured grid with 40,466 mesh points was deformed using Radial Basis Functions (RBFs). Regression Ordinary Kriging was used to construct surrogate models for its robustness. The objective function is described by

$$\min c_d \quad \text{s.t.} \quad c_{l,\text{target}} = 0.72 \tag{1}$$

The settings of the refinement strategies are shown in Table 1. Different optimization results in Table 2 indicate that SBO is a global optimization method and is more efficient than the Subplex. In addition, the hybrid refinement strategy is able to enhance the local region of the surrogate model more efficiently than the standard EI-based refinement. Although the optimum obtained with the hybrid refinement strategy is slightly better than that using the enhanced hybrid refinement strategy, the latter is more efficient if the infill samples are computed in parallel in each refinement cycle. Figure 2 compares pressure distributions of the optimized geometries with that of the baseline. The Subplex is seen to have extended the laminar extensions on the upper surface, while the SBOs resulted in longer laminar extensions on the upper surfaces.

Table 2 Results of optimizing the NLF0416 airfoil

Optimization strategy	c_l	Opt. (c_d) (d. c.)	c_{dv} (d.c.)	c_{dp} (d.c.)	Trans. pts.		Nr. of cycles	Nr. of CFD comp.	Nr. of proc. used	Wall clock time(s)
					Xtr_U	Xtr_L				
Baseline	0.7193	82.30	53.58	28.72	0.3330	0.5679	×	1	8	ignored
Subplex	0.7209	69.08	44.79	24.29	0.5415	0.5461	500	681	8	327716.8
SBO (Pure EI)	0.7196	64.41	39.35	25.06	0.6833	0.5570	100	122	12	44615.7
SBO (Hybrid)	0.7197	62.97	37.54	25.43	0.7377	0.5461	100	222	24	51137.4
SBO (Enhanced)	0.7201	63.58	37.33	26.25	0.7595	0.5461	50	218	36	24945.7

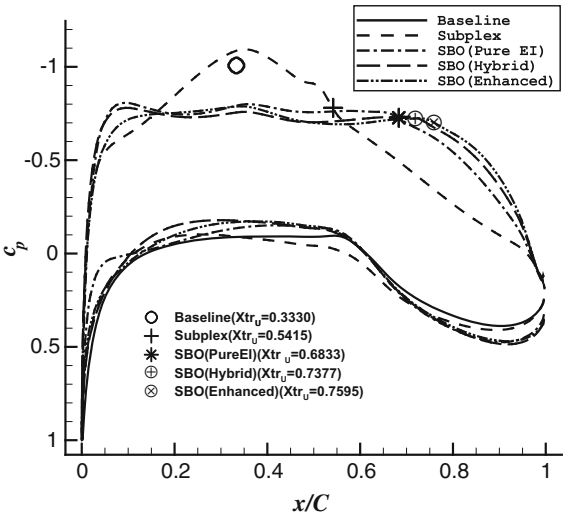

Fig. 2 Comparison of pressure distributions

3.2 Optimization of a Korn Airfoil at Two Design Points

The goal of the second test case is to validate if the SBO framework can efficiently handle multiple design variables and multiple design points. The baseline geometry is the Korn airfoil with the thickness of 15 % of the chord. The freestream conditions at the two design points are a Mach number of 0.66 and a Reynolds number of 1.45e7, and a Mach number of 0.4 and a Reynolds number of 1.2e7, respectively. The DLR TAU RANS solver combined with the Spalart-Allmaras turbulence was used and the transition points were predicted using the e^N-method ($N = 11.5$). The geometry was parameterized with 26 Bezier bumps using the in-house parameterization tool GenGeo. The structured baseline grid with 46,800 mesh points was generated by an in-house structured mesh generator. Regression Ordinary Kriging was chosen to construct surrogate models. To obtain better performance at the maximum cruise velocity as well as at the maximum climb velocity, the objective function was defined as

$$\min \left(c_{d,\text{design point 1}} + c_{d,\text{design point 2}}\right) \text{ s.t. } \begin{array}{r} \text{thickness} \geq 0.150115 \\ c_{l,target,design\ point\ 1} = 0.24 \\ c_{l,target,design\ point\ 2} = 0.44 \end{array} \quad (2)$$

As there was no previous knowledge of the optimum, the optimization was carried out in two steps: in the first step, SBO was performed based on the baseline Korn airfoil; in the second step, SBO with the same settings was performed, using the optimized geometry from the first step as the baseline.

Table 3 Settings of the refinement strategies

Cases	DoE (RLHS)	Settings of the refinements (The number stands for refinement cycles)	Optimizers for refinement		
			EI	KE	Cost
Enhanced	39	(EI + KE + Cost) (0 ∼ 100) Start shrinking design space after 70 cycles	DE + CG (3 start. pts)	DE	CG (3 start. pts)

Table 4 Results for optimizing the Korn airfoil at two design points

Profile	c_l	c_d(d. c.)	c_{dp}(d. c.)	c_{Dv}(d. c.)	c_m	xtr_U	$\mathbf{xtr}_L$
Design point 1: $M = 0.66$, $c_{l,target} = 0.24$, $Re = 1.45 \times 10^7$.							
Korn	0.24	63.18	21.72	41.45	0.13736	0.250	0.248
SBO	0.24	34.35	9.97c	24.39	0.10071	0.635	0.612
LC2	0.24	34.49	10.02	24.88	0.08984	0.584	0.658
Design point 2: $M = 0.40$, $c_{l,target} = 0.44$, $Re = 1.20 \times 10^7$							
Korn	0.44	70.44	21.60	48.82	0.11390	0.130	0.352
SBO	0.44	34.93	9.96	24.97	0.08702	0.659 ∼ 0.647	0.633 ∼ 0.623
LC2	0.44	37.17	10.65	26.52	0.07790	0.599	0.670

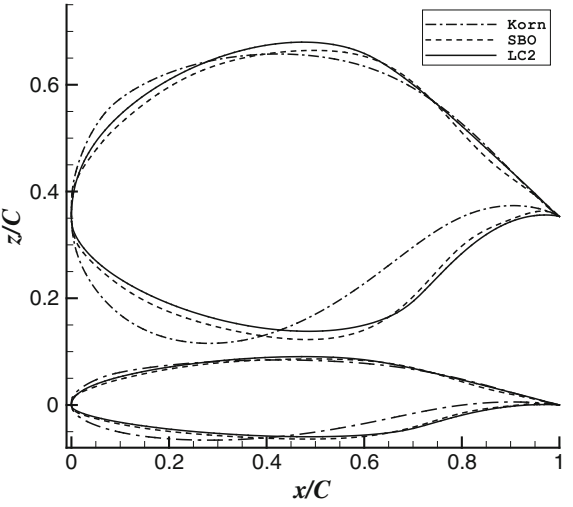

Fig. 3 Comparison of the geometries

The settings for the refinement strategy are shown in Table 3. The results from SBO are compared with those of the baseline geometry from the inverse design (coined LC2 [11]) in Table 4. Figure 4 shows that the thickness distributions of LC2 and the optimized geometry are similar, while the camber distributions are somewhat different. Figure 5 indicates that the optimized geometry features a little longer laminar extension on the upper surface, but a little shorter laminar extension

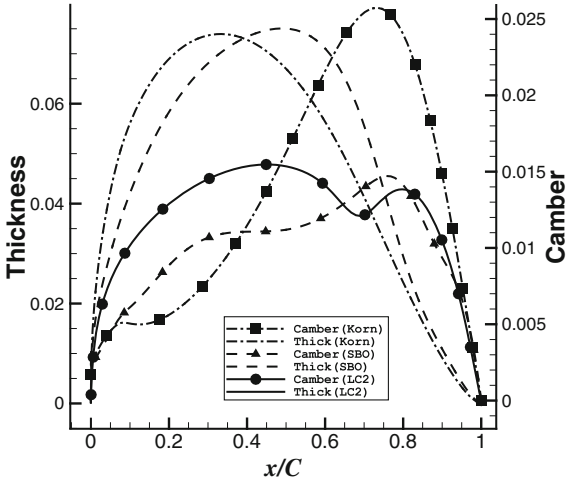

Fig. 4 Comparison of the thicknesses and cambers

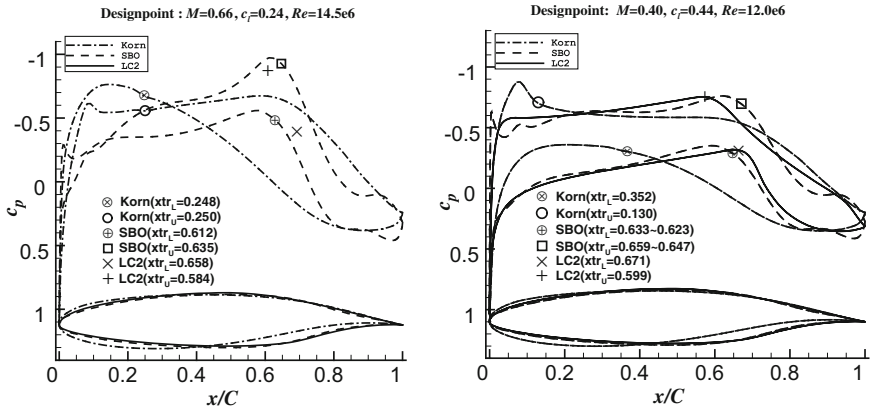

Fig. 5 Comparison of pressure distributions at two design points

on the lower surface in comparison with LC2. Small pressure peaks are seen to arise around the leading edge of the optimized geometry due to the parameterization and the baseline geometry. Figure 6 compares the polars of the baseline, the optimized geometry and the LC2. The optimized geometry has lower drag between the two design points than LC2, while the low drag buckets of LC2 are wider. In the opinion of the author, this is due to the described pressure peaks, which grow fast as the angle of attack increases outside the design range, for it can cause the transition point to quickly move to the leading edge, which results in a sharp increase of the drag.

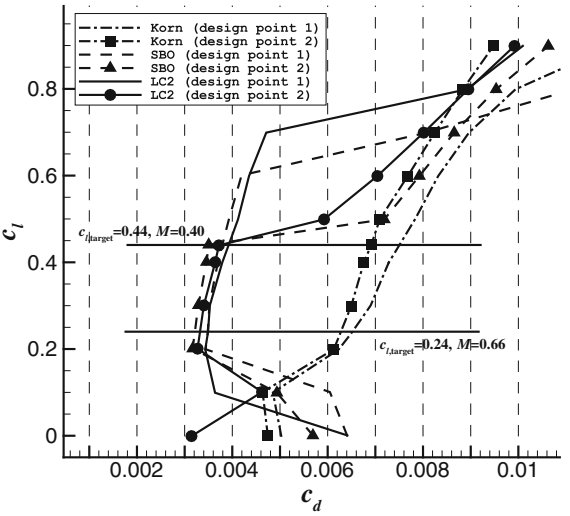

Fig. 6 Comparison of polars of the baseline, the optimized geometry from SBO and the LC2

4 Conclusions

Surrogate-based optimization (SBO) is an efficient global optimization method. Out of different sample refinement strategies, the hybrid refinement strategy can be more efficient in enhancing the accuracy of the surrogate model than the standard individual refinement strategies. The enhanced hybrid sample refinement outperforms others due to its good balance in the local exploitation and the global exploration of the design space. The developed optimization methodology can evaluate the effect of different design points automatically during the refinement.

Despite this, the optimization method shows limitations of setting the design boundaries of the design space in case that no previous knowledge of the optimum is available. Further studies are needed to determine when and how to shrink the design space more effectively.

References

1. Li, C.-H., Brezillon, J., Görtz, S.: A Framework for Surrogate-Based Aerodynamic Optimization, Proceedings ODAS 2011. Toulouse, France (2011)
2. Jeong, S., Obayashi, S.: Efficient global optimization (EGO) for multi-objective problem and data mining. Proc. Congr. Evol. Comput. **2005**(3), 2138–2145 (2005)
3. Brezillon, J., Abu-Zurayk, M.: Aerodynamic Inverse Design Framework using Discrete Adjoint Method, 17th DGLR-Fach-Symposium der STAB. Berlin, Deutschland (2010)
4. Han, Z.-H.: Response Surface Model (RSM) Toolbox Version 1.3.4: User's Guide, German Aerospace Center (DLR), Institute of Aerodynamics and Flow Technology, (2010)
5. Brodersen, O., Hepperle, M., Ronzheimer, A., Rossow, C.-C., Schöning, B.: The parametric grid generation system megacads, numerical grid generation in computational field simulations.

In: Proceedings of the 5th International Conference, Soni, pp. 353–362. Mississippi State University (1996)
6. Gerhold, T., Friedrich, O., Evans, J., Galle, M.: Calculation of complex three-dimensional configurations employing the DLR-TAU-code, AIAA paper (1997) pp. 97–167
7. McKay, M.D., Beckman, R.J., Conover, W.J.: A comparison of three methods for selecting values of input variables in the analysis of output from a computer code. Technometrics **21**(2), 239–245 (1979)
8. Bates, S.J., Sienz, J., Langley, D.S.: Formulation of the Audzu-Eglais uniform Latin Hypercube design of experiments. Adv. Eng. Softw. **34**, 493–506 (2003)
9. Viana, F.A.C., Venter, G., Balabanov, V.: An algorithm for fast optimal Latin hypercube design of experiments. Int. J. Numer. Meth. Eng. **82**, 135–156 (2010)
10. Sacks, J., Welch, W.J., Mitchell, T.J., Wynn, H.P.: Design and analysis of computer experiments. Stat. Sci. **4**(4), 409–423 (1989)
11. Köster, H., Horstmann, K.H., Rohardt, C.H.: Aachen RWTH. DGLR-Bricht **90–06**, 111–115 (1990)

Efficient Quantification of Aerodynamic Uncertainty due to Random Geometry Perturbations

Dishi Liu and Stefan Görtz

Abstract The effort of quantifying the aerodynamic uncertainties caused by uncertainties in the airfoil geometry is hindered by the large number of the variables and the high computational cost of the CFD model. To identify efficient methods addressing this challenge, four promising methods, gradient-enhanced Kriging (GEK), gradient-assisted polynomial chaos (GAPC), maximum entropy method and quasi-Monte Carlo quadrature are applied to a test case where the geometry of an RAE2822 airfoil is perturbed by a Gaussian random field parameterized by nine independent variables. The four methods are compared in their efficiency of estimating some statistics and probability distribution of the uncertain lift and drag coefficients. The results show that the two surrogate method, GEK and GAPC, both utilizing gradient information obtained by an adjoint CFD solver, are more efficient in this situation. Their advantage is expected to increase as the number of variables increases.

1 Introduction

Aerodynamic modelings could be subject to uncertainties in the geometry of the aircraft and hence the system response quantities (SRQ). Quantifying the uncertainties associated with the SRQ enhances the reliability of the model and enables robust design optimization. This uncertainty quantification (UQ) process is usually done in a probabilistic framework, in which the input uncertainties are parameterized by

D. Liu (✉) · S. Görtz
DLR Institut für Aerodynamik und Strömungstechnik, Lilienthalplatz 7,
38108 Braunschweig, Germany
e-mail: Dishi.Liu@dlr.de

S. Görtz
e-mail: Stefan.Goertz@dlr.de

A. Dillmann et al. (eds.), *New Results in Numerical and Experimental Fluid Mechanics IX*,
Notes on Numerical Fluid Mechanics and Multidisciplinary Design 124,
DOI: 10.1007/978-3-319-03158-3_7,

random variables, and the consequent uncertainties in the SRQ are quantified by determining the probability distribution, or some statistical moments, of the SRQ.

However, two things hinder the effort of propagating the uncertainty from the input to the SRQ. One is the high computational cost of CFD, the other is the the large number of variables representing the geometric uncertainties. The former makes the traditional sampling methods such as Monte-Carlo and its variance-reduced variants (e.g. Latin Hypercube method) not practical because of their slow error convergence rate, while the latter invokes the "curse of dimensionality" that prohibits the use of tensor-product quadratures and tensor product stochastic collocation methods. In [10] and [13] sparse grid quadratures were employed in aerodynamic UQ problems due to uncertain airfoil geometry. Nevertheless as pointed out in [11] in case of a high number (e.g. $\geq$9) of variables, even sparse grid methods suffer limitations in applicability.

Recently, some methods addressing this challenge are gaining more attention, e.g. point-collocation non-intrusive polynomial chaos (NIPC) methods [9], Kriging methods [7] and maximum entropy (ME) methods [14]. The first two establish surrogate models that are cheaper to evaluate and perform UQ based on a large number of samples evaluated on the surrogate model. In [6] Kriging is shown to outperform Monte Carlo and Latin Hypercube methods in estimating the mean value of a bivariate Rosenbrock function. The maximum entropy method directly estimates the probability distribution function (pdf) of the SRQ by maximizing its entropy under the condition that some known statistical moments are honored. One common characteristic of the three methods is that they all admit scattered sampling scheme which leads to two virtues, i.e. robustness w.r.t. failed samples (due to, e.g., poor convergence, as often observed in CFD) and flexibility w.r.t. admission of an arbitrary number of samples. The latter virtue not only enables incorporation of pre-existing or additional samples as well as run-time adaptive sampling, but also makes the methods practical and convenient for problems with high number of variables. These features render the three methods more promising in the UQ using CFD models with geometric uncertainties. However, their relative performance for this particular problem remains to be compared.

In this work we use the Kriging, point-collocation NIPC and maximum entropy methods, and (for the purpose of comparison) also the quasi-Monte Carlo method to quantify the uncertainty in the lift and drag coefficients of an RAE2822 airfoil with randomly perturbed geometry and compare their efficiency. The number of CFD model evaluations is kept small ($\leq$200) in this numerical comparison to make it relevant to large-scale industrial applications.

2 Test Case

We consider the inviscid flow around the RAE2822 airfoil at a Mach number of 0.73 and an angle of attack of 2.0 degrees. The source of uncertainty is assumed to be the randomly perturbed airfoil geometry which is modeled by a Gaussian

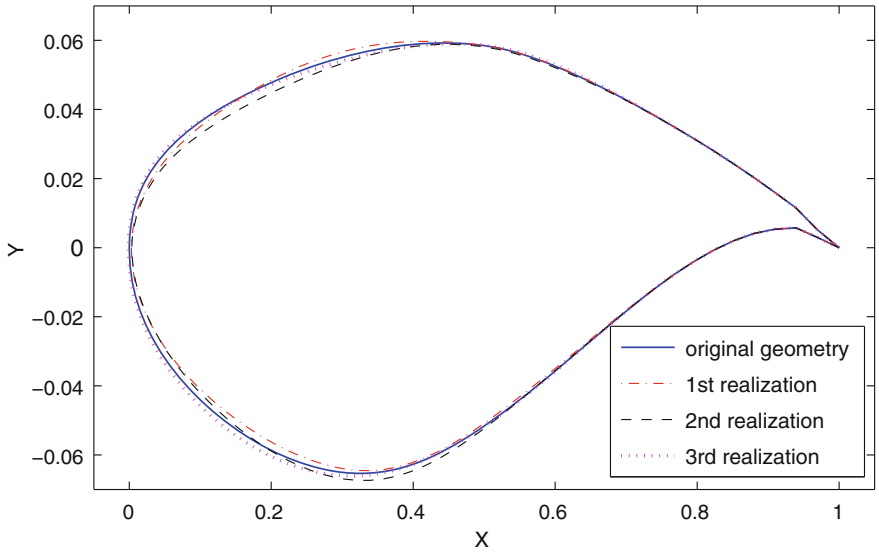

Fig. 1 Three realizations of the randomly perturbed airfoil geometry, with the perturbations three-times exaggerated

random field. By a Karhunen-Loève discretization the random field is approximated and parameterized by nine independent Gaussian variables that fill a vector $\boldsymbol{\xi} = \{\xi_1, \ldots, \xi_9\}$. A detailed description of this test case can be found in [13]. Figure 1 exemplifies three realizations of the perturbed RAE2822 airfoil geometry in which the shown perturbations are purposely exaggerated three times to make them observable.

This test case is used to set up a CFD simulation that takes the input variables $\boldsymbol{\xi} = \{\xi_1, \ldots, \xi_9\}$ and yields the lift and drag coefficients, C_ℓ and C_d, of the randomly perturbed airfoil. Hereafter the model is denoted as $f(\boldsymbol{\xi})$ in this paper. We compare the efficiency of the candidate methods in estimating some target statistics including the mean (μ_ℓ, μ_d), the standard deviation (σ_ℓ, σ_d), and the exceedance probabilities $P_{\ell,\kappa} = \text{Pro}\{C_\ell < \mu_\ell - \kappa \cdot \sigma_\ell\}$ and $P_{d,\kappa} = \text{Pro}\{C_d > \mu_d + \kappa \cdot \sigma_d\}$ with $\kappa = 2, 3$ of C_ℓ and C_d respectively. The accuracy of the statistics is judged by comparing with reference statistics obtained by QMC integration with a large sample number $(N = 5 \times 10^5)$.

3 Methods

Four UQ methods are applied to the test case. They include two surrogate modeling methods, i.e. gradient-enhanced Kriging (GEK) and gradient-assisted point-collocation polynomial chaos (GAPC), and two direct sampling methods, i.e. maximum entropy (ME) method and quasi-Monte Carlo (QMC) quadrature.

Since the gradients of the SRQ with respect to all nine variables are computed by an adjoint solver at an additional cost of approximately one evaluation of the CFD model, to count in this additional cost we introduce the term *elapse time-penalized sample number* $M = 2N$ for the two gradient-employing methods and $M = N$ for the rest, with N being the number of evaluations of the CFD model. The comparison was then made in term of M rather than N.

The CFD solver we use is the DLR-TAU code [5]. The geometry perturbation is implemented by using a mesh deformation tool based on radial basis functions incorporated in the DLR-TAU code as described in [8].

3.1 Quasi-Monte Carlo Quadrature

Quasi-Monte Carlo (QMC) quadrature [2] evaluates the CFD model with the variables $\boldsymbol{\xi}$ chosen to be elements of a *low discrepancy* sequence which achieves a higher degree of uniformity with respect to a given pdf than the pseudo-random sequence used in Monte Carlo methods does. The statistics of the SRQ are directly computed from the samples with the error bound of order $\mathcal{O}(N^{-1}(\log N)^d)$ in which d is the number of variables. In this work we use the Niederreiter low discrepancy sequence which in [12] is considered the most efficient if d is large. The Niederreiter sequence is generated by the program from [1].

3.2 Maximum Entropy Method

The maximum entropy (ME) method [14] approximates the pdf of the SRQ based on the sampled statistical moments. Let s represent the SRQ, in this work we assume its pdf takes the form of an exponential function of s, i.e. $P(s, \boldsymbol{\lambda}) = \exp[-(1 + \sum_{k=0}^{4} \lambda_{k+1} s^k)]$, with parameters $\boldsymbol{\lambda}$ maximizing the entropy:

$$\mathscr{E}[P(s, \boldsymbol{\lambda})] = -\int P(s, \boldsymbol{\lambda}) \ln P(s, \boldsymbol{\lambda}) \mathrm{d}s$$

under the constraints that the moments up to the fourth order are honored, i.e.

$$\int s^k P(s, \boldsymbol{\lambda}) \mathrm{d}s = \mathfrak{m}_k \ , \quad k = 0, 1, 2, 3, 4$$

The entropy maximizing parameters $\boldsymbol{\lambda}$ are identified by a two-phase technique, i.e. a genetic algorithm to find a promising starting point, followed by a Newton iteration as in [16], finalizing the local maximization.

The same set of samples as in the QMC quadrature are used to compute the moments $\mathfrak{m}_k$. The exceedance probabilities are obtained by integrating the $P(f, \boldsymbol{\lambda})$ over the corresponding sub-domain.

3.3 Gradient-Enhanced Kriging

Kriging [4] approximates $f(\boldsymbol{\xi})$ by a weighted linear combination of samples, i.e.,

$$\hat{f}(\boldsymbol{\xi}) = \gamma(\boldsymbol{\xi}) + \sum_{i=1}^{N} w_i(\boldsymbol{\xi}) f(\boldsymbol{\xi}_i)$$

where $f(\boldsymbol{\xi}_i)$ are N samples of SRQ, this process can also be viewed as an interpolation among the samples. The functions $\gamma(\boldsymbol{\xi})$ and $w_i(\boldsymbol{\xi})$ are determined by minimizing the variance of the error $\varepsilon = f(\boldsymbol{\xi}) - \hat{f}(\boldsymbol{\xi})$ with the constraint that the expectation of ε is zero and an assumption that $f(\boldsymbol{\xi})$ honors a spatial correlation model. We use direct gradient-enhanced Kriging (GEK) [3] that incorporates gradient information as secondary samples by an extended spatial correlation model that accommodates gradients. The GEK enforces the sampled gradients in the model. We implement GEK using the *Surrogate-Modeling for Aero-Data Toolbox (SMART)* [7] developed at DLR, opting for ordinary Kriging and a correlation model of spline type which is considered the most efficient for UQ in aerodynamic simulations in [11]. The hyper-parameters of the correlation model is fine-tuned to fit the sampled data by a maximum likelihood estimation [17].

For this UQ job we first establish a GEK surrogate model of $f(\boldsymbol{\xi})$ based on QMC samples of the CFD model, and compute the target statistics from a large number (10^5) of QMC sample on the surrogate model.

3.4 Gradient-Assisted Point-Collocation Polynomial Chaos (GAPC)

According to Wiener [15], $f(\boldsymbol{\xi})$ can be approximated by a truncated *polynomial chaos expansion* (PCE)

$$\hat{f}(\boldsymbol{\xi}) = \sum_{j=0}^{K} c_j \Psi_j(\boldsymbol{\xi}) \tag{1}$$

where Ψ_j is Hermite polynomial chaos (PC). The total number of terms is $K = (p + d)!/(p!d!)$ with d the number of variables and p the order of PC. A point-collocation polynomial chaos method is introduced in [9]. Here we use a gradient-employing version of it, i.e. the coefficients c_j are determined by solving the following system,

$$\boldsymbol{\Psi c} = \boldsymbol{f}$$

$\boldsymbol{\Psi}$ is a $N(1+d) \times K$ matrix where the first N rows are the values of the PC terms evaluated at N sample points, the second N rows the values of the PC's partial derivatives with respect to the first variable evaluated at N sample points, and so on until the partial derivatives with respect to the d-th variable. $\boldsymbol{f}$ is a vector of length $N(1+d)$ filled with sampled SRQ and the d derivatives at N points. $\boldsymbol{c}$ contains the K coefficients. The K is chosen to be half of the number of "conditions", $N(1+d)$, for the best performance according to [9].

For this UQ job we first establish a GAPC surrogate model of $f(\boldsymbol{\xi})$ based on QMC samples of the CFD model, and compute the mean and the variance of $f(\boldsymbol{\xi})$ directly from the coefficients,

$$\mu = c_0 \,, \qquad \sigma^2 = \sum_{j=1}^{K} (c_j)^2 \cdot \mathbb{E}[\Psi_j^2(\boldsymbol{\xi})] \tag{2}$$

The exceedance probabilities are computed from a large number (10^5) of QMC sample on the surrogate model.

4 Results and Discussion

The results of the efficiency comparison about C_ℓ are shown in Figs. 2 and 3. Those about C_d is not included due to the limit of size for this paper, they show the same "pattern" of efficiency in the methods as those about C_ℓ do. Figure 2 shows the errors of the four methods in estimating the target statistics of C_ℓ as a function of M. It is observed there that the two surrogate sampling-based methods, GEK and GAPC, are more efficient than the ME and QMC methods since the former two reduce their errors faster, and the GEK seems the most efficient one. Figure 3 shows the approximated pdf of C_ℓ obtained by GEK, GAPC and ME, comparing with the reference pdf. There we see that for the same computational effort, $M = 50$, GEK yields the most accurate pdf, followed by GAPC and ME. This is consistent with their relative performance in estimating the statistics.

The authors attribute the relatively better performance of the surrogate sampling-based methods to the fact that they utilize more information than the others with the same computational effort M, i.e. they use $(1+d)\frac{M}{2}$ conditions (SRQ samples and gradients) while the others use M conditions (SRQ samples only). As d, the number of variables, increases, this advantage is expected to increase. This is due to the cheaper cost of obtaining gradients by an adjoint solver given that the number of SRQ's is smaller than d.

From the results we also see that being theoretically equal to QMC in estimating statistical moments, the ME method only performs slightly better than QMC in estimating exceedance probabilities. The assumption of an exponential function for

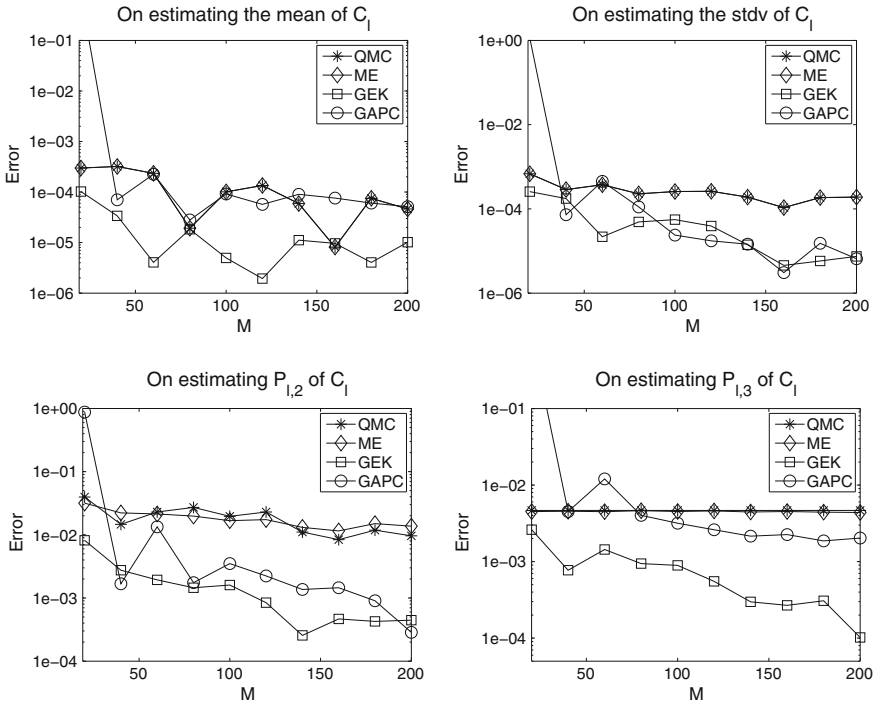

Fig. 2 Error in estimating mean, standard deviation (*upper row*) and exceedance probabilities (*lower row*) of C_ℓ

pdf in the ME method,though being oftenly adopted, might not be optimum for this particular problem.The results also show that GAPC seems not better than GEK in estimating exceedance probabilities. This could be explained by the tendency of "over shooting" of polynomial chaos in the outskirts of the domain as extrapolations are made there.

Nevertheless, the ME and GAPC method have their strong point that we have no burden of parameter optimization in running these methods.

5 Summary

Aerodynamic uncertainty quantification (UQ) problems arise from airfoil geometry perturbations are characterized by the numerousness of variables and high computational cost. To investigate efficiency of methods dealing this challenging we applied four methods that are robust in handling this problem, namely gradient-enhanced Kriging (GEK), gradient-assisted point-collocation polynomial chaos (GAPC), maximum entropy (ME) method and quasi-Monte Carlo (QMC) quadrature, to a test case in which the geometry of an RAE2822 airfoil is randomly perturbed. The four meth-

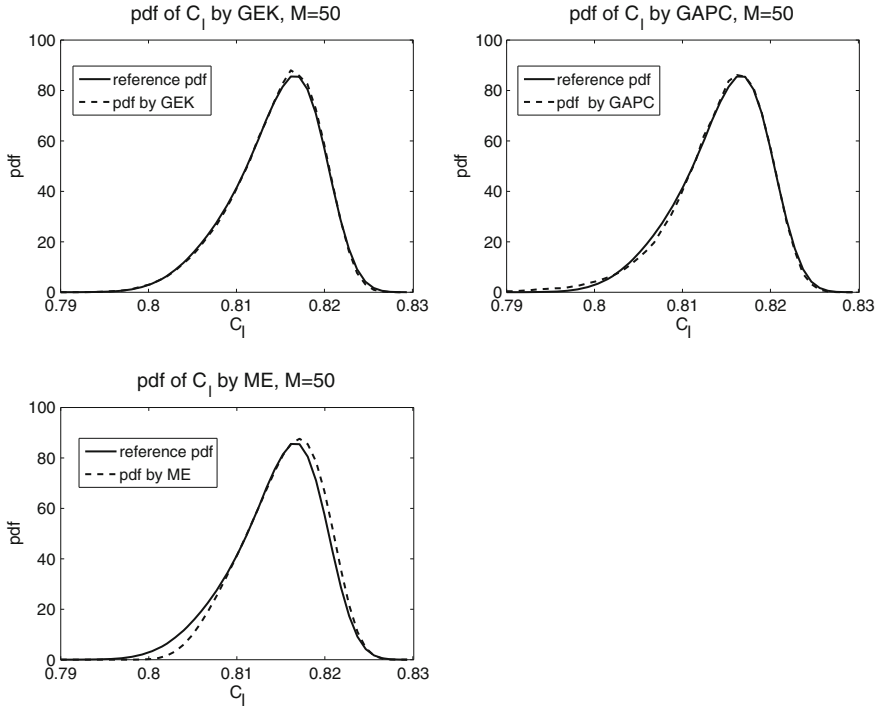

Fig. 3 Estimated pdf of C_ℓ using GEK, GAPC and ME methods, $M = 50$

ods were compared in their efficiency in estimating some statistics and probability distribution of the uncertain lift and drag coefficients. The results show that if the gradients can be obtained by relatively smaller cost than the system response quantity (SRQ), the sampling-based surrogate methods, GEK and GAPC, have an edge over the other two direct sampling-based methods. The GEK method is the most efficient, especially when the sample number is relatively small and in estimating the exceedance probabilities.

Acknowledgments The German national joint research project MUNA Management and Minimisation of Uncertainties and Errors in Numerical Aerodynamics has been funded by the German Ministry of Economics within the Luftfahrtforschungsprogramm IV under contract number 20A0604A.

References

1. Bratley, P., Fox, B.L., Niederreiter, H.: Programs to generate Niederreiter's low-discrepancy sequences. ACM Trans. Math. Softw. **20**(4), 494–495 (1994)
2. Caflisch, R.E.: Monte Carlo and quasi-Monte Carlo methods. Acta Numerica **7**, 1–49 (1998)

3. Chung, H.-S., Alonso, J.J.: Using gradients to construct cokriging approximation models forhigh-dimensional design optimization problems. AIAA paper 2002–0317 (2002)
4. Cressie, N.: Statistics for Spatial Data. Wiley, New York (1991)
5. Gerhold, T., Friedrich, O., Galle, M., Evans, J.: Calculation of complex three-dimensional configurations employing theDLR-TAU-Code. AIAA paper 97–0167 (1997)
6. Giunta, A.A., Eldred, M.S., Castro, J.P.: Uncertainty quantification using response surface approximation. In: 9th ASCE Specialty Conference on Probabolistic Mechanics and Structural Reliability, Albuquerque, New Mexico, USA (2004)
7. Han, Z.H., Görtz, S., Zimmermann, R.: Improving variable-fidelity surrogate modeling via gradient-enhancedkriging and a generalized hybrid bridge function. J. Aeros. Sci. Technol. (2012)
8. Heinrich, R., Kroll, N., Neumann, J., Nagel, B.: Fluid-structure coupling for aerodynamic analysis and design: a DLRperspective. AIAA paper 2008–561 (2008)
9. Hosder, S., Walters, R.W., Balch, M.: Efficient sampling for non-intrusive polynomial chaos applicationswith multiple uncertain input variables. AIAA paper 2007–1939 (2007)
10. Litvinenko, A., Matthies, H.G.: Sparse data formats and efficient numerical methods for uncertaintiesquantification in numerical aerodynamics. In: ECCM IV: Solids, Structures and Coupled Problems in Engineering (2010)
11. Liu, D.S.: A best practice guide: efficient quantification of aerodynamic uncertainties. Technical report, DLR, 2012. IB 124–2012/2
12. Niederreiter, H.: Random Number Generation and Quasi-Monte Carlo Methods. SIAM, Philadelphia (1992)
13. Schillings, C., Schulz, V.: On the influence of robustness measures on shape optimization withstochastic uncertainties. Technical report, Trierer Forschungsbericht 12–2, Universität Trier, 2012
14. Sobczyk, K., Trcebicki, J.: Approximate probability distributions for stochastic systems: maximumentropy method. Comput. Methods Appl. Mech. Eng. **168**(1–4), 91–111 (1999)
15. Wiener, N.: The homogeneous chaos. Amer. J. Math. **60**, 897–936 (1938)
16. Zellner A., Highfield, R.A.: Calculation of maximum entropy distributions and approximation ofmarginal posterior distributions. J. Econometrics **37**, 195–209 (1988)
17. Zimmermann, R.: Asymptotic behavior of the likelyhood function of covariance matricesof spatial gaussian processes. J. App. Math. (2010). Article ID 494070

Fluid-Dynamic Optimization of the Cabin Air Outlet Do728-KLA with Adjoint Sensitivity Analysis

Anne Lincke, Gerrit Lauenroth, Thomas Rung and Claus Wagner

Abstract This chapter is concerned with shape optimization based on continuous adjoint sensitivity analysis with respect to fluid-dynamic cost functions such as uniformity of flow or pressure loss. The solution of the primal and the corresponding adjoint incompressible Reynolds-averaged Navier-Stokes (RANS) equations leads to the sensitivity, which specifies in combination with a normal vector and a proper step size, how body contours should be modified in order to obtain an improvement of the cost function toward a local minimum. Focal point is the application to an aircraft cabin air outlet. According to the specification of the sensitivity the initial geometry is deformed. A further RANS simulation illustrates numerically that the cost function notably improves. Additionally, Particle Image Velocimetry (PIV) measurements are accomplished in order to validate the numerical results.

1 Introduction

The adjoint sensitivity analysis has become an established technique for shape optimization when many degrees of freedom are present [1–3]. Contrary to generic optimization methods, which require at least one RANS simulation for each design

A. Lincke (✉) · T. Rung
Institute for Fluid Dynamics and Ship Theory, Hamburg University of Technology, Hamburg, Germany
e-mail: anne.lincke@tuhh.de

T. Rung
e-mail: thomas.rung@tuhh.de

G. Lauenroth · C. Wagner
Institute of Aerodynamics and Flow Technology, Department Fluid Systems, German Aerospace Center (DLR), Göttingen, Germany
e-mail: gerrit.lauenroth@dlr.de

C. Wagner
e-mail: claus.wagner@dlr.de

A. Dillmann et al. (eds.), *New Results in Numerical and Experimental Fluid Mechanics IX*, Notes on Numerical Fluid Mechanics and Multidisciplinary Design 124,
DOI: 10.1007/978-3-319-03158-3_8,

parameter, the computational cost of the adjoint shape optimization process is independent of the number of degrees of freedom. The continuous adjoint approach is based on an augmented cost function, which includes the primal governing equations (here the RANS equations) as constraints, which have to be satisfied in the computational domain. Application of the variational operator to the augmented cost function leads to the adjoint RANS equations and the sensitivity equation, which indicates the behavior of the cost function with the variation of the shape. Subsequently, gradient-based optimization techniques like steepest-descent might guide the morphing process of the shape toward a local minimum of the cost function. The ansatz is restricted to small variations in surface-normal direction as the variation is linearized. This chapter will focus upon the application of adjoint sensitivity analysis to an aircraft cabin air outlet of the Dornier Do728 jet (Do728-KLA). The governing cost function is uniformity of the flow at the outlet with respect to a reference velocity U_d. Steady-state simulations, solving primal and adjoint RANS equations, are performed with the open-source finite volume solver open field operation and manipulation (OpenFOAM) [4]. Additionally, PIV measurements are performed, which maintain the veracity of the numerical results.

2 Theory

We consider a fluid-dynamic cost function $J\,(u_i,\,p,\,b)$, which depends on the primal flow properties velocity u_i, pressure p, and the shape b, according to [5, 6]. The object is to minimize the cost function J by changing the shape b of the design surface Γ_dsg provided that the primal incompressible RANS equations are fulfilled on the flow domain Ω. Hence, the problem can be stated as

$$\min J\,(u_i,\,p,\,b) \;\text{ subject to} \tag{1}$$

$$R_i = \frac{\partial}{\partial x_j} u_i u_j + \frac{\partial p^*}{\partial x_i} - \frac{\partial}{\partial x_j}\left[2\nu_\mathrm{g} S_{ij}\right] - f_i = 0 \tag{2}$$

$$Q = -\frac{\partial u_i}{\partial x_i} = 0\ , \tag{3}$$

where R_i and Q denote the residual form of the momentum and continuity equation, with the effective kinematic viscosity $\nu_\mathrm{g} := \nu + \nu_\mathrm{t}$ as sum of kinematic turbulent and molecular viscosity, shear stress tensor $S_{ij} = \frac{1}{2}\left(\frac{\partial u_i}{\partial x_j} + \frac{\partial u_j}{\partial x_i}\right)$, the modified mean pressure $p^* = \frac{p+\frac{2}{3}k\rho}{\rho}$ with density ρ and turbulent kinetic energy k, and f_i a constant body force. Thus, we have a constrained optimization problem, which can be handled by enhancement with proper Lagrangian multipliers $\hat{u}_i$, $\hat{p}$, which are denoted as adjoint velocity and adjoint pressure. In this manner, we obtain the augmented cost function $\tilde{J}$

$$\tilde{J} := J + \int_{\Omega} \hat{u}_i R_i + \hat{p} Q \, d\Omega \ . \tag{4}$$

The variational operator δ is applied to the augmented cost function $\tilde{J}$, consisting of convective, local, and geometric variations due to a displacement of the design b

$$\delta\tilde{J} := \delta J + \int_{\Omega} \hat{u}_i \delta R_i + \hat{p}\delta Q \, d\Omega \ . \tag{5}$$

Integration by parts leads to a form where variations of primal flow variables can be factored out. The remainder are the adjoint RANS equations

$$-2u_j \hat{S}_{ij} = \frac{\partial}{\partial x_j}\left(2\nu_{\mathrm{g}}\hat{S}_{ij} - \hat{p}\delta_{ij}\right) \tag{6}$$

$$\frac{\partial \hat{u}_i}{\partial x_i} = 0 \tag{7}$$

with $\hat{S}_{ij} := \frac{1}{2}\left(\frac{\partial \hat{u}_i}{\partial x_j} + \frac{\partial \hat{u}_j}{\partial x_i}\right)$, and the adjoint boundary conditions for wall, inlet

$$\hat{u}_{\mathrm{t}} = 0, \tag{8}$$

$$\hat{u}_{\mathrm{n}} = -\frac{\partial j_{\Gamma}}{\partial p} \tag{9}$$

$$\frac{\partial \hat{p}}{\partial n} = 0 \ , \tag{10}$$

and for the outlet

$$\hat{p} = u_i \hat{u}_i + u_{\mathrm{n}}\hat{u}_{\mathrm{n}} + \nu_{\mathrm{g}}\frac{\partial \hat{u}_{\mathrm{n}}}{\partial n} + \frac{\partial j_{\Gamma}}{\partial u_{\mathrm{n}}} \tag{11}$$

$$0 = u_{\mathrm{n}}\hat{u}_{\mathrm{t}} + \nu_{\mathrm{g}}\frac{\partial \hat{u}_{\mathrm{t}}}{\partial n} + \frac{\partial j_{\Gamma}}{\partial u_{\mathrm{t}}}, \tag{12}$$

where j_{Γ} denotes the boundary-declared objective functional integrand, n denotes the normal and t the tangential component. The above boundary conditions are valid for ducted flows with typical inlet, outlet, and wall boundary conditions, assuming *frozen turbulence*, i.e. $\delta\nu_{\mathrm{g}} = 0$, for the cost function J, evaluated at the surface Γ_{obj}, disjoint to the design boundary Γ_{dsg}, i.e. $\Gamma_{\mathrm{dsg}} \cap \Gamma_{\mathrm{obj}} = \emptyset$, and for Γ_{dsg} defined on walls only. Note that these derivations do not impose a condition for the adjoint pressure $\hat{p}$; the zero gradient boundary condition of p at wall and inlet is applied to $\hat{p}$ as well, in order to ensure the well-posedness of the adjoint equation system (see [5]). The solution of the primal and adjoint flow equations leads to the sensitivity

$$\frac{\partial \tilde{J}}{\partial n} = -\int_{\Gamma_{\mathrm{dsg}}} \nu_{\mathrm{g}}\frac{\partial u_{\mathrm{t}}}{\partial n}\frac{\partial \hat{u}_{\mathrm{t}}}{\partial n} d\Gamma_j, \tag{13}$$

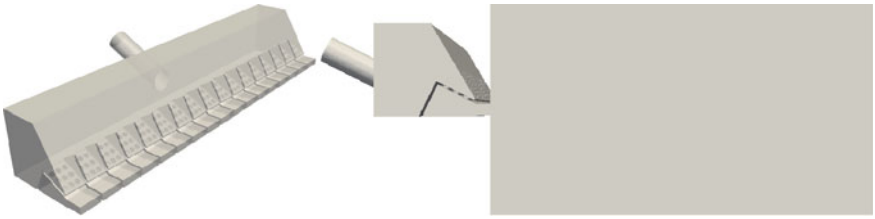

Fig. 1 Geometry of the cabin air outlet Do728, with box (*right*) for simulating the outflow

which displays the gradient of the cost function and does not depend on variations of primal flow properties. Contrary to the discrete-adjoint method, the continuous adjoint technique starts with a volume-based sensitivity (5) and ends up with a surface-based sensitivity which avoids the calculation of metrics variations over the computational domain. By combination of the sensitivity with the reference normal vector and a proper step size the application of a gradient-based optimization approach like steepest-descent leads to an optimized design.

3 Cabin Air Outlet Do728-KLA

The geometry of the cabin air outlet Do728-KLA consists of a 178 mm long circular duct with a diameter of 57 mm, followed by a 185 mm (length) $\times$ 1000 mm (width) $\times$ 165 mm (height) angled chamber, including a deflector and 17 hole plates, and subsequently 17 air outlets (see Fig. 1).
The object is to minimize the cost function *uniformity of the velocity at the outlet* with respect to a desired velocity U_d

$$J = \oint_{\Gamma_\mathrm{obj}} \frac{1}{2} (U - U_\mathrm{d})^2 \, d\Gamma \ , \tag{14}$$

which is evaluated at the outlet segments. Furthermore, the design boundary consists of the basement of the chamber and the deflector. The desired velocity U_d is set to $U_\mathrm{d} = (0.8916\ 0\ 0)$ due to fulfilment of mass conservation. Via adjoint sensitivity analysis the optimization is performed, i.e. the primal and adjoint RANS equations are solved numerically.

4 Numerical Simulation

A semi-implicit pressure linked equation (SIMPLE) solver is used for solving the primal and the adjoint RANS equations numerically. The Reynolds-number, based on the diameter of the pipe, is $Re = 27.000$ with an inlet velocity magnitude of $|\mathbf{u}| = 7 \, \frac{\mathrm{m}}{\mathrm{s}}$. Turbulence is modeled via the high-Re $SST\ k - \omega$ turbulence model.

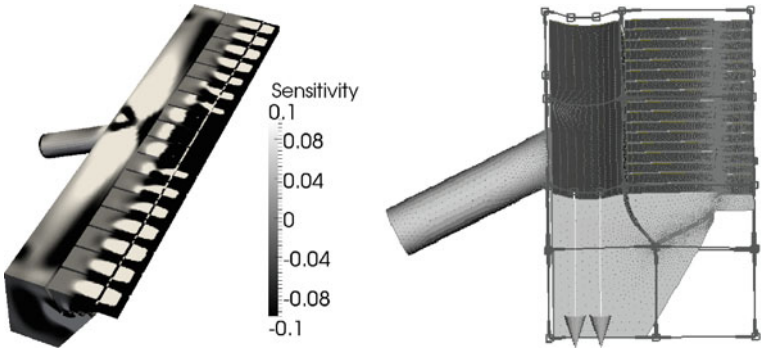

Fig. 2 Contour plot of sensitivity for original geometry (*left*) and morphing model with optimized geometry (*right*) of the cabin air outlet Do728. The deformation of the surface mesh is increased in the *middle* of the cabin air outlet

Besides, the boundaries are assigned to typical ducted flow properties, consisting of inlet, outlet, and wall. After a satisfactory convergence (with an initial residual value of $1e^{-6}$ based on the current values of primal and adjoint fields), the sensitivity is computed in a postprocessing step. Note that for this case the supplementary *advection term* which arises in the adjoint equations is neglected for convergence reasons, see [3]. The cost function is evaluated for the mesh with a plenum behind the cabin air outlet (Fig. 1, right) in a cell zone, which corresponds to the outlet of the mesh without plenum (Fig. 1, left), and is normalized with the volume of the cell zone. The evaluation of the cost function for the original design results in a value of $J = 0.08027 \frac{\mathrm{m}^2}{\mathrm{s}^2}$. The sensitivity (Fig. 2, left) is automatically mapped to the morphing parameters of automatic net-generation for structural analysis (ANSA) [7] and the mesh is morphed accordingly (see Fig. 2, right).
A second RANS simulation is performed for the deformed mesh. The cost function is evaluated again after a satisfactory convergence and has a value of $J = 0.0714 \frac{\mathrm{m}^2}{\mathrm{s}^2}$. It shows an improvement of 11 % compared to the initial value of the cost function. As the gradient-based optimization technique steps toward a local minimum with every design cycle, we perform a second design cycle based on the morphed mesh and the primal and adjoint velocity fields obtained from it, which generates an improvement of 13 % ($J = 0.0699 \frac{\mathrm{m}^2}{\mathrm{s}^2}$) compared to the initial value, which is a further improvement of 2 %. The total pressure loss improved 1 %. Figure 3 illustrates the results for the velocity magnitude of the initial geometry and of the deformed geometries.

5 Experimental Validation

To validate the results of the RANS simulation, the homogeneity of the flow velocity of the original and the improved air outlet is investigated experimentally using PIV, see [8]. To conduct PIV, the fluid is seeded with tracer particles, which are small

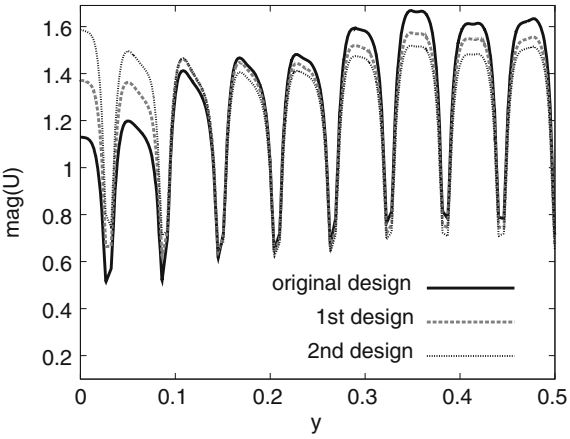

Fig. 3 Velocity magnitude along one half of the outlet (x-axis) for different shapes

enough to follow the flow. The particles are illuminated with a planar laser beam. The magnitude of the inlet velocity is $|\mathbf{u}| = 7\,\frac{\mathrm{m}}{\mathrm{s}}$.

Two pictures of the particles are taken with a small time difference. Using the software PIVview, the flow velocity field can be calculated from the particle displacement computed from the two pictures taken at different times. The experimental setup is depicted in Fig. 4 and consists of a Nd:YAG laser, whose beam is shaped with a light-sheet optic to illuminate the measurement region.

The air flowing through the outlet is supplied by a radial fan and the flow velocity is measured with a volumetric flow meter. The cutting plane is positioned orthogonal and central to the outlet segments. Furthermore, DEHS seeding (see Table 1) is added to the flow at the inlet of the radial fan. Due to safety reasons and to prevent external influences on the studied flow, the setup is encased with a curtain to avoid scattered light. All details of the PIV measurement are listed in Table 1. A comparison of the measured velocity fields in horizontal planes is presented in Fig. 5. Regarding the homogeneity of the flow, the original and the improved outlet geometries produce considerably different velocity distributions. The averaged velocity field of the original outlet, shown in Fig. 5 (left), is characterized by pronounced maxima, whereas the flow of the modified outlet generates a more homogeneous mean flow outside the outlet (see Fig. 5, right).

In Fig. 6 the velocity distribution, obtained from the PIV measurement, is directly compared to the velocity field from the numerical simulations at a distance of 5 cm from the air outlet.

The velocity distribution obtained from the experiments is comparable to the velocity distribution from the numerical simulations. The differences can be explained by measuring inaccuracy and modeling errors in the RANS calculation. However, both results show clearly the improvement of the homogeneity at the outlet.

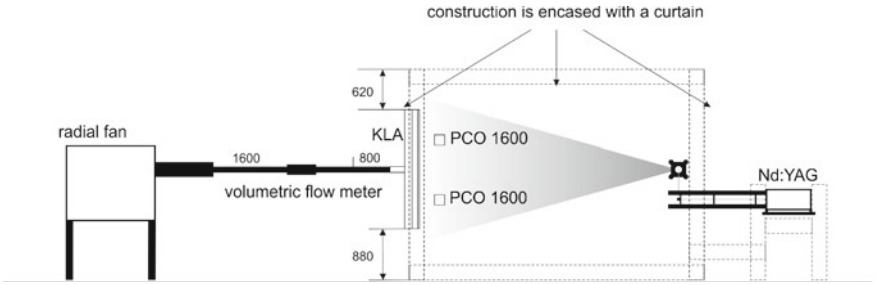

Fig. 4 PIV measurement setup

Table 1 PIV measurement parameter

Laser	2 × neodymium-doped yttrium aluminum garnet (N_d:YAG) laser 532 nm 350 mJ, repetition rate 10 Hz
Cameras	2 × PCO1600, resolution: 1600 × 1200 pixel
Light-sheet optics	−150 mm biconcave, 300 mm, F 100 mm Zyl.
Scattering particles	Di-Ethyl-Hexyl-Sebacat (DEHS) particles, size: 0.5–1.5 µm
Volume-flow rate	287–4300 l/min with an accuracy of +/– 2.5 %, typical: 1080 l/min
Fan	Steplessly variable radial fan
Fabrication of the outlet	Rapid prototyping with PA2200
Field of view	2 × 600 mm × 420 mm
Interrogation window	12 × 12 mm
# averaged vector fields	694
Vector distance	6 × 6 mm

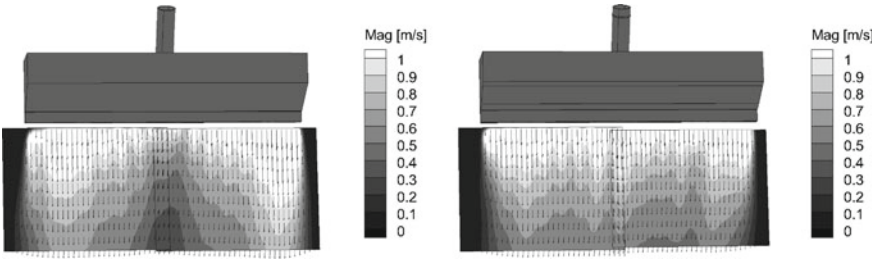

Fig. 5 PIV velocity field, original (*left*) and improved (*right*) outlet in horizontal planes

6 Summary and Conclusion

The shape of the cabin air outlet Do728-KLA was optimized via adjoint sensitivity analysis with respect to the cost function uniformity of flow at the outlet. Therefore, the primal and adjoint RANS equations were solved numerically and, combined with the steepest descent approach and a mesh morphing tool, the sensitivity directly led to an improved design. Two design cycles have been executed. After the first design

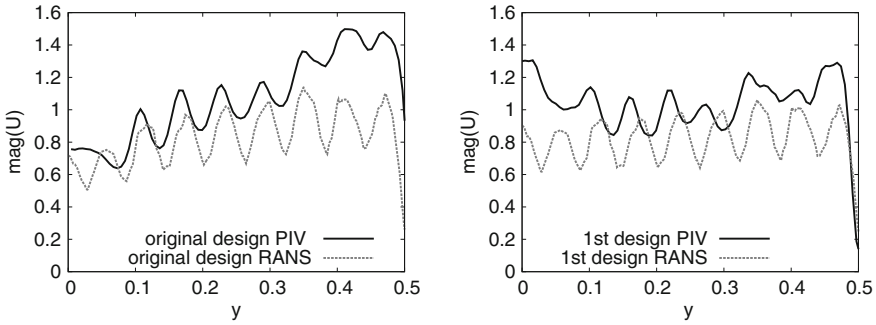

Fig. 6 Comparison of the computed and measured velocity magnitude distribution in the *center* of the outlet plane for the initial (*left*) and the modified (*right*) design

cycle an improvement of 11 % for the cost function was obtained. A second design cycle led to a further improvement of 2 %.
PIV measurements werde accomplished to support the numerical results. Computed and measured velocity distributions, obtained at a distance of 5 cm from the air outlet, are compared and agree well. The results clearly show the improvement of the homogeneity of the velocity distribution at the outlet. Therefore, the experiments confirm the geometrical modification proposed by the RANS simulations. Thus, in spite of the performed simplifications (neglection of the advection term, *frozen turbulence*) the adjoint sensitivity analysis led to a significant improvement of the cost function.

Acknowledgments The first author is grateful to the German Ministry of Economy and Technology (BMWi) funding the project PROTEG under the aegis of LUFO4 framework program.

References

1. Jameson, A.: Aerodynamic design via control theory. J. Sci. Comput. **3**, 233–260 (1988)
2. Pironneau, V.: On optimum design in fluid mechanics. J. Fluid Mech. **64**, 97–110 (1974)
3. Löhner, R., Soto, O.: On the computation of flow sensitivities from boundary integrals. In: 42nd AIAA Aerospace Sciences Meeting and Exhibit, AIAA-2004-0112, American Institute of Aeronautics and Astronautics (2004)
4. OpenFOAM: The Open Source CFD Toolbox. User Guide Version 1.6 (2009)
5. Othmer, C.: A continuous adjoint formulation for the computation of topological and surface sensitivities of ducted flows. Int. J. Numer. Meth. Fluids **58**, 861–877 (2008)
6. Stück, A., Rung, T.: Adjoint RANS with filtered shape derivatives for hydrodynamic optimisation. Comput. Fluids **47**(1), 22–32 (2011)
7. ANSA version 13.2.1 User's Guide, BETA CAE Systems S.A. (2011)
8. Raffel, M., Willert, C.E., Wereley, S.T., Kompenhans, J.: Particle Image Velocimetry. Springer, New York (2007)

Part III
Turbulence Research and Turbulence Modeling

Geometrical Features of Streamlines and Streamline Segments in Turbulent Flows

Philip Schaefer, Markus Gampert, Fabian Hennig and Norbert Peters

Abstract Streamlines constitute natural geometries in turbulent flows. In this work streamlines are segmented based on local extrema of the field of the absolute value of the velocity along the streamline coordinate. Streamline segments are parameterized based on their arclength and a theoretical scaling of the mean length with the geometric mean of the Kolmogorov length and the Taylor microscale is derived and found to be in good agreement with direct numerical simulations.

1 Introduction

One approach which has greatly benefited from the recent advances in high performance computing in turbulence research is to analyze turbulent inherent geometries. In this spirit, vortex structures have been identified and analyzed for instance by She et al. [1] and Kaneda et al. [2]. However, vortex tubes and sheets do not allow a unique and space-filling decomposition of the flow field into unambiguous sub-ensembles. This problem was overcome by Wang and Peters [3, 4] in their concept of dissipation elements, an approach which has its roots in early works by Gibson [5] who analyzed the role of extreme points in turbulent scalar mixing processes. This concept, based on gradient trajectories, allows the decomposition of turbulent scalar fields into smaller sub-units. By calculating gradient trajectories in direction of ascending and descending scalar gradients, a local minimum and a local maximum point are reached. Dissipation elements are then defined as the spatial region from which all gradient trajectories reach the same pair of maximum and minimum points in a scalar field. The most important feature of dissipation elements is that they are space-filling and unambiguous, meaning that at any instant in time the

P. Schaefer (✉) · M. Gampert · F. Hennig · N. Peters
Institut für Technische Verbrennung, Templergraben 64, 52056 Aachen, Germany
e-mail: pschaefer@itv.rwth-aachen.de
http://www.itv.rwth-aachen.de

A. Dillmann et al. (eds.), *New Results in Numerical and Experimental Fluid Mechanics IX*,
Notes on Numerical Fluid Mechanics and Multidisciplinary Design 124,
DOI: 10.1007/978-3-319-03158-3_9,

turbulent scalar field can be decomposed in a determined manner. Then, based on the much simpler conditional statistics within the dissipation elements and the knowledge of their statistical distribution (in terms of joint probability density functions) the complicated statistics of the entire scalar field can be reconstructed. Successful examples of this approach can be found in [6, 7]. However, one major shortcoming of the theory of dissipation elements is that it is only applicable to turbulent scalar fields. In order to also apply this successful theory to the turbulent velocity field itself, Wang [7] proposed to study streamlines in turbulent velocity fields. The geometrical properties of particle paths (the analogon to streamlines in an evolving turbulent field) have for instance been studied by Rao [8] and Braun et al. [9], whose ideas have been extended to the geometrical properties of streamlines by Schaefer et al. [10]. Streamlines are not Galilei invariant, meaning that the chosen frame of reference determines the streamline topology. Thus, one has to choose an appropriate frame of reference when analyzing turbulent flow fields based on streamlines. In the course of this work this frame of reference will be the fluctuating velocity field with zero mean as from a geometrical point of view we are only interested in the geometry and topology of the fluctuating field, which is often used to isolate "pure" turbulent physics without the interaction with solid walls, mean gradients or alike. As streamlines are a-priori infinitely long, we follow [7] and partition streamlines into segments based on local extreme points of the absolute value u along the streamline, i.e. points where the projected gradient $u_s = t_i \partial u / \partial x_i = 0$ vanishes. These points have been shown [11] to constitute an isosurface in space. Then, as in the context of dissipation elements, we parameterize streamlines by their arclength l and the velocity difference at the end points Δ. This work is concerned with the probability density function of the length l and the scaling of the mean length l_m.

2 Direct Numerical Simulation

In the following we will list the specific numerical procedures used for the different cases, whose parameters are summarized in Table 1. All cases have in common that a pseudo-spectral method in space and a second-order Adams-Bashforth method in time are used. The computations are performed in a periodic box of length 2π and aliasing errors are eliminated by isotropic truncation using the $2/3$ rule. Computations were performed on an IBM BlueGene/P machine at the research center Jülich.

- **Homogeneous isotropic decaying turbulence**: For the two decaying turbulence cases the initial velocity field is random and isotropic and is generated so that it satisfies a prescribed energy spectrum. The initial energy spectrum is taken from [12], for details, see [13].
- **Homogeneous isotropic forced turbulence**: For the forced case we employ a forcing scheme proposed by [14]. The DNS of the forced case reaches a steady state after several hundred iterations at which all statistical quantities fluctuate around a mean value. For details, see [15].

Table 1 Parameters of the different DNS cases

DNS case	1	2	3	4
Flow type	Decaying	Decaying	Forced	Shear
No. of grid cells	1024^3	1024^3	1024^3	1024^3
Reynolds number Re_λ	50	116	206	300
Viscosity ν	$5 \cdot 10^{-4}$	$1 \cdot 10^{-4}$	$2.0 \cdot 10^{-3}$	$5 \cdot 10^{-4}$
Kinetic energy k	$4.9 \cdot 10^{-2}$	$3.4 \cdot 10^{-2}$	12.0	3.07
Dissipation ε	$1.3 \cdot 10^{-2}$	$5.9 \cdot 10^{-3}$	11.3	1.39
Kolmogorov scale η	0.01	$3.6 \cdot 10^{-3}$	$5.2 \cdot 10^{-3}$	$3.1 \cdot 10^{-3}$
Taylor length λ	0.139	$7.6 \cdot 10^{-2}$	0.146	0.105
Integral time τ_{int}	3.88	5.76	1.06	2.21
Kolmogorov time τ_η	0.196	0.130	0.013	0.019
Resolution $\Delta x/\eta$	0.610	1.69	1.19	1.98
Mean shear S	–	–	–	1.5

- **Homogeneous shear turbulence**: For this flow we use a coordinate transformation with a moving frame attached to the mean flow, cf. [16]. However, to reset the distortion of the attached grid a remeshing procedure is periodically applied. For a detailed description of the algorithm see [17].

3 A Model for the Length Distribution of Streamline Segments

Based on prior works, Schaefer et al. [11] derived a model equation for the normalized probability density function of the length of streamline segments $\tilde{P}(\tilde{l}) = l_m P(l/l_m)$,

$$\frac{\partial \tilde{P}(\tilde{l},\hat{\tau})}{\partial \hat{\tau}} + \frac{\partial}{\partial \tilde{l}}\left[\tilde{a}_1(\tilde{l})\tilde{P}(\tilde{l},\hat{\tau})\right] = \Lambda_c\left(2\int_0^\infty \tilde{P}(\tilde{l}+\tilde{z},\hat{\tau})d\tilde{z} - \tilde{l}\tilde{P}(\tilde{l},\hat{\tau})\right) + 2\Lambda_a\left(\int_0^{\tilde{l}} \frac{\tilde{y}}{\tilde{l}}\tilde{P}(\tilde{l}-\tilde{y},\hat{\tau})\tilde{P}(\tilde{y},\hat{\tau})d\tilde{y} - \tilde{P}(\tilde{l},\hat{\tau})\right). \tag{1}$$

For a detailed derivation of Eq. 1 the reader is referred to [11]. In the following the different terms will briefly be discussed and related to their physical sources. The different terms in Eq. 1 represent the different mechanisms which influence the temporal length evolution of streamline segments belonging to a length class l. The first term on the l.h.s. is the unsteady term which in the numerical solution is sought to vanish to obtain a steady solution. The second term on the l.h.s. describe so called "slow changes" of streamline segments, where $\tilde{a}_1$ denotes the normalized drift velocity in phase space.

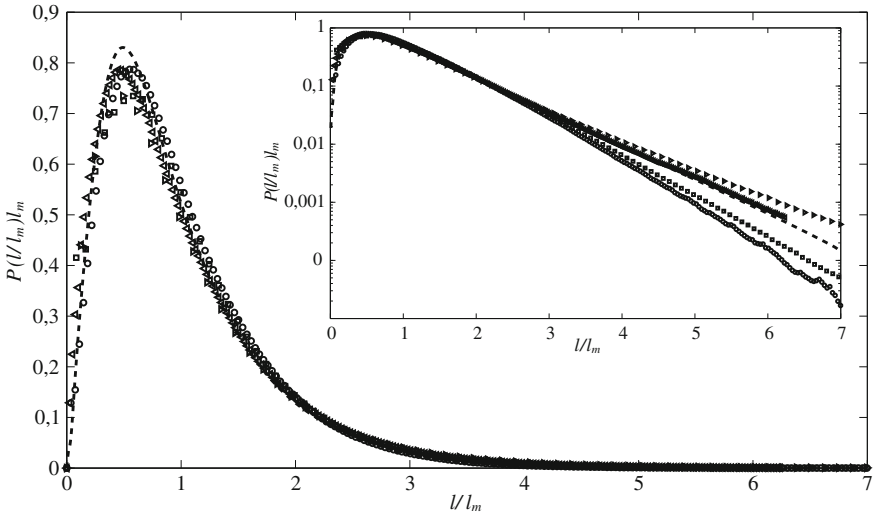

Fig. 1 Comparison of the normalized pdf $\tilde{P}(\tilde{l})$ from DNS cases 1–4 with the model solution (Eq. 1)

On the other hand streamline segments are subject to so called "fast changes" which are attributed to the local random distortion of the velocity field which yields non-local abrupt changes in the geometry of the streamline segment. These fast changes result in the four integral terms on the r.h.s. of Eq. 1 which have been modeled as a stationary Poisson like cutting- and reconnection process with the two frequencies Λ_c (cutting frequency, corresponds to the new creation of extrema within streamline segments and results in the cutting of the latter) and Λ_a (reconnection frequency, corresponds to the disappearance of extrema and the subsequent reconnection of two adjacent streamline segments).

Figure 1 shows the normalized pdfs $\tilde{P}(\tilde{l})$ obtained from the four DNS cases (symbols) and the steady solution of Eq. 1 where for the drift velocity the ansätze obtained in [11] have been used. A quite good agreement of the DNS data with the model can be observed, revealing the linear rise at the origin as well as the exponential tails, which are further highlighted in the log-lin inset. The maximum of all pdfs occur at $\tilde{l} \approx 0.5$ with a value of $\tilde{P}_{max} \approx 0.75$ where the model slighty overpredicts the maxima of the DNS data which in themselves vary slightly from one DNS case to another. As the different data collapse well, the Reynolds number independence predicted by the model can be confirmed with a further independence of the type of the flow under consideration as the data not only contains homogeneous isotropic decaying cases, but also a forced and a homogeneous shear flow. In addition, the model shows that the only relevant length scale of the distribution of the length of streamline segments is the mean length l_m. This raises the question how the mean length scales with turbulent length scales of the flow under consideration, a question that will be adressed in the following.

4 Scaling of the Mean Length of Streamline Segments

In order to reconstruct the dimensional pdf of a particular flow from the normalized quasi-universal model solution one needs the scaling of the mean length l_m with characteristic mean turbulent quantities. Such a scaling is proposed in the following based on dimensional grounds.

Along a streamline the arclength s serves as a one-dimensional coordinate and the variation of the absolute value $u(s)$ can be viewed as a one-dimensional variation along s. Let us in this context determine the life-time of an extreme point. The vicinity of an extreme point is mainly diffusion controlled so that in a coordinate system moving with it (Lagrangian view) we can model the evolution of the u profile by a simple diffusion equation

$$\frac{\mathrm{D}u}{\mathrm{D}t} \approx \nu \frac{\partial^2 u}{\partial s^2}. \tag{2}$$

Within this framework we can estimate its characteristic life-time t_a as

$$t_a \propto \frac{l_a^2}{\nu}, \tag{3}$$

where l_a denotes its characteristic size.

It can be estimated as follows by an expansion of the scalar u field around it, yielding

$$l_a^2 \propto \frac{u_0}{u_{ss}}. \tag{4}$$

where u_0 is the value of the scalar at the extreme point and $u_{ss} = \partial^2 u/\partial s^2$ its second derivative in direction of the streamline evaluated at the extreme point which is located at s_0. Figure 2 illustrates the scenario along a streamline and displays all relevant scales.

Assuming statistical independence of u_0 (being a large scale quantity) and u_{ss} (being a small scale quantity) at the extreme point let us average over all extrema to obtain

$$\langle l_a \rangle \propto \left(\frac{\langle u_0^2 \rangle^{1/2}}{\langle u_{ss}^2 \rangle^{1/2}} \right)^{1/2}. \tag{5}$$

Note the similarity to the result obtained by Rice's theorem, cf. [18, 19], for the mean distance between zero crossings of u, i.e. the mean distance of stagnation points. However, in our case the second derivative comes into play as we are considering the zero crossings of the gradient of u rather than of u itself.

Following Kolmogorov's similarity hypothesis [20, 21], the r.m.s. of the second derivative u_{ss}, being a purely small scale quantity, should scale solely with the mean energy dissipation ε and the viscosity ν yielding

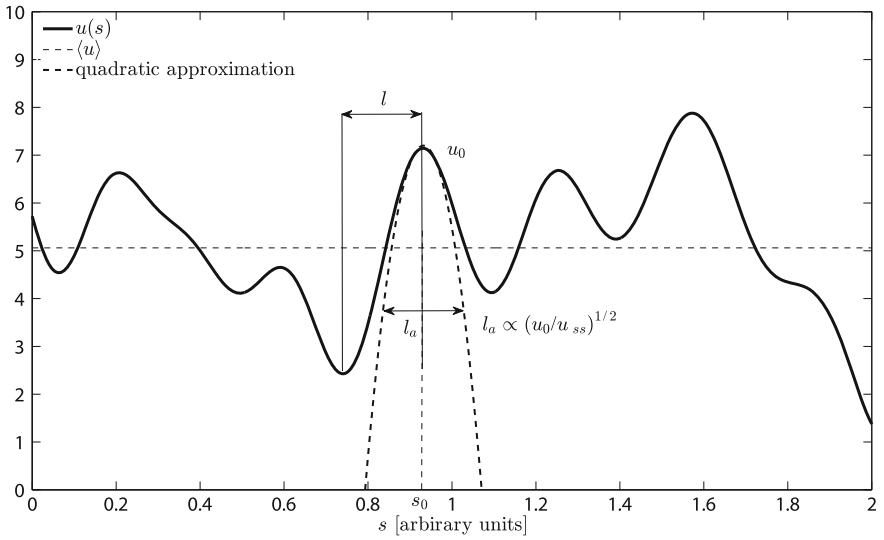

Fig. 2 Local expansion of the u profile in an extremum along the streamline coordinate

$$\langle u_{ss}^2 \rangle^{1/2} \propto \varepsilon^{3/4} \nu^{-5/4}. \tag{6}$$

Note that a similar scaling, namely that of the variance of the solenoidal part of the acceleration in the Navier-Stokes equations (i.e. the viscous term) has been confirmed by [22]. Additionaly, we have

$$\langle u_0^2 \rangle^{1/2} \propto u_{rms}, \tag{7}$$

so that with Eq. 6 we obtain the following scaling of the mean size of extrema of u along streamlines

$$\langle l_a \rangle \propto \left(u_{rms} \varepsilon^{3/4} \nu^{-5/4} \right)^{1/2} \propto \lambda Re_\lambda^{-1/4} \propto (\lambda \eta)^{1/2} \tag{8}$$

with the Kolmogorov scale η and the Taylor microscale λ.

Figure 3 shows that the above scaling of the mean length of streamline segments is valid for all four cases under consideration and thus seems to hold over a broad range of Reynolds numbers. While the ratio of l_m with neither the Kolmogorov length scale nor the Taylor microscale yields a Reynolds number independent constant, the value of the constant for a normalization following the scaling of Eq. 8 yields a constant $C_{lm} \approx 2.9$ for all three cases where only the shear case, probably due to the anisotropic influence of the constant shear gradient, yields a slightly larger value than the three other cases. This finding is further highlighted in Fig. 3 where the ratio l_m/λ and the ratio $l_m/(\lambda\eta)^{1/2}$ is shown over the Taylor based Reynolds number in

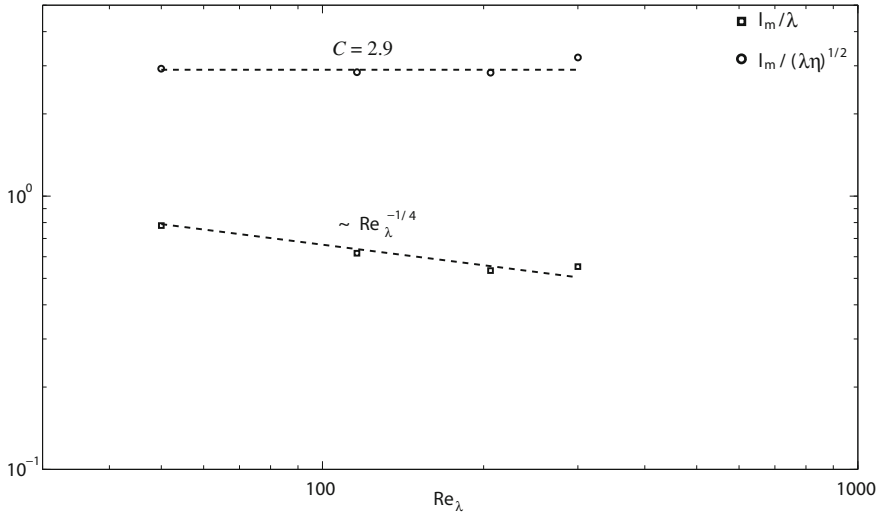

Fig. 3 Scaling of the mean length of streamline segments with the Taylor microscale and the new scaling (Eq. 8) over the Taylor based Reynolds number from DNS cases 1–4

a double logarithmic plot, indicating a clear scaling with $Re_\lambda^{-1/4}$ of the former and a Reynolds number independent constant of the latter. With this scaling relation and the model solution of the pdf the length distribution of streamline segments $P(l)$ of any turbulent flow can be reconstructed.

5 Concluding Remarks

The new scaling of the mean length of streamline segments has been found to be valid for a limited range of Reynolds numbers accessible through DNS of simple turbulent flows. It remains to show in the future that the scaling also holds for more complex flows, such as wall-bounded flows or free shear flows. In addition, it would be desirable to investigate flows at higher Reynolds numbers which might only be attainable through experiments. While streamlines constitute natural geometries in turbulent flows, they are also very special lines in the flow field. It thus remains for future work to investigate the meaning of this new scaling in a more general setting. Thinking even further into the future, geometrical aspects of streamlines and streamline segments and their scaling laws might lay a foundation for formulating an LES model which uses the intrinsic coordinates locally attached to streamlines and might proove useful to simplify the task of closing the a-priori unclosed subgrid terms.

Acknowledgments This work was funded by the Deutsche Forschungsgemeinschaft under Grant Pe 241/38-2 and supported by the Gauss Center for Supercomputing.

References

1. She, Z.S., Jackson, E., Orszag, S.A.: Intermittent vortex structures in homogeneous isotropic turbulence. Nature **344**, 226–228 (1990)
2. Kaneda, Y., Ishihara, T.: High-resolution direct numerical simulation of turbulence. J. Turbulence **7**, N20 (2006)
3. Wang, L., Peters, N.: The length scale distribution function of the distance between extremal points in passive scalar turbulence. J. Fluid Mech. **554**, 457–475 (2006)
4. Wang, L., Peters, N.: Length scale distribution functions and conditional means for various fields in turbulence. J. Fluid Mech. **608**, 113–138 (2008)
5. Gibson, C.H.: Fine structure of scalar fields mixed by turbulence I. zero gradient points and minimal gradient surfaces. Phys. Fluids **11**, 2305–2315 (1968)
6. P. Schaefer, M. Gampert, J.H. Goebbert, L. Wang, N. Peters: Testing of different model equations for the mean dissipation using Kolmogorov flows. Flow, Turb. Comb. **85**, 225–243 (2010)
7. Wang, L.: On properties of fluid turbulence along streamlines. J. Fluid Mech. **648**, 183–203 (2010)
8. Rao, P.: Geometry of streamlines in fluid flow theory. Def. Sci. J. **28**, 175–178 (1978)
9. Braun, W., De Lillo, F., Eckhardt, B.: Geometry of particle paths in turbulent flows. J. Turbulence **7**, N62 (2006)
10. Schaefer, P.: Curvature statistics of streamlines in various turbulent flows. J. Turbulence **13**, N28 (2012)
11. Schaefer, P., Gampert, M., Peters, N.: The length distribution of streamline segments in homogeneous isotropic decaying turbulence. Phys. Fluids **24**, 045104 (2012)
12. Mansour, N.N., Wray, A.A.: Decay of isotropic turbulence at low Reynolds number. Phys. Fluids **6**, 808–814 (1993)
13. Schaefer, P., Gampert, M., Peters, N.: Asymptotic analysis of homogeneous isotropic decaying turbulence with unknown initial conditions. J. Turbul. **12**, N30 (2011)
14. Overholt, M.R., Pope, S.: A deterministic forcing scheme for direct numerical simulations of turbulence. Comput. Fluids **27**, 11–28 (1998)
15. Gampert, M., Goebbert, J.H., Schaefer, P., Gauding, M., Peters, N., Aldudak, F., Oberlack, M.: Extensive strain along gradient trajectories in the turbulent kinetic energy field. New J. Phys. **13**, 043012 (2011)
16. R.S. Rogallo.: Numerical experiments in homogeneous turbulence. NASA T.M., 81315. NASA Ames Research Center, Moffett Field (1981)
17. L. Wang.: Geometrical description of homogeneous shear turbulence using dissipation Element Analysis. PhD thesis, RWTH-Aachen, Germany (2008)
18. Rice, S.O.: Mathematical analysis of random noise. Bell Syst. Tech. J. **23**, 282–332 (1944)
19. Rice, S.O.: Mathematical analysis of random noise. Bell Syst. Tech. J. **24**, 46–156 (1945)
20. Kolmogorov, A.N.: The local structure of turbulence in an incompressible viscous fluid for very large Reynolds numbers. Dokl. Akad. Nauk SSSR **30**, 301–305 (1941a)
21. Kolmogorov, A.N.: Dissipation of energy under locally isotropic turbulence. Dokl. Akad. Nauk SSSR **32**, 16–18 (1941b)
22. Vedula, P., Yeung, P.: Similarity scaling of acceleration and pressure statistics in numerical simulations of isotropic turbulence. Phys. Fluids **11**, 1208–1220 (1999)

Numerical Investigation of the Combined Effects of Gravity and Turbulence on the Motion of Small and Heavy Particles

Christoph Siewert, Rudie Kunnen, Matthias Meinke and Wolfgang Schröder

Abstract Numerical studies [1, 2] show that the influence of gravity and turbulence on the motion of small and heavy particles is not a simple superposition. However, in [3] it is shown that these studies may be artificially influenced by the turbulence forcing scheme. In the present study, a new numerical setup to investigate the combined effects of gravity and turbulence on the motion of small and heavy particles is presented, where the turbulence is only forced at the inflow and is advected through the domain by a mean flow velocity. Within a transition region the turbulence develops to a physical state which shares similarities with grid-generated turbulence in wind tunnels. In this flow, trajectories of about 43 million small and heavy particles are advanced in time. It is found that for a specific particle inertia the particles fall faster in a turbulent flow compared with their fall velocity in quiescent flow. Additionally, specific regions within the turbulent vortices cannot be reached by the particles as a result of the particle vortex interaction. Therewith, the particles tend to cluster outside the vortices. These results are in agreement with the theory of Dávilla and Hunt [4].

1 Introduction

Heavy particles transported in turbulent carrier flows are important for several applications, e.g. planetary science, plankton species, spray combustion in diesel engines, volcano ash, dust, spore, and pollen spreading, and droplet growth in clouds. Hence,

C. Siewert (✉) · M. Meinke · W. Schröder
Institute of Aerodynamics, RWTH Aachen University, Wüllnerstrasse 5a,
52062 Aachen, Germany
e-mail: c.siewert@aia.rwth-aachen.de

R. Kunnen
Fluid Dynamics Laboratory, Department of Applied Physics, Eindhoven University
of Technology, P.O. Box 513, 5600 MB Eindhoven, The Netherlands

A. Dillmann et al. (eds.), *New Results in Numerical and Experimental Fluid Mechanics IX*,
Notes on Numerical Fluid Mechanics and Multidisciplinary Design 124,
DOI: 10.1007/978-3-319-03158-3_10,

many investigations have been performed. However, physical explanations for some phenomena are still missing. This is mainly due to the large range of scales involved. Therefore, in the past mostly theoretical investigations have been performed (e.g. [5]). About 20 years ago the computational power reached a level which enabled simulations of the particle trajectories in turbulent flows. An effect called "particle clustering" or "preferential concentration" was discovered [6]. Heavy particles of intermediate inertia are centrifuged out of vortices and tend to gather in regions of high strain (low vorticity).

In numerical simulations the dissipation range has to be fully resolved since the particle motions are mainly governed by the smallest scales of turbulence. Therewith, numerical simulations are restricted to intermediate Taylor-scale Reynolds numbers Re_λ due to the computational effort. So the separation of scales may be an issue. To the authors' knowledge the highest Re_λ concerning particle-laden turbulent flows was reached in [7]. Based on these data physical explanations for the phenomena of particle clustering were found. However, the influence of gravity on the particle phase was neglected in this study. In [8] it is pointed out that the fall velocity of the heavy particle significantly shortens the particle vortex interaction time and therewith the presence of gravity alters the preferential concentration effect. This is numerically supported by [1].

All numerical studies in the literature utilize the same generic periodic setup wherein the largest scales of turbulence are forced. In [3] it was recently shown that this could be problematic because the preferential concentration depends on the employed large scale forcing scheme. Therefore, a completely different setup is presented with similarities to grid-generated turbulence in wind tunnels. Synthetic turbulence is forced only at the inflow plane and advected through the domain by a mean flow velocity. Therewith, the flow evolves according to the Navier-Stokes equations and a decaying isotropic turbulence can be found. In this flow the combined effects of turbulence and gravity on the motion of small and heavy particles are investigated.

2 Setup

The flow field generated in this study shares similarities with grid-generated turbulence in wind tunnel experiments. A detailed description can be found in [9]. A slice through the domain is shown in Fig. 1. The domain boundaries are furnished with a sponge layer to avoid spurious oscillations due to reflections [10]. At the outflow boundary the pressure is kept constant and the wall-normal velocity gradients are set to zero. At the inflow plane the synthetically generated turbulent fluctuations $\mathbf{u}'$ are added to the mean advection velocity $\mathbf{U}$. The Reynolds number $Re_L = \frac{UL}{\nu}$ is 80,000 with the domain length L and the kinematic viscosity ν. At the inflow boundary, also the particles are released into the flow. The gravity direction is opposed to the mean flow direction. Therewith, the particle duration of stay within the domain is increased and after a specific time interval the particle motions are independent

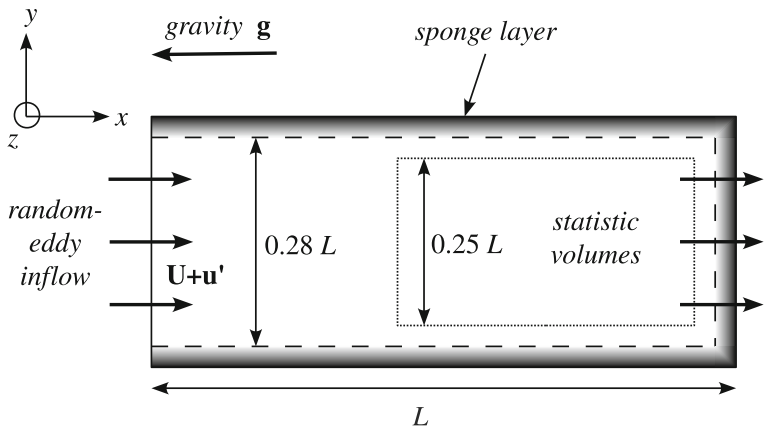

Fig. 1 Sketch of the domain setup. The z and the y layout are the same. At the inflow plane synthetic turbulence is added to the mean advection velocity. The remainder of the domain boundary is furnished with a sponge layer. Gravity points in the opposite direction as the mean flow direction. Turbulence and particle statistics are gathered in several consecutive statistic volumes at the downstream end of the domain

of the initial release conditions. Downstream of this initial transition region the turbulence and particle statistics are gathered in consecutive statistic volumes, which are characterized by different turbulence intensities, see Fig. 3a. The vertical extent of the downstream volumes is chosen small enough to ensure that the statistics are unaffected by the presence of the sponge layers.

3 Flow Phase

The turbulent fluctuations are generated by a method following [11]. The main idea is to generate synthetic fluctuations that match a prescribed Reynolds stress tensor on average. Therefore, the fluctuations consist of a large number of individual Fourier modes, here 200 were used. They are chosen randomly but fulfill the continuity equation. However, the fluctuations obey the momentum equation only on average. Besides the particle initial release conditions that is why an initial transition region is needed.

The flow solver used here is a general purpose solver developed and successfully applied at the Institute of Aerodynamics at RWTH Aachen [10]. It solves the integral form of the Navier-Stokes equations for compressible flows with a finite volume method. The flow simulated here is essentially incompressible, hence the Mach number is set to $Ma = 0.1$. Since a DNS is intended, the domain is discretized into cubic cells with a side length corresponding to the Kolmogorov length η_K, leading to a total number of about 53 million cells.

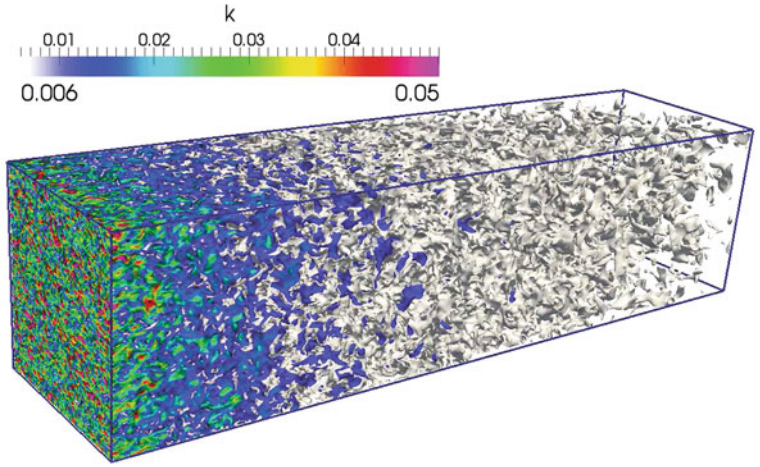

Fig. 2 Contours (0.24, 0.2, 0.18, 0.12, 0.08, 0.04, and 0.001) of the instantaneous turbulent kinetic energy k/U^2

After an initial period of $8 \times \frac{L}{U}$, turbulence statistics are gathered over $20 \times \frac{L}{U}$. Since there is no mean shear in the flow, turbulence is only produced at the inflow. Downstream, the turbulent kinetic energy k decays due to viscous damping. For grid turbulence it was shown that the decay is of the form $k(t) = k_0 \left(\frac{t}{t_0}\right)^n$, with $n = -1.3$ [12]. A snapshot is shown in Fig. 2 to provide a qualitative picture of this decay. The decay of the turbulent kinetic energy is very distinct.

The turbulent kinetic energy dissipation rate ϵ is decaying following $\epsilon(t) = -\frac{dk}{dt} = \epsilon_0 \left(\frac{t}{t_0}\right)^{n-1}$. This temporal dependence can be related to a spatial one due to the constant mean flow velocity U by Taylor's hypothesis, where $t = \frac{x}{U}$. Figure 3a shows the dissipation rate ϵ over the spatial coordinate x in a logarithmic plot. It can be seen that ϵ is nearly constant at the inflow, but further downstream it decays with the theoretical decay exponent of -2.3. The size of the transition region can be estimated from this plot. After only $1/8$ of the total domain length a physical state is reached, which means that the flow has evolved from the synthetic inflow distribution to a fully developed state, this is defined by the solution of the conservation equations. All statistic volumes are located further downstream, see the symbols in Fig. 3a.

Figure 3b shows a one-dimensional velocity spectrum at the position of the first statistic volume. The -7 law of the dissipation range down to the Kolmogorov length is well resolved. The inertia range is rather small. Re_λ has a value of around 20 and is weakly depending on the streamwise coordinate. In any case, there is no restriction to scale-up the current method to reach higher turbulent intensities besides the larger computational effort. An advantage of the current method is that the dependency on the dissipation rate can be checked within a single computation. The turbulence is spatially decaying and therewith the particles are advected through areas of different turbulence intensities.

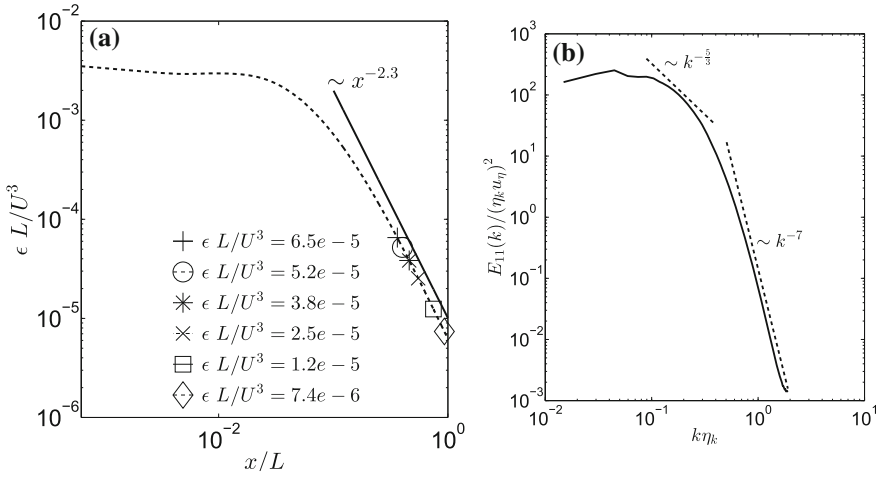

Fig. 3 Flow field characterization: **a** Streamwise evolution of the turbulent kinetic energy dissipation rate ϵ. The *solid line* represents the -2.3 scaling typical for grid-generated spatially evolving turbulence. Additionally the streamwise locations of the statistic volumes are indicated by symbols. **b** One-dimensional energy spectrum of the simulated turbulence at the position of the first statistic volume. The additional lines depict $k^{-\frac{5}{3}}$ and k^{-7} scaling, respectively

4 Particle Phase

The particles considered here are small (ratio of the particle radius to the Kolmogorov length $\frac{a_p}{\eta_K} \ll 1$) and heavy (ratio of the particle density and the fluid density $\frac{\rho_p}{\rho_f} = 843$). Within this limit the equation of motion [13] can be simplified to

$$\frac{d\mathbf{v}_p}{dt} = \frac{f_D}{\tau_p}\left[\mathbf{u}_f\left(\mathbf{x}_p\right) - \mathbf{v}_p\right] + \mathbf{g}\ , \tag{1}$$

with $\mathbf{v_p}$ the particle velocity, $\mathbf{u_f}$ the fluid velocity at the particle position $\mathbf{x_p}$ interpolated by a tricubic least square method, the gravity force $\mathbf{g}$, a non-linear Stokes drag correction f_D, and the particle response time $\tau_p = 2a_p^2\rho_p/9\nu\rho_f$. A total number of about 45 million particles in 20 different radii classes are advanced simultaneously in the turbulent flow described above. Due to the small volume fraction (9×10^{-5}) occupied by the particles, one-way coupling is assumed such that the influence of the particles on the flow field and the particle interaction is neglected.

The ratio of the particle response time and the flow time scale is called Stokes number St. Because of the small particle sizes, the Kolmogorov time scale is the appropriate time scale [1]. Particles with a very small inertia follow the flow similar to fluid tracers. In the opposite limit of very large inertia the particles are hardly affected by the turbulence. If the particle and turbulent time scale match, particles are driven out of the vortices and gather in regions of high strain [14]. This particle

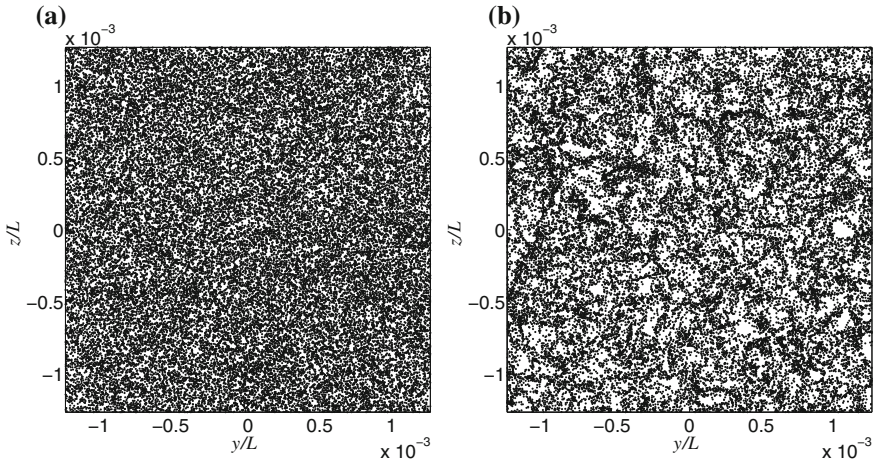

Fig. 4 Visualization of the clustering effect. The particle positions are displayed in a slice perpendicular to the streamwise direction. The particle sizes are increased to have the same value for better visibility and comparability. **a** $St \ll 1$ and **b** $St \sim 1$

clustering is measured by a so called radial distribution function (RDF) g_{11} [1]. It compares the number of contacting particles within one instant of the simulation with the number of contacting particles expected for a random spatial distribution of the same total amount of particles. Figure 4 shows the preferential concentration effect by displaying the particle positions in a slice. In (a) the particle Stokes number is much smaller than unity resulting in a homogeneous particle distribution. For a particle Stokes number of unity (b) many regions without particles and as a result regions with particle clusters can be found.

In the presence of gravity and turbulence the behavior discussed above is altered. Gravity and turbulent acceleration are not simply superposed as Eq. (1) might suggest, but there are combined effects. Without turbulence the particles would fall with their so-called terminal velocity $v_t = \tau_p g / f_D$ (derived from Eq. (1)). Hence, the relative importance of gravity and turbulence can be evaluated by the non-dimensional settling velocity Sv which is the ratio of the terminal velocity and the Kolmogorov velocity scale $Sv = v_t / u_\eta$ [8]. If the ratio is high, the particles sediment faster through the vortex than its turnover time. In this case gravity dominates the motion of the particles compared to turbulence due to the small particle-vortex interaction times. Thus, Dávilla and Hunt [4] suggest to rescale the Stokes number by the non-dimensional settling velocity resulting in the particle Froude number $F_p = St\ Sv^2$. They predict that for $F_p \sim 1$ the average turbulent falling velocity is higher than the laminar one because the particles preferentially pass vortices on their downward motion side. Additionally, they state that due to their inertia, particles cannot reach certain areas of the vortices. Hence, the particles gather elsewhere.

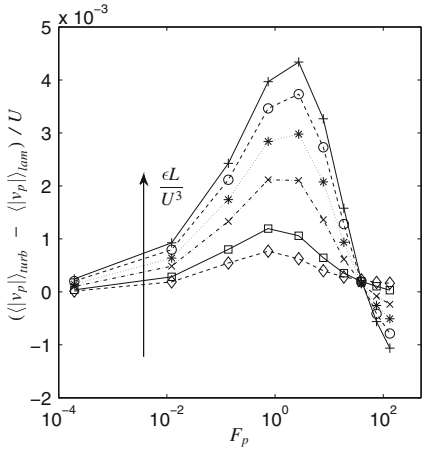

Fig. 5 Difference between the averaged turbulent and the laminar falling velocities over the particle radius. The symbols indicate the dependency on the dissipation rate (see Fig. 3)

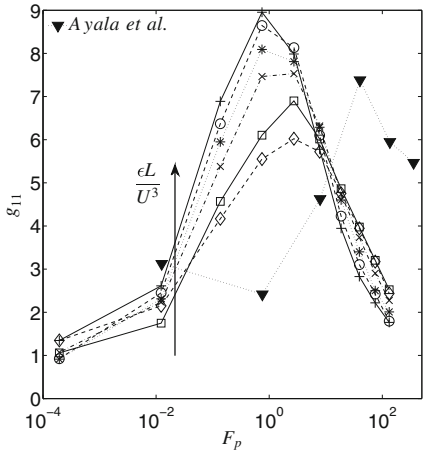

Fig. 6 RDF g_{11} over the particle radius. The empty symbols indicate the dependency on the dissipation rate (see Fig. 3). The filled symbols represent data from [2]

5 Results

In the following, the numerical results are compared with the theory explained in the previous section. In Fig. 5 the difference between the averaged turbulent and the laminar falling velocities is plotted as a function of the particle Froude number. Additionally, the dependency of this difference on the turbulence intensity, respectively the dissipation rate ϵ, is indicated. In fact, for $F_p \sim 1$ particles fall faster the higher the turbulence intensity of the carrier fluid is. For $F_p > 40$ the effect is inversed and weaker. It fits exactly the predictions in [4] described above. Despite the totally different setup, the same tendency was found in [2].

The particle clustering effect is depicted in Fig. 6 by means of the RDF values as a function of the particle Froude number depending on the dissipation rate. It

can be seen that the particles in the considered size range generally tend to cluster ($g_{11} > 1$). From small to big particles the clustering effect becomes stronger and reaches a pronounced maximum value for $F_p \approx 1$. In [2] the position of the maximum value is at $F_p \approx 40$ which corresponds to $St \sim 0.6$. At this value of St the strongest effect was found in [7] neglecting the influence of gravity. This is surprising because of the otherwise good quantitative agreement with the data of Ayala et al. [2]. The differences might be originated in the spatial decay of the turbulence in this study and/or the periodicity of the domain and the large scale forcing scheme in the studies reported in the literature. However, based on the existing data it remains unclear what causes this difference and which result is more physically correct. Therefore, it is planned to numerically simulate a laboratory experiment to answer this question.

6 Conclusion

A new numerical setup is presented to investigate the combined effects of gravity and turbulence on the motion of small and heavy particles. The turbulence is only forced at the inflow and is advected through the domain by a mean flow velocity. Within a transition region the turbulence develops to a physical state which shares similarities with the grid-generated turbulence in wind tunnel experiments. In this flow trajectories of about 43 million small and heavy particles are advanced in time. The theoretical predictions of Dávilla and Hunt [4] are confirmed. For a particle Froude number $F_p \sim 1$ the particles fall on average faster with a higher dissipation rate. Due to their inertia particles might preferentially choose the downward motion side of the vortices they pass. In this study the particle clustering is strongest for $F_p \sim 1$. This is in contrast to other numerical simulations in the literature. It remains unclear which result is more physically correct.

The funding of this project under grant number SCHR 309/39 by the Deutsche Forschungsgemeinschaft is gratefully acknowledged.

References

1. Woittiez, E.J.P., Jonker, H.J.J., Portela, L.M.: On the combined effects of turbulence and gravity on droplet collisions in clouds: a numerical study. J. Atmos. Sci. **66**, 1926–1943 (2009)
2. Ayala, O., Rosa, B., Wang, L.P., Grabowski, W.W.: Effects of turbulence on the geometric collision rate of sedimenting droplets. Part 1. Results from direct numerical simulation. New J. Phys. **10**, 075015 (2008)
3. Rosa, B., Parishani, H., Ayala, O., Wang, L.P., Grabowski, W.W.: Kinematic and dynamic pair collision statistics of sedimenting inertial particles relevant to warm rain initiation. J. Phys. Conf. Ser. **318**, 072016 (2011)
4. Dávila, J., Hunt, J.C.R.: Settling of small particles near vortices and in turbulence. J. Fluid Mech. **440**, 117–145 (2001)
5. Saffman, P.G., Turner, J.S.: On the collision of drops in turbulent clouds. J. Fluid Mech. **1**, 16–30 (1956)

6. Squires, K.D., Eaton, J.L.: Preferential concentration of particles by turbulence. Phys. Fluids **3A**, 1169–1178 (1991)
7. Bec, J., Biferale, L., Cencini, M., Lanotte, A.S., Toschi, F.: Intermittency in the velocity distribution of heavy particles in turbulence. J. Fluid Mech. **646**, 527–536 (2010)
8. Grabowski, W.W., Vaillancourt, P.: Comments on preferential concentration of cloud droplets by turbulence: effects on the early evolution of cumulus cloud droplet spectra. J. Atmos. Sci. **56**, 1433–1436 (1999)
9. Kunnen, R.P.J., Siewert, C., Meinke, M., Schröder, W., Beheng, K.: Numerically determined geometric collision kernels in spatially evolving isotropic turbulence relevant for droplets in clouds. Atmos. Res. **127**, 8–21 (2013)
10. Hartmann, D., Meinke, M., Schröder, W.: An adaptive multilevel multigrid formulation for Cartesian hierarchical grid methods. Comput. Fluids **37**, 1103–1125 (2008)
11. Batten, P., Goldberg, U., Chakravarthy, S.: Interfacing statistical turbulence closures with large-eddy simulation. AIAA J. **42**(3), 485–492 (2004)
12. Pope, S.B.: Turbulent Flows. Cambrigde University Press, Cambrigde (2000)
13. Maxey, M.R., Riley, J.J.: Equation of motion for a small rigid sphere in a nonuniform flow. Phys. Fluids **26**, 883–889 (1983)
14. Sundaram, S., Collins, L.R.: Numerical considerations in simulating a turbulent suspension of finite-volume particles. J. Comput. Phys. **124**, 337–350 (1996)

On "Adaptive Wall-Functions" for LES of Flow and Heat Transfer

G. John-Puthenveettil and S. Jakirlić

Abstract Present work is concerned with the modelling of near-wall region in turbulent flow configurations including heat transfer in the framework of a Large-Eddy Simulation. The relevant development focuses on a universal wall treatment implying one functional dependency being valid across all characteristic zones of a wall boundary layer providing smooth and seamless transition from viscosity-affected immediate wall vicinity to the fully-turbulent outer part of inner layer with underlying log-law for both velocity and temperature fields. The present wall-function model was formulated on the basis of the so-called Compound Wall Treatment proposed by Popovac and Hanjalic [10] within the RANS framework. A slightly modified expression coupled with an appropriate algorithm for the determination of the instantaneous wall shear stress is formulated and applied in LES of a plane channel flow and flow over a backward facing step subjected to external wall heating in a Reynolds number range and flow and passive scalar transport in a model of swirl combustor.

1 Introduction

A Large Eddy Simulation (LES) of high Reynolds number flow configurations requests an appropriately fine mesh to be used; it relates in particular to the immediate wall-vicinity. Accordingly, one of the most important issues in LES of wall-bounded flows is the near-wall treatment. The numerical grid resolving all scales up to a relevant extent has to be refined not only in the wall-normal direction but also in the streamwise and spanwise directions aiming at capturing appropriately structural characteristics of the instantaneous flow field. Such circumstances are especially

G. John-Puthenveettil · S. Jakirlić (✉)
Darmstadt University of Technology, Institute of Fluid Mechanics and Aerodynamics/Center of Smart Interfaces, Petersenstr. 17, 64287 Darmstadt, Germany
e-mail: s.jakirlic@sla.tu-darmstadt.de

A. Dillmann et al. (eds.), *New Results in Numerical and Experimental Fluid Mechanics IX*, Notes on Numerical Fluid Mechanics and Multidisciplinary Design 124,
DOI: 10.1007/978-3-319-03158-3_11,

pronounced at higher Reynolds numbers as the size of the smallest eddies near the wall is progressively reduced. Instead of carrying out a wall-resolved LES a reasonable alternative is to use the "wall-function" concept for the wall treatment enabling significant coarsening of the near-wall grid resolution. The instantaneous wall-shear stress matching the instantaneous tangential velocity at the wall-nearest grid point is to be captured and applied as boundary condition at the wall. When using the standard wall functions relying on the law-of-the-wall for velocity field $U^+ = In(Ey^+)/k$ it has to be ensured that the wall-closest grid point is placed in the logarithmic layer. In cases that for instance involve separation and reattachment the dimensionless wall distance y^+ of the wall-adjacent grid point varies throughout the flow. Consequently, it is difficult to assure having the first grid node positioned in the logarithmic layer at the entire wall length. By taking a wall function expression blending between linear law (exact velocity profile pertinent to the viscous sublayer: $U^+ = y^+$) and logarithmic law ("fully-turbulent" region) being valid in all three characteristic zones of a boundary layer, i.e. viscous sublayer, buffer layer and logarithmic layer independent of the position of the wall-next computational node, this problem can be remedied. Work on the so-called "universal wall functions"—some other denotations, as e.g. hybrid or generalized wall functions are also in use—have been experienced growing popularity in the recent years, especially within the Reynolds-Averaged Navier Stokes (RANS) framework in conjunction with different turbulence models: Esch and Menter [3], Knopp et al. [8], and Popovac and Hanjalic [10]. The works of Werner and Wengle [13] and Temmerman et al. [11] can be consulted with respect to the wall-functions-like wall-region treatment within the LES methodology. The objective of the present work is an appropriate adaptation of the Popovac and Hanjalic's [10] RANS proposal for LES of wall-bounded flow configurations subjected to wall heating.

2 Hybrid Wall Functions (HWF) for LES: Rationale

Starting point of the present development is the recent work of Popovac and Hanjalic [10] on a unified wall function formulation which, depending on the position of the wall-closest computational node, blends between the exact boundary conditions (with numerical node positioned in the viscous-sublayer) as the lower bound and the high-Reynolds wall function formulation (node positioned in the log-law layer) as the upper bound. This so-called Compound Wall Treatment (CWT), employed in the RANS framework in conjunction with their ζ-f turbulence model, relies on the early Kader's (1981) proposal for the temperature profile:

$$\Theta^+ = \mathrm{Pr}\, y^+ e^{-\Gamma_\Theta} + \left[\alpha \ln\left(y^+\right) + \beta\,(\mathrm{Pr})\right]\Theta^+ e^{-1/\Gamma_\Theta} \tag{1}$$

with $\Gamma_\Theta = 0.001(\mathrm{Pr}y^+)^4/1 + 5Pr^3y^+$, $\beta = (3.85Pr^{1/3} - 1.3)^2 + 2.12\ln(\mathrm{Pr})$ and $\alpha = 2.12$. This approach has been employed by Popovac and Hanjalic for the derivation of a wall function for the velocity by setting $\mathrm{Pr} = 1$ in Eq. (1):

$$U^+ = y^+ e^{-\Gamma_1} + \left[\frac{1}{\kappa\psi}\ln\left(Ey^+\right)\right]e^{-1/\Gamma_2} \quad \text{with} \quad \Gamma_1 = \Gamma_2 = \frac{0.01\left(y^+\right)^4}{1+5y^+} \tag{2}$$

with the von Karman constant $\kappa = 0.41$ and $E = 8.3$. In the present formulation the blending functions Γ_1 and Γ_2 take following forms

$$\Gamma_1 = \frac{0.0045\left(y^+\right)^{4,2}}{15+y^+} \quad \text{and} \quad \Gamma_2 = \frac{0.018\left(y^+\right)^4}{15+5y^+} \tag{3}$$

The parameter Ψ represents a non-equilibrium function in the CWT-model accounting for tangential pressure gradient effects and convection. In the present work this function takes the unity value, implying the use of the standard "equilibrium" wall-functions. This is experience obtained with the CWT model application in real-life flow configurations; accordingly, the simplification $\Psi = 1$ contributes to increased numerical robustness, Basara et al. [2]. The performances of both CWT and present formulations are displayed in Fig. 1 showing the semi-log plot of mean velocity profile in a plane channel.

Numerical method. The computational results presented were obtained by using the in-house code Flow Analysis by Solving Transport Equations Simulating Turbulence (FASTEST), which uses a finite volume method for block-structured, body-fitted, non-orthogonal, hexahedral meshes. The velocity-pressure coupling is ensured by the pressure-correction method based on the SIMPLE algorithm. The convective transport of all variables was discretised by a second-order, central differencing scheme. Time discretisation was accomplished applying the Crank-Nicolson scheme.

For more details about numerical method and the algorithm used for the determination of the instantaneous wall shear stress see John-Puthenveettil [6].

3 Results and Discussion

Figures 3, 4, 5, 6, 7, 8, 9, 10, 11, and 12 illustrate the performance of the proposed wall-function model applied to a channel flow and a flow over a backward facing step subjected to wall heating and a flow and mixing in a combustor channel with secondary air injection.

Fully-developed channel flow subjected to wall heating. The performance of the present hybrid wall function is first evaluated in a plane channel flow at the target friction Reynolds numbers $\mathrm{Re}_\tau = 590/640$ (DNS: Moser et al. [9] / Abe et al. [1]) and $\mathrm{Re}_\tau = 2003$ (DNS by Hoyas and Jimenez [4]), corresponding to the bulk Reynolds numbers $\mathrm{Re}_\mathrm{m} = 22000/24000$ and $\mathrm{Re}_\mathrm{m} \approx 87000$ respectively. The dimensions of the flow domain are $2\pi\mathrm{h}$, $2\mathrm{h}$, $\pi\mathrm{h}$, with h representing the half channel height, Fig. 2. Periodic boundary conditions are applied in the streamwise and spanwise direction. In all simulations the dynamic Smagorinsky model is chosen to account for the subgrid scales. Different grid resolutions (with grid nodes distributed uniformly

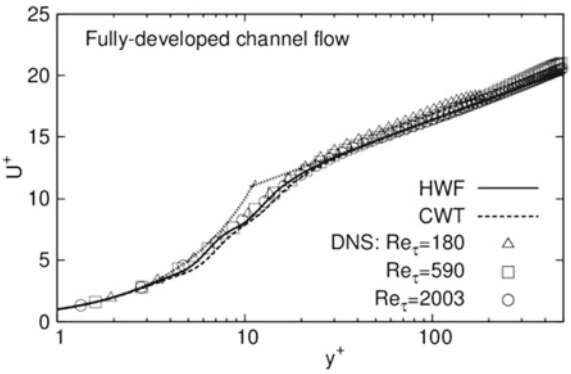

Fig. 1 Mean velocity profile arising from the present hybrid wall function method in comparison with CWT and DNS data for the channel flow at $Re_\tau = 180$, 590 and 2003

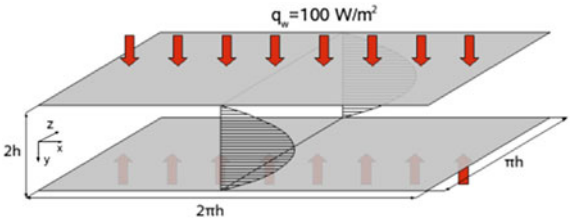

Fig. 2 Schematic of the plane channel flow considered

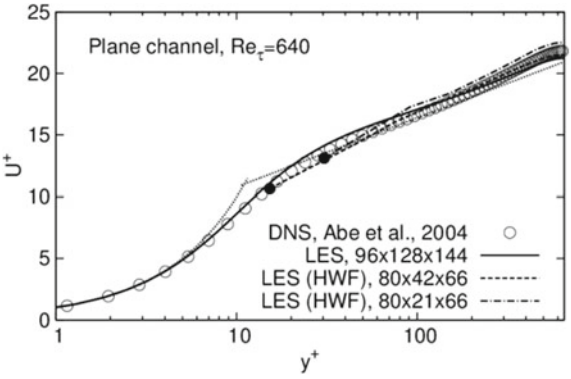

Fig. 3 Semi-log plot of the mean velocity profiles obtained using different grid sizes

in all three coordinate directions) providing the position of the wall-adjacent grid node in the viscous sublayer (dimensionless wall distance at $y^+ < 5$), buffer layer ($y^+ \approx 15$) and logarithmic region ($y^+ \approx 30$–40) were used, Figs. 3, 4 and 5. Velocity and temperature profiles show good agreement with available DNS results following closely the logarithmic-law. The Reynolds stress distribution, corresponding to the grid with the wall-next node situated in the buffer layer, was, apart of the immediate wall-vicinity, captured in a good agreement with available DNS data; the agreement improves further with the Reynolds number increase. The results are of comparable quality with those obtained by Temmerman et al. [11].

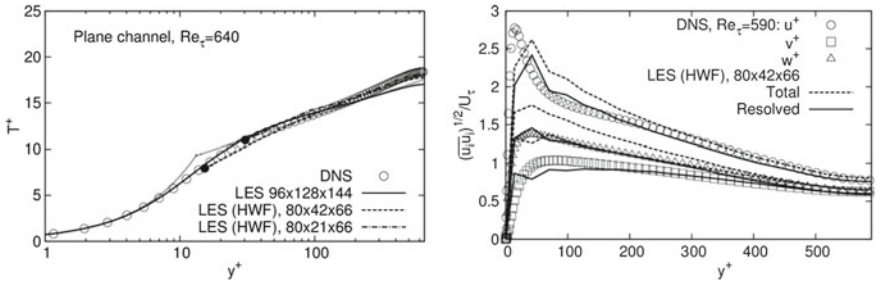

Fig. 4 Semi-log plot of the mean temperature profiles obtained using different grid sizes (*left*) and Reynolds stress component profiles (*right*) in the channel flow at $\mathrm{Re}_\tau = 590/640$

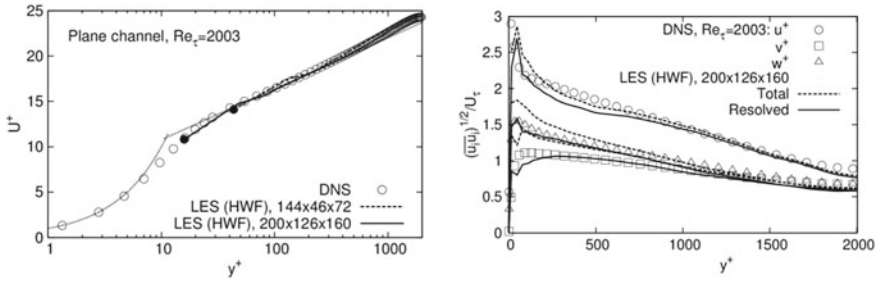

Fig. 5 Semi-log plot of the mean velocity profiles obtained using different grid sizes (*left*) and Reynolds stress component profiles (*right*) in the channel flow at $\mathrm{Re}_\tau = 2003$

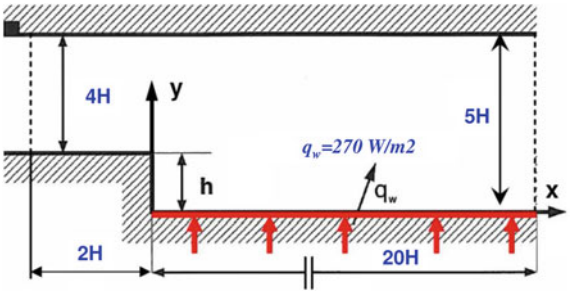

Fig. 6 Schematic of the flow over a backward-facing step with external wall heating

Flow over a backward-facing step subjected to wall heating. The configuration investigated experimentally by Vogel and Eaton [12] is chosen as the next test case. This is a suitable case to test the performance of the present hybrid wall functions under conditions of scalar transport in separated flows. The Reynolds number based on the step height H (= 38 mm) is $\mathrm{Re_H} = 28000$. The dimensions of the flow domain can be taken from Fig. 6. The flow in the inflow channel corresponds to a developing boundary layer with the thickness $\delta = 40.55$ mm at $\mathrm{x/H} = -2$. The unsteady inflow planes are generated using Klein's et al. [7] inflow generation method applied to the results obtained by a Second-Moment

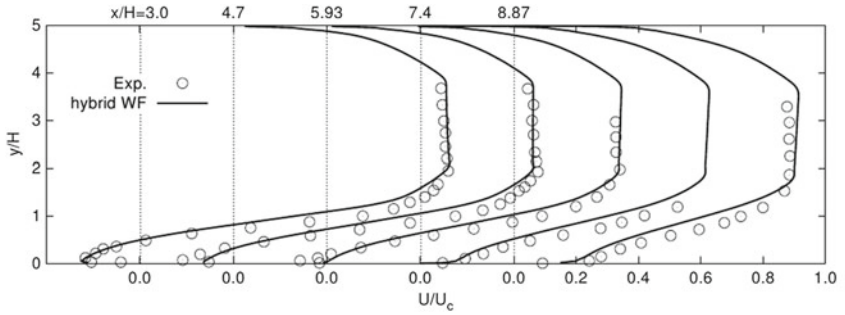

Fig. 7 Evolution of the mean streamwise velocity profile in the flow over a backward-facing step with external wall heating

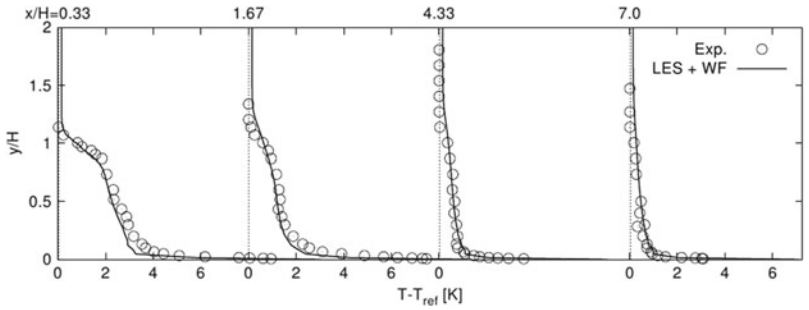

Fig. 8 Evolution of the mean temperature profile in the flow over a backward-facing step with external wall heating

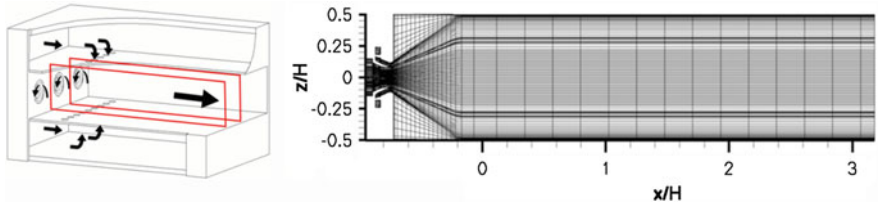

Fig. 9 Schematic of the combustor channel of a gas turbine and corresponding numerical grid

Closure model by doing a separate computation of a respective boundary layer. In the spanwise direction periodic boundary conditions are imposed. At the outlet the zero-gradient boundary condition is chosen. Along the walls, the hybrid wall function for velocity and temperature are applied. The surface heat flux at the bottom wall of the expanded channel amounts to $270\,\mathrm{W/m^2}$. The other walls are considered to be adiabatic. The Prandtl number is 0.71. The grid resolution providing the position of the wall-closest grid node $y^+ \approx 5$–12 (lower value is documented at the streamwise position corresponding approximately to the secondary reattachment region at $x/H \approx 1$–2) along the lower wall consisted of $20 \times 79 \times 60$

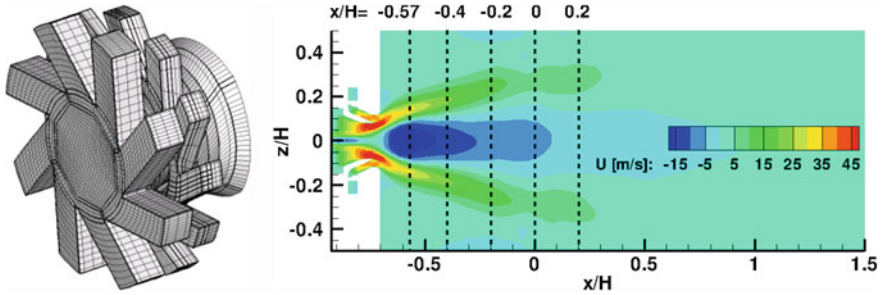

Fig. 10 Air blast nozzle and corresponding numerical grid (*left*) and computationally obtained time-averaged axial velocity contours in the vertical mixing channel plane (*right*)

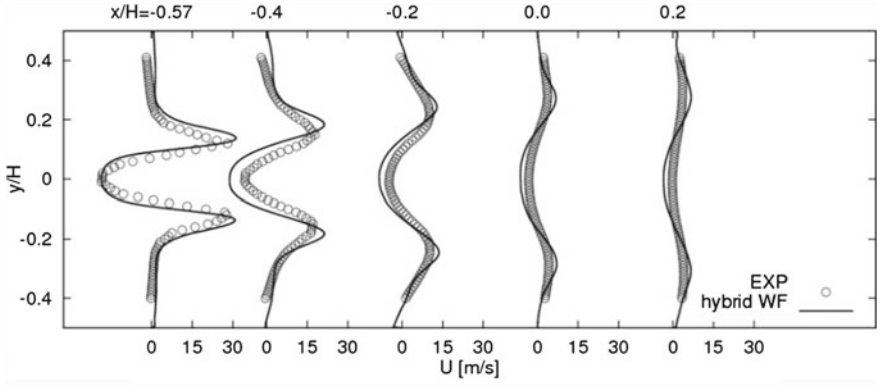

Fig. 11 Evolution of the mean axial velocity profile at selected streamwise positions in the vertical mixing channel plane

(inlet channel) and $176 \times 100 \times 60$ (expansion) grid cells -1.15 Mio. grid cells in total; a coarser grid with the near-wall resolution corresponding to $y^+ \approx 5$–36 was also tested. The averaging process is carried out for nearly 33 flow through times. The flow is averaged both in time and in the spanwise direction. Figures 7 and 8 display the mean velocity and mean temperature profile developments. Computationally obtained results are compared with the experimental data at five selected streamwise locations. An overall good agreement between the simulation and experiment can be seen. It is noticeable that the simulation predicts a somewhat shorter recirculation region: $x/H \approx 6.0$ compared to 6.7 obtained experimentally. A somewhat higher turbulence intensity (not shown here) in the separated shear layer is in accordance with a shorter flow reversal zone. The proposed wall function model shouldn't be automatically blamed for this deviation; in the case of an LES the resolution in both streamwise and spanwise directions as well as the inflow conditions, related mostly to the level of inflow turbulence, play a decisive role with respect to this issue.

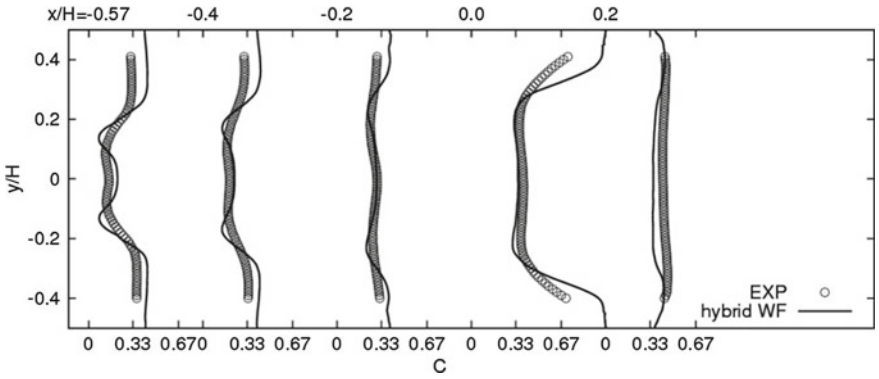

Fig. 12 Evolution of the mean concentration profiles profile at selected streamwise positions in the vertical mixing channel plane

Flow and mixing in a swirl combustor channel with secondary air injection. Finally, the present hybrid wall function formulation is tested by simulating the mixing process in an annular gas turbine combustor model. This complex flow configuration implies a swirling flow and secondary air jets being injected into the chamber, Jakirlic et al. [5]. The flow in the annular combustor is assumed to be nearly periodic in circumferential direction. Therefore, one single segment of the combustor, consisting of a swirler and a subsequent rectangular channel, is included in the computational domain, see Figs. 9 and 10. In the spanwise direction of the channel periodic boundary conditions are applied. At the outlet the convective exit boundary condition is applied. It was sufficient to prescribe a constant velocity distribution at the inlets of the swirler since the flow becomes highly perturbed after passing through the swirler. The flow enters the inlet ducts in the first row of the swirler with a velocity of $u_1 = 28.46\,m/s$ and in the second row with a velocity of $u_2 = 35.33\,m/s$ respectively. The Reynolds number of the flow based on the channel height and the bulk velocity at the outlet is $Re = 15800$. The momentum flux ratio J representing the momentum ratio between the secondary flow through the injected jets (injected into the chamber through six orifices of diameter $d = 12\,mm$ in the top and bottom wall respectively, Fig. 9) and the main flow is $J = 100$; it indicates how deep the secondary air jet penetrates into the main flow. The simulation is performed under isothermal and non-reacting conditions. The turbulent concentration flux is modelled applying the simple gradient diffusion hypothesis. The computational grid consists of around 870,000 cells. The first grid points off the wall are at positions $y^+ \approx 15$–25. The flow in the combustion chamber is characterized by a swirl-induced flow reversal, the recirculation in the corners and by the interaction of these regions with the main flow, Fig. 10. The computational results are compared with the PIV measurements, see e.g. Jakirlic et al. [5]. Figures 11 and 12 depict the streamwise velocity and concentration (representing the fraction of the secondary air entering the flow through the orifices) profiles at five different streamwise positions. The results

of the simulation performed using the hybrid wall functions agree reasonably well with the experimental values. It can be observed that a somewhat larger opening angle of the flow behind the swirler compared to the experimental findings indicates a more intensive spreading.

4 Conclusions

Predictive performances of the presently formulated "adaptive wall-functions" for the near-wall region treatment in the LES framework were illustrated by computing several flow configurations including wall heating featured by separation and swirl. The feasibility of the proposed model was checked in a plane channel flow in a range of Reynolds numbers up to $\mathrm{Re}_\tau = 2003$ ($\mathrm{Re}_\mathrm{m} \approx 87000$) by employing different grid resolutions providing the next-to-the-wall grid node is situated at different distances corresponding to all three characteristic boundary layer zones: viscous sublayer, buffer layer and logarithmic layer. Corresponding Reynolds stress distribution was captured in a good agreement with available DNS data. Similarly good agreement is documented in the case of the mean velocity, temperature and concentration profile developments in the separated and swirling flow in the backward-facing step geometry and a swirl-combustor model.

References

1. Abe, H., Kawamura, H., Matsuo, Y.: Surface heat-flux fluctuations in a turbulent channel flow up to Re_τ=1020 with Pr=0.025 and 0.71. Int. J. Heat Fluid Flow **25**, 404–419 (2004)
2. Basara, B., Aldudak, F., Schrefl, M., Jakirlić, S., Hanjalić, K., Tropea, C., Mayer, J.: Experimental Investigations and Computations of Unsteady Flow past a Real Car Using a Robust Elliptic Relaxation Closure with a Universal Wall Treatment. SAE technical paper series, paper no. 2007–01-0104, pp. 1–11 (2007)
3. Esch, T., Menter, F.R.: Heat Transfer Predictions Based on Two-Equation Turbulence Models with Advanced Wall Treatment. In: Hanjalic et al. (eds.), Turbulence, Heat and Mass Transfer 4, pp. 633–640. Begell House Inc., West Redding (2003)
4. Hoyas, S., Jimenez, J.: Scaling of the velocity fluctuations in turbulent channels up to $Re_\tau = 2003$. Phys. Fluids **18**(011702) (2006)
5. Jakirlić, S., Kniesner, B., Kadavelil, G., Gnirß, M., Tropea, C.: Experimental and computational investigations of flow and mixing in a single-annular combustor configuration. Flow Turbul. Combust. **83**(3), 425–448 (2009)
6. John-Puthenveettil, G.: Computational modelling of complex flows using eddy-resolving models accounting for near-wall turbulence. Ph.D. thesis, Technische Universität, Shaker Verlag, Darmstadt (ISBN 978-3-8440-1760-1) (2012)
7. Klein, M., Janicka, J., Sadiki, A.: A digital filter based generation of inflow data for spatially developing direct numerical or large-eddy simulations. J. Comp. Phys. **186**, 652–665 (2003)
8. Knopp, T., Alrutz, T., Schwamborn, D.: A grid and flow adaptive wall-function method for RANS turbulence modelling. J. Comp. Phys. **220**, 19–40 (2006)
9. Moser, R.D., Kim., J., Mansour, N.N.: Direct numerical simulation of turbulent channel flow up to Re_τ = 590. Phys. Fluids **11**(4), 943–945 (1999)

10. Popovac, M., Hanjalic, K.: Compound Wall Treatment for RANS Computation of Complex Turbulent Flows and Heat Transfer. Flow Turbul. Combust. **78**, 177–202 (2007)
11. Temmerman, L., Leschziner, M.A., Mellen, C.P., Fröhlich, J.: Investigation of wall function approximations and subgrid-scale models in large eddy simulation of separated flow in a channel with streamwise periodic constrictions. Int. J. Heat Fluid Flow, **24**(2), 157–180 (2003)
12. Vogel, J.C., Eaton, J.K.: Combined heat transfer and fluid dynamic measurements downstream of a backwards-facing step. ASME J. Heat Transfer **107**, 922–929 (1985)
13. Werner, H., Wengle, H.: Large-Eddy Simulation of Turbulent flow over and around a Cube in a plane Channel. In: Launder et al. (Eds.), Turbulent Shear Flows 8, pp. 155–168. Springer, New York (1993)

The Influence of the Diffusion Model on the Separation Sensitivity of Differential Reynolds Stress Models

Bernhard Eisfeld

Abstract Three different diffusion models are coupled with the SSG/LRR-ω Reynolds stress model. The different model versions are applied to three characteristic aerodynamic test cases. While there is very little influence on the pressure distribution, some differences are observed in the predicted skin friction, revealing the more complex diffusion models to enhance the sensitivity to separation.

1 Introduction

The development of Computational Fluid Mechanics (CFD) methods during the past decades has been such successful that numerical flow simulation has become a standard method in the design of modern aircraft. Consequently there is a vision for almost entirely relying on simulation results in the future.

However in off-design conditions the quality of CFD simulations depends on the ability to correctly predict flow separation, which in turn depends on the correct description of the effects of turbulence. In principle, scale-resolving methods like Large Eddy Simulations (LES) should allow highly accurate predictions of separating turbulent flows, but the effort needed is currently beyond the scope of most engineering applications. For this reason, engineering applications mainly rely on methods based on the Reynolds averaged Navier-Stokes (RANS) equations, where the ability to predict separation highly depends on the respective turbulence model. In particular so-called eddy-viscosity models (EVM), modeling the effects of turbulence simply by a flow dependent increase in viscosity, often appear to be of limited accuracy for predicting separated flows [8].

B. Eisfeld (✉)
Institute of Aerodynamics and Flow Technology, German Aerospace Center (DLR),
Lilienthalplatz 7, 38108 Braunschweig, Germany
e-mail: Bernhard.Eisfeld@dlr.de

A. Dillmann et al. (eds.), *New Results in Numerical and Experimental Fluid Mechanics IX*,
Notes on Numerical Fluid Mechanics and Multidisciplinary Design 124,
DOI: 10.1007/978-3-319-03158-3_12,

For this reason so-called Differential Reynolds Stress Models (DRSM) have been developed, employing the transport equations for the individual Reynolds stresses instead of making an eddy-viscosity assumption. In this context the important process of mean turbulence production is treated exactly, while, nevertheless, the remaining terms in the Reynolds stress transport equation still need to be modelled together with a transport equation for some length scale supplying variable. Although being numerically demanding, DRSMs have been demonstrated to be applicable to complex aerodynamic flow problems with modest effort [7]. Furthermore, in several cases improved results have been obtained compared to EVMs [5].

Nonetheless there is still a need for improving the prediction of separation which requires studying the influence of the various model terms. In general, separation is associated with unsteady flow. Therefore the application of steady RANS based methods to separating flows appears reasonable only if, on the macroscopic level, the associated unsteadiness is small. This is assumed to be the case as long as separation bubbles remain small, which is the focus of the current study.

In a previous chapter it has been shown that the choice of the length scale supplying equation can have a significant effect on the pattern of shock-induced separation [6]. The current paper is devoted to the effects of different formulations of the diffusion term in the Reynolds stress transport equation.

In principle, the formulations could be assessed within the framework of a term-by-term analysis by comparing their predictions to the corresponding term extracted from DNS data. This has been done e.g. by Hanjalić for plane channel flow at low Reynolds number [9]. However, in the current paper the focus is on aerodynamic flows at higher Reynolds number so that the comparison is made on the overall flow prediction, when varying the diffusion model only.

2 Diffusion Modelling

For weakly compressible flow the transport equation for the specific Reynolds stress components $\widetilde{R}_{ij}$ can be formally written as

$$\frac{\left(\overline{\rho}\widetilde{R}_{ij}\right)}{\partial t} + \frac{\partial}{\partial x_k}\left(\overline{\rho}\widetilde{U}_k\widetilde{R}_{ij}\right) = \overline{\rho}P_{ij} + \overline{\rho}\Pi_{ij} - \overline{\rho}\epsilon_{ij} + \overline{\rho}D_{ij}, \tag{1}$$

where $\overline{\rho}$ is the mean density, $\widetilde{U}_k$ the components of the mass-weighted mean velocity, t the time and x_k the spatial Cartesian coordinates. The terms on the right hand side represent the components of the production term, $\overline{\rho}P_{ij}$, of the pressure-strain correlation, $\overline{\rho}\Pi_{ij}$, of the dissipation term, $\overline{\rho}\epsilon_{ij}$, and of the combined diffusion term

$$\overline{\rho}D_{ij} = \frac{\partial}{\partial x_k}\left(\overline{\tau'_{ik}u''_j} + \overline{\tau'_{jk}u''_i}\right) - \frac{\partial}{\partial x_k}\left(\overline{\rho u''_i u''_j u''_k}\right) - \frac{\partial}{\partial x_k}\left(\overline{p'u''_i}\delta_{jk} + \overline{p'u''_j}\delta_{ik}\right), \tag{2}$$

where u_i'' represents the components of the velocity fluctuations, p' is the fluctuating pressure and τ_{ij}' refers to the fluctuating viscous stress components. The viscous diffusion term is given by

$$\overline{\tau_{ik}' u_j''} + \overline{\tau_{jk}' u_i''} = \overline{\mu} \frac{\partial \widetilde{R}_{ij}}{\partial x_k}. \tag{3}$$

The turbulent transport term $\overline{\rho u_i'' u_j'' u_k''}$ is generally agreed to be represented by a diffusive flux, driven by the gradients of the Reynolds stress components [4], but various forms have been suggested. Shir [14] employs the so-called simple gradient diffusion hypothesis (SGDH), defining

$$\overline{\rho u_i'' u_j'' u_k''} = -C_s \frac{\overline{\rho}\widetilde{k}}{\epsilon} \widetilde{k} \frac{\partial \widetilde{R}_{ij}}{\partial x_k}, \tag{4}$$

where $\widetilde{k} = \frac{1}{2}\widetilde{R}_{ii}$ is the specific kinetic turbulence energy, and ϵ is the isotropic dissipation rate that is provided by a respective transport equation.

Daly and Harlow [3] replace the scalar diffusion coefficient in the simple gradient diffusion model by a tensor, obtaining

$$\overline{\rho u_i'' u_j'' u_k''} = -C_s \frac{\overline{\rho}\widetilde{k}}{\epsilon} \widetilde{R}_{kl} \frac{\partial \widetilde{R}_{ij}}{\partial x_l}, \tag{5}$$

which is called the generalized gradient diffusion hypothesis (GGDH).

As one can see, neither the simple nor the generalized gradient model is fully symmetric with respect to all three indices i, j, k as it should be according to the definition of the turbulent transport term. For this reason Hanjalić and Launder [10] extend the GGDH formulation such that

$$\overline{\rho u_i'' u_j'' u_k''} = -C_s \frac{\overline{\rho}\widetilde{k}}{\epsilon} \left(\widetilde{R}_{il} \frac{\partial \widetilde{R}_{jk}}{\partial x_l} + \widetilde{R}_{jl} \frac{\partial \widetilde{R}_{ik}}{\partial x_l} + \widetilde{R}_{kl} \frac{\partial \widetilde{R}_{ij}}{\partial x_l} \right), \tag{6}$$

which will be called HL model in the following.

The above models are investigated in conjunction with the so-called SSG/LRR-ω model [7], combining the Speziale-Sarkar-Gatski model (SSG) [15] in the far field with the Launder-Reece-Rodi model (LRR) [11] near the wall. The isotropic dissipation rate is determined from Menter's so-called baseline ω-equation [12] via $\epsilon = C_\mu \widetilde{k}\omega$, where $C_\mu = 0.09$. This requires the diffusion coefficient C_s to vary from the LRR-values near the wall to the SSG-values further apart. Table 1 lists the respective bounding values.

Concerning the pressure diffusion terms $\overline{p' u_i''}$, DNS data seem to indicate that their contribution is negligible except near walls [9]. However, if not modeled explicitly, their effect is implicitly included in the coefficient of the turbulent transport [13].

Table 1 Bounding values of the diffusion coefficient C_s with $\sigma^* = 0.5$ and $C_\mu = 0.09$

	SGDH	GGDH	HL
LRR	$\sigma^* C_\mu$	$\frac{3}{2}\sigma^* C_\mu$	$\frac{9}{14}\sigma^* C_\mu$
SSG	$\frac{2}{3}$ 0.22	0.22	0.08

3 Simulation Results

The respective diffusion models have been implemented into the DLR TAU code, solving the compressible RANS equations together with the respective turbulence equations based on a Finite Volume discretization. All results have been obtained using a formally second order accurate central discretization scheme with artificial dissipation for the RANS equations and a second order accurate upwind scheme for the turbulence equations.

3.1 Flat Plate

The flow over a flat plate with zero pressure gradient is a classical test case for any type of turbulence model, where the prediction of the skin friction distribution and the agreement with the log-law

$$u^+ = \frac{1}{\kappa} \ln y^+ + C \tag{7}$$

is of particular interest. In this equation $u^+ = U/u_\tau$ is the non-dimensional velocity and $y^+ = y/(\nu/u_\tau)$ the non-dimensional wall distance with the friction velocity $u_\tau = \sqrt{\tau_w/\rho}$, the kinematic fluid viscosity ν and the local shear stress at the wall τ_w as scaling parameters. The log-law parameters are usually assumed to be $\kappa \approx 0.41$ and $C \approx 5$.

Figure 1 (left) compares the predicted skin friction distribution with the experiments by Wieghardt as evaluated by Coles [2]. There is only very little difference between the three diffusion models, nevertheless close inspection reveals that with SDGH the highest and with HL the lowest skin friction values are predicted throughout. Figure 1 (right) shows virtually no difference in the non-dimensional velocity profiles $u^+ = f(y^+)$ except for the outer edge of the boundary layer, which directly reflects the small difference in skin friction, since $u^+_{edge} = \sqrt{C_f/2}$. Nevertheless it should be noted that the slope of the predicted profiles is steeper than the reference one, although the same value of $\kappa = 0.41$ has been used in the calibration of the turbulence model.

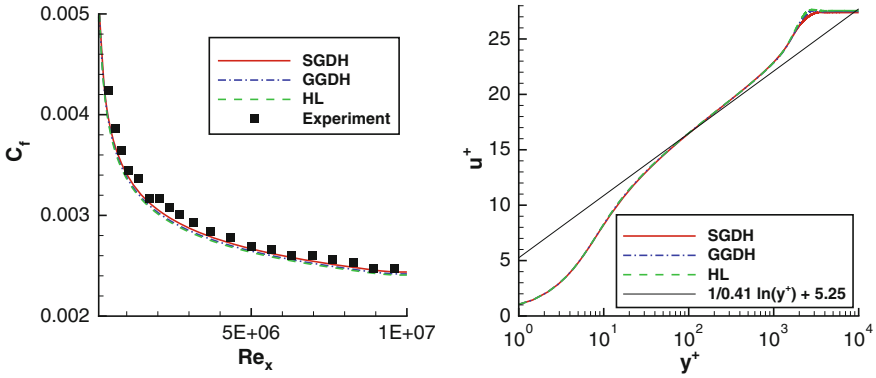

Fig. 1 Flat plate. Skin friction distribution (*left*) and log-law (*right*)

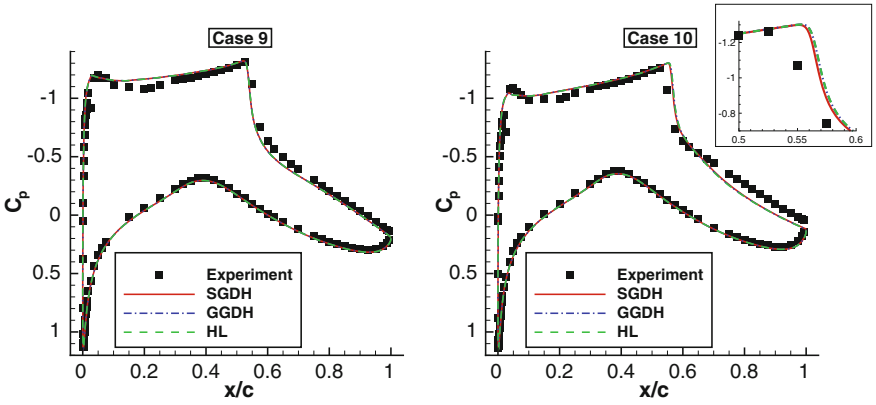

Fig. 2 RAE 2822. Pressure distributions for Case 9 (*left*) and Case 10 (*right*)

3.2 RAE 2822 Airfoil

The flow around the RAE 2822 airfoil [1] for conditions called Case 9 (Mach number $Ma = 0.73$, Reynolds number $Re = 6.5e6$, incidence $\alpha = 2.8°$) and Case 10 (Mach number $Ma = 0.75$, Reynolds number $Re = 6.2e6$, incidence $\alpha = 2.8°$) is a standard test case for evaluating the predictive capability of turbulence models in transonic flows. Figure 2 shows the respective pressure distributions predicted with the SSG/LRR-ω model and the different diffusion models compared to the experiment. As one can see there is virtually no difference in the C_p-results, except for Case 10, where SGDH predicts the shock slightly upstream of the other solutions.

Nevertheless there are differences in the predicted skin friction distributions, as depcited in Fig. 3. In particular immediately downstream the shock C_f is lower for the GGDH and HL diffusion models, leading to a distinctly larger shock induced

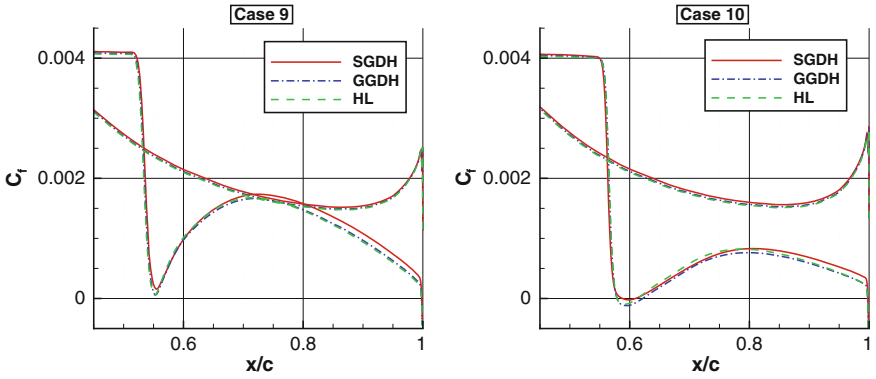

Fig. 3 RAE 28202. Skin friction distributions for Case 9 (*left*) and Case 10 (*right*)

separation zone for Case 10 ($C_f < 0$). Interestingly, after separation HL gives the steepest increase of C_f, leading to an earlier re-attachment than with GGDH. Anyway, the predicted separation bubbles are too shallow to be displayed reasonably.

3.3 Aérospatiale A Airfoil

The flow around the Aérospatiale A Airfoil serves as a test case for predicting pressure induced trailing edge separation under high lift conditions, where the Mach number $Ma = 0.15$, the Reynolds number $Re = 2.1e6$ and the incidence $\alpha = 13.3°$. Under these conditions a laminar separation bubble occurs on the suction side near the leading edge which is closed by setting transition at 12 % chord. On the pressure side transition is fixed at 30 % chord [8].

Figure 4 (left) shows the pressure distribution obtained with the SSG/LRR-ω model combined with the different diffusion models in comparison to experiments. As one can see, in general the suction peak is overestimated, while the pressure level at the trailing edge is somewhat too low. Nevertheless there is virtually no difference between the different diffusion models.

In contrast, the skin friction towards the trailing edge, shown in Fig. 4 (right), is predicted higher with SGDH than with the other models, resulting in a notably smaller trailing edge separation ($C_f < 0$). The scatter of the F1 experimental data does not allow a definite statement on which of the predictions is closest to the measurements. The F2 experimental data imply a larger trailing edge separation, indictaing an improvement by GGDH an HL, but the data are considered less reliable [8].

Figure 5 shows the streamlines near the trailing edge, indicating the separation pattern predicted by the different diffusion models. Consistent with the higher skin friction, with SGDH the separation bubble is markably shallower than with the other models. With GGDH and HL the separation bubble has a similar and higher maximum

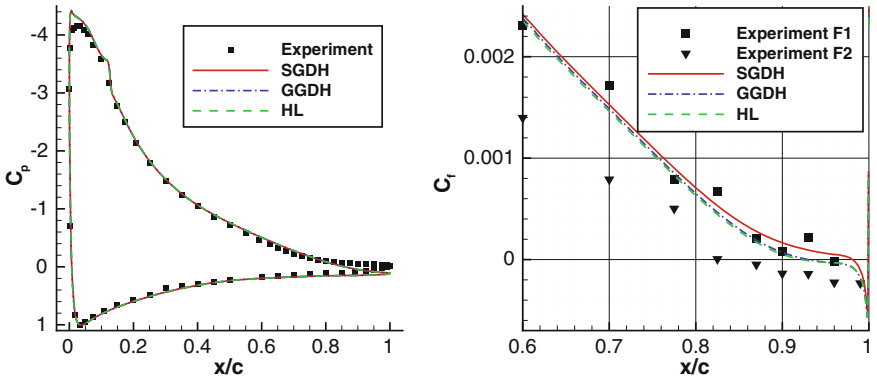

Fig. 4 Aérospatiale A airfoil. Pressure distribution (*left*) and skin friction distribution (*right*)

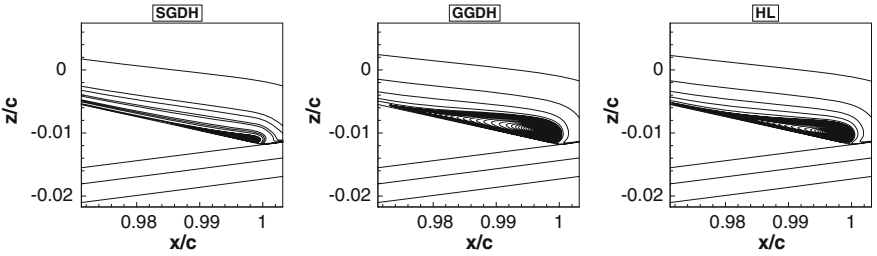

Fig. 5 Aérospatiale A airfoil. Streamlines near trailing edge for SGDH (*left*), GGDH (*center*) and HL (*right*)

thickness, but differs in shape. While with GGDH the bubble seems to grow more or less constantly from the beginning, with HL the bubble remains relatively shallow for a long distance, until it grows fairly rapidly towards the trailing edge.

4 Conclusion

Three different diffusion models have been combined with the SSG/LRR-ω Reynolds stress turbulence model and applied to typical test cases for aerodynamic flows. All diffusion models are based on the gradient diffusion hypothesis, where the diffusion coefficient is a scalar for simple gradient diffusion (SGDH) and a tensor for generalised gradient diffusion (GGDH). The Hanjalić-Launder model (HL) can be considered as an extension of GGDH, which fulfils the symmetry conditions of the modeled turbulent transport term.

For the flow over a flat plate with zero pressure gradient there is little difference between the predicted skin friction, where SGDH yields slightly higher values than the other models. As required, the log-law is represented equally well with all models.

For the transonic flow around the RAE 2822 airfoil, Case 9 and Case 10, the pressure distributions are also almost identical, and there is hardly any visible influence on the shock position. Nevertheless the skin friction differs in particular directly downstream of the shock. Especially for Case 10, with GGDH and HL a larger shock induced separation region is predicted than with SGDH.

Similarly, for the flow around the Aérospatiale A airfoil at $\alpha = 13.3°$ incidence the predicted pressure distributions do not show any significant dependence on the diffusion model. Nevertheless there is an influence on the size and the shape of the trailing edge separation. Again, SGDH yields the smallest recirculation zone, whereas GGDH and HL give larger separation bubbles that differ in shape. Comparison with experimental data seems to indicate a slight improvement by the latter models.

Thus it is confirmed that the influence of the diffusion model is generally relatively small [13]. Nevertheless separation onset and the size of recirculation zones may depend on its details, where the major difference is observed between SGDH, which appears to be the least sensitive to separation, and the other models. The differences between the GGDH and HL results are significantly smaller so that for practical applications the simpler GGDH seems to be a reasonable choice.

Note that no particular convergence problems have been encountered with any of the diffusion models. Note also that with the most complex HL diffusion model particularly good convergence rates have been observed.

References

1. Barche, J. (ed.): Experimental data base for computer program assessment. AGARD-Report AGARD-AR-138 (1979)
2. Coles, D.E., Hirst, E.A.: Proceedings of the Computation of Turbulent Boundary Layers-1968 AFOSR-IFP-Standford Conference, Vol. 2 (1968)
3. Daly, B.J., Harlow, F.H.: Transport equations of turbulence. Phys. Fluids **13**, 2634–2649 (1970)
4. Durbin, P.A., Pettersson Reif, B.A.: Statistical Theory and Modeling for Turbulent Flows. Wiley, Chichester (2001) (reprint 2003)
5. Eisfeld, B.: Numerical simulation of aerodynamic problems with a Reynolds stress model. In: Rath, H.-J., Holze, C., Heinemannm, H.-J., Henke, R., Hönlinger, H. (eds.) New Results in Numerical and Experimental Fluid Mechanics V. Notes on Numerical Fluid Mechanics and Multidisciplinary Design, vol. 92, pp. 413–419. Springer, Heidelberg (2006)
6. Eisfeld, B.: The influence of the length scale equation of the simulation results of aerodynamic flows using differential reynolds stress models. In: Dillmann, A., Heller, G., Klaas, M., Kreplin, H.-P., Nitsche, W., Schröder, W. (eds.) New Results in Numerical and Experimental Fluid Mechanics VII. Notes on Numerical Fluid Mechanics and Multidisciplinary Design, vol. 112, pp. 83–90. Springer, New York (2010)
7. Eisfeld, B., Brodersen, O.: Advanced turbulence modelling and stress analysis for the DLR-F6 configuration. AIAA-Paper 2005-4727 (2005)
8. Haase, W. Aupoix, B., Bunge, U., Schwamborn, D. (eds.): FLOMANIA—A European Initiative on Flow Physics Modelling. Notes on Numerical Fluid Mechanics, vol. 94, Springer, Berlin (2006)
9. Hanjalić, K.: Advanced turbulence closure models: a view of current status and future prospects. Int. J. Heat Fluid Flow **15**, 178–203 (1994)

10. Hanjalić, K., Launder, B.E.: A Reynolds stress model of turbulence and its application to thin shear flows. J. Fluid Mech. **52**, 609–638 (1972)
11. Launder, B.E., Reece, G.J., Rodi, W.: Progress in the development of a Reynolds-stress turbulence closure. J. Fluid Mech. **68**, 537–566 (1975)
12. Menter, F.R.: Two-equation eddy-viscosity turbulence models for engineering applications. AIAA Journal **32**, 1598–1605 (1994)
13. Pope, S.B.: Turbulent Flows. Cambridge University Press, Cambridge (2000)
14. Shir, C.C.: A preliminary study of atmospheric turbulent flow in the idealized planetary boundary layer. J. Atmos. Sci. **30**, 1327–1339 (1973). Cited according to [13]
15. Speziale, C.G., Sarkar, S., Gatski, T.B.: Modelling the pressure-strain correlation of turbulence: an invariant dynamical systems approach. J. Fluid Mech. **227**, 245–272 (1991)

DNS and LES of Turbulent Mixed Convection in the Minimal Flow Unit

Christian Kath and Claus Wagner

Abstract We performed Direct Numerical Simulations (DNS) and Large Eddy Simulation (LES) of turbulent mixed convection in the minimal flow unit. DNS of turbulent isothermal channel flow have been conducted to demonstrate the predictive capability of the second order accurate finite volume method we used. For the mixed convection case we obtained that the turbulence intensity increases due to bouyancy. Consequently, we reduced the spanwise width of the domain to show that turbulence can be sustained for mixed convection. Additionally, we launched a LES of mixed convection with the dynamic Smagorinsky model. The obtained LES results agree well with the corresponding DNS data.

1 Introduction

Research on wall-bounded turbulent flows is of considerable interest for many technological applications. It is also well known that the improved understanding of the transport phenomena closed to walls are of major importance for development of more sophisticated turbulence models. Various researchers summarized the experimental and numerical results of the last years on this subject in annual reviews. Most cited and with the largest impact on research on this subject were [1] and [2]. For the latest review on this topic the reader is referred to [3]. One major issue of these reviews are the development of coherent structures in the turbulent boundary layer. They are found in the viscous sublayer and buffer regions, where the bulk of the near-wall turbulence-production takes place [4]. In channel flows, these structures are alternating narrow streaks of fluid, which move at different speeds in streamwise direction [2]. Fluid from low-speed streaks is transported into the outer region while high-speed streaks receive fluid from the wall-distant zone.

C. Kath (✉) · C. Wagner
German Aerospace Center (DLR), Institute of Aerodynamics and Flow Technology, SCART, Göttingen, Germany
e-mail: christian.kath@dlr.de

A. Dillmann et al. (eds.), *New Results in Numerical and Experimental Fluid Mechanics IX*, Notes on Numerical Fluid Mechanics and Multidisciplinary Design 124,
DOI: 10.1007/978-3-319-03158-3_13,

In order to understand the complex interactions between coherent structures, Jiménez and Moin [5] (hereafter, JM) made several Direct Numerical Simulations (DNS) of turbulent channel flows in different narrow boxes. The idea was to isolate a single low-speed streak in a minimal channel. They have shown that there is minimal set of span- and streamwise widths, in which a turbulent boundary layer can be sustained. An interesting result was that the low-order statistics are in good agreement to those of DNS in the "full" channel in the regions close to the walls, although the minimal box seemed to be too small to adequately represent the turbulent flow in the region away from the wall. Furthermore, it turned out that there are active and passive periods, in which the turbulent boundary layer relaminarizes at one wall of the minimal channel. Indeed, this characteristic was not seen during experimental investigations so far. As they decreased the size of the spanwise width further, they observed the decay of the whole turbulent channel flow to a laminar state.

JM validated this simulations based on a study of the empirical correlation between the wall shear stress and the bulk velocity in channel flows by Dean [6]. The latter predicts that the size of the coherent structures decreases with increasing wall shear stress, while the turbulence production is considerbly enhanced. In this regard several reports (e. g. [7, 8]) point out that buoyancy severely modifies the shear stress in mixed convection. Thus, the primary objective of this work is to obtain and analyse results of turbulent mixed convection in the minimal flow unit and to show if a turbulent flow in a domain smaller than that of JM can be sustained. Finally, results of LES are compared with those of DNS of turbulent mixed convection.

2 Governing Equations and Numerical Method

2.1 Direct Numerical Simulations

The finite volume method solves the time-dependent, incompressible governing equations based on the Boussinesq approximation. They read:

$$\frac{\partial u_i}{\partial x_i} = 0 \tag{1}$$

$$\frac{\partial u_i}{\partial t} + \frac{\partial}{\partial x_j}(u_j u_i) = -\frac{1}{\rho}\frac{\partial p}{\partial x_i} + \nu \frac{\partial^2 u_i}{\partial x_j \partial x_j} + \alpha(T - T_m) g_i \delta_{i2} + F\delta_{i1} \tag{2}$$

$$\frac{\partial T}{\partial t} + \frac{\partial}{\partial x_j}(u_j T) = \kappa \frac{\partial^2 T}{\partial x_j \partial x_j} \tag{3}$$

For space discretization, second-order central differencing is used for all terms. The second-order implicit Crank-Nicolson scheme is used for time discretization. The discretized pressure and velocity fields are coupled with a PISO algorithm [9]. A sketch of the minimal flow unit and the coordinate system is illustrated in Fig. 1.

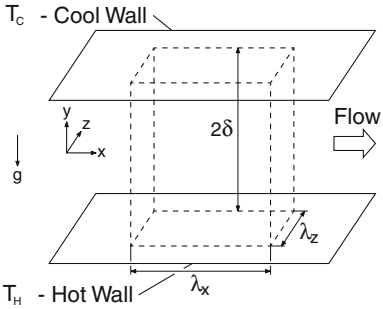

Fig. 1 Geometry of the computational domain with periodic boundary conditions in x- and z-direction

The boundary conditions in both the stream- and spanwise directions are periodic, while top and bottom boundaries are physical walls with no-slip and impermeability conditions. Additionally, the walls temperature is prescribed values $T_H = 274.9\,\mathrm{K}$ and $T_C = 271.4\,\mathrm{K}$, respectively. Throughout this chapter we will use the thermodynamic properties of air for all fluid simulations, i. e. the kinematic viscosity $\nu = 1.35\mathrm{e}-5\,\mathrm{m}^2/\mathrm{s}$, the thermal diffusivity $\kappa = 1.898\mathrm{e}-5\,\mathrm{m}^2/\mathrm{s}$, the density $\rho = 1.276\,\mathrm{kg}/\mathrm{m}^3$ and the thermal expansion coefficient $\alpha = 3.674\mathrm{e}-3\,\mathrm{K}^{-1}$. The buoyancy force acts in wall-normal direction, as well as the gravitational acceleration g. In order to maintain a constant volume flux in the channel flow, we use a forcing function F in the x-direction in the momentum equations. It represents a streamwise mean pressure gradient that needs to be updated at each time step to maintain a prescribed volume flux. The Reynolds number characterising the flow is $Re = u_m\delta/\nu = 2000$ according to JM, where $\delta = 0.18\,\mathrm{m}$ is the channel half width and u_m the volume averaged velocity. Thus, for the Grashof number $Gr = \alpha g\delta^3\Delta T/\nu^2 = 4e^6$, we get an Archimedes number of $Ar = Gr/Re^2 = 1$. As a result of the additionally acting buoyancy force, the wall shear stress is different on both walls. Thus, the friction velocity $u_\tau = \sqrt{\tau_w/\rho}$ and the friction Reynolds number $Re_\tau = u_\tau\delta/\nu$ are the averaged values of the hot and cold wall. In order to define the computational grid, we used the empirical approximation of Pope [10] to predict the friction Reynolds number $Re_\tau = 0.09\,(2\,Re)^{0.88}$. The calculated value of $Re_\tau = 133$ applies to an isothermal simulation. For the simulations of mixed convection the resulting friction Reynolds number is expected to be higher. Therefore, for these simulations we used a even finer grid with a spatial resolution of $\Delta x^+ = 4$ and $\Delta z^+ = 2$ in streamwise and spanwise directions, respectively. The grid is refined in the wall-normal direction, such that the first node at the wall is located at $y_w^+ = 0.1$ and the central spacing is $\Delta y_c^+ = 2.5$. Here, the "+" superscript denotes wall units $\Delta x_i^+ = u_\tau\Delta x_i/\nu$. The physical domain size ($L_x \times L_y \times L_z$) was set to $\pi\ \delta \times 2\,\delta \times \delta$ with a $108 \times 136 \times 68$ grid. As initial condition, we used an instantaneous flow field produced in a DNS of a fully developed turbulent flow of a "full" channel. Before statistical averaging was started, all simulations were processed until no remarkable change in general flow behaviour and the low-order statistical moments was observed. Additionally, we simulated a isothermal turbulent

channel flow in the minimal box of JM to analyse the predictive capabilities of the used finite volume method. For the latter simulation, the momentum Eq. (2) were decoupled from the energy Eq. (3) by setting the buoyancy term to zero.

2.2 Large Eddy Simulations

The following governing equations for the LES are formally obtained by tophat-filtering Eqs. (1)–(3) using a filter width which corresponds to the grid spacing of the coarser LES grid.

$$\frac{\partial \widetilde{u}_i}{\partial x_i} = 0 \tag{4}$$

$$\frac{\partial \widetilde{u}_i}{\partial t} + \frac{\partial}{\partial x_j}(\widetilde{u}_j \widetilde{u}_i) = -\frac{1}{\rho}\frac{\partial \widetilde{p}}{\partial x_i} - \frac{\partial \tau_{ij}}{\partial x_j} + \nu \frac{\partial^2 \widetilde{u}_i}{\partial x_j \partial x_j} + \alpha(\widetilde{T} - T_m) g_i \delta_{i2} + F\delta_{i1} \tag{5}$$

$$\frac{\partial \widetilde{T}}{\partial t} + \frac{\partial}{\partial x_j}(\widetilde{u}_j \widetilde{T}) = -\frac{\partial h_j}{\partial x_j} + \kappa \frac{\partial^2 \widetilde{T}}{\partial x_j \partial x_j} \tag{6}$$

where $\tau_{ij} = \widetilde{u_i u_j} - \widetilde{u}_i \widetilde{u}_j$ and $h_j = \widetilde{u_j T} - \widetilde{u}_j \widetilde{T}$ are the subgrid-scale (SGS) stress tensor and the subgrid-scale heat flux (HF) vector, respectively. These two terms take into account the effect of SGS turbulence and need to be modelled to close the system of governing equations.

We used the dynamic process introduced by Germano [11] and Lilly [12], together with Smagorinsky model [13]. The dynamic Smagorinsky model is known for its features of self-calibration, is free from empirical constants and artificial near-wall damping functions and allows for some backscattering of turbulent kinetic energy from the subgrid-scales to the grid scales. It models the trace-free SGS stress tensor with a function of the resolved strain rate tensor $\widetilde{S}_{ij}$: $\tau_{ij} - \tau_{kk}/3\ \delta_{ij} = -2C_S \widetilde{\Delta}^2 |\widetilde{S}| \widetilde{S}_{ij}$ where $\widetilde{S}_{ij} = (\partial \widetilde{u}_i/\partial x_j + \partial \widetilde{u}_j/\partial x_i)/2$, $|\widetilde{S}| = (2\widetilde{S}_{ij}\widetilde{S}_{ij})^{0.5}$ and $\widetilde{\Delta}$ is the filter width. Following the procedure of [12] we minimize the residual of the Germano identity and obtain $C_S = -(M_{ij}L_{ij})/(M_{ij}M_{ij})$. This equation introduces the resolved Leonard type stress $L_{ij} = \langle \widetilde{u}_i \widetilde{u}_j \rangle - \langle \widetilde{u}_i \rangle \langle \widetilde{u}_j \rangle$ and a differential tensor $M_{ij} = \alpha_{ij} - \widetilde{\beta_{ij}}$ with $\alpha_{ij} = 2\langle \widetilde{\Delta} \rangle^2 |\langle \widetilde{S} \rangle| \langle \widetilde{S} \rangle_{ij}$ and $\beta_{ij} = 2\widetilde{\Delta}^2 |\widetilde{S}| \widetilde{S}_{ij}$. The dynamic model relies on two different filtering operations based on which the model coefficient C_S can be determined. The finer filter is the implicit grid filter ($\sim$) and the coarser filter is the so called test-grid filter ($<>$). In order to avoid negative values for C_S, we applied spatial plane and time averaging of the model coefficient C_S. The dynamic HF model is based on the eddy thermal diffusivity concept in analogy to Fourier's law and was introduced by [14]. It reads: $h_j = -\kappa_t\ \partial \widetilde{T}/\partial x_j = -\nu_t/Pr_t\ \partial \widetilde{T}/\partial x_j = -Pr_t^{-1} C_S \widetilde{\Delta}^2 |\widetilde{S}| \partial \widetilde{T}/\partial x_j$. Here, the SGS eddy thermal diffusivity is κ_t, the SGS eddy viscosity is ν_t and the SGS Prandtl number is the fixed value $Pr_t = 0.5$ as proposed by [14]. The LES was performed on a coarser grid, with $21 \times 88 \times 13$ points in

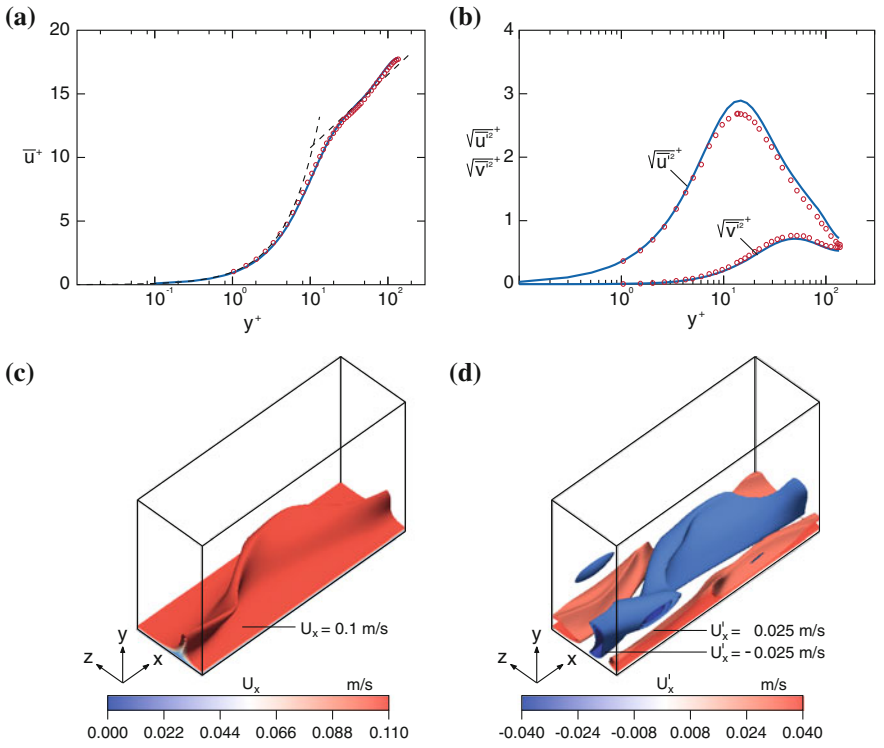

Fig. 2 **a** Mean velocity profile in wall coordinates: DNS (*blue line*) and JM (*red circles*). **b** Root-mean-square (rms) velocity fluctuations in wall coordinates: DNS (*blue line*) and JM (*red circles*). Isosurfaces of instantaneous streamwise velocity component **c** ($u_x = 0.1\,\mathrm{m/s}$) and streamwise velocity fluctuations **d** ($u'_x = 0.025\,\mathrm{m/s}$ and $u'_x = -0.025\,\mathrm{m/s}$)

the x-, y- and z-directions, respectively. Since the domain size was maintained the realized spatial resolution is $\Delta x^+ = 30$, $\Delta z^+ = 15$, $y_w^+ = 0.5$ and $\Delta y_c^+ = 15$, respectively.

3 Results

3.1 DNS of Isothermal Channel Flow

In order to demonstrate the reliability and of the applied second-order accurate finite-volume method used, we simulated turbulent isothermal channel flow in the minimal flow unit of JM. The generated mean streamwise velocity and turbulence intensities profiles in wall coordinates are presented in Fig. 2. Note that the quantities with the $(+)$ superscript are normalized with the friction velocity u_τ. In Fig. 2a, the mean

velocity profile agrees well with the JM data. Furthermore, the profiles of the rms velocity fluctuations shown in Fig. 2b are in good agreement with the JM data as well. There are only small discrepancies in the rms value of the streamwise velocity component in the buffer layer. To demonstrate that the coherent structure discussed above is obtained in the considered minimal flow unit, we illustrated such a structure with isosurfaces of the instantaneous velocity field obtained for some time step in Fig. 2c. We observe one single low-speed streak in the minimal flow unit, which organizes the production of turbulence. The field of velocity fluctuations which is computed by subtracting the mean streamwise velocity component from the instantaneous field shown Fig. 2c is visualized in Fig. 2d. It can be seen that the low-speed streak is surrounded by streaks of high-speed fluid.

3.2 DNS of Mixed Convection

As mentioned above a higher wall shear stress is obtained for turbulent mixed convection. This leads to a increased friction Reynolds number $Re_\tau = 191$. Thus the realized spatial resolution in wall units of the DNS of mixed convection reduces to $\Delta x^+ = 5.7$, $\Delta z^+ = 2.9$, $y_w^+ = 0.14$ and $\Delta y_c^+ = 3.6$, respectively. The predicted mean streamwise velocity, shown in Fig. 3a, agrees well with the law of the wall in the viscous sublayer. Though, farther away from the wall the streamwise velocity values are lower due to the higher turbulence intensity obtained for mixed convection as shown in Fig. 3b. Contrary to the isothermal case, the wall-normal velocity fluctuations are much higher far away from the wall. The corresponding mean temperature profile and the rms temperature fluctuations are presented in Fig. 3c and d, respectively. These graphs show that a turbulent thermal boundary layer develops close to the wall where the mean temperature values $\overline{\theta} = (\overline{T} - T_m)/\Delta T$ significantly deviate from the center temperature $T_m = (T_H + T_C)/2$ as the peaks in the rms temperature fluctuations reveal. In the middle of the channel the rms temperature fluctuations decrease to a minimum. In order to demonstrate that the size of the coherent structures has reduced due to the increased wall shear stress, isosurfaces of the streamwise velocity are presented in Fig. 4a and b. Note, that the scales of Fig. 4a and b are the same as the one of Fig. 2c and d, respectively. The comparison reveals that smaller scales develop for mixed convection which underlines the enhancing effect of buoyancy. In this respect the streaks became thinner and shorter than the single streak observed for the isothermal case. We also performed a number of additional DNS of turbulent mixed convection for which we successively reduced the size of the spanwise width of the domain. The result was that we obtained a turbulent channel flow up to a spanwise width $\lambda_z^+ = 38.2$ (i. e. $L_z = 0.2\delta$).

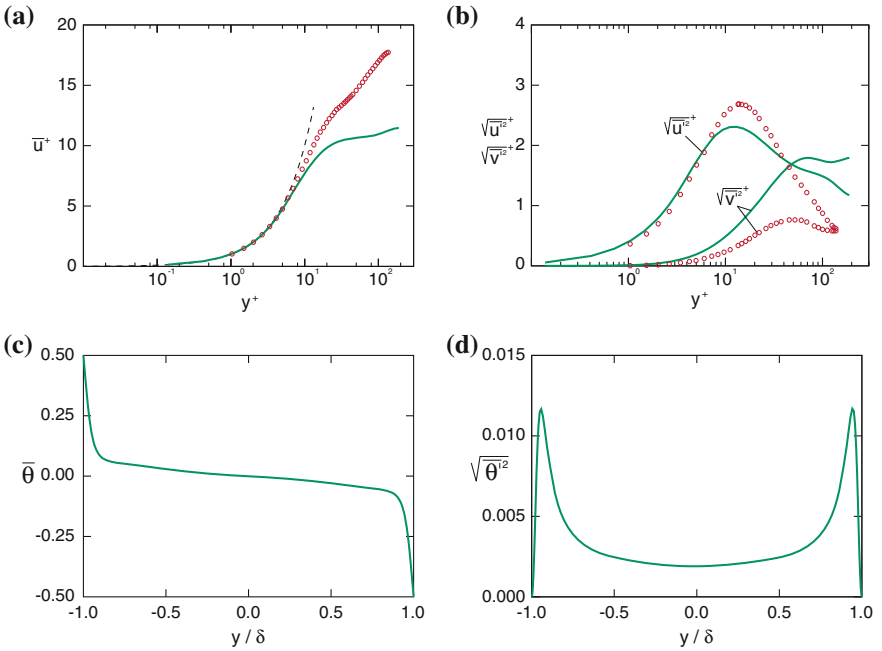

Fig. 3 **a** Mean velocity profile in wall coordinates: mixed (*green line*) and JM (*red circles*). **b** Mean turbulent rms velocity fluctuations in wall coordinates (*green line*) and JM (*red circles*). **c** The normalized mean temperature profile in global coordinates. **d** Mean turbulent rms temperature fluctuations in global coordinates

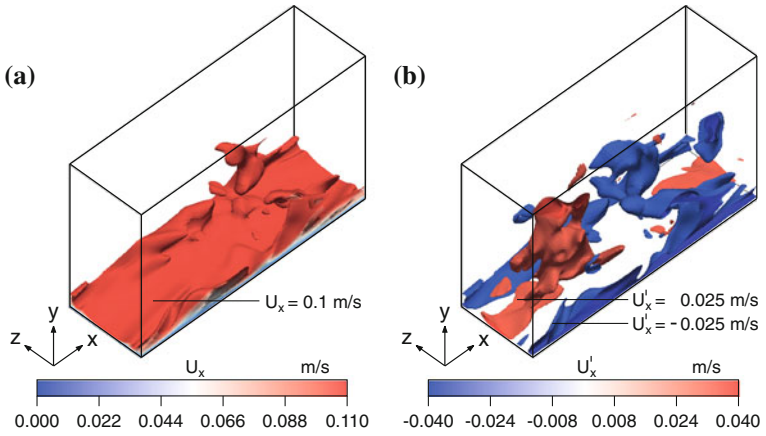

Fig. 4 Coherent structures in mixed convection visualized using isosurfaces of the instantaneous streamwise velocity component in **a** ($u_x = 0.1\,\mathrm{m/s}$) and the streamwise velocity fluctuations in **b** ($u'_x = 0.025\,\mathrm{m/s}$ and $u'_x = -0.025\,\mathrm{m/s}$)

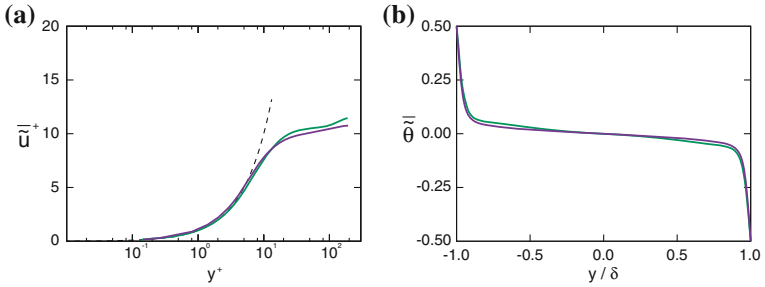

Fig. 5 **a** Mean velocity profile in wall coordinates: DNS (*green line*) and LES (*violet line*). **b** The normalized mean temperature profile in global coordinates: DNS (*green line*) and LES (*violet line*)

3.3 LES of Mixed Convection

The results of the LES are illustrated in Fig. 5a and b. The mean streamwise velocity profile in Fig. 5a matches the DNS data quite well, but it slightly underpredicts the velocity in the region far away from the wall. Fig. 5b additionally shows the normalized temperature profile, which is underpredicted by the LES at the hot wall and overpredicted at the cold wall. Nevertheless, the LES data obtained are in good agreement with the DNS data.

4 Summary

In order to show that the finite-volume method, we used, is accurate enough, we performed a DNS of a turbulent flow in the minimal flow unit for an isothermal case. The spatial resolution realized in this DNS was shown to be fine enough to resolve all relevant turbulent scales. This was confirmed since the DNS results are in good agreement with the reference data by JM. Furthermore, we have also identified similar coherent structures in the minimal flow unit. Since buoyancy increases the wall shear stress, we performed a DNS of turbulent mixed convection. Analysing the results we showed that the streaks became thinner and shorter than in the isothermal case. The analysis of the mean flow field and rms velocity and temperature fluctuations further revealed that buoyancy significantly enhances the production of turbulence. Consequently, we performed additional DNS of turbulent mixed convection for which we successively reduced the size of the spanwise width of the domain and still obtained a self-sustaining turbulent flow. Finally, we conducted a LES of mixed convection with the dynamic Smagorinsky model with spatial plane and time averaging of the model coefficient. The comparison of DNS and LES results revealed that the mean quantities are in good agreement.

References

1. Cantwell, B.J.: Organized motion in turbulent flow. Annu. Rev. Fluid Mech. **13**, 437–515 (1981)
2. Robinson, S.K.: Coherent motions in the turbulent boundary layer. Annu. Rev. Fluid Mech. **23**, 601–639 (1991)
3. Jiménez, J.: Cascades in wall-bounded turbulence. Annu. Rev. Fluid Mech. **44**, 27–45 (2012)
4. Kim, J., Moin, P., Moser, R.: Turbulence statistics in fully developed channel flow at low Reynolds number. J. Fluid Mech. **177**, 133–166 (1987)
5. Jiménez, J., Moin, P.: The minimal flow unit in near-wall turbulence. J. Fluid Mech. **225**, 221–240 (1991)
6. Dean, R.B.: Reynolds number dependence of skin friction and other bulk flow variables in two-dimensional rectangular duct flow. J. Fluids Eng. **100**, 215–223 (1978)
7. Kasagi, N., Nishimura, M.: Direct numerical simulation of combined forced and natural turbulent convection in a verticqal plane channel. Int. J. Heat Fluid Flow **18**, 88–99 (1997)
8. Davidson, L., Čuturić, D., Peng, S.-H.: DNS in a plane vertical channel with and without buoyancy. In: Hanjalić, K., Nagano, Y., Tummers, M.J. (eds.) Turbulence Heat and Mass Transfer, pp. 401–408. Begell House, New York (2003)
9. Issa, R.I.: Solution of the implicitly discretised fluid flow equations by operator-splitting. J. Comput. Phys. **62**, 40–65 (1986)
10. Pope, S.B.: Turbulent Flows, p. 279. Cambridge University Press, Cambridge (2000)
11. Germano, M., Piomelli, U., Moin, P., Cabot, W.H.: A dynamic subgrid-scale eddy viscosity model. Phys. Fluids A **3**, 1760–1765 (1991)
12. Lilly, D.K.: A proposed modifications of the Germano subgrid-scale closure method. Phys. Fluids A **4**, 633–635 (1992)
13. Smagorinsky, J.: General circulation experiments with the primitive equations. Mon. Wea. Rev. **91**, 99–164 (1963)
14. Moin, P., Squires, K., Cabot, W., Lee, S.: A dynamic subgrid-scale model for compressible turbulence and scalar transport. Phys. Fluids A **3**, 2746–2757 (1991)

Turbulence Resolving Simulations of the Flow About a Tandem Cylinder and a Rudimentary Landing Gear

Dieter Schwamborn, Axel Probst, Roland Kessler, Mariafrancesca Valentino and Keith Weinman

Abstract Scale-resolving simulations of two separated flows using the DLR codes TAU and THETA are presented and compared to reference data. For a tandem cylinder the compressible TAU code is shown to yield equally good results as other flow solvers, and the incompressible THETA code allows for efficient and accurate mean-flow predictions of a rudimentary landing gear. Thus, the maturity of the applied models and the numerical solvers for flows with massive separation is demonstrated.

1 Introduction

During the last decade new turbulence resolving methods with less computational effort than Direct Numerical Simulation (DNS) or Large Eddy Simulation (LES) have gained wide spread interest, following the pioneering work of Spalart et al [1] on Detached Eddy Simulation (DES). These methods have been further developed with respect to both the underlying turbulence models and a highersophistication,

D. Schwamborn (✉) · A. Probst · R. Kessler · K. Weinman
DLR, Institute of Aerodynamics and Flow Technology, Göttingen, Germany
e-mail: dieter.schwamborn@dlr.de

A. Probst
e-mail: axel.probst@dlr.de

R. Kessler
e-mail: roland.kessler@dlr.de

K. Weinman
e-mail: keith.weinman@dlr.de

M. Valentino
formerly: DLR, now at ICON Process ad Technology Consulting GmbH, Institute of Aerodynamics and Flow Technology, Göttingen, Germany
e-mail: m.valentino@iconcfd.com

A. Dillmann et al. (eds.), *New Results in Numerical and Experimental Fluid Mechanics IX*, Notes on Numerical Fluid Mechanics and Multidisciplinary Design 124,
DOI: 10.1007/978-3-319-03158-3_14,

like the Delayed DES (DDES) [2] and the Improved Delayed DES (IDDES) [3]. Additionally, they have inspired other approaches such as Scale Adaptive Simulation (SAS) [4].

Recently the European project ATAAC ("Advanced Turbulence Simulation for Aerodynamic Application Challenges") led by DLR has been finished, which concentrated on the development and assessment of such models with respect to flows relevant for the aeronautical industry. In ATAAC the assessment process was based on a number of fundamental "stepping stone" test cases and industrial "application challenges" [5]. Here, results for two fundamental test cases obtained with the DLR codes TAU [6] and THETA [7], respectively, are presented and compared with experimental data as well as results from other partners in ATAAC. These test cases are the NASA Tandem Cylinder [8] and the Boeing Rudimentary Landing Gear [9].

2 Numerical Approach

The applied DLR flow solvers TAU [6] and THETA [7] share the same data structure based on unstructured grids with mixed cell types (e.g. tetrahedra, hexahedra, prisms). For scale-resolving simulations the TAU code solves the compressible flow equations with 2nd order accuracy both in space (i.e. central scheme with matrix dissipation) and time (i.e. dual-time stepping). Low-Mach-number preconditioning is applied for incompressible flows, but convergence rates are still limited in this regime.

The THETA code solves the incompressible equations using a projection method. The linear systems resulting from the implicit time discretization are solved by the matrix-free version of a Krylov method. The code is 2nd order accurate in space and time.

On the physical side three different scale-resolving models are applied: The DDES switches from RANS to LES depending on the local grid spacing, but it applies a shielding function to retain attached boundary layers in RANS mode. The IDDES uses specific sensor functions and a filter-width modified in the near-wall region to provide wall-modelled LES capabilities. The third model, SAS, applies a grid-independent sensor based on the von-Kármán length and is regarded as 2nd generation URANS model.

3 Applications

The simulations of the two ATAAC stepping stone test cases presented here applied the DLR flow solvers TAU and THETA. The Tandem cylinder was computed with the TAU code only, but as it was found that the THETA code was more computationally efficient by a factor of 3–5 for such essentially incompressible flows, THETA was employed for the Rudimentary Landing Gear allowing simulations with three different modelling approaches.

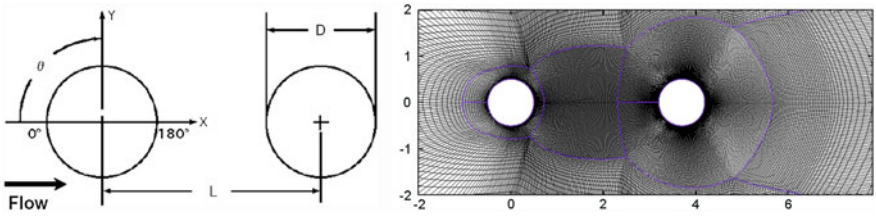

Fig. 1 Sketch of the tandem cylinder configuration and close-up of the grid near the cylinders

3.1 The NASA Tandem Cylinder

A number of experiments with regard to the Tandem Cylinder flow have been performed at NASA Langley Research Center, e.g. [8]. This flow is relevant for airframe noise configurations (e.g. struts and hoses on a landing gear), and has therefore been chosen as a representative stepping stone in the ATAAC project. It is used to test the capability of different turbulence modelling approaches to properly reproduce the following complex flow phenomena: separation of the turbulent boundary layer, roll-up of the free shear layer, unsteady massively separated flow in both wakes, and the unsteady wake of the downstream cylinder. Considering noise, an accurate prediction of the unsteady pressure field of the configuration is of high importance.

The flow properties in the experiment were: $D = 0.05715$ m; $L = 3.7$ D and $U = 44$ m/s at 292 K resulting in a Reynolds number of $1.66 \cdot 10^5$ based on D. As the boundary layer on both cylinders was tripped ahead of their separation, performing "fully turbulent" simulations seemed nevertheless justified. The grid for these simulations was provided by NTS (St. Petersburg) and used by most contributing partners. The block-structured mesh consists of about 12 million grid points in 150 parallel planes spanning a width of 3 D. The cell size in the focus region close to and between the cylinders is 0.02 D, with $y^+ \sim 1$ at the walls. As lateral boundary conditions periodicity was assumed, and the upper and lower boundaries (at $y = \pm 6.22$ D) were treated as inviscid walls (i.e. symmetry planes). Figure 1 shows the geometrical setup and the grid close to the cylinders. More details on the partner codes and the mesh can be found in [5].

The results shown here are all based on DDES simulations with either the Spalart-Allmaras (SA) or the kω-SST model as the RANS basis, except for NLR's XLES approach which acts however similar to a kω-based (D)DES. Figure 2 shows the pressure coefficient on the surface of both cylinders averaged both in span and time, where all calculations were performed with a time step of $\Delta t = 0.02$ D/U. The averaging time was at least in the order of 100 convective time units (CTU = D/U), and even much longer averaging did not result in essential differences. Unlike URANS calculations (not shown here) all results are in good or at least satisfactory agreement with the experiment, with a slight advantage for the SA-based approaches.

Switching to the unsteady part of the pressure presented in Fig. 3 the situation changes in so far as the scatter between the results is now much larger, especially

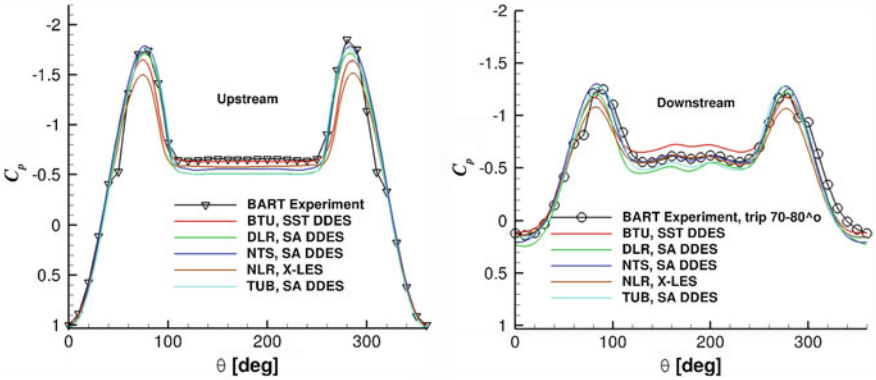

Fig. 2 Mean pressure coefficient on the upstream (*left*) and downstream (*right*) cylinder

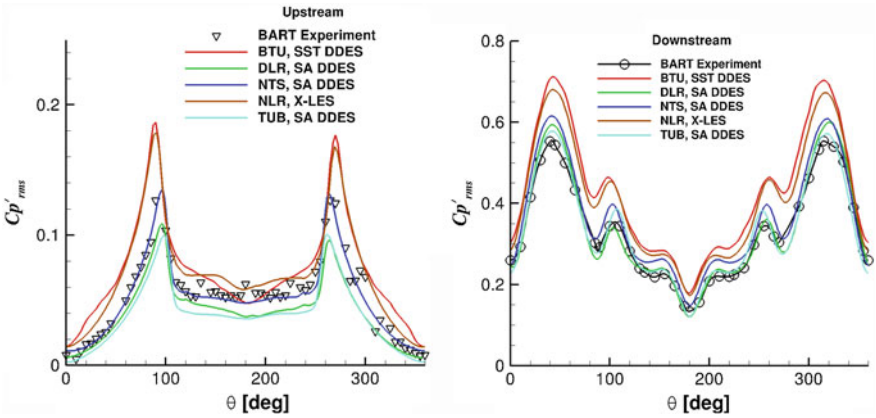

Fig. 3 Mean of the pressure fluctuations on the first (*left*) and second (*right*) cylinder; note the different scale on the downstream cylinder, which is "noisier" than the upstream one

on the second cylinder (note the different scale!). Although no method is perfect everywhere, it seems that the SA-based results are again a bit closer to the experiment, especially those by NTS (with a 4th order method), which might indicate that a higher order discretization is favourable for resolution of unsteady effects.

Figure 4 depicts the mean velocity distributions along the center line between the cylinder and after the second one. While the agreement of all simulations with the experiment is excellent in the wake behind the rear cylinder, most approaches indicate a too long recirculation zone behind the front cylinder, with the DLR result being in good agreement. Comparing the resolved turbulent kinetic energy in the same regions (Fig. 5; only components normal to the cylinder axis) the situation worsens drastically: the scatter is quite large and only the NLR result is close to the experiment in both areas.

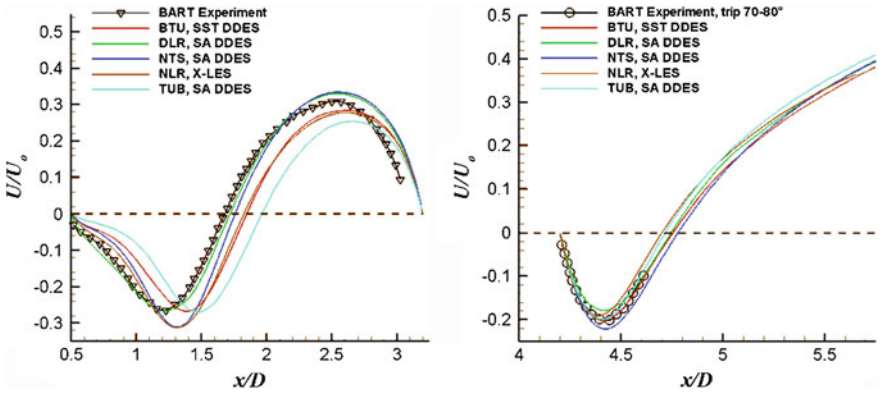

Fig. 4 Center line velocity between cylinder (*left*) and in the wake of the rear cylinder (*right*)

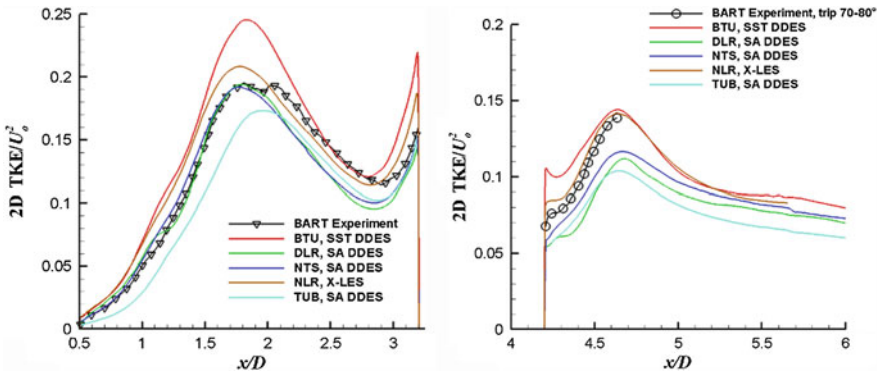

Fig. 5 Distribution of the in-plane part of the resolved turbulent kinetic energy along the centerline between the cylinders (*left*) and behind the second cylinder (*right*)

3.2 The Rudimentary Landing Gear

The second ATAAC test case presented here is the "Rudimentary Landing Gear" (RLG), an experiment for validation of hybrid approaches proposed by Spalart, funded by Boeing and performed by NAL, Bangalore [9]. A specialty of this case is that all struts and axles of the configuration are rectangular resulting in separation at the edges, thus reducing the sensitivity to the Re-number, which is $Re_D = 10^6$ based on wheel diameter. For the same reason the wheels are tripped and can be modelled as fully turbulent in the simulations. As the flow can be considered incompressible ($U_\infty = 40$ m/s) the simulations were performed with the DLR THETA code, which is faster than TAU in this case. This allows for a comparison of three different approaches with less effort, i.e. SA-DDES, SA-IDDES and kω-SST-based SAS. A structured mesh with 11 million grid points was used, providing a mean cell size of about 0.04 D in the resolved regions behind the landing gear. The time step

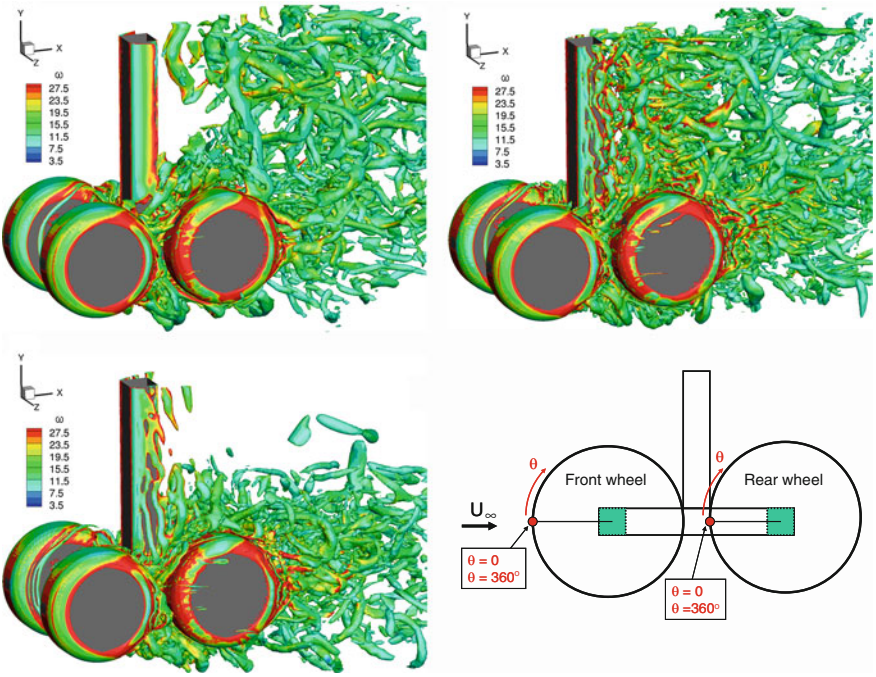

Fig. 6 Flow structures visualized by iso-surfaces of vorticity-coloured Q-criterion: SA-DDES (*top left*), SA-IDDES (*top right*) and SAS (*bottom left*); sketch of RLG (*bottom right*)

in all simulations was chosen as 0.005 D/U_∞. The averaging time interval was 130 CTU (with CTU $= D/U_\infty$) for SA-IDDES, and 50 CTU in the SA-DDES and SAS computations, respectively.

A qualitative impression of the flow is given in Fig. 6 depicting turbulent structures in the flow. While the structures are very similar in the wheel area, the three models perform clearly different in the area behind the main strut: the IDDES starts to resolve structures already in the shear layer on the side of the strut (due to its reduced filter width), whereas the SAS exhibits no structures. The latter indicates that the SAS remains in URANS mode, as e.g. in simulations of the backward facing step, where artificial turbulence is needed to make the SAS switch to resolving mode. The DDES stays first in URANS mode due to the shielding of the boundary layer and thus delays the development of turbulent content compared to IDDES.

Figure 7 provides a comparison of pressure data on the wheels. On the front wheel the mean data of the simulations and the experiment are in almost perfect agreement, which is also true for the rear wheel with two exceptions: firstly, all models alike yield a deviation from the experiment in the area, where eddies from the front wheel impinge on the lower front of the rear one at Θ about 320°. Secondly, the IDDES shows a difference just behind the 90° position indicating earlier deceleration and separation. These deviations from the experiment find their counterparts in a higher

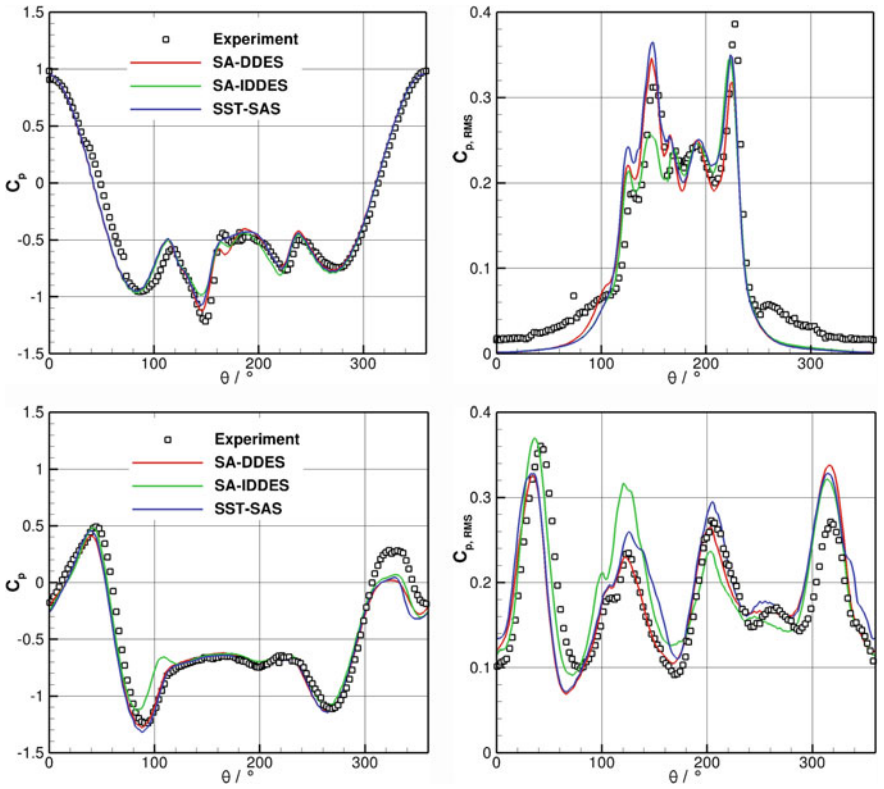

Fig. 7 Comparison of the models regarding mean (*left*) and fluctuating (*right*) pressure along a circumferential line on the front (*top*) and rear (*bottom*) wheel (for Θ see sketch in Fig. 6)

rms-pressure value in the same locations, while this quantity is otherwise in satisfactory agreement. The reasons for these deviations are not yet understood, but have also been found by other partners in ATAAC. Another difference seen in Fig. 7 remains unclear as well, i.e. the experiment exhibits small but non-zero rms-values already in the stagnation area of the front wheel. This could hint to a sound source in the wind tunnel.

Figure 8 gives an impression of the flow along the wheel surface, visualized by oil flow in the experiment and mean skin-friction lines in the computation. As the models only yield minor differences, just IDDES is exemplarily shown. Overall good qualitative agreement is observed in the distinct vortical flow regions, although some irregularities and asymmetries in the simulation may indicate insufficient time averaging of the required flow gradients close to the wall.

Figure 9 provides acoustics-related data in form of the sound pressure level (SPL). In the first location on the rear of the main strut the IDDES predicts a higher level than the other approaches which is in line with the earlier resolution of turbulent eddies in Fig. 6, but unfortunately too high compared with the experiment. Furthermore

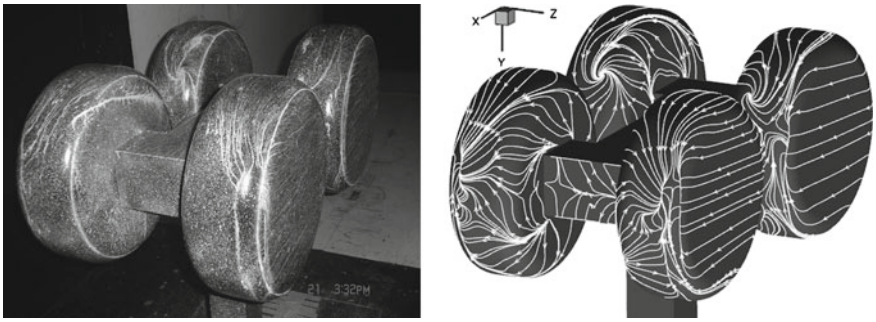

Fig. 8 Rear view of the flow structure on the wheels from oil flow (*left*) and IDDES (*right*)

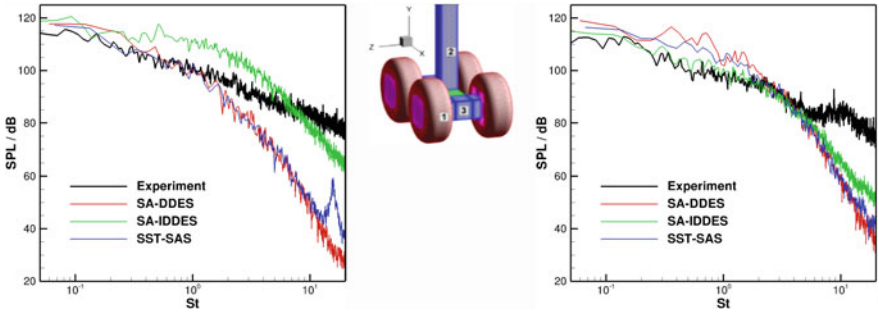

Fig. 9 Sound pressure level on the rear of the strut (pos. 2; *left*) and the axle (pos. 3, *right*)

we find a too fast drop of the SPL with increasing frequency due to insufficient numerical resolution. At the rear of the axle all numerical results converge again. Here, the IDDES is somewhat closer to the experiment but still dropping too fast. The high-frequency peak for SAS at pos. 2 may be attributed to local numerical instabilities.

4 Conclusions

Turbulence resolving flow simulations of two test cases with massive separation from the ATAAC project have been assessed, using DLR's flow solvers TAU and THETA as well as different physical models. For these highly-unsteady flows, where conventional URANS approaches are clearly infeasible, all tested variants of Detached-Eddy Simulation and the Scale-Adaptive Simulation are shown to offer great benefits in both compressible and incompressible formulations. Although the mean flow data and to a certain extend even the fluctuations can be predicted satisfactorily for engineering purposes, the results are still not accurate enough in an aero-acoustic sense.

Acknowledgments The results in this publication were obtained in the framework of the European ATAAC project, which was funded by the European Community under Contract No. ACP8-GA-2009-233710-ATAAC. The authors are grateful to Boeing and Philippe Spalart for releasing the experimental data of the RLG.

References

1. Spalart, P.R., Jou, W.-H., Strelets, M., Allmaras, S.R.: Comments on the Feasibility of LES for Wings and on the Hybrid RANS/LES Approach. Advances in DNS/LES. In: Proceedings of the First AFOSR International Conference on DNS/LES (1997)
2. Spalart, P.R., Deck, S., Shur, M.L., Squires, K.D., Strelets, M.K., Travin, A.: A new version of detached-eddy simulation, resistant to ambiguous grid densities. Theor. Comput. Fluid Dyn. **20**(3), 181–195 (2006)
3. Shur, M.L., Spalart, P.R., Strelets, M.K., Travin, A.K.: A hybrid RANS-LES approach with delayed-DES and wall-modelled LES capabilities. Int. J. Heat Fluid Flow **29**(6), 1638–1649 (2008)
4. Menter, F.R., Egorov, Y.: A scale-adaptive simulation model using two-equation models. AIAA paper 2005–1095, Reno/NV (2005)
5. Schwamborn, D., Strelets, M.: ATAAC—an EU-project dedicated to hybrid RANS/LES methods. In: Fu, S., Haase, W., Peng, S.H., Schwamborn, D. (eds.) Program in Hybrid RANS/LES Modelling, Notes on Numerical Fluid Mechanics and Multidisciplinary Design, vol. 117 (2012)
6. Schwamborn, D., Gardner, A., von Geyr, H., Krumbein, A., Lüdeke, H., Stürmer, A., Development of the TAU-Code for aerospace applications. In: 50th NAL International Conference on Aerospace Science and Technology, 2008-06-26–2008-06-28, Bangalore. http://www.nal.res.in/nal50/incast/incast/01-Invited%20Talk%20Full%20papers/IT-13.pdf
7. Kessler, R., Rütten, M., Pennecot, J.: Simulation of the flow in a human nose. In: New Results in Numerical and Experimental Fluid Mechanics VII, Notes on Numerical Fluid Mechanics and Multidiscipliary Design, vol. 112, pp. 521–528. Springer, Berlin, (2010)
8. Jenkins, L.N., Neuhart, D.H., McGinley, C.B., Choudhari, M.M., Khorrami, M.R.: Measurements of unsteady wake interference between tandem cylinders. AIAA Paper 2006–3202 (2006)
9. Venkatakrishnan, L., Karthikeyan, N., Mejia, K.: Experimental studies on a rudimentary four wheel landing gear. AIAA-2011-0354 (2011)

Superstructures in a Turbulent Boundary Layer Under the Influence of an Adverse Pressure Gradient Investigated by Large-Scale PIV

D. Schanz, T. Knopp, A. Schröder, M. Dumitra and C. J. Kähler

Abstract The flow of a turbulent boundary layer under the influence of an adverse pressure gradient was investigated using a large-scale, high-resolution PIV setup. Wall-normal vector fields with a length of 1.7 m (ultimately over 3.0 m) and a resolution below one mm were stitched from multiple camera views. Re_θ was measured to be 4,600 at the end of a long flat plate preceding the pressure gradient. Within this dataset long, stretched regions with positive or negative streamwise velocity fluctuations can be observed in singular snapshots. These so-called 'super-structures' (or 'very large-scale motions') were already identified in undisturbed turbulent boundary layers [1], pipe flows [2], and in flows under the influence of an adverse pressure gradient [3, 4]. These measurements either used PIV with a limited measurement region or probe-measurements assuming frozen turbulence. As already described in other publications, a reliable capture of very long flow phenomena proved to be problematic due to spanwise meandering. The structures move in and out of the two-dimensional measurement plane used in the presented experiment, reducing their perceived extent. However, in many snapshots the meandering is of a low scale, so that large parts of the structures could be imaged. In order to characterize the occurring flow structures, two-point-correlations were performed, yielding the average structure size in the course of the adverse pressure gradient for different heights above the wall. Average sizes of 1.6–3.2 δ were found, with an increase in structure length with the advance of the pressure gradient. Especially smaller-scale structures near the model wall increase in size as they are driven from the wall,being stretched

D. Schanz (✉) · T. Knopp · A. Schröder
Deutsches Zentrum für Luft- und Raumfahrt e.V. (DLR), Institut für Aerodynamik und Strömungstechnik, Bunsenstr. 10, 37073 Göttingen, Germany
e-mail: Daniel.Schanz@dlr.de

M. Dumitra · C. J. Kähler
Institute for Fluid Mechanics and Aerodynamics, Universität der Bundeswehr, München, Germany

A. Dillmann et al. (eds.), *New Results in Numerical and Experimental Fluid Mechanics IX*, Notes on Numerical Fluid Mechanics and Multidisciplinary Design 124,
DOI: 10.1007/978-3-319-03158-3_15,

in the process. Further measures to identify singular super-structures instead of applying statistical approaches—which are biased by the huge number of small structures and the meandering of the large ones—are discussed.

1 Introduction

Jiménez [5] showed that eddies with streamwise lengths of 10–20 δ are present in the logarithmic region of wall-bounded flows by compiling results from existing measurements and numerical simulations. Kim and Adrian [2] found streamwise energetic modes with wavelengths up to 14 pipe radii within fully developed turbulent pipe flow. They accounted the alignment of packets of hairpin-vortices as responsible for the creation of such structures and termed them 'very large scale motion' (VLSM).

Indications of the existence of similar flow structures within the log-region of turbulent boundary layers (TBLs) were given by Tomkins and Adrian [6], as well as Ganapathisubramani et al. [7]. They were able to document the existence of long stripes of negative or positive streamwise velocity fluctuations (u') within these domains. Both publications relied on measurements using the method of particle imaging velocimetry (PIV) with a streamwise length of the investigation area around two times the boundary layer thickness (δ). Therefore the full extent of the found structures could not be examined.

Hutchins and Marusic [1] and again Marusic et al. [8] confirmed these results using a similar PIV-setup. Additionally they performed measurements using a hot-wire rake, covering a spanwise distance of more than one δ with eleven hot-wire probes. By applying Taylor's hypothesis on the obtained time-series, they were able to extract quasi-instantaneous snapshots of the flow structures at several heights above the wall. In many of these snapshots very long structures of positive and negative u' can be seen, frequently exceeding a length of 20 δ. These regions of negative and positive u' typically appear besides each other and show a meandering behavior in spanwise direction. The authors account this meandering for the fact that the length scales indicated by single-point statistics were much shorter (around 6 δ). Due to the large extent of the found features, the authors termed them 'superstructures'.

As shown by DNS data [4], these superstructures seem to directly interact with small-scale structures near the wall (leaving a 'footprint'). This impact on the conditions near the wall is of particular interest, as the large-scale structures underlie outer scaling (their extent is dependent on δ and therefore also the Reynolds number), while it was assumed that near-wall structures do not. The interaction of large and small-scale structures challenges this assumption. A further examination of the formation and evolution of superstructures in different flow conditions is therefore of interest for a better understanding of turbulent flows in general.

Rahgozar and Maciel [3, 4] investigated large and very large-scale structures in a turbulent boundary layer subjected to a strong adverse pressure gradient (APG). Horizontal measurement planes with a height of 3 δ at different heights and streamwise locations were investigated using PIV. It was found that the general features

of large flow structures are retained under the presence of an APG, however the frequency of appearance decreases. Especially in the lower parts of the boundary layer the appearance of high- and low-speed streaks diminishes in comparison to a zero-pressure-gradient case.

For this study, large-scale PIV-data of a TBL within a slowly rising adverse pressure gradient is analyzed with respect to the sizes of the occurring structures; indications of the presence of superstructures within this flow regime are gathered.

2 Experimental Setup

The experimental data was gained in context of the DLR-internal project 'Rettina'. The aim of the project was to generate an experimental dataset suitable for the extraction of possible enhancements and/or modifications of the law of the wall for flows within a pressure gradient [9, 10].

A large model was designed that allowed maximizing the achievable Reynolds number, smooth changes of the pressure gradient and good measurability of the flow properties. Figure 1 shows the model in top view. Spanning over 12 m, it consists of a long flat plate with superelliptic nose that allows the buildup of a TBL of significant thickness. The deflection is achieved by a 1.5 m-long arc with large curvature radius, followed by a 0.8 m long flat plate, inclined at an angle of 13° relative to the main flat plate. The flow is directed back by another arc, followed by a flat plate. At the end of the model a 1.5 m-long flap can be used to ensure symmetric flow conditions at the nose.

An appropriate wind tunnel was found with the 'Atmospheric Wind Tunnel' at the Universität der Bundeswehr in Munich. The 22 m long test section with a cross section of 2×2 m allowed for huge dimensions of the model, wind speeds up to 40 m/s are achievable; the measured turbulence level is 0.1 %.

In order to be able to describe the development of the flow characteristics for all pressure regions—from the undisturbed boundary layer, over the onset of the deflection to the fully developed pressure gradient—a large scale PIV-setup was used.

Eight high-resolution PCO 4,000-Cameras with 11 Megapixel each were installed in series on top of the wind tunnel, observing a total region of over 3 m in the vicinity of the APG. Figure 2 shows the approximated fields of view of all cameras. Seven cameras used 100 mm-lenses, while one camera, connecting the main areas of interest, used a 50 mm-lens. The described camera system allowed retaining a high spatial resolution, in spite of the very large investigation area. For the work presented in this chapter, only the four cameras downstream (labeled 1–4) were used.

Illumination was realized using two partially overlapping light sheets, generated by two double pulse lasers. The flow was seeded with DEHS droplets, having an average diameter of approx. 1 μm. The gained images were correlated using an iterative multigrid algorithm with image deformation. A final window size of 24×24 pixels (16×16 in case of camera 1), combined with an overlap of 66 %, yields a

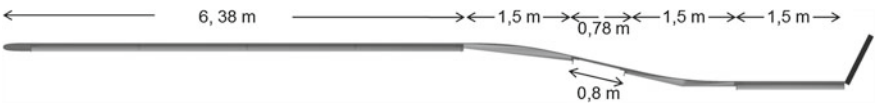

Fig. 1 *Top view* of the model installed upright in the center of the wind tunnel, with flow being directed past both sides. The flap at the end is used to compensate for circulation around the model

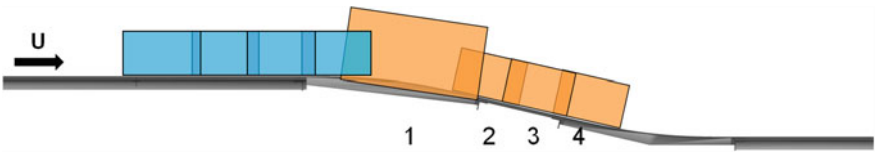

Fig. 2 Fields of view for the eight PCO 4,000 cameras. The four cameras used within this work are numbered 1, 2, 3, 4 in streamwise direction

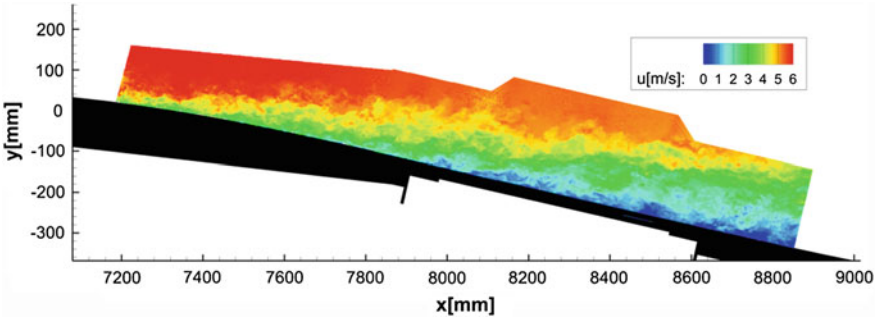

Fig. 3 Instantaneous snapshot of u-velocity for U = 6 m/s (stitch of four camera views)

vector spacing of approx. 0.65 mm (1 mm for camera 1). A more detailed description of the experiment can be found in [11].

The calculated vector fields for each camera are combined according to the calibration to yield one continuous vector field of approx. 1.7 m length and around 20 cm wall-normal height. Figure 3 shows an example of the instantaneous velocity field as seen by the four cameras considered.

Using a free stream velocity of $U = 6\,\mathrm{m/s}$, a boundary layer thickness of $\delta_{99} = 106\,\mathrm{mm}$ was measured at the end of the long flat plate. Around 6,000 independent snapshots were taken at a frequency of 1 Hz, allowing for converged statistics. Figure 4 shows the averaged u-velocity.

3 Structure Characterization

Looking at instantaneous streamwise fluctuations (see Fig. 5) it is obvious that patterns resembling the sought-after superstructures can be identified. In the rear part of the APG a stretched region of slow fluid can be seen that spans a length

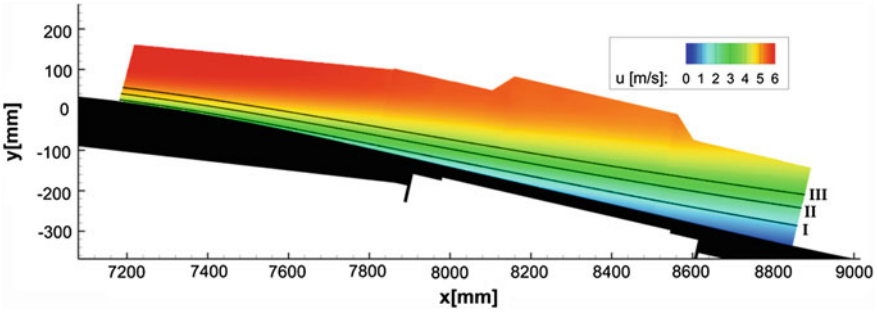

Fig. 4 Averaged u-velocity for a free stream velocity of U = 6 m/s. Streamtraces starting at y = 0.04 δ(I), y = 0.17 δ(II) and y = 0.32 δ(III)

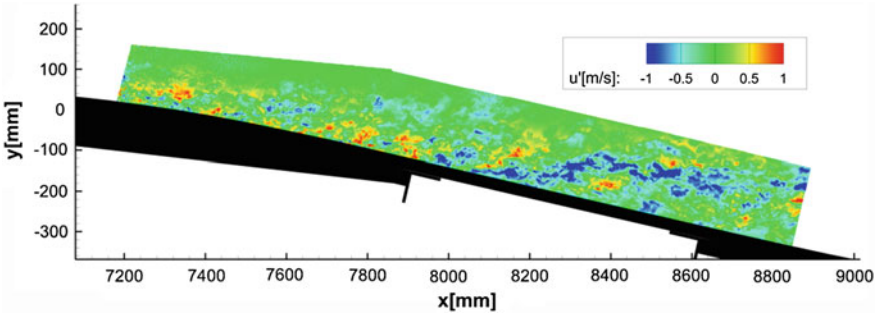

Fig. 5 Instantaneous streamwise velocity fluctuations, derived from the velocity field shown in Fig. 3

of around 80 cm (∼8 δ), before it exists the investigation area. Evidence for similar structures can be found in many instantaneous snapshots, though the features often seem to be more disturbed and broadened compared to the hot-wire results in [1]. As can be seen in Fig. 5, the structures are mostly angled to the (tilted) wall and seem to be stretched in the direction of the main flow. This inclination does not seem to change noticeably with progression of the pressure gradient.

As to be able to describe the structures' evolution within the growing influence of the APG, streamtraces were extracted from the averaged velocity data. Along these streamtraces, two-point correlations of streamwise velocity fluctuations (R_{uu}) were performed in order to extract general features of the occurring structures and their development in time. The fixed points of the two-point correlations were positioned at 45 equidistant points following along the streamtraces. This approach was chosen, assuming that occurring structures should mostly follow the mean flow. Three streamtraces with starting points at different heights above the wall (y = 0.04 δ (I), y = 0.17 δ (II) and y = 0.32 δ (III)) were examined—see Fig. 4.

Figures 6 and 7 show exemplary correlation results for two fixed points on streamtrace II. The correlation plane at the onset of the APG (Fig. 6) shows a streamwise

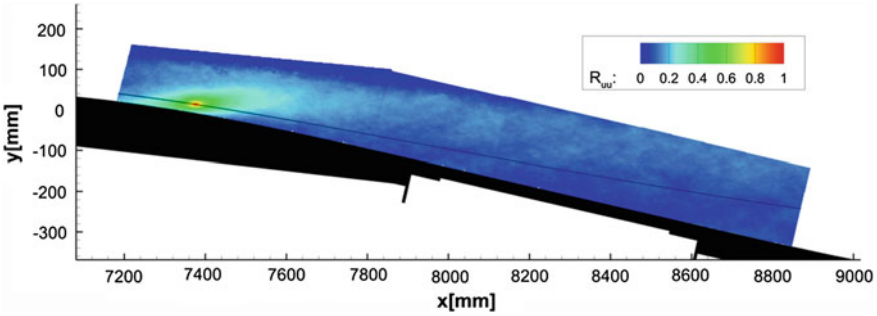

Fig. 6 Two-point correlation of streamwise velocity fluctuation (R_{uu}) for a fixed point on streamline II in the early stages of the adverse pressure gradient

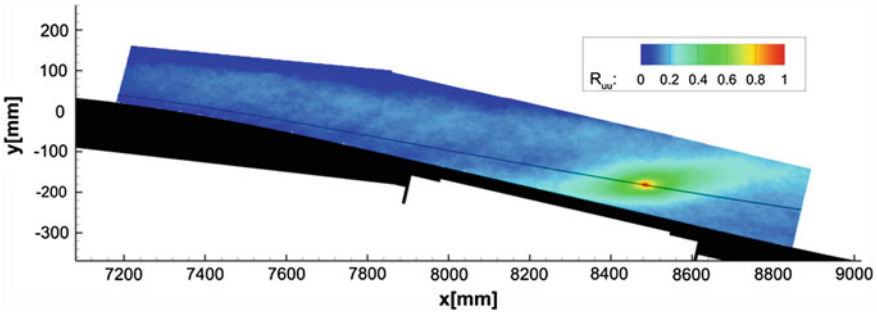

Fig. 7 Two-point correlation of streamwise velocity fluctuation (R_{uu}) for a fixed point on streamline II in the later stages of the adverse pressure gradient

elongation of around 250 mm, indicating the presence of structures with an average length of 2–3 δ. The inclination of the correlation figure is around 10° relative to the main flow direction. In case of an undisturbed TBL, the value of this inclination would be 11–13°.

The characteristic shape of the correlation figure stems from the presence of hairpin-like vortices, which are typically inclined at an angle of around 45° relative to the wall (see e.g. [12]). The averaging of the occurring structures, as done by the process of two-point-correlation, results in the elliptical shape with inclination towards the wall (see [1] for an example in a zero-pressure-gradient case).

Looking at the results at a later stage of the APG (Fig. 7), it is evident that the correlation is broadened and the peak is smeared out. The occurring structures are stretched in length by the force of the APG and widened by the increasing turbulence within this region. Still, the inclination of the correlation figure is fixed at a value of approx 10°. The structures may be convected with the flow, as well as deformed by the occurring forces, but their general direction and orientation remains unchanged.

In order to quantify the development of structure sizes within the APG, the integral length scale of all considered two-point-correlations was calculated:

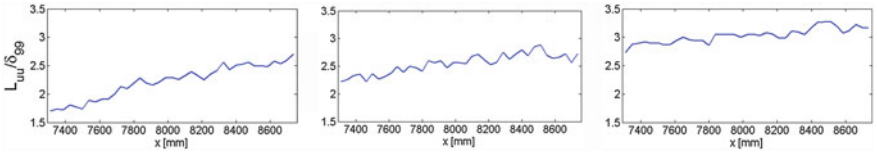

Fig. 8 Spatial development of the integral length scale for two-point-correlations along streamtraces I (*left*), II (*middle*) and III (*right*)

$$L_{uu}(r) = \int_{-\infty}^{\infty} R_{uu}(r)\, ds$$

This value gives a measure of the averaged elongation of the structures along the direction of the line integral. In this case, the line integral was chosen to run along the extracted streamtrace (as indicated in Figs. 6 and 7). L_{uu} was evaluated for all 45 fixed points of the two-point correlations along streamtraces I, II and III, giving the development of structure sizes within the growing influence of the APG.

Figure 8 shows the results of these calculations. In case of streamtrace I, which is positioned close to the wall ($y = 0.04\,\delta$) at the upstream edge of the interrogation volume, the structures clearly gain in size while following the streamtrace: averaged structure sizes of around 1.6 δ are found at the beginning (at $x \approx 7300$ mm), which increase to around 2.6 δ at the end of the interrogation volume (at $x \approx 8700$ mm). The streamtrace is clearly lifted from the model wall by the APG, the flow being on the verge of detachment. The smaller-scale structures near the wall are stretched significantly during this process and gain in size.

This effect is less pronounced in the regions higher up the TBL: the increase in structure size is far less pronounced in case of the other streamtraces. For streamtrace II initial structure sizes of around 2.2 δ can be seen, which rise to a maximum of around 2.8 δ at the end of the interrogation volume. For streamtrace III the initial size of approx. 2.8 δ rises to around 3.2 δ in the final stages of the APG. The increase in structure size seems to be connected to the relative growth of wall distance with the course of the streamtrace. Actual structure sizes may be slightly underestimated by this approach, as the maximum extent of the correlation figure is not along the streamtrace, but along the inclination relative to the main flow. It has to be stressed that very long structures are singular events that cannot be adequately captured by two-point correlations, as these constitute averages of all occurring flow phenomena. Additionally, large structures are often not imaged entirely due to spanwise meandering, reducing the perceived structure size.

4 Conclusion and Outlook

By performing successive two-point-correlations along streamtraces of the flow under the influence of an adverse pressure gradient, it was possible to document the development of averaged structure-sizes and-orientation. It can be seen that structures spanning multiple δ can be found on a regular basis, which grow in size with increased distance to the model wall. The presence of the pressure gradient both stretches and widens the flow features.

With respect to the sought-after super-structures these investigations showed to be not suitable to extract a great deal of relevant information. Though it is clear that very long structures persist within the APG-region (see Fig. 5), their occurrence is irregular; statistical approaches, such as two-point-correlations, are biased by smaller structures. Therefore, the real length of such structures ($>8\,\delta$ by visual inspection of the data, $20\,\delta$ as given in [1]) could not be confirmed in the scope of the conducted investigations.

One obstacle in the observation of super-structures in the available dataset is the spanwise meandering of the structures, described in [1]. As the PIV measurement plane is oriented in wall normal direction it is possible that existing super-structures move in and out of the measurement plane within one single snapshot. If this is the case, the real extent of the structures will be masked to the measurement. However, for a subset of the measurements the meandering is of such a small scale that the whole structure is visible. In order to identify such cases and to extract viable information, other examination methods are needed, such as conditional averaging or pattern-recognition, similar to the methods applied in [3].

In the scope of such an investigation, the additional data from the four upstream cameras, observing the undisturbed boundary layer and the early onset of the APG, would be included. By this, occurring structures could be captured at their full length, and the whole process of structure development within the pressure gradient could be described.

Furthermore, measurements on the same model using tomographic PIV [13] are planned. These investigations could simultaneously show the meandering tendency of the occurring structures, as well as document their wall-normal appearance.

References

1. Hutchins, N., Marusic, I.: Evidence of very long meandering features in the logarithmic region of turbulent boundary layers. J. Fluid Mech. **579**, 1–28 (2007)
2. Kim, K.C., Adrian, R.J.: Very large-scale motion in the outer layer. Phys. Fluids **11**, 417–422 (1999)
3. Rahgozar, S., Maciel, Y.: Low and high-speed structures in the outer region of an adverse-pressure-gradient turbulent boundary layer. Exp. Therm. Fluid Sci. **35**, 1575–1587 (2011)
4. Rahgozar, S., Maciel, Y.: Statistical analysis of low-and high-speed large-scale structures in the outer region of an adverse pressure gradient turbulent boundary layer. J. Turbul. **13**, 46 (2012)

5. Jiménez, J.: The Largest Scales of Turbulent Wall Flows, pp. 137–154. CTR Annual Research Briefs. University, Stanford (1998)
6. Tomkins, C.D., Adrian, R.J.: Spanwise structure and scale growth in turbulent boundary layers. J. Fluid Mech. **490**, 37–74 (2003)
7. Ganapathisubramani, B., Longmire, E.K., Marusic, I.: Characteristics of vortex packets in turbulent boundary layers. J. Fluid Mech. **478**, 35–46 (2003)
8. Marusic, I., McKeon, B.J., Monkewitz, P.A., Nagib, H.M., Smits, A.J., Sreenivasan, K.R.: Wall-bounded turbulent flows at high Reynolds numbers: recent advances and key issues. Phys. Fluids **22**, 065103 (2010)
9. Knopp, T.: Entwurf eines Experimentes einer turbulenten Grenzschicht mit starkem Druckgradienten bei hohen Reynoldszahlen zur Entwicklung von Wandgesetzen bei Druckgradienten, DLR-IB 224–2011 C 106 (2011)
10. Knopp, T., Schanz, D., Schröder, A., Dumitra, M., Cierpka, C., Hain, R., Kähler C.J.: Experimental investigation of the log-law for an adverse pressure gradient turbulent boundary layer flow at $\mathrm{Re}_\theta = 10000$, Flow Turbul. Combust. (2013). doi:10.1007/s10494-013-9479-3
11. Dumitra, M., Schanz, D., Schröder, A., Kähler, C. J.: Large-scale turbulent boundary layer investigation with multiple camera PIV and hybrid evaluation up to single pixel resolution. In: 9th International Symposium on PIV, Japan (2011)
12. Ganapathisubramani, B., Longmire, E.K., Marusic, I.: Experimental investigation of vortex properties in a turbulent boundary layer. Phys. Fluids **18**, 055105 (2006)
13. Elsinga, G., Scarano, F., Wieneke, B., van Oudenheusen, B.W.: Tomographic particle image velocimetry. Exp. Fluids **41**, 933–947 (2006)

Part IV
Laminar Flow Control and Transition

Impact of Forward-Facing Steps on Laminar-Turbulent Transition in Subsonic Flows

Christopher Edelmann and Ulrich Rist

Abstract The influence of forward-facing steps on laminar-turbulent transition is studied with both direct numerical simulation and linear stability theory. N-factor envelopes are calculated for inflow Mach numbers 0.15 and 0.8 at varying step positions and step heights. Very good agreement between direct numerical simulation and linear stability theory is archived. By comparing N-factor envelopes with and without step, the impact of steps can be captured by an additional amplification factor ΔN in the e^N method. It is found that ΔN is a function of streamwise position, step location, step height and Mach number.

1 Introduction

The influence of forward-facing steps on laminar-turbulent transition is studied with both direct numerical simulation and linear stability theory. The present work is part of the DLR project VER^{2}SUS in which a simplified suction system for Hybrid Laminar Flow Control (HLFC) is to be verified. With HLFC the drag of future aircraft can be reduced and thus fuel efficiency is enhanced by sustaining laminar flow over a bigger part of the wing. Even small imperfections on the wing surface can reduce the region of laminar flow by moving the transition location towards the leading edge. As manufacturing is only possible with certain tolerances, imperfections are unavoidable and it is necessary to study the impact of steps, gaps and roughness on the stability of the boundary layer flow. The e^N method (Van Ingen [7] and Smith and Gamberoni [6]) is the most popular tool for predicting laminar-turbulent transition up to today. It is based on the idea, that transition occurs when a certain amplification factor N_{tr} is reached. To incorporate the influence of steps, Crouch et al. [2] use the idea, that the N-factor evaluated for a smooth surface N_s can be reduced by a factor ΔN

C. Edelmann (✉) · U. Rist
Universität Stuttgart, Institut für Aerodynamik und Gasdynamik, Pfaffenwaldring 21, 70569 Stuttgart, Germany
e-mail: edelmann@iag.uni-stuttgart.de

A. Dillmann et al. (eds.), *New Results in Numerical and Experimental Fluid Mechanics IX*, Notes on Numerical Fluid Mechanics and Multidisciplinary Design 124,
DOI: 10.1007/978-3-319-03158-3_16,

$$N_{tr} = N_s - \Delta N. \tag{1}$$

A correlation for ΔN would enable an a-priori estimate of the influence of forward-facing steps on the transition location. Crouch et al. [2] argue that their results lead to $\Delta N = 1.6H/\delta^*$, but state that this relation is a fit for data from runs with adverse pressure gradient, while it is a rough upper bound for their favorable pressure gradient data. Perraud et al. [4] found a more complicated relationship for the influence of steps on the N-factor. They state that the influence of a step decays downstream of the step and ΔN is therefore not only a function of step height but also of the momentum thickness Reynolds number Re_Θ.

In the following, methods for evaluating N- and ΔN-Factor curves with step from both direct numerical simulation and linear stability theory are explained. Results for subsonic cases are presented and compared with results and correlations from literature.

2 Methods

2.1 Problem Formulation

The flow around forward-facing steps at two different inflow Mach numbers, 0.15 and 0.8 is studied numerically with two-dimensional simulations and with linear stability theory. The steps are located on a flat plate without pressure gradient at Reynolds numbers based on the step location between $Re_S = 330{,}000$ and $Re_S = 2{,}450{,}000$. The governing equations are the unsteady, compressible Navier-Stokes equations. They are written in Cartesian tensor notation with conservative variables and in non-dimensional form as

$$\frac{\partial \rho}{\partial t} + \frac{\partial \rho u_j}{\partial x_j} = 0 \tag{2}$$

$$\frac{\partial \rho u_i}{\partial t} + \frac{\partial \rho u_i u_j}{\partial x_j} = -\frac{\partial p}{\partial x_i} + \frac{\partial \tau_{ij}}{\partial x_j} \tag{3}$$

$$\frac{\partial E}{\partial t} + \frac{\partial (E+p) u_j}{\partial x_j} = \frac{\partial u_i \tau_{ij}}{\partial x_j} + \frac{\vartheta}{(\gamma - 1) Re\, Pr\, Ma^2} \cdot \frac{\partial T}{\partial x_j}, \tag{4}$$

where ρ, ρu_i, E are the conservative variables with density ρ, velocity components u_i and total energy E. Furthermore, t denotes time, p pressure, T temperature and ϑ the thermal conductivity. The fluid is assumed to be Newtonian and a calorically perfect gas. The heat capacity ratio $\gamma = c_p/c_v$ is fixed to $\gamma = 1.4$ for all simulations, which corresponds well to the thermodynamic properties of air. The Prandtl number is set to $Pr = 0.71$. The variation of the dynamic viscosity with temperature is accounted for by Sutherland's law.

2.2 DNS Code

The DNS code NS3D was originally written by Babucke [1] and is subject to continous development. For the spatial discretization in streamwise (x) and wall-normal (y) direction finite differences are implemented. To satisfy a high accuracy on the one hand and to achieve a good scalability on the massive parallel Cray XT6 system on the other hand, 8th-order explicit finite differences are used. Grid deformation is done by mapping the generally non-uniform physical grid to a perpendicular uniform computational grid. Boundary conditions for both sub- and supersonic flows are available. To introduce controlled disturbances in the flow, blowing and suction at the wall is possible. Spatial filtering and selected frequency damping are implemented, as well.

2.3 Linear Stability

Only a short introduction on linear stability theory (LST) follows, further details including its historical development are given by Mack [3]. For the derivation of the stability equations, three assumption are necessary. First, the baseflow is a steady solution of the Navier-Stokes equations. Second, fluctuations are small. Third, the baseflow is considered parallel. Under these assumptions, the compressible Navier-Stokes equations (Eqs. 2–4) can be linearized and split into a steady primary state and a time varying perturbation. With the fluctuations being dealt with in wave form, the temporal problem can be reduced to a generalized eigenvalue problem. To solve the spatial problem, the temporal solver (Schmidt and Rist [5]) is advanced by iterating the streamwise wavenumber α_i such that the temporal amplification rate ω_i vanishes and the spatial eigenvalue is obtained.

3 Results

3.1 Baseflow with Step

For the subsequent studies of the N-factor development, a baseflow with step has to be calculated for each case. The numerical scheme used is the same as used for the direct numerical simulation of a wave-packet later on (see sect. 3.2).

The grid for the baseflow calculations is stretched in both x- and y-direction as on the one hand, a very fine grid is necessary around the step location and on the other hand a sufficient domain length and height is needed. Initial conditions are obtained using a compressible self-similar solution. All cases are converged in time until a steady state is reached. Cases where no steady state could be reached are neglected for the present study. Important parameters for the cases studied can be found in Table 1.

Table 1 Baseflow Simulations with Step

Case	Ma_∞	T_W	Re_S	Re_H	H/Θ_S	L_1/H	L_2/H
1	0.15	1	3.3×10^5	1656	≈ 4.4	≈ 5.2	≈ 1.7
2	0.15	1	3.3×10^5	920	≈ 2.4	≈ 1.3	–
3	0.15	1	2.45×10^6	2543	≈ 2.4	≈ 4.4	≈ 1.1
4	0.8	1	2.45×10^6	400	≈ 0.4	≈ 0.3	–
5	0.8	1	2.45×10^6	2640	≈ 2.4	≈ 4.7	≈ 1
6	0.8	1	2.45×10^6	4440	≈ 4.1	≈ 13.1	≈ 7.6
7	0.8	Adiabatic	2.45×10^6	2816	≈ 2.4	≈ 4.2	≈ 0.8

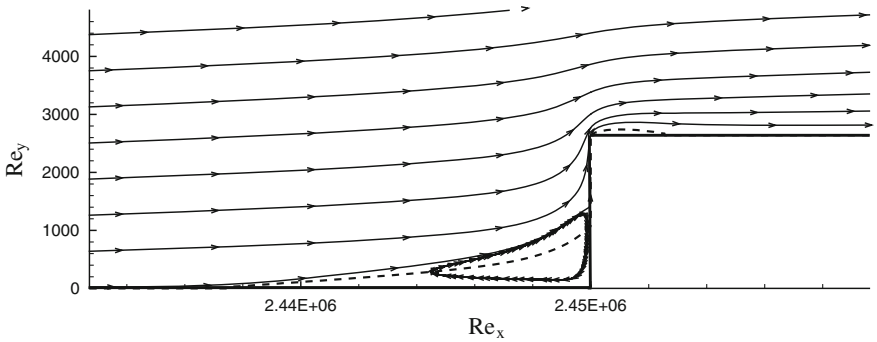

Fig. 1 Baseflow around the step geometry for case 5 ($Ma = 0.8$, $Re_S = 2{,}450{,}000$, $Re_H = 2640$). Region of reversed streamwise flow visualized by a *dashed line*. y-direction is stretched by a factor of two

The main characteristics of the baseflow are roughly the same for all cases studied. Thus, the example of a case at $Ma = 0.8$, with step position $Re_S = 2{,}450{,}000$ and step height $Re_H = 2640$ ($H/\Theta \approx 2.4$) is used. Figure 1 shows a zoom on the region around the step. Two separation bubbles can be seen. A first one in front of the step and a second one immediately at the step corner. The first separation zone is approximately 4.7 step heights long and much bigger than the second one, which is only one step height long and especially much flatter.[1] In Fig. 2a–d profiles of streamwise velocity u at four streamwise positions are shown for two grid resolutions. Hereby, "refined" means a grid refinement in both x- and y-direction by a factor of two. Both results are found to be in very good accordance. At position $Re_x = 2{,}000{,}000$ a typical laminar boundary layer profile can be seen. In Fig. 2b a profile directly in front of the step, inside the separated zone is shown. Only marginally negative velocities are observed. $Re_x = 2{,}450{,}080$ is a position immediately past the step. Here, a small sub-boundary layer, starting at the step corner, can be seen, while the outer profile remains nearly unchanged. At $Re_x = 2{,}800{,}000$ the sub-boundary layer has vanished and the original flat plate boundary layer is almost completely recovered.

[1] In case 4, the first separation bubble is very small and no second separation zone can be found.

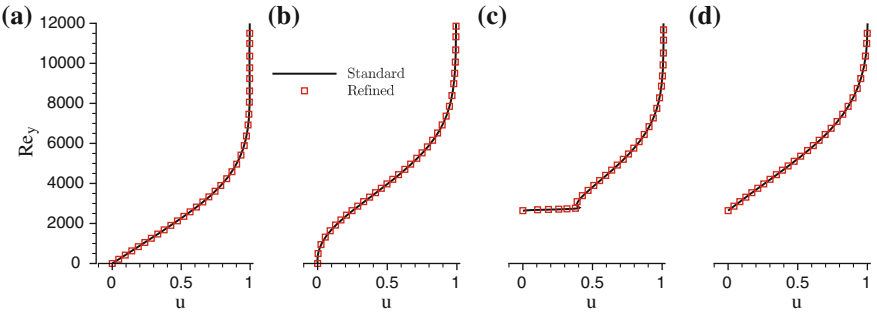

Fig. 2 Profiles of streamwise velocity u for case $Ma = 0.8$, $Re_S = 2{,}450{,}000$, $Re_H = 2640$ at four different streamwise positions. **a** $Re_x = 2{,}000{,}000$ **b** $Re_x = 2{,}445{,}000$ **c** $Re_x = 2{,}450{,}080$ **d** $Re_x = 2{,}800{,}000$

3.2 N-Factor by DNS

One possibility to gain N-factor curves is the direct simulation of disturbances. Thereby disturbances are introduced in the steady baseflow, their development is numerically simulated and amplitudes of the flow variables are analyzed. As a wide band of frequencies is of interest, a wave-packet is used in the present study. This wave-packet is introduced into the steady baseflow by suction and blowing at the wall over a short time at the beginning of the simulation. It is of great importance that the magnitude of the disturbances stays in the linear regime. Thus, the amplitude of the wave packet needs to be very small. As the comparison with results from linear stability theory shows best accordance with results using the streamwise velocity component u, only this flow variable is considered below. Maximum amplitudes along the wall normal coordinate for every frequency analyzed ($A(x)$) are calculated. Subsequently, n-factor curves for each frequency[2] are computed with

$$n(x) = ln\left(\frac{A(x)}{A_0}\right), \tag{5}$$

where A_0 is the maximum amplitude along y at the streamwise position where the considered frequency is amplified for the first time. The envelope of all curves is formed and a frequency-independent result $N(x)$ is obtained. Important for an accurate evaluation is the precise value of A_0. First of all, this means that the locations where the frequencies of interest are amplified for the first time lies inside the integration domain. By comparing results with step with those without step it is possible to calculate a $\Delta N(x)$ for each case. In Fig. 3 the evaluation of $\Delta N(x)$ is illustrated with two cases at $Ma = 0.15$ and step position $Re_S = 330{,}000$ (case 1 and case 2). On the left, the N-factor curves for both cases with step and the reference flat plate case are shown, while on the right the resulting ΔN development is plotted.

[2] Note the small letter used here, in contrast to the capital letter used for the envelope later on.

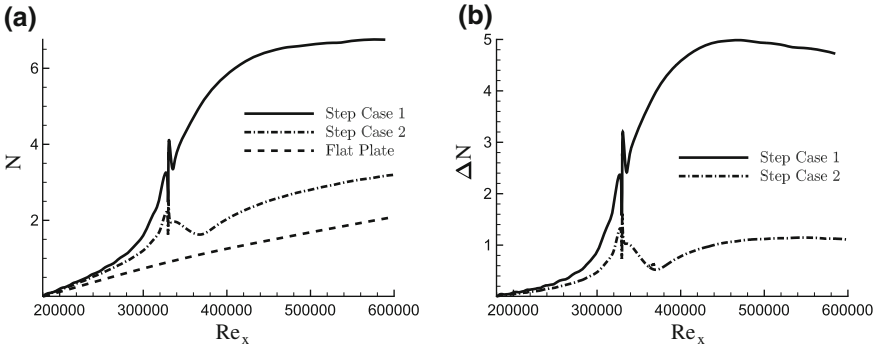

Fig. 3 N and ΔN development for cases at Mach 0.15, calculated from DNS results

3.3 N-Factor by LST

From the DNS results, the ΔN development far downstream of the step remains unclear as computational costs for the evaluation of N-factor curves by DNS are high and only a relatively small domain can be used. However, the development far downstream of the step seems crucial for the correct evaluation of correlation laws. That is why LST is used to evaluate N-factors in a very long domain. n-factors for every frequency are calculated with

$$n(x) = -\int_{x_0}^{x} \alpha_i(\tilde{x}) d\tilde{x}. \tag{6}$$

where the integration of the spatial amplification rates for a certain frequency begins at the location where it is amplified for the first time. $N(x)$ is again obtained by taking the envelope of all n-factor curves. In Fig. 4a results from LST are compared with results from DNS on the one hand and results from Perraud et al. [4][3] on the other hand. A very good accordance is observed. Figure 4b shows the N-factor development after the step and a comparison with results by Perraud et al. [4]. It can be seen that N-factor curves with and without step approach each other far downstream, which means a decreasing ΔN along x. The accordance with results by Perraud et al. [4] is again good, though present N-factors are overall a little higher.

3.4 Influence of Parameters and Comparison with Correlations

The influence of parameters on the ΔN-factor is visualized in Fig. 5. A step with the same relative step height H/Θ but larger Re_S shows an overall larger ΔN (see cases 2 and 3). Compressibility has a damping influence on ΔN (see cases 3 and

[3] Perraud et al. conducted a numerical study. They first calculated a baseflow with an incompressible method and calculated N-factors by a subsequent stability analysis.

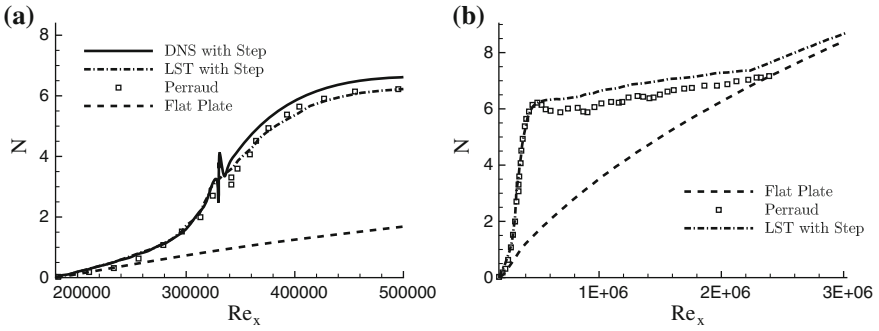

Fig. 4 Comparison of N-factor results from LST for case 1 with results from DNS and from Perraud et al. [4]

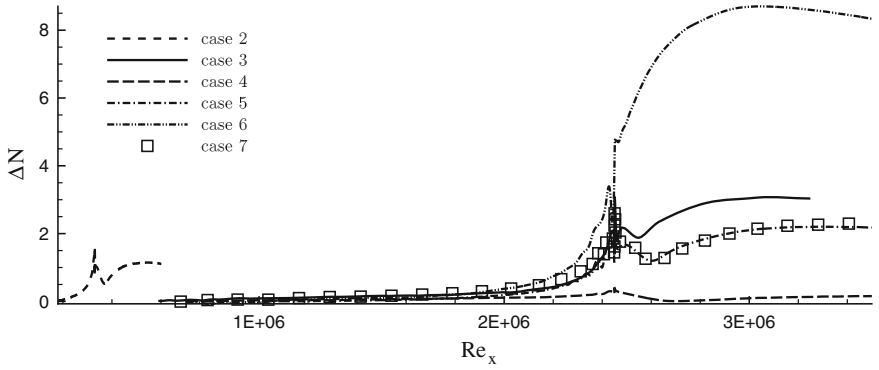

Fig. 5 Influence of step position, step height, Mach number and wall temperature on ΔN. All results from DNS calculations

5), while nearly no influence of wall temperature is observed (see cases 5 and 7). The influence of step height is visualized by cases 4, 5 and 6. In Fig. 6 correlations by Perraud et al. [4] and Crouch et al. [2] are compared with present results. The correlation by Perraud et al. [4] gives a good fit for data at $Re_S = 330{,}000$[4] but fails in other cases. The general approach however seems promising as a streamwise varying ΔN can be modeled. The correlation by Crouch et al. [2] may be a good estimate at a certain coordinate in some cases but is not capable of catching the general trend of a streamwise varying ΔN.

[4] This is a case used by Perraud et al. to establish their correlation.

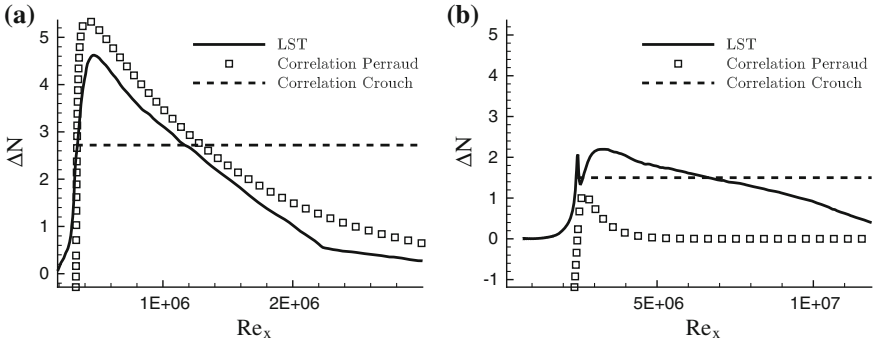

Fig. 6 Comparison of Correlations for ΔN-factor with LST results. **a** Case 1 **b** Case 3

3.5 Conclusion

N-factor curves for varying parameters at subsonic speeds are calculated with both DNS and LST. A very good agreement between results calculated with both methods as well as with results by Perraud et al. [4] is achieved. It is found that ΔN is a function of streamwise position, step location, step height and Mach number. For the same relative step height in terms of boundary layer momentum thickness, no dependency on the wall temperature was found. Correlations for ΔN from literature showed poor agreement with present results in most cases. However it is thought, that the approach by Perraud et al. [4] looks promising.

References

1. Babucke, A.: Direct numerical simulation of noise-generation mechanisms in the mixing layer of a jet. Ph.D. thesis, Universität Stuttgart (2009)
2. Crouch, J., Kosorygin, V., Ng, L.: Modeling the effects of steps on boundary-layer transition. In: Govindarajan, R. (ed.) IUTAM Symposium on Laminar-Turbulent Transition of Fluid Mechanics and Its Applications, vol. 78, pp. 37–44. Springer, Netherlands (2006)
3. Mack, L.M.: Boundary-layer linear stability theory. In: Special Course on Stability and Transition of Laminar Flow, vol. 709, pp. 379–409 (1984)
4. Perraud, J., Arnal, D., Seraudie, A., Tran, D.: Laminar-turbulent transition on aerodynamic surfaces with imperfections. In: RTO AVT. Prague (2004)
5. Schmidt, O.T., Rist, U.: Linear stability of compressible flow in a streamwise corner. J. Fluid Mech. **688**, 569–590 (2011)
6. Smith, A.M.O., Gamberoni, N.: Transition, pressure gradient and stability theory. Technical Report ES-26388, Douglas Aircraft Company, El Segundo Division, El Segundo, California (1956)
7. van Ingen. J.: A suggested semi-empirical method for the calculation of the boundary layer transition region. Technical report (1956)

Interaction of a Cylindrical Roughness Element and a Two-Dimensional TS-Wave

Benjamin Plogmann, Werner Würz and Ewald Krämer

Abstract Roughness induced transition in the leading edge region of airfoils is one of the challenges in the design of highly efficient wind turbine blades especially with respect to various inflow turbulence levels. The present experimental investigation discusses, therefore, the interaction of a laminar boundary layer perturbed by a single, 2D disturbance mode with a cylindrical roughness element at medium height. High and low speed streaks in the roughness wake suggest the presence of a counter-rotating vortex pair. A significantly increased amplification of the disturbance mode downstream of the roughness in comparison to the zero roughness height case leads to the formation of 3D structures with a dominant spanwise length scale corresponding to the roughness diameter. However, these 3D structures are only very weakly distinctive far downstream.

1 Introduction

Boundary layer transition in the leading edge region of airfoils is usually inherent with a significant increase in aerodynamic drag and decrease in lift followed by a performance loss. For the design of highly efficient airfoils and wind turbine blades a detailed understanding of roughness induced transition especially with respect to different inflow turbulence levels is required, since the airfoil leading edge can easily be contaminated by insects or be prone to surface corrosion. In general, roughness elements are distinguished based on their shape and on their height. Depending on the roughness shape 2D roughness steps, 3D isolated roughness elements and distributed, 3D roughness elements can be separated [9].

B. Plogmann (✉) · W. Würz · E. Krämer
Institute of Aerodynamics and Gas Dynamics (IAG),
Pfaffenwaldring 21, 70569 Stuttgart, Germany
e-mail: plogmann@iag.uni-stuttgart.de

A. Dillmann et al. (eds.), *New Results in Numerical and Experimental Fluid Mechanics IX*,
Notes on Numerical Fluid Mechanics and Multidisciplinary Design 124,
DOI: 10.1007/978-3-319-03158-3_17,

Based on the height of the roughness element, a distinction into three different ranges is suggestive, since flow phenomena leading to transition downstream of the roughness alter significantly not only depending on the shape but also with increasing roughness height in relation to the boundary layer displacement thickness: For low roughness heights (i), base flow velocity variations caused by the roughness element are small. Nevertheless, such small-scale velocity variations as caused by small roughness elements can result in an energy transfer from free stream disturbances to boundary layer instability modes (Tollmien Schlichting (TS) waves) via receptivity as first shown in the experiments by Aizin and Polyakov [2] and also by Goldstein [6] using the triple deck analysis. Since the receptivity process is very sensitive to the frequency of the disturbance and the height of the roughness a linear relationship in-between roughness height and TS-wave amplitude is only present below a certain threshold for the roughness height [13].

For roughness heights in a medium range (ii), a distinct mean flow velocity distortion downstream of the roughness element results in a considerable change of the boundary layer stability characteristics. Moreover, the receptivity process at the roughness element reaches a non-linear stage [13]. Downstream of the roughness element the excited disturbance modes may undergo transient growth [5], which is, however, strongly dependent on the receptivity process at the roughness element. For 2D roughness elements the downstream evolving disturbances are at first 2D, before the flow develops a 3D nature in the process of transition [8]. In contrast, 3D roughness elements highly favor the development of different vortical structures (horse-shoe shaped vortex wrapped around the front side of the roughness and a trailing vortex rising vertically in the wake of the roughness) directly at the (cylindrical) roughness [10]. The particular vortical structures are, however, highly sensitive to the roughness shape.

For roughness heights close to or larger than the displacement thickness (iii), a strong mean flow distortion causes highly nonlinear effects. Hence, transition occurs close to the roughness element and is also referred to as bypass transition. Detailed investigations were conducted by Acarlar and Smith [1] and Klebanoff et al. [7] showing that different vortical structures appeared to lead to turbulence in the inner (close to the surface) and outer region of the boundary layer, which is hinted at by two inflection points in the mean flow velocity profile. Again, the vortical structures strongly depended on the particular roughness shape.

Within this context, the present investigation focuses on the interaction of a laminar boundary layer with a cylindrical roughness element located in stage (ii). The experiments are conducted in an airfoil leading edge region at a Reynolds number of $Re = 6 \cdot 10^6$ to achieve a close alignment to operational conditions of wind turbines. Moreover, the model is equipped with a disturbance source upstream of the roughness element giving the possibility to model different inflow turbulence levels. In the present study the laminar boundary layer is, therefore in a first step, perturbed by a single, 2D TS-wave upstream of the roughness.

2 Experimental Setup and Data Acquisition

The experiments were conducted in the Laminar Wind Tunnel of the IAG, which is of Eiffel type. Due to several screens in the inlet section and an effective contraction ratio of 20:1 a very low longitudinal turbulence level of $Tu_x = 0.02\,\%$ ($f = 10-5000$ Hz, $u_\infty = 30$ m/s) is obtained. For the experiments a particularly designed airfoil section (*BE72* [11]) was employed having a similar pressure gradient in the leading edge region as the NACA $64_3 - 418$ airfoil, which can be regarded a typical airfoil for wind turbine applications. However, the pressure distribution in the trailing edge section of the *BE72* was significantly modified in order to reduce the model chord length ($c = 2.4$ m). Therewith, experiments can be conducted at a typical Reynolds number for wind turbine applications ($Re = 6 \cdot 10^6$) and at low free stream velocity ($u_\infty = 20$ m/s). The pressure gradient at the roughness position was close to zero corresponding to an angle of attack of $\alpha = 4.4°$.

A cylindrical roughness element (diameter $d_r = 20$ mm) is integrated into the model at a streamwise location of $x/c = 0.15$. Using a linear actuator with a minimal incremental motion smaller than 0.1μm the roughness can be displaced in a range of $0 < \delta_{1,ref} < 1.5$. Additionally, the roughness height is measured with a laser-triangulation system with a resolution of 0.15 μm corresponding to 0.2 % of the boundary layer displacement thickness. For the excitation of the disturbance modes upstream of the roughness element a very thin slit is integrated into the model surface at $x/c = 0.1$ and via tubes connected to 128 individually controllable micro-loudspeakers. Employing a 128 channel signal generator [3] with a common quartz based clock, disturbance modes in a wide streamwise and spanwise wave number range can be excited.

For the hot-wire measurements the same clock as for the excitation of the disturbance modes is used enabling phase-locked measurements. The hot-wire signal is split into AC and DC part. The AC part is high-pass filtered and amplified. AC and DC part of the signal are acquired with a 18-Bit AD converter (NI USB-6289). For the spectral analysis the total of 32,768 samples for each point is split into eight blocks and ensemble-averaged in the temporal domain prior to a transformation into the spectral domain via Fast Fourier transform (FFT). For the evaluation of the spanwise wavenumber spectra via Complex FFT points are interpolated to an equidistant grid in a range $-7.5 < z/d_r < 7.5$. The spanwise wavenumber β is non-dimensionalized by the roughness diameter, without considering 2π. Hence, $\beta d_r = 1$ corresponds to a wavelength equal to d_r. For further details on the experimental setup compare Plogmann et al. [12].

3 Results

3.1 Base Flow Characteristics

Experiments are conducted in a close to zero pressure gradient boundary layer as can be seen from the velocity at the boundary layer edge being almost constant

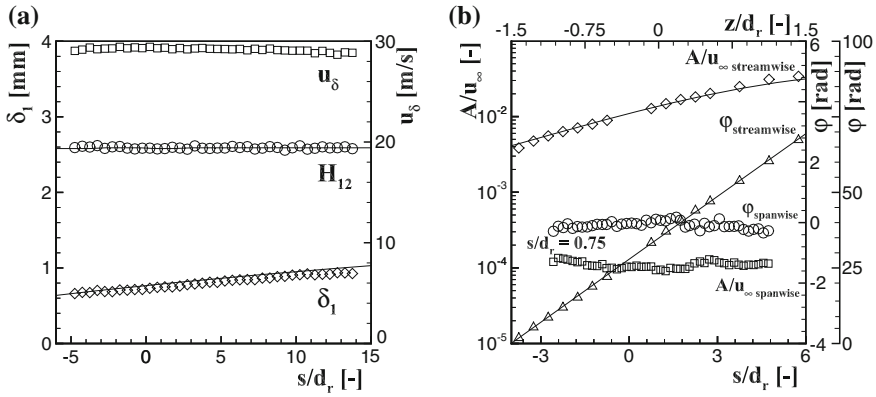

Fig. 1 Comparison of measured (symbol) and calculated (line) base flow characteristics (**a**) and measured (symbol) and calculated (line, LST) TS-wave characteristics of mode $f_1 = 549$ Hz (**b**) for $h/\delta_{1,ref} = 0$

(Fig. 1a). Hence, the shape factor is constant and close to the value of the Blasius boundary layer ($H_{12} = 2.591$). The displacement thickness at the position of the roughness element is $\delta_{1,ref} = 0.72$. Both for the displacement thickness (δ_1) and the shape factor (H_{12}) a good agreement in-between measured and calculated values is obvious. For further details on the base flow see [11].

At the roughness position boundary layer disturbances are convectively amplified in a range $270 < f < 690$ Hz according to linear theory. In the present experiments a single, 2D TS-wave with frequency $f_1 = 549$ Hz, which is in the range of the most amplified disturbances at the roughness position, was excited upstream of the roughness. Figure 1b shows the streamwise development of the TS-wave amplitude and phase for zero-roughness height in comparison to linear theory. Only minor variations in the spanwise distribution of the TS-wave amplitude and phase reveal a good two-dimensionality of the excited mode downstream of the roughness element for zero roughness height.

3.2 Mean Flow Distortion

The following results focus on the influence of the roughness element at $h/\delta_{1,ref} = 0.5$ on the laminar boundary layer, which is perturbed by the single, 2D TS-wave mode f_1. At first, Fig. 2 shows the mean flow velocity distortion caused by the roughness element. Clearly, in the near wake of the roughness element the mean flow velocity is considerably reduced with the highest velocity distortion being present in the centerline region at a wall normal distance corresponding to the roughness height. Further downstream the mean flow distortion in the centerline region is considerably decreasing and the maximum is shifted off the wall to approximately $y/\delta_{1,ref} = 1$. Therefore, at $s/d_r = 7$ the undisturbed boundary layer profile is recovered on the centerline, as can be deduced from a mean flow distortion being in the order of 1–2 %.

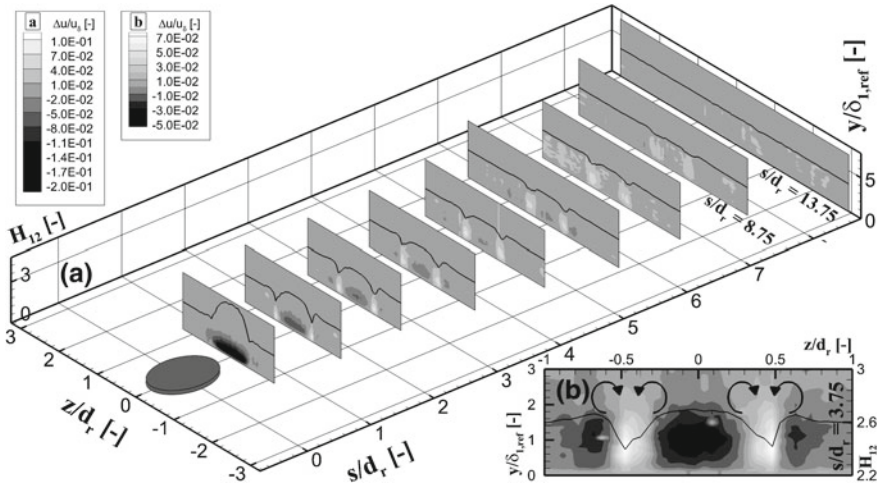

Fig. 2 Mean flow distortion and shape factor (*black line*) for $h/\delta_{1,ref} = 0.5$, (**a**) streamwise development downstream of the roughness element and (**b**) at $s/d_r = 3.75$

Moreover, regions of increased or decreased velocity, so-called streaks, form out of center downstream of the roughness. Two high speed streaks are present at spanwise positions of $z/d_r = \pm 0.5$ corresponding to the edges of the roughness. The amplitude of the low speed streaks, which are located on the outer edges of the high speed streaks, respectively, is considerably lower compared to the amplitude of the high speed streaks. In the streamwise development the wall normal maximum of these streaks is shifted off the wall in compliance with the observations made in the centerline region. Starting at $s/d_r = 4.75$ a considerable amplitude decrease of the high speed streaks can be observed. Only small scattering in the spanwise shape factor distribution at $s/d_r = 13.75$ shows that the undisturbed mean flow velocity profile ($H_{12} = 2.59$) is nearly recovered in the entire spanwise domain, in which the mean flow was affected by the roughness.

In agreement with observations by Wang [14], the observed streaks persist at a constant spanwise scale in the streamwise evolution. From these high and low speed streaks the presence of two counter-rotating vortex pairs in the wake of the roughness can be inferred as indicated in Fig. 2b and also described by Legendre and Werle [10]. Hence, the trailing vortex pair shifts low momentum fluid away from the wall in the center (lift-up effect), while both vortex pairs (trailing and horse shoe vortex) contribute to the formation of the high speed streaks on the edges of the roughness, which entrain high-momentum fluid towards the wall. Finally, the low speed streaks on the outer edges of the high speed streaks are a consequence of the horse-shoe vortex pair. Clearly, low speed streaks result in an increase of the shape factor while the shape factor is considerably reduced in regions with high speed streaks.

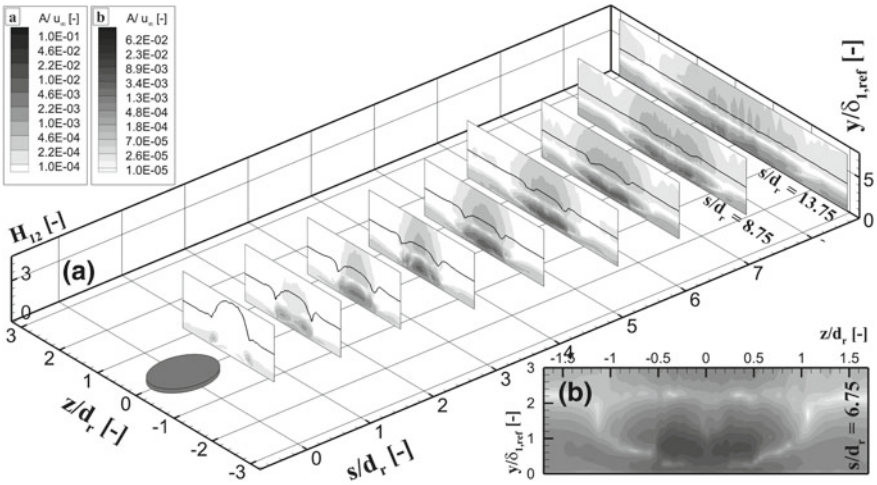

Fig. 3 Streamwise amplitude development of the disturbance mode f_1 and shape factor (*black line*) (**a**) and amplitude distribution of f_1 in the wall-normal spanwise plane at $s/d_r = 6.75$ (**b**)

3.3 Disturbance Roughness Interaction

Below, the influence of the cylindrical roughness element on the initially 2D disturbance mode with a frequency of $f_1 = 549$ Hz and a maximum wall-normal amplitude of $A/u_\infty = 0.01\,\%$ at the position of the roughness element is considered. Directly downstream of the roughness element a strong amplification at the edges of the roughness element leads to the formation of two peaks in the spanwise amplitude distribution with a wall normal maximum at $y/\delta_{1,ref} = 0.9$ (Fig. 3a). In the centerline region, however, the amplitude is considerably damped due to the significantly decreased mean flow velocity immediately downstream of the roughness element (Fig. 2). Hence, the interaction of the roughness element and the 2D disturbance mode results, at first, in the excitation of 3D modes in a wide spanwise wave number range predominately in the inner region of the boundary layer (compare Fig. 4a). The amplitude of these 3D modes is, however, considerably lower compared to the 2D mode.

In the downstream development the two amplitude peaks at the edges of the roughness element move towards the center before merging to a common peak at $s/d_r = 2.75$ (Fig. 3a). At the same time local minima develop at spanwise positions of $z/d_r = \pm 0.5$ corresponding to the edges of the roughness element. From the comparison to the spanwise distribution of the shape factor it is obvious that these local minima in the spanwise amplitude distribution coincide with the high speed streaks caused by the two vortex pairs in the wake of the roughness element. Therefore, the most significant influence of the roughness element on the amplification of the excited mode f_1 is, at first, restricted to the spanwise extent of the roughness element. The strong amplification in the centerline region and the influence of the

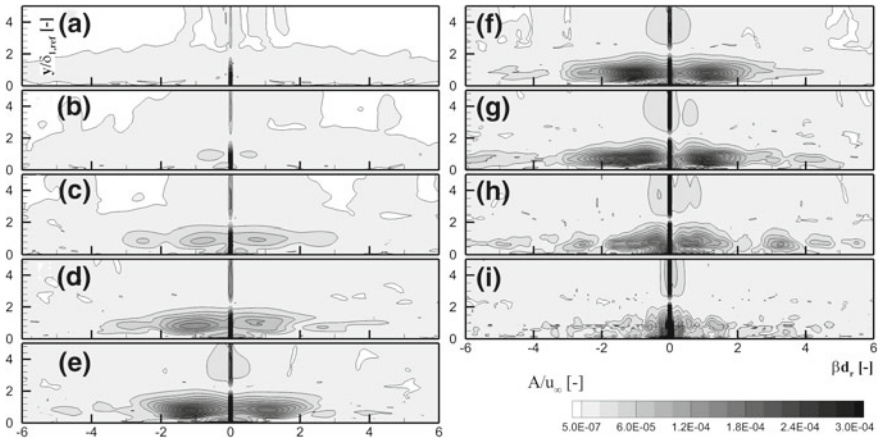

Fig. 4 Spanwise wavenumber spectra of the disturbance mode f_1 in the wall-normal spanwise plane at $s/d_r = 0.75, 1.75, 2.75, 3.75, 4.75, 5.75, 6.75, 8.75, 13.75$ (**a**–**i**)

high speed streaks at the edges of the roughness element lead to the formation of a dominant 3D mode ($\beta d_r = 1$) out of the broadband nature of the 3D structures immediately downstream of the roughness element (Fig. 4). This mode ($\beta d_r = 1$) develops in the inner region of the boundary layer ($y/\delta_{1,ref} < 2$) with its maximum located near $y/\delta_{1,ref} = 0.8$ and is considerably amplified in streamwise direction. The spanwise length scale corresponds to the roughness diameter and can, therewith, clearly be linked to the interaction with the roughness element. In the outer region of the boundary layer only 3D modes of broadband character without the presence of dominant peaks can be observed.

Only further downstream ($s/d_r = 4$) the minima at $z/d_r = \pm 0.5$ start to move outwards while a wavy type structure develops in-between these two minima (Fig. 3b). The increasing spanwise extent, in which the mode f_1 is affected by the interaction with the roughness element coincides with the amplitude decrease of the high speed streaks (compare also Fig. 2). Moreover, the amplitude of the mode f_1 reaches a maximum close to $s/d_r = 5$ before being slightly damped as can also be deduced from the amplification on the centerline (Fig. 5). In contrast, the (undisturbed) mode f_1 is further growing in regions, which are not affected by the interaction with the roughness element. Hence, the 3D structures in spanwise direction are considerably damped as can also be seen in Fig. 3a. This observation is consistent with a strong damping of the most significant 3D mode ($\beta d_r = 1$) observed in the spanwise wavenumber spectra (see Fig. 4g–i). At $s/d_r = 13.75$ only minor scattering in the spanwise wavenumber spectra is present showing that no significant 3D modes, especially with respect to the roughness element, persist far downstream. In agreement, De Paula et al. [4] found that 3D modes excited by a cylindrical roughness element are damped for low disturbance amplitudes at the roughness element. However, in comparison to present investigation ($A/u_\infty = 0.01$) the disturbance mode amplitude at the roughness position was considerably higher ($A/u_\infty = 0.45$).

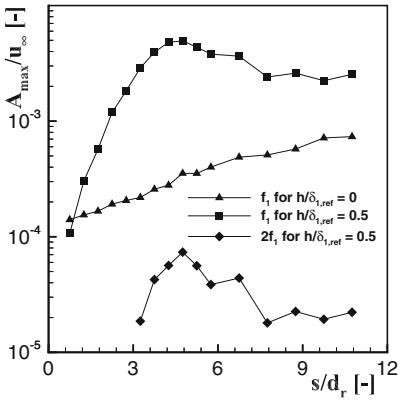

Fig. 5 Amplification of mode f_1 and $2f_1$ on roughness. centerline for $h/\delta_{1,ref} = 0$ and $h/\delta_{1,ref} = 0.5$

Finally Fig. 5 shows that the strong amplification of the fundamental mode f_1 downstream of the roughness element is connected with a transfer of energy into the harmonic mode $2f_1$. Comparing the amplification of the fundamental and the harmonic mode shows that both modes experience a very similar growth behavior. However, the total amplitude of the harmonic mode is considerably lower as can also be seen from the comparison of Fig. 6a, b. Clearly, comparing the amplitude of the fundamental and the harmonic mode in the wall-normal spanwise plane supports the argument that the highest energy transfer from the fundamental to the harmonic mode is present in regions of maximum amplitude for the fundamental mode.

4 Conclusion

The interaction of a laminar boundary layer perturbed by a 2D, TS-mode with a cylindrical roughness at $h/\delta_{1,ref} = 0.5$ was investigated. High and low speed streaks in the wake of the roughness reveal the presence of two counter-rotating vortex pairs. In the downstream development the streak amplitude is, at first, nearly constant before decreasing significantly. Far downstream the undisturbed boundary layer profile is, therefore, recovered in the entire spanwise domain.

The interaction of the 2D, low amplitude TS-mode with the cylindrical roughness element results, at first, in a strong amplification in the centerline region, which is accompanied by an energy transfer from the excited fundamental into the first harmonic mode. The high speed streaks at the edges of the roughness lead to the formation of spanwise minima in the disturbance amplitude. The evolving 3D structures show a dominant spanwise length scale, which can be attributed to the roughness diameter.

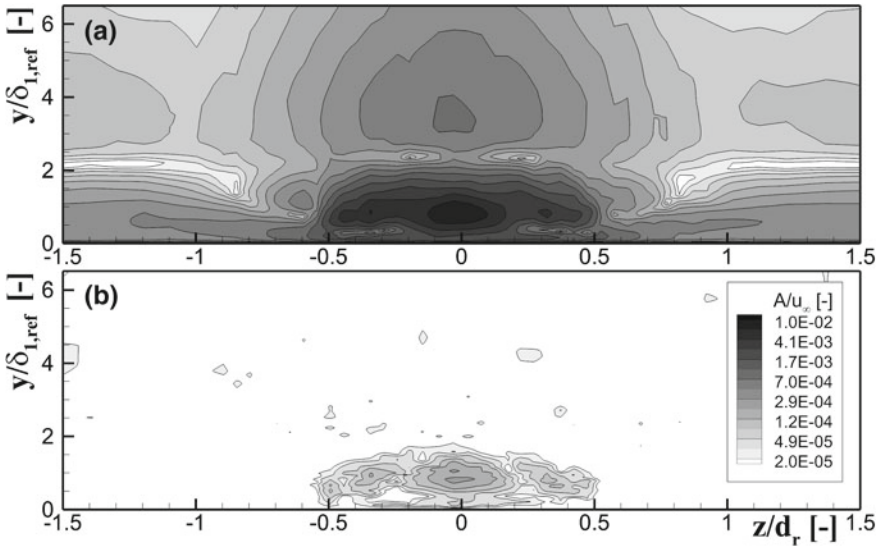

Fig. 6 Comparison of amplitude distribution for mode f_1 (**a**) and $2f_1$ (**b**) in the wall-normal spanwise plane at a streamwise position of $s/d_r = 4.75$

Further downstream, as the amplitude of the high speed streaks decreases, the spanwise extent, in which the disturbance mode is affected by the interaction with the roughness element, starts to spread considerably. At the same time a significant decrease in the amplitude of the 3D structures is observed. Therefore, no dominant 3D modes resulting from the influence of the roughness element on the low amplitude TS-mode persist far downstream.

References

1. Acarlar, M., Smith, C.: A study of hairpin vortices in a laminar boundary-layer. Part 1. J. Fluid Mech. **175**, 1–41 (1987)
2. Aizin, L., Polyakov, N.: Acoustic generation of Tollmien-Schlichting waves over local unevenness of surfaces immersed in streams. Preprint 17, Akad. Siberian Div, Nauk USSR (1979)
3. De Paula, I., Würz, W. et al.: Generation of seeds of subharmonic resonance in an airfoil boundary-layer transition initiated by modulated TS-waves. 15th ICMAR, Novosibirsk (2010)
4. De Paula, I., Würz, W., Medeiros, M.: Experimental study of Tollmien-Schlichting wave interaction with a shallow 3D roughness element. J. Turb. **9**, 1–23 (2008)
5. Ergin, F., White, E.: Unsteady and transitional flows behind roughness elements. AIAA J. **44**(11), 2504–2514 (2006)
6. Goldstein, M.: Scattering of sound waves into Tollmien-Schlichting waves by small streamwise variations in surface geometry. J. Fluid Mech. **154**, 509–529 (1985)
7. Klebanoff, P., Cleveland, W., Tidstrom, K.: On the evolution of a turbulent boundary-layer induced by a three-dimensional roughness element. JFM **237**, 101–187 (1992)

8. Klebanoff, P., Tidstrom, K.: Mechanism by which a two-dimensional roughness element induces boundary-layer transition. Phys. Fluids **15**(17), 1173–1188 (1972)
9. Lachmann, G. (ed.): Boundary layer and flow control. 637–656 and 657–681. Pergamon Press (1961)
10. Legendre, R., Werle, H.: Toward the elucidation of three-dimensional separation. Ann. Rev. Fluid Mech. **33**, 129–154 (2001)
11. Plogmann, B., Würz, W., Krämer, E.: Interaction of a laminar boundary layer with a cylindrical roughness element near an airfoil leading edge. AIAA 2012–3077 (2012)
12. Plogmann, B., Würz, W., Krämer, E.: Interaction of a three-dimensional roughness element with a TS-wave near an airfoil leading edge. 16th ICMAR, Kazan (2012)
13. Saric, W., Hoos, J., Radezsky, R.: Boundary layer receptivity of sound with roughness. Boundary Layer Stability and Transition to Turbulence. (1991)
14. Wang, Y.: Instability and transition of boundary layer flows disturbed by steps and bumps. Ph.D. thesis, Queen Mary College, University of London (2004)

Effects of a Discrete Medium-Sized Roughness in a Laminar Swept-Wing Boundary Layer

Holger B. E. Kurz and Markus J. Kloker

Abstract Direct numerical simulations of the effects of a cylindrical roughness element in the laminar 3-d boundary layer on the upper surface of a swept wing are performed. The roughness element generates streamwise vortices, where one is persistently growing in streamwise direction due to crossflow instability. By varying the roughness height, the onset of secondary instability of this crossflow vortex and ultimate transition to turbulence varies also in streamwise direction. When reaching the "effective", i.e. the flow-tripping roughness height, the linear crossflow-instability regime is bypassed and breakdown to turbulence occurs in close vicinity to the element due to a global instability.

1 Introduction

For the development of future transport aircraft the reduction of fuel consumption has become a central aspect. As the decrease of total skin friction drag by transition delay on the wings and tailplanes is a promising means, there is great interest in a better understanding of the transition process. In respect of laminar wing design, an assessment of the required surface quality is necessary for both active and passive control approaches. In particular, the impact of discrete roughness is of interest. Since transport aircraft typically have swept-back wings, the consideration of a corresponding 3-d boundary layer is stringently required in order to capture the features of the inherent crossflow (CF) instability. Schrader et al. [1] investigated numerically the linear receptivity of a 3-d boundary layer to shallow roughness elements. Tempelmann et al. [2] concluded that linear receptivity can be assumed for roughness

H. B. E. Kurz (✉) · M. J. Kloker
Institute of Aerodynamics and Gas Dynamics, University of Stuttgart, Stuttgart, Germany
e-mail: kurz@iag.uni-stuttgart.de

M. J. Kloker
e-mail: kloker@iag.uni-stuttgart.de

A. Dillmann et al. (eds.), *New Results in Numerical and Experimental Fluid Mechanics IX*,
Notes on Numerical Fluid Mechanics and Multidisciplinary Design 124,
DOI: 10.1007/978-3-319-03158-3_18,

heights up to 10 % of the local boundary-layer displacement thickness. The EU-project RECEPT has set its sights on improving the understanding of the receptivity process in such boundary layers, especially for cases where non-linear effects are no longer negligible. In this context, direct numerical simulations (DNS) with medium-sized roughness elements on a swept modified NACA 671-215 profile near cruise conditions are performed at the IAG. Additionally, a 2-d setup is employed for comparison. Cylindrical roughness elements in 2-d boundary layers generate pairs of transiently appearing counter rotating vortices with ensuing velocity streaks, where the rotational direction of the vortices depends on the flow configuration. In the present case of a 3-d boundary layer, a spanwise oriented array of roughness elements is utilized to generate regularly spaced crossflow vortices. The vortex system behind an element becomes asymmetric, where vortices are suppressed if their rotational direction does not correspond to the CF vortex rotation sense.

2 Configuration

The geometry under consideration is the laminar profile NACA 671-215 as shown in Fig. 1 with a chord length of $\bar{L} = 2.0\,\mathrm{m}$ (overbar denotes dimensional values), hereafter used as reference length for non-dimensionalization unless otherwise stated. The lower side was modified in order to avoid separation in the given configuration. The baseflow past the profile has been computed with the Reynolds-Averaged Navier-Stokes (RANS) solver TAU at a sweep angle of $\beta = 35°$ and an angle of attack of $\alpha = -6.1°$, measured perpendicular to the leading edge. This configuration ensures that the boundary layer on the upper surface is dominated by CF instability, while Tollmien-Schlichting modes are not amplified upstream of $x = 0.7$. The free stream Mach number is chosen such that subsonic flow on the upper surface with respect to the absolute value of the velocity is ensured, in order to avoid shocks and expansions at the discrete 3-d roughness element. Therefore, the cruise Mach number is set to $Ma_\infty = 0.65$ obtained with $\bar{Q}_\infty = 192\,\mathrm{m/s}$ at an altitude of 12,000 m; the chord Reynolds number is $Re_\mathrm{L} = \bar{U}_\infty \cdot \bar{L}/\bar{\nu} = 6.9 \cdot 10^6$. As the zero-lift angle is approximately $\alpha_0 = -3°$, the airfoil in fact produces negative lift with $c_\mathrm{L} = -0.33$ with respect to the total free-stream velocity at $Ma_\infty = 0.65$, and the stagnation point is found at $x = 0.01$ on the upper side.

The transition locations on the upper and lower side are predicted by means of the classical e^N method. Linear growth rates are obtained from the stability solver LILO included in TAU. LILO employs the temporal approach, spatial growth rates are obtained through Gaster's relation. An edge streamline is chosen as integration path for the N-factor calculation, in approximation of the wave propagation path. Transition on the upper side is found at $x = 0.1$ where $\mathrm{N_{CF}}$ for steady modes reaches the critical value of 9; on the lower side CF and TS waves are amplified. Transition is triggered by $\mathrm{N_{TS}}$ reaching 12 at $x = 0.2$. An interaction of CF and TS modes is neglected, which seems reasonable as $\mathrm{N_{CF}}$ does not exceed a value of 4 on the lower side. Since the RANS result serves as initial solution for the subsequent

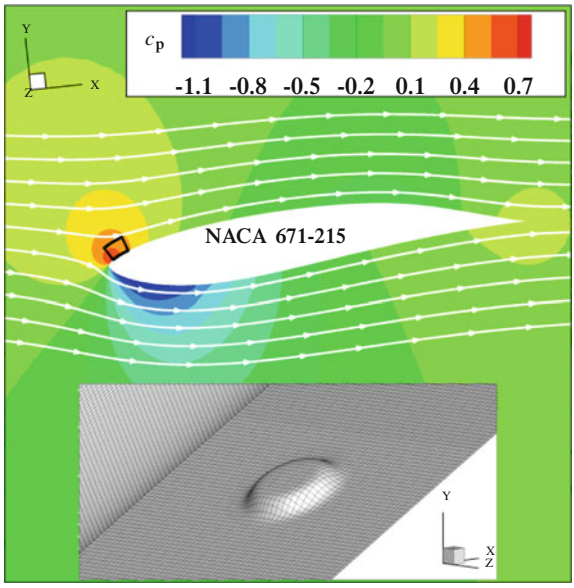

Fig. 1 Flow-field crosscut perpendicular to the leading edge ($z = \text{const.}$), $\alpha = -6.1°$ measured in body-fixed coordinate system x-y-z. Pressure coefficient c_p given with respect to free-stream velocity $Q_\infty = 192$ m/s. *Black box* near leading edge depicts DNS domain. *Frame* shows meshed roughness element with $k = 1.0$

DNS where a modeled transition is not desired, transition on the upper side is fixed farther downstream at $x = 0.2$ to provide a useful laminar stretch. A comparison of the spatial growth rates of both flow solutions shows a negligible upstream influence of the transition location.

For comparative reasons, a 2-d baseflow at identical angle of attack has been computed by omitting the spanwise velocity component of the free stream, leading to an identical Re_L. Further, transition is fixed at the same locations as in the swept case.

The converged RANS baseflow is interpolated to a high-resolution DNS subdomain by means of a third-order Lagrangian interpolation based on structured data. The extent is indicated in Fig. 1 by the black box near the leading edge. To account for differences in the numerical schemes and errors due to the interpolation, the initial solution is further converged using the in-house (D)NS code (NS3D) without introduction of disturbances. In a second step, the final DNS domain is gained by cropping the inflow and free-stream boundaries, again settled by steady (D)NS before a roughness element is introduced.

The spanwise extent of the DNS domain, corresponding to the z-direction, is set to $\lambda_z = 2 \cdot 10^{-3}$ according to the spanwise wavelength of the most amplified steady mode gained by linear stability theory. The final streamwise extent is $0.015 \leq x \leq 0.05$ (cf. Fig. 1). Two grid resolutions are used for the computations to check for resolution effects: resolution # 0 with $14 \cdot 10^6$ points, and resolution # 1 with $57 \cdot 10^6$ points ($N_x \times N_y \times N_z = 2368 \times 188 \times 128$). Both grids have the same spatial extent and wall-normal resolution, but for resolution # 1 the number of points in wall-parallel planes is doubled. At the inflow boundary, a characteristic boundary

condition is utilized to allow upstream-running waves to leave the domain. In a buffer zone upstream of the outflow boundary, the conservative variables are forced back to the initial solution. For the undisturbed flow, an adiabatic wall is considered, while all the flow variables at the free-stream boundary are fixed. In spanwise direction, the boundaries are periodic. For basics of the numerical method, the careful extension to and verification of asymmetric 3-d flows, see Friederich and Kloker [3].

A cylindrical roughness element with a diameter of $d = 5 \cdot 10^{-4}$ is placed at $x = 0.02$ (center). The edges are blended to the surface by a hyperbolic tangent with a maximum slope angle of 45° for all heights. An insert in Fig. 1 shows a roughness element in the DNS grid. The element is meshed by elevating the respective points of the wall boundary according to the geometric definition. The roughness height $k = \bar{k}/\bar{\delta}_{1,\mathrm{s}}$ is in the order of $\delta_{1,\mathrm{s}}$, being defined as the displacement thickness of the undisturbed 3-d boundary layer at the roughness element in the edge-streamline system with $\delta_{1,\mathrm{s}}(x = 0.02) = 8.5 \cdot 10^{-5}$ and $Re_{\delta 1,\mathrm{s}}(x = 0.02) = 519$. The relevant dimensionless quantity for the assessment of a roughness element in a boundary layer is the Reynolds number based on the height and the magnitude of the wall-parallel velocity vector of the undisturbed flow at this distance from the wall:

$$Re_{\mathrm{kk,s}} = \frac{\bar{k} \cdot |\bar{\mathbf{u}}_{\mathrm{wp}}(\bar{k})|}{\bar{\nu}} \,. \tag{1}$$

Three roughness elements with $k = 1.0/1.5/2.0$ are investigated, correponding to aspect ratios of $0.170/0.255/0.340$ and $Re_{\mathrm{kk,s}} = 296/581/912$, respectively. The element with $k = 1.0$ in the 2-d baseflow without spanwise velocity component yields $Re^{\mathrm{2d}}_{\mathrm{kk,s}} = 207$. All DNS are carried out without forcing of unsteady disturbance modes, making the uncontrolled numerical background noise the only unsteady forcing. For the simulations with roughness element, the wall boundary condition is set to isothermal.

While the DNS is conducted in a domain conforming to the surface curvature of the wing profile as shown in Fig. 1, the results are transformed to a coordinate system with s being the arc-length along the contour in the x-y-plane and n pointing in the wall-normal direction, and subsequently straightened for evaluation. The respective velocity components are denoted as u, v and w. For the 3-d cases, the system is subsequently rotated about the n-axis by $\phi_{\mathrm{r}} = 55°$ to align with the CF vortices and denoted by the subscript r. The origin is defined by the center of the roughness element.

3 Results

Boundary-layer properties are summarized in Fig. 2, showing a continuous acceleration of the boundary-layer edge velocity $u_{\mathrm{s,e}}$ and a corresponding decrease of the local edge-streamline angle ϕ_{e}. The CF reaches a maximum of $0.094 \cdot u_{\mathrm{s,e}}$ at $x = 0.04$. The stability analysis for steady ($\omega = 0$) CF modes shows a maximum amplification at $x = 0.03$ at a spanwise wavenumber corresponding to $\lambda_{\mathrm{z}} = 0.002$, cf. Fig. 3.

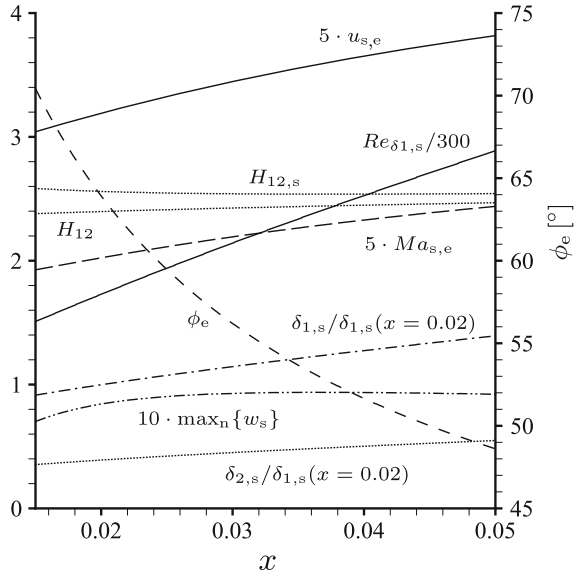

Fig. 2 Streamline oriented boundary-layer parameters in DNS domain: edge velocity $u_{s,e}$, displacement thickness $\delta_{1,s}$, momentum thickness $\delta_{2,s}$, shape parameter $H_{12,s}$(H_{12} in chordwise system), local Reynolds number $Re_{\delta 1,s}$, local edge Mach number $Ma_{s,e}$, maximum of crossflow $\max_n\{w_s\}$, edge-streamline angle ϕ_e

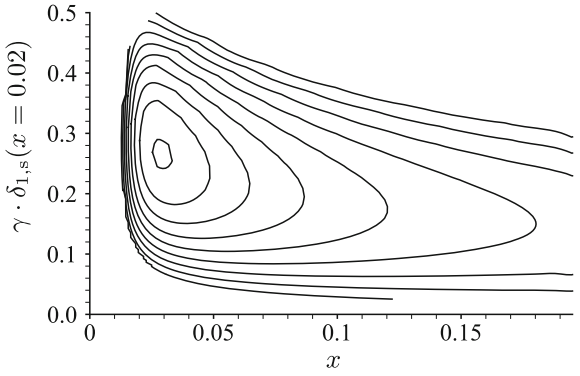

Fig. 3 Spatial amplification rates α_i for unstable steady CF modes in the laminar stretch on the upper surface, normalized by $\delta_{1,s}(x = 0.02) = 8.5 \cdot 10^{-5}$. The outer *line* marks $\alpha_i = 0$, $\Delta\alpha_i = -0.002$

In the 2-d case without spanwise velocity component and $k = 1.0$, a pair of counter-rotating wake vortices emerges behind the roughness element, see Fig. 5a. The rotational direction of the wake vortex pair conforms to a horseshoe vortex, creating a high-speed streak along the downstream centerline. In literature, high- or low-speed streaks and corresponding opposite rotation senses of the vortices are documented depending on many parameters. We note that the present element is subjected to an accelerated boundary layer. The vortices decay some roughness diameters downstream the element since these steady disturbances are not amplified in the accelerated boundary layer. Note the difference between $Re_{kk,s}$ and $Re^{2d}_{kk,s}$ when comparing this result to the 3-d case.

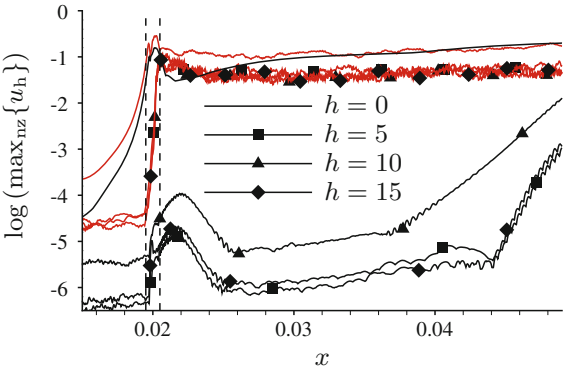

Fig. 4 Temporal amplitudes u_h of selected frequency harmonics $h = \omega/\omega_0$ for $k = 1.0$ (*black*) and $k = 2.0$ (*red*), obtained from a Fourier analysis based on the fundamental frequency $\omega_0 = 328$, $h = 1$. *Dashed lines* indicate roughness

The respective element in the 3-d baseflow (Fig. 5b) gives rise to a set of horseshoe vortices with alternating rotational direction near the element. However, only one prevailing pair of counter-rotating vortex legs seems to govern the near field behind the roughness element. While the vortex rotating opposed to the CF vortex sense is suppressed shortly downstream of the element, the dominant vortex—rotating in the basic CF direction near the wall—persists and triggers the evolution of the expected streamwise CF vortex. Additionally, wake vortices rotating in the same direction transiently appear. A snapshot of the near wake in the rotated r-system is given in Fig. 6a, where isolines of the downstream velocity component u_r show a continuous deformation along the downstream coordinate s_r. Further downstream, alongside the primary CF vortices, small vortices with a reverse rotation sense near the wall emerge, see Fig. 6b. Periodic structures can be observed between the primary CF vortices, indicating the presence of secondary instability that amplifies unsteady disturbances from the numerical background. This scenario is in accordance with structures found by, i.a., Bonfigli and Kloker [4]. A temporal Fourier analysis allows an assessment of the actual onset of secondary instability. The angular frequency $\omega_0 = 328$ of the CF wave reaching the largest spatial growth rate was chosen as a reference for the analysis. The results are shown in Fig. 4 (black lines). The tenth temporal harmonic exhibits exponential growth starting at $x = 0.037$ and reaching a level of 10^{-2} at the end of the domain. Velocity contours and the distribution of the temporal amplitudes u_h of the tenth harmonic in a crosscut in Fig. 6b compare well with z-modes in literature, see, e.g., Wassermann and Kloker [5] and Friederich and Kloker [3].

Increasing the element height to $k = 1.5$ substantially alters the near wake of the element. The Fourier amplitudes shoot up right behind the element, remaining at a level of 10^{-1} in the entire domain, indicating turbulent flow. The case with $k = 2.0$ exhibits an even sharper rise (Fig. 4, red lines) and slightly larger amplitudes right behind the element. Since the growth rate of unsteady modes is beyond typical convective growth rates, this behavior indicates a global instability in the near wake

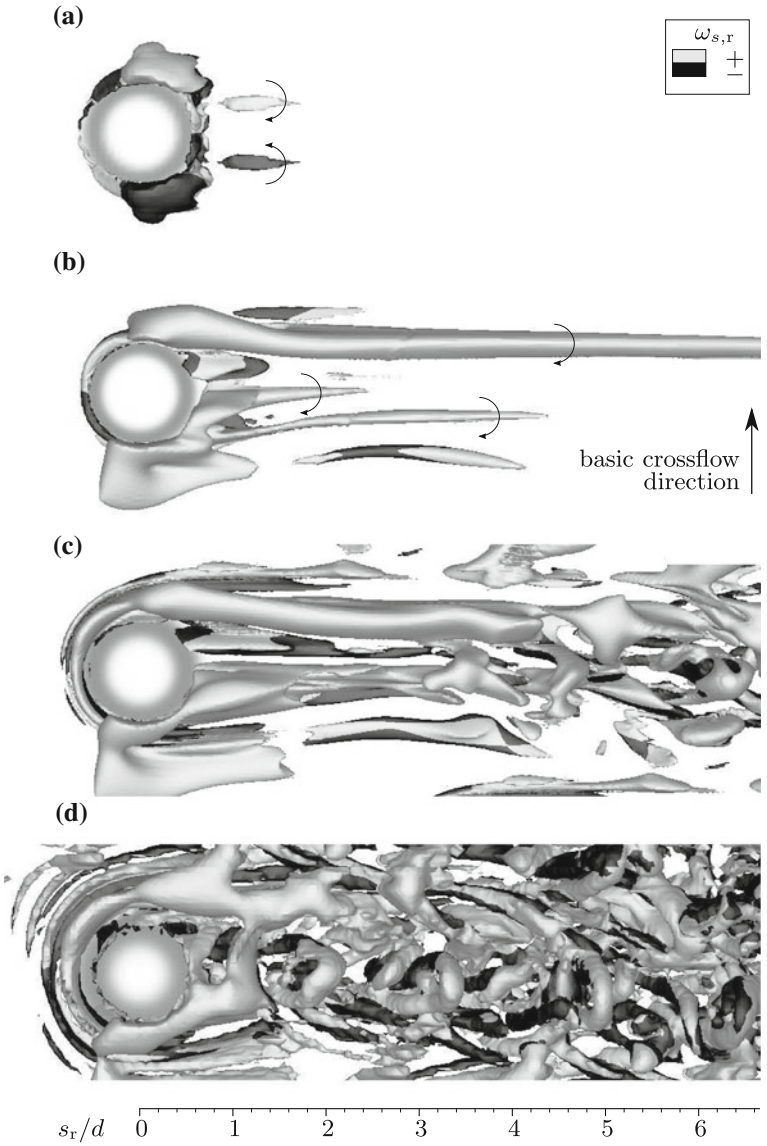

Fig. 5 Vortex systems in the near wake for different roughness-element heights and baseflows, isosurfaces at $\lambda_2 = -20000$, structures above roughness elements are blanked out. *Black* and *white* shading indicates sign of streamwise vorticity $\omega_{s,\mathrm{r}}$. **a** 2-d case with $k = 1.0$: vortices damped shortly behind element, **b** 3-d case with $k = 1.0$: steady CF vortex is triggered, **c** 3-d case with $k = 1.5$: convectively unstable recirculation region sheds unsteady structures, **d** 3-d case with $k = 2.0$: global instability

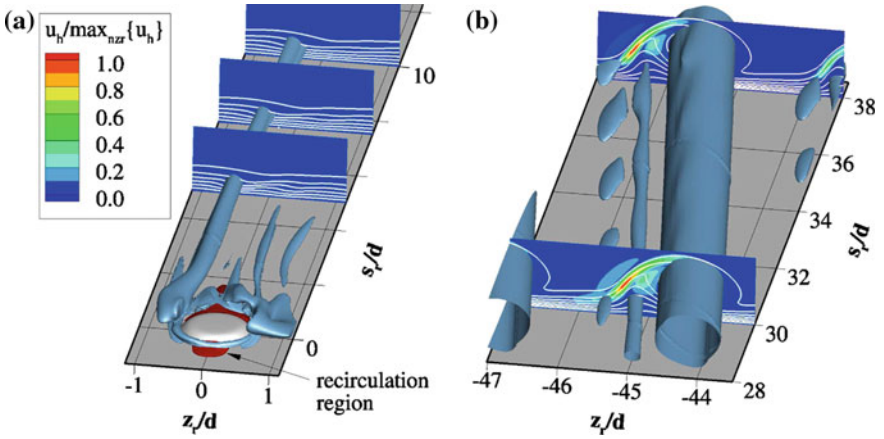

Fig. 6 Near and far wake of roughness element with $k = 1.0$ in rotated wall-parallel coordinate system, rotation angle $\phi_r = 55°$, coordinates normalized by roughness-element diameter d. Vortices visualized by isosurfaces at $\lambda_2 = -20000$ (**a**) and $\lambda_2 = -8000$ (**b**), structures above roughness element are blanked out. *Red* recirculation region is defined by $u_r = 0$. *Slices* show contours of normalized temporal amplitudes $u_h / \max_{nzr}\{u_h\}$ of $h = \omega/\omega_0 = 10$ and *isolines* of u_r

of the element for $k = 2.0$, whereas the $k = 1.5$ case seems to be on the verge of it.

Isosurfaces of the λ_2-criterion at $k = 1.5$ still show basic features of the horseshoe vortex with one persisting leg that was already observed at $k = 1.0$, cf. Fig. 5b, c. However, unsteady structures emerge from the recirculation region and interact with the steady streamwise vortices, causing the latter to periodically break up into smaller structures. In fact, this behavior suggests that 3-d effects due to CF may play a minor role in the near global-instability cases.

A further increase to $k = 2.0$ as shown in Fig. 5d leads to an immediate dominance of the unsteady behavior with a rapid growth and ultimate breakdown to non-periodic, chaotic flow; primary and secondary (convective) instability can not be distinguished. As structures shed by the spanwise periodic roughness array strongly interact with adjacent elements, λ_z is likely to be a relevant parameter for the downstream evolution of the flow past elements at this height.

4 Conclusions

Cylindrical roughness elements in the investigated 3-d boundary layer produce (nonlinear) wake vortices that are either damped or supported by the basic crossflow, depending on their rotational sense and thus their affinity to pure crossflow vortices. With growing roughness height, the recirculation region behind the element gains in

importance regarding the evolution of the flow. Two essentially different scenarios are observed: Up to a roughness height of $k = \bar{k}/\bar{\delta}_{1,s} = 1.0$, $Re_{kk} = 296$, a single persisting (crossflow) vortex is observed in the far wake of the element which becomes secondarily unstable within the DNS domain. In contrast, the near wake of elements with a height of $k = 2.0$, $Re_{kk} = 912$, is governed by a global instability around the element. This mechanism is a changeover of the strong convective instability found for $k = 1.5$, where steady streamwise vortices are still present behind the element and are broken up by interaction with the prevailing unsteady structures shed from the separated near-wake region.

The effective, i.e. directly flow-tripping roughness Reynolds number for the latter scenario is still to be determined, however the present findings are in accordance with estimations of $Re_{kk,crit}$ ranging from 325 to approximately 800 for 2-d flows as summarized by Klebanoff et al. [6]. Note that in the 3-d situation here (i) the effective roughness Reynolds number is in the range of the critical roughness Reynolds number for 2-d flows, the latter typically defining the boundary between completely ineffective and transition-promoting roughness, and (ii), any small roughness gives rise to exponentially amplified steady disturbances without external forcing, rendering the critical roughness Reynolds number smaller than in 2-d base flows.

Acknowledgments The financial support by the European Commission through the FP7 project 'RECEPTivitiy and amplitude-based transition prediction' (ACPO-GA-2010-265094) and the provision of computational resources by the Federal High Performance Computing Center Stuttgart (HLRS) are gratefully acknowledged.

References

1. Schrader, L.-U., Brandt, L., Henningson, D.S.: Receptivity mechanisms in three-dimensional boundary-layer flows. J. Fluid Mech. **618**, 209–241 (2009)
2. Tempelmann, D., Schrader, L.-U., Hanifi, A., Brandt, L., Henningson, D.S.: Swept-wing boundary-layer receptivity to localised surface roughness. J. Fluid Mech. **711**, 516–544 (2012)
3. Friederich, T., Kloker, M.J.: Control of the secondary cross-flow instability using localized suction. J. Fluid Mech. **706**, 470–495 (2012)
4. Bonfigli, G., Kloker, M.J.: Secondary instability of crossflow vortices: validation of the stability theory by direct numerical simulation. J. Fluid Mech. **583**, 229–272 (2007)
5. Wassermann, P., Kloker, M.J.: Mechanisms and passive control of crossflow-vortex-induced transition in a 3-d boundary layer. J. Fluid Mech. **456**, 49–84 (2002)
6. Klebanoff, P.S., Cleveland, W.G., Tidstrom, K.D.: On the evolution of a turbulent boundary layer induced by a three-dimensional roughness element. J. Fluid Mech. **237**, 101–187 (1992)

Wing Design Based on a Tapered Wing Natural Laminar Flow Airfoil Catalogue

Judith Frfr. von Geyr, Fedime von Knoblauch zu Hatzbach, Arne Seitz, Thomas Streit and Georg Wichmann

Abstract In this work airfoil and wing design results using a sectional conical wing method for analysis and design are presented. This method allows the design of swept tapered wing sections. It is useful for transonic Natural Laminar Flow (NLF) design, where sweep and tapering of the wing has to be taken into account. In the first part of this work a transonic tapered wing NLF airfoil catalogue was generated. Different airfoils were designed by varying the design Mach and Reynolds numbers, lift coefficient, leading-edge sweep and airfoil thickness. In the second part a NLF wing was designed for a short range aircraft wing-body configuration. Using the airfoils from the catalogue a wing was obtained with an acceptably large transition region and small shocks on the upper side. Due to the fuselage influence the inner lower wing required further design. For this purpose a 3D inverse design method was used.

1 Introduction

The challenge of integrating a laminar technology into a transport aircraft is considered in the European integrated technology demonstrator "Smart Fixed Wing Aircraft" (SFWA) [1]. SFWA is part of the Joint Technology Initiative (JTI) Clean Sky which aims to develop, integrate and demonstrate technologies that will contribute significantly to achieve the ACARE 2020 vision project. ACARE 2020 contemplates four goals to be reached in the year 2020: 50 % reduction of CO_2 emissions through drastic reduction of fuel consumption, 80 % reduction of NO_x (nitrogen oxide) emissions, 50 % reduction of external noise and green product life cycle (design, manufacturing, maintenance and disposal/recycling). Figure 1, on the left side, shows

J. F. von Geyr · F. von Knoblauch zu Hatzbach · A. Seitz · T. Streit (✉) · G. Wichmann
Institute of Aerodynamics and Flow Technology, DLR Braunschweig, Lilienthalplatz 7, 38108 Braunschweig, Germany
e-mail: Th.Streit@dlr.de

A. Dillmann et al. (eds.), *New Results in Numerical and Experimental Fluid Mechanics IX*, Notes on Numerical Fluid Mechanics and Multidisciplinary Design 124,
DOI: 10.1007/978-3-319-03158-3_19,

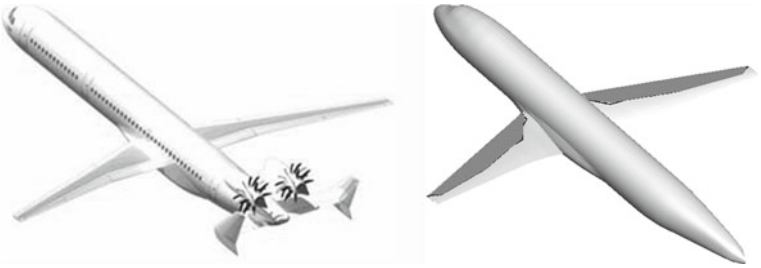

Fig. 1 Short/medium range concept configuration: On the *left side* SFWA concept configuration including various key technologies to improve performance [1]. On the *right side* wing-body short range aircraft configuration considered in this work. On the wing laminar/turbulent boundary layer regions are shown *dark*/*light grey*

a typical SFWA short medium range concept [1] transport configuration integrating different key technologies.

This work presents contributions to SFWA which consider the design of Natural Laminar Flow (NLF) airfoils and wings. This is one of various key technologies which together are considered to achieve the ACARE 2020 vision project. Overviews of laminar flow technology including progress achieved in the past and future challenges are given in Seitz et al [2] and Hansen [3]. In the first part of this work a transonic tapered wing NLF airfoil catalogue was generated [4]. For a variation of design and geometry parameters different airfoils were designed. The catalogue is used for applications within SFWA. The catalogue can also be used to provide a high fidelity data basis for pre design of NLF and to calibrate computationally fast empirical methods. Taking into account the tapering is important for transonic laminar design since: at the nose crossflow instability (CFI) is significantly determined by the leading-edge sweep, while transonic properties like shock strength is determined by the sweep at the shock position. Therefore, numerical solutions obtained with 2.5D methods which allow solutions for infinite swept wings are inadequate for NLF tapered wing design. The sectional conical method [5] takes into account the different sweep due to tapering. An advantage of the sectional conical method is that similarly as the 2.5D methods, it allows the design of tapered airfoils with a computational effort corresponding to a 2D solution. The numerical sectional conical method is also denominated 2.75D method. For the wing definition, these designed airfoil sections can be used in regions where the flow is conical, i.e. isobar lines follow constant percent chord lines. This is the case for most of the wing, except for wing regions close to the body or to the tip where the flow shows large three-dimensional properties. In the second part of this work a NLF wing was designed using the airfoils from the NLF catalogue. A wing-body configuration (see right side Fig. 1) is considered with the wing planform corresponding to the SFWA short range aircraft (SRA) concept.

The used numerical methods are described in Sect. 2. The NLF airfoil catalogue is considered in Sect. 3. Results for the NLF wing design are presented in Sect. 4. Conclusions are given in Sect. 5.

2 Used Numerical Methods

Meshes were generated using the DLR in-house mesh generation software [6, 7], for structured wing-body configurations. In order to obtain RANS solutions for the wing, the mesh resolves the boundary layer with 32 cells. Since the main effect of the body on the wing flow is the displacement of the flow by the body, the body is only modelled with an inviscid boundary condition. Many design iterations have to be performed, therefore for the design a coarse mesh with $257 \times 81 \times 41$ points was utilised. The wing surface was resolved by 161×33 (chord direction $\times$ span direction) points. Stability analysis is performed on corresponding fine mesh solutions with $531 \times 113 \times 81$ points and with 321×65 (chord direction $\times$ span direction) points for the wing surface. In order to estimate the body viscous drag also a body alone mesh was generated with resolved boundary layer. The analysis and design CFD solutions were computed using the FLOWer inverse design code [8, 9]. The RANS equations were solved using the Baldwin-Lomax turbulence model to enable numerically stable computations. For the design of swept tapered wing airfoils the sectional conical method [5] has been implemented into FLOWer. Induced and wave drag are estimated using the program MegaDrag [10]. Transition positions were determined using the STABTOOL program [11]. The program uses the linear stability theory with the e^N method. It provides N-factors for Tollmien-Schlichting (TS) N-factors N_{TS} and crossflow (CF) N-factors N_{CF}. STABTOOL is applied in three steps: PREPCP, COCO and LILO; PREPCP pre-processes the input pressure distributions in order to prepare them for boundary layer calculation. COCO performs compressible boundary layer calculation for the stability analysis, which is performed by LILO. LILO uses a N_{TS}/N_{CF} method, in which N_{TS} is obtained by using the constant wave angle ψ strategy at frequencies covering the complete range of unstable waves, and N_{CF} is obtained by considering only stationary instabilities, using either the constant wavelength strategy or the constant spanwise wavenumber ß* strategy. LILO results were obtained for incompressible N_{TS}/N_{CF} factors.

3 Transonic Tapered NLF Airfoil Catalogue

The NLF airfoil catalogue includes several airfoils designed for a set of parameter combinations namely lift coefficient c_L, Mach number, Reynolds-Number, leading-edge sweep and maximum airfoil thickness. Tapering corresponds to the SRA concept planform. This parameters are varied around the values $Ma_\infty = 0.75$, $Re_c, = 15$ Mill., leading-edge sweep $\varphi_{LE} = \varphi_{LE\_SRA}$, $c_l = 0.65$, $t/c_{max} = 10.5\,\%$ for outer wing airfoils and $Ma_\infty = 0.75$, $Re_c, = 25$ Mill., $\varphi_{LE} = \varphi_{LE\_SRA}$, $c_l = 0.60$, $t/c_{max} = 12.5\,\%$ for inner wing airfoils. The outer/inner wing is defined by span position larger/smaller than the wing kink span position. The airfoils were designed using the 2.75D method. The considered design parameter blocks are given in Table 1.

Table 1 NLF airfoil catalogue design parameter blocks

	Wing position	Varied parameters	Constant parameters
Block 1	Outer	Re_C	M_∞, φ_{LE}, $\varphi_{TE.}$ c_l, t/c_{max}
Block 2	Outer	t/c_{max}, Re_C	M_∞, φ_{LE}, $\varphi_{TE,}$ c_l,
Block 3	outer	φ_{LE}, $\varphi_{TE,}$ Re_C	M_∞, c_l, t/c_{max}
Block 4	Outer	φ_{LE}, $\varphi_{TE,}$ M_∞	Re_C, c_l, t/c_{max}
Block 5	inner	t/c_{max}, Re_C	M_∞, φ_{LE}, $\varphi_{TE.}$ c_l
Block 6	Inner	φ_{LE}, $\varphi_{TE,}$ M_∞	Re_C, c_l, t/c_{max}

For the sweep variation in block 3 and block 6 the wing is sheared. The airfoil catalogue consists of 13 airfoils which take into account 43 design points. For each design point a polar was computed. In addition solutions were obtained for a Mach number variation $M = M_{design} \pm 0.03$ at design c_l.

Since the 2.75D method is a 3D solution for a tapered wing the obtained numerical pressure drag also includes induced drag besides boundary layer induced viscous drag. For the NLF airfoil catalogue the viscous pressure drag was estimated by designing an equivalent 2.5D geometry using inverse design. Target pressure distribution is the 2.75D Cp distribution and used 2.5D sweep is the 2.75D local sweep at the shock position. Transition positions for the 2.5D solutions were set according to the transition position obtained by the 2.75D solution. In future it is planed to avoid the additional work of designing the equivalent 2.5D airfoil by estimating the viscous pressure drag directly from the 2.75D solution using boundary layer analysis estimates.

4 NLF Wing Design

The NLF wing design is performed for a wing-body configuration with a wing planform corresponding to the SFWA new Short Range Aircraft (SRA) planform. Selected cruise design conditions are: $M_\infty = 0.75$, $h = 36000$ ft. Considered off-design flow conditions are $0.73 \leq M_\infty \leq 0.78$, $0.84 \leq c_{L/}\, c_{Lcruise} \leq 1.08$. Besides the planform, constrains were imposed on thickness and load distribution. For the aft-swept wing geometry a first step configuration was defined using 6 airfoils from the catalogue. An initial NLF wing-body geometry was provided by Airbus. In the first step no further geometry modifications were performed, except for the twist and thickness modifications required in order to satisfy the corresponding load and thickness constraints specified in consultation with Airbus. The results of the first step configuration showed an acceptably laminar boundary layer extent at the upper wing side as well as a low wave drag characteristic. Since for the most part of the wing no further design was necessary, these results indicate the usefulness of the 2.75D design. Figure 2 shows a good agreement between the pressure distribution of the 2.75D airfoil result from the profile catalogue [4] and the results of the corresponding

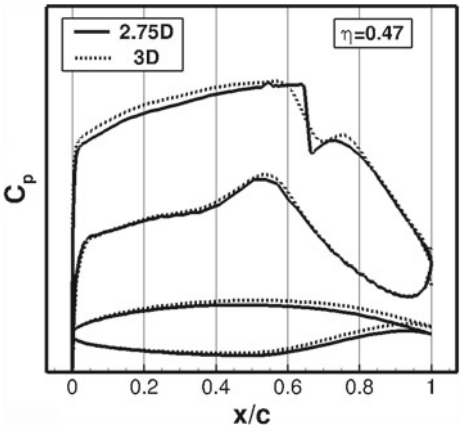

Fig. 2 Comparison of pressure distribution for same local lift between 2.75D result for used catalogue airfoil and wing section at $\eta = 0.47$ span position

section obtained for the 3D wing-body result, compared at the same local lift, for a wing section with normalized span position $\eta = 0.47$ (span is normalized with wing semispan s). The stronger shock of the 2.75D result is caused by a finer mesh. In order to estimate the body viscous drag, a full turbulent body alone solution was obtained. At the initial configuration cruise incidence the viscous drag amounts to 18.76 % of the total initial NLF drag (body viscous drag included). In comparison to the initial NLF configuration the new total drag was reduced by 1.6 %. The wave drag part was reduced by 0.4 %. In comparison to the initial configuration with turbulent boundary layer total drag was reduced by 10.8 %.

In a next step, the 3D inverse design [8] was used in order to obtain a larger region with laminar boundary layer especially on the lower side. A 3D design method is required especially at the inner wing, for regions close to the wing-body intersection. Results showed a downstream displacement of the lower side transition line leading to an additional reduction in total drag. Figure 3 shows the transition line position results for step 1, intermediated design results and final design result. For the inner wing, due to crossflow instability, the transition line could not be displaced further downstream without violating a leading-edge radius constraint. This constraint was violated in design steps 6 and 7 in Fig. 3. Figure 4 shows the total drag components based on cruise total drag of the final NLF design. Note that the skin friction and viscous pressure drag have similar contributions. Results for the local drag laminar benefit and local wave drag are given in Fig. 5. The laminar drag benefit $c_{d\,\mathrm{lam.\,ben.}}$ is the additional viscous drag, obtained for the same pressure distribution for a full turbulent boundary layer in comparison to the drag obtained with transition. Here this difference is estimated using the empirical estimates [12] for skin friction benefit and profile drag benefit:

$$c_{df} = 0.032 x_{tr} (M/M_\infty)/\log_n(Re_c),\ c_{dp} = 0.20 x_{tr} (M/M_\infty)(C_{pte} - C_{pm})/Re_c^{0.28} \quad (1)$$

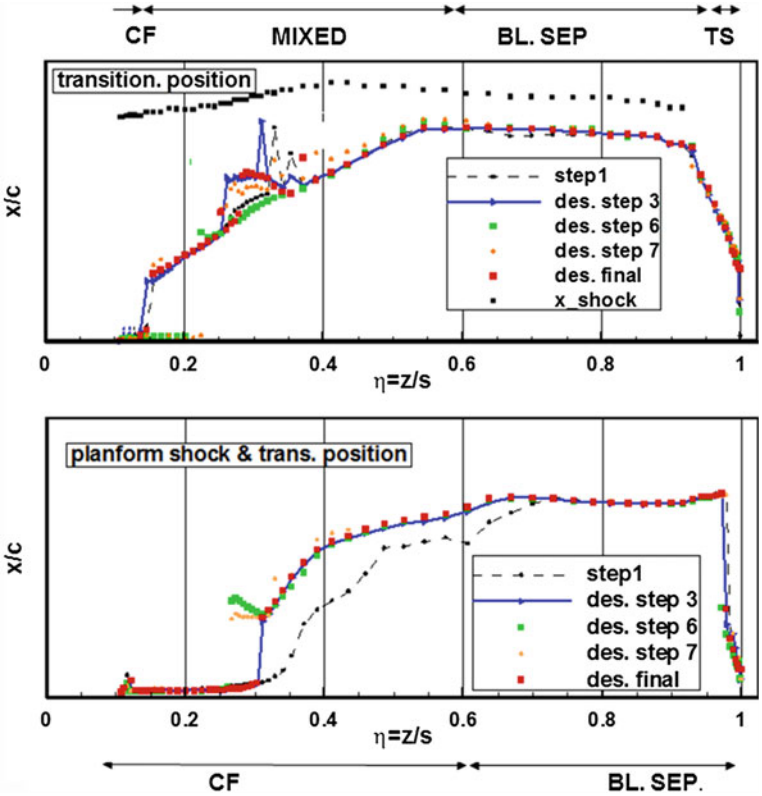

Fig. 3 Transition line position for upper and lower wing side for step 1 (wing constructed with NLF airfoil catalogue) configuration and intermediate and final designed configurations. For the upper wing also the shock position is given. The relevant transition mechanism is indicated: *CF* crossflow, *TS* Tollmien-Schlichting, mixed transition, *BL. SEP.* laminar boundary layer separation

where x_{tr} is the transition location in terms of x/c, C_{pm} is a term related to the magnitude of the pressure rise at the pressure minimum, and C_{pte} is the trailing-edge pressure. In the case of transonic flow the relevant drag benefit is computed by subtracting the wave drag from the viscous drag benefit. It is denoted $c_{d\,ben\,trans}$. In comparison to the initial NLF configuration the final design total drag was reduced by 2.3 %. The wave drag part was reduced by 0.5 %. In comparison to the initial configuration with turbulent boundary layer total drag was reduced by 11.0 %. A further improvement of laminar extent in the inner wing region cannot be achieved with NLF design alone. Assuming a suction panel for the inner wing up to a span position $\eta = 0.25$ and setting the transition position for $\eta < 0.25$ at the same x/c transition position than at $\eta = 0.25$ (except for a turbulent wedge with origin at the nose of the intersection between wing and body) leads for the upper side to a further

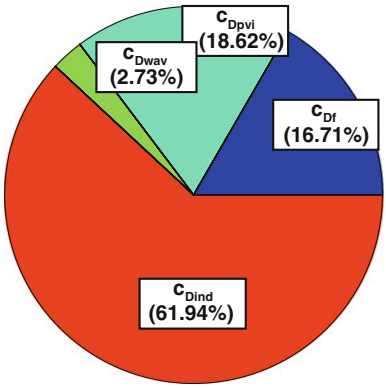

Fig. 4 Drag components: induced drag C_{Dind}, wave drag C_{Dwav}, skin friction $C_{Df,}$ viscous pressure drag C_{Dpvi}. Based on total drag of final design without viscous body drag

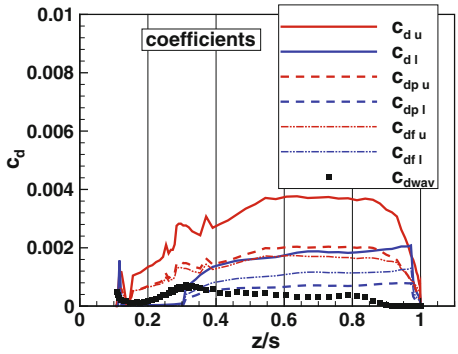

Fig. 5 local drag laminar benefit and local wave drag as function of normalized span. The indices u/l denote the *upper/lower side*. Benefits are given for local drag (denoted c_d), its friction drag component (denoted c_{df}) and its viscous pressure drag (denoted c_{dp})

total drag reduction of 0.9 %. However, this is an estimate for the pure aerodynamic drag reduction without considering the additional weight and suction power penalties due to the HLF technology (hybrid laminar flow).

Off-design solutions with transition for the final designed wing were obtained for flow conditions with $0.73 \leq M_\infty \leq 0.78$, $0.84 \leq c_{L/}c_{Lcruise} \leq 1.08$. Contour plots for wave drag $c_{D\,wav}$ and NLF transonic benefit drag c_{Dben_trans} are given in Fig. 6. Aerodynamic efficiency M_∞ L/D contours are given in Fig. 7. Small wave drag is obtained around the design point (crossed circle). The wave drag rise for high lift and high Mach number is compensated by the reduced viscous drag due to the laminar boundary layer. In comparison to the design point drag of the initial NLF configuration, this compensation extends to a large off-design region. Similarly the aerodynamic efficiency shows a region of extended off-design improvement.

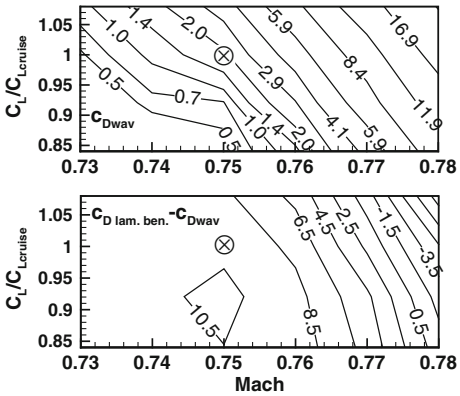

Fig. 6 Contours for $c_{D\,wav}$ (*upper side*) and $c_{D\,ben\_trans}$ (*lower side*), normalized with the initial NLF configuration design point total drag, in percent

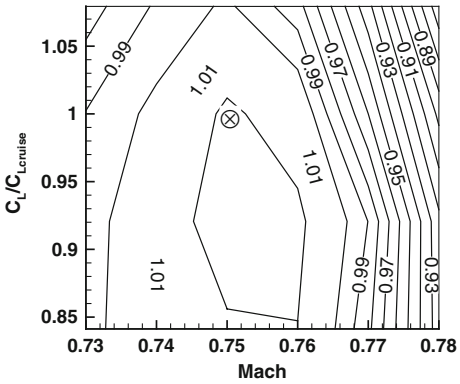

Fig. 7 Aerodynamic efficiency normalized with the initial NLF configuration design point aerodynamic efficiency

5 Conclusion

In this work airfoil and wing design results using a sectional conical wing method for analysis and design are presented. This method allows the design of swept tapered wing sections with a computational effort which is slightly higher than a 2D computation. The method is useful for transonic NLF design, where the sweep and tapering of the wing has to be taken into account. In the first part of this work a transonic tapered wing NLF airfoil catalogue was generated. For a variation of the parameters Mach number, Reynolds number, lift coefficient, wing leading-edge sweep and airfoil thickness, different airfoils were designed. In the second part a NLF wing was designed for a short range aircraft wing-body configuration. Using the airfoils from the catalogue with twist and airfoil thickness scaling modifications due to spanwise lift and thickness distributions constraints a wing was obtained with acceptably large transition region and small shocks on the upper side. Since for the most part of the wing no further design was necessary, these results indicate the usefulness of the NLF sectional conical design. Due to the influence of the body

further design was required for the inner lower wing part. In this region the conical approximation does not apply and a 3D inverse design method was used. In comparison to the initial NLF configuration at the design point the final design total drag was reduced by 2.3 %. The wave drag part was reduced by 0.5 %. In comparison to the initial configuration with turbulent boundary layer the total drag was reduced by 11.0 %. Furthermore, a region of improved off-design results was obtained.

Acknowledgments The research leading to these results has received funding from the European Union's Seventh Framework Programme (FP7/2007-2013) for the Clean Sky Joint Technology Iniative under grant agreement number CSJU-GAM-SWFA-2008-001.

References

1. Clean Sky at a Glance. Bringing sustainable air transport closer. http://cleansky.eu/content/document/clean-sky-glance Feb 2012
2. Seitz, A., Horstmann, K.H.: Design studies on NLF and HLFC applications at DLR., In: 27th International Congress on the Aeronautical Sciences. Nice, France, 19–24 Sept 2010
3. Hansen, H.: Laminar flow technology—the airbus view. In: 27th International Congress on the Aeronautical Sciences. Nice, France, 19–24 Sept 2010
4. von Knoblauch, F., von Geyr, J., Streit, Th, Seitz. A.: SFWA-ITD technical report: natural laminar flow airfoil catalogue. Braunschweig (2011)
5. Streit, Th., Wichmann, G, Campbell, R., von Knoblauch zu Hatzbach, F.: Implications of conical flow for laminar wing design and analysis. In: AIAA 2011–3808, 29th AIAA Applied Aerodynamics Conference. Honolulu, Hawaii, 27–39 June 2011
6. Wichmann, G.: Untersuchung zur Flügel-Rumpf-Interferenz durch Anwendung eines Eulerverfahrens für kompressible Strömung. Dissertation, Institut für Strömungstechnik, Technische Universität Braunschweig, ZLR-Forschungsbericht (1993)
7. Streit, Th., Wichmann, G., Rohardt C.-H.: Nachrechnung und Entwurf von transsonischen Tragflügeln für die DO-728/DO-928. DLR IB-129-99/13 (1999)
8. W. Bartelheimer.: Ein Entwurfsverfahren für Tragflügel in transsonischer Strömung (A design method for wings in transonic flow). Published in German, Dissertation TU Braunschweig, DLR-Forschungsbericht 96–30, Deutsche Forschungsanstalt für, Luft- und Raumfahrt e.V. (1996)
9. FLOWer Installation and User Manual, Release 2007, Doc.-Nr. FLOWer1-2007.1, Institut für Aerodynamik und Strömungstechnik, DLR.
10. Kreuzer, P.: MEGADRAG Installations und Benutzerhandbuch (für FLOWer 114). Technische Universität Darmstadt, BMBF Projekt Widerstandanalyse (1999)
11. Schrauf, G.: Lilo 2.1, User's Guide and Tutorial. GSSC technical report 6 (2006)
12. Campbell, R.L., Campbell, M.L., Streit, Th.: Progress toward efficient laminar flow analysis and design. In: AIAA 2011–3527, 29 th AIAA Applied Aerodynamics Conference, Honolulu, Hawaii, 27–39 June 2011

Experimental and Numerical Investigations of the Laminar Airfoil NLF9

René-Daniel Cécora and Henning Rosemann

Abstract The flow around a 2D laminar airfoil is investigated using wind tunnel experiments as well as computational fluid dynamics, employing both sub- and supercritical freestream conditions. In the transonic cases, an interaction of the compression shock and the boundary layer on the upper airfoil surface takes place, leading to transition and, for high angles of attack, shock-induced separation.

1 Introduction

Reduction of fuel and emissions is an important challenge for aircraft industry, leading to an increased interest in the usage of laminar wings. In recent years, the German Aerospace Center (DLR) participated in several investigations concerning laminarization of aircraft flow, with a special interest in natural laminar flow (NLF). The measurements presented in this paper were part of an investigation about the design of modern airfoils with NLF capabilities for regional aircrafts. Both subsonic ($M = 0.3$) and transonic ($M = 0.62$) flow regimes were tested, cooling of the flow allowed to reach Reynolds numbers in the range of 6 million to 15 million. Along with high-quality pressure distributions, the heat flux from the airfoil surface into the boundary layer was measured to indicate laminar-turbulent transition. Furthermore the drag coefficient was determined by wake measurements.

R.-D. Cécora (✉)
Institute of Fluid Mechanics, Technische Universität Braunschweig,
38108 Braunschweig, Germany
e-mail: r-d.cecora@tu-bs.de

H. Rosemann
Institute of Aerodynamics and Flow Technology, German Aerospace Center,
37073 Göttingen, Germany

A. Dillmann et al. (eds.), *New Results in Numerical and Experimental Fluid Mechanics IX*,
Notes on Numerical Fluid Mechanics and Multidisciplinary Design 124,
DOI: 10.1007/978-3-319-03158-3_20,

Table 1 Comparison of experimental data and results of numerical simulation

Case		α	C_L	C_D	M	$Re/10^6$	$x_{tr,upper}$	$x_{tr,lower}$
56	Experiment	0°	0.370	0.0063	0.3002	5.97	0.45–0.55	0.55–0.60
	JHh-v2	−1.2°	0.372	0.0052			0.51	0.53
68	Experiment	5°	0.921	0.0098	0.2998	5.97	0.15–0.25	0.55–0.60
	JHh-v2	3.53°	0.921	0.0097			0.11	0.56
91	Experiment	1°	0.615	0.0051	0.6185	15	0.00–0.30	0.50–0.60
	JHh-v2	−0.39°	0.615	0.0054			0.45	0.49
95	Experiment	3°	0.912	0.0062	0.6214	15	0.45–0.50	0.55–0.60
	JHh-v2	1.40°	0.915	0.0075			0.47	0.53
112	Experiment	6°	1.302	0.0177	0.6207	15	0.40–0.50	0.55–0.60
	JHh-v2	4.3°	1.303	0.0223			0.48–0.49	0.55
121	Experiment	1°	0.614	0.0056	0.6208	10.1	0.45–0.50	0.55–0.60
	JHh-v2	−0.35°	0.615	0.0057			0.46	0.52
124	Experiment	1°	0.615	0.0061	0.6189	6	0.45–0.55	0.55–0.60
	JHh-v2	−0.29°	0.614	0.0062			0.47	0.54

Computational Fluid Dynamics (CFD) is essential for the development of new aircraft technology. The quality of CFD simulations strongly depends on the chosen turbulence model. Most of the turbulence models currently used by aircraft industry are based on the Boussinesq assumption, which shows discrepancies in complex flows including flow separation, streamline curvature or strong effects of stress anisotropy. On the contrary, Reynolds-stress models (RSM) directly calculate transport equations for all elements of the Reynolds-stress tensor, hence the Boussinesq assumption is discarded. Consequently turbulent stress anisotropy can be captured naturally, at the cost of higher computational effort. At the Institute of Fluid Mechanics of TU Braunschweig, a slightly modified version of the Reynolds-stress model by Jakirlić and Hanjalić [1] was implemented into the DLR flow solver TAU [2], which uses the homogeneous part of the dissipation rate as length scale variable [3]. This model has already shown its capabilities to simulate flows of aircraft aerodynamics [3, 4], the application to laminar airfoils including transition prediction is discussed in this work.

A summary of the different flow conditions and simulation results is found in Table 1.

2 Experimental Setup

The DNW-KRG (Fig. 1) is a blow-down cryogenic wind tunnel based on the Ludwieg-Tube concept [5] for high Reynolds number research in transonic flow. Operating at stagnation pressures up to 1 MPa and charge temperatures T_c down to 100 K, it is possible to achieve Reynolds numbers up to 60×10^6 based on a model chord of 150 mm (2–D). The run time varies between 0.6 s and 1.0 s, depending on the fluid temperature. Pressure fluctuations in the flow for the conditions used here were measured to $c_{p,rms} \approx 0.0025$, see also [6] and [7].

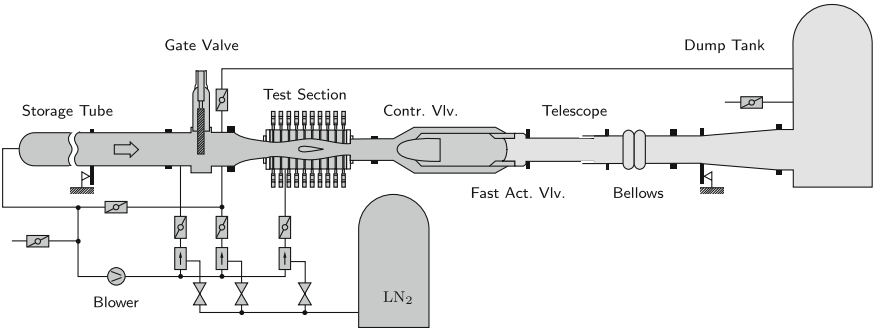

Fig. 1 Schematic illustration of the Cryogenic Ludwieg-Tube Göttingen (DNW-KRG)

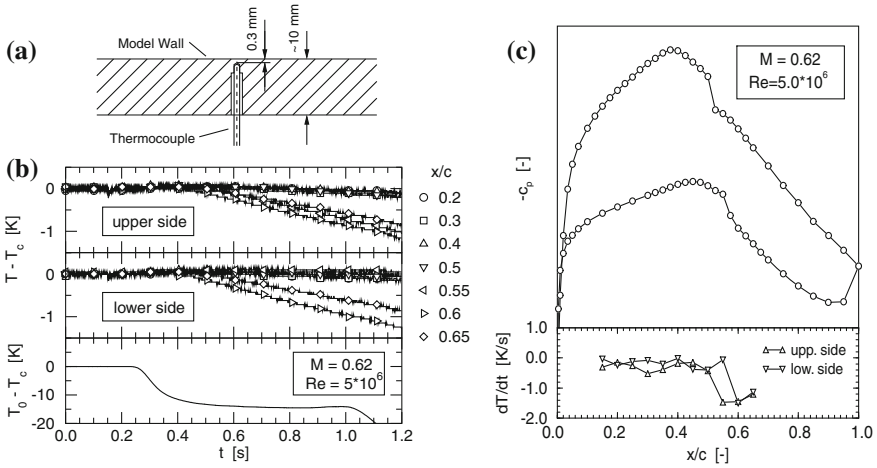

Fig. 2 Transition detection by thermocouples

The test section with a width of 400 mm, a height of 350 mm and a total lenght of 2,000 mm is equipped with adaptive horizontal walls. The shape of the flexible upper and lower wall is determined by a non-iterative Cauchy method from the deflection of the walls and the wall pressure distribution [6].

The NLF9 airfoil model with a chord length of $c = 180$ mm was mounted in the side-walls of the test section. It was equipped with 71 pressure taps and 26 thermocouples mounted only 0.3 mm underneath the skin, as shown in Fig. 2a, for transition measurements.

Due to the unsteady expansion process in a Ludwieg Tube during start-up, the total temperature drops by about 3 % at $M = 0.3$ and about 5 % at $M = 0.7$, yielding temperature differences of 8.5 K and 14 K, respectively, between flow and model, when the flow is established, see Fig. 2b (lower diagram).

The corresponding time-traces of the thermocouples show very little temperature change during the run for the upstream positions, whereas the distinct cooling visible

downstream of $x/c \geq 0.55$ on the upper and $x/c \geq 0.60$ on the lower side indicates a turbulent boundary layer by its larger heat flux.

This is confirmed by an evaluation of the temperature gradients and comparison with the measured pressure distribution, Fig. 2c, which shows signatures of laminar separation bubbles at $x/c \approx 0.56$ on the lower and at $x/c \approx 0.52$ on the upper side. This agrees perfectly with the steps in the temperature gradient.

Drag was determined with a wake rake positioned on the center axis of the test section 310 mm downstream of the trailing edge of the model.

Static and wake pressures were measured by a PSI System 8400 equipped with Scanivalve ZOC 14 and PSI ESP-32SL modules (50 psi and 45 psi range, respectively) with a nominal accuracy of ± 0.05 % FS. All data were averaged over a time window of 0.1 s close to the end of the run time to determine mean values. The remaining interferences of the horizontal walls were estimated to $\Delta\alpha \leq 0.01°$ and $\Delta M \leq 0.001$.

3 Computational Fluid Dynamics

All simulations shown in this work have been carried out using the DLR-TAU Code [2], solving the Favre- and Reynolds-averaged Navier-Stokes equations on hybrid unstructured grids with second order accuracy. The steady-state solver was applied with a central spatial discretization scheme, a three-level multigrid scheme was used to accelerate convergence. Closure of the equation system was achieved with the Reynolds-stress turbulence model JHh-v2 [4].

Transition locations on the upper and lower surface of the airfoil were predicted by the transition module of the DLR-TAU solver [8], which uses linear stability theory to determine amplification rates for different instability types. By integrating the amplification rates along the airfoil contour, N-factors are calculated and the e^N-method can be applied. The critical N-factor of transition was set to $N_{crit} = 7$. In order to overcome an unphysical damping of turbulence in the transition region due to low-Re damping terms, prescription of Reynolds stresses at the transiton point was applied [9].

The mesh-generation software Gridgen V15 [10] was used to create a 2D hybrid mesh, containing 78,000 points. The structured part around the airfoil comprises 472×97 points, followed by a structured wake region with 75×232 points and surrounded by an unstructured mesh with a radius of 100 cord lengths. The grid can be seen in Fig. 3. Grid dependencies were investigated with a refined 2D mesh (factor 2 in both directions), no remarkable influence on the solution could be found.

To compensate for effects of the wind tunnel side walls, the angle of attack was reduced in the simulations until the measured lift coefficient was matched.

Due to the occurrence of oscillating separation bubbles, the Cases 95, 112 and 124 were simulated using the unsteady RANS solver of the DLR-TAU Code, which comprises a dual-time-stepping scheme.

In order to estimate the influence of the chosen turbulence model, simulations using the SST model by Menter [11] have been performed for all test cases. No

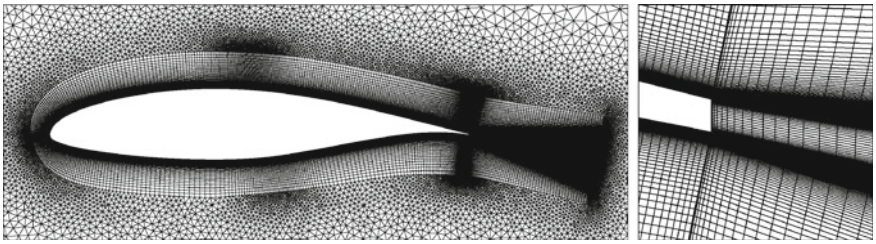

Fig. 3 2D hybrid grid

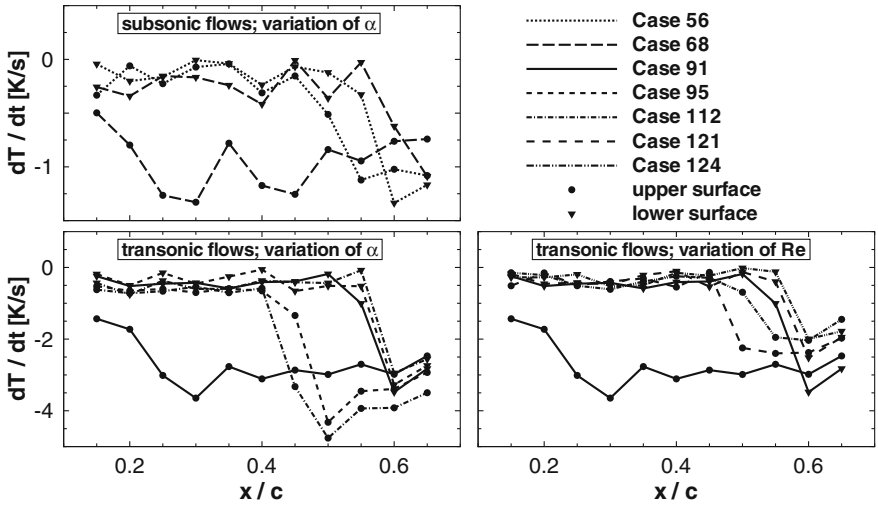

Fig. 4 Experimentally measured heat flux

significant differences could be found between the pressure distributions of both turbulence models, likewise the predicted transition locations show only minor deviations.

4 Results

All measured heat flux distributions are shown in Fig. 4. Contrary to the main idea of laminar airfoils, transition on the upper surface occurs near the airfoil nose for the Cases 68 and 91. In all other Cases transition is found between $x/c = 0.4$ and $x/c = 0.6$, both on the upper and lower surface.

A comparison of measured and simulated pressure distributions of the two subsonic cases can be seen in Fig. 5, showing a good agreement in Case 56. Applying a higher angle of attack (Case 68), the suction peak is underestimated in the simulation. The existence of a suction peak and following pressure rise in Case 68 explains the earlier discussed transition location near the airfoil nose on the

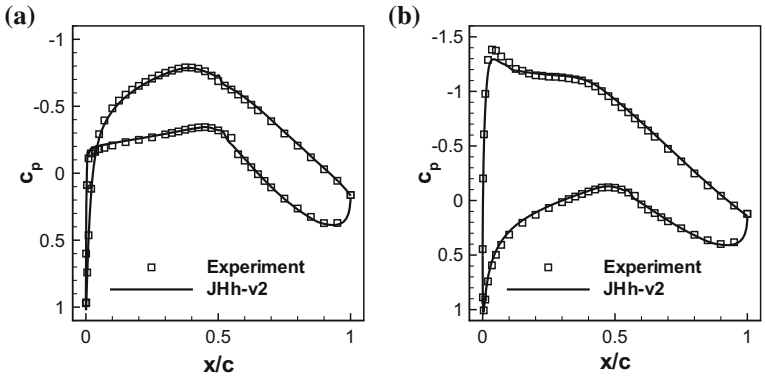

Fig. 5 NLF 9 airfoil: pressure distributions. **a** Case 56, **b** Case 68

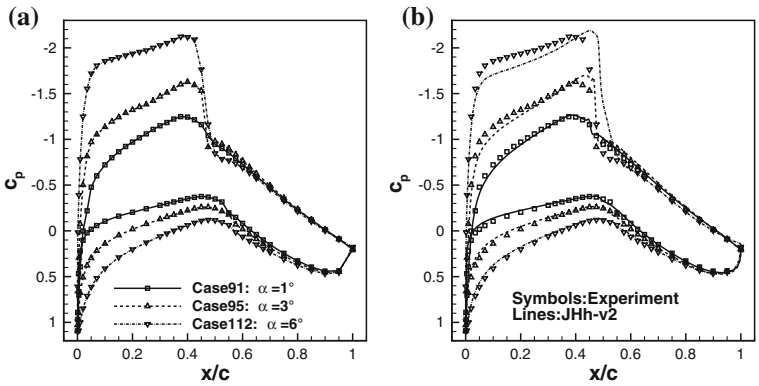

Fig. 6 Pressure distribution for different angles of attack: Ma $= 0.62$, Re $= 15 \times 10^6$. **a** Experimental data, **b** comparison with simulations

upper surface, which is predicted correctly by the transition module in the simulations (Table 1).

All five investigated test cases with M $= 0.62$ develop a region of supersonic flow above the upper surface, they can therefore be considered as transonic test cases. Experimental pressure distributions for three different angles of attack are shown in Fig. 6a. It is noticable that on the upper surface the location of minimum pressure, and likewise the shock location, remains the same when increasing the angle of attack, while the shock strength rises. In the simulations however, the shock location moves slightly downstream with increasing angle of attack, leading to a higher lift coefficient. In order to achieve the same lift coefficient as the experiments for the Cases 95 and 112, the angle of attack has to be reduced by 1.6° and 1.7°, respectively. From the comparison of pressure distributions in Fig. 6b it can be noticed that the pressure on the upper surface near the airfoil nose is overestimated in both Cases,

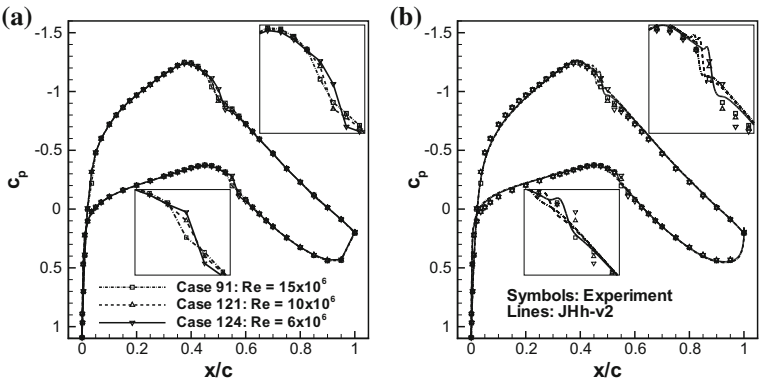

Fig. 7 Pressure distribution for different Reynolds numbers: Ma $= 0.62$, $\alpha = 1°$. **a** Experimental data, **b** comparison with simulations

indicating a too low angle of attack. The kink in the steep pressure rise at the shock of Case 112, which can only be found in the simulations, is due to a shock-induced separation bubble. Contrary to Case 68, the pressure distribution of Case 91 gives no explanation for the early transition on the upper surface, which has most likely been triggered by disturbances from surface roughness. Accordingly we find a deviation of the numerical transition prediction and the measured location. A good agreement of the transition locations can be found for the higher angles of attack in the Cases 95 and 112.

In Fig. 7a, the influence of the Reynolds number on the experimental pressure distributions can be seen. Both on the upper and lower surface, a longer region of moderate pressure rise upstream of the shock is found for the lower Reynolds numbers. This is due to the stronger tendency of laminar boundary layers to develop weak oblique compression shocks that combine to a so-called λ-shock, while turbulent boundary layers tend to develop a stronger compression without preceding oblique shocks [12]. The location of the steepest pressure gradient moves upstream with rising Reynolds number. The shock induces a rapid increase of boundary-layer thickness and displacement thickness, observable in the small pressure plateau on the upper surface downstream of the shock. Since this effect is comparatively higher for laminar boundary layers, the plateau is more distinct for the lower Reynolds numbers in Case 121 and Case 124. In the simulation of Case 124, a small laminar separation bubble is found on the lower surface, leading to an unsteady oscillation of the transition location.

While the experiments of Case 91 measure transition on the upper surface near the airfoil nose, it is predicted by the simulations near the shock location (Table 1). Hence the simulated shape of the pressure distribution in the shock region is similar for all three Reynolds numbers, as can be observed in Fig. 7b. Equal to the experiments, the shock location moves slightly upstream with rising Reynolds numbers. Directly upstream of the shock, a small wiggle in the simulated pressure distributions can

be noticed, which is due to the unphysically rapid onset of Reynolds stresses at the transition location. The high gradient of Reynolds stresses in streamwise direction directly contributes to the momentum equation and is compensated by the local negative pressure gradient.

5 Conclusion

A comparison of experimental and numerical investigations of the flow around the laminar airfoil NLF9 has been presented. The test cases contain both subsonic and transonic flow, including variation of the angle of attack and of the Reynolds number. Besides measuring pressure distributions, transition locations could be determined experimentally from the heat flux on the airfoil surface, additionally the drag coefficient was measured. On the numerical side, RANS/URANS simulations with a Reynolds-stress model including transition prediction have been performed. For the subsonic cases, a good agreement of the simulations with the experimentally measured pressure distributions and transition locations was achieved. A comparison of the transonic pressure distributions shows a moderate movement of the simulated shock locations towards the trailing edge with rising angle of attack, which is not found in the experiments. A mentionable influence of the turbulence model could not be found.

Acknowledgments The authors gratefully acknowledge the "Bundesministerium für Bildung und Forschung" who funded the numerical part of this research within the frame of the joint project *ComFliTe* (funding number 20 A 06 04 G).

References

1. Jakirlić, S., Hanjalić, K.: A new approach to modelling near-wall turbulence energy and stress dissipation. J. Fluid Mech. **459**, 139–166 (2002)
2. Kroll, N., Rossow, C.-C., Schwamborn, D.: The MEGAFLOW-Project—Numerical Flow Simulation for Aircraft. Progress in Industrial Mathematics at ECMI 2004. Springer, Berlin (2005)
3. Probst, A., Radespiel, R.: Implementation and extension of a near-wall Reynolds-stress model for application to aerodynamic flows on unstructured meshes. AIAA Paper 2008–770 (2008)
4. Cécora, R.-D., Eisfeld, B., Probst, A., Crippa, S., Radespiel, R.: Differential Reynolds stress modeling for aeronautics. AIAA-Paper 2012–0465 (2012)
5. Ludwieg, H.: Der Rohrwindkanal. Z. Flugwiss. Weltraumforsch. **3**, 206–216 (1955)
6. Rosemann, H.: The Cryogenic Ludwieg-Tube at Göttingen. In: Special Course on Advances in Cryogenic Wind Tunnel Technology, AGARD-R-812. DLR, Cologne, Germany, 20–24 May (1996)
7. Koch, S.: Zeitliche und räumliche Turbulenzentwicklung in einem Rohrwindkanal und deren Einfluss auf die Transition an Profilmodellen. Forschungsbericht DLR-FB-04-19, DLR (2004)
8. Krimmelbein, N., Radespiel, R.: Transition prediction for three-dimensional flows using parallel computation. Comput. Fluids **38**(1), 121–136 (2009)
9. Probst, A., Radespiel, R., Rist, U.: Linear-stability-based transition modeling for aerodynamic flow simulations with a near-wall Reynolds-stress model. AIAA J. **50**(2), 416–428 (2012)

10. Pointwise Inc.: Gridgen User Manual, Version 15. http://www.pointwise.com (2011)
11. Menter, F.R.: Two-equation Eddy-viscosity turbulence models for engineering applications. AIAA J. **32**(8), 1598–1605 (1994)
12. Ackeret, J., Feldmann, F., Rott, N.: Investigations of Compression Shocks and Boundary Layers in Gases Moving at High Speed. NACA Technical Memorandum No. 1113 (1947)

Reconstruction of a Disturbance Flow Field from Wall Measurements of Tollmien-Schlichting Waves

Arne Seitz

Abstract In 2001, flight tests were performed in order to learn more about boundary layer transition induced by free-stream excited Tollmien-Schlichting waves. A sixty four element hot-film array, placed on the right hand wing of DLR's flying test-bed LFU-205, was used to measure the wall shear stress fluctuations provoked by these instabilities while propagating in the laminar boundary layer. In the present work, a procedure was developed that allows the reconstruction of the disturbed flow field above the hot-film sensors from the wall measurements by employing linear stability analysis. The reconstruction delivers the fluctuations of all flow quantities, i.e. disturbance velocity components, pressure, temperature and density. A comparison of the reconstructed longitudinal disturbance velocity component u' with hot-wire measurements shows good qualitative agreement.

1 Introduction

Tollmien-Schlichting waves are well known as primary instabilities in transition of boundary layers from laminar to turbulent flow. But only a few experiments are known to the author that deal with the technically relevant case of free-stream (or naturally) excited Tollmien-Schlichting waves in a wing boundary layer in free-flight. Lee et al. [1] measured instability frequencies, but no information on propagation directions, wavelengths etc. were gained. Peltzer and Nitsche [2] used arrays of surface hot-wires and piezo sensors to detect naturally and artificially excited instabilities on a sailplane wing as an input for Direct Numerical Simulations (DNS).

At the German Aerospace Center DLR, in 2001 in-flight experiments with the flying test bed LFU-205 were performed (Seitz [3]). A multi-element hot-film array, placed on the right hand wing of the flying test-bed LFU-205, was used to sense skin

A. Seitz (✉)
Institute of Aerodynamics and Flow Technology, DLR, Braunschweig, Germany
e-mail: arne.seitz@dlr.de

A. Dillmann et al. (eds.), *New Results in Numerical and Experimental Fluid Mechanics IX*,
Notes on Numerical Fluid Mechanics and Multidisciplinary Design 124,
DOI: 10.1007/978-3-319-03158-3_21,

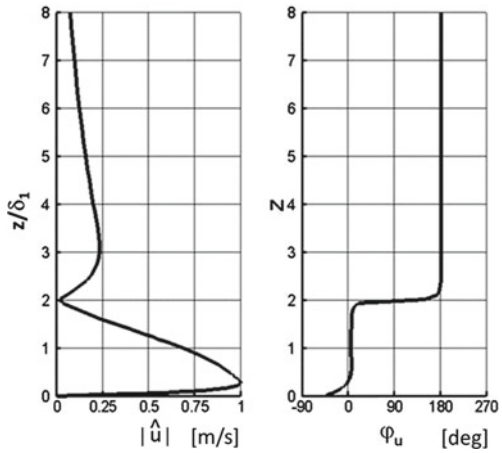

Fig. 1 Eigenfunction $\hat{u}$ of velocity disturbance u' in terms of absolute value and phase angle

friction fluctuations provoked by Tollmien-Schlichting waves propagating in the laminar boundary layer. In the present work, the previously acquired experimental data are utilized to reconstruct the disturbance flow field in the boundary layer above the hot-film sensors by employing linear stability theory. The reconstruction delivers the fluctuations of all flow quantities, i.e. disturbance velocity components, pressure, temperature and density.

In the following paragraphs, first the acquisition of the experimental data, which are the basis of the reconstruction, will be presented followed by a description of the methodology used for reconstruction. Finally, for the selected test case results and a comparison of the reconstructed longitudinal velocity component u′ with hot-wire data acquired during the in-flight experiment of Horstmann and Miley [4] are given.

2 The Experimental Data

2.1 Wall Measurement of Tollmien-Schlichting Waves

In Fig. 1 the typical longitudinal disturbance velocity profile (eigenfunction respectively) of a single Tollmien-Schlichting wave is depicted. Its amplitude and phase function correspond with the wave ansatz from temporal linear stability theory:

$$u'(x, y, z, t) = |\hat{u}(z)| \cdot e^{\omega_i t} \cdot \cos(\alpha x + \beta y - \omega_r t = \varphi_u(z)) \cdot \tag{1}$$

Using the definition for wall shear stress, it may be derived from Eq. (1) that a velocity disturbance u' provokes a fluctuating skin friction according to

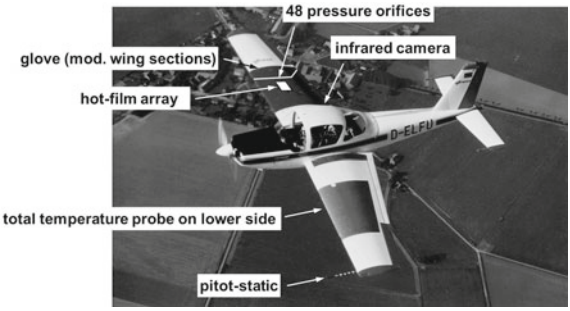

Fig. 2 Flying test-bed LFU-205 with instrumentation

$$\tau'_w(x, y, t) = \mu \frac{d|\hat{u}(z)|}{dz}|_{z=0} \cdot e^{\omega_i t} \cdot \cos(\alpha x + \beta y - \omega_r t = \varphi_u(z)), \qquad (2)$$

with $\hat{\tau}_w = \mu(d|\hat{u}|/dz)|_{z=0}$ being the amplitude and x, y, z the streamwise, spanwise and wall normal coordinates. Obviously, Tollmien-Schlichting instabilities leave traces at the wall which contain all the information about the waves like frequency $f = 2\pi\omega_r$, wave numbers α, β, and amplification ω_i.

Hot-films are the adequate type of sensor to measure these traces or skin friction fluctuations respectively. The principle of hot-film anemometry is based on convective heat transfer from an electrically heated sensing element. Cooling of the element by the flow then depends upon the magnitude of the wall shear stress and, hence, a relation exists between wall shear stress τ_w and the electric voltage needed to keep the sensor at a constant temperature. The instantaneous anemometer output voltage $e = E_0 + e'$ then may be split up into a mean value E_0 that is linked to the mean shear stress τ_{w0} and a fluctuating part e', which can be related to τ'_w via a calibration procedure. Details of the calibration procedure as well as an error analysis (on which the accuracy of all quantities subsequently derived from the wall shear stress fluctuations depends) are given in [3].

2.2 The In-Flight Experiment

Figure 2 shows the flying test-bed LFU-205 of DLR. It is a light aircraft equipped with a laminar glove made from composite material on the right hand wing. The airfoil in the glove region was especially designed to allow for a moderate growth of Tollmien-Schlichting waves in a constant pressure region or under a slightly adverse pressure gradient (Horstmann et al. [5]). Depending on speed and altitude, the LFU-205 can be operated at chord Reynolds numbers ranging roughly between $Re_C = 4 \cdot 10^6$ and 10^7, while the Mach number does not exceed $Ma_\infty = 0.3$.

In order to measure the actual pressure distribution, the wing is equipped with 48 orifices in one chordwise row. An infrared thermovision system installed in the cockpit of the aircraft is used to monitor the location of turbulence onset in the glove region. Further instrumentation comprises a pitot-static located on the left wing-tip

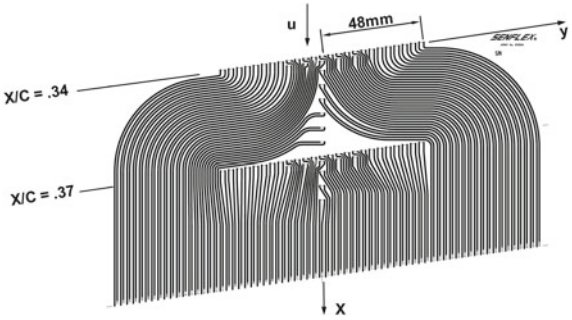

Fig. 3 Sixtynine element hot-film array placed on right hand wing of the LFU-205

and a total temperature probe on the lower side of the left hand wing. Data gained from these probes are utilized to compute free stream values of velocity, static pressure, static temperature and density as well as Mach and Reynolds number.

Although the wing of the LFU-205 is slightly swept forward and tapered (quarter chord sweep $-7°$, taper ratio 0.5) no significant cross-flow develops, so the boundary layer may be considered two-dimensional. Therefore, the instabilities found are essentially Tollmien-Schlichting waves. Their propagation in the laminar boundary layer was measured with the 69 element hot-film array shown in Fig. 3.

Sensor elements on the array are arranged mainly in two spanwise rows on constant chord positions of $x/c = 0.34$ and $x/c = 0.37$. Each row consists of 25 sensors being 4 mm apart in spanwise direction. Both rows are connected by a chordwise column of 7 sensors on the center line of the array. Additional sensors are short coupled (2.5 mm distance in chordwise direction) to the elements of both main rows.

The hot-films were operated in the constant temperature (CTA) mode, with the temperature being held at $T = 150$ °C. The fluctuating parts of the sensor signals were sampled simultaneously for one second at a rate of 48 kHz.

From the experimental data basis gained in the 2001 flight-test campaign, measuring point no. 18 taken during test-flight 8 was selected for the purpose of the present work, i.e. the disturbance flow field reconstruction. Figure 4 shows the respective glove pressure distribution $C_P(x/c)$, the free-stream values of velocity U_∞, static pressure p_∞ and static temperature T_∞ as well as an infrared image of the glove region.

As can be seen in the infrared image, the onset of turbulence occurs at a chord position of about $x/c = 0.45$, i.e. well down-stream of the hot-film array. A linear stability analysis of boundary layer velocity profiles (calculated on basis of the measured pressure distribution) showed that the point of neutral stability is located at $x/c = 0.105$. Therefore, in this case the instability growth takes place in the presence of a slightly adverse pressure gradient.

As an example for the measurement of the wall shear fluctuations, in Fig. 5a 10 ms long cut out from the 1 s long time histories τ'_w of eleven sensor elements located around the center line y = 0 mm of the hot-film array at a chord position of $x/c = 0.37$ is presented.

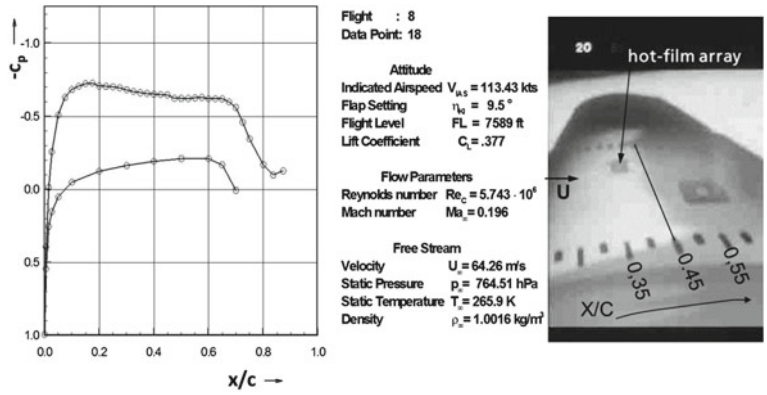

Fig. 4 Pressure distribution, free-stream quantities and infrared image of measuring point 8/18

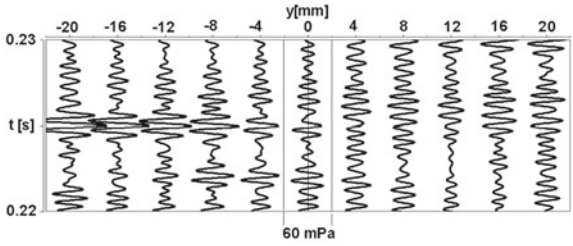

Fig. 5 Time histories $\tau_w'(x, y, t)$ of sensors on spanwise row at $x/c = 0.37$

3 Reconstruction of the Disturbance Flow Field

As indicated by Eqs. (1) and (2), a strong relationship exists between wall shear stress fluctuations that are provoked by Tollmien-Schlichting waves in experiment and their theoretical eigenfunction that can easily be determined by local linear stability analysis. Subsequently it will be shown, how this relationship can be utilized to reconstruct the disturbance flow field above a spanwise row of hot-film sensors from the wall measurements. The procedure consists essentially of four steps and will be exemplarily conducted for the sensor row at $x/c = 0.37$ on basis of the data presented in the previous paragraph.

In the first step of the reconstruction all Tollmien-Schlichting waves that are involved in the skin friction fluctuations have to be identified. This is accomplished by a discrete Fourier decomposition in time and space of records $\tau_w'(x = const, y, t)$ from an equally spaced spanwise row of n_s sensors sampled at m discrete time steps. This yields the amplitude $\hat{\tau}_w$ as a function of k-th disturbance frequency $f = 2\pi\omega_r$ and q-th spanwise wave number

$$\hat{\tau}_w(f_k, \beta_q) = |\hat{C}_{k,q}|, \tag{3}$$

Here, the $\hat{C}_{k,q}$ are the complex Fourier coefficients according to

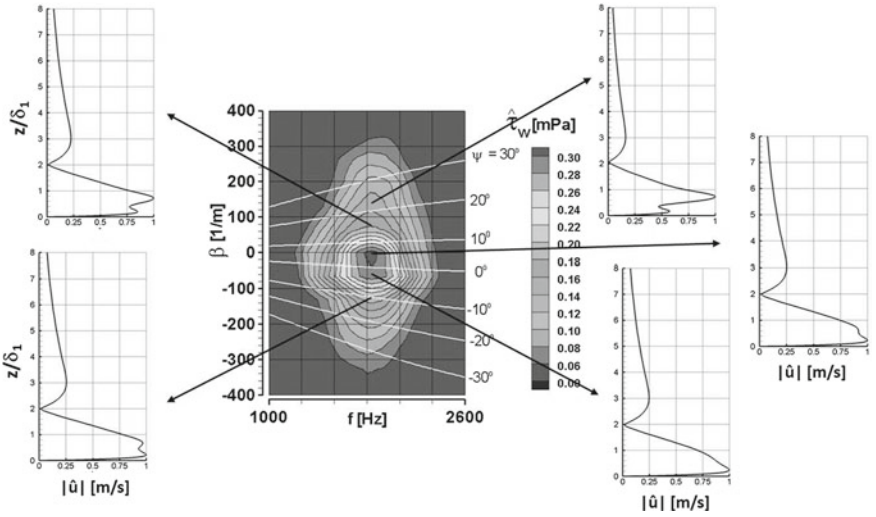

Fig. 6 Frequency-spanwise-wavenumber spectrum of time histories $\tau'_w(x/c) = 0.37, y, t$ and absolute values of eigenfunctions $\hat{u}(Z)$ for selected Tollmien-Schlichting modes

$$\hat{C}_{k,q} = \frac{2}{m(n_s - 1)} \sum_{j=0}^{m-1} \sum_{p=\frac{n_s-1}{2}}^{+\frac{n_s-1}{2}} \tau'_w(j, p) \cdot e^{i(-2\pi f_k - \beta_q y)}. \tag{4}$$

Additionally, with $\Delta\varphi(f_k, \beta_q) = \tan^{-1}(Im(\hat{C}_{k,q})/Re(\hat{C}_{k,q}))$ the relative phase shift between individual modes is obtained. It should be noted that Tollmien-Schlichting waves are well-defined through the specification of two of their parameters like frequency f (or angular frequency ω_r, respectively) and spanwise wave number β. The streamwise wave number α then is a dependent variable which can be determined by the dispersion relation $\omega = \omega(\alpha, \beta)$.

In the second step of the reconstruction the complex eigenfunctions $\hat{u}(z)$, $\hat{v}(z)$, $\hat{w}(z)$ (disturbance velocity components), $\hat{p}(z)$ (pressure), $\hat{T}(z)$ (temperature) and $\hat{\rho}(z)$ (density) of all Tollmien-Schlichting modes identified in the first step are calculated by local linear stability analysis employing the COSAL code (Malik and Orszag [6]). The laminar mean flow at sensor positions ($x/c = 0.37$; $-48\,\text{mm} \leq y \leq 48\,\text{mm}$), which is needed as an input for the stability analysis, is computed on basis of the measured glove pressure distribution $C_P(x/c)$ with a boundary layer method for swept and tapered wings (Kaups and Cebeci [7]).

In Fig. 6 the result of the Fourier decomposition, i.e. the frequency-spanwise-wavenumber amplitude spectrum is shown. Lines of constant angle ψ indicate the propagation direction of Tollmien-Schlichting waves relative to the local edge flow. Furthermore, Fig. 6 depicts the absolute value of five of the $\hat{u}(z)$ eigenfunctions of step two of the reconstruction in order to illustrate their variability (in total 14,400 modes were investigated). However, it is noticeable that the maximum amplitude of all eigenfunctions shown is 1 m/s. This is due to the fact that linear stability analysis solves a

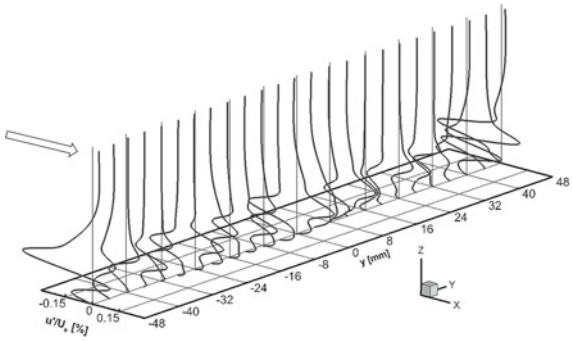

Fig. 7 Reconstructed disturbance velocity $u'(x/c = 0.37, y, z, t)$ at $t = 0.0189$ s

set of homogenous ODE's, meaning that the theoretically determined eigenfunctions are not well-defined, or, in other words, any arbitrarily chosen constant K may be multiplied to eigenfunctions $\hat{u}(z)$, $\hat{v}(z)$, $\hat{w}(z)$, $\hat{p}(z)$, $\hat{T}(z)$, $\hat{p}(z)$ and they will still be a solution of the linearized stability equations for a set of eigenvalues α, β, ω. Therefore, the goal of the third step of the reconstruction is to specify constant K so that the theoretical amplitudes match real world physics, an idea already expressed in 1935 by Schlichting [8], who designated K "Intensitätsfaktor" (intensity or scaling factor). This task is accomplished by employing the relationship between wall shear stress amplitude $\hat{\tau}_w$ and eigenfunction $\hat{u}(z)$ already expressed in Eq. (2):

$$\hat{\tau}_w(f_k, \beta_q) = \mu(d|K(f_k, \beta_q) \cdot \hat{u}(z, f_k, \beta_q)|/dz)|_{z=0}. \tag{5}$$

Equation (6) delivers after rearrangement:

$$K(f_k, \beta_q) = \hat{\tau}_w(f_k, \beta_q)/\mu(d|\hat{u}(z, f_k, \beta_q)|/dz)|_{z=0}. \tag{6}$$

Once intensity factors $K(f_k, \beta_q)$ have been specified, in a fourth step the disturbance flow field is finally reconstructed by superposing the scaled modes in a backward Fourier transform in time and space for all wall distances z, carefully taking into account the phase shift $\Delta\varphi(f_k, \beta_q)$ between individual Tollmien-Schlichting waves.

Figure 7 shows as an example the reconstructed longitudinal velocity disturbance $u'(x/c = 0.37, y, z, t)$ above the downstream row of hot-film sensors at an arbitrarily chosen instant of time. Of course, the question arises if the reconstruction delivers the correct disturbance flow field. An ultimate proof would require to measure in an experiment disturbance velocity u' and provoked wall shear stress fluctuation τ'_w at exactly the same time; however, currently this seems not to be feasible.

Nevertheless, an indirect comparison can be made using the data collected during an in-flight experiment with the LFU-205 by Horstmann and Miley [4]. They used hot-wires which were traversable normal to the wall in order to determine RMS (root mean square) values of disturbance velocity u' at different wall distances. The result for a data point similar (with respect to the stability situation) to the one used for the present work is shown in Fig. 8. A good qualitative agreement can be found

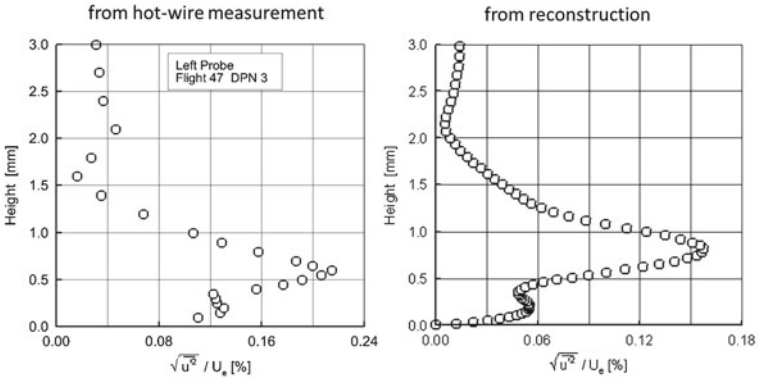

Fig. 8 Comparison of wall normal RMS distributions of longitudinal disturbance velocity u'

between wall normal RMS distributions u' of from hot-wire measurements and reconstruction, indicating that the methodology for reconstruction developed here does make sense.

4 Summary

A methodology based on linear stability analysis was developed that allows for the reconstruction of a disturbance flow field from the measurement of wall shear stress fluctuations provoked by Tollmien-Schlichting waves. The reconstruction delivers the fluctuations of all flow quantities, i.e. disturbance velocity components, pressure, temperature and density. A comparison of the reconstructed longitudinal disturbance velocity component u′ with hot-wire measurements shows good qualitative agreement. It is planned to use the reconstructed quantities of the disturbance flow as initial values for a direct numerical simulation of the transition process on the LFU-205 wing.

References

1. Lee, C.C., Obara, J., Wusk, M.S.: Flight-measured disturbance instabilities in laminar flow. AIAA Paper-90-1283 (1990)
2. Peltzer, I., Nitsche, W.: In-flight and wind tunnel measurements of natural and of controlled instabilities on a laminar flow airfoil. In: IUTAM Symposium on Laminar-Turbulent Transition. Fluid Mechanics and Its Applications, Vol. 79, 261–266. Springer, Netherland (2006)
3. Seitz, A: Freiflug-Experimente zum Übergang laminar-turbulent in einer Tragflügelgrenzschicht. DLR-Forschungsbericht FB-2007-01, Braunschweig (2007)
4. Horstmann, K.-H., Miley, S.J.: Data report on flight and wind-tunnel investigations of Tollmien-Schlichting waves on an aircraft wing. DLR IB-129-91/18 (1991)

5. Horstmann, K.-H., Quast, A., Redeker, G.: Flight and wind-tunnel investigations on boundary layer transition at Reynolds numbers up to 10^7. ICAS Proc. **2**, 979–986 (1988)
6. Malik, M.R., Orszag, S.A.: Efficient computation of the stability of three-dimensional compressible boundary layers. AIAA-Paper 81–1277, (1981)
7. Kaups, K., Cebeci, T.: Compressible laminar boundary layers with suction on swept and tapered wings. J. Aircr. **14**, 661–667 (1977)
8. Schlichting, H.: Amplitudenverteilung und Energiebilanz der kleinen Störungen bei der Plattenströmung. Nachr. d. Ges. d. Wiss. zu Göttingen, Math.-Phys. Klasse **1**, 47–78 (1935)

Flight Measurements Under Turbulent Atmospheric Conditions

Andreas Reeh, Michael Weismüller and Cameron Tropea

Abstract A complete investigation of the influence of atmospheric turbulence on airfoils requires in-flight experiments and in the present report the integration of a comprehensive measurement system into a motorized glider is described. The system allows for simultaneous measurements of the onflow quantities and the aerodynamic response of a wing section, emphasizing the investigation of the laminar-turbulent transition of the wing boundary layer. Characteristic experimental results are presented which underline the need for in-flight testing.

1 Introduction

Turbulence has an important influence on atmospheric flow processes. It is produced by shear layers generated through processes like wind shear at inversion layers, thermal convection and orographic interference [1]. The latter two processes are typically found in the lowest layer of the troposphere, the atmospheric boundary layer which usually reaches altitudes between 1 and 2 km. The effects on aircraft flying through turbulent air are unsteady variations of the onflow conditions. The nature of atmospheric turbulence implies turbulence production at large length scales in the order of several hundred meters [2]. Large eddies become unstable and transfer their energy into multiple smaller eddies which continue to decay in an energy cascade (see Batchelor [3]). The process continues until viscosity becomes important at small length scales, where the kinetic energy is eventually dissipated. Therefore, aircraft flying through turbulence experience onflow disturbances caused by the random appearance of turbulent eddies of different scales and intensities [4, 5]. Length scales in the order of several chord lengths as well as length scales in

A. Reeh (✉) · M. Weismüller · C. Tropea
Fachgebiet Strömungslehre und Aerodynamik, Technische Universität Darmstadt, Flughafenstr. 19, 64347 Griesheim, Germany
e-mail: a.reeh@sla.tu-darmstadt.de

A. Dillmann et al. (eds.), *New Results in Numerical and Experimental Fluid Mechanics IX*, Notes on Numerical Fluid Mechanics and Multidisciplinary Design 124,
DOI: 10.1007/978-3-319-03158-3_22,

order of the wing boundary-layer thickness may affect loads and the aerodynamic performance [6]. Flight through turbulent air poses a complex problem which cannot be thoroughly simulated in wind-tunnel experiments or numerical computations. Only in-flight experiments offer simultaneous access to all relevant effects and their interactions. While previous in-flight studies focussed on the characterization of the onflow turbulence [2, 4, 5] or the investigation of airfoil flow under calm conditions [7–9], experiments taking account of all relevant aerodynamic quantities in flight through turbulent air have only begun [6] and these are described in the present work.

2 Experimental Setup

The platform for the flight experiments is a Grob G109b motorized glider. Due to its clean aerodynamic shape and its excess in engine power, the turbocharged G109b offers adequate climbing and gliding performance for practical flight-testing procedures. Several characteristics make this motorized glider an almost ideal platform for in-flight experiments at low Mach numbers. By using the aircraft as a glider during the measurements acoustic noise, structural vibrations and electromagnetic disturbances from the engine are completely avoided and thus cannot interfere with the receptivity and the transition process of the boundary layer or the measurement equipment. Furthermore, the wing planform has a high aspect ratio of 15.9 and negligible forward sweep with slight dihedral making it ideal for two-dimensional airfoil flow investigations. In addition, the layout of the wing is a simple trapezoid formed by a single laminar airfoil (Eppler E580). The only movable parts are the ailerons and the air brakes on the upper side of the wing. Between these flight control elements there is considerable space for instrumentation. All these features tremendously facilitate the construction of a wing glove mantling the original wing in the spanwise section between the air brake and the aileron (Fig. 1 and 2).

The laminar wing glove is the primary test section for the in-flight experiments. It was designed and built by Weismüller [6] to meet some very specific goals. First of all, it must house the measurement equipment without affecting the structure of the wing for certification compliance. The resulting higher weight and the increased thickness of the wing glove need to be compensated for in order to maintain the original flight handling qualities within the targeted flight envelope. Therefore, the lift and drag coefficients of the wing-glove airfoil have been optimized to countervail the asymmetric wing configuration. Besides this basic flight-mechanic requirement, a well-defined pressure distribution on the wing glove is essential for the boundary-layer transition investigations. A specific airfoil geometry was designed in an iterative process using the inverse methods of the airfoil design program Xfoil [10] and the vortex lattice tool AVL to test the aircraft configuration. The result is the MW-166-39-44-43 laminar airfoil. Its most important design parameters can be found in Table 1. The airfoil offers long laminar runs on the upper and the lower side avoiding sharp increases of the pressure gradient. Only on the lower side for the last 20 % of the

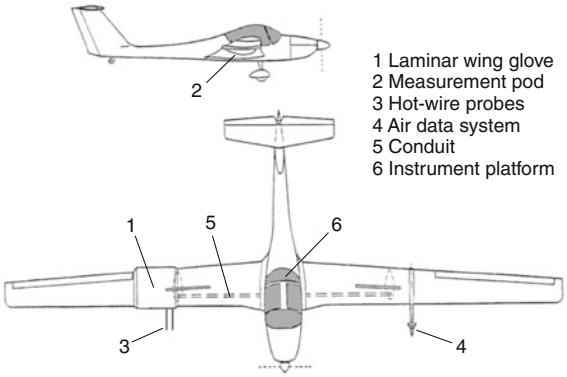

Fig. 1 The G109b research aircraft

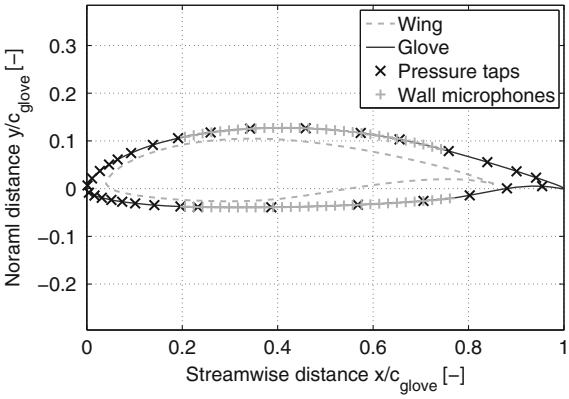

Fig. 2 Sensor allocation on the airfoil

Table 1 Airfoil geometry parameters normalized by the chord length

	Thickness	Camber	Leading edge radius	Chord length
Wing (E580)	0.161 ($x/c = 0.36$)	0.041 ($x/c = 0.61$)	0.010	1.09 m (mean)
Glove (MW)	0.166 ($x/c = 0.39$)	0.044 ($x/c = 0.43$)	0.013	1.35 m

chord ($c = 1.35\,\text{m}$), a sharp increase is necessary to match the boundary condition at the trailing edge. While natural transition on the upper side is encountered for the entire flight envelope ($-3° \leq \alpha \leq 8°$, $2 \cdot 10^6 \leq \text{Re} \leq 4 \cdot 10^6$), on the lower side the boundary layer stabilizes for positive angles of attack, suppressing natural transition. In order to avoid a laminar separation bubble on the lower side, the boundary layer is tripped with a zig-zag tape turbulator at $x/c = 0.77$. In the region before the trip strip, pressure increases or decreases can be obtained by varying the angle of attack in gliding flight. In Fig. 4 the pressure distribution for a negative angle of attack is presented and a positive pressure gradient in the region $0.1 \leq x/c \leq 0.8$ can be

observed. The pressure gradient directly affects the amplification rates of instabilities inside the boundary layer.

The wing glove has a rectangular planform with a width of 1.5 m. It was built in milled molds using carbon and fiberglass composites. In order to store sensors, amplifiers and A/D-converters, a storage pod on the lower side of the wing glove was inevitable. Furthermore, two booms pointing into the free stream are necessary to capture the onflow quantities 0.9 m in front of the leading edge. Nonetheless, an important criterion for the wing glove was the two-dimensionality of the flow at the centerline, where the transition measurements are taken. Nearly two-dimensional boundary-layer flow is highly desirable to facilitate comparisons with theoretical predictions and enable simpler numerical simulations. The whole modified wing configuration, including the described measurement installations, were simulated with the CFD-software ANSYS CFX. The results of the simulations confirmed a nearly undisturbed flow at the centerline for the flying conditions under consideration. The cross-flow velocity at the edge of the boundary layer in the relevant region for the transition investigations is below 2 % of the free-stream velocity and can thus be neglected. The design and construction of the wing glove as well as the verification of the flow quality is covered in detail in the work of Weismüller [6].

The measurement system comprises various probes and sensors, among which only the relevant ones for the investigations discussed in Sect. 3 will be described here. By far, the most striking modification of the research aircraft is the laminar wing glove on the starboard wing. It includes boom-mounted hotwire probes to characterize the onflow, miniature pressure sensors to obtain the pressure distribution and wall microphones to investigate the transition process.

Two X-wire probes are used to obtain information on all three velocity components and both angles, the angle of attack and the side slip angle. The hotwires are operated by Dantec 54T30 miniature constant temperature anemometers. Prior to a flight experiment a calibration wind-tunnel is positioned directly in front of the probe booms and the X-wires are calibrated with the effective angle method from Bradshaw [11]. It proved to be very convenient and accurate [12] for incidence angles below 10°. A difficulty was encountered with the compensation of the temperature differences between flight and calibration on the ground. Several analytical compensation formulas were tested but none of them yielded completely satisfying results, producing velocity differences of up to 8 % compared with pitot-static measurements. It was thus decided to use a linear correction formula [13]. In order to preserve precision, hotwire results in Sect. 3 are given as deviations from the mean quantities, which are correctly obtained with the reference system described below.

For the measurement of the instantaneous pressure distribution, 32 Sensortechnics HCL-12X5P pressure transducers are distributed on the wing section and custom signal conditioners are used. The piezoelectric working principle and the short tube lengths of less than 0.1 m between the measurement taps and the sensors guarantee a fast response to pressure changes. Besides the static calibration, a dynamic calibration was carried out to further improve the temporal resolution and to adjust the sensor responses up to frequencies of 100 Hz. A calibration device generating calibrated sinusoidal pressure signals was connected to every pressure tap and dif-

ferent frequencies with fixed amplitudes were applied. A forward-backward Fourier transform procedure is carried out to correct the frequency response of each sensors. Although the pressure transducers are used for detecting unsteady load variations ($f < 50\,\text{Hz}$), their frequency response is not suited for the investigation of high frequency boundary-layer instabilities ($f > 500\,\text{Hz}$).

Transition detection and investigation is accomplished through streamwise rows of PMO-4015 back-electret wall microphones on the lower as well as on the upper side of the wing glove. Each row consists of 32 microphone capsules with a diameter of 4 mm. The microphones are operated and the signals amplified by custom electronic units. The microphones are installed directly beneath the surface minimizing the dead volume and they are connected to the flow by openings with a diameter of 0.2 mm. The individual sensor responses are matched through an in-situ array calibration using a reference microphone and an acoustic white-noise source positioned at a distance of 4 m from the array in the most sound-absorbing laboratory available. Calibration formulas according to Mish [14] are applied. Due to some malfunctioning microphones on the upper side, only the results for the micropohone row on the lower side could be obtained with a meaningful spatial resolution. For state-of-the-art sailplane airfoils, transition on the lower side is particularly sensitive to angle of attack changes possibly deteriorating performance in high-speed flight through turbulent conditions.

On the port-side wing a flight log is installed on a rugged boom pointing into the free stream. It serves as an accurate measurement reference for the quantities static pressure, dynamic pressure, temperature and relative humidity. The tip of the boom is a wind vane with two degrees of freedom. The actual position of the vane is detected with potentiometers. Although the wind vane has a certain inertia and is not suited for high frequency measurements, it provides a robust and reliable sensor for the angle of attack and the side slip angle.

In flight testing the adjustment of constant and reproducible experimental conditions presents a challenge due to pilot inaccuracies, meteorological changes and the inevitable effects of turbulence. In order to guarantee reproducible conditions, specific care must be taken when choosing the experimental flight strategies. For typical investigations the pilot tries to adjust predefined angles of attack in gliding flight and to keep them constant during the data acquisition. The Reynolds number based on the chord length varies according to the ambient conditions. However, the pilot needs to react to sudden disturbances of the angular momentum balance, especially when flying through turbulent air. An elaborate experimental flight control strategy was developed and translated into a simple pilot display for accurate and comfortable flight testing. The software filters (low-pass) the angle information of the flight log in real time enabling the pilot to correct long-wave deviations of the desired angle of attack and the desired side slip angle. This procedure is appropriate since the pilot is not able to correct the high-frequency angle of attack fluctuations occurring even in flight through moderately turbulent conditions. Depending on the targeted angle

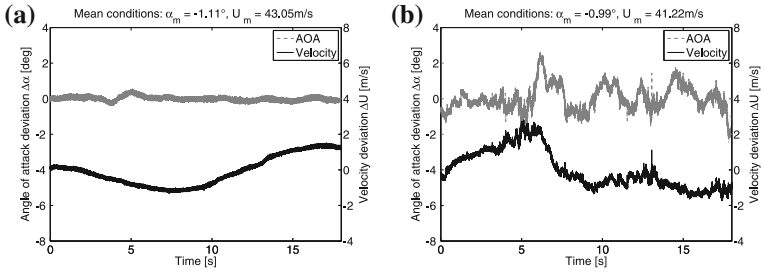

Fig. 3 Different onflow conditions. **a** Calm air. **b** Moderately turbulent air

of attack, the stability characteristics of the boundary layer can be controlled. Low angles of attack cause an adverse pressure gradient on the lower side of the wing glove promoting natural transition.

3 Experimental Results

In the following the effects for exemplary flight through calm and moderately turbulent air are compared. The mean angle of attack and the mean Reynolds number are very similar in both cases, as can be seen in the titles of Fig. 4(a) and (b). Figure 3 shows the deviations from the mean of the angle of attack and the mean velocity magnitude for typical measurement intervals. Under calm air conditions the pilot is able to keep the angle of attack almost constant with deviations smaller than 0.2°. The velocity deviates more than 1m/s in a long waveform due to the phugoid motion of the aircraft. The behavior for turbulent air conditions is completely different. In addition to the increased small-scale disturbance level, larger deflections appear irregularly in the time traces. The random fluctuations with amplitudes of up to 2.5° in the angle of attack and 2.5 m/s in the velocity magnitude do not appear to be closely correlated. Turbulent conditions with much larger fluctuations have often been detected, but are omitted for the investigation of the prevalent moderately turbulent conditions. A decomposition of the velocity deviation into chordwise and normal components is not shown here. Nevertheless, the normal velocity fluctuations translate into the shown angle of attack variations which have preeminent effect on laminar-turbulent transition on the lower side of the wing glove. They lead to a modification of the pressure gradient which in turn determines the boundary-layer stability.

The measured mean pressure distribution is compared to the results of the two-dimensional, steady airfoil analysis program Xfoil in Fig. 4. Good agreement between measurements and theory can be observed in both cases. In order to illustrate the effects of the unsteady onflow conditions, error bars depict the maximum deviations of the pressure coefficient C_p at the measurement stations. While in calm air there are only slight deviations from the mean pressure distribution, considerable fluctu-

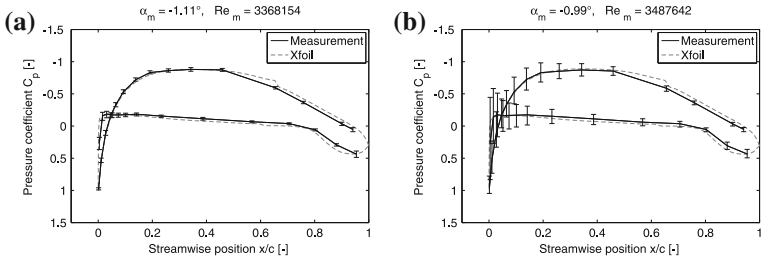

Fig. 4 Comparison of the pressure distributions for different turbulence conditions. **a** Calm air. **b** Moderately turbulent air

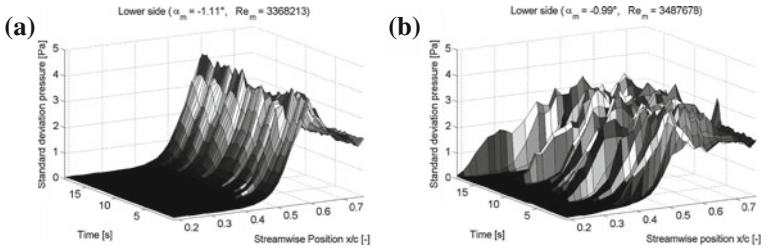

Fig. 5 Time evolution of transition on the lower side of the wing glove. **a** Calm air. **b** Moderately turbulent air

ations are present in moderately turbulent air, especially in the leading edge region. The instantaneous pressure distributions no longer correspond to steady theory. The integral of the product of the pressure and the surface normal vector along the airfoil surface yields the acting pressure force vector per width which correlate to the temporal changes in the angle of attack. Reeh et al. [15] show that the magnitude of the resulting lift coefficient can only be explained by unsteady airfoil theory in the moderately turbulent case. The resulting variations of the pressure gradient may also affect the development of the boundary layer and the transition process.

Natural transition is initiated by boundary-layer instabilities which are excited by the onflow disturbances in a particular flight environment. Initially too small to be measured, the instabilities amplify according to the stability properties of the boundary layer depending strongly on the pressure gradient. Before the breakdown to the fully turbulent boundary layer the fluctuation energy of all flow quantities continuously rises until reaching a peak in the narrow transition region. Within this region intermittency increases rapidly as the disturbances lose their deterministic behavior. The fluctuation magnitude of all flow quantities eventually drops to an intermediate level in the turbulent part of the boundary layer. The standard deviation of the microphone signals, i.e. the root mean square (rms) of the pressure fluctuations directly at the wall, is a very convenient quantity for the characterization of the transition process. In Fig. 5 the time evolution of transition measured with the wall microphones on the lower side of the wing glove is presented in terms of pressure

rms-values. The plots were created by dividing the microphone time traces into overlapping intervals and determining the standard deviation for each interval. A time interval of 0.5 s and 50 % overlap proved to be a convenient choice for an accurate representation. In the calm air case disturbance amplification starts smoothly at a temporally constant streamwise position. For the moderately turbulent case massive displacements of the amplification region are observed, which are induced by the angle of attack deviations illustrated in Fig. 3.

4 Conclusions and Outlook

The elaborate experimental setup enables simultaneous measurements of the onflow characteristics and the aerodynamic effects of atmospheric turbulence on a laminar wing section. In flight through calm air the airfoil flow behaves according to the predictions from two-dimensional, steady theory. Flight through turbulent air leads to random, unsteady variations of the onflow quantities, especially for the angle of attack. The airfoil pressure distribution evolves unsteadily, leading to deviations in the lift curve compared to steady theory. The development of the boundary layer is affected by the unsteady pressure distribution. Even though the transition location correlates with the angle of attack variations, differences in the boundary-layer development are expected due to the unsteady airfoil behavior. Comparisons with numerical boundary-layer investigations and a more comprehensive analysis of the experimental results are given by Reeh et al. [15].

References

1. Wyngaard, J.C.: Atmospheric turbulence. Ann. Rev. Fluid Mech. **24**, 205–233 (1992)
2. MacCready, P.B.J.: The inertial subrange of atmospheric turbulence. J. Geophys. Res. **67**, 1051–1059 (1962)
3. Batchelor, G.K.: The application of the similarity theory of turbulence to atmospheric diffusion. Quart. J. Roy. Meteorol. Soc. **76**, 133–146 (1950)
4. Riedel, H., Sitzmann, S.: In-flight investigation of atmospheric turbulence. Aerosp. Sci. Technol. **5**, 301–319 (1998)
5. Zanin, B.Y.: Transition at natural conditions and comparison with the results of wind tunnel studies. In: Laminar-Turbulent Transition, pp. 541–546. Springer, Berlin (1984)
6. Weismüller, M.: A new approach to aerodynamic performance of aircraft under turbulent atmospheric conditions. Ph.D. thesis, TU Darmstadt, http://tuprints.ulb.tu-darmstadt.de/2934/ (2011)
7. Erb, P.: Untersuchung der Grenzschichttransition im Flugversuch. Ph.D. thesis, Technische Universität Darmstadt (2002)
8. Seitz, A., Horstmann, K.H.: In-flight investigation of Tollmien-Schlichting waves. IUTAM Symposium on One Hundred Years of Boundary Layer Research, pp. 115–124 (2006)
9. Peltzer, I.: Comparative in-flight and wind tunnel investigation of the development of natural and controlled disturbances in the laminar boundary layer of an airfoil. Exp. Fluids **44**, 961–972 (2008)

10. Drela, M.: Xfoil: an analysis and design system for low reynolds number airfoils. In: Mueller, T. (ed.) Low Reynolds Number Aerodynamics. Lecture Notes in Engineering, vol. 54, pp. 1–12 (1989)
11. Bradshaw, P.: An Introduction to turbulence and its measurement. Pergamon Press, Oxford (1971)
12. Bruun, H.H., Nabhani, N., Fardad, A.A., Khan, M.A., Hogarth, E.: Calibration and analysis of X hot-wire probe signals. Meas. Scie. Technol. **1**, 782–785 (1990)
13. Abdel-Rahman, A., Tropea, C., Slawson, P., Strong, A.: On temperature compensation in hot-wire anemometry. Meas. Sci. Technol. **20**, 315–319 (1987)
14. Mish, P., Devenport, W.: An experimental investigation of unsteady surface pressure on an airfoil in turbulence. Technical report, NASA (2003)
15. Reeh, A.D., Weismüller, M., Tropea, C.: Free-flight investigation of transition under turbulent conditions on a laminar wing glove. AIAA Paper 2013–994

Part V
Rotorcraft Aerodynamics

Numerical Investigation of the Influence of the Model Installation on Rotor Blade Airfoil Measurements

K. Richter, A. D. Gardner and S. H. Park

Abstract For the assessment of the aerodynamic performance of helicopter rotor blade airfoils, accurate wind tunnel measurements of the undisturbed airfoil flow around the airfoil model are necessary, and accurate wind tunnel tests are challenging. Three-dimensional CFD simulations were performed for the subsonic flow around a rotor blade airfoil model in the adaptive-wall test section of the Transonic Wind Tunnel Göttingen to investigate the influence of different types of model installations. The results revealed that the strength of the side-wall influence depends on the model installation and that a small gap between the wind tunnel model and the side wall changes the flow at the junction of model and side wall significantly.

1 Introduction

The design of helicopter rotor blade airfoils is usually concluded by wind tunnel experiments. Two-dimensional airfoil measurements are conducted for the validation of the numerical design and for the assessment of the aerodynamic performance in the entire application range of the airfoil. Aerodynamic databases are generated to feed industrial flight mechanic tools and flight performance tools. Therefore, an accurate measurement of the undisturbed airfoil flow around the model is necessary.

At the DLR, two-dimensional rotor blade airfoil measurements are typically performed in the Transonic Wind Tunnel Göttingen (DNW-TWG). The 1×1 m adaptive-

K. Richter (✉) · A. D. Gardner
DLR, Bunsenstr. 10, 37073 Göttingen, Germany
e-mail: kai.richter@dlr.de

A. D. Gardner
e-mail: tony.gardner@dlr.de

S. H. Park
Konkuk University,1 Hwayang-dong, Gwangjin-gu, Seoul143-701, Republic of Korea
e-mail: pish@konkuk.ac.kr

A. Dillmann et al. (eds.), *New Results in Numerical and Experimental Fluid Mechanics IX*,
Notes on Numerical Fluid Mechanics and Multidisciplinary Design 124,
DOI: 10.1007/978-3-319-03158-3_23,

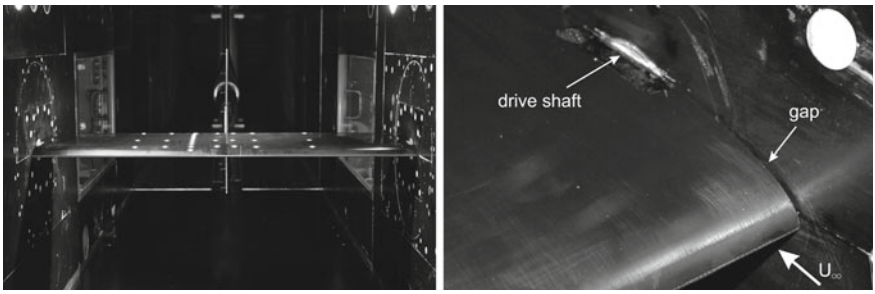

Fig. 1 Rotor blade airfoil model OA209 in the adaptive-wall test section of the DNW-TWG (*left*) and close-up view of the model installation at the wind tunnel side wall (*right*)

wall test section is used to minimize the interference effects of upper and lower walls by the adaptation of the wall shape to the prevailing flow condition. In this test section, two types of airfoil model installations can be used. For static measurements, the model can be flush mounted between the side walls. The model spans the entire test section and has a breadth of exactly $b = 1{,}000$ mm. For pitching airfoil measurements, gaps between the model and the side walls are mandatory to ensure the freedom of movement. For this purpose, models are build with a reduced span of 997 mm to have $s = 1.5$ mm gaps on both sides. Since the size of the gap is small compared to the test section size ($s/b = 0.15\,\%$), the aerodynamic influence of the different installations was in the past considered to be negligible. Figure 1 shows the OA209 rotor blade airfoil model installed in the wind tunnel and a close-up view of the model/side-wall junction.

The OA209 is a well known rotor blade airfoil which is used on helicopter main rotors. At the DLR, a two-dimensional OA209 airfoil model ($b = 997$ mm) exists [1] that was frequently used in wind tunnel measurements. The measurements have normally been of good quality but some results showed an unexpected behavior that could not be explained by simple two-dimensional flow assumptions. In these cases, the measured static lift curve has a lower slope $\mathrm{d}c_l/\mathrm{d}\alpha$ than the numerical results, leading to a difference in the angle of attack between 2D CFD and experiment of up to $\Delta\alpha \approx 2^\circ$ when compared at constant lift, shown in Fig. 2 for $M = 0.31$ and $Re = 1.15 \times 10^6$. Investigations with respect to the influences of the usual experimental and numerical parameters, such as freestream offsets, boundary layer transition, model deformation, computational grid and turbulence models, all showed effects much smaller than those necessary to explain the discrepancy. The three-dimensionality of the flow around the airfoil was investigated and the gap between the model and the side wall was suspected of playing a role in reducing the slope of the lift curve. In order to investigate the influence of the different model installations on the flow around the OA209 airfoil model, two-dimensional CFD simulations of the airfoil and three-dimensional simulations of the model in the DNW-TWG adaptive-wall test section were conducted in the frame of the DLR/Konkuk MoU on Helicopter Aeromechanics, and the results are discussed in this paper.

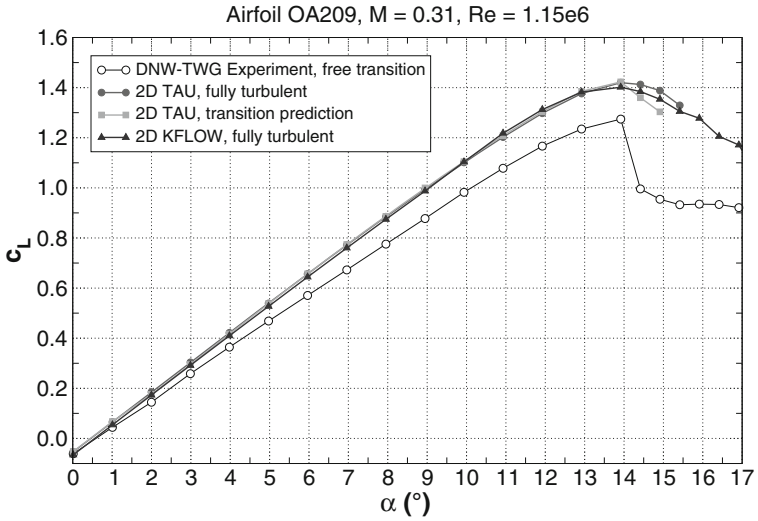

Fig. 2 Measured and two-dimensional numerical lift curves for the OA209 rotor blade airfoil at $Re = 1.15 \times 10^6$ and $M = 0.31$

2 Numerical Setup

Two-dimensional steady RANS simulations were performed with the structured KFLOW code [2] and the unstructured DLR-TAU code [3] on standard structured and hybrid grids, respectively. Three-dimensional RANS simulations were conducted with DLR-TAU on hybrid grids generated with the commercial grid generation software CENTAUR [4]. The 3D grids meshed a symmetric half of the DNW-TWG adaptive-wall test section with curved upper and lower walls using the adapted wall shapes measured in the experiment. The nozzle and the settling chamber were used in addition, as shown in Fig. 3, to obtain a side wall boundary layer profile close to measured values. Both the wind tunnel walls and the model surfaces were treated as viscous walls with 30 prismatic layers on the wind tunnel walls and 40 layers on the model. The height of the first layer was adjusted to $y^+ \approx 1$ and the height of the prism stack was adjusted to the respective boundary layer thickness. The inflow boundary condition was given with the total pressure p_0 and the total density ρ_0 from the experiments, the pressure at the exit plane p_{exit} was adjusted to reach the correct free stream pressure p_∞ in the test section. In the wind tunnel center section a symmetry plane was used.

Grids were generated for three geometric configurations. For the simulation of the realistic OA209 wind tunnel situation, the airfoil was modelled with a half-span of $b/2 = 498.5$ mm, a gap of $s = 1.5$ mm and a part of the drive shaft (40 mm diameter) within the test section. For the simulation of the model installation without a gap, the side wall gap and the drive shaft were removed, and the model was extended to the side wall to have a half-span of exactly $b = 500$ mm. For the simulation

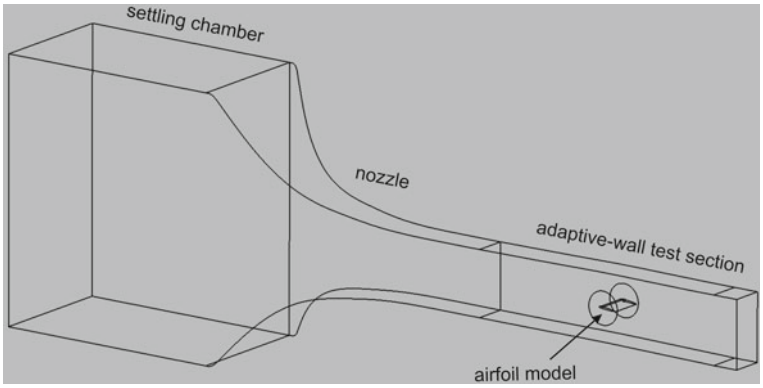

Fig. 3 Numerical setup of the OA209 rotor blade airfoil model in the DNW-TWG adaptive-wall test section used for 3D TAU simulations

of a quasi two-dimensional situation, the wind tunnel configuration without a gap was gridded without prisms on the side wall, which was set as an inviscid wall, in contrast to the viscous treatment for the first and second configuration. A limited grid convergence study was performed by a stepwise refinement of the grid on the model surface and in a volume containing the junction of the model and the side wall, in order to ensure an appropriate grid resolution and to reduce the grid influence on the simulation. As a result, maximum surface and volume cell sizes of $s/c = 0.3\,\%$ were used in the junction area for the detailled investigation of the near-wall flow and for a compensation of the CENTAUR-typical reduction of the height of the prismatic layers in the junction region. Away from the side wall, the airfoil model was resolved with a maximum surface cell size of $s/c = 1\,\%$. In the configuration with the gap, the gap was extremely well resolved with at least 20 grid points over the width of the gap. For the different configurations, the sizes of the grids varied between 6×10^6 (inviscid side wall) and 16×10^6 points (viscid side wall).

Steady simulations were performed for each of the configurations for three angles of attack $\alpha \in [0°, 5°, 10°]$ at $M = 0.31$ and $Re = 1.15 \times 10^6$. Both the 2D and the 3D computations were conducted fully-turbulent and with the Spalart-Allmaras turbulence model [5].

3 Results

The numerical simulations of the different model installations revealed significant differences in the flow near the wind tunnel side wall, causing changes at the model center section.

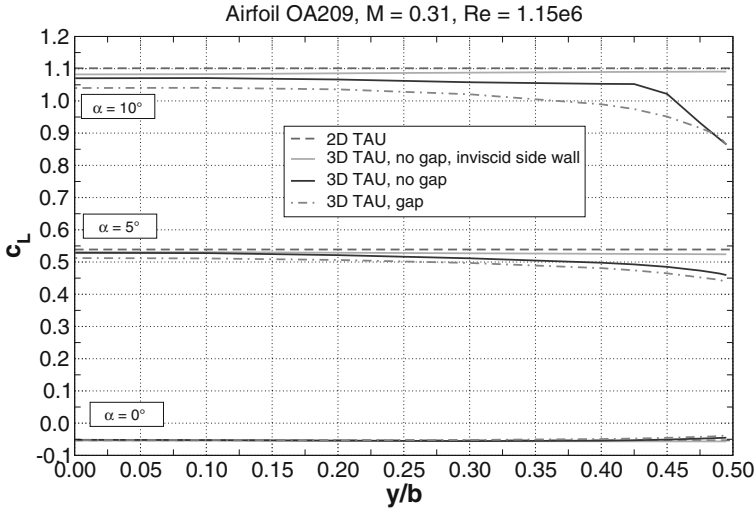

Fig. 4 Spanwise lift distribution on the model extracted from 3D TAU simulations (center section at $y/b = 0$, side wall at $y/b = 0.50$)

3.1 Quasi 2D

The quasi two-dimensional configuration was simulated with the wind tunnel side wall treated as an inviscid wall. Since no side wall boundary layer develops in this case, the side wall influence in the test section is completely removed. The flow through the test section is then similar to a test section of infinite width. The comparison of this 3D flow result with the results from 2D simulations allows the investigation of the influence of the adapted upper and lower wind tunnels walls on the airfoil flow. The results show that the adapted walls only have a very small influence on the flow around the model. The pressure distributions are in good agreement with the 2D results. The spanwise lift distribution of the 3D airfoil model without gap and with inviscid side walls, shown in Fig. 4 for $\alpha \in [0°, 5°, 10°]$, shows slightly lower values than for the 2D lift since the wall adaptation also accounts for the side wall boundary layers which are not present in these 3D simulations.

3.2 Model Installation Without a Gap

The model installation without a gap shows a flow behavior near the side wall which is similar to what is known from other airfoil investigations [6]. Due to the interaction of the boundary layers on the side wall and the wind tunnel model, a corner separation develops on the model upper side. The separation starts at the model trailing edge at small angles of attack and grows both upstream and spanwise with increasing angle

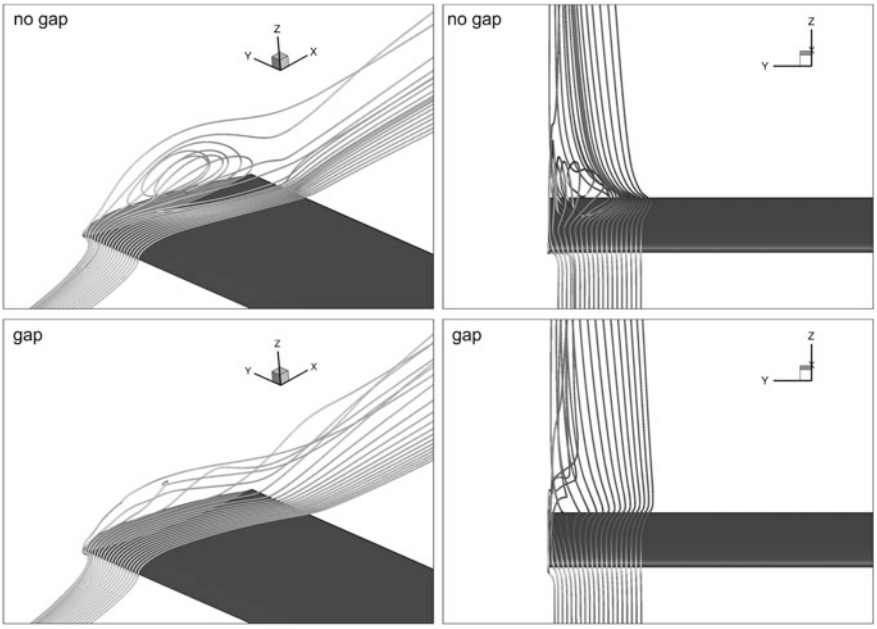

Fig. 5 Streamlines of the near-wall upper surface airfoil flow without a gap (*top row*) and with a gap (*bottom row*) both at $M = 0.31$, $Re = 1.15 \times 10^6$ and $\alpha \approx 10°$

of attack. At high angles, a large recirculation region forms which diverts the upper side model flow to the model center, as indicated by the streamlines of the near-wall flow in Fig. 5 (top row), and the upper side flow is accelerated by the blockage. The spanwise lift distribution in Fig. 4 reveals that the sectional lift significantly reduces near the side wall ($y/b = 0.50$) for the model at $\alpha \in [5°, 10°]$ and that the sectional lift rapidly increases with increasing distance from the wall. For $\alpha = 0°$, neither a corner separation occurs nor a side-wall influence is visible. Spanwise constant flow conditions are reached near the model center at $y/b = 0.0$. For $\alpha \in [5°, 10°]$, a lift reduction in the center section of $\Delta c_L \approx -2.0$ to $-2.5\,\%$ compared to the 2D flow solution remains and indicates that the side wall influence of the model installation without the gap extends to the model center section. Therefore, the slope of the lift curves also reduces slightly as shown in Fig. 6. For a fair comparison with the uncorrected experimental data, the lift integration of the CFD results was performed using only data from the positions of the pressure sensors in the experiment.

3.3 Model Installation with a Gap

The model installation with a gap shows a completely different flow topology near the side wall compared to the installation without a gap. Although the gap is small

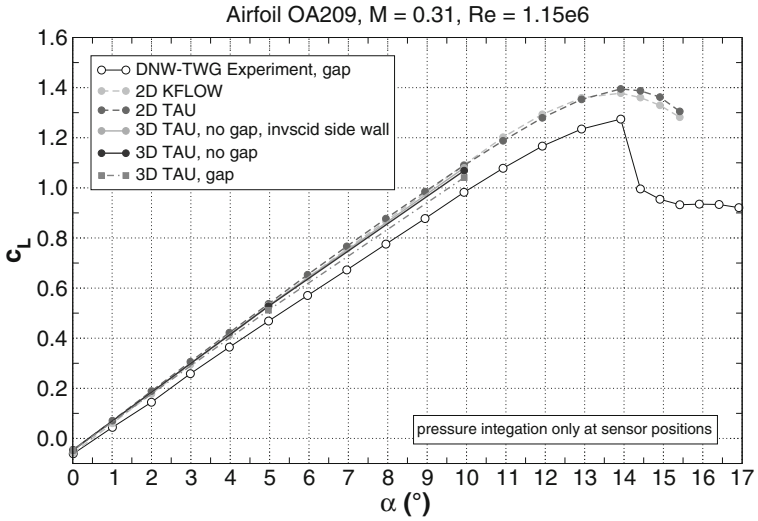

Fig. 6 Experimental and numerical lift curves for the OA209 rotor blade airfoil in the DNW-TWG wind tunnel at $Re = 1.15 \times 10^6$ and $M = 0.31$

compared to the test section size and although it is totally submerged in the wind tunnel side wall boundary layer, the pressure difference between the upper and lower model sides causes a flow through the gap from bottom to top. The flow through the gap forms a jet in the upper side model flow very near the wall, and causes a suction of the flow in the areas in which the corner separation occurred without the gap. This changes the near-wall flow drastically and leads to the absence of a corner separation on the model upper side. Therefore, the upper side flow is much less diverted to the model center. Figure 5 (bottom row) indicates that the flow on the model upper side is much less disturbed than on the model installed without the gap.

The flow through the gap uses only air from the lower side model flow. Figure 7 shows the streamlines of the flow through the gap. The bright streamlines represent the gap flow upstream of the drive shift, and the dark streamlines the flow downstream of the drive shaft. The streamlines are ejected above the model and roll up into two vortices, one vortex for each part of the gap upstream and downstream of the drive shaft. Both vortices have a clockwise sense of rotation, i.e. upwards at the side wall and downwards away from the wall. The upstream vortex originates from the model leading edge, whereas the downstream vortex starts with a short delay downstream of the shaft, at the position where the first streamline reaches the model upper side. As both vortices increase their distance from the side wall with age, the vortex from upstream of the shaft is always located further away from the wall than the vortex downstream of the shaft. In the cases investigated, no merging of the vortices was observed. Figure 7 also shows that, despite the small width of the gap, a significant portion of the spanwise inflow is entrained in the gap. The spanwise extent increases with the model angle of attack and was $y/b \approx 5\,\%$ for $\alpha = 10°$. Due to the mass flow

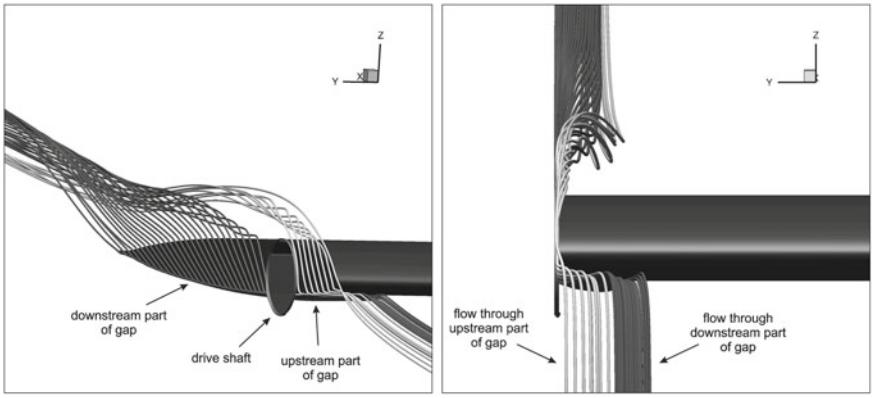

Fig. 7 Streamlines of the flow through the gap between model and side wall at $Re = 1.15 \times 10^6$, $M = 0.31$ and $\alpha \approx 5°$

leaving the lower side model flow, the rest of the lower side flow is decelerated on its way from the leading edge to the trailing edge. For the installation with the gap, the side wall influence, therefore, mainly occurs on the model lower side, whereas it occurs on the upper side for the installation without the gap.

Despite the differences in the near-wall flow topology, the effect of the different model installations on the side wall influence is similar. The spanwise lift distribution in Fig. 4 shows that the lift reduction at the side wall is nearly the same for both configurations. The sectional lift also increases with increasing distance from the wall but the increase is slower than that of the installation without the gap. The side wall influence is stronger for the configuration with the gap and spanwise flow gradients are still present in the model center. The lift reduction in the center increases to $\Delta c_L \approx -5.0$ to -5.5 % compared to the 2D CFD result for $\alpha = 5°$ and $\alpha = 10°$, respectively. This causes a further decrease of the slope of the lift polar as shown in Fig. 6 and a reduction of the difference in lift between CFD and experiment in the order of 50 %. The origin of the remaining differences is still unknown.

4 Conclusions

Three-dimensional CFD simulations were performed for the subsonic flow around a rotor blade airfoil model in the adaptive-wall test section of the Transonic Wind Tunnel Göttingen to investigate the influence of different types of model installations. The results revealed that a small gap between the wind tunnel model and the side wall changes the near-wall flow significantly. A model installation without a gap causes the development of a corner separation. An installation with a gap leads to a siginifcant flow through the gap suppressing the separation. The resulting side wall influence is similar for both configurations but larger for the installation with a gap.

References

1. Geissler, W., Dietz, G., Mai, H., Bosbach, J., Richard, H.: Dynamic stall and its passive control investigations on the OA209 airfoil section. 31st European Rotorcraft Forum, Florence, Italy (2005)
2. Park, S.H., Kwon, J.H.: Implementation of k-ω turbulence models in an implicit multigrid method. AIAA J. **42**(7), 1348–1357 (2004)
3. Gerhold, T., Friedrich, O., Evans, J., Galle, M.: Calculation of complex three-dimensional configurations employing the DLR-TAU-Code. AIAA-97-0167, AIAA 35th Aerospace Sciences Meeting and Exhibit, Reno (NV) (1997)
4. Kallinderis, Y., Khawaja, A., McMorris, H.: Hybrid prismatic/tetrahedral grid generation for complex geometries. AIAA J. **34**(2), 291–298 (1996)
5. Spalart, P.R., Allmaras, S.R.: A one-equation turbulence model for aerodynamic flows. AIAA-92-0439, AIAA 30th Aerospace Sciences Meeting and Exhibit, Reno (NV) (1992)
6. Richter, K., Rosemann, H.: Numerical simulation of wind tunnel wall effects on the transonic flow around an airfoil model. In: Rath, H.-J. et al. (eds.) Notes on Numerical Fluid Mechanics and Multidisciplinary Design: New Results in Numerical and Experimental Fluid Mechanics, vol. VIII, pp. 525–532 (2013)

Flow Simulation of a Five: Bladed Rotor Head

Moritz Grawunder, Roman Reß, Victor Stein, Christian Breitsamter and Nikolaus A. Adams

Abstract This work presents an alternative approach for modeling rotating helicopter rotor heads including the cyclic pitch motion of blade cuffs. In contrast to the standard method employing the chimera overset grid approach, a sliding mesh interface in combination with deforming meshes is employed for this purpose. The results are obtained through numerical simulations based on the incompressible unsteady Reynolds averaged Navier–Stokes equations. The employed approach, including the mesh parameters, is presented in detail in this work. Furthermore, the present results are verified against trends observed in literature for similar cases. Finally, the impact of the cyclic pitch motion on the flow in the wake of an isolated rotating rotor head is analyzed.

1 Introduction

Increasing efficiency and productivity requirements for helicopter necessitate a significant reduction of parasite drag for next generation helicopter [1]. The main rotor head of helicopter contributes considerably to the aerodynamic drag in cruise, accounting for up to 30 % of the total parasite drag [2]. A reduced parasite rotor head drag level decreases the required power to maintain high-speed forward flight, leading to an increase in range, maximum speed and payload. Thus reducing main rotor head drag can improve rotorcraft efficiency and productivity significantly. Therefore, over the last decade, numerous research efforts addressed the expansion of the prediction capabilities of numerical flow simulation for helicopter rotor head [3–10]. The employed numerical methods generally solve the steady or unsteady

M. Grawunder (✉) · R. Reß · V. Stein · C. Breitsamter · N. A. Adams
Lehrstuhl für Aerodynamik und Strömungsmechanik, Technische Universität München,
Boltzmannstr. 15, 85748 Garching bei München, Germany
e-mail: moritz.grawunder@aer.mw.tum.de
website: http://www.aer.mw.tum.de

A. Dillmann et al. (eds.), *New Results in Numerical and Experimental Fluid Mechanics IX*,
Notes on Numerical Fluid Mechanics and Multidisciplinary Design 124,
DOI: 10.1007/978-3-319-03158-3_24,

Reynolds-Averaged-Navier–Stokes (RANS) equations. In some cases, the solved equations are extended to hybrid methods like zonal LES or DES. Consistent for all modeling approaches for rotating rotor heads with or without cyclic pitch motion is the application of Chimera grids. The Chimera technique allows relative motion of stationary and moving domains through interpolation in overlapping grid regions. It is shown that the rotation of the rotor head both for isolated rotor head or rotor head with fuselage configurations does not affect the occurring drag. However, the lift production is changed significantly when taking the rotation or even the cyclic pitch motion of the blade cuffs into account [4, 8]. In this work, a different approach for modeling rotating rotor heads including cyclic pitch motion is adapted with ICEM/ANSYS CFX, extending the work of Vogel et al. [11]. Instead of applying the Chimera overset grid approach, a sliding mesh interface in combination with mesh deformation is employed. The modeling approach is similar to the simulation strategy presented by Steijl and Barakos for rotors with discrete blade geometries [12]. In our work, unstructured grids are employed to resolve a high level of geometric details on the rotor head. The obtained results for an isolated rotor head are discussed with respect to the impact of the cyclic pitch motion on body forces and wake structure.

2 Model Geometry and Configurations

Figure 1 depicts the design of the investigated bearing-less five-bladed rotor head model in detail (scale 1:5). This model features the rotor mast (1), swash plate (2), pitch rods (3), scissors (4), lead/lag dampers (5), blade cuffs (6) and the hub cap (7). The model geometry reproduces the real helicopter geometry for all components except the flexbeam elements and connecting bolts. The flexbeam elements have to be omitted to be able to model the cyclic pitch motion of the blade cuffs. The blade cuffs are truncated at the first aerodynamic section of the blade in the radial direction. In order to analyze the impact of the cyclic pitch motion on the aerodynamic characteristics two cases are investigated. These cases are a rotating isolated rotor head with and without cyclic pitch motion. Equation 1 describes the cyclic pitch motion in terms of the blade pitch angle Θ at variable blade azimuth angles Ψ as a function of the collective Θ_0, lateral cyclic Θ_C and the longitudinal cyclic Θ_S pitch.

$$\Theta(\Psi) = \Theta_0 + \Theta_C \cos(\Psi) + \Theta_S \sin(\Psi). \tag{1}$$

For the case without cyclic pitch motion the blade cuffs are fixed at the collective pitch attitude Θ_0. Flapping and lead-lag motions are omitted. The cyclic motion of the swash plate and control rods are neglected as well. Hence the clearance between the control rods and blade cuffs varies with azimuth. An azimuth angle $\Psi = 0°$ corresponds to a blade position where the blade pitch axis of one blade is parallel to the free stream direction and the blade tip is pointing downstream. Trim conditions are derived from the real helicopter in forward flight.

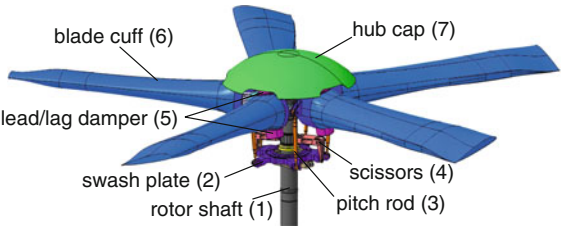

Fig. 1 Five-bladed rotor head model

Fig. 2 Mesh parameter

Paramter	Inner Domain	Outer Domain
number of surface elements	577,542	-
first prism layer height	0.001 mm	-
number of prism layers	22	-
prism expansion ratio	1.28	-
total prism layer height	0.8120 mm	-
number of prism elements	11,153,868	-
number of tetra elements	7,537,224	2,390,427
max tetra size	0.018 D	1.36 D
total number of elements	19,286,282	2,390,427
total number of nodes	6,978,638	403,090

3 Mesh Topology and Numerical Setup

In order to model the rotating rotor head, the computational domain splits up into an inner and an outer part. The inner domain includes the rotor head, whereas the outer domain covers the far field, see Fig. 3. For the actual meshing of the investigated configurations, performed with ANSYS ICEM CFD, unstructured meshes are employed, see Fig. 4. Recent publications show that an unstructured approach is appropriate for this type of simulation [10]. The meshing of the rotor head is performed for the blade stubs in their collective position. This provides two advantages. First the solution with and without cyclic pitch motion are computed on the same mesh. Second the required mesh displacement for the cyclic case is confined to a minimum. To obtain the initial cyclic pitch for each blade the mesh is 'pretensioned'. This is performed by rotating the blade cuffs to their initial position in a pre-run. The meshing itself is performed in two steps. In a first step the surface mesh is calculated applying the octree algorithm. Then the prism layers and the tetrahedral volume mesh is obtained with the Delaunay algorithm. To resolve the rotor head wake more precisely, the volume mesh is refined in a region extending up to two rotor head diameters D downstream. Details about the mesh characteristics are presented in Fig. 2. The resulting dimensionless wall function y^+ is always below 1. To simulate the rotation of the rotor head a sliding mesh interface between the inner and outer domain is applied. The cyclic pitch motion of the blade cuffs is modeled by updating the associated surface mesh geometry in accordance to the blade cuff kinematics. The volume mesh is updated by applying quasi-steady non linear diffusion equations. The mesh quality is found to be maintained best during the simu-

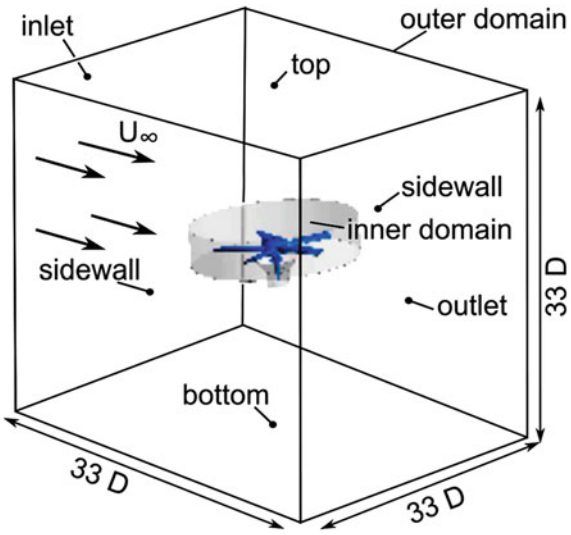

Fig. 3 Computational domain

lation, if the diffusion coefficient is set proportional to the inverse of the cell volume. In accordance to the wind tunnel experiments, the free stream velocity at the domain inlet is 40 m/s. This corresponds to a Reynolds number of $Re/D = 2.59 * 10^6$. The rotational speed of the scaled rotor head is set such that the advance ratio is equal to the parameter of the real helicopter, resulting in an angular velocity ω of $100.8\frac{1}{s}$. The computation, performed with ANSYS CFX, is conducted by solving the incompressible unsteady Reynolds averaged Navier–Stokes equations. Choosing the incompressible equation is justified, since the maximum Mach number at the tip of the blade cuff M_{tip} is $= 0.2$. The discretization in space and time is realized by employing the high resolution scheme and the implicit second order backward Euler method, respectively. The applied turbulence model is the Menter SST model. During the first four revolutions the time step corresponds to an azimuthal step of $\Delta\Psi = 3.21°$. Afterwards, the increment in azimuth angle is reduced to $\Delta\Psi = 1.07°$ for two further revolutions. Only the results of the final revolution are included in our analysis. The validity of the chosen mesh characteristics and the numerical setup could be demonstrated in earlier publications. In [1] the authors show that the setup is sufficient to resolve the flow about a helicopter configuration with a truncated tailboom and rotating rotor head for the case without cyclic pitch. The results agree to within 5 and 6 % with the experimental drag and lift characteristics, respectively. The missing fuselage in the present analysis is a known limitation to the validity for the authors. This abstraction of the problem is accepted to reduce the computational effort for the presented proof of concept.

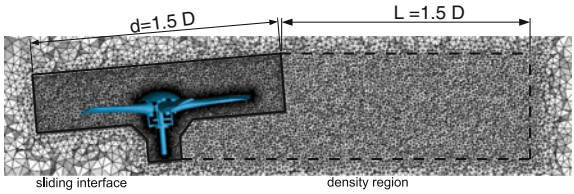

Fig. 4 Mesh topology at the center of the domain

4 Analysis and Discussion

First the azimuthal drag coefficient characteristics of the rotating isolated rotor head with and without cyclic pitch are discussed, see Fig. 5 (left). The time dependend drag coefficient features a five per revolution characteristic period with a phase shift of 72°. This meets the expectation that the dominant characteristics depend on the rotor angular velocity and the number of blades. Furthermore, the independence of the average drag over one rotor revolution $\bar{C}_D$ of the cyclic pitch input, found in literature for similar configurations, is confirmed [4, 8]. The relative difference between the two cases in $\bar{C}_D$ is below 2 %. Figure 5 (right) depicts the resulting drag decomposition per component. Only one chart for both cases is presented since no differences in the drag components is observed. The biggest contributor to the drag of the isolated rotor head are the blade cuffs with 52 %. Another 42 % of the total rotor head drag are equally distributed on the hub cap, rotor shaft and the control parts (swash plate, scissors and control rods). These results are also in good agreement with what was observed in other studies [11]. Figure 6 (left) depicts the azimuthal lift coefficient characteristics for both the case with and without cyclic pitch. The time dependent lift coefficient features the same five per revolution characteristic. One notable difference between the two cases with and without cyclic pitch motion is the level of produced lift. If the cyclic pitch motion is included the lift produced at the rotor head drops by a factor of 4. Figure 6 (right) shows that this difference in lift is associated to a reduction of produced lift at the blade cuffs. The averaged lift produced over one rotor head cycle at the blade cuffs is reduced by an order of magnitude by applying cyclic pitch input. Furthermore, the cyclic pitch motion reduces the once per revolution lift fluctuation by approximately 12 %. Both effects are associated to the trim of the rotor blade cuffs according to the azimuthal position. Similar to the entire rotor blades this trim leads to significantly reduced lift production on the advancing side and a slightly increased lift on the retreating side. Thus the lift is reduced and in better balance over one rotor cycle.

Figures 7 and 8 depict the structures in the wake of the rotating isolated rotor head at three different azimuth positions with and without cyclic pitch, respectively. The structures in the wake are visualized through iso-surfaces of the Q-Critrerion colored with the dimensionless streamwise vorticity. Furthermore, for each azimuth position, dimensionless streamwise vorticity contours are depicted in a cut-plane one rotor head diameter downstream of the rotor head.

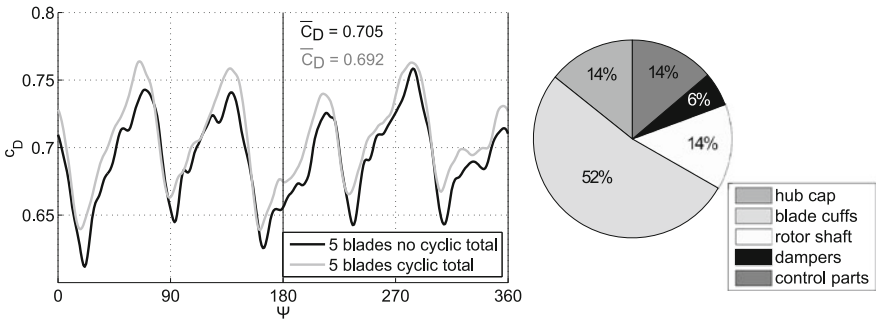

Fig. 5 Azimuthal drag characteristics of the isolated rotor head with and without cyclic pitch input (*left*) and corresponding rotor head drag breakdown (*right)*

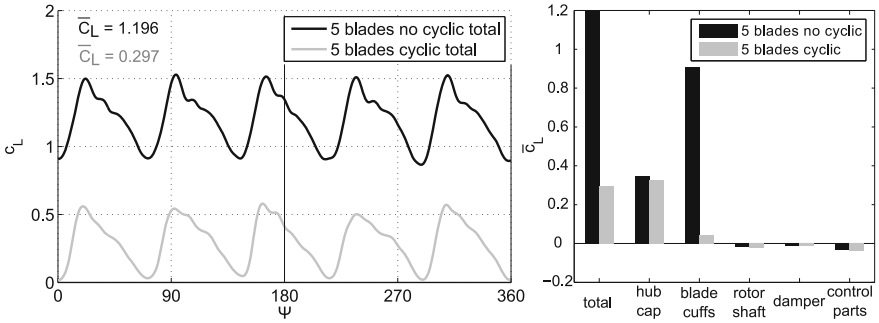

Fig. 6 Azimuthal lift characteristics of the isolated rotor head with and without cyclic pitch input (*left*) and corresponding rotor head lift breakdown (*right*)

For both cases with and without cyclic pitch, the dominant structures in the wake are associated to lift producing rotor head components, i.e. the blade cuffs and the hub cap. In effect of the lift producing hub cap, a counter rotating vortex pair is shed into the wake called left and right hub cap vortex (LHCV/RHCV). Furthermore, the blade cuffs generate tip vortices (BCTV). The BCTV's are numbered according to the associated blade. The blade pointing downstream at azimuth position $\Psi = 0°$ is assigned blade number 1. The remaining blades are serially numbered in the anti-clockwise direction. In the case without cyclic pitch input the BCTV generated at the advancing blade cuffs is considerably stronger than on the retreating side. This uneven vorticity distribution is even amplified in the wake through super-positioning of different BCTV's, e.g. BCTV-2 and BCTV-3 at $\Psi = 50°$. As expected, based on the discussion of azimuthal lift coefficient characteristics, this asymmetry is reduced for the case including the cyclic pitch motion. It is a known limitation to the authors that the BCTV's would not occur on a rotor with complete rotor blades.

The main difference for the case with and without cyclic pitch is the structure of the wake on the advancing blade side. Without cyclic pitch motion the advancing blades angle of attack is too large to maintain attached flow at the blade cuffs. The

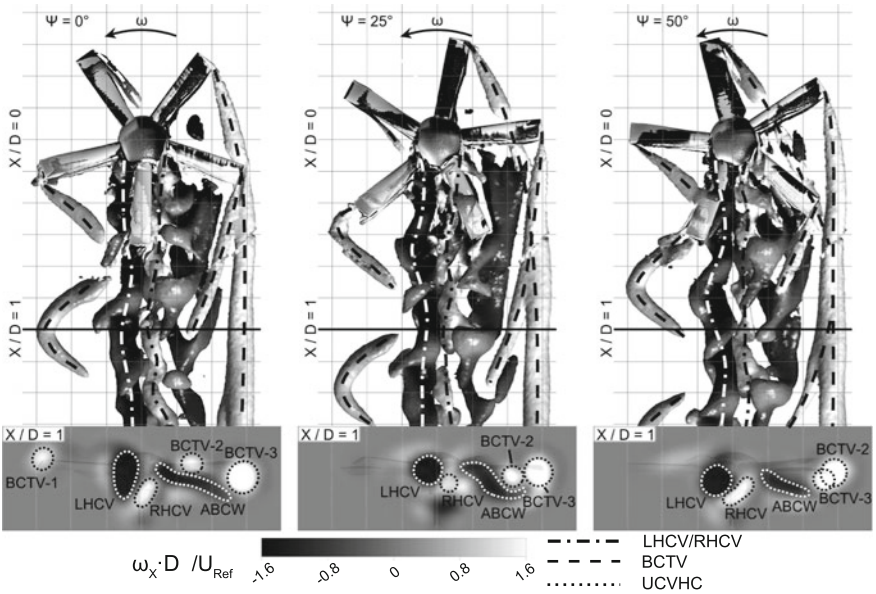

Fig. 7 Vortex Structures in the wake of the isolated rotating rotor head configuration—no cyclic

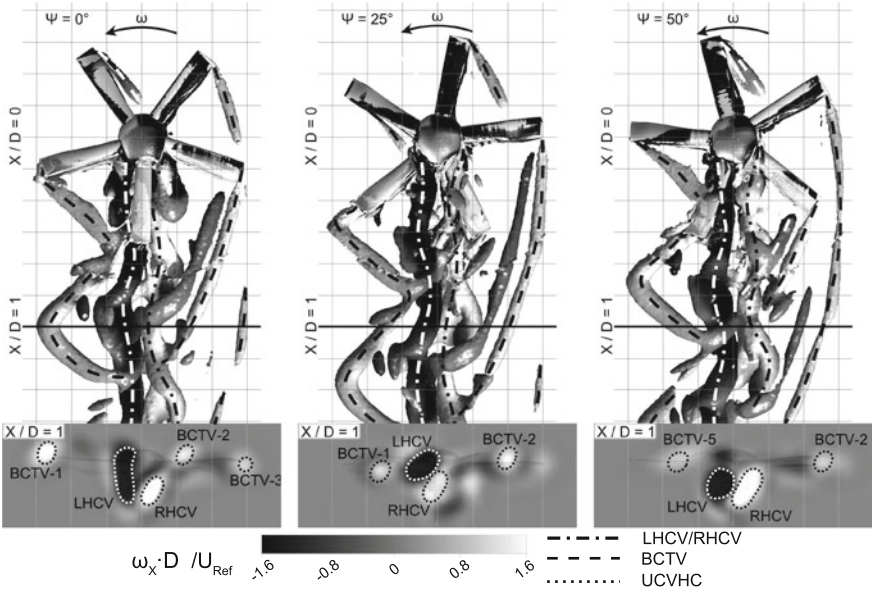

Fig. 8 Vortex Structures in the wake of the isolated rotating rotor head configuration—cyclic

occurring separation results in a region of negative axial vorticity termed advancing blade cuff wake (ABCW). The vorticity in the ABCW region is caused through three-dimensional effects within the separation bubble at the rotating blade cuff. If the cyclic pitch motion is considered the blade pitch angle on the advancing side is reduced. This confines the separation region to a small area close to the trailing edge and the blade cuff root. In these areas the blade cuff shape is comparatively blunt and separation occurs independently of blade angle of attack. Thus the ABCW region is reduced to an extent that it could not be clearly identified in the cut-plane at X/D = 1.

5 Conclusion

The main objective of this work was to demonstrate the capability of our simulation strategy to model the flow about rotating rotor heads including cyclic pitch motion of the blade cuffs. In contrast to previous work performed, employing the chimera technique for this purpose, a sliding mesh approach in combination with deforming meshes is chosen. For this purpose unsteady Reynolds averaged Navier–Stokes simulations were performed for an isolated rotating rotor head with and without cyclic pitch. It is shown that the employed approach, excluding the cyclic pitch motion, is capable of predicting lift and drag coefficients within 6 % of existing wind tunnel data in the presence of the fuselage and skid-landing-gear. Furthermore, the concept is evaluated by comparing the observed trends in drag and lift coefficient characteristics against those found in literature. The present results reproduce these trends qualitatively well. Finally, the impact on the wake of an isolated rotating rotor head with and without cyclic pitch motion is performed. It is shown that the intensity and spatial distribution of vorticity in the wake is affected considerably through cyclic pitch.

Overall, the employed simulation strategy seems capable of solving the problems of interest at the same level of confidence as other simulation strategies found in literature. The next step is the quantitative verification of the methods quality. For this purpose the configuration including the rotating rotor head with cyclic pitch, fuselage and skid-landing-gear will be simulated. Similar to results of the same configuration omitting cyclic pitch, these results can then be validated with existing wind tunnel data.

Acknowledgments The research leading to these results received funding from the European Community's Seventh Framework Program (FP/2007–2013) for the Clean Sky Joint Technology Initiative under grant agreement number 270563. The authors would like to thank project partner Eurocopter Deutschland GmbH for the fruitful collaboration and valuable support. Furthermore, special thanks are addressed to ANSYS CFX for providing the flow simulation software.

References

1. Grawunder, M., Reß, R., Breitsamter, C., Adams, N.A.: Flow Characteristics of a helicopter fuselage configuration including a rotating rotor head. In: 28th International Congress of the Aeronautical Sciences, Brisbane (2012)
2. Sheehy, T.W.: A general review of helicopter hub drag data. J. Am. Helicopter Soc. **22**(2), 2–10 (1977)
3. D'Alascio, A., Berthe, A.: Industrial use of computational fluid dynamics in the helicopter design process. In: American Helicopter Society 58th Annual Forum, Montreal (2002)
4. Le Chuiton, F., Kneisch, T., Schneider, S., Krämer, P.: Industrial validation of numerical aerodynamics about rotor heads: towards a design optimisation at eurocopter. In: 35th European Rotorcraft Forum, Southampton (2009)
5. Wake, B., Hagen, E., Ochs, S., Matalanis, C., Scott, M.W.: Drag prediction with an unstructured flow solver. In: American Helicopter Society 65th Annual Forum, Grapevine (2009)
6. Borie, S., Mosca, J., Sudre, L., Benoit, C., Péron, S.: Influence of rotor wakes on helicopter aerodynamic behaviour. In: 35th European Rotorcraft Forum, Southampton (2009)
7. Bridgeman, J.O., Lancaster, G.T.: Physics-based analysis methodology for hub drag prediction. In: American Helicopter Society 66th Annual Forum, Phoenix (2010)
8. Kneisch, T., Krauss, R., d'Alascio, A., Schimke, D.: Optimised rotor head design for an economic helicopter. In: 37th European Rotorcraft Forum, Gallarate (2011)
9. Dombroski, M., Egolf, T.A.: Drag prediction of two production rotor hub geometries. In: American Helicopter Society 68th Annual Forum, Fort Worth (2012)
10. Hill, M., Louis, M.: Rotating hub drag prediction methodology. In: American Helicopter Society Specialist's Conference on Future Vertical Lift Aircraft Design, San Francisco (2012)
11. Vogel, F., Breitsamter, C., Adams, N.: Aerodynamic investigations on a helicopter main rotor hub. In: American Helicopter Society 66th Annual Forum, Phoenix (2010)
12. Steijl, R., Barakos, G.: Computational analysis of rotor-fuselage interactional aerodynamics using sliding-plane CFD method. In: 34th European Rotorcraft Forum, Liverpool (2008)

Blade Shape Design: Trim Acceleration for Fluid-Structure Coupled Simulations of an Isolated Rotor in Forward Flight

Martin Hollands, Manuel Keßler and Ewald Krämer

Abstract The fluid-structure coupled and trimmed simulation of a helicopter rotor in forward flight is a computationally intensive task, hence it is a limiting factor for optimization studies of rotor blades. Therefore, the possibility of reducing the necessary trim iterations is investigated. Firstly, the quality criterion lift over drag is found to differ only slightly between a three and a four component trim while the three component trim requires less trim iterations. Secondly, the initial trim conditions for new blade shape geometries are predicted based on existing simulation results. For the present study a two dimensional parametric area resolved with 15 results is used for the interpolation of global quality criteria such as power and lift over drag as well as local properties such as the thrust distribution. The beneficial effect on the rotor trim using interpolated initial conditions is demonstrated.

1 Introduction

In the present study the blade shape design of a five bladed isolated helicopter rotor in forward flight is examined. The optimization of helicopter rotor blades in forward flight condition requires fluid-structure coupled simulations which have to be trimmed to a steady flight state in order to obtain comparable results of different rotor blade geometries. These Computational Fluid Dynamics (CFD) simulations are com-

The authors would like to thank the aerodynamic department of Eurocopter and the German Federal Ministry of Economy and Technology (BMWi) for its funding in the framework of FTEG-ECO-HC under grant 20H0803. We would also like to thank the members of the Helicopters and Aeroacoustics group at the IAG for their contribution.

M. Hollands (✉) · M. Keßler · E. Krämer
Institut für Aerodynamik und Gasdynamik, Universität Stuttgart, Pfaffenwaldring 21, 70569 Stuttgart, Germany
e-mail: martin.hollands@iag.uni-stuttgart.de;
http://www.iag.uni-stuttgart.de

A. Dillmann et al. (eds.), *New Results in Numerical and Experimental Fluid Mechanics IX*, Notes on Numerical Fluid Mechanics and Multidisciplinary Design 124,
DOI: 10.1007/978-3-319-03158-3_25,

putationally costly and are thus limiting the amount of parameters of an optimization. It is therefore of interest to investigate the possibility to reduce computational time as well as to predict loads and moments for new blade geometries to reduce the amount of necessary CFD calculations.

2 Computational Setup

2.1 Computational Methods

The aeroelastic simulations are realized by coupling the structure and flight mechanics code *HOST* from Eurocopter [1] with the flow solver *FLOWer* from DLR [2]. Within *HOST* the blade is modeled by an Euler-Bernoulli beam with rigid elements, connected with virtual joints as detailed in [3]. *FLOWer* solves the unsteady Reynolds Averaged Navier-Stokes (RANS) equations with a spatial second order central difference method. In time an implicit dual time-stepping method by Jameson [4] is applied using implicit residual smoothing and a three level multi-grid to accelerate convergence. Turbulence is modeled with the Wilcox $k-\omega$ model [5]. A time step equivalent to 1° with up to 80 sub-iterations is used. The coupling between *HOST* and *FLOWer* is conducted with a weak fluid-structure coupling method [6] exchanging periodic loads and deformation states within each trim iteration. The iteration process starts with an initial deformation and trim state calculated by *HOST* on the basis of two dimensional Blade Element Theory. The deformation state is passed from *HOST* to *FLOWer* in form of weighting factors for modal shapes. These result from a modal decomposition with the Rayleigh-Ritz method of the deformation state coming from the beam elements [3]. For the determination of the aerodynamic loads and moments with *FLOWer*, 4/5 revolutions of the five bladed rotor equal to 288° of simulation time are computed in each trim iteration to achieve a periodic solution within the CFD calculation. These loads and moments are transferred back to *HOST* and the vector $\boldsymbol{F}_{HOST}^{n+1}$ is calculated as follows:

$$\boldsymbol{F}_{HOST}^{n+1} = \boldsymbol{F}_{2D}^{n+1} + \left(\boldsymbol{F}_{3D}^{n} - \boldsymbol{F}_{2D}^{n}\right) \tag{1}$$

with $\boldsymbol{F}_{2D}$ being the internal loads and moments vector based on two dimensional aerodynamics, $\boldsymbol{F}_{3D}$ the vector coming from *FLOWer* and n being the current trim iteration. The solution is converged, if $\boldsymbol{F}_{2D}^{n}$ of the actual trim iteration is equal to $\boldsymbol{F}_{2D}^{n+1}$ of the next iteration step. Then $\boldsymbol{F}_{HOST}^{n+1}$ depends only on $\boldsymbol{F}_{3D}$ and thus the deformation and trim state is based only on the CFD solution.

2.2 Mesh Setup

Blade motion and deformation is realized using the Chimera technique [7] implemented in *FLOWer*. The five individual blade meshes are embedded in a Cartesian

background mesh. In the area of the rotor blades a hole is defined and cells of the background mesh within this hole definition are blanked. Each blade mesh has 1.4 mio. cells and a boundary layer resolution of 28 cells, with the height of the first boundary layer cell being at $y^+ < 1$. The background mesh is resolved with 1.6 mio. cells.

2.3 Interpolation Method

In order to accelerate the trim process and to reduce the amount of necessary trim cycles, a good estimation for the initial trim condition is required. The currently used Blade Element Theory in *HOST* yields initial trim control angles which are up to 2° off from the final trimmed control angles in fast cruise speed condition. Hence the effect of interpolating the initial condition for a new blade design from previously conducted CFD solutions of similar blade designs is examined. For this purpose the interpolation with Radial Basis Functions (RBF) as detailed for instance in [8] and implemented in the python module *scipy* [9] is used for the present study. A value y at position $\boldsymbol{x}$ is determined from m data points at the location $\boldsymbol{x_i}$ by the sum:

$$y(\boldsymbol{x}) = \sum_{i=1}^{m} \lambda_i \phi(||\boldsymbol{x} - \boldsymbol{x_i}||) \tag{2}$$

with the weighting coefficients λ_i and ϕ being a radial basis function. For the present case the inverse multiquadric: $\phi = 1/\sqrt{1 + (r/\epsilon)^2}$ was selected as radial basis function, with $r = ||\boldsymbol{x} - \boldsymbol{x_i}||$ and ϵ being set to an average length of the interpolation area.

3 Results

For the present study the results from the two dimensional parametric area, already examined in [10], is taken as data basis for investigating the effect of a different trim method and of the application of interpolation methods to determine an initial trim state. A schematic of the two parameters radial position $a = r/R$ and chord length $b = c_{max}/c_{avg}$ is given in Fig. 1 with r being the local radial position, R the rotor radius, c_{max} the maximum and c_{avg} the average chord length. The distance Δ is kept constant at $0.075\,R$. The chord length at the blade tip c is determined dependent on a and b to obtain blades with the same thrust weighted average chord length. The results obtained in [10] are shown in Fig. 2a. An optimum in the region of $a = 0.9 - 0.92$ and $b = 1.15 - 1.175$ is found.

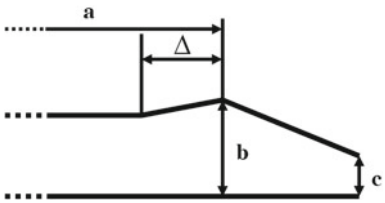

Fig. 1 Schematic of examined parameters a and b

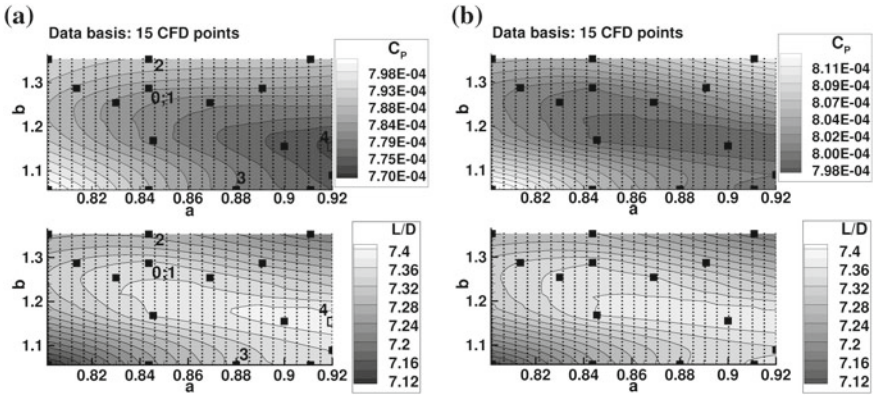

Fig. 2 Power coefficient C_P and lift over drag L/D. **a** 3 component trim; [11], **b** 4 component trim

3.1 Trim Process

In previous studies [10] and [11] a three component trim of the pilot controls collective pitch, longitudinal and lateral cyclic pitch, was used to obtain a steady flight state. While the objectives thrust (T), pitching and rolling moment of the rotor then are equal for different blade geometries, this is not the case for force components tangential to the rotor disc F_T. Hence, a varying lift $L = T \cdot cos(\theta) - F_T \cdot sin(\theta)$ and propulsive force $X = T \cdot sin(\theta) + F_T \cdot cos(\theta)$ is obtained with θ being the rotor shaft angle. Based on the assumption of a constant drag force of the helicopter fuselage, which has to be overcome by the propulsive force of the rotor, a blade geometry producing less propulsive force requires a higher inclination of the rotor disc. This has a negative effect on the performance of the rotor. Thus, a performance criterion has to include not only the consumed power of the rotor but also its propulsive force, when using a three component trim. A common criterion is the Lift over Drag ratio L/D defined in [12] as:

$$\frac{L}{D} = \frac{L}{\frac{P}{v_\infty} - X}, \tag{3}$$

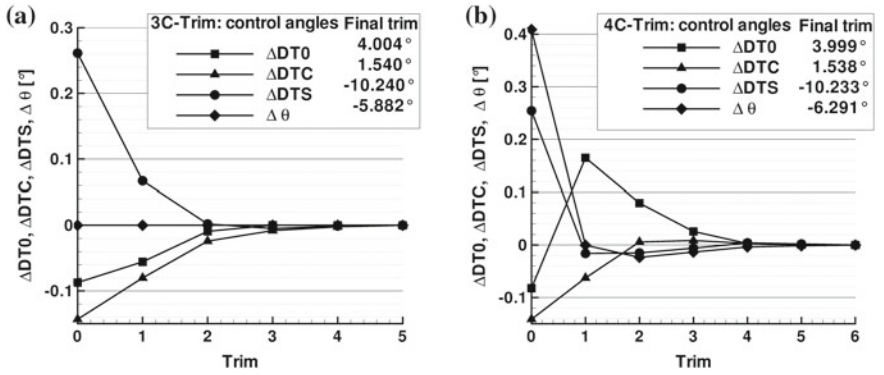

Fig. 3 Trim convergence of control angles. **a** 3 component trim, **b** 4 component trim

where P is the power and v_∞ the forward flight speed. This criterion is investigated taking the results presented in [10] with a three component trim and comparing them to the results trimming the rotor with the three pilot controls and additionally the rotor shaft angle to meet the objectives lift, propulsive force, rolling and pitching moment of the rotor. Figure 2a shows the results for the power coefficient C_P and L/D of the three component trim (3C). Black filled squares indicate the CFD results while the values at the small dots are interpolated using Kriging interpolation. Figure 2b shows the corresponding results for the four component trim (4C). In Fig. 2a both plots of C_P and L/D show an improvement towards higher values of a and towards $b \approx 1.15$. Yet L/D decreases faster towards lower or higher values of b than C_P. In contrast C_P and L/D of Fig. 2b show the same contour lines. Yet as defined in Eq. (3), L/D reaches a maximum if C_P shows a power minimum. The direct comparison of the L/D plot in Fig. 2a with the corresponding plot in Fig. 2b shows a fairly good qualitative agreement between the two trimming methods. Also quantitatively a deviation of less than 0.025 in L/D for all 15 CFD solutions is found. For the results with 4C-trim the calculations conducted with 3C-trim were carried on. In average two trim iterations were required to obtain a converged solution of a 4C-trim with a change of the trim controls of less than 0.01°. An additional calculation at $a = 0.88$, $b = 1.19$ starting with the same initial condition was conducted two times with 3C and 4C-trim to estimate the additional effort for the 4C-trim (Fig. 3a, b). The figures show the difference between the values of the trim controls and the final trimmed solution of the control angles over the trim iteration. The final values are indicated in the corresponding plot legend. Generally for the 15 CFD solutions the 4C-trim has only little influence on cosine (DTC) and sine (DTS) cyclic pitch angles with a variation of about 0.05°, while the collective pitch (DT0) varies up to 0.1°, and there is an about 0.25−0.4° elevated rotor shaft angle θ. In terms of computational effort one trim iteration more is required for obtaining a converged 4C-trim.

3.2 Prediction of Initial Trim Loads

Interpolation methods such as radial basis functions can not only be applied to global values such as performance criteria, but also to local values such as blade loads and moments. The application is presented in Fig. 4a–d. While Fig. 4a shows exemplarily the CFD result of the thrust-coefficient divided by the solidity of the rotor at position $(a, b) = (0.84, 1.29)$, Fig. 4b plots the difference between the CFD solution at the corresponding position to the CFD solution at $(a, b) = (0.92, 1.14)$. It represents thus the difference caused by a geometric variation. Figure 4c, d are the difference plots between an interpolated solution at position (0.84, 1.29) and their CFD solution. For Fig. 4c all CFD solutions, shown in Fig. 2a with black filled squares, except the interpolated point have been used for interpolation, yet for Fig. 4d only 5 points have been selected out of the CFD data basis to perform the interpolation: The four points in the corner of the parametric area and the point at position (0.87, 1.25). Although the interpolation error is increased in Fig. 4d compared to Fig. 4c the error range is still small compared to a representative geometric effect shown in Fig. 4b. Larger errors are only found for positions at the border of the parametric area. Namely for position (0.88, 1.06) local errors are above 10 %.

In Fig. 5a–c the final trimmed solution of the control angles is compared to the initial condition calculated by *HOST*, to the next existent CFD solution and to the interpolated solution. The *HOST* solution shows the result determined by internal two-dimensional aerodynamics $\boldsymbol{F}^0_{2D}$ of Eq. 1, as usually used for trim zero. Secondly, for the initial condition from the nearest neighbour, the existing final trim solution $\boldsymbol{F}^n_{3D}$ as well as $\boldsymbol{F}^n_{2D}$ is taken as trim zero ($n = 0$). Yet, within *HOST* the blade geometry is updated to the new blade and the deformation and trim state of the first trim iteration is calculated. Finally, for the interpolation the trim with the solution of the nearest neighbour $\boldsymbol{F}^0_{3D}$ and $\boldsymbol{F}^0_{2D}$ is continued. But, instead of performing a CFD calculation in the first trim iteration, the solution $\boldsymbol{F}^1_{3D}$ is interpolated. Consequently the trim state for the second trim iteration is obtained by *HOST*.

Five different cases are investigated in detail for their trim behaviour. The resulting trim controls are drawn over the five cases in Fig. 5. Case 0 and 1 is based on the parameter set $(a, b) = (0.84, 1.29)$ (see also Fig. 2a for the position of the different cases). For case 0 the next neighbour is taken at position (0.83, 1.25), while case 1 was calculated with a remote point (0.80, 1.06) to examine the methods when only few CFD points are available. While the solution of the nearest neighbour is already close to the target value for case 0, also for case 1 with the remote point from the corner of the parametric area a good prediction can be found. The interpolation does not yield any benefit when the solution of the nearest neighbour is already close to the target value, whereas the predicted result can be improved in case 1. The same behaviour is also found for other cases: 2 with parameter set (0.84, 1.35) and neighbour (0.84, 1.29) as well as 3 with set (0.88, 1.06) close to (0.91, 1.06). Case 4 was newly calculated and therefore used to compare the effect of different starting points on the trim process. It is at the position (0.92, 1.14) with the close point (0.92, 1.09). Figure 6a shows the control angles of the close point (0.92, 1.09) at trim 0. Trim

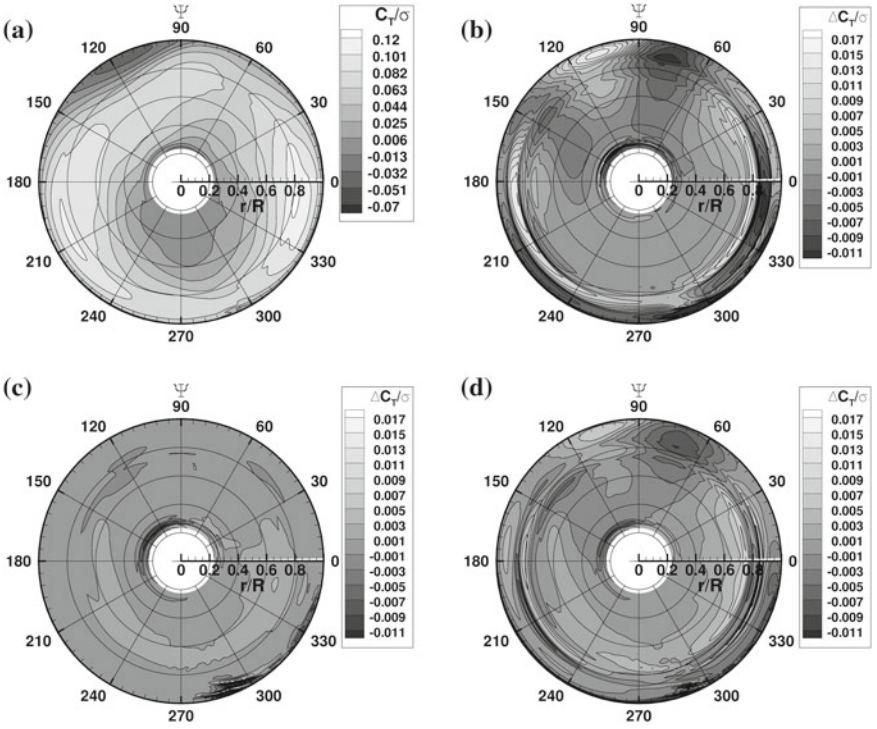

Fig. 4 Thrust coefficient. **a** CFD solution at (a, b) = (0.84, 1.29), **b** Δ = (CFD at (a, b)=(0.84, 1.29)—CFD at (a, b) = (0.92, 1.14), **c** Δ = (Interpolated—CFD solution) at (a, b) = (0.84, 1.29) using 14 points as data basis, **d** Δ = (Interpolated—CFD solution) at (a, b) = (0.84, 1.29) using only 5 points as data basis

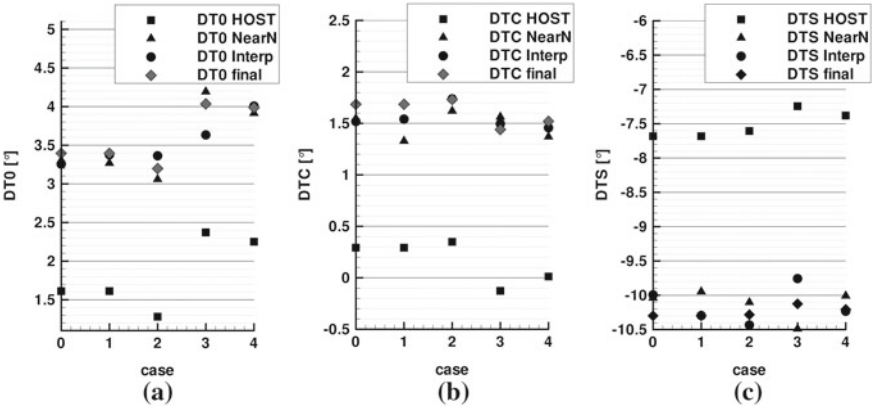

Fig. 5 Initial condition of trim controls for different cases. **a** Collective pitch **b** Lateral cyclic **c** Longitudinal cyclic

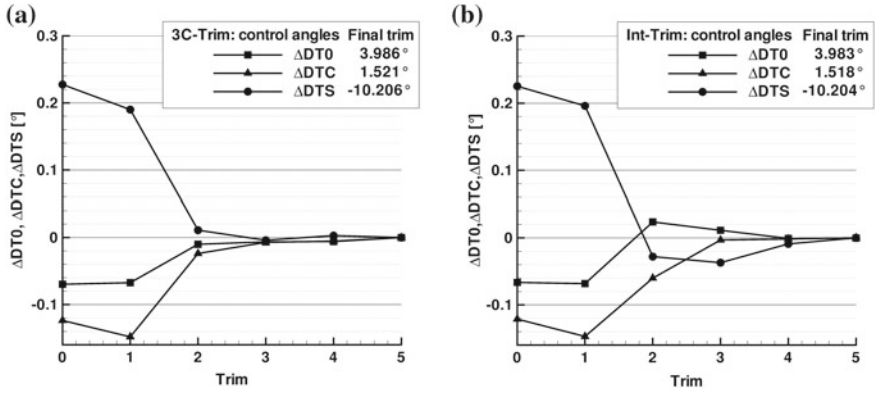

Fig. 6 Trim convergence of control angles for 3 component trim, case 4. **a** initial trim, nearest neighbour **b** with interpolated initial solution

iteration 1 is thus the first CFD calculation. While the predicted values for trim 1 still have a significant offset from the final solution, directly after the first CFD computation the trim converges rapidly, yet with a small oscillation in trim 4. Figure 6b starts with the same values as Fig. 6a, but this time iteration 1 is interpolated and trim 2 is the first CFD calculation. The trim shows a similar convergence. As the oscillation in trim 4 of Fig. 6a is only slightly above the trim termination condition of 0.01°, both methods need about the same amount of CFD calculations to converge. Starting the trim process with trim 0 from *HOST* requires 7 CFD calculations for convergence. Overall a reduction of 3–4 iterations can be achieved by using a blade shape design with similar geometric properties and interpolating the initial trim condition from existing geometries. As one trim iteration with 288 time-steps requires 7–8 h wall clock time with 160 CPUs on the CRAY XE6 of the High performance computing center stuttgart (HLRS), 3,400–5,000 CPU h can be saved for each simulation by using this interpolation method.

4 Conclusion

A comparison between a three and a four component trim of an isolated rotor was performed by investigating 15 different blade shape geometries varied in the two parameters radial position and extension of maximum chord length. It was shown, that reliable results are obtained using a three component trim with lift over drag ratio as performance criterion. Thereby one trim iteration less is required than performing the four component trim. Another acceleration of the trim process is achieved by using the final trimmed CFD result from an existing geometry with similar parameters as initial solution for the rotor trim. Additionally an interpolation of loads and moments for the following trim step, instead of their calculation with CFD, results in trim

controls which are close to the final trimmed controls. Only in the case of an existing CFD solution, which is already very close to the target point, there is in some cases a slight drawback of using the interpolated solution. Overall there is a benefit of three to four trim iterations less, using the solution of a nearby CFD solution as start condition for the trimming process as well as for using the interpolated solution. As expected, interpolated results become less accurate towards the boundary of the parametric area and thus, the benefit is likely to be smaller.

References

1. Benoit, B., Dequin, A.M., Kampa, K., von Grünhagen, W., Basset, P.M., Gimonet, B.: HOST, a general helicopter simulation tool for Germany and France. In: American Helicopter Society, 56th Annual Forum. pp. May 2–4, Virginia Beach, Virginia USA (2000)
2. Kroll, N., Eisfeld, B., Bleecke, H.M.: Flower. Notes Numer. Fluid Mech. **71**, 58–68 (1999)
3. Dietz, M.: Simulation der Umströmung von Hubschrauberkonfigurationen unter Berücksichtigung von Strömungs-Struktur-Kopplung und Trimmung. Ph.D. thesis, Universität Stuttgart (2009)
4. Jameson, A.: Time dependent calculations using multigrid, with applications to unsteady flows past airfoils and wings. In: AIAA 10th Computational Fluid Dynamics Conference. p. 91–1596, Honolulu, Hawaii, USA (1991)
5. Wilcox, D.C.: Turbulence Modeling for CFD, 3nd edn. DCW Industries Inc., München (2006)
6. Altmikus, A., Wagner, S., Beaumier, P., Servera, G.: A comparison: weak versus strong modular coupling for trimmed aeroelastic rotor simulations. In: American Helicopter Society, 58th Annual Forum. pp. 697–710, Montreal, Canada (2002)
7. Benek, J.A., Steger, J.L., Dougherty, F., Buning, P.G.: Chimera: a grid-embedding technique. In: NASA techdocs, p. 86N32242. No. 19860022770 April 1986
8. Wright, G.B.: Radial Basis Function Interpolation: Numerical and Analytical Developments. Ph.D. thesis, University of Colorado, Boulder (2003)
9. The Scipy Community: Numpy and Scipy Documentation SciPy Reference Guide (September 2012), http://docs.scipy.org/doc/scipy/reference/generated/scipy.interpolate.Rbf.html
10. Hollands, M., Keßler, M., Krämer, E.: Influence of an-/dihedral and of different blade shapes on performance and aeroacoustics of an isolated rotor. In: 38th European Rotorcraft Forum, ERF, Amsterdam, Netherlands (2012)
11. Hollands, M., Keßler, M., Altmikus, A., Krämer, E.: Trade study: influence of different blade shape designs on forward flight and hovering performance of an isolated rotor. In: 37th European Rotorcraft Forum, ERF, Gallarate, Italy (2011)
12. Leishman, J.G.: Principles of Helicopter Aerodynamics, 2nd edn. Cambridge Aerospace Series. Cambridge University Press, Cambridge (2006)

Numerical Investigations of a Back-Flow Flap for Dynamic Stall Control

K. Kaufmann, A. D. Gardner and K. Richter

Abstract Numerical investigations with the DLR TAU Code demonstrate that an actuated back-flow flap on the suction side of an OA209 helicopter airfoil is able to improve the dynamic stall behavior. When the flow begins to stall, the flap is extended which interferes with the back-flow. This weakens the dynamic stall vortex and consequently the peak in the pitching moment peak is reduced.

1 Introduction

Dynamic stall occurs on the retreating rotor blade of a helicopter during maneuver and fast forward flight. The phenomenon is characterized by the development of a vortex starting at the front of the airfoil. This first leads to a lift overshoot, but as the vortex moves downstream high drag and pitching moment peaks appear leading to high structural loads. Thus, flight conditions which cause dynamic stall over a large area of the rotor blade are excluded from the flight envelope. Therefore, a large number of dynamic stall control devices including leading edge suction [1], fluidic control devices [2], leading edge vortex generators [3] and leading edge slats [4] have already been tested with the aim of decreasing the pitching moment and drag peaks while improving the lift.

Static investigations by Meyer [5] show that a back-flow flap on the top of an airfoil near the trailing edge can increase the lift by 10–18 %. In the current study, an actuated flap on the suction side of an OA209 airfoil was tested to improve the dynamic stall (DS) behavior [6, 7]. Because dynamic separation is different from the static case, the ideal flap position had to be found. Therefore, three different flap configurations with a hinge joint at 10 % (Flap I), 40 % (Flap II) and 70 % (Flap III)

K. Kaufmann (✉) · A. D. Gardner · K. Richter
German Aerospace Center (DLR), Institute of Aerodynamics and Flow Technology,
Bunsenstraße 10, 37073 Göttingen, Germany
e-mail: kurt.kaufmann@dlr.de

A. Dillmann et al. (eds.), *New Results in Numerical and Experimental Fluid Mechanics IX*,
Notes on Numerical Fluid Mechanics and Multidisciplinary Design 124,
DOI: 10.1007/978-3-319-03158-3_26,

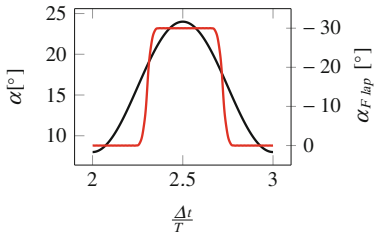

Fig. 1 Angle of attack of the airfoil (*black*) and angle of the flap (*red*) over a pitching period

chord were tested. All flaps had a length of 10 % of the airfoil's chord. When the dynamic stall vortex begins to move downstream the flap is extended. This weakens the dynamic stall vortex and the pitching moment is reduced. The flap is kept in this position until the flow begins to reattach, then the flap is closed. The movement of the airfoil and the flap over one pitching cycle is shown in Fig. 1. First, computations of an oscillating airfoil without a flap were carried out to analyze the dynamic stall behavior of the airfoil. Subsequently calculations of an oscillating airfoil with a closed flap were carried out to investigate the influence of the installation of the flap and the flow around the airfoil. Finally, calculations of the oscillating airfoil with a moving flap were carried out to determine the effect of the moving flap.

2 Numerical Method

Two-dimensional unsteady Reynolds-averaged Navier-Stokes (URANS) computations were undertaken with the DLR TAU code [8]. A DS test case with a pitching OA209 airfoil and the following parameters was carried out: $Ma = 0.14$, $Re = 9.2 \times 10^5$, $\alpha = 16° \pm 8°$ and the reduced frequency $\omega^* = \frac{2\pi f_{osc} c}{U_\infty} = 0.1$. Hybrid grids were created with the unstructured grid generator Centaur^{TM}. A fine grid was created with the preferences of Richter et al. [9] using 60 prismatic layers, to provide a reference grid-converged solution. The relative movement between flap and airfoil was realized by using the Chimera technique [10]. This technique uses one body fixed grid for the airfoil (black) and one for the flap (red) (Fig. 2). In the overlapping area the flow information is interpolated between the two grids for each time-step, requiring a strong local mesh refinement in this area. In order to reduce computation time, the chimera grid used only 30 prismatic layers, and a comparably coarse single-block grid with 30 layers was created to show the effect of the coarsening. The height of the first prismatic layer and the stretching factor were adjusted to reach a $y^+ \approx 1$ and the boundary layer thickness, respectively. All computations were fully turbulent using the Spalart-Allmaras turbulence model [11], although the Reynolds number is quite low. Previous investigations [9] have found that this is an acceptable simplification, because at the angles of attack relevant to the deep stall, the top of the airfoil is fully turbulent, with transition at the leading edge. The URANS computations used 1,000

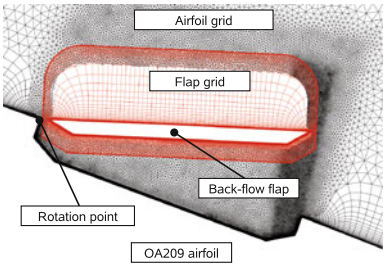

Fig. 2 Chimera technique in the area of the back-flow flap with *red* flap grid and *black* airfoil grid

inner iterations and 2,000 iterations per period as in [9]. After two pitching cycles, convergence has been reached assuming a maximum difference of 1.5 % between the lift coefficient of the second and third period.

3 Results

In Fig. 3 the lift coefficient (left) and the pitching moment (right) are plotted for one pitching period for the configuration without flap on the coarse grid (black) using the DS test case: $Ma = 0.14$, $Re = 9.2 \times 10^5$, $\alpha = 16° \pm 8°$ and $\omega^* = 0.1$. Starting at the minimum angle of $\alpha = 8°$ the lift coefficient rises linearly until $\alpha = 18°$ on the upstroke while the pitching moment is slowly, also linearly decreasing. Then the gradient of the lift slowly starts to fall due to separation at the trailing edge. At about $\alpha = 20°$ the dynamic stall vortex is formed at the front of the airfoil leading to a sudden increase of the lift and to a drop of the pitching moment. The maximum lift of $C_l = 2.33$ is reached at $\alpha = 21.1°$. While the vortex is moving downstream the lift coefficient is kept high and the pitching moment has a negative peak reaching its minimum of $C_m = -0.536$ at $\alpha = 22°$. These rapid changes in the pitching moment are the major concern of dynamic stall, causing high structural loads. As the vortex leaves the trailing edge the lift coefficient suddenly reduces and reaches a local minimum of $C_l = 0.98$ at $\alpha = 22.8°$ while the pitching moment rapidly increases. Subsequently, a new vortex develops at the front of the airfoil leading to a second maximum of the lift coefficient of $C_l = 1.56$ at $\alpha = 23.3°$. When the vortex moves downstream a second smaller negative pitching moment peak with a value of $C_m = -0.277$ at $\alpha = 23.5°$ is created. At the maximal angle of attack of $\alpha = 24°$, the lift coefficient is oscillating at low values and the pitching moment rises continuously on the downstroke until the flow reattaches. Comparing the results of the computations without a flap in Fig. 3 on the fine single-block grid (red) and on the coarse single-block grid (black) showed, that the coarse grid is sufficiently resolved for an engineering estimate of the effect of the flap. Although true convergence is not reached, all relevant flow structures for dynamic stall are contained in the flow.

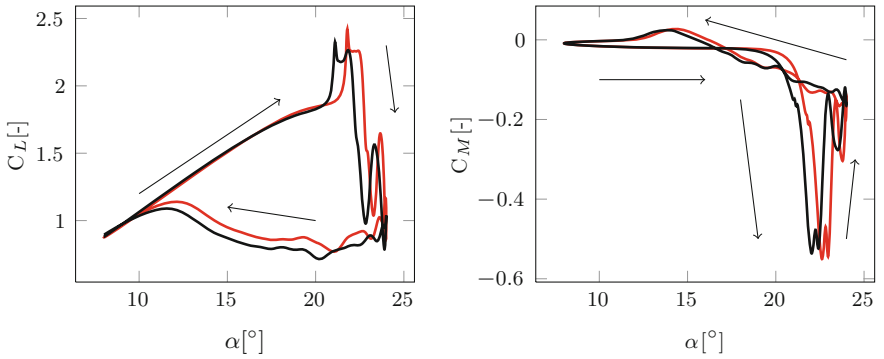

Fig. 3 URANS computations without flap on the fine grid (*red*) and on the coarse grid (*black*) over one pitching period: *Left* = Lift, *Right* = Pitching moment

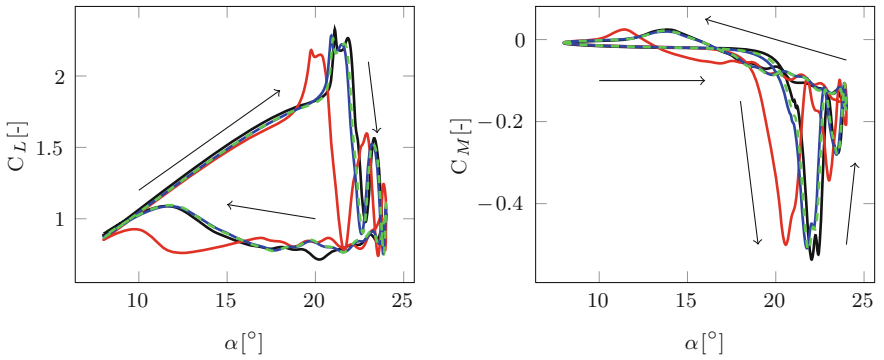

Fig. 4 URANS computations without flap (*black*) and with closed flaps at 10 % (*red*), 40 % (*blue*) and 70 % (*green*) over one pitching period: *Left* = Lift, *Right* = Pitching moment

In Fig. 4, the configuration without a flap (black) is compared with the configurations with a flap I, II and III at 10 % (red), 40 % (blue) and 70 % (green) chord using the same DS test case. The flaps are kept closed for the whole pitching period to investigate the influence of their installation. At small angles all curves are quite similar. The air circulation caused by the gaps between the airfoil and the flaps influences the flow around the airfoil and leads to a smaller gradient of the lift coefficients and to earlier flow separation as shown in Fig. 5. Flap I has the most significant impact on the flow, because the flap is placed in the region of the suction peak. The maximum lift at $\alpha = 19.7°$ drops by 7.7 %, the flow separation starts 1.4° earlier and the flow begins to reattach much later than without a flap. The influence of flap II and III is much lower. The maximum lift coefficient at $\alpha = 20.9°$ drops by 2.1 % and the flow separation starts 0.2° earlier. The closed flaps don't seem to have any effect on the reattachment of the flow.

The coefficient of lift (left) and the pitching moment (right) for the three flap configurations are shown in Fig. 6 comparing one pitching period where the flap is

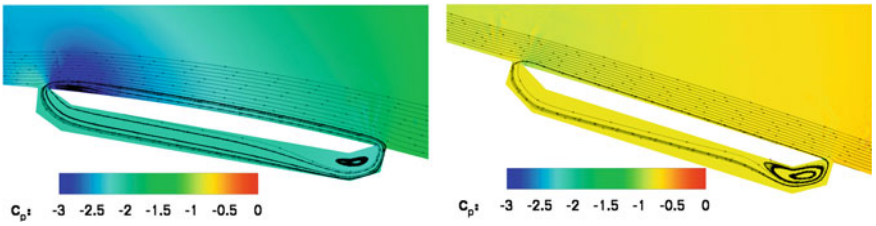

Fig. 5 Airflow around flap configuration I (*left*) and flap configuration II (*right*)

kept closed (black) and one pitching period with moved flap (red). The flap starts to extend at $\alpha = 16°$ and is fully extended at $\alpha = 20.5°$ on the upstroke (Fig. 1). The flap stays in the extended position of $\alpha_{Flap} = -30°$, then the flap is closed from $\alpha = 20°$ to $\alpha = 15°$ on the downstroke of the airfoil. In the two upper diagrams of Fig. 6 the lift coefficient (left) and the pitching moment (right) for the flap configuration I at 10 % is pictured. The first changes can be detected at $\alpha = 18°$. The lift coefficient of the case with the moving flap starts to rise earlier than that of the case with a closed flap. The maximum lift coefficient is reached at the same angle of attack but is 2.2 % smaller. In contrast to the case with the closed flap the lift coefficient drops directly after reaching the maximum. The lift then descends to a value of $C_l = 0.64$. The second peak is 10 % lower than with the closed flap configuration. On the downstroke when the flow is separated, larger fluctuations in the lift coefficient are seen. However, the DS behavior is improved by the movement of the flap reducing the first pitching moment peak by 17 % and the second peak by 22 %. Additionally the absolute values of the drag peaks which appear during the shedding of the first and second vortices are reduced by 13 % and by 15 %, respectively.

In the two diagrams in the middle of Fig. 6 the lift coefficient (left) and the pitching moment (right) of flap configuration II at 40 % chord are pictured. The movement leads to an increase in the lift between $\alpha = 18°$ and $\alpha = 20°$ on the upstroke. Furthermore, both DS vortices begin to move downstream earlier. Thus, the maximum lift is already reached at $\alpha = 20.5°$ and is 10 % lower. The second lift peak at $\alpha = 22.7°$ is 20 % lower. Almost no effect of the movement can be detected on the reattachment of the flow. A significant improvement can be seen in the pitching moment. The pitching moment starts to drop when the flap is extended between $\alpha = 18°$ and $\alpha = 19°$ on the upstroke, as a vortex is formed downstream of the extended flap. Then there is a plateau in the pitching moment at $C_m = -0.14$ until the dynamic stall vortex starts to move downstream at $\alpha = 20.5°$ and the pitching moment drops. At $\alpha = 21.3°$ the minimum value of $C_m = -0.337$ is reached which is 34 % less than in the reference case because the extended flap breaks down the vortex into smaller, weaker parts. The second dynamic stall vortex is also weakened by the flap configuration II. The pitching moment peak is 31 % less than in the reference case. As with flap configuration I, the drag is reduced by 28 % at the first maximum and by 29 % at the second maximum. In contrast to flap configurations I

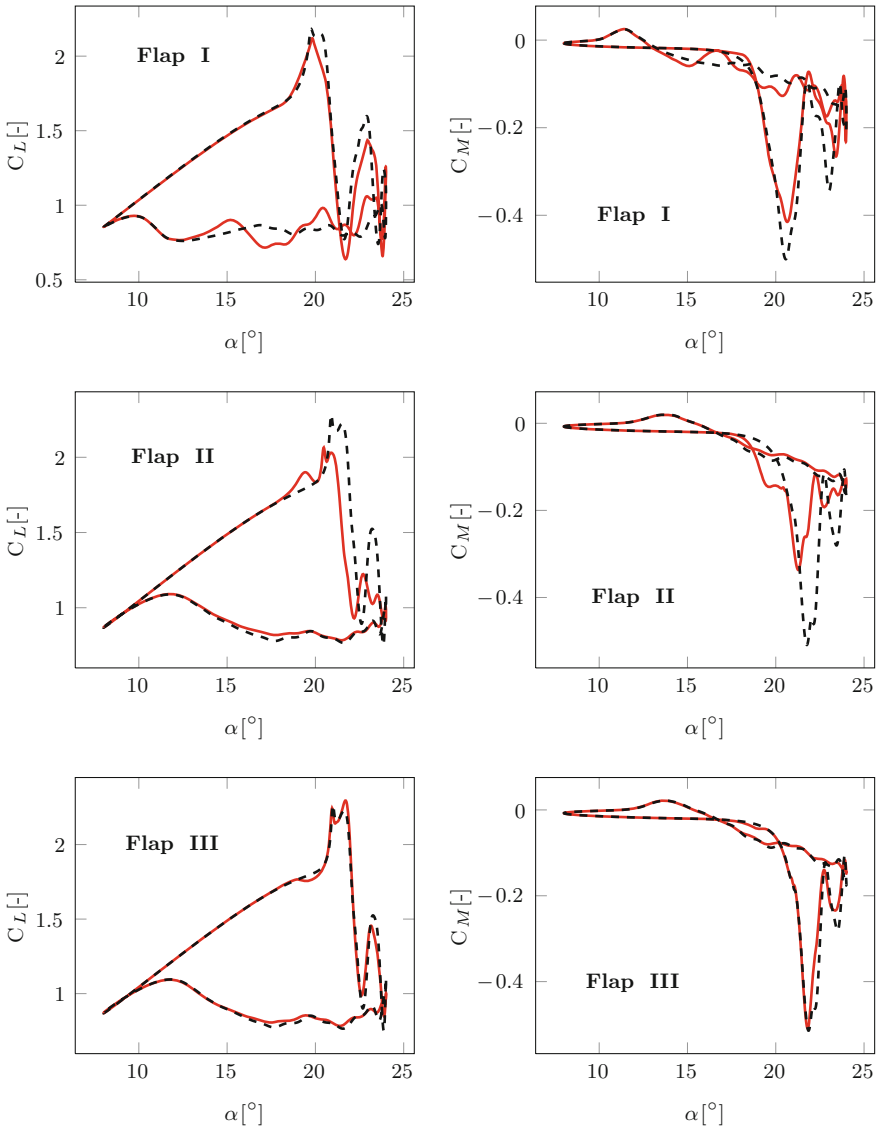

Fig. 6 URANS computations with the flap configuration at 10, 40 and 70 % chord for the closed flap (*black*) and the moving flap (*red*) over one pitching period for: *Left* = Lift, *Right* = Pitching moment

and II, the movement of flap III shows almost no effect, as shown in the bottom row of Fig. 6.

Figure 7 illustrates the change in the flow due to the flap movement at 40 % chord length (Flap II). The flow field with the pressure distribution and the streamlines around the pitching airfoil is pictured for the closed flap (left) and the moving flap

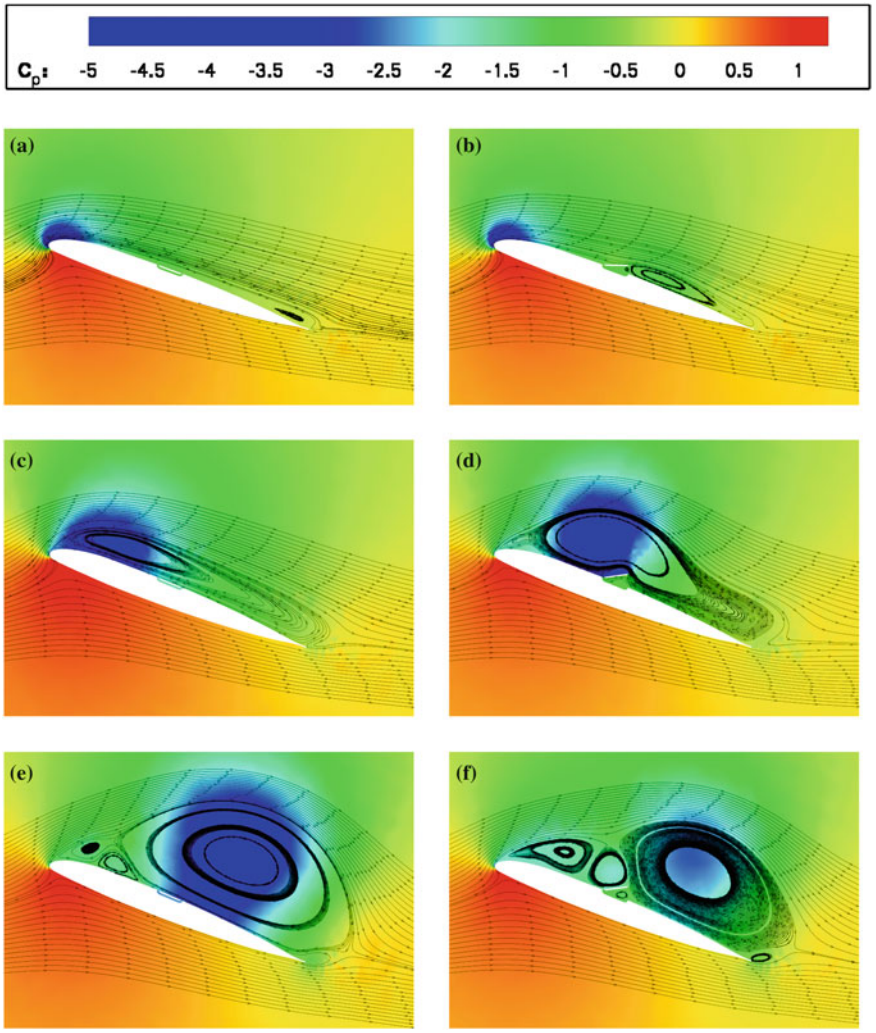

Fig. 7 Flow pattern around the airfoil of the closed flap (*left*) and the moving flap (*right*) for the flap configuration at 40 % chord length. All snapshots are during the upstroke ↑

(right). In Fig. 7a, b the airfoils are shown on the upstroke at $\alpha = 19°$. In Fig. 7a separation starts at the trailing edge while in Fig. 7b the flap is starting to extend and the airflow is separated directly behind the flap. Figure 7c, d show the flow field when maximum lift is reached. While the dynamic stall vortex is still rolling up at the front of the airfoil in the case with the closed flap (Fig. 7c), the vortex in Fig. 7d is already moving downstream and reaches the maximum lift when the vortex is in the region of the extended flap. Figure 7e, f show the flow fields around the flaps when

the maximum pitching moment is reached. Here the largest differences can be seen. Due to the movement of the flap the dynamic stall vortex is split into smaller, weaker vortices which reduce the pitching moment and the drag peaks.

4 Conclusion

The numerical investigations showed that an actuated back-flow flap is able to improve the dynamic stall behavior. The best results were achieved with the flap at 40 % chord. The pitching moment peak was reduced by 34 % and the mean drag coefficient was reduced by 28 %. When keeping the flap closed this configuration also showed good results compared to the test case without a flap. Further computations will be carried out to improve the flap length, position and movement. Finally, experimental investigations will be carried out in a wind tunnel model in 2014.

References

1. Alrefai, M., Acharya, M.: Controlled leading-edge suction for management of unsteady separation over pitching airfoils. AIAA J. **34**(11), 2327–2336 (1996)
2. Gardner, A.D., Richter, K., Rosemann, H.: Numerical investigation of air jets for dynamic stall control on the OA209 airfoil. Aeronaut. J. **1**(1), 69–82 (2011). doi:10.1007/s13272-011-0002-z
3. Heine, B., Mulleners, K., Joubert, G., Raffel, M.: Dynamic stall control by passive disturbance generators. In: 29th AIAA Applied Aerodynamics Conference, Honolulu, Hawaii, USA 27–30 June 2011
4. Carr, L.W., Chandrashekara, M.S., Wilder, M.C., Noonan, K.W.: The effect of compressibility on suppression of dynamic stall using a slotted airfoil. AIAA Paper 1998–332, January 1998
5. Meyer, R.K.J.: Experimentelle Untersuchungen von Rückstromklappen auf Tragflügeln zur Beeinflussung von Strömungsablösungen. Dissertation TU Berlin, Mensch-und-Buch-Verlag (2000)
6. DLR: Rotorblatt mit integrierter passiver Oberflaechenklappe. Deutsches Patent DE 10 2010 041 111 A1. Accessed 22 Mar 2012
7. Kaufmann, K.: Numerische Untersuchung einer Rückstromklappe zur Dynamic Stall-Kontrolle. Diplomarbeit, Universität Stuttgart (2012)
8. Schwamborn, D., Gardner, A.D., von Geyr, H., Krumbein, A., Lüdeke, H., Stürmer, A.: Development of the TAU-Code for aerospace applications. In: 50th NAL INCAST, Bangalore, India, 26–28 June 2008
9. Richter, K., Le Pape, A., Knopp, T., Costes, M., Gleize, V., Gardner, A.D.: Improved two-dimensional dynamic stall prediction with structured and hybrid numerical methods. AHS J. **56**(4), 1–12 (2011)
10. Schwarz, T.: The overlapping grid technique for the time accurate simulation of rotorcraft flows. In: 31st ERF, Florence, Italy, 13–15 September 2005
11. Spalart, P.R., Allmaras, S.R.: A one equation turbulence model for aerodynamic flows. AIAA Paper 92–0439, 1992

Adaptation of the Dynamic Rotor Blade Modelling in CAMRAD for Fluid-Structure Coupling Within a Blade Design Process

Christian Stanger, Martin Hollands, Manuel Keßler and Ewald Krämer

Abstract In this paper two different methods to adapt the structural model in blade design due to geometric changes are introduced. The first method is based on scaling laws, whereas the second method uses the solution of a linear system of equations. To evaluate the effect of the adaptation of the structural dynamics, trimmed and fluid-structure coupled CFD simulations for different adaptations were performed. The effects are discussed with the help of global values like collective pitch and required rotor power as well as local aerodynamics and structural dynamics. The impact of the different parameters is analysed and it is shown that the adaptation is not negligible without a loss of accuracy.

1 Introduction

The aerodynamics of a helicopter in forward flight are characterized by an unsteady, however periodic flow-field. Due to the oscillating forces resulting out of this flow field, the structural dynamics of the rotor blade is excited. With the elasticity of the blades, this leads to a periodic deformation of the blade which simultaneously influences the aerodynamic characteristics of the blade. Blade torsion causes different angles of attack as well as flapping and lagging movement influence the induced

C. Stanger (✉) · M. Hollands · M. Keßler · E. Krämer
Institute of Aerodynamics and Gasdynamics, University of Stuttgart, Pfaffenwaldring 21, 70569 Stuttgart, Germany
e-mail: Stanger@iag.uni-stuttgart.de

M. Hollands
e-mail: Hollands@iag.uni-stuttgart.de

M. Keßler
e-mail: Kessler@iag.uni-stuttgart.de

E. Krämer
e-mail: Kraemer@iag.uni-stuttgart.de

A. Dillmann et al. (eds.), *New Results in Numerical and Experimental Fluid Mechanics IX*, Notes on Numerical Fluid Mechanics and Multidisciplinary Design 124,
DOI: 10.1007/978-3-319-03158-3_27,

velocity. Hence, there is a significant interaction between aerodynamics and structural dynamics in rotorcraft technology.

For the blade design process this characteristic of a rotor blade has to be considered. Therefore the simulation of fluid dynamics (CFD) is coupled with the simulation of structural dynamics (CSD) and an aerodynamic model of the blade is necessary as well as a structural model. The blade grids, for the CFD simulation can be created automatically on the basis of the blade geometry and there are also many approaches to generate a structural model of a given blade (cf. [1]). But in the pre-design phase, the exact composition of the blade is unknown and these methods cannot be applied. Thus the structural model of a preferably similar blade is used so far. This deficit in modelling is resolved with the present work by demonstrating two methods for the adaptation of the dynamic model of a rotor blade due to geometrical changes.

2 Methods to Adapt the Structural Model

2.1 Composition of the Structural Model in CAMRAD II

CAMRAD II [2] is an aeromechanical analysis tool of helicopters. For this research it is applied to calculate the blade movement and deformation resulting from aerodynamic forces. Its beam component implements two different structural models (cf. [3]), in this paper the Euler-Bernoulli beam theory with an elastic axis is used. The parameters of this structural model can be divided into three groups. The first group, geometric parameters, are coordinates and angles. The second group are stiffness parameters which define the correlation between forces and displacements and the third group are inertia parameters which define the correlation between forces and accelerations. To generate a structural model of a rotor blade, all parameters, denoted by p, have to be defined on different radial positions. To estimate the structural model of a new rotor blade (*modified blade*, index *mod*), it is required that the structural model of a similar blade (*reference blade*, index *ref*) is known. The correlation between reference and modified blade can be derived now at an arbitrarily chosen cross section.

For all geometric parameters it is assumed, that each cross section of the reference blade can be transformed to the modified blade by scaling in chord and thickness direction (cf. Fig. 1). The scaling factors

$$\alpha = \frac{a_{mod}}{a_{ref}} \quad \text{and} \quad \beta = \frac{b_{mod}}{b_{ref}} \tag{1}$$

are defined as the ratios of the lengths of reference and modified blade. Due to the assumption that reference and modified blade are similar, all coordinates can be converted by a multiplication with the corresponding scaling factor. This geometric adaptation is the state of the art, however the adaptation of stiffness and inertia parameters is so far neglected.

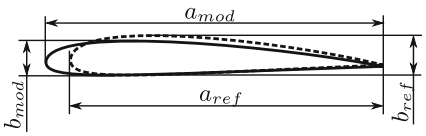

Fig. 1 Scaling of a cross section

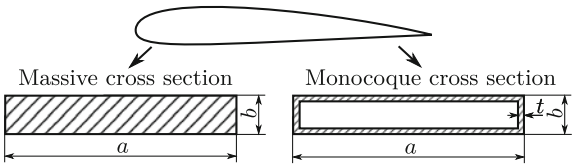

Fig. 2 Transition of an airfoil to a simpler geometry using the example of a rectangle

2.2 Scaling Method

Idea. With respect to the required lightweight construction of rotor blades, the method allows a selection between the scaling of a massive cross section (MA, $\mu = 1$) and the scaling of a monocoque cross section with a thin wall (MO, $\mu = 0$) or a combination of these two scalings ($\mu = 0 \ldots 1$). Hence the scaling factor ν of any stiffness and inertia parameter can be written as a combination of these two scaling factors

$$\nu = \mu \cdot \nu_{MA} + (1 - \mu) \cdot \nu_{MO} \qquad \text{with} \qquad \nu = \frac{p_{mod}}{p_{ref}}. \tag{2}$$

To derive the scaling factors ν_{MO} and ν_{MA}, the airfoil is reduced to a simpler geometry like a rectangle (cf. Fig. 2). It is assumed, that Young's modulus E, shear modulus G and density ρ are constant at the considered area.

Mathematical Derivation of the Scaling Factors. All stiffness and inertia parameters are zeroth or second moments of area. Zeroth moments of area are, e.g. extension stiffness or mass to length ratio. Their scaling factors as a function of the length ratios can be found in Table 1. In the important case of equal scaling, the scaling factor for a monocoque cross section is independent of the airfoil, otherwise it depends on thickness to chord ratio δ. Second moments of area are, e.g. bending or torsion stiffness. In contrast to zeroth order moments, second order moments depend on their reference axis and on the distance between the axis and the center of gravity z_0. Scaling factors for radial moments like torsion stiffness can be calculated by the weighted average of the two axial scaling factors. A detailed mathematical derivation can be found in [4].

Table 1 Scaling factors for zeroth and second moments of area

Order of moment of area	0th	2nd (x-axis)	
Massive cross section	$\alpha\beta$	$\alpha\beta^3$	with $\delta = \frac{b_{ref}}{a_{ref}}$
Monocoque cross section	$\frac{\alpha+\delta\,\beta}{1+\delta}$	$\beta^2 \frac{3\alpha a^2\delta^2+a^2\beta\delta^3+12(\alpha+\beta\delta)z_0^2}{3a^2\delta^2+a^2\delta^3+12(1+\delta)z_0^2}$	

2.3 LSE-Method

Idea. The errors due to the simplifications made for the scaling method have been analysed (cf. [4]). The biggest effects has the derivation of the scaling factors for a rectangle instead for the used airfoil and the unknown weighting-factor μ. To avoid these simplifications, a second method has been developed.

Within this method, characteristic blade values $\underline{m}$ are calculated. They are expected to be constant at reference and modified blade. These values can be calculated by solving a linear system of equations (LSE)

$$\underline{m} = \mathbf{A}_{ref}^{-1} \cdot \underline{p}_{ref} \qquad \text{with} \qquad \mathbf{A}_{ref} = f\left(\underline{q}_{ref}\right), \tag{3}$$

where $\underline{p}$ is the vector of all dynamic parameters p_j and $\mathbf{A}$ is the blade-matrix, which is a function of the airfoil geometry $\underline{q}$. With the knowledge of $\underline{m}$, the structural model of the modified blade can be calculated by

$$\underline{p}_{mod} = \mathbf{A}_{mod} \cdot \underline{m} \qquad \text{with} \qquad \mathbf{A}_{mod} = f\left(\underline{q}_{mod}\right). \tag{4}$$

Description of the Model. For the characteristic blade values, an improved and more realistic blade model is used. A beam at the quarter-chord line is added to the monocoque. This structure can take up longitudinal and shear forces, thus two characteristic blade values are Et and Gt. (cf. Fig. 3a). The additional stiffness of the beam is modelled with a central stiffness EA_B and $2EA_B$ at the ends, which can take up bending moments, too.

It is assumed that monocoque and beam have a constant density to Young's modulus ratio $\frac{\rho_{MO}}{E}$ and the infill is made of one material with the density ρ_{MA} (cf. Fig. 3b). The trim-mass is modeled with m_{trim} at the nose. The function to calculate the blade-matrix $\mathbf{A}$ can be derived by the definition of each parameter. For example, the extension stiffness of the whole cross section is the sum of all components

$$EA = (\ell_{MO} + \ell_B)\, Et + EA_B + 2EA_B. \tag{5}$$

Every other parameter can be derived accordingly. For torsion stiffness, a correlation between J and the wall thickness can by derived using Bredt-Batho formula.

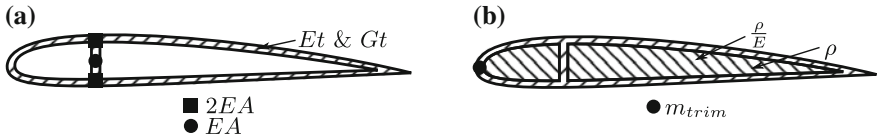

Fig. 3 Modeled blade for LSE method. **a** Model for stiffness. **b** Model for inertia

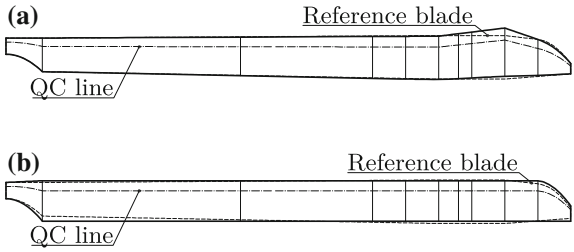

Fig. 4 Horizontal projection of the two test cases and the reference blade

With a known airfoil shape, all values depending on the airfoil like perimeter ℓ_{MO}, height of beam ℓ_B, area or second moments of area can be calculated numerically.

3 Effects of the Adapted Structural Model

3.1 Definition of the Test Cases

To analyse the effects of the adaptation of blade's structural model, a reference blade was chosen. Its geometry was changed in two test cases, as can be seen in Fig. 4. Test case *IncChord* (cf. Fig. 4a) is predominantly effected by the geometric parameters, in contrast to test case *RefChord* (cf. Fig. 4b), where primarily cross sections are scaled and not moved.

Five different adaptations of the structural model were made. First, the structural model of the reference blade was used with no adaptations (*NA*). For a comparison to the state of the art method, a test case was performed where only the geometric parameters were adapted (*OG*). Two cases for the scaling method were executed. First with the scaling factors for a massive cross section (*MA*), and second with the scaling factors for a monocoque cross section (*MO*). The fifth structural model was generated with the LSE method (*LSE*).

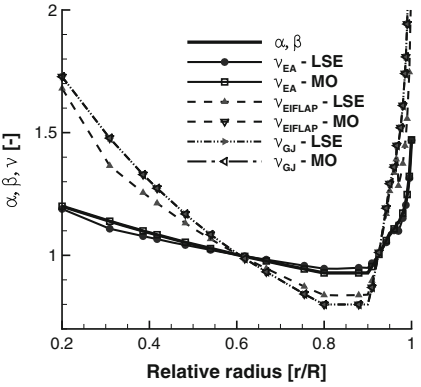

Fig. 5 Comparison of some normed stiffness parameters for test case *RefChord*

3.2 Effects on Structural Model

As can be seen in Fig. 4b, for test case *RefChord*, airfoil cross sections are scaled up in the first half of the rotor blade and at the tip and scaled down in the second half of the blade. Due to equal scaling ($\alpha = \beta$), with scaling method monocoque, extension stiffness scaling factor is proportional to α. Scaling factors for extension stiffness, calculated with the various methods do not show significant deviations (Fig. 5). The scaling factors for second moments of area like flapping bending stiffness EI_{FLAP} and torsion stiffness GJ calculated with the scaling method monocoque are proportional to the third power of α. The same behaviour is seen with $\nu_{GJ,LSE}$ in the special case of equal scaling. For bending stiffness, differences between the methods are bigger than for extension stiffness, but still both methods show similar results, especially in the context of the quite big scaling factors used here. At the tip region, markable differences between the two methods are present. It can be expected, that blade structure in reality is not in accordance with the LSE model for radii greater than 0.9. Thus, probably LSE method is closer to reality at the mid part of the blade, whereas the scaling method is to be preferred at the tip region.

3.3 Effects to Fluid-Structure CFD-CSD Coupled Simulations

Setup. For each test case and for each structural model, fluid-structure coupled CFD-CSD simulations have been performed for a trimmed isolated main rotor in cruise conditions. The used CSD program was CAMRAD II [2] and the CFD-solver was FLOWer [5]. The control angles were calculated by CAMRAD II to achieve the prescribed thrust as well as pitch and roll moment. Data exchange between CSD and CFD was once per revolution with a temporal resolution of 1° per timestep. Convergence was reached, if the change in all control angles between the previous and the actual iteration was less than 0.02°, which took 5–7 iterations. The total

CFD-setup consisted of 6.8 million cells, which includes 1.32 million cells for each of the 4 blades meshes and 1.54 million cells for the background grid.

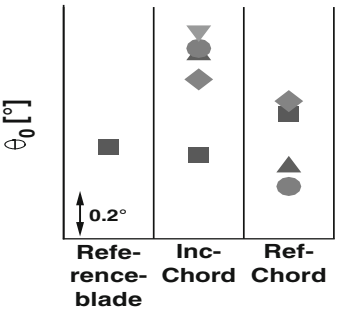

Fig. 6 Collective pitch

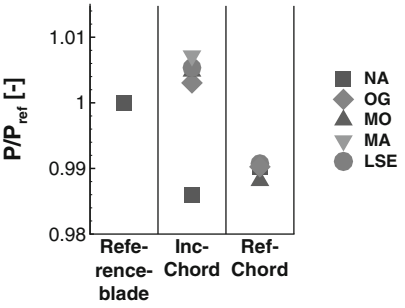

Fig. 7 Required power, referred to reference blade

Collective Pitch and Required Rotor Power. The collective pitch is shown in Fig. 6. It can be seen, that the effect of the adaptation of the structural model with up to 0.6° is not negligible. The main effects for test case *IncChord* result from the change of the geometric parameters. The collective pitch of the solution for test case *OG* is quite close to the other solutions and between the different methods, there is no significant difference. On the contrary for test case *RefChord* stiffness and inertia parameters are more important. Only adapting the geometry parameters almost does not have any effect. This emphasizes that the difference between the scaling method monocoque and the LSE method is quite small.

It was expected that a changed collective pitch has an impact on the required rotor power, too. This was verified by the simulations for test case *IncChord* (cf. Fig. 7). The increased pitch leads to an increased power. In contrast, a raised power requirement cannot be found for test case *RefChord*. Although the collective pitch was affected by the adaptation of the structural model, there is no appreciable difference for the rotor power. This is caused by the increased torsion stiffness for small radii which requires a smaller collective pitch for the same angles of attack.

Thrust. To discuss the effects of the adaptation of the structural model on aerodynamics, the rotor thrust is considered. Figure 8 shows the integrated blade thrust normalized by the average thrust for test case *IncChord*. In contrast to the retreating blade, the advancing blade in the area of $0° \leq \psi \leq 120°$ shows obvious differences. As already observed for the collective pitch, deviations between the different scaling methods do also not exist here. The effect, that for this test case the geometric parameters dominate can be seen as well.

To analyse the places where the adaptation leads to changes, it is useful to consider the difference between a simulation with an adapted structural model and the simulation with the non adapted model over the rotor-disc. This is shown in Fig. 9 for the normalized radial force gradient for the LSE method, normalized by the ideal

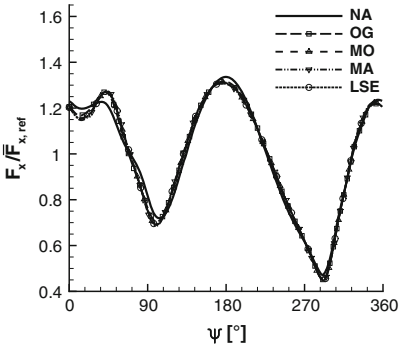

Fig. 8 Normalized integrated blade thrust for test case *IncChord*

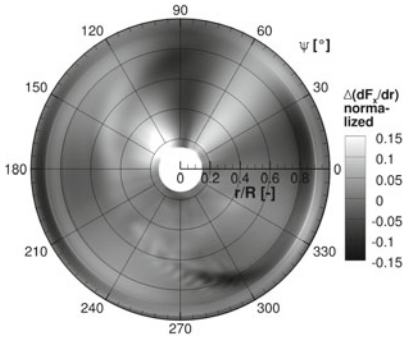

Fig. 9 Normalized difference of blade thrust for LSE method for test case *IncChord* to reference blade

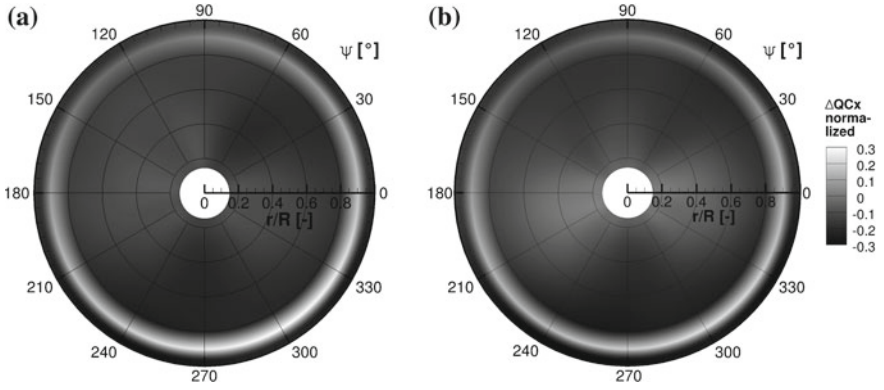

Fig. 10 Normalized difference of flapping movement for test case *IncChord*. **a** Monocoque cross section. **b** Massive cross section

thrust distribution. In a wide area, the differences are quite small. But especially at the advancing blade side, there are some quite small areas with significant differences up to 15 %.

Flapping Movement. The biggest effects of the adapted structural model are expected at the structural dynamics. Figure 10 shows the normalized differences for the flapping movement of the quarter-chord line for the two simulations of test case *IncChord* with the scaling method. Figure 10a shows the normalized deviation with the scaling for a monocoque and Fig. 10b for a massive cross section. The precone angle is used as reference value. Noticeable is the change of sign at $0.9\,R$. This is exactly the radial position with the biggest geometric change (cf. Fig. 4a). The flapping movement is the only value, where differences between the adaptation methods can be found. Due to the upscaling of the tip region, the blade becomes heavier for a massive than for a monocoque scaling. Thus centrifugal forces increase for a

massive scaling and the cone angle decreases. This is the reason why all differences in Fig. 10b are smaller than in Fig. 10a.

Nearby, the changed structural model has effects on eigenfrequencies and mode shapes, too. For flapping movement the amplitudes of the excited frequencies for NA, MO and LSE method are nearby the same. For lagging movement and torsion oscillation, amplitudes vary up to 20 %. A detailed analysis can be found in [4].

4 Conclusion and Outlook

Two different methods to adapt the structural model to geometric changes in blade design have been introduced. It was shown, that this adaptation is not negligible. For example, collective pitch is affected by up to 0.6° and rotor power by up to 2 % in the considered test cases. The areas in the rotor-disc which cause these differences are quite small, but these local differences are quite high with up to 15 %. Although the two used blade models for the scaling and the LSE method are different, the results of both methods are similar. The influence of the different parameter groups strongly depends on the modifications which were made.

Compared to other modelling approaches (cf. [1]), the introduced methods are very simple, and they can be executed, even if the exact composition of the blade is unknown. A reference blade is required and results will depend on the quality of this model. Due to the fact that no measured values are known, all evaluations are based on assumptions. It can be expected, that more detailed approaches will show better results, if the composition of the blade is known. The lack of measured values is a deficit which should be resolved in future. The automatic adaptation is implemented in the process chain for the flight mechanics program CAMRAD II, in future tasks this can be expanded to other programs like HOST [6] as well.

Acknowledgments The authors would like to thank Eurocopter Deutschland GmbH for its support. We also thank the members of the Helicopters and Aeroacoustics group at the IAG for their input and experience.

References

1. Hodges, D.H.: Review of composite rotor blade modelling. AIAA J. **28**(3), 561–565 (1990)
2. Johnson, W.: Comprehensive analytical model of rotorcraft aerodynamics and dynamics. Johnson Aeronautics Analytical Methods, Palo Alto (2007)
3. Johnson, W.: Rotorcraft dynamics models for a comprehensive analysis. In: American Helicopter Society Forum, Washington (1998)
4. Stanger, C.: Erweiterung des Prozesses zur Rotorblattoptimierung um automatische Anpassungen der Strukturmodellierung. Studienarbeit, Institut für Aerodynamik und Gasdynamik, Universität Stuttgart (2012)
5. Kroll, N., Eisfeld, B., Bleecke, H.M.: Flower. In: Kroll, N., Eisfeld, B., Bleecke, H.M. (eds.) Notes on Numerical Fluid Mechanics, vol. 71, pp. 58–71. Vieweg, Braunschweig (1999)
6. Benoit, B., et al.: HOST-Helicopter overall simulation tool-user manual. Eurocopter, France, Marignane (1997)

Part VI
Convective Flows

Flight Testing of Alternative Ventilation Systems for Aircraft Cabins

J. Bosbach, A. Heider, T. Dehne, M. Markwart, I. Gores and P. Bendfeldt

Abstract Cabin displacement ventilation (CDV) has been evaluated for the first time in a real passenger aircraft cabin under flight conditions. Two ventilation systems, i.e. pure CDV and a hybrid ventilation (HV) system, which provides 30 % of the total volume flow rate through the lateral mixing ventilation outlets, were tested in an A320 aircraft. While pure CDV was found to provide low air velocities, high heat removal efficiencies and a very good dynamic performance regarding control of the air temperatures, the hybrid system, still allowing for comfortable flow velocities and good heat removal efficiencies, was shown to significantly improve the cooling and heating rates at the cabin surfaces. With both systems, the local temperature in the passenger zone is distributed very homogeneously among the investigated seat and aisle positions.

1 Introduction

The atmosphere in passenger aircraft cabins, which is generated by the environmental control system (ECS), is essential for the health and thermal comfort of the travelers. Thereby the duties of the ECS are threefold: first, the cabin pressure has to be adjusted with respect to the flight level, yet kept at a healthy level. Second, the passengers have to be supplied with fresh air, and third the heat loads in the cabin, caused by the passengers themselves as well as board electronics, have to be removed in order to keep the temperature at a comfortable level. Though the ECS is a complex system,

J. Bosbach (✉) · A. Heider · T. Dehne
Institute of Aerodynamics and Flow Techology, German Aerospace Center (DLR),
Bunsenstr. 10, 37073 Göttingen, Germany
e-mail: Johannes.Bosbach@dlr.de

M. Markwart · I. Gores · P. Bendfeldt
Environmental Control Systems, Airbus Operations GmbH, Kreetslag 10,
21129 Hamburg, Germany

A. Dillmann et al. (eds.), *New Results in Numerical and Experimental Fluid Mechanics IX*,
Notes on Numerical Fluid Mechanics and Multidisciplinary Design 124,
DOI: 10.1007/978-3-319-03158-3_28,

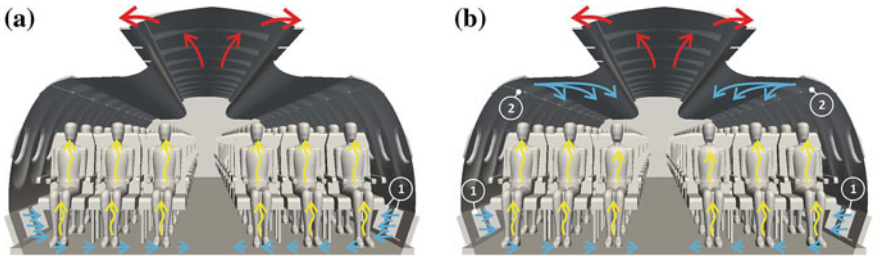

Fig. 1 Alternative ventilation methods for aircraft cabins. **a** Cabin displacement ventilation (CDV), **b** hybrid ventilation (HV). The involved air outlets are indicated in **b** by *1* (CDV outlets) and *2* (lateral MV outlets)

constituted by a variety of different subsystems, the air flow through the passenger cabin ("ventilation") has turned out to be essential in order to address the above mentioned aspects.

Nowadays employed ventilation systems are based on the principle of mixing ventilation (MV), where fresh air is blown into the cabin via jets of rather high momentum [1]. The shear layers generated by these jets cause entrainment of recirculated air and thus efficient mixing before the air leaves the cabin at floor level. While MV usually results in homogeneous temperature distributions, its cooling efficiency is limited by a high amount of short circuit flows. Further, among other potential drawbacks, MV is known to be prone to draught, and exsiccation of mucosa.

Since displacement ventilation (DV) is expected to be far less susceptible to many of these issues, it is investigated since a few years as an alternative for air conditioning of aircraft cabins (CDV—cabin displacement ventilation) [2–6]. CDV relies upon injection of fresh air into the cabin with low velocity at floor level, where it generates a "lake of fresh air", see Fig. 1a. Near the thermal loads, like e.g. passengers, the fresh air heats up and rises due to buoyancy prior to extraction at ceiling level. Like this, each thermal load generates its own fresh air bubble. As a result, much lower fluid velocities and turbulence levels are expected. However, all of the studies reported so far were either based on computational fluid dynamics (CFD) or conducted on a laboratory scale. Validation of the advantages under real conditions, which is the aim of our study, has still been lacking.

2 Alternative Ventilation Systems for Aircraft Cabins

To overcome the deficiencies of MV, CDV and personalized air distribution systems are mostly studied in the literature. Müller et al. [2] studied and compared MV, CDV and HV (see Fig. 1b) in an A320 mock-up cabin section. They investigated temperature and velocity distributions as well as local mean votes of test persons. At CDV, very low flow velocities were observed, indicating a significant reduction of

the draft risk as compared to MV. However, this finding was accompanied by the occurrence of a vertical temperature stratification, which requires proper control in order not to exceed comfort critical values. Zhang et al. studied MV, an under-floor CDV and a personalized air distribution system in a Boeing 767 aircraft cabin section using computational fluid dynamics (CFD) [3]. They found that MV generated the most uniform air temperature, but the highest air velocities and CO_2 concentrations, while the personalized air distribution system created the best cabin environment. Yin et al. [4], who compared MV and CDV in the same configuration by CFD, recommend CDV for use in future airplanes because CDV was found to lessen the local CO_2 concentrations and to improve the relative humidity without causing condensation risks. Recently, a ceiling based cabin displacement ventilation (CCDV) system was investigated in a Dornier 728 aircraft cabin under laboratory conditions and compared to MV and CDV regarding velocity and temperature distributions as well as efficient heat removal [6]. In total six different ventilation scenarios, involving hybrid CCDV/CDV cases were studied. CDV was found to provide the lowest velocity levels and the most efficient heat removal of the investigated scenarios with the drawback of the strongest vertical temperature stratification. However, adjusting the flow split between CDV and CCDV allows well to balance out these parameters to the desired value.

Our study (see also [5]) extends the above cited literature, in that it aims at proving the potential benefits of CDV for the first time under real flight conditions, i.e. at a realistic fluid density and thus characteristic numbers. To our knowledge, this is the first time that the dynamic performance of the different aircraft cabin ventilation concepts is addressed.

3 Aircraft

3.1 General Description

As test platform for the ground and flight tests, the "Advanced Technology Research Aircraft" (ATRA) of the German Aerospace Center (DLR), which is an Airbus A320-232 (MSN659) and the largest test bed of the DLR fleet, was chosen.

3.2 Cabin Layout

Approximately one half of the ATRA cabin was refurbished to CDV, see Fig. 2, allowing for a measurement section, which extended from frame number 46 to 62. The latter was separated by foam walls of 0.4 m thickness on each side from the rest of the cabin in order to ensure thermal insulation and to prevent air flow in longitudinal direction. The front part of the cabin was used to install the operator, measurement and dummy power supply racks.

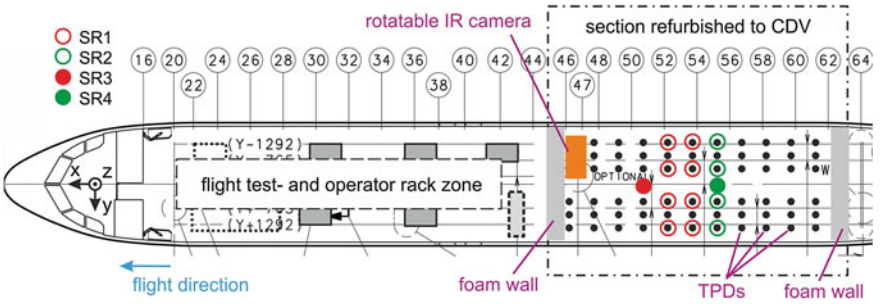

Fig. 2 Cabin layout and the relevant components of the cabin flight test installation

3.3 Integration of Cabin Displacement Ventilation

CDV outlets were installed in place of the original dado[1] panels, see Fig. 1a. They have a total active surface of 3.68 m^2 in the measurement section. The preexisting lateral MV outlets were kept in place in order to generate hybrid ventilation, see Fig. 1b. In both scenarios, the used air left the cabin through the pre-existing openings and gaps of the ceiling outlets.

4 Flight Test Installation

A cabin flight test installation (FTI), comprising 63 thermal passenger dummies and in total more than 200 sensors installed in the test section, see Fig. 2. It is described briefly in the following—for details see [5].

The thermal passenger dummies (TPDs) were arranged in 11 seat rows in the measurement section at a seat pitch of 31 in. and operated under constant heat flux conditions. Measurements in the fluid were conducted using four different types of sensor-racks, which we refer to as SR1, SR2, SR3 and SR4, see Fig. 2. SR1 and SR2 were positioned near the TPDs and placed their sensors 5 cm apart from the TPD surface, i.e. close, yet outside the boundary layers. The SR1s comprised combined omnidirectional velocity and temperature probes at three levels and a reference temperature sensor (RTD—resistance temperature detector), whereas the SR2s comprised RTDs at 10 levels. SR3 and SR4 were placed in the aisle. SR3 was equipped with combined omnidirectional velocity and temperature sensors at 6 levels, while SR4 comprised RTDs at 12 levels. 24 RTDs were glued with painted aluminum tape on the interior floor, hat-rack, side-panel, windows and ceiling panel surfaces. 20 additional RTDs were installed in the CDV, lateral and ceiling air outlets.

Complementary to the surface sensors, a programmable, step motor driven, automatically rotatable infrared camera set-up was installed in the front of the

[1] "dado" is an architectural term, which describes the lower portion of a wall.

Table 1 Test conditions in measurement section during steady climate scenarios

	CDV ground	CDV flight	HV ground	HV flight
$\mathbf{q}_V$ (l/s)	743(7)	721	732	717(2)
$\mathbf{P}_{TPD}$ (kW)	4.73	4.73	4.73	4.73
$\mathbf{P}_{Cable}$ (kW)	0.40	0.40	0.40	0.40
$\mathbf{P}_{light}$ (kW)	2.00	2.00	2.00	2.00
p (hPa)	1022	768	1024	768(5)
Ma	0	0.78	0	0.78
ALT (ft)	16	37154..37251	16	37267..38339

q_V volume flow rate, P_{TPD} total heating power of TPDs, P_{Cable} total heating power of TPD supply cables, P_{light} total heating power of cabin illumination, p cabin pressure, Ma Mach number, ALT altitude. If the variations exceed the last digit, the standard deviations are given in brackets

measurement section. The appliance allows taking a panorama image of the whole cabin interior every minute.

Further sensors, not relevant for the following discussions, were installed [5].

5 Investigated Scenarios

Two ventilation scenarios are discussed in the following: pure CDV and HV, where 30 % of the air was supplied by the lateral MV outlets. Both scenarios were studied under static and dynamic conditions. Table 1 summarizes the conditions for the steady scenarios. In addition, both systems have been investigated under transient conditions, i.e. upon sudden, stepwise changes of the inflow temperature. The other parameters of these dynamic scenarios are comparable to the ones listed in Table 1.

6 Experimental Results

6.1 Static Scenarios

An overview of the fluid velocity and temperature level is given in Fig. 3. A local temperature, T_{loc}, has been defined as the average of the air temperature at ankle, knee, chest and head level (z = 0.07, 0.55, 0.88 and 1.25 for SR1; z = 0.05, 0.6, 0.8, and 1.3 for SR2). At SR3 and SR4, similar height levels, corresponding to a standing person have been used (z = 0.05, 0.63, 1.14, and 1.70 for SR3; z = 0.05, 0.65, 1.25, and 1.65 for SR4). The mean temperatures were averaged again over the same y-position in three ($|y| > 0$), respectively two (y = 0, aisle) seat rows, see Fig. 3a.

In all scenarios, a very homogeneous distribution of the local temperature is found. Even if the aisle is considered, the maximal deviation from the mean value of all

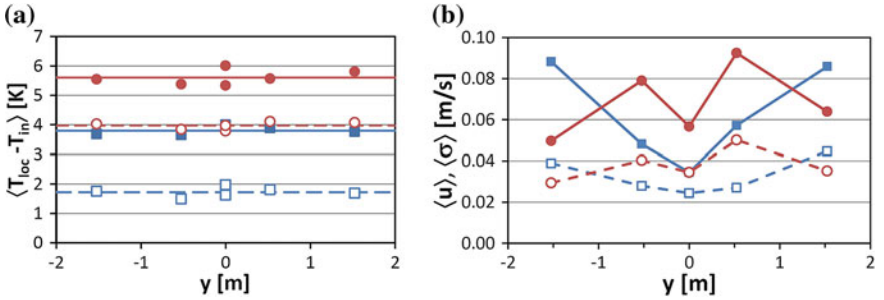

Fig. 3 Mean quantities evaluated near the TPDs and in the aisle for CDV and HV as a function of the position (y-coordinate) for CDV (*squares, blue*) and HV (*circles, red*). **a** Local temperatures during flight (*filled symbols*) and on ground (*open symbols*). *Lines* depict mean of respective data. **b** Flow velocity magnitudes (*filled symbols*) and spatiotemporal standard deviations (*open symbols*) during flight. The *lines* are just a guide to the eye

measures is as low as 0.27 K. This finding supports the image of the fresh air lake, which homogeneously distributes the air between the heat loads, regardless of the lateral injection into the cabin. The mean local temperature is always lower for the ground as compared to flight cases due to the higher fluid density and thus specific heat capacity per volume. At HV, the local mean temperature is significantly higher as compared to CDV, which indicates a larger amount of short circuit flows. The latter is caused by the lateral MV air jets, which homogeneously mix up with the warm cabin air, leading to the typical fact, that a considerable fraction of fresh air bypasses the heat loads and directly leaves the cabin at ceiling level. As a result, the cooling efficiency is lower for HV as compared to CDV, which in turn provides the lowest local fluid temperatures and thus the highest cooling efficiency.

Figure 3b unveils the mean velocity magnitudes and their spatiotemporal standard deviations, evaluated similar to the mean temperatures in Fig. 3a. For averaging, the sensors at ankle, knee and head level (z = 0.07, 0.55 and 1.25 m) were considered (SR1). In the aisle, the sensors at z = 0.05, 0.63, 1.14, and 1.7 m were considered (SR3). The mean fluid velocities and fluctuations are well below 0.1 m/s for both systems, and thus the draught risk is very low [7]. Though, a characteristic distribution between the cabin position in y-direction can be observed, reflecting the influence of the outlets at CDV (window seats) as well as the momentum of the lateral air jets at HV (aisle seats).

6.2 Dynamic Behavior

While both, HV and CDV, lead to homogeneous surface temperature distributions under static climate conditions [5], large differences in the performance are observed under dynamic conditions: Fig. 4 shows the surface temperature changes after an abrupt reduction of the inflow temperature by approximately 12K (“pull-down”),

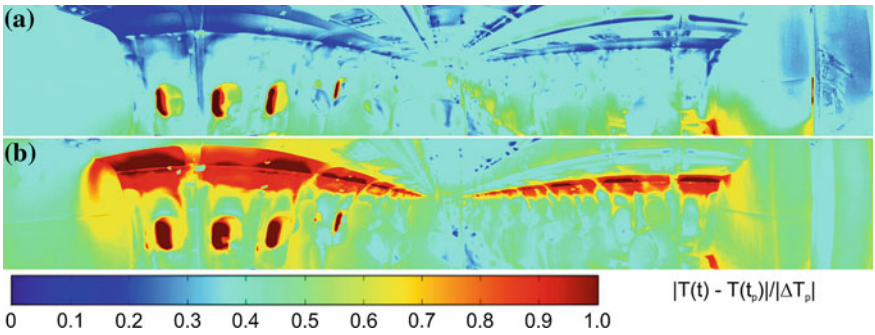

Fig. 4 Surface temperature distributions after pull-down, T(t), relative to the initial distributions $T(t_p)$ and normalized to ΔT_p for **a** CDV flight and **b** HV flight at $t\text{-}t_p = 2000$ s

measured during flight with the rotatable infrared camera. At CDV, the surface temperature changes proceed from the lower to the upper cabin part and stay below 50 % of the applied temperature jump even after 2000 s in most parts. Using HV, the surface temperature changes are much larger, and the distribution is qualitatively different: Even though they carry only 30 % of the volume flow rate, the lateral air jets induce a significant gain in surface cooling rates in their surroundings. After 2000 s, most of the cabin surfaces reach more than 50 % of the applied temperature jump.

In order to further characterize the cooling performance of HV and CDV, the temperature response of the RTDs at different height levels and fluid positions have been evaluated accordingly, see Fig. 5a. Clearly the curves deviate from simple exponentials, which would lead to straight lines in the chosen scaling. We ascribe this to the heat exchange between fluid and surfaces of the cabin interior parts like hat-racks, side panels etc., which act as heat reservoirs and thus limit the dynamics of the whole system. However, the response time increases with z for CDV, reflecting the global flow direction, and the temperature changes of the air are much faster than for the surfaces. The dynamics is further characterized in Fig. 5b by $t_{0.3}$, which is the time, that a certain mean temperature needs to reach 30 % of the applied temperature jump $\Delta T_p(t)$.

While $t_{0.3}$ is smaller for CDV and $z < 1$ m, HV is generally faster for $z > 1$ m and at the upper cabin surfaces. On the floor, which is influenced by the heat reservoir of the cargo compartment, very high $t_{0.3}$ are observed. We conclude, that the convection based air guidance principle of CDV supports fast air temperature changes in the passenger zone due to the fact, that fresh air is attracted by and thus quickly exchanged at the heat loads. Supply of fresh air to and thus efficient cooling of the passive cabin surfaces, however, is strongly supported by the pressure gradients and turbulence induced by the lateral MV outlets at HV. Comparison of pull-up and pull-down for HV unveils significant differences in the $t_{0.3}$ distribution, stemming from the fact, that the lateral air jet is affected by buoyancy forces, which have opposite sign in

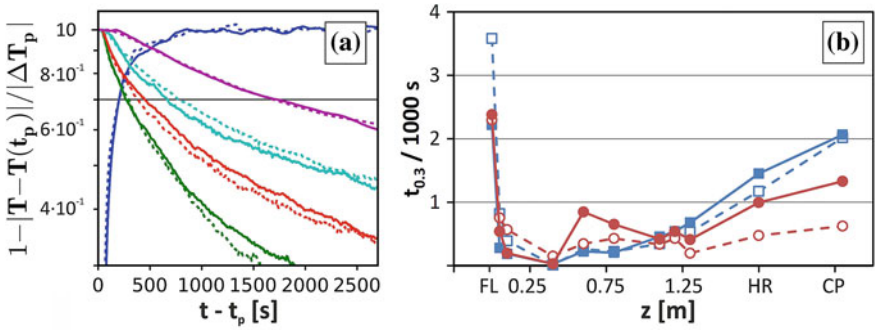

Fig. 5 **a** Normalized temperature differences as a function of time during "pull-up" (*solid lines*) and "pull-down" (*dotted lines*) for "CDV flight". *Blue* incoming air, *green* mean of all SR2 sensors at z = 0.4 m, *red* mean of all SR2 sensors at z = 0.6 m, *cyan* mean of all SR2 sensors at z = 1.3 m, *magenta* mean of all RTDs at ceiling, side-panels, hatracks and floor surfaces. **b** $t_{0.3}$ for different positions for CDV (*squares*) and HV (*circles*) during "pull-down" (*filled symbols*) and "pull-up" (*open symbols*). The values for $0 < z < 1.75$ m correspond to the mean fluid temperatures in the passenger zone. In addition, $t_{0.3}$ is given for the sensors at floor (FL), hat-rack (HR) and ceiling panel (CP) surfaces. The *lines* are just a guide to the eye

both scenarios. We think that the change of the $t_{0.3}$ distribution between pull-up and pull-down is a consequence of premature jet separation [1] during pull-down.

7 Conclusions

CDV and HV have been evaluated for the first time under flight conditions in an A320 aircraft. In addition to the stationary performance, the dynamic behaviour was investigated. Our measurements unveil homogeneous lateral temperature distributions and low flow velocity levels in the passenger zone for both systems. The different fluid temperature levels for HV and CDV directly reflect the higher cooling efficiency of the CDV system, which also provides a better performance regarding control of the air temperatures in the passenger zone. The HV system, however, relying partly upon classical jet ventilation, exhibits higher surface cooling rates as compared to CDV.

Acknowledgments This project was supported by the German Federal Ministry of Economics and Technology under the grant numbers 20K0806D, 20K0806A and 20K0702A on the basis of a decision of the German Bundestag. The responsibility of the content is the authors. We thank all colleagues at Airbus Operations and the German Aerospace Center, who contributed to the successful preparation and performance of the ground and flight tests.

Supported by:

on the basis of a decision
by the German Bundestag

References

1. Kühn, M., Bosbach, J., Wagner, C.: Experimental parametric study of forced and mixed convection in a passenger aircraft cabin mock-up. Build. Environ. **44**(5), 961–970 (2009)
2. Müller, D., Schmidt, M., Müller, B.: Application of a Displacement Ventilation System for Air Distribution in Aircraft Cabins, AST 2011, March 31–April 1. Hamburg, Germany (2011)
3. Zhang, T., Chen, Q.: Novel air distribution systems for commercial aircraft cabins. Build. Environ. **42**(4), 1675–1684 (2007)
4. Yin, S., Zhang, T.A.: A New Under-Aisle Displacement Air Distribution System for Wide-Body Aircraft Cabins, Building Simulation 2009. Glasgow, Scotland, pp. 1030–1036, (2009)
5. Bosbach, J., Heider, A., Dehne, T., Markwart, M., Gores, I., Bendfeldt, P.: Evaluation of cabin displacement ventilation under flight conditions. In: ICAS2012, paper 304, September 23–28. Brisbane, Australia (2012)
6. Bosbach, J., Lange, S., Dehne, T., Lauenroth, G., Hesselbach, F., Allzeit, M.: Alternative ventilation concepts for aircraft cabins. CEAS Aeronaut. J. **4**(3), 301–313 (2013)
7. Ergonomics of the thermal environment—Analytical determination and interpretation of thermal comfort using calculation of the PMV and PPD indices and local thermal comfort criteria, DIN ISO 7730:2005(E)

Large-scale Coherent Structures in Turbulent Mixed Convective Air Flow

Andreas Westhoff, Johannes Bosbach and Claus Wagner

Abstract We report on an experimental study of mixed convective air flow in a cuboidal container with an inlet and outlet slot at $\mathcal{A}r = 3.3$, $\mathcal{R}e = 1.0 \times 10^4$, $\mathcal{R}a = 2.4 \times 10^8$ at a fluid pressure of $P = 11.6\,\mathsf{bar}$. Particle image velocimetry were performed with the objective to identify the dynamics of the large-scale circulations. In addition, we applied temperature measurements to determine the heat transport. Due to the unsteady nature of mixed convection in the present configuration, the velocity vector fields were subjected to a proper orthogonal decomposition in order to extract the predominant coherent structures. The analysis uncovers two structures consisting of three and four thermally induced large-scale circulations, which are arranged in longitudinal direction. Further, we found that the dynamics and the topology of the convection rolls strongly influences the heat transport between the container‘s inlet and outlet.

1 Introduction

Convection describes the process of heat transport due to the movement of ensembles of molecules within fluids. In general, a distinction is made between two basic types of convective flows: thermal convection, also referred to as free or natural convection, and forced convection. The expression thermal convection is given to the category of flows, which are driven by externally induced temperature gradients, while in forced convection, the motion of fluid and the transport of heat is governed by pressure gradients, e.g. caused by pumps or fans. If both coexist and have the same order of magnitude, the flow is termed as mixed convection. Mixed convection is characterised

A. Westhoff (✉) · J. Bosbach · C. Wagner
Simulation Center of Aerodynamic Research in Transportation (SCART), German Aerospace Center (DLR), Institute of Aerodynamics and Flow Technology, Bunsenstraße 10, 37073 Göttingen, Germany
e-mail: andreas.westhoff@dlr.de

A. Dillmann et al. (eds.), *New Results in Numerical and Experimental Fluid Mechanics IX*, Notes on Numerical Fluid Mechanics and Multidisciplinary Design 124,
DOI: 10.1007/978-3-319-03158-3_29,

by the non-dimensional numbers: the Rayleigh number $\mathcal{R}a = {}^{g\alpha\Delta\Theta H^3}/_{\nu\kappa}$ as a measure for the thermal convective flow, the Reynolds number $\mathcal{R}e = {}^{UH}/_{\nu}$ for the forced flow and the Prandtl number $\mathcal{P}r = {}^{\nu}/_{\kappa}$ for the fluid properties. Here g denotes the gravitational acceleration, α the thermal expansion coefficient, $\Delta\Theta$ the characteristic temperature difference, H the characteristic height, ν the kinematic viscosity, κ the thermal diffusivity and U the characteristic velocity. In addition, the Archimedes number $\mathcal{A}r = {}^{\mathcal{R}a}/_{\mathcal{R}e^2\mathcal{P}r} = {}^{\Delta\Theta\alpha g L^3}/_{U^2}$ is another frequently used parameter to characterise mixed convection. It represents the ratio of buoyancy to inertia forces. Convective flows with $\mathcal{A}r \ll 1$ are predominated by inertia forces and can be assigned to forced convection. If $\mathcal{A}r \gg 1$, the flow is governed by buoyancy forces and it is referred to as thermal convection. Convective flows with $\mathcal{A}r \approx 1$, i.e. if inertia and buoyancy forces have the same order of magnitude, belong to the regime of mixed convection.

The phenomenon convection, and in particular, mixed convection, occurs abundantly in nature and is of utmost importance in numerous applications. Often, convective flows emerge on large scales, like in meteorology [8], indoor air-conditioning [4] or other technical applications [1, 5]. Consequently, a direct experimental study requires often an unreasonable effort or is even impossible. To overcome that issue, a concept of spatial scaling [12] is utilised to obtain high characteristic numbers on laboratory scales. In accordance with this concept, the characteristic velocity U and the fluid pressure were adjusted to obtain the characteristic numbers comparable to a container whose spatial dimensions would be larger by a factor five. Here, we present and discuss results of turbulent mixed convective air flow in a cuboidal container with the focus on the dynamics of the thermally induced large-scale circulations and their influence on the heat transport.

2 Experimental Setup

A sketch of the container's geometry is illustrated in Fig. 1. In principle, the enclosure corresponds to a Rayleigh-Bènard container, consisting of a rectangular box with a quadratic cross-section, isothermally heated from below and cooled from above. The aspect ratios are $\Gamma_{\mathsf{LH}} = {}^{\mathsf{length}}/_{\mathsf{height}} = 5$ and $\Gamma_{\mathsf{WH}} = {}^{\mathsf{width}}/_{\mathsf{height}} = 1$.

In addition, the container is equipped with an air inlet and outlet (Fig. 1). The inlet is placed at the top and the outlet at the bottom. Both slots are located on the same side and span over the whole length, where the height of the inlet and outlet is $H_{\mathsf{in}} = 0.05 \times H$ and $H_{\mathsf{out}} = 0.03 \times H$ respectively. To guarantee well-defined and reproducible inflow conditions the container is additionally equipped with an inflow channel. Thus, at the inlet slot a fully developed velocity profile is obtained. The outlet is equipped with a channel to provide an undisturbed outflow. This configuration ensures well-defined forced convective flow.

The dimensions of the experimental setup are listed in the table of Fig. 1, where H denotes the height, L the length, W the width, H_{in} the height of the inlet channel,

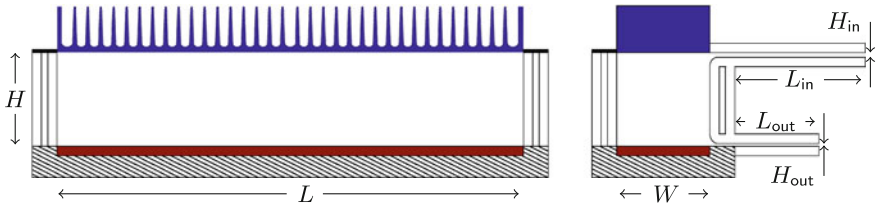

H	L	W	H_{in}	H_{out}	L_{in}	L_{out}
100	500	100	5	3	150	110

Fig. 1 Sketch of the container's geometry with an aspect ratio of 1 : 1 : 5 and the corresponding lengths. All dimensions are in mm

H_{out} the height of the outlet channel, L_{in} the length of the inlet channel and L_{out} the length of the outlet channel.

The measurements were performed in the High Pressure Wind Tunnel Göt- tingen (HDG). The HDG is a Göttingen-type closed circuit low speed wind tunnel, which can be operated at fluid pressures up to 100 bar. The function of the HDG in the experiments is twofold. The HDG allows the adjustment of the fluid pressure and supplies the cooling of the ceiling. The measurements of this study are performed at an ambient pressure $P \approx 11.6$ bar.

With the objective to determine the characteristic temperature difference $\Delta\Theta$, the setup is equipped with numerous temperature sensors. Here, eight sensors are placed shortly below the surface of the top and bottom plate. Further, five sensors are placed into the outlet slot in order to verify the heat transport between the container's inlet and outlet.

3 Proper Orthogonal Decomposition (POD)

For the present configuration, a key feature is the formation of large-scale coherent roll structures. To examine the structure formation and their dynamics, Particle Image Velocimetry (PIV) [6] was utilised in the longitudinal cross-section $Y = 0.5 \times W$ to measure planar velocity vector fields. However, for the parameters of this study, mixed convection is turbulent and far from equilibrium. To this end, the velocity vector fields were subjected to a Proper Orthogonal Decomposition (POD). It was applied to an ensemble of 4,800 velocity vector fields to extract the topology of the predominant large-scale coherent flow structures and their trajectories in time. For practical applications basically two methods of the POD exist: the direct method introduced by Berkooz et al. [2] and the snapshot method by Sirovic [9]. For the analysis of the present data, the latter method was used.

Considering, an ensemble of vectorfields fields $\left\{\mathbf{u}^{(n)}\right\}$ and $\mathbf{u} = \mathbf{u}(\mathbf{x})$, where $\mathbf{x}$ denotes the spatial coordinates; the basic objective of the POD procedure is to find a new basis of orthonormal functions, as a linear combination

$$\mathbf{u}^{(\mathsf{n})}(\mathbf{x}, t_{\mathsf{n}}) = \sum_{\mathsf{k}=1}^{\mathsf{n}} \zeta_{\mathsf{k}}(t)\Psi_{\mathsf{k}}(\mathbf{x}). \tag{1}$$

Since the functions of the new basis are linearly independent, the eigenfunctions $\{\Psi_{\mathsf{n}}(\mathbf{x})\}$ are commonly termed as coherent structures. The corresponding eigenvalues can be interpreted as the kinetic energy. In principle, higher eigenvalues are obtained for eigenmodes, which represents larger structures. Thus, the eigenmodes with the largest eigenvalues often represent large-scale coherent structures. Hence, to identify large-scale structures, the eigenvalues are a valid indicator to identify the eigenmodes of interest. The eigenvectors $\zeta_{\mathsf{n}}(t)$ are functions of time and represent the trajectory in time of the corresponding coherent structures.

4 Results

In mixed convection, the formation of flow structures is determined by the mutual interplay of forced and thermal convection. Depending on the ratio of inertia to buoyancy forces, numerous coherent flow states are reached. For $\mathcal{A}r = 3.33$, the formation of flow structures is primarily governed by buoyancy forces. Figure 2 illustrates the time-averaged velocity vector field (Fig. 2a) and the two coherent structures (Figs. 2b and 2c) with the highest eigenvalues. Here, the magnitude of the velocity vectors are colour-coded and normalised with the characteristic mean inflow velocity U. Regarding, the coherent structures, the magnitude Ψ_{n} of the eigenfunctions are normalised as well. Furthermore, the velocity vectors and the vectors, reconstructed from the eigenfunction of the corresponding in plane velocity components, are scaled to one.

However, the time-averaged velocity field reveals just a phantom flow field, which never develops in the flow. It is the superposition of coherent flow states. Consequently, an analysis of the flow based on the time-averaged velocity field is obviously not promising. To find the large-scale coherent structures which are representative for the flow a POD was utilised on the in-plane velocity components of the instantaneous velocity fields. Figures 2b and 2c show the topology of the first and second mode coherent structure Ψ_1 and Ψ_2 representing the POD modes with the highest eigenvalues.

The coherent structure of the first mode discloses four almost symmetrically arranged counter-rotating large-scale circulations (LSC) with a preferred location of rising hot air in the centre region $X \approx 0.5 \times L$ and at the lateral walls. Accordingly, descending cold air is located at $X \approx 0.25 \times L$ and $X \approx 0.75 \times L$. A closer inspection of the coherent structure reveals that the LSCs centre is shifted towards the region of rising hot air. Moreover, a significant broadening of the horizontal flow at the top, relative to the flow over the heating plate, is observed. Both effects result from the interplay of the forced mean wind with thermal convection rolls. Besides the structure of four longitudinally arranged LSCs the POD uncovers another coherent structure, which is composed of large-scale roll structures. The structure Ψ_2 represents a pattern, which consists of three counter-rotating LSCs (Fig. 2c).

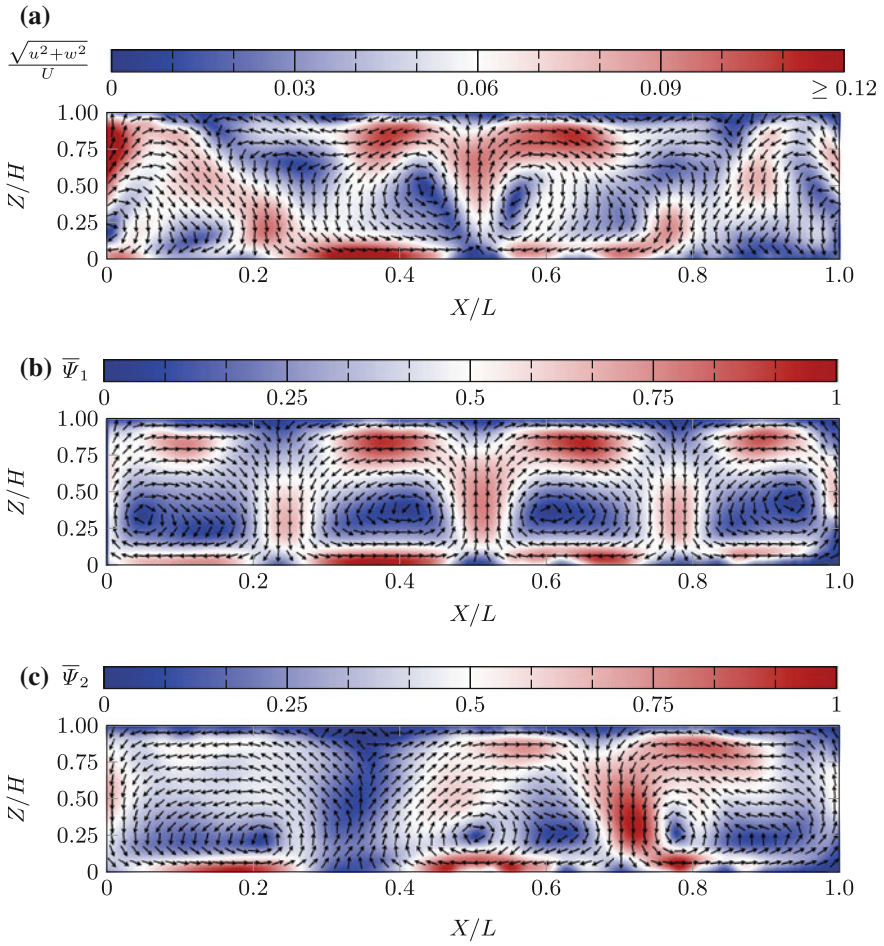

Fig. 2 Thermally induced lare-scale coherent structures in the longitudinal cross-section $Y = 0.5 \times W$ for $\mathcal{A}r = 3.33$, $\mathcal{R}e = 1.01 \times 10^4$ and $\mathcal{R}a = 2.39 \times 10^8$ under high pressure conditions $P = 11.6$. **a** The time-averaged in-plane velocity vector field. **b** The topology of the first POD mode coherrent structure Ψ_1. **c** The topology of the second POD mode coherrent structure Ψ_2

To determine the dynamics of the coherent structures Ψ_1 and Ψ_2, the time developing coefficients were analysed. The time developing coefficient of the first mode (Fig. 3 (black)) corresponds to the coherent structure consisting of four LSCs. Eigenvector ζ_1 reveals two periods $1{,}250\,\mathsf{s} \lesssim t \lesssim 2{,}750\,\mathsf{s}$ and $3{,}600\,\mathsf{s} \lesssim t \lesssim 7{,}200\,\mathsf{s}$, where the structure of four LSCs is present. Further, the change of the LSC rotational direction is indicated by the conversion. On the contrary, within the first period $0\,\mathsf{s} \lesssim t \lesssim 1{,}250\,\mathsf{s}$ and during $2{,}750\,\mathsf{s} \lesssim t \lesssim 3{,}600\,\mathsf{s}$, ζ_1 is approximately zero and the coherent structure of the second POD mode is predominant.

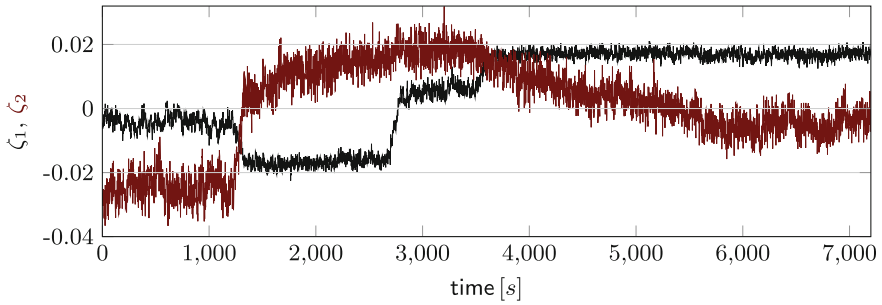

Fig. 3 The time developing coefficient of the first two POD modes ζ_1 and ζ_2 in the cross-section $Y = 0.5 \times L$ at $\mathcal{A}r = 3.33$, $\mathcal{R}e = 1.01 \times 10^4$ and $\mathcal{R}a = 2.39 \times 10^8$

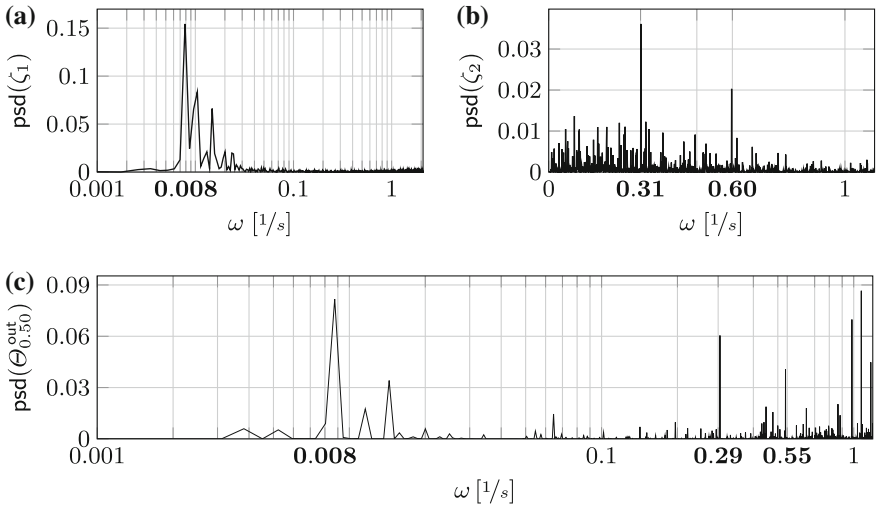

Fig. 4 The power spectrum of the first mode eigenvector of POD in the *longitudinal cross-section* $Y = 0.5 \times W$ (**a**), second mode eigenvector of POD in the *vertical cross-section* $X = 0.5 \times L$ (**b**) and the outlet temperature time series at $X = 0.5 \times L$ (**c**)

Besides the identification of sudden break-ups and flow reversals of the roll structures, the Fourier analysis of the POD eigenvectors reveals a time-periodic behaviour of the large-scale coherent structures. A very low characteristic frequency of the first mode $\omega = 2\pi f \approx 0.008\,\mathrm{s}^{-1}$ (Fig. 4a) is found. The physical process, which underlies this very low-frequency oscillation cannot fully be disclosed with the present data. However, due to studies of LSC in Rayleigh-Bènard convection [3] it seems reasonable to assume that this frequency has its origin in a torsional movement of the thermal convective roll structures. In addition, the eigenvectors of the POD in the vertical cross-section uncovers characteristic frequencies. The frequency $\omega \approx 0.6\,\mathrm{s}^{-1}$, for instance, corresponds to the mean angular velocity of the thermal convection rolls for the state of four counter-rotating LSCs. Moreover, this frequency indicates

that the thermal convection rolls rotate with a single frequency over hundreds of cycles, although the bulk is turbulent. Besides these two POD modes, several other POD modes are found, including characteristic frequencies. A detailed discussion and analysis of all these frequencies would go beyond the scope of the discussion in this chapter.

In the end, the time periodic dynamics of the LSCs influence the heat transport between the container's inlet and outlet. The power spectrum of the temperature time series in the outlet slot discloses characteristic frequencies, which correlate to those found in the power-spectra of the time developing coefficients of the dominant POD modes. For instance, the power spectrum of the temperature time series in the outlet slot at $X = 0.5 \times L$ (Fig. 4c) shows a similar time periodic behaviour like ζ_1 and ζ_2. Furthermore, the power spectrum of the temperature time series discloses peaks at $\omega \approx 1.0\,\mathrm{s}^{-1}$. These frequencies are almost similar to the angular velocity of the forced mean wind $\omega = 1.1\,\mathrm{s}^{-1}$ in the vertical cross-section $X = 0.5 \times L$. The angular velocities were calculated from velocity vector fields measured for isothermal flow at the same $\mathcal{R}e$ [10]. The finding of these frequencies shows a clear influence of the forced convective flow on the heat transfer, although the flow is primarily governed by thermal convection.

Regarding structure formation and dynamics, the results are in good agreement with findings in a lager container with the same geometry at similar characteristic numbers [11]. As well, there a coherent structure of four counter-rotating LSCs was found. However, clear differences can be identified. For instance, the measurements in the large container just reveal one large-scale coherent structure. A reason for the absence of additional coherent flow states is that the measurement was randomly performed within a period where the flow was featured by one coherent structure only, without any flow reversals or other erratic flow features. First results of temperature measurements with measuring times of several days substantiate this assumption. The study reveals flow reversals and sudden break-ups of the LSC also in the larger container [7]. These findings show that the dynamics of the large-scale structures are more complex as previously assumed [11].

5 Summary

Turbulent mixed convective air flow was experimentally studied in a cuboidal container at a fluid pressure $P = 11.6$ for $\mathcal{A}r = 3.3$, $\mathcal{R}a = 2.4 \times 10^8$, $\mathcal{R}e = 1.01 \times 10^4$ and $\mathcal{P}r = 0.7$. The container is uniformly heated from below and cooled from above. Additionally, it is equipped with an inlet and outlet slot. With the objective to identify the flow structures and their dynamics, PIV was performed in the longitudinal cross-section $Y = 0.5 \times W$. In addition, measurements of the temperature were conducted to determine the heat transport.

A POD was subjected to the ensemble of instantaneous velocity vector fields to identify large-scale coherent structures, their dynamics and the influence on the heat transport between the inlet and outlet slot. The POD discloses a predominant coher-

ent structure, which consists of four counter-rotating LSCs arranged in longitudinal direction. In addition, a second POD mode was found, which represents a coherent structure composed of three counter-rotating LSCs. The analysis of the corresponding time developing coefficients brings to light: flow reveals, sudden breakups and spontaneous re-organisation of the large-scale roll structures. Moreover, a frequency analysis of the POD time developing coefficients and the temperature time series at the outlet discloses numerous characteristic frequencies. The finding of similar frequencies in the time developing coefficients of the predominant large-scale coherent structures and the time series of the temperature at the outlet clearly shows that the dynamics of the forced and thermal convection rolls strongly influences the heat transport between the inlet and outlet of the container.

However, due to the long-time dynamics of the coherent structures, in particular, for higher Ar, measurements have to be performed over a longer period in order to uncover the full dynamics of the large-scale flow pattern. Nevertheless, we showed that it is possible to extract the prominent flow features from these relative short measurement periods by POD.

References

1. Baïri, A.: Nusselt-Rayleigh correlations for design of industrial elements: experimental and numerical investigations of natural convection in tilted square air filled enclosure. Heat Mass Transf. **42**, 56–63 (2008)
2. Berkooz, G., Holmes, P., Lumley, L.J.: The proper orthogonal decomposition in the analysis of turbulent flows. Annu. Rev. Fluid Mech. **25**, 539–575 (1993)
3. Funfschilling, D., Brown, E., Ahlers, G.: Torsional oscillations of the large-scale circulation in turbulent Rayleigh-Bénard convection. J. Fluid Mech. **607**, 119–139 (2008)
4. Linden, P.F.: The fluid mechanics of natural ventilation. Annu. Rev. Fluid Mech. **31**, 201–238 (1999)
5. Prvulovic, D., Tolmac, S., Lambic, M.: Convection drying in the food industry. Agric. Eng. Int. CIGR Ejournal **9**(9), 1–13 (2007)
6. Raffel, M., Willert, C.E., Kompenhans, J.: Particle Image Velocimetry. Springer, Berlin (1997)
7. Schmeling, D., Bosbach, J., Wagner, C.: Oscillations of the large-scale circulation in turbulent mixed convection in a closed rectangular cavity. Exp. Fluids, **54**(5), 1–15. Springer-Verlag (2013). doi:10.1007/s00348-013-1517-3
8. Silva Dias, P.L., Schubert, W.H., DeMaria, M.: Large-scale response of the tropical atmosphere to transientconvection. J. Atmos. Sci. **32**(9), 1244–1252 (1983)
9. Sirovich, L.: Turbulence and the dynamics of coherent structures part I: coherent structures. Quart. Appl. Math. **45**(3), 561–571 (1987)
10. Westhoff, A.: Spatial scaling of large-scale circulations and heat transport in turbulent mixed convection. PhD thesis, Georg-August University School of Science (GAUSS) (2012)
11. Westhoff, A., Bosbach, J., Schmeling, D., Wagner, C.: Experimental study of low-frequency oscillations and large-scale circulations in turbulent mixed convection. Int. J. Heat Fluid Flow **31**(5), 794–804 (2010)
12. Westhoff, A., Grabinski, N., Bosbach, J., Wagner, C., Thess, A.: Scaling of turbulent mixed convection under high pressure. In: Fifth International Symposium on Turbulence and Shear Flow Phenomena, vol. 2, pp. 505–510 (2007)

Numerical Simulation of the Air Flow and Thermal Comfort in Aircraft Cabins

Mikhail Konstantinov, Waldemar Lautenschlager, Andrei Shishkin and Claus Wagner

Abstract Results of a numerical study of the air flow and the thermal comfort of the passengers in an aircraft cabin which includes thermal radiation effects are presented. The computations have been performed by coupling flow simulations with the Computational Fluid Dynamics (CFD) code OpenFOAM with finite element simulations of the heat transport within the passengers using the code THESEUS-FE. With the latter the bodies of passengers are modeled based on various layers with different heat transport characteristics to account for effects like blood flow, skin, clothing as well as activity levels and ambient humidity. Computations of the flow, the thermal radiation and the modeled passenger comfort in the cabin of the Airbus A320 and Do728 are discussed. The predicted numerical temperature distributions in the cabin of Do728 have been supported by experimental measurements.

1 Introduction

Thermal comfort and the well-being of passengers in aircraft cabin are important criteria for airlines to purchase a specific aircraft. The thermal comfort of passengers sin particular is influenced by the air flow, the temperature distribution and the thermal radiation in a specific cabin configuration. The thermal comfort prediction in an aircraft cabin further depends on the numerous thermal sources, one of which is the passenger itself. Conventionally, in computations using Computational Fluid Dynamics (CFD) methods, the thermal boundary conditions are prescribed at the passenger/cabin air interface in terms of either the specified heat flux or isothermal temperature distributions. In this respect the passenger is considered as a passive heat source [1–3]. There are also more sophisticated thermal comfort models which

M. Konstantinov (✉) · W. Lautenschlager · A. Shishkin · C. Wagner
German Aerospace Center, Institute of Aerodynamics and Flow Technology, SCART,
Bunsenstraße 10, 37073 Göttingen, Germany
e-mail: mikhail.konstantinov@dlr.de

A. Dillmann et al. (eds.), *New Results in Numerical and Experimental Fluid Mechanics IX*,
Notes on Numerical Fluid Mechanics and Multidisciplinary Design 124,
DOI: 10.1007/978-3-319-03158-3_30,

consider a human body to consist of several layers with different heat conductivities and capacities also taking into account the heat transport in the cardiovascular system and the influence of clothing on the thermal comfort. Additionally, the influence of human activity levels and the ambient humidity on human physiology is also considered, albeit in empirical form.

The thermal comfort simulations presented below are based on a coupling of the finite volume method OpenFOAM which solves the unsteady Reynolds-averaged Navier-Stokes (URANS) equations using the Boussinesq approximation with the commercial finite element code, THESEUS-FE, developed by P+Z Engineering GmbH (FIALA-Manikin-Model) [4]. The model implemented in the latter considers all relevant thermo-physiological effects of a human body as described by D. Fiala et al. [5, 6]. It computes the so-called Zhang local sensation indices which describe the feeling temperature in a range from "very cold" to "very hot" [7]. Based on the latter the Zhang local comfort indices are evaluated which describe the sense of comfort in a range from "very uncomfortable" to "very comfortable" [8]. Using the coupled approach, computations of the flow and thermal comfort of passengers in cabin of the A-320 and the Do728 have been performed and are discussed below. Additionally, the calculated results are compared with those of subjective comfort studies obtained with of test persons in Do728 cabin.

2 Comfort Model

The heat transfer problems solved with THESEUS-FE software [4] are based on a thermal manikin the so-called FIALA-Manikin Model. The body of the latter is considered to consist of 54 body segments. For our simulations we reduced the number of segments to 14. So the head, the face and the neck of the FIALA-Manikin are combined to one segment of our Thermal Comfort Model (TCM). Further, one segment represents the torso. There are also the left and right segments of the upper arm, lower arm, hand, upper leg, lower leg and foot. Each these body segments consist of several material layers. Additionally, it is possible to define an individual clothing layer for any of the above discussed segments. Finally, it must be noted that the core of each segment has own attributes and that gender effects as well as differences in the human thermoregulation are not reflected. The distribution of body elements is shown in Fig. 1.

For each body segment the following partial differential equation is solved for all layers to describe the energy changes at each material point:

$$\rho c \frac{\partial T}{\partial t} = k \left(\frac{\partial^2 T}{\partial r^2} + \frac{\omega}{r} \frac{\partial T}{\partial r} \right) + q_m + \rho_b c_b w_b \left(T_{b,a} - T \right) \tag{1}$$

Here ρ is the density, c—the specific heat, k—the thermal conductivity, T—the temperature, q_m—the metabolic heat flow density, w_b—the blood perfusion rate and $T_{b,a}$—the calculated arterial temperature. The term $\rho_b c_b w_b (T_{b,a} - T)$ describes the

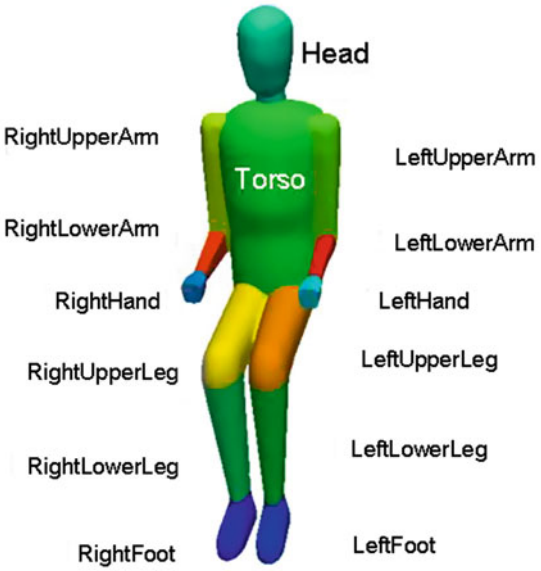

Fig. 1 Partitioning the body elements for calculation of local comfort indices

heating due to the arterial blood flow. Blood circulation is of vital importance for the dissipation of heat within the human body [5, 6]. The brain temperature would reach unrealistic values of more than 70 °C in a simulation without blood circulation. Body elements are simplified considering them as cylinders with the exception of the head (sphere) and r is a body element radius. The dimensionless parameter ω is 1 for cylindrical body elements (for example leg) and 2 for spherical body element (head). Thus, Eq. (1) describes the law of energy conservation at each material point of a layer that might represent skin, fat, muscle, bone, brain etc.

The local clothing properties of each garment were predicted using the model of McCullough [9]. The clothing is defined with thickness, clothing resistance, evaporate resistance, non-structural mass and specific heat. With the FIALA-Manikin surface (T_{sf}) and skin (T_{sk}) temperatures are computed. For calculations of the convective and radiative heat transport in complete aircraft cabins the value of T_{sf} is of major importance.

Different comfort evaluation indices can be modeled in our approach. First, an equivalent temperature T_{eq} is determined according to

$$T_{eq} = T_{sf} - \frac{q_{real}}{h_{cal}}, \tag{2}$$

$$q_{real} = R + C + E, \tag{3}$$

where q_{real}, R, C and E symbolize the realistic, radiation, convection and evaporation heat flux densities. Evaporation is estimated and calculated in THESEUS-FE by

a prescribed humidity. Further, h_{cal} denotes the combined heat transfer coefficient of this environment ($h_r + h_c$), where h_r is the radiation and h_c the convection heat transfer coefficient. The equivalent temperature denotes the temperature of homogeneous room with a radiation background temperature equal to the air temperature and the low relative air speed.

The equivalent temperature and any other comfort indices (e.g. both Zhang indices) were calculated by THESEUS.

The Zhang local Sensation Index (SI) is defined as a function of following parameters

$$SI = f\left(T_{sk,i}, \frac{dT_{sk,i}}{dt}, \overline{T}_{sk,i}, \dot{T}_{hy}\right), \tag{4}$$

where $T_{sk,i}$ is the skin temperature of the body segment i and T_{hy} – the hypothalamus temperature. The resulting sensation scale ranges from: 4—"very hot", 3—"hot", 2—"warm", 1—"slightly warm", 0—"neutral", −1—"slightly cool", −2—"cool", −3—"cold", −4—"very cold".

Based on Eq. (5) the Zhang Local thermal comfort index (Lc) is computed taking into account the Overall Thermal Sensation (So)

$$Lc_i = f\,(SI_i, So) \tag{5}$$

Zhang local comfort index ranges from 4—"very comfortable", 2—"comfortable", 0—"just comfortable" to −2—"uncomfortable", −4—"very uncomfortable". For details on the calculation of So the reader is refereed to [8].

3 OpenFOAM-THESEUS Coupling

For the data exchange between the flow simulations using OpenFOAM and the thermal comfort computation with THESEUS the following interface was developed. At the beginning of the simulations the initial temperature of the all body surfaces of the passengers is prescribed as follows: head—T = 308 K, torso—T = 308 K, the upper arms—T = 306 K, lower arms—T = 306 K, hands—T = 307 K, upper legs—T = 305 K, lower legs—T = 304 K and feet—T = 304 K. Using these initial conditions the Reynolds-averaged Navier-Stokes (RANS) simulations are started. After 100 iterations the heat flux densities due to radiation and convection are computed and written into an output file. From this file THESEUS obtains the heat flux densities and calculates a new set of surface temperature boundary conditions by solving the Eq. (1) of the FIALA-Manikin model. To obtain a good convergence of the solution in THESEUS-FE the number of inner iterations/time steps was chosen to be 10. Additionally steady state conditions as residual of 5e-4 have been prescribed. The results are an estimate of the response of a typical human body to the specified thermal loading. Further, an "equivalent" temperature which is used to assess the thermal comfort, as well as surface (and skin) temperatures are computed. The

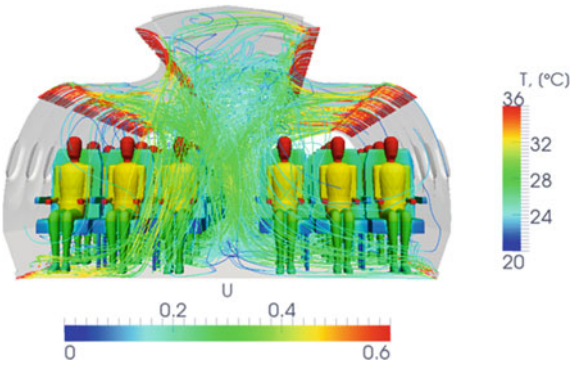

Fig. 2 Streamlines emerging from *inlet* surfaces and surface temperature distribution in A320

latter are then passed on to the RANS simulations by updating the surface temperature boundary condition through an intermediate output file. The whole procedure is repeated every 10 iterations.

4 Results of Coupled Simulations

The flow simulations were performed solving the RANS equations with the finite volume code OpenFOAM together with THESEUS-FE. The air flows in the cabins of the A320 and the Do728 were investigated. For a A320 segment the computational domain features 6 rows and 36 passengers, while for the Do728 cabin 3 rows and 15 passengers were considered. This means that for the passengers in the A320 cabin $14 \times 36 = 504$ separate body segment boundary conditions were needed while $14 \times 15 = 210$ body segment boundary conditions were used for Do728 cabin. At all air inlet planes the volume flux and its temperature value were prescribed. At the walls representing the sides, bottom, ceiling and windows temperature and heat flux were calculated. For the light-bands in A320 cabin the heat flux density of 300 W/m^2 was given. The unstructured grids used for A320-computations consisted of 22 Mio. cells and 14 Mio. cells for the Do728 cabin.

The conducted turbulent flow simulations include modeling of thermal surface to surface radiation. They were carried out with the "buoyantBoussinesq" solver of OpenFOAM by Engys. It solves the RANS equations together with k-ω/SST model. The computed velocity and temperature fields in the A320 cabin are presented in Fig. 2, where streamlines of the mean velocity emerging from the inlet and the resulting surface temperature distributions are visualized. At the four inlets region the volume flux and the temperature of 19 °C were prescribed. The calculated mean temperature in the cabin A320 reaches the value of 22.5 °C.

As mentioned above, heat flux densities on the passenger's surfaces are first computed and then passed on to the finite-element code THESEUS-FE. The latter updates the surface body temperatures with the FIALA-Manikin model. With

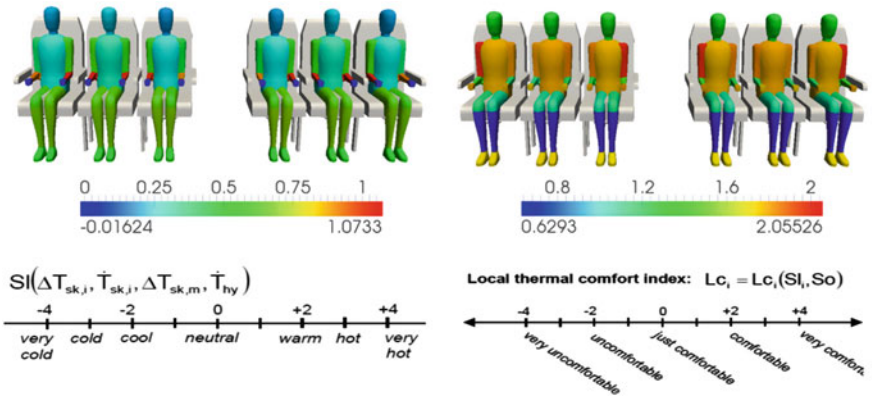

Fig. 3 Predicted distribution of the Zhang Sensation and the Local Comfort indices on the passengers in a row of the A320 cabin

these new temperature boundary conditions at the passenger surfaces the RANS simulations are continued. Additionally several comfort parameters such as the perceived temperature are also provided by THESEUS-FE. The calculated surface and skin temperature underline that a realistic choice of clothing data is important for the below discussed thermal comfort predictions. The latter is obtained by making use of the Zhang sensation and local comfort indices which are presented in Fig. 3. The analysis of these indices reveals the correlation between perceived temperature and the perceived comfort for each body segment of the passenger dummies. Thus, a perceived "neutral" temperature at the hands leads to comfortable situation, while a "slightly warm" perceived temperature at the lower arm is perceived as not comfortable.

5 Comparison of the Predicted and Measured Temperatures

The several experiments with test persons were carried out in the Do728 cabin test facility. In these test series the perceived thermal comfort was determined by analyzing questionnaires which were filled out by test persons. The experimental boundary conditions are reflected in the CFD simulations. To reach the mean cabin temperature of 24 °C the initial temperature of 17 °C at all four inlet regions was given. The total volume flux in experiment was about 47 *l/s* per passenger row. The CFD calculations were performed for cabin segment of 3 rows and the flux value was scaled accordingly.

During these test series the surface temperatures were additionally measured with a "VarioCAM" high resolution infrared camera. In Fig. 4 the measured and computed mean surface temperature on the body segments of passengers in one row are presented.

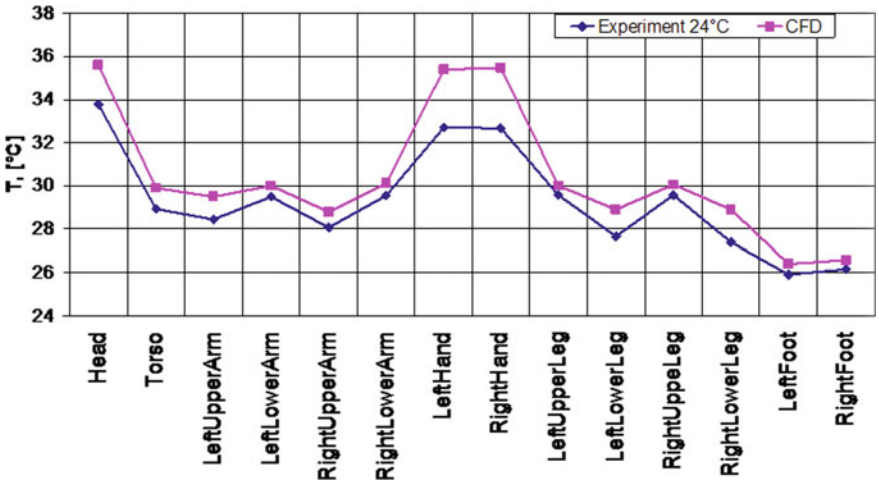

Fig. 4 Comparison of the computed (*magenta*) and measured (*blue*) mean temperature distribution on the body segments of one row of 5 passengers obtained at the cabin temperature $T_{cabin} = 24\,^{\circ}\mathrm{C}$

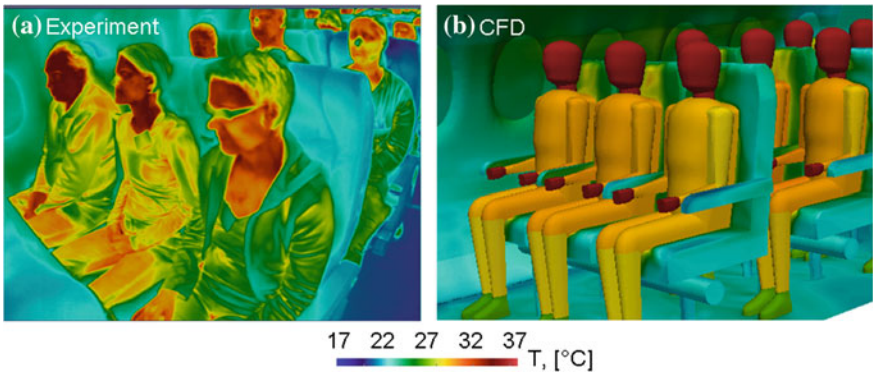

Fig. 5 Comparison of the measured (*left*) and the computed (*right*) surface temperature distribution in the cabin of Do728 at a mean temperature of $T_{cabin} = 24\,^{\circ}\mathrm{C}$

By postprocessing the infrared pictures for each body element have been adopted in one polygon in which the mean temperature value was determined. Although, the temperatures on the head and hands differ by about 2 °C the overall agreement is qualitatively good. Probably infrared camera has not enough resolution for these domains. For the investigated case the mean aircraft cabin temperature amounted to $T = 24\,^{\circ}\mathrm{C}$. Additionally, the comparison of predicted and measured surface temperatures in the Do728 cabin is shown in Fig. 5 in the same temperature interval. Again, a qualitative agreement is obtained. The major reasons for the observed quantitative differences are the differences in clothing in the test series and the computations.

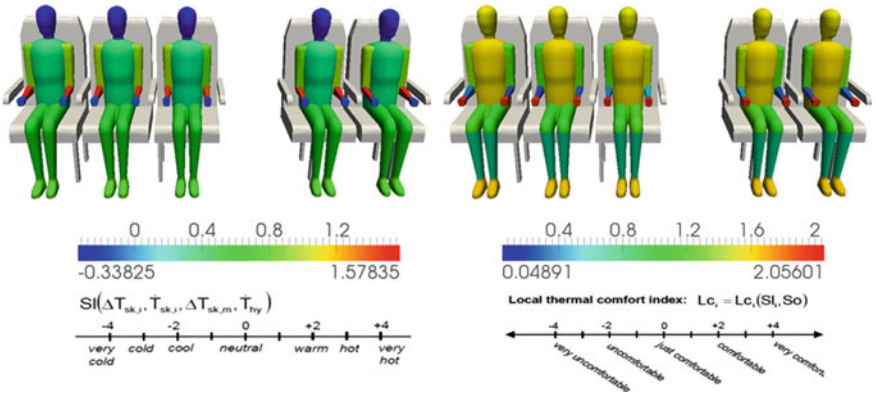

Fig. 6 Zhang sensation (*left*) and local comfort (*right*) indices in the cabin of Do728

Finally, the obtained Zhang indices for this test case are visualized in Fig. 6. The sensation index values of the heads and hands reveal a nearly neutral comfort sensation. At the lower arms the indices are higher which indicates that there the temperature might be perceived as slightly to warm. Still, the predicted local comfort values show, that the heads, hands, torso and feet perceive the conditions as comfortable. Only, the lower arms are reflected as just comfortable a “warm" sensation index.

6 Conclusions

The presented numerical thermal comfort predictions are based on the solution of the Reynolds-averaged Navier-Stokes equations using the Boussinesq approximation and modeling of surface to surface thermal radiation in two different aircraft cabins and the coupling with the finite element code THESEUS. The latter allows to simulate the heat transport within the passengers and the perceived temperature and comfort of passengers. It was shown that with the presented approach a qualitative and quantitative thermal comfort prediction is possible. The analysis of the results further revealed that a proper modeling of the clothing is of particular importance for a realistic prediction of the thermal radiation within cabin. The comparison of the results obtained in numerical simulations and those of test series with human beings in the Do728 cabin demonstrates a good agreement.

Acknowledgments We thank Dr. Stefan Paulke from P+Z Engineering GmbH for helpful discussions and perfect suggestions.

References

1. Rütten, M., Konstantinov, M., Wagner, C.: Analysis of cabin air ventilation in the Do728 test facility based on high-resolution thermography. Deutsches Luft- und Raumfahrtkongress 2008, Darmstadt (2008)
2. Konstantinov, M., Rütten, M., Lambert, M., Wagner, C.: Strahlung als wesentlicher Faktor der numerischen Simulation von Flugzeugkabineninnenströmungen für Komfortvorhersagen. Deutsches Luft- und Raumfahrtkongress 2009, ID: 121285, Aachen (2009)
3. Müller, D., Schmidt, M., Otto, S., Gores, I., Markwart, M.: Fully automated simulation process for comfort predictions in aircraft cabins. IndoorAir 2008 (2008)
4. THESEUS-FE Theory Manual, Version 4.0. P+Z Engineering GmbH, Munich (2011)
5. Fiala, D.: Dynamic Simulation of Human Heat Transfer and Thermal Comfort. Ph. D. Thesis. Inst. Energy and Sustainable Development, De Montfort University Leicester (1998)
6. Fiala, D., Lomas, K.J., Stohrer, M.: Computer prediction of human thermoregulatory responses to a wide range of environmental conditions. Int. J. Biometeorol. **45**, 143–159 (2001)
7. Zhang, H., Arens, E., Huizenga, C., Han, T.: Thermal sensation and comfort models for non-uniform and transient environments: Part I: Local sensation of individual body parts. J. Building and Environment. **45**, 380–388 (2010)
8. Zhang, H., Arens, E., Huizenga, C., Han, T.: Thermal sensation and comfort models for non-uniform and transient environments: Part II: Local comfort of individual body parts. J. Build. Environ. **45**, 389–398 (2010)
9. McCullough, E.A., Jones, B.W.: Huck J: A Comprehensive data base for estimating clothing insulation. ASHRAE Trans. **91**, 316–328 (1985)

Highly-Resolved Numerical Simulations of High Rayleigh and Reynolds Number Indoor Ventilation in a Generic Room

Olga Shishkina and Claus Wagner

Abstract We conduct Direct Numerical Simulations (DNS) and Large Eddy Simulations (LES) of turbulent mixed convection in parallelepiped convective cells with heated parallelepiped obstacles inside, which represents indoor ventilation in a generic room. The considered Reynolds number $\mathcal{R}e$ based on the velocity of the inlet flow and the width of the inlet ducts is up to $\mathcal{R}e = 1.0 \times 10^3$ (and 1.5×10^5 if based on the height of the cell) and the Grashof number $\mathcal{G}r$ based on the height of the generic room and the temperature difference of the heated obstacles and the cooled inlet flows is up to $\mathcal{G}r = 2.8 \times 10^{10}$. The flow for $\mathcal{R}e = 1.5 \times 10^5$, $\mathcal{G}r = 2.8 \times 10^{10}$ and the length of the domain $\widehat{L} = 5$ m is studied by means of LES based on the Smagorinsky model. The results of the simulations reveal a strong dependency of the global flow structures on the Grashof number $\mathcal{G}r$, Archimedes number $\mathcal{A}r$ and the length of the domain.

1 Introduction

Mixed convection, which is the dominant transport process in indoor ventilation (for reviews and references see [9, 14]), is characterized by complex transport mechanisms resulting from the interaction of natural and forced convection. Responsible for the former type of convection is the buoyancy force resulting from temperature induced density differences, while forced convection is driven by an imposed pressure gradient.

In the past turbulent mixed convection of air in simplified geometries has been investigated mainly in experiments. For example, Schmeling et al. [10] considered a rectangular convection cell, Fitzgerald and Woods [4] a parallelepiped container

O. Shishkina (✉) · C. Wagner
German Aerospace Center (DLR), Institute of Aerodynamics and Flow Technology, Göttingen, Germany
e-mail: Olga.Shishkina@dlr.de

A. Dillmann et al. (eds.), *New Results in Numerical and Experimental Fluid Mechanics IX*, Notes on Numerical Fluid Mechanics and Multidisciplinary Design 124,
DOI: 10.1007/978-3-319-03158-3_31,

heated from below by uniform heat sources and Gladstone and Woods [6] a naturally ventilated room with a heated floor and two openings to a cold exterior.

Most of the numerical investigations of mixed convection have been conducted either for laminar flows as reported, for example, by Ehrhard [3], or if a turbulent flow was considered, by solving the Reynolds-averaged Navier-Stokes (RANS) equation with different types of turbulence models. A comparative study by Costa et al. [2] and Blay et al. [1] who tested some available turbulence models revealed large discrepancies between the RANS predictions of mixed convection, for which they made the turbulence models responsible. In particular, Blay et al. [1] found that some of the RANS simulations predicted large-scale circulations rotating in the opposite directions, although the same physical parameters were specified.

Therefore, accurate Direct Numerical Simulations (DNS) or well-resolved Large Eddy Simulations (LES) databases for a generic ventilated room are need-ed, which can be used as references in the development of reliable turbulence models for accurate predictions of mixed convection in complicated domains with external and internal walls.

2 Computational Domain and Governing Equations

In the present work we investigate by means of DNS and LES mixed convection flows in a box with four parallelepiped ducts, attached to two opposite vertical walls as shown in Fig. 1.

The length, height and width (without ducts) of the domain are denoted as $\widehat{L}$, $\widehat{H}$ and $\widehat{D}$, respectively. Through two thin ducts, located at the top of the side walls, cold air enters the domain. The length, height and width of the inlet ducts are $\widehat{L}$, $\widehat{H}/150$ and $\widehat{W} = \widehat{H}/30$, respectively. Two outlet ducts with the sizes $\widehat{L} \times \widehat{H}/20 \times \widehat{W}$ are situated at the bottom of the side walls. Inside the box there are four heated parallelepiped obstacles which are elevated at $\widehat{H}/20$ from the floor and are orientated in a parallel manner to each other. The length, height and width of the obstacles are $\widehat{L}$, $\widehat{H}/5$ and $\widehat{D}/10$, respectively, and the distance between the two central obstacles equals $\widehat{D}/5$. The distances between the other obstacles or between the most left/right obstacle and the nearest side walls amount to $\widehat{D}/10$. In all our simulations rooms of the height $\widehat{H} = 3$ m were considered.

The investigated mixed convection flows are driven by inertia and buoyancy forces, while neither of them dominates, i.e. the Archimedes number $\mathcal{A}r$, $\mathcal{A}r \equiv \mathcal{G}r/\mathcal{R}e^2$ is around one. Thus, these type of convection flows is determined by the Grashof number and Reynolds number

$$\mathcal{G}r = \alpha g \widehat{H}^3 \Delta \widehat{T}/\nu^2, \quad \mathcal{R}e = \widehat{H}\widehat{u}_{inlet}/\nu,$$

respectively, where α denotes the thermal expansion coefficient, ν the kinematic viscosity, g the gravitational acceleration and $\Delta\widehat{T}$ the temperature difference between

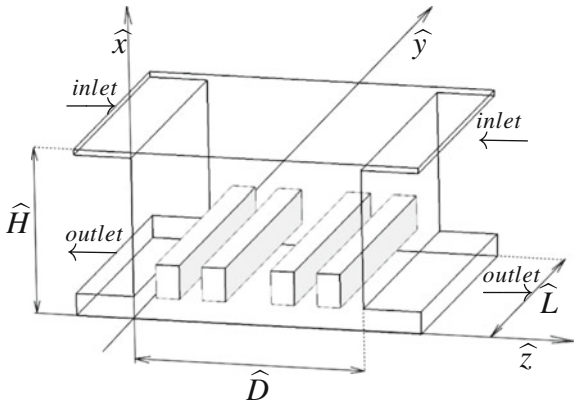

Fig. 1 Sketch of the generic ventilated room of length $\widehat{L}$, width $\widehat{D}$ and height $\widehat{H}$

the isothermal heated obstacles and colder inlet flows. Further, $\widehat{H}$ denotes the height of the container and $\widehat{u}_{inlet}$ the maximum center velocity of the inlet flow.

In the Boussinesq approximation, the system of the momentum, energy and continuity equations for the velocity $\widehat{\mathbf{u}}$, temperature $\widehat{T}$, and pressure $\widehat{p}$ reads

$$\widehat{\mathbf{u}}_t + \widehat{\mathbf{u}} \cdot \nabla \widehat{\mathbf{u}} + \rho^{-1} \nabla \widehat{p} = \nu \Delta \widehat{\mathbf{u}} + \alpha g (\widehat{T} - \widehat{T}_0) \widehat{\mathbf{e}}_x, \tag{1}$$

$$\widehat{T}_t + \widehat{\mathbf{u}} \cdot \nabla \widehat{T} = \kappa \Delta \widehat{T}, \quad \nabla \cdot \widehat{\mathbf{u}} = 0, \tag{2}$$

where $\widehat{\mathbf{u}}_t$ and $\widehat{T}_t$ denote the time derivatives of the velocity and temperature fields, respectively, ρ the density, κ the thermal diffusivity, $\widehat{T}_0 = 0.5(\widehat{T}_H + \widehat{T}_C)$, where $\widehat{T}_H$ is the temperature of the heating obstacles, $\widehat{T}_C$ the temperature of the cool inlet flows and $\widehat{\mathbf{e}}_x$ the vertical unit vector.

The considered boundary conditions are the following. The temperature of the inlet flows and obstacles is fixed to $\widehat{T}_C$ and $\widehat{T}_H$, respectively, while at the outlets and outer rigid walls adiabatic boundary conditions $\partial \widehat{T} / \partial \mathbf{n} = 0$ are prescribed, where $\mathbf{n}$ is the wall normal vector.

The highest considered Reynolds number, based on the height of the inlet ducts and the center velocity in the inlets, $\mathcal{R}e_{inlet} = \mathcal{R}e/150 \approx 1.0 \times 10^3$ corresponds to a laminar duct flow, therefore a parabolic profile of the horizontal velocity component u_z in vertical x-direction was prescribed at the inlets. The other two velocity components of the inlet flow are set to zero. At the outer boundaries of the outlet ducts the Neumann conditions were set, $\partial \widehat{\mathbf{u}} / \partial \mathbf{n} = 0$, while at all solid walls $\widehat{\mathbf{u}} = 0$ according to no-slip conditions.

To non-dimensionalize the governing Eqs. (1), (2), we use the following reference length $\widehat{x}_{ref} = \widehat{D}$ and velocity $\widehat{u}_{ref} = \left(\alpha g \widehat{D}\, \Delta \widehat{T}\right)^{1/2}$, which lead to the following reference time $\widehat{t}_{ref} = \widehat{x}_{ref} / \widehat{u}_{ref}$. Further, the reference temperature and pressure are defined as $\widehat{T}_{ref} = \Delta \widehat{T} \equiv \widehat{T}_H - \widehat{T}_C$ and $\widehat{p}_{ref} = \widehat{u}_{ref}^2 \, \rho$, respectively. Thus, we obtain the following system of the governing dimensionless equations in the Boussinesq approximation

$$\begin{aligned} \mathbf{u}_t + \mathbf{u}\cdot\nabla\mathbf{u} + \nabla p &= \Gamma^{-3/2}\mathcal{G}r^{-1/2}\Delta\mathbf{u} + T\mathbf{e}_x, \\ T_t + \mathbf{u}\cdot\nabla T &= \Gamma^{-3/2}\mathcal{G}r^{-1/2}\mathcal{P}r^{-1}\Delta T, \quad \nabla\cdot\mathbf{u} = 0. \end{aligned} \tag{3}$$

Here, $\mathbf{u}$ is the dimensionless velocity vector-function, T the temperature, $\mathbf{u}_t$ and T_t their time derivatives, p the pressure, $\Gamma = \widehat{D}/\widehat{H}$ the aspect ratio of the generic room and $\mathcal{P}r = \nu/\kappa$ the Prandtl number. Thus, the dimensionless temperature equals $T_H = 0.5$ at the obstacles and $T_C = -0.5$ at the inlets.

3 Finite-Volume Ansatz and Computational Mesh

Equation (3) are discretized following the volume-balance procedure by Schumann and solved by a finite-volume method, originally developed by Schmitt et al. [5]. The DNS code has been advanced by implementing a semi-implicit time integration scheme and fourth-order discretization in space [13] and the von Neumann numerical stability criterion [12]. To conduct DNS of turbulent thermal convection in domains without any periodical directions, e.g. with rigid outer walls, a direct Poisson solver which is based on the separation of variables method [7] was implemented. Further advancement of the code was done with the capacitance matrix technique, described in detail in [11], which made it possible to conduct simulations in domains with internal rigid walls, using computational meshes, which are non-equidistant in all three directions and regular in one direction along the obstacles and irregular in other two directions. The correct implementation of the above-described changes was verified in DNS of turbulent natural convection in cuboid domains [7] as well as in parallelepiped domains with obstacles [11].

To conduct Large-Eddy Simulations with the Smagorinsky model [16] for $\mathcal{G}r = 2.8 \times 10^{10}$ and $\mathcal{R}e = 1.5 \times 10^5$ and the domain length of $\widehat{L} = 5$ m, we used a computational mesh with $320 \times 386 \times 600$ nodes in x-, y- and z- directions, respectively. The nodes distribution presented in Fig. 2 reflects the mesh diameter at different locations, which is especially fine around the heated obstacles and near walls of the room and the attached ducts for inlet and outlet flows. The corresponding minimal and maximal mesh widths in different directions are: $\Delta x_{min} = 2.0 \times 10^{-4}$, $\Delta x_{max} = 3.3 \times 10^{-3}$, $\Delta y_{min} = 1.1 \times 10^{-4}$, $\Delta y_{max} = 1.1 \times 10^{-3}$, $\Delta z_{min} = 2.5 \times 10^{-4}$ and $\Delta z_{max} = 7.9 \times 10^{-3}$.

4 Investigation of Indoor Ventilation by Means of LES

Applying the top-hat filtering to the Eq. (1) one obtains:

$$\frac{\partial \overline{u}_i}{\partial t} + \frac{\partial}{\partial x_j}\left(\overline{u_i u_j}\right) = -\frac{1}{\rho}\frac{\partial \overline{p}}{\partial x_i} + 2\nu\frac{\partial}{\partial x_j}\overline{S_{ij}} + \alpha g(\overline{T} - \widehat{T}_0)\,\delta_{i1},$$

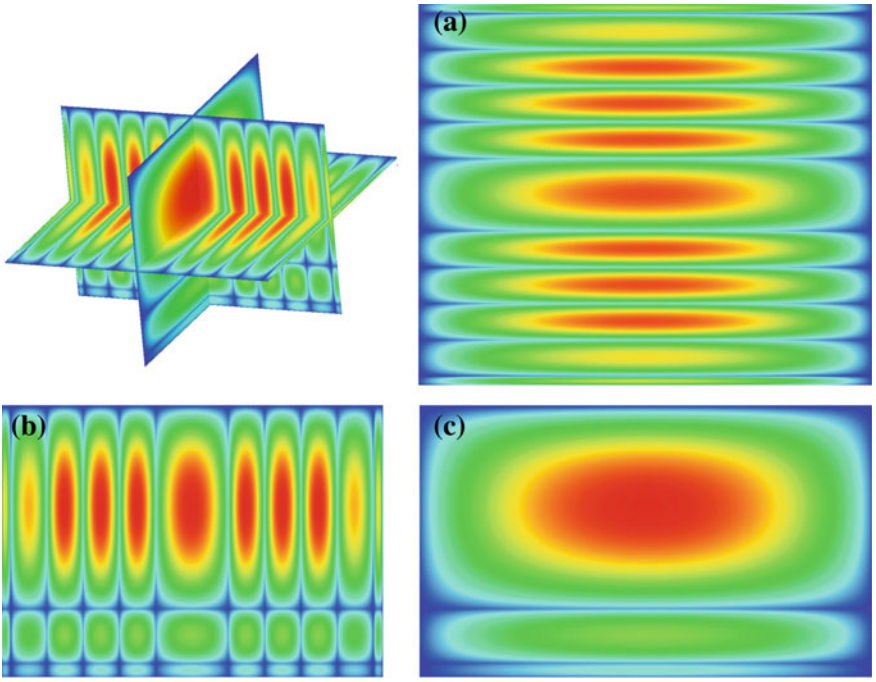

Fig. 2 Colour-scaled distribution of grid points of the structured mesh in **a** x-direction, **b** y-direction and **c** z-direction. Colour scale goes from *blue* (zero) through *green* to *red* (10^{-3})

where $\overline{S_{ij}} = 0.5\left(\partial\overline{u}_i/\partial x_j + \partial\overline{u}_j/\partial x_i\right)$ is the rate-of-strain tensor, δ_{ij} is the Kronecker symbol and the overline denotes the filtering of the corresponding dimensional quantity. Introducing the residual stress tensor $\tau_{ij} = \overline{u_i u_j} - \overline{u_i}\,\overline{u_j}$, one further obtains:

$$\frac{\partial\overline{u}_i}{\partial t} + \frac{\partial}{\partial x_j}\left(\overline{u_i}\,\overline{u_j}\right) = -\frac{1}{\rho}\frac{\partial\overline{p}}{\partial x_i} + 2\nu\frac{\partial}{\partial x_j}\overline{S_{ij}} - \frac{\partial\tau_{ij}}{\partial x_j} + \alpha g(\overline{T} - \widehat{T}_0)\,\delta_{i1}.$$

Applying the eddy viscosity model $\tau_{ij} - \tau_{kk}\delta_{ij}/3 = -2\nu_\tau\overline{S_{ij}}$, where $\nu_\tau = (C_s h)^2\sqrt{2\overline{S_{ij}}\,\overline{S_{ij}}}$ is the turbulent eddy viscosity, h the local mesh diameter, and C_s is a constant, which in our simulations was taken equal to 0.2, one obtains:

$$\frac{\partial\overline{u}_i}{\partial t} + \frac{\partial}{\partial x_j}\left(\overline{u_i}\,\overline{u_j}\right) = -\frac{1}{\rho}\frac{\partial\overline{p}}{\partial x_i} + 2(\nu + \nu_\tau)\frac{\partial}{\partial x_j}\overline{S_{ij}} + \alpha g(\overline{T} - \widehat{T}_0)\,\delta_{i1}.$$

Distribution of the obtained turbulent eddy viscosity ν_τ for $\mathcal{G}r = 2.8 \times 10^{10}$, $\mathcal{R}e = 1.5 \times 10^5$ in three central cross sections is presented in Fig. 3. As one can

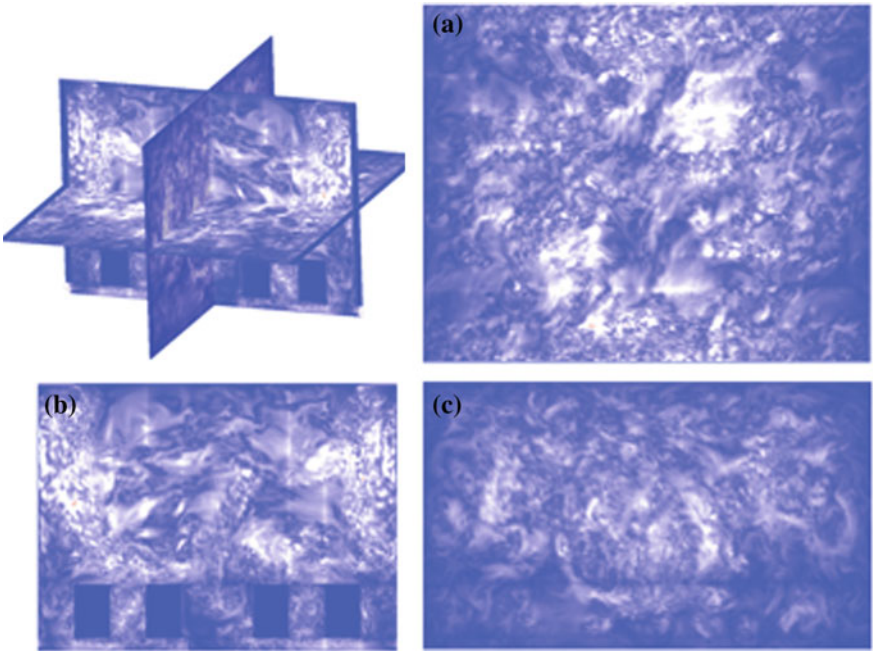

Fig. 3 Distribution of the turbulent eddy viscosity ν_τ across **a** x-direction, **b** y-direction and **c** z-direction for $\mathcal{G}r = 2.8 \times 10^{10}$, $\mathcal{R}e = 1.5 \times 10^5$. Colour scale goes from *white* (zero) to *blue* ($\nu_\tau/\nu = 8.5 \times 10^{-2}$)

see, its values vary between zero and 8.5 % of the real (kinematic) viscosity and ist distribution is inhomogeneous.

In Fig. 4 instantaneous distributions of the temperature and velocity magnitude are presented at different locations, namely at 50 % of the height, length and width of the domain for $\mathcal{G}r = 2.8 \times 10^{10}$, $\mathcal{R}e = 1.5 \times 10^5$. Comparing the obtained results with those for a shorter room with $\widehat{L} = 80\,\text{cm}$ (see [15]), one concludes that with increasing length of the domain the flow start to develop also in y-direction (Fig. 4a, b). In the shorter room the flow was almost homogeneous along the obstacles with the only exception in the vicinity of the vertical walls.

Further, in the long room (present case) the thermal plumes emission is the highest not in the center ($y/\widehat{L} = 0.5$) as it was observed in the short room [15], but in two regions between the center and the walls ($y/\widehat{L} \approx 0.25$ and 0.75, see Fig. 4a, e).

In contrast to the pure forced convection (studied in [8] and not shown here), where the flow in the core of the domain goes downwards, in the mixed convection we always obtained an upflow in the central part of the container. A different sense of rotation of the large-scale circulation in the cases of mixed and forced convection was obtained due to the dominance of buoyancy over inertia in the considered mixed convection case.

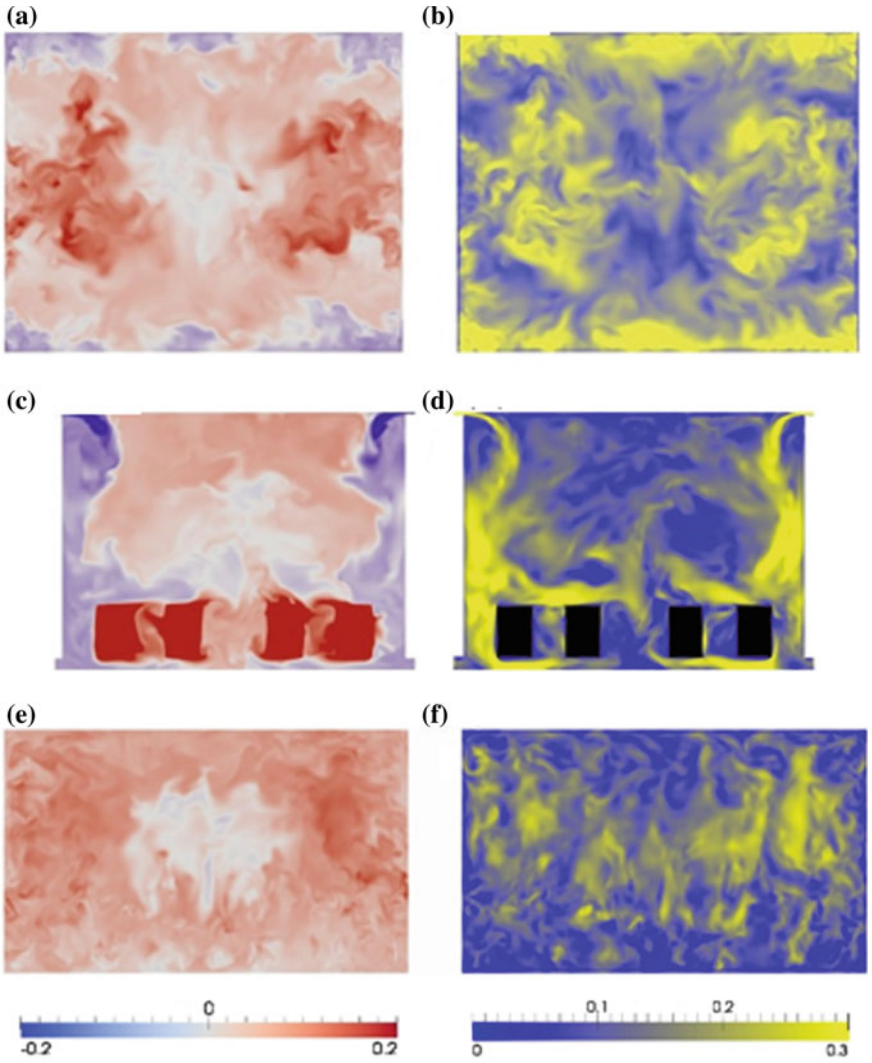

Fig. 4 Instantaneous distributions of the temperature (**a, c, e**) and velocity magnitude (**b, d, f**) in three central cross-sections: $x/\widehat{H} = 0.5$ (**a, b**), $y/\widehat{L} = 0.5$ (**c, d**) and $z/\widehat{D} = 0.5$ (**e, f**) for $\mathcal{G}r = 2.8 \times 10^{10}$, $\mathcal{R}e = 1.5 \times 10^5$

5 Conclusions

By means of DNS and LES, we investigate turbulent mixed convection in parallelepiped convective cells with heated parallelepiped obstacles inside, which represents indoor ventilation in a generic room. Cold air enters the cell through thin ducts located at the side walls close to the top, and warmer air leaves the cell through

the outlet ducts located also at the side walls but close to the bottom. The case of Reynolds number $\mathcal{R}e = 1.5 \times 10^5$ and Grashof number $\mathcal{G}r = 2.8 \times 10^{10}$ is studied in LES with Smagorinsky model.

As the DNS and LES results show, for a fixed Grashof number and geometry of the domain, the global flow is determined by the balance between buoyancy and inertia, i.e. by the Archimedes number $\mathcal{A}r$. Thus, a downflow in the central part of the domain for lower $\mathcal{A}r$ (if the forced convection dominates over the natural one) or an upflow for $\mathcal{A}r > 1$ was observed.

Further, the global flow structures for $\mathcal{A}r$ around 1 are not fully determined by Grashof number, they also depend strongly on the length of the domain. Thus, an increase of the domain length by a similar geometry and the same Reynolds and Grashof numbers lead to different large-scale circulations of air inside the room. The flow always becomes more turbulent and three-dimensional with growing $\mathcal{G}r$ and the length of the generic room. In a room with the length of 5 m the highest thermal plume intensity is obtained at a distance about 1–1.5 m from the vertical walls and not in center of the domain, as it was obtained previously in DNS of mixed convection in a domain with the length of 80 cm by a similar geometry and the same Reynolds and Grashof numbers.

The authors acknowledge financial support by the Deutsche Forschungsgemeinschaft (DFG) under grant WA/1510-11.

References

1. Blay, D., Mergui, S., Niculae, C.: Confined turbulent mixed convection in the presence of a horizontal buoyant wall jet. Fundam. Mixed Convection **213**, 65–72 (1992)
2. Costa, J., Oliveira, L., Blay, D.: Test of several versions for the $k-\epsilon$ type turbulence modelling of internal mixed convection flows. Int. J. Heat Mass Transf. **42**, 4391–4409 (1999)
3. Ehrhard, P.: Laminar mixed convection in two-dimensional far wakes above heated/cooled bodies: model and experiments. J. Fluid Mech. **439**, 165–198 (2001)
4. Fitzgerald, S., Woods, A.: Transient natural ventilation of a room with a distributed heat source. J. Fluid Mech. **591**, 21–42 (2007)
5. Friedrich, R., Schmitt, L.: Numerische Simulation turbulenter Grenzschichten (Large-Eddy-Simulation). Technical report, TU München (1982) No. 82/2
6. Gladstone, C., Woods, A.: On buoyancy-driven natural ventilation of a room with a heated floor. J. Fluid Mech. **441**, 293–314 (2001)
7. Kaczorowski, M., Shishkin, A., Shishkina, O., Wagner, C.: Development of a numerical procedure for direct simulations of turbulent convection in a closed rectangular cell. In: C. Tropea et al., (eds) New Results in Numerical and Experimental Fluid Mechanics VI, Notes on Numerical Fluid Mechanics and Multidisciplinary Design. **96**, 381–388. Springer Verlag (2008)
8. Körner, M., Shishkina, O., Wagner, C., Thess, A.: Properties of large-scale flow structures in an isothermal ventilated room. Building and Environment. **59**, 563–574 (2013)
9. Linden, P.: The fluid mechanics of natural ventilation. Annu. Rev. Fluid Mech. **31**, 201–238 (1999)
10. Schmeling, D., Westhoff, A., Kühn, M., Bosbach, J., Wagner, C.: Large-scale flow structures and heat transport of turbulent forced and mixed convection in a closed rectangular cavity. Int. J. Heat Fluid Flow **32**, 889–900 (2011)

11. Shishkina, O., Shishkin, A., Wagner, C.: Simulation of turbulent thermal convection in complicated domains. J. Comput. Appl. Maths **226**, 336–344 (2009)
12. Shishkina, O., Wagner, C.: Stability conditions for the Leapfrog-Euler scheme with central spatial discretization of any order. Appl. Num. Anal. Comp. Maths **1**, 315–326 (2004)
13. Shishkina, O., Wagner, C.: A fourth order accurate finite volume scheme for numerical simulations of turbulent Rayleigh-Bénard convection in cylindrical containers. C. R. Mecanique **333**, 17–28 (2005)
14. Shishkina, O., Wagner, C.: Modelling the influence of wall roughness on heat transfer in thermal convection. J. Fluid Mech. **686**, 568–582 (2011)
15. Shishkina, O., Wagner, C.: A numerical study of turbulent mixed convection in an enclosure with heated rectangular elements. J. Turbulence **13**(22), 1–21 (2012)
16. Smagorinsky, J.: General circulation experiments with the primitive equations. i. the basic equations. Mon. Weather Rev. **91**, 99–164 (1963)

Influence of the Geometry on Rayleigh-Bénard Convection

Sebastian Wagner, Olga Shishkina and Claus Wagner

Abstract Direct numerical simulations (DNS) of Rayleigh-Bénard convection in a cube and a cylinder with equal diameter and height are performed to investigate the main responses of the system, namely heat flux and motion. Differences in the latter two quantities for the two geometries suggest a transition between different flow states in the cube, which is not observed in the cylinder due to its rotational symmetry. A method is introduced to analyse the flow dynamics in the cube, which relies on the temperature distribution at the lateral walls. It reveals that above a certain Rayleigh number the global flow structure in the cube is organized in a diagonal manner and not longer parallel to the walls, which leads to differences in the heat flux and the kinetic energy in the cylindrical and the cubic sample.

1 Introduction

Rayleigh-Bénard convection (RBC) as a model system for many convective flow problems occurring in nature and technology is usually studied in terms of the Oberbeck-Boussinesq (OB) approximation [1]. Within this approximation, the flow is determined by the dimensionless temperature gradient, Rayleigh number Ra, and a fluid parameter, Prandtl number Pr. Besides the dynamical similarity, forced by equal Pr and Ra, flow setups must be geometrically similar to lead to similar solutions.

The geometry is usually parameterised by one (or more) aspect ratios, e.g. diameter/height for a cylinder. In DNS of Rayleigh-Bénard convection in cylindrical samples filled with air the influence of the aspect ratio on the mean heat flux is reported to be small [2], while experiments in rectangular containers filled with water do not show any significant influence [3] at all. From two-dimensional DNS, it is known

S. Wagner (✉) · O. Shishkina · C. Wagner
German Aerospace Center (DLR), Institute of Aerodynamics and Flow Technology, Simulation Center of Aerodynamic Research in Transportation (SCART), Göttingen, Germany
e-mail: Sebastian.Wagner@DLR.de

A. Dillmann et al. (eds.), *New Results in Numerical and Experimental Fluid Mechanics IX*, Notes on Numerical Fluid Mechanics and Multidisciplinary Design 124,
DOI: 10.1007/978-3-319-03158-3_32,

[4, 5] that the mean heat flux is significantly influenced by changes in the global flow structure occurring for small aspect ratios. In addition, a theoretical attempt [6] exists trying to explain the influence of the aspect ratio. The latter is based on differences between the boundary layers attached to the vertical and horizontal walls. These differences are discussed for different flow structures (called "plate filling" and "laterally restricted"), but the occurrence of this flow structures are not understood and therefore, the applicability of the theory is questionable.

The aspect ratio is of course not sufficient for describing the geometry, since e.g. a cube and a cylinder, both with aspect ratio one, are still not similar geometries. To our knowledge, the only study comparing the flow in different geometries in a direct way deals with a cylindrical and a rectangular convection cell of equal volume and height, i.e. different aspect ratio, for large Ra [7]. The comparison reveals, that the temperature and velocity fluctuations in the center of the convection cell differ considerably, in particular, regarding the scaling with Ra. This means, that the influence of the geometry is not negligible at all for high Ra.

In the present study, the geometry's influence on the flow within two cavities with equal aspect ratio is investigated. We performed direct numerical simulation (DNS) of the flow in a cube and a cylinder with equal diameter and height (Sect. 2). The main integral responses of the system, namely the Nusselt number (vertical heat flux) and the Reynolds number (motion) and their Ra-dependence, are compared (Sect. 3.1). They show a strong influence of the geometry especially, for small Ra. To understand these differences a method is introduced to analyse the global flow structure and its instantaneous dynamics (Sect. 3.2).

2 Methodology

DNS of RBC are performed in a cube and a cylinder with equal diameter and height. A fourth-order accurate finite volume code in cylindrical [8, 9] and in Cartesian coordinates [10, 11], respectively, is used to solve the dimensionless governing equations in OB approximation:

$$\partial_t \mathbf{u} + \mathbf{u} \cdot \nabla \mathbf{u} = -\nabla p + \sqrt{\frac{Pr}{Ra}} \nabla^2 \mathbf{u} + \theta \mathbf{e}_z,$$

$$\partial_t \theta + \mathbf{u} \cdot \nabla \theta = \sqrt{\frac{1}{RaPr}} \nabla^2 \theta, \quad \nabla \cdot \mathbf{u} = 0.$$

As reference quantities we use the free-fall velocity $\sqrt{\alpha g \Delta H}$ and the height H have been used. The temperature is made dimensionless by $\theta = (T - T_M)/\Delta$ with $T_M = (T_{\text{bottom}} + T_{\text{top}})/2$ and $\Delta = T_{\text{bottom}} - T_{\text{top}}$. The boundary conditions for the considered domains are defined as follows. Top and bottom plates are isothermal with $T_{\text{bottom}} > T_{\text{top}}$, while the vertical walls are adiabatic. Further, no-slip and impermeability conditions are set on all walls. All material properties are considered

to be constant except of the density in the buoyancy term, which is assumed to depend linearly on the temperature. The fluid is a (heavy) gas, i.e. $Pr = \nu/\kappa = 0.786$, and the Rayleigh number $Ra = \alpha g \Delta H^3/(\nu\kappa)$ is varied between 10^5 and 10^7. Here, ν is the kinematic viscosity, κ the thermal diffusivity, α the isobaric thermal volume-expansion coefficient, g the gravitational acceleration and H the height of the convection cell. The resolution of the simulation is chosen according to [12] and [13].

3 Results

To investigate the influence of the geometry the two main responses of the system, motion and vertical heat flux, and their dependence on *Ra* are investigated. A further analysis of the flow structure in the cube is performed and the obtained results are compared to the flow structure in the cylinder.

3.1 Integral Responses of the System

The two main responses of the system, motion and heat flux from bottom to top, can be expressed by integral quantities, namely, the Reynolds number *Re* and the Nusselt number *Nu*. The latter is the ratio of the integral vertical heat flux of the system and the heat flux which would occur in a solid body under the same conditions. It reads in dimensionless formulation

$$Nu = \left\langle \sqrt{PrRa}\, u_z \theta - \frac{\partial \theta}{\partial z} \right\rangle_{A_z,t}, \tag{1}$$

where A_z is the area of the cross-section orthogonal to the $z-$direction.

For natural convection the definition of the Reynolds number *Re* is more complex, since the choice of the characteristic velocity and length are rather arbitrary. For convenience, we choose the height H as reference length and calculate a reference velocity from the volume-and time-averaged kinetic energy of the flow, i.e.

$$Re = \sqrt{\frac{Ra}{Pr}} \sqrt{\langle \mathbf{u}^2 \rangle_{V,t}}\,. \tag{2}$$

For both quantities, *Nu* and *Re*, a large variety of results from DNS and measurements exist to which good agreement is found [14, 15]. Further, there are different theories to describe their dependence on *Ra* and Pr, among which the theory by Grossmann and Lohse [16] should be mentioned here. However, none of the theories sufficiently consider the geometry of the sample.

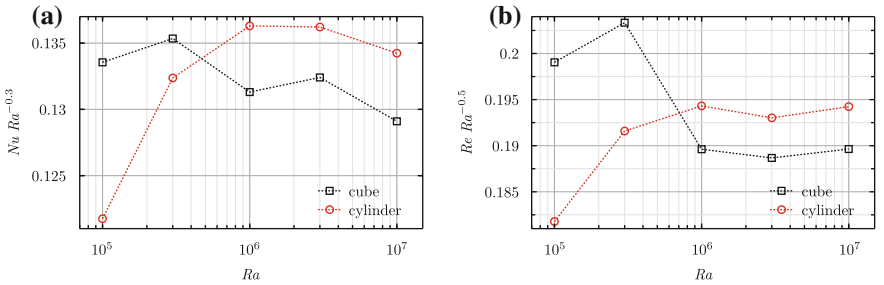

Fig. 1 Ra-dependence of **a** the reduced Nusselt number $NuRa^{-0.3}$ and **b** the reduced Reynolds number $ReRa^{-0.5}$ for cube and cylinder (with equal diameter and height) and $Pr = 0.786$

The comparison of Nu and Re obtained in the cube and in the cylinder in our DNS are shown in Fig. 1. For clarity, both quantities are reduced by a certain power of Ra. Deviations between the cube and the cylinder case up to 10 % for Nu and even up to 60 % for Re are found. For small Ra, the cube case is characterised by larger Nu and Re, while for larger Ra it is vice versa. Nevertheless, the scaling with Ra is found to be similar for large Ra. This tendency is also correct for even larger Ra as it is pointed out in [15]. Further, there is no universal scaling law $Nu \sim Ra^{\alpha}$ with constant α (and for Re as well) (cf. [14]). This is explained in theory [16] by a change between different regimes. Nevertheless, the steep drop in Re and Nu for the cube for $Ra \approx 10^6$ must be studied in more detail. To do so, in the next subsection the flow structure in the cube is further analysed.

3.2 Flow Structure

As it has been shown previously [14], the structure of the global flow in a cylindrical sample with aspect ratio one is not much influenced by an increase in Ra. Further, the transition from a stationary equilibrium to an instationary one takes place between $Ra = 10^5$ and $Ra = 3 \times 10^5$. This leads to a steep increase in the reduced Nusselt and Reynolds number (cf. Fig. 1). The latter is also obtained for the cubic sample, but for Ra around 10^6, both quantities decrease. To analyse this drop, a method already used for the cylinder [14] is adopted to the cube. When warm fluid is rising close to the vertical wall, this leaves a temperature footprint on the wall, as shown in Fig. 2 for the time-averaged temperature. If the height z_0, at which the arithmetic mean temperature (of top and bottom plate) is reached, is located close to the top plate, warm fluid is moving upward close to this wall, and if it is located close to the bottom plate, cold fluid is moving downwards. This information is available in instantaneous temperature fields as well. The latter are saved for the whole domain four times per dimensionless time unit $H/\sqrt{\alpha g \Delta H}$. For all corners (①: $x = 0, y = 0$), (②: $x = 0, y = H$), (③: $x = H, y = H$),(④: $x = H, y = 0$) the height z_0 is

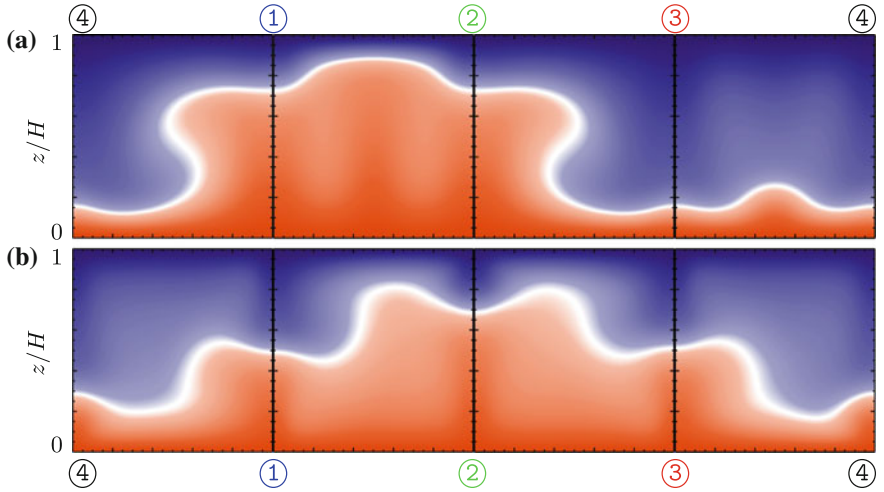

Fig. 2 Time-averaged temperature distribution (*red* warm, *blue* cold, *white* arithmetic mean temperature) on the vertical walls of the cube for **a** $Ra = 10^5$ **b** $Ra = 10^6$ and $Pr = 0.786$. The circled numbers mark the corners for the instantaneous analysis

identified in the instantaneous temperature fields. The four time-series $z_0(t)$ reflect the global flow structure in the cube and its development in time.The time-series, for the *Ra*-interval in which the drop in *Nu* and *Re* appears, are displayed in Fig. 3b, d, f.[1] Additionally, the corresponding isosurfaces of the time-averaged temperature are presented in Fig. 3a, c, e. Both reveal a change in the global flow structure from a flow approximately parallel to the vertical walls ($Ra = 10^5$) to a flow which is organised in a diagonal manner ($Ra = 10^6$). As a consequence, the flow for $Ra = 10^5$ is rising at the corners ① and ② and between them as Figs. 2a and 3a reveal. The other limit is reached for $Ra = 10^6$ for which the warm fluid rises in the corner ② and cold fluid is moving downward in the corner ④ (cf. Figs. 2b and 3e). In between, for $Ra = 3 \times 10^5$, the global flow structure is oriented already slightly diagonal but still shows a large component in direction parallel to the walls.

Of course, this information is not only visible in the temperature field but also, in more detail in the time-averaged velocity field. In Fig. 4, the time-averaged velocity field in the vertical slice at the height of the averaged thickness of the thermal boundary layer $z_{\mathrm{slice}}/H = (2Nu)^{-1}$ close to the bottom plate is depicted. In colour the magnitude of the vertical velocity is shown, while the superimposed vector-field displays the velocity components within the slice. It becomes obvious that the flow fields are more complicated than it seems from the temperature distribution. For $Ra = 10^5$, the flow is mainly pointing from the right to the left (cf. Fig. 4a), while for $Ra = 10^6$ it is spreading over the whole area but has a dominant diagonal component. This means that the length corresponding to the large scale flow for the diagonal flow

[1] It should be noted that for symmetry reasons the corners can be interchanged by rotating and mirroring the domain. This has been done to simplify the comparison between the different *Ra*.

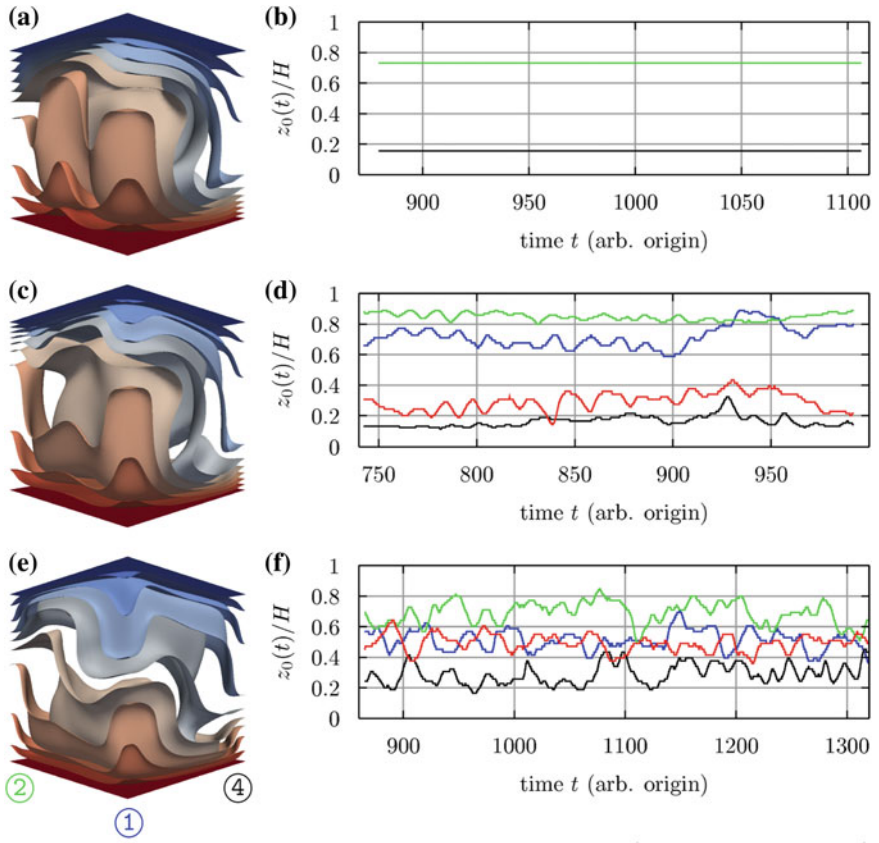

Fig. 3 Isosurfaces of the time-averaged temperature (*red* warm, *blue* cold) and corresponding time-histories of the height z_0 as defined in the text (*blue*: corner ①, *green*: corner ②, *red*: corner ③, *black*: corner ④), for **a**, **b** $Ra = 10^5$, **c**, **d** $Ra = 3 \times 10^5$ and **e**, **f** $Ra = 10^6$, $Pr = 0.786$. Note that in Fig. 3b the *blue* and *red lines* are not visible because they collapse with the *green* and *black line*, respectively

is rather $\sqrt{2}H$ (diagonal of the bottom plate) than simply H. This leads to an *effective aspect ratio* larger than one, while for the flow parallel to the walls it is one.

The results for a cylindrical sample [2] reveal that Nu for $Ra \in [10^7, 10^9]$ is decreasing when the aspect ratio is increased above one. In an experimental study [3] using water (i.e. $5.18 \leq Pr \leq 7.03$) Nu is found to be independent of the aspect ratio larger than one. Since the dependence on the aspect ratio seems to be more pronounced for smaller Pr, as two-dimensional simulations suggest [4], it can be suggested that the difference in Nu might be connected to this change in the effective aspect ratio. If in addition, boundary layers of Prandtl-Blasius type are assumed, as as it is often done for RBC in the considered Ra-range, Nu and Re are related by $Nu^2 \sim Re$ [12], which makes the drop of Re reasonable.

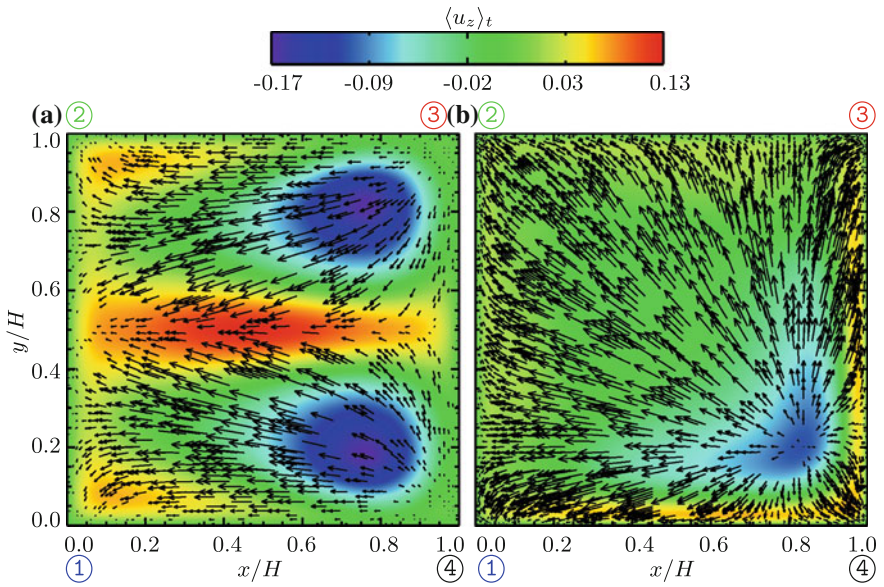

Fig. 4 Horizontal slice at height $z_{\text{slice}}/H = (2Nu)^{-1}$ of the time-averaged vertical velocity (colour coded) with superimposed velocity vectors within this plane for **a** $Ra = 10^5$ and **b** $Ra = 10^6$, $Pr = 0.786$

For the physical mechanism behind the decrease in Re, we find the following possible explanation: When the global flow is changing to a diagonal structure, the warm fluid rises in the corner of the cube. This means that the viscous boundary layers close to two walls are dissipating kinetic energy of the rising fluid. Contrary, for the cylindrical sample and for the global flow in the cube with a structure parallel to the walls, the warm fluid is rising mainly close to one wall, which might lead to a higher Re. To separate the effect of different effective aspect ratios from the influence of corner effects, further simulations are required.

4 Summary

DNS of RBC have been performed in a cylindrical container with equal height and diameter and in a cubic container, for $Pr = 0.786$ and $Ra \in [10^5, 10^7]$. The main responses of the system, motion and heat flux, expressed by Nu and Re have been evaluated and compared. Large differences between the two geometries in absolute values as well as in their scaling with Ra have been found. Most interesting is a drop of Nu and Re around $Ra = 10^6$ in case of the cube. While both quantities are larger for the cube for $Ra = 10^5$, it is vice versa for $Ra = 10^7$. This drop seems to correspond to a change in the global flow structure in the cube, which does not

occur in case of the cylinder. The main feature of the cubic geometry in the contrast to the cylindrical one is the presence of two characteristic lengths, namely the side length and the length of the diagonal of the plates. While for smaller *Ra* the flow is organized parallel to the vertical walls, it is organized in a diagonal manner for larger *Ra*.

It is further found that the scaling of *Nu* and *Re* is similar for larger *Ra*, eventhough the absolute values differ. This remaining difference might be caused by the arbitrary choice of geometries, and in particular the choice of the cube's aspect ratio. For large *Ra* rather the diagonal of the cube's bottom plate is characteristic for the flow. Thus, for future studies a comparison of a cylinder and a box-shaped container, with equal effective aspect ratio based on this characteristic length, seems reasonable.

Acknowledgments The authors would like to thank Matthias Kaczorowski and Tomasz Czarnota for updating the computational code in Cartesian coordinates and acknowledge support by the Deutsche Forschungsgemeinschaft (DFG) under grant SH405/3-1.

References

1. Ahlers, G., Grossmann, S., Lohse, D.: Heat transfer and large scale dynamics in turbulent Rayleigh-Bénard convection. Rev. Mod. Phys. **82**, 503–537 (2009)
2. Bailon-Cuba, J., Emran, M.S., Schumacher, J.: Aspect ratio dependence of heat transfer and large-scale flow in turbulent convection. J. Fluid Mech. **655**, 152–173 (2010)
3. Zhou, Q., Liu, B.F., Li, C.M., Zhong, B.C.: Aspect ratio dependence of the heat transport by turbulent Rayleigh-Bénard convection in rectangular cells. J. Fluid Mech. **710**, 260–276 (2012).
4. van der Poel, E.P., Stevens, R.J.A.M., Lohse, D.: Connecting flow structures and heat flux in turbulent Rayleigh-Bénard convection. Phys. Rev. E **84**, 045303 (2011)
5. van der Poel, E.P., Stevens, R.J.A.M., Sugiyama, K., Lohse, D.: Flow states in two-dimensional Rayleigh-Bénard convection as a function of aspect ratio and Rayleigh number. Phys. Fluids **24**, 085104 (2011)
6. Grossmann, S., Lohse, D.: On geometry effects in Rayleigh-Bénard convection. J. Fluid Mech. **486**, 105–114 (2003)
7. Daya, Z.A., Ecke, R.E.: Does turbulent convection feel the shape of the container. Phys. Rev. Lett. **87**, 184501 (2001)
8. Shishkina, O., Wagner, C.: A fourth order accurate finite volume scheme for numerical simulations of turbulent Rayleigh-Bénard convection in cylindrical containers. C. R. Mec. **333**, 17–28 (2005)
9. Horn, S., Shishkina, O., Wagner, C.: On non-Oberbeck-Boussinesq effects in three-dimensional Rayleigh-Bénard convection in glycerol. J. Fluid Mech. **691**, 52–68 (2012)
10. Kaczorowski, M., Shishkin, A., Shishkina, O., Wagner, C.: Development of a numerical procedure for direct simulations of turbulent convecxtion in a closed rectangular cell. In: New Results in Numerical and Experimental Fluid Mechanics VI, Volume 96 of Notes on Numerical Fluid Mechanics and Multidisciplinary Design, Springer, Dordrecht, pp. 381–388 (2008)
11. Shishkina, O., Shishkin, A., Wagner, C.: Simulation of turbulent thermal convection in complicated domains. J. Comput. Appl. Math. **226**, 336–344 (2009)
12. Shishkina, O., Stevens, R.J.A.M., Grossmann, S., Lohse, D.: Boundary layer structure in turbulent thermal convection and its consequences for the required numerical resolution. New J. Phys. **12**, 075022 (2010)

13. Wagner, S., Shishkina, O., Wagner, C.: Numerical investigation of the spatial resolution requirements for turbulent Rayleigh-Bénard convection. submitted to Springer (2012)
14. Wagner, S., Shishkina, O., Wagner, C.: Boundary layers and wind in cylindrical Rayleigh-Bénard cells. J. Fluid Mech. **697**, 336–366 (2012)
15. Kaczorowski, M., Xia, K.-Q.: Turbulent flow in the bulk of Rayleigh-Bénard convection: small-scale properties in a cubic cell. J. Fluid Mech. **722**, 596–617 (2013)
16. Grossmann, S., Lohse, D.: Scaling in thermal convection: a unifying view. J. Fluid Mech. **407**, 27–56 (2000)

Part VII
Aerodynamics and Aeroacoustics of Ground Vehicles

An Experimental and Numerical Investigation of the Near Wake Field of a Tractor-Trailer Configuration

Johannes Haff, Joachim Tschech, Hugues Richard, Sigfried Loose and Claus Wagner

Abstract An experimental and numerical study was performed with a 1/15th scaled model of a typical European tractor-trailer configuration. The objective was to develop a new and practicable passive method which reduces the aerodynamic pressure drag by controlling the unsteady velocity field behind the trailer. The experiments included the measurement of the pressure distribution on the trailer base, the velocity wake based on particle image velocimetry and the resulting aerodynamic loads. A trailer underbody equipped with a full fairing and a rear diffuser with side plates is shown to reduce the aerodynamic drag coefficient by 2.4 %. The direct influence on the trailer wake and the resultant base pressure of the trailer is presented. The results of the also conducted Computational Fluid Dynamics (CFD) predictions confirm the effect of the drag reducing add-on devices on the velocity and pressure field in accordance to the experimental data.

J. Haff (✉) · J. Tschech · H. Richard · S. Loose · C. Wagner
German Aerospace Center (DLR), Institute of Aerodynamics and Flow Technology, SCART, Bunsenstr. 10, 37073 Göttingen, Germany
e-mail: Johannes.Haff@dlr.de;
http://www.dlr.de

J. Tschech
e-mail: Joachim.Tschech@dlr.de

H. Richard
e-mail: Hugues.Richard@dlr.de

S. Loose
e-mail: Sigfried.Loose@dlr.de

C. Wagner
e-mail: Claus.Wagner@dlr.de

A. Dillmann et al. (eds.), *New Results in Numerical and Experimental Fluid Mechanics IX*, Notes on Numerical Fluid Mechanics and Multidisciplinary Design 124,
DOI: 10.1007/978-3-319-03158-3_33,

1 Introduction

The main part of goods traffic in Europe is organised by road freight transport with tractor-trailer configurations. This is a result of the high flexibility and infrastructure density of this transportation system. Nevertheless, the overload of the road capacity, the high energy consumption and its negative environmental impact require a significant development in the future.

A reduction of the energy consumption with its positive effect on the environmental compatibility can be realised by making use of lightweight construction, new materials, progresses in the development of tires with a reduced rolling resistance and improved propulsion systems as well as the optimisation of the vehicle aerodynamics.

From the aerodynamic point of view, a tractor-trailer is a bluff body with most unfavourable flow characteristics. Confirmed by numerous research studies, e.g. Gilhaus [1], there is still a high potential for the reduction of aerodynamic pressure drag, the major part of the total aerodynamic drag of a tractor-trailer configuration. Most of the pressure drag is associated with the low-pressure field behind the trailer as shown by Cooper [2]. Maximum vehicle dimensions specified by the European Community [3] and the requirement for a maximum transport capacity define the geometric shape for truck manufacturers in Europe. Thus, there is not much space for geometrical changes.

The results of the wind tunnel experiment reveal that a trailer with an underbody fairing and a rear diffuser reduces aerodynamic drag by manipulating the trailer wake. The use of side and splitter plates optimises this drag reducing potential. The objective of this research study is to understand the effect of a rear diffuser on the near wake flow structures and the base pressure distribution of a tractor-trailer based on experimental and numerical results. All investigations were performed at zero yaw angle without the consideration of cross-flow effects. The influence of realistic ground flow conditions was investigated by CFD whereas in the experiment no moving ground and no wheel rotation was simulated.

2 Experimental Setup

The experimental part of this study was performed in the Side Wind Test Facility Göttingen (SWG) which is a conventional closed-loop wind tunnel powered by a 0.5 MW engine with a maximum freestream velocity of 65 m/s in the empty test section. The test section has a cross-sectional area of 2.4 $\times$ 1.6 m (width $\times$ height) and a length of 9 m.

A 1/15th scaled model (Fig. 1) of a typical European tractor-trailer configuration with a two-axle tractor and a three-axle trailer was used. For more information about the truck model the reader is referred to Haff [4].

The model was installed on a ground board of 2.6 m in length and 1.2 m in width 230 mm above the wind tunnel floor to eliminate contamination from the developing

Fig. 1 Wind tunnel setup in the SWG test section

wind tunnel boundary layer and to minimise the ratio of the boundary layer displacement thickness to the model ground clearance (Fig. 1, left). The blockage ratio of the test setup to the cross-sectional area of the test section was 4.1 %.

A 3-component piezo-electric force transducer type 9257B from Kistler was installed inside the model (Fig. 1, right). For the accurate measurement of the aerodynamic loads, a distance of 2 mm was set between the model wheels and the ground board surface. For all tested configurations, the pressure distribution on the trailer rear was measured with 36 unsteady pressure transducers type 8510B-1 from Endevco, a 1 psi high sensitive piezoresistive pressure transducer with a resonance frequency of 55 kHz. The pressure transducers were installed in small cavities directly at the rear side to resolve high frequencies in the pressure series. The force and pressure signals were recorded with a sampling frequency of 2 kHz over 45 s for each configuration. The reproducibility of the force and pressure measurement setup was investigated by the analysis of 20 single measurements with a standard deviation of the drag coefficient of $\Delta C_D = 0.00084$ (0.14 % of the full-scale output) and with $\Delta C_P = 0.0018$ (1.35 %) for the mean base pressure coefficient.

A PIV system was installed outside the test section to measure the unsteady wake velocity field behind the trailer. A Q-switched dual oscillator Nd:YAG laser with a pulse energy of 200 mJ from Litron and two thermoelectric cooled CCD cameras from PCO with a resolution of 2048 x 2048 pixels and a dynamic range of 14 bit were used. As tracer particles droplets of DEHS (Di-Ethyl-Hexyl-Sebacat) with a mean diameter of 0.6 μm were injected behind the test section.

Two different configurations were investigated. A baseline configuration (Fig. 2, left) representing a typical European tractor-trailer configuration and the proposed drag reduction concept with the trailer underbody equipped with a full fairing and a rear diffuser as shown in Fig. 2, right. The full fairing reduces the ground clearance to 35 % of the baseline case. With a width of 65 % of the model width ($W_m = 0.168$ m) the construction was installed along the full trailer length. The rear diffuser geometry consisted of a flat shaped diffuser wall with a constant axial length of 0.8 of the model width. Side plates were installed on both sides of the diffuser. The diffuser angles

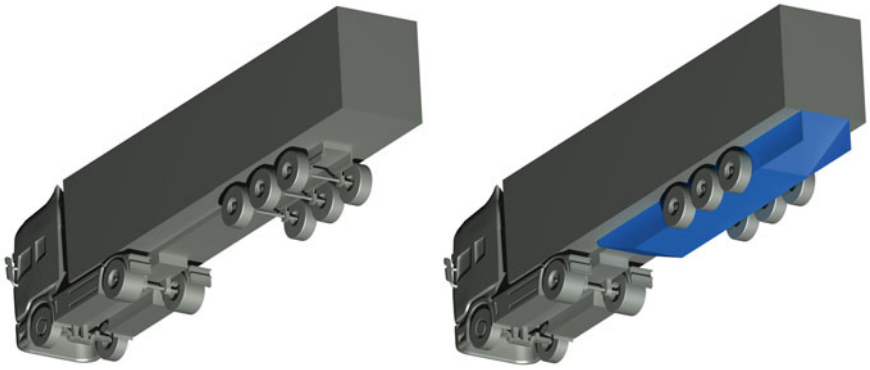

Fig. 2 Baseline configuration (*left*) and configuration with a 25° rear diffuser (*right*)

experimentally tested were 0°, 10°, 12.5°, 15° and 25°. All investigations were performed at zero yaw angle and for a Reynolds number of 6.50×10^5 based on the model width and the freestream velocity.

3 Numerical Flow Simulations

In the past decades CFD was established in the industrial development processes since it was shown that they can reduce the risk of potential design failures. In this study, CFD is used for the verification of the experimental results and to investigate the effect of the drag reduction method on the flow field characteristics around the model.

Thus, the wind tunnel experiment in the SWG was simulated with the open source "Computational Fluid Dynamics (CFD)"-code OpenFOAM by Joachim Tschech within the scope of a master thesis at DLR in 2012. Steady-state and unsteady Reynolds-averaged Navier-Stokes simulations were conducted using the k-ω SST turbulence model implementation in OpenFOAM. A hybrid-structured-unstructured grid consisting of 26 million cells was used. The flow region close to the model was solved by a continuous wall function. The non-dimensional wall distance y+ is below the required maximum of 50 for the used turbulence model. The simulation was started from uniform flow generated with the simple potential flow solver. After reaching a quasi steady-state the solution process was changed either to the steady or unsteady mode. In case of the unsteady RANS simulation a time step of 0.5 ms was used to set a Courant number <1 with a simulation time of 3 s. The force data were time averaged over 2,000 time steps to provide the statistical flow fields used for the comparison to the measurements.

A priori we performed grid independence simulations to investigate if the grid is sufficiently fine for resolving the large-scale flow structures in the wake behind the

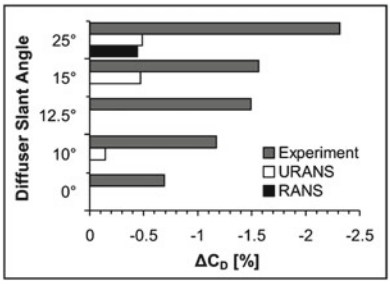

Configuration		Measured and Predicted Drag Coefficient			Relative deviation to the experimental data	
		Experiment	RANS	URANS	RANS	URANS
Baseline Configuration		0.585	0.594	0.589	1.59%	0.61%
Diffuser Slant Angle	0°	0.581	-	-	-	-
	10°	0.578	-	0.588	-	1.65%
	12.5°	0.576	-	-	-	-
	15°	0.576	-	0.586	-	1.73%
	25°	0.572	0.592	0.586	3.54%	2.49%

Fig. 3 Measured and predicted drag reduction of the diffuser configurations referred to the baseline case (*left*) and overview of all experimental and numerical drag force results (*right*)

trailer. In accordance to the experiments all numerical simulations were performed for a Reynolds number of 6.50×10^5. After an insufficient prediction of the measured drag force reduction between the baseline case and the most efficient configuration with a diffuser angle of 25° with the calculation of the steady-state RANS equations the performance of a unsteady flow solver was tested. In summary, the diffuser angles simulated were 25° with RANS and 10°, 15° and 25° with URANS.

4 Results and Discussion

The experimentally and numerically obtained aerodynamic drag coefficient C_D is presented in Fig. 3 for the baseline case and all investigated diffuser configurations. A reduction of the aerodynamic drag coefficient at increasing diffuser slant angles was measured in the wind tunnel experiment with a maximum reduction of 2.4 % at an angle of 25° compared to the baseline configuration.

The comparison of the measured and predicted drag coefficients revealed that the latter are overestimated. The relative deviations for increasing slant angles are about one order of magnitude lower. Apart from the absolute prediction concerning the experimental data the relative deviation between the baseline case and the configuration with a maximum investigated diffuser angle is comparable between steady-state and unsteady RANS. In general, the estimation of the aerodynamic loads with CFD is challenging particularly for the separated flow region behind a tractor-trailer configuration. It is well-known that the wake velocity field behind the trailer and the resultant base pressure distribution on the trailer back significantly affect the aerodynamic pressure drag. Due to a similar prediction of the relative reduction in aerodynamic drag between the steady-state and the unsteady case the following discussion is based on the results of the steady-state RANS simulations.

The visualisations in Figs. 4 and 5 show the flow field in the trailer's wake in a vertical streamwise plane of the model centerline in a side view. The velocity magnitude was determined from the two in-plane velocity components and was nor-

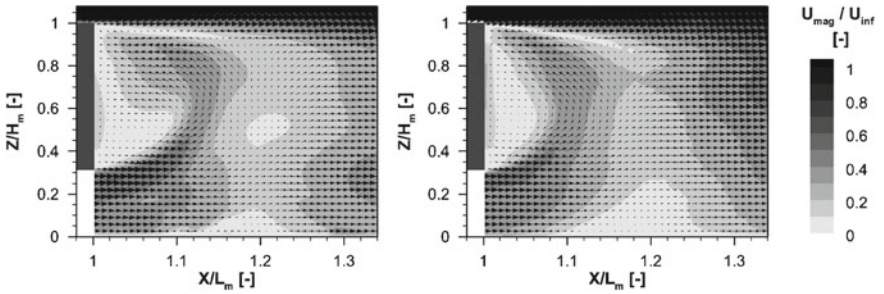

Fig. 4 Mean velocity magnitude contour plot and mean velocity vector field of the baseline configuration in the model symmetry of the steady-state RANS simulation (*left*) and the experiment (*right*)

malised with the freestream velocity. Additionally, every fifth vector of the mean velocity vector field is superimposed. The flow direction is from left to right with the trailer base shown as a grey cube on the left side. The length scales are based on the model dimensions. For the comparison of the experimentally and numerically obtained wake flow structures, the same spatial resolution of both data sets has been realised. The wake field region was resolved with an evaluation mesh size of 2 mm defined in both spatial dimensions. For the experimental analysis of the particle images an evaluation window size of the same order was defined. The window size was set to 24 $\times$ 24 pixels with a 50 % overlap and delivered a velocity vector every 1.87 mm. Thus, the resolution of the numerical and the experimental data are comparable. As shown in Fig. 4, right, the near wake is characterised by a recirculation region extending over the entire trailer box height. A second small counter-rotating vortex is located downstream the trailer base.

The RANS flow field of the baseline configuration qualitatively agrees with the measured wake as presented in Fig. 4, left. However, the predicted mean recirculation zone does not extend up to the upper trailing edge and the second counter-rotating vortex is located closer to the trailer base. Besides, the length of the measured mean recirculation zone X_R with 96 % of the trailer box height H_B is smaller than the predicted length of $X_R/H_B = 1.11$. Since the mean wake field is strongly correlated to the trailer's underbody flow with a much weaker influence of the upper shearing layer, it seems that a faster underbody flow leads to an increased length of the recirculation zone.

In addition, the mean wake field of the experimental and numerical data is presented in Fig. 5 for the most effective diffuser angle of 25°. In accordance to the baseline configuration the recirculation zone length is overpredicted in the numerical simulation by around 21.2 % with $X_R/H_B = 1.43$–1.18 in the experiment. A reduced vertical extension of the predicted recirculation zone can be also observed. Figures 4 and 5 reveal a similar effect of the rear diffuser on the measured and predicted mean velocity wake. At a diffuser angle of 25° the length of the recirculation zone is increased by around 22.9 % in the experiment compared to 28.8 % in the

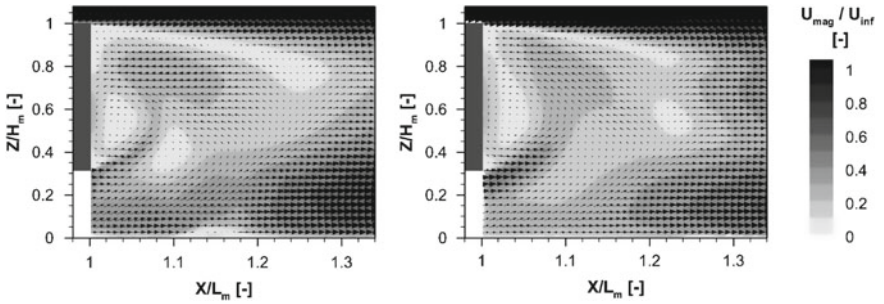

Fig. 5 Mean velocity magnitude contour plot and mean velocity vector field of the configuration with 25° rear diffuser in the model symmetry of the steady-state RANS simulation (*left*) and the experiment (*right*)

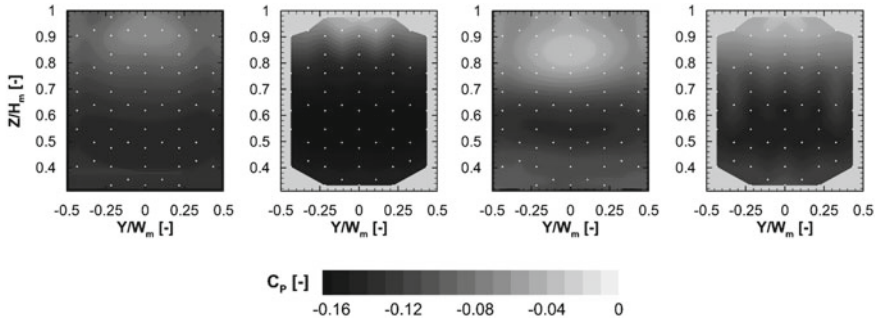

Fig. 6 Mean pressure coefficient at the trailer base of the baseline configuration (*CFD*(**a**), *Exp*.(**b**)) and with the 25° rear diffuser (*CFD*(**c**), *Exp*.(**d**))

simulation. Further, a more upward directed underbody flow with reduced mean flow velocities is obtained.

Another feature of the modified wake field presented in Fig. 5 is a three-dimensional flow effect indicated by a local velocity drop in the region of $X/L_m = 1.1$ and $Z/H_m = 0.4$ in the numerical and around $X/L_m = 1.12$ and $Z/H_m = 0.35$ in the experimental results. The study of the numerical results arrived at the conclusion that the observed flow phenomenon seems to be induced by a counter-rotating vortex pair generated by the diffuser shape. Stereoscopic PIV performed in a section cut orthogonal to the freestream direction confirmed the existence of two longitudinal vortices in the trailer's wake. A wake topology similar to that of the inclined rear end of an Ahmed body, which is the benchmark case in vehicle aerodynamics, is generated. Several research studies, e.g. Han [5], show the development of a counter-rotating vortex pair behind an Ahmed Body and a drag reducing effect at increasing slant angles.

The measured and predicted distributions of the mean pressure coefficient on the trailer base are presented in Fig. 6 for both investigated configurations.

The pressure tap location in the experiment is indicated by white dots with the pressure measured only at half of the trailer base. The experimental data are characterised by higher magnitudes than the predicted ones with a pressure gradient in vertical direction (Fig. 6b, d) whereas the numerical results reveal a local pressure rise in the upper part of the trailer base (Fig. 6a, c). Further, a correlation of the mean base pressure and the mean flow velocities close to the trailer base can be observed. High vertical flow velocities induce a low-pressure region and high base pressures are related to flow stagnation.

For the 25° rear diffuser configuration the average of the base pressures is increased by around 21.9 % in the experiment and 19.8 % in the simulation. In consistence to the experimental data the mean base pressure of the simulation is based on the pressure tap location in the experiment. In the experiment, the difference of the resultant pressure force on the trailer base is of the same order of magnitude as the reduction in drag force measured with the force transducer. Thus, the major part of aerodynamic drag reduction is induced by the manipulation of the low-pressure region behind the trailer. The simulations with moving ground predicted the same tendency of the base pressure characteristic whereas the difference between the baseline case and the configuration with 25° rear diffuser is less developed than at stationary ground conditions.

The overpredicted length of the recirculation zone in the numerical data is in accordance to the underpredicted base pressures and could explain the deviation in the predicted aerodynamic drag coefficient. We therefore plan simulations with a more sophisticated turbulence modulation to improve the prediction of the aerodynamic drag coefficient.

5 Conclusions

An experimental and numerical research study has been performed with a scaled model of a tractor-trailer configuration to investigate the drag reducing potential of a trailer with full fairing and a rear diffuser. A reduction of the aerodynamic drag coefficient of 2.4 % has been measured at the maximum investigated diffuser slant angle of 25°. Further, a significant influence of the trailer modifications on the mean velocity wake and the resultant base pressure distribution could be observed. Steady-state RANS simulations have confirmed the experimental results. Similar effects on the mean wake field structures and the base pressure distribution have been observed. The influence of the rear diffuser on the mean base pressure rise is of the same order of magnitude for the experiments and the simulations.

References

1. Gilhaus, A., Hau, E., Künster, R., Potthoff, J.: Über den Luftwiderstand von Fernlastzügen, Ergebnisse aus Modellmessungen im Windkanal Teil I+II. Automobil- Industrie 9/79, pp. 125–137 (1979) + 3/80, pp. 45–62 (1980)
2. Cooper, K.: Truck aerodynamics reborn— lessons from the past. SAE PaperNo. 2003–01-3376 (2003)
3. Official journal of the European communities. Council directive 96/53/EG (1996)
4. Haff, J., Jönsson, M., Richard, H., Loose, S.: Experimental investigation on a detailed European tractor-trailer configuration. Euromech Colloquium 509, Berlin (2009)
5. Han, T.: Computational analysis of three-dimensional turbulent flow around a bluff body in ground proximity. AIAA J. **27**(9) (1989)

Experimental Study of the Pressure Rise due to Tunnel Entry of a High-Speed Train

Daniela Heine and Klaus Ehrenfried

Abstract Entering a tunnel a high-speed train generates a pressure wave, which propagates along the tunnel and is partly reflected at the opposite tunnel portal. This wave leads to some severe problems like loads on the installations inside of the tunnel, discomfort of the passengers or even micro-pressure waves at the end of the tunnel. The tunnel-simulation facility Göttingen (TSG) was built in order to analyse these pressure changes and to develop systems, which smooth the pressure increase and reduce the pressure-depending problems in train-tunnel entry. The TSG is a moving-model rig, which allows a very realistic investigation of train-tunnel interaction. The train used is an ICE3-model made of carbon fiber scaled 1:25. The train speed ranged from 30 up to 45 m/s. The results of the experiments done in the TSG show, that the pressure gradient can be reduced by about 45 % using an extended, vented tunnel portal.

1 Introduction

When a train enters a tunnel a complicated system of pressure waves arises, which leads to many problems due to the passage of a high-speed train through a railway tunnel. The changes in pressure affect the installations inside of the tunnel as well as the train's structure in a negative way. Furthermore the comfort of the passengers can be compromised. So most high-speed trains are sealed to protect the passengers from the pressure waves. The sealing requires a reinforced construction of the inter-car connections and special measures at the airconditioning systems. By that

D. Heine (✉) · K. Ehrenfried
German Aerospace Center DLR, Department Fluid Systems, Bunsenstr. 10,
37073 Göttingen, Germany
e-mail: daniela.heine@dlr.de

K. Ehrenfried
e-mail: klaus.ehrenfried@dlr.de

A. Dillmann et al. (eds.), *New Results in Numerical and Experimental Fluid Mechanics IX*,
Notes on Numerical Fluid Mechanics and Multidisciplinary Design 124,
DOI: 10.1007/978-3-319-03158-3_34,

the weight of the train and its operating expenses are increased. Another problem with the generated waves occurs at the tunnel exit. When a compression wave propagates through a very long tunnel it can steepen and form a weak shock wave. At the tunnel exit such a shock wave would be emitted as a boom, which would have an unacceptable impact on the surrounding environment. To suppress the emission of pressure waves from the exit, modern tunnels are equipped with tunnel-entrance hoods, which have a larger cross section than the tunnel and which have extra windows through which air is vented out of the hood (see [1]). The hood reduces the initial pressure gradient and by that the onset of the non-linear steepening of the compression wave is delayed. In the past 15 years several theoretical and experimental studies of tunnel portals with different geometries were performed (see. e.g. [2]–[9]). For example Howe et al. ([2]) present a theoretical model which predicts the pressure gradient for the case of a tunnel hood where also the effect of windows is included. To validate their theoretical results experiments were conducted in a moving model rig (see [3]) where an axis-symmetric train model in scale 1:127 can be accelerated up to 450 km/h. However the influence of a complex tunnel portal is not completely understood. For example in the portals of the Katzenbergtunnel (for further informations: [1]) the air is vented from the hood into adjacent chambers before is exhaust to the surrounding. The effect of such chambers is not addressed in the theoretical approaches cited above. To test complex portal geometries in model scale the tunnel-simulation facility Göttingen (TSG) was build. It is a moving model rig, where train models scaled between 1:20 and 1:100 can be used. In the present paper it is shown that the effect of an extended tunnel portal can be investigated in this new facility. The experiments were performed with an 1:25 scaled ICE3 model. To check if the results are reasonable, the measured height of the compression wave is compared to different theoretical estimations.

2 Pressure Changes During the Passage of a Train Through a Tunnel

When a train passes a tunnel a complicated system of waves is generated. First a compression wave arises when the train head enters the tunnel. When the rear end of the train reaches the tunnel an expansion wave evolves. Both waves propagate into the tunnel at the speed of sound c. When they arrive at an observer far inside the tunnel first the pressure increases and then it drops back to roughly its initial value due to the expansion wave. The pressure decreases further when the train passes the observation point. The under-pressure beside the train can be explained by the flow around the train. Additionally waves which were reflected from the distant tunnel exit and waves which are generated when the train leaves the tunnel arrive at the observer. Hence, two or more waves might superpose at the observation point especially when the tunnel is relatively short.

2.1 Estimation of the Height of the First Pressure Rise

In literature several expressions can be found to estimate the height of the initial pressure rise Δp in the case of a train entering a tunnel without special tunnel hood. In general the pressure rise depends on the speed of the train U and the blockage ratio $\beta = A_z/A_t$ where A_z is the cross section of the train and A_t the one of the tunnel.
Assuming $\beta \ll 1$ Howe [4] derived from an acoustic analogy the relation

$$\Delta P_{Howe} = \frac{\rho U^2 \beta}{\left(1 - M^2\right)} . \tag{1}$$

where ρ is the density and $M = U/c$ the Mach number. Taking higher order effects into account Howe et al. [2] obtained

$$\Delta P_{Howe,ext} = \frac{\rho U^2 \beta}{\left(1 - M^2\right)} \cdot (1 + \beta) . \tag{2}$$

This extended expression gives a much better approximation for realistic values of β which can get up to 0.2 or even slightly higher. Using a completely different approach Ozawa derived the equation (see [5])

$$\Delta P_{Ozawa} = \frac{\rho U^2 \cdot \left(1 - \Phi^2\right)}{2 \cdot (1 - M)\left(M + \Phi^2\right)} \tag{3}$$

with $\Phi = 1 - \beta$. All three presented relations for ΔP are based on theoretical descriptions where the shear layer from the exit flow out of the tunnel entrance is treated in a simplified way. This shear layer occurs when the air displaced by the train is pushed backwards out of the tunnel entrance and the flow separates at the edge of the portal as it is illustrated in Fig. 1. Other viscous effects like the boundary layer at the train or the tunnel wall are neglected. To describe the generation of compression waves in tunnel portals with an entrance hood and to take the viscous drag on the train into account Howe et al. [2] developed a more sophisticated theory. This approach leads to an expression for the height of the initial pressure rise in the form

$$\Delta P_{Entrance} = P_E + P_D + P_W + P_J \tag{4}$$

where the contributions of different effects are summed up. P_E is the contribution of the entry wave, P_D represents viscous effects like the train boundary layer, P_W describes the influence of windows in the hood, and P_J is the contribution of the wave which occurs when the train passes the junction between hood and tunnel.

For a tunnel without hood P_W and P_J vanish, and P_E corresponds to the right hand side of Eq. (2). P_D can be estimated taking Eq. (23) from ref. [2]. This is done here to compare the experiments with a theory where the boundary layer on the train

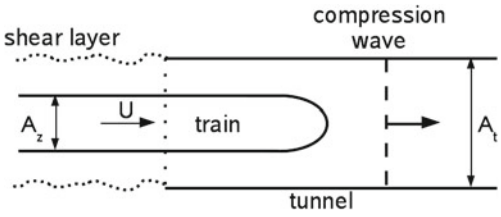

Fig. 1 Airflow while the train enters the tunnel

is taken into account. By estimating the pressure rise due to the viscous drag P_D the friction coefficient is supposed to be $\mu \approx 0.053$ (see [2]). The measurement position and time are the position of the pressure transducer (here: $x = 4.42$ m) and the time when the maximum in pressure is detected ($t \approx 0.043$ s). For further information see [2].

3 Experiments

The experiments were performed in the moving model rig of the DLR Göttingen using a 1:25 scaled ICE3 train model. The model tunnel is a section of a circular tube with a closed bottom which corresponds to a modern single-track railway tunnel like the Katzenbergtunnel [1] in the scale of 1:30. For the first tests a smaller scaled tunnel was used to obtain stronger effects and a better signal to noise ratio also at lower velocities. The resulting ratio of cross-sectional areas is $\beta \approx 0.23$.

The moving model rig has three sections: a catapult where the models are accelerated, the test section where the model tunnel is installed, and a brake consisting of a chamber around the track which is filled with polystyrene spheres. The catapult itself contains elements of an ancient Roman ballista and of the catapult of a modern aircraft carrier. It is designed to accelerate a 1 kg-model up to 100 m/s. In the present experiments the typical velocity is about 40 m/s, which goes along a maximum acceleration of 800 m/s^2 .

The concept of the moving-model rig has many advantages when transient aerodynamics are to be studied. In a conventional wind tunnel it is not possible to investigate the train-tunnel passage as realistic as in a moving-model rig. There are other facilities, which allow the investigation of transient effects, like the TRAIN Rig (*TR*ansient *A*erodynamics *IN*vestigation) of the University Birmingham in Derby (see [10] or [11]) or a moving-model rig at the Railway Technical Research Institute (RTRI) in Tokyo (see [3]). The RTRI-facility is twodimensional axisymmetric. Therefore the models are not as realistic as the TSG or TRAIN-rig models, but they perfectly suffice to study train-tunnel passages.

In Fig. 2 a photo of the ICE3 train model is shown. The model consists of three cars and has a length of 2.77 m. The model tunnel has a length of 10 m. As seen in Fig. 2 it can be equipped with a hood which acts as an extended tunnel portal (cf. [12]). The dimensions of the hood and the tunnel are given in Fig. 3. The pressure inside of the

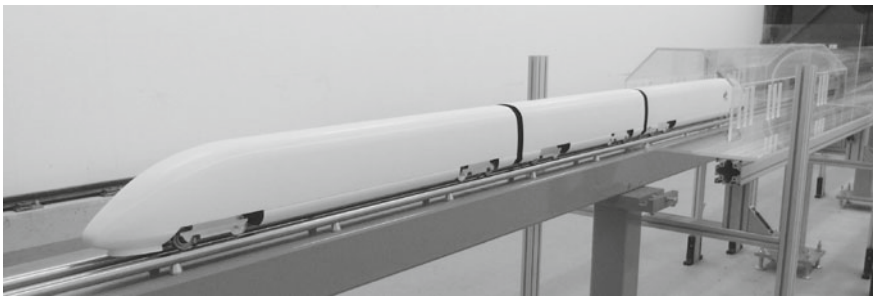

Fig. 2 ICE3-model with tunnel and tunnel hood

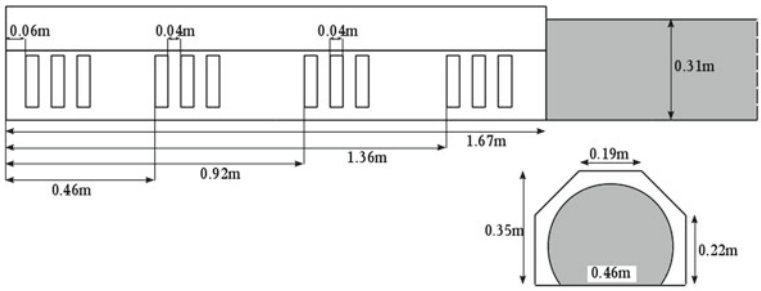

Fig. 3 Tunnel hood with wimensions (schematic)

tunnel was measured with piezoresistive pressure transducers (20 Endevco-sensors, model 8,510B-1, 1psi). Additionally, four light barriers were used to monitor the velocity of the train. The train velocity was varied from 37 to 46 m/s.

4 Results

4.1 Experiments Without Extended Tunnel Portal (Clear Configuration)

To obtain an overview of the behaviour of the pressure waves inside the model tunnel, experiments without extended tunnel portal were performed at several train velocities. Figure 4a shows the pressure-time histories at three different positions in the tunnel for the case $U = 42$ m/s. Each curve represents six independent tests, which were averaged to reduce the noise. The deviation of the train velocity was smaller that 1 %, thus it is allowed to average the data. The time $t = 0$ s is the moment, when the train nose enters the tunnel.

The pressure waves due to train-tunnel entry can be clearly correlated with the expected pressure changes. The black curve depicts the pressure at the first sensor

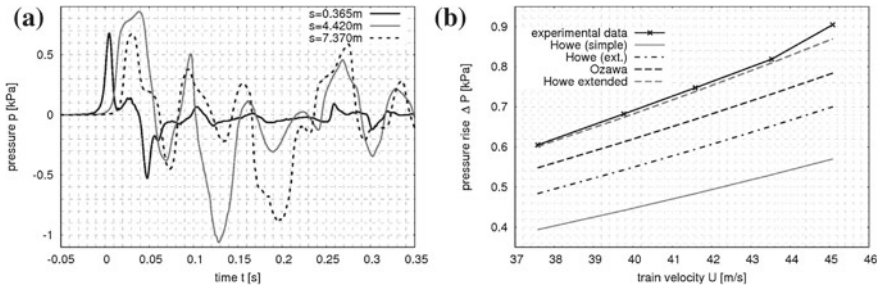

Fig. 4 Results of the measurements without extended tunnel portal **a** Pressure-time history at three positions in the tunnel

near the tunnel entrance. After the first pressure rise, the pressure decreases due to the train passage at the sensor. The second decrease in pressure is due to the entry of the train's rear end into the tunnel. The following pressure fluctuations are relatively weak, because at this position close to the entrance the waves superpose destructively with their own reflections. The other two curves show more clearly the reflections of the pressure waves. Furthermore, a pressure wave is generated due to the train leaving the tunnel, which is visible after $t = 0.23$ s in the grey and the dashed curves.

Figure 4b shows a comparison of the experimentally determined height of the first pressure rise ΔP with the theoretically expected ones. Generally, the experimental values are higher than theoretical predictions. Only the curve "Howe incl. drag" obtained with the extended theory of Howe et al. [2], where the viscous drag is taken into account, shows quite good agreement with the experiments. There 20 % of the pressure rise is due to the viscous drag. The influence of the drag can be seen by comparing the curves "Howe (ext.)" and "Howe incl. drag". The only difference in the evaluation of the pressure rise is the viscous drag. All theoretical estimations, which neglect the effect of the boundary layer on the train, show a large deviation. Literally the train is thickened by the boundary layer which leads to an effectively larger blockage ratio β and by that to a larger pressure rise.

4.2 Experiments With Extended Tunnel Portal (Hood Configuration)

To enlarge the rise time Δt of the pressure, an extended tunnel portal was installed. Figure 5 shows the resulting pressure-time history at the position $x = 4.42$ m from the tunnel entrance with the train velocity $U = 42$ m/s. To see the influence of the hood, the second curve depicts the pressure inside the tunnel at the same position without extended portal. Due to the tunnel hood, the pressure inside the tunnel rises earlier than without hood, because also a compression wave is generated, when the

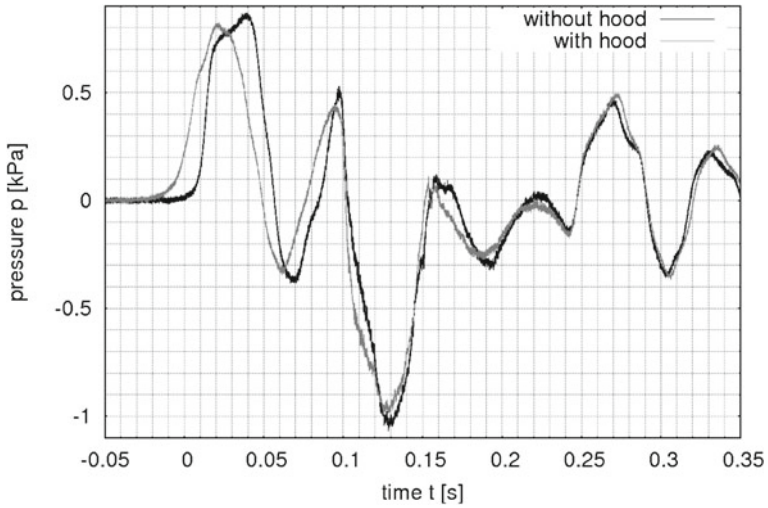

Fig. 5 Comparison between the pressure-time histories without and with hood

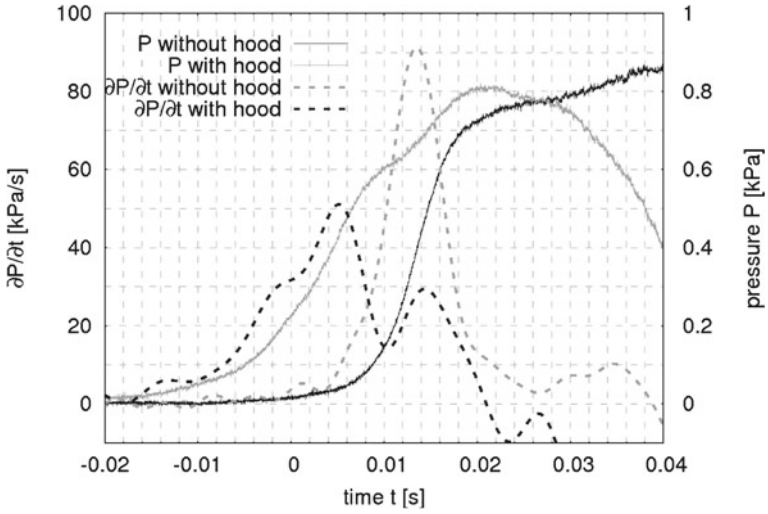

Fig. 6 Pressure gradient without and with tunnel hood

train enters the hood. A part of the air, which is pushed forwards by the train and the pressure wave, exhausts through the portal vents, whereas the other part of the air enters the tunnel. Therefore, the pressure inside the tunnel increases, before the train reaches the tunnel. Entering the tunnel, the train causes an additional compression wave, so that the pressure reaches its maximum. The final height of the pressure rise is not significantly affected by the portal. But, since the pressure rise starts earlier, the pressure gradient is smaller with than without portal. This is demonstrated in Fig. 6,

where the temporal derivation of the pressure is depicted. With hood, the maximum of the pressure gradient is about 44 % smaller compared to the case without tunnel hood.

5 Conclusion

It was demonstrated that the generation of pressure fluctuations due to the passage of a train through a tunnel can be investigated in model scale using the moving model rig of the DLR in Göttingen. The experimentally obtained height of the pressure rise agrees very well with the theoretical estimation if the effect of viscous drag is taken into account.

With the tunnel hood used in the experiments, the pressure gradient can be decreased by about 44 %. This is a promising result when one considers, that the tunnel hood was only utilized in one configuration so far. By adapting the size of open portal windows to the size and velocity of the train, the portal efficiency most probably can be improved. This has to be shown in further investigations.

References

1. Hieke, M., Gerbig, C., Tielkes, T., Deeg P.: Mastering micro-pressure wave effects: countermeasures at the Katzenberg Tunnel and Introduction of a new German regulation to get micro-pressure wave emissions under control. In: World Congress on Railway Research, 2003
2. Howe, M.S., Iida, M., Maeda, T., Sakuma, Y.: Rapid calculation of the compression wave generated by a train entering a tunnel with a vented hood. J. Sound Vib. **297**, 267–292 (2006)
3. Howe, M.S., Iida, M., Fukuda, T., Maeda, T.: Theoretical and experimental investigation of the compression wave generated by a train entering a tunnel with a flared portal. J. Fluid Mech. **425**, 111–132 (2000)
4. Howe, M.S.: Mach number dependence of the compression wave generated by a high-speed train entering a tunnel. J. Sound Vib. **212**(1), 23–36 (1998)
5. Ozawa, S.: Studies on the micro-pressure wave radiated from a tunnel exit. RTRI R. **1121**, (1979)
6. Vardy, A., Howe, M.S.: Rapid prediction of train nose entry pressure gradients. In: Proceedings of the 13th International Symposium on Aerodynamics and Ventilation of Vehicle Tunnels, vol. 2, pp. 429–443 (2009)
7. Heine, D., Ehrenfried, K.: Experimental study of the compression-wave generation due to train-tunnel entry. In: Proceedings of the First International Conference on Railway Technology, Civil-Comp Press, Stirlingshire, (2012). ISBN 978-1-905088-53-9, doi:10.4203/ccp.98.163
8. Howe, M.S., Cox, E.A.: Reflection and transmission of a compression wave at a tunnel portal. J. Fluids and Struct. **20**, (2005)
9. Rèty, J.-M., Grègoire, R.: Numerical simulation of the pressure wave generated when a train enters a tunnel. TRANSAERO-Projekt, (2002)
10. Johnson, T., Dalley, S.: 1/25 Scale Moving Model Tests for the TRANSAERO Project. Springer, TRANSAERO-Project (2002)
11. Johnson, T., Holding, J.: Better understanding of high speed train slipstream velocities. In: 6th World Congress on Railway Research, Edinburgh, 2003
12. Hieke, M.: Specification of Moving Model Tests. DB Systemtechnik, Munich, (2010)

Aerodynamic Loads Induced by Passing Trains on Track Side Objects

Sabrina Rutschmann, Klaus Ehrenfried and Andreas Dillmann

Abstract The aerodynamic loads on a sphere induced by the head pressure pulse of a passing train are calculated using potential flow theory. The results are compared with experimental data which were measured in a moving model rig. The loads were calculated using two different theoretical approaches. They show good agreement with the experimentally obtained results even though in the theoretical model the geometry of the train and the embankment is simplified.

1 Introduction

Passing trains induce aerodynamic loads on track side objects. To guarantee the safety of waiting passengers on platforms guidelines are required for the speed of trains driving through stations and for the safety distance between passengers and the platform edge. The European "Technical Specification for Interoperability (TSI)" [1] specifies several demands passing trains have to fulfill. Among other things the induced flow velocity and the generated pressure fluctuations at certain points are limited. But the velocity or pressure values obtained in a TSI acceptance procedure at only few test positions do not give for example the dependency of induced loads on the distance or the geometry of an object. Therefore it is desirable to have a reliable prediction tool for the aerodynamic loads as a function of all relevant parameters like the train speed, the train geometry, the geometry of the object, and the distance between train and object.

The flow field around a train can be split into three regions: The first one is the pressure wave generated by the head of the train—the head pressure pulse—the second one is the boundary layer next to the train and the third one is the wake

S. Rutschmann (✉) · K. Ehrenfried · A. Dillmann
German Aerospace Center DLR, Institute of Aerodynamics and Flow Technology,
Bunsenstrasse 10, 37073 Göttingen, Germany
e-mail: Sabrina.Rutschmann@DLR.de

A. Dillmann et al. (eds.), *New Results in Numerical and Experimental Fluid Mechanics IX*,
Notes on Numerical Fluid Mechanics and Multidisciplinary Design 124,
DOI: 10.1007/978-3-319-03158-3_35,

behind the train. The present paper concentrates on the head pressure pulse. It is widely accepted that the flow around the train head can be accurately described using potential flow theory. The boundary layer in the head region is relatively small. Only for trains with extremely blunt heads, where separation occurs, significant deviations from a potential flow field may be observed. Steinheuer [2] describes a panel method to compute the potential flow around a train head. He presents results for different head geometries and a validation of the numerical results with model and full scale experiments. Additionally Steinheuer [2] introduces a simplified potential flow model to compute the induced loads on track side objects. But the presented model is restricted to an axial-symmetric head geometry and to cylindrical objects. In the present paper a potential flow model is introduced which is more flexible with respect to the geometry of the train head but still requires only little computational effort. In the first tests a sphere is used as track side object. The numerical results obtained with this model are validated with experiments in a moving model rig. Finally a further simplification of the theoretical model is presented which requires even less computational effort but which can be extended in a straightforward way to different object geometries.

2 Potential Flow Model

2.1 Generation of Train Contour

The train is modeled as potential flow body in homogeneous flow using three monopole sources of equal strength Q_* in the train head. Corresponding sinks are located in the tail [3]. The source positions were adjusted to have a geometry similar to the ICE 3 [4]. All sources and sinks are mirrored at the x-y-plane to simulate a floor. This gives in total $n = 12$ sources/sinks. The collection of streamlines starting from the stagnation point is interpreted as the surface of the train as it is shown in Fig. 1. The velocity potential ϕ in the reference system of the train is the sum of the solutions of the Laplace-equation $\Delta\phi = 0$ for the homogeneous flow and for the sources/sinks. It holds

$$\phi_{Train} = u_\infty x - \sum_{i=1}^{n} \frac{Q_i}{4\pi} \frac{1}{\sqrt{(x - x_i)^2 + (y - y_i)^2 + (z - z_i)^2}} , \qquad (1)$$

where x_i,y_i and z_i are the coordinates of the positions of the sources/sinks and $Q_i = \pm Q_*$ their strengths. The first source in the train head defines the position $x = 0$. For a given cross section A of the train and train velocity u_∞ the source strength Q_* can be calculated using

$$3Q_* = A \cdot u_\infty. \qquad (2)$$

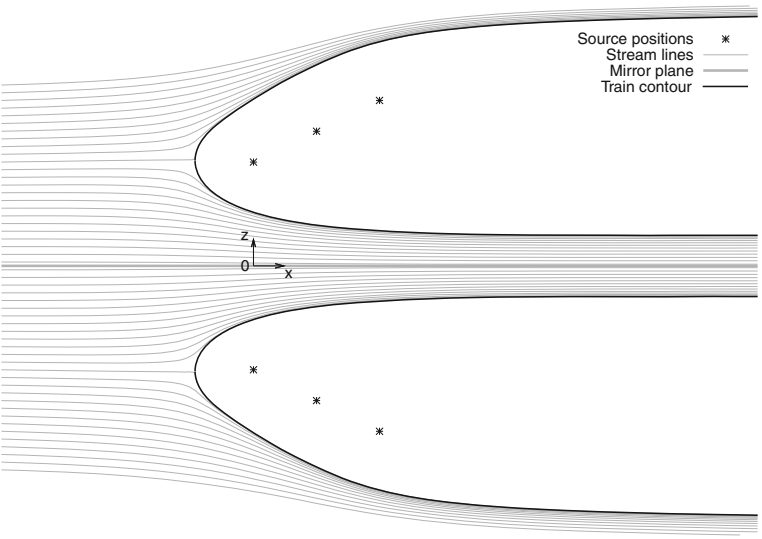

Fig. 1 Cut through the y = 0 plane: stream lines and contour of the train with mirror plane and mirror train

2.2 Generation of a Track Side Object

In the present tests a sphere is taken as generic track side object. It is generated by a dipole moving with flow velocity u_∞ in x-direction. Consequently the time-dependent dipole potential reads

$$\phi_D(t) = -\frac{1}{4\pi}\left(\frac{Q_x(t)\big(x - x_D(t)\big)}{r^3} - \frac{Q_y(t)\big(y - y_D\big)}{r^3} - \frac{Q_z(t)\big(z - z_D\big)}{r^3}\right), \quad (3)$$

with $x_D(t) = x_0 + u_\infty t$. Q_x, Q_y and Q_z are the dipole moments in the respective directions and $r = \sqrt{(x - x_D(t))^2 + (y - y_D)^2 + (z - z_D)^2}$ is the distance from the dipole. The dipole moments, describing the sphere, are calculated using control points $\vec{T}_i$ on the sphere's surface. Two diametric points are taken in the direction of each dipole. For example, at the control position $\vec{T}_1 = R\,(1\ 0\ 0) + \vec{x}_D(t)$ the boundary condition

$$\left.\frac{\partial \phi_D}{\partial x}\right|_{\vec{T}_1} + \left.\frac{\partial \phi_{Train}}{\partial x}\right|_{\vec{T}_1} = 0, \quad (4)$$

should hold on the impermeable surface. Since there are two control points for each dipole moment the problem is overdetermined. The strength of a dipole moment is chosen so that the sum of the square residuals of the two respective conditions is minimized.

2.3 Calculation of the Unsteady Loads

The aerodynamic loads on a sphere are calculated by numerical integration of the pressure on the sphere's surface. The pressure is computed using the unsteady Bernoulli-equation

$$\frac{\partial \phi}{\partial t} + \frac{\vec{u}^2}{2} + \frac{p}{\rho_0} = \text{const.} = \frac{p_0}{\rho_0} \ . \tag{5}$$

Here, p_0 and ρ_0 are the ambient conditions and ϕ is the sum of the velocity potential of train and sphere. The temporal derivative of ϕ is calculated numerically using the difference quotient.

3 Experimental Setup

To verify the theoretical considerations,experiments in the "Tunnel-Simulation-Facility" in Göttingen (TSG), Germany [5] have been performed. In this facility, models are accelerated by a hydraulic catapult and are moving freely through the test section. A three-parted ICE 3 [4] model in scale 1:25 was used in the experiment. An embankment as required in the TSI-norm [1] was installed. This differs from the plane floor used in the theoretical model. The sphere as generic track side object is realized by polystyrene spheres of different sizes. They were fixed at an one-component cantilever balance (cf. [6]).

4 Comparison of Potential Flow Theory with Experiments

The aerodynamic loads were measured for a train velocity of $u_\infty = 37.7\,\text{m/s}$ and the track distance of the sphere was $y_D = 0.92 \cdot D$, where $D = 0.12\,\text{m}$ was the width of the train model. The radius of the sphere was $R = 0.17 \cdot D$. For each condition the experiment was repeated five times and the results were averaged to reduce the internal noise from the balance as well as external vibrations which were propagating from the floor into the mounting of the balance. In Fig. 2 the measured force coefficients in x- and y-direction are compared to the calculated ones.

The peak at $x/D = 0$ is the force induced by the head pressure pulse, while the one at $x/D \approx 22$ is caused by the passing tail of the train. The reason for the smaller peaks in between are the inter-car gaps. Although the model geometries are different, the measured and calculated forces do not differ much. The existing differences are supposedly owed by the different train and floor geometries. In particular for the force induced by the head pressure pulse, good agreement is obtained. This agreement justifies the general assumption that the interaction between train and object can be described by potential theory. In contrary, large deviations are obtained in the

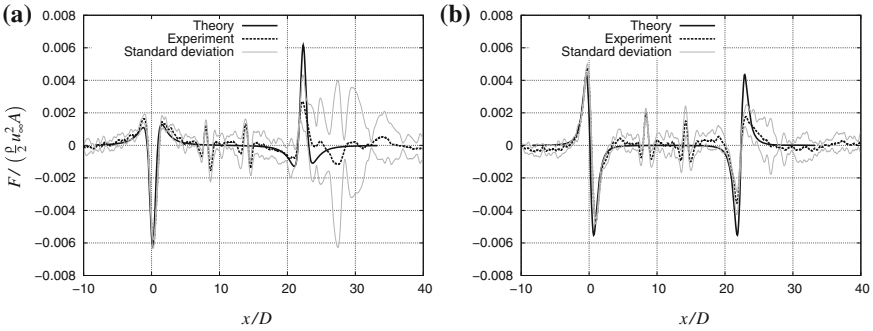

Fig. 2 Comparison of the aerodynamic loads in (**a**) direction of travel and (**b**) in lateral direction, between experiment (*black*) and theory (*red*) for a sphere with $R = 0.17 \cdot D$, a track distance of $y_D = 0.92 \cdot D$ and a flow velocity $u_\infty = 37.7$ m/s

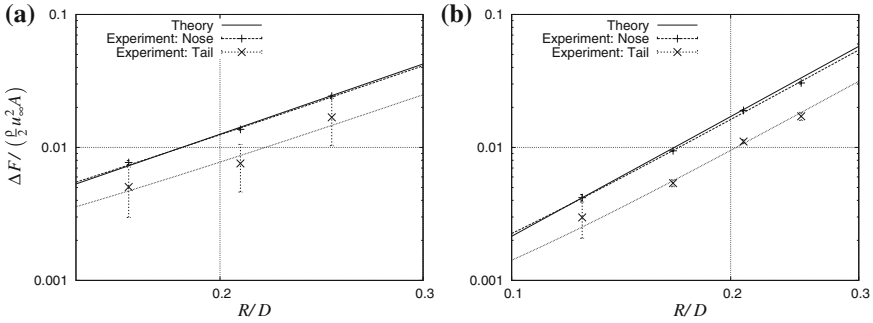

Fig. 3 Dependence of the loads on a sphere on the sphere radius, $u_\infty = 37.7$ m/s, $y_D = 0.92 \cdot D$. **a** x-direction and **b** y-direction

tail region, which is influenced stronger by viscous effects. Further, the standard deviation in this region is no longer an indicator for measurement uncertainty but for turbulent fluctuations. The latter are more significant in direction of travel than across to it.

In the following it is considered how the force scales with the sphere radius. Figure 3 shows the force amplitude obtained in experiments compared to the calculated ones for different sphere radii between $R = 0.125 \cdot D$ and $R = 0.25 \cdot D$. Here ΔF is the peak-to-peak amplitude of the force during the head passage. Good agreement is obtained for all considered radii. In addition it is found, that the amplitude is proportional to the cube of the radius. Note, that this is in contrast to the simplified model of Steinheuer [2] where the amplitude scales with the surface area of the object.

Since in steady aerodynamic loads are typically proportional to the surface area of an object it is reasonable to assume that in the present case unsteady effects are dominating. Recapitulating Bernoulli's equation (5), it is expected, that the unsteady

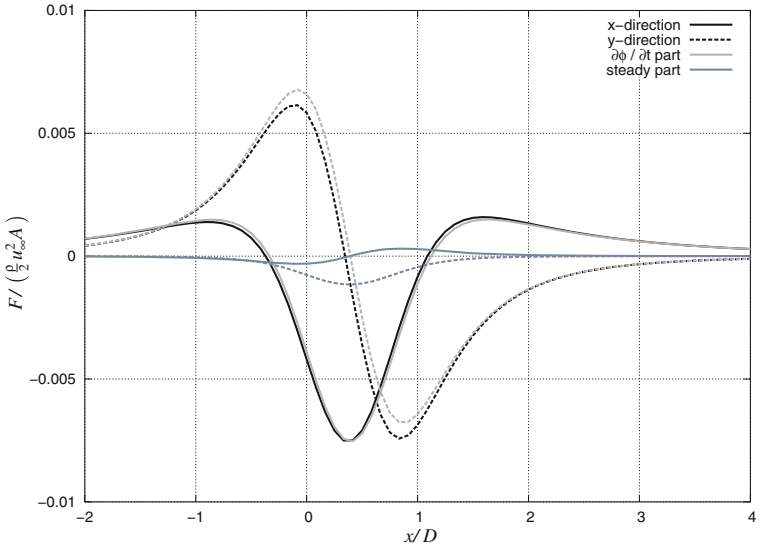

Fig. 4 Steady (*dark-gray*) and unsteady part (*light-gray*) of the force and total force (*black*) on the sphere with $R = 0.17 \cdot D$ in x-direction (*solid*) and y-direction (*dashed*), at a track distance of $y_D = 0.83 \cdot D$ and a flow velocity of $u_\infty = 37.7$ m/s

part $\partial\phi/\partial t$ is larger than the $\vec{u}^2/2$. To check this assumption, in Fig. 4 both parts are compared for the head pressure pulse. Indeed the unsteady part is dominating the force.

5 Simplified Model for the Calculation of Aerodynamic Loads

The results in the previous section show that the force on the sphere is dominated by linear effects which are related to the time derivative $\partial\phi/\partial t$ of the flow potential. The situation appears to be similar to the case where a force on a sphere is caused by the scattering of a plane acoustic wave. Of course in the acoustic case compressibility effects may be important in contrast to the incompressible flow considered above. But if the wave length λ of the incoming wave is large compared to the radius R of the sphere the acoustic field in the vicinity of the sphere corresponds in good approximation to an incompressible, potential flow field. The acoustic wave causes an acceleration of the fluid at the position of the sphere. The sphere obstructs this acceleration which requires a force acting on the fluid. For a relative large wave length in the sense $\lambda \gg R$ the scattering problem is typically treated [7] by splitting up the acoustic field in the undisturbed incoming wave and a scattering part which corresponds to the field of a transversely oscillating sphere. The velocity of the oscillating sphere $\vec{u}_{\text{osc}}$ is opposite to the velocity of the incoming wave $\vec{u}_{\text{inc}}$.

According to this approach the force which acts on the sphere can be split up in the force $\vec{F}_{\text{osc}}$ acting on the oscillating sphere and the force $\vec{F}_{\text{inc}}$ which results from the integration of the pressure p_{inc} of the undisturbed incoming wave over the surface of the sphere. Following [8] the former is given as

$$\vec{F}_{\text{osc}} = -\frac{2}{3}\pi R^3 \rho_0 \frac{\partial \vec{u}_{\text{osc}}}{\partial t}. \tag{6}$$

Note that this relation only holds for the considered case $\lambda \gg R$. This means that the sphere is compact in the acoustic sense and that in the vicinity of the sphere the spatial variation of $\vec{u}_{\text{inc}}$ and $\nabla\, p_{\text{inc}}$ can be neglected. Hence, the integration of the pressure over the sphere leads to

$$\vec{F}_{\text{inc}} = -\frac{4}{3}\pi R^3 \nabla\, p_{\text{inc}}.$$

Using $\vec{u}_{\text{osc}} = -\vec{u}_{\text{inc}}$ together with the linearized Euler equation the time derivative $\partial \vec{u}_{\text{osc}}/\partial t$ can be replaced by $(1/\rho_0)\nabla\, p_{\text{inc}}$. This gives for the total force acting on the sphere

$$\vec{F} = \vec{F}_{\text{inc}} + \vec{F}_{\text{osc}} = -2\pi R^3 \nabla\, p_{\text{inc}}. \tag{7}$$

As above the resulting force is proportional to the cube of the radius R.

The approach used in the scattering problem is now adopted to calculate the forces on the sphere during the train passage. Therefore in a first step the undisturbed, steady, potential flow around the train without sphere is calculated. Then the pressure gradient in this undisturbed flow at the position of the sphere is taken as $\nabla\, p_{\text{inc}}$ and the force on the sphere is calculated using Eq. (7). By shifting the position of the sphere along the train the temporal evolution of the force can be obtained easily without computing an unsteady solution. Of course, in contrast to the considered acoustic case the flow field around the train head is three-dimensional and the pressure gradient is not spatially constant. At the position of the sphere the iso-surfaces of the pressure field have a curvature unlike the wave fronts in a plane acoustic wave. But for a tiny sphere which is very small compared to the width or length of the train head the radius of this curvature is relative large and in the vicinity of the sphere the pressure gradient is approximately constant. Hence, this approach implies beside the neglection of nonlinear effects the assumption that the radius R is much smaller than the dimensions of the train. In Fig. 5 the x and y-components of the resulting force are shown as a function of the train position relative to the sphere. For comparison the corresponding results computed with the method described in Sect. 2 are depicted. In the presented case the radius of the sphere is $R = 0.17\, D$. This means that the sphere was not really tiny compared to the train width. Nevertheless the results obtained using the simplified approach are in quite good accordance with the results from the unsteady computations. It seems that the inhomogeneities in the pressure field of the train do not have a strong influence on the resulting force and that indeed the process is dominated by the local obstruction of the accelerated flow.

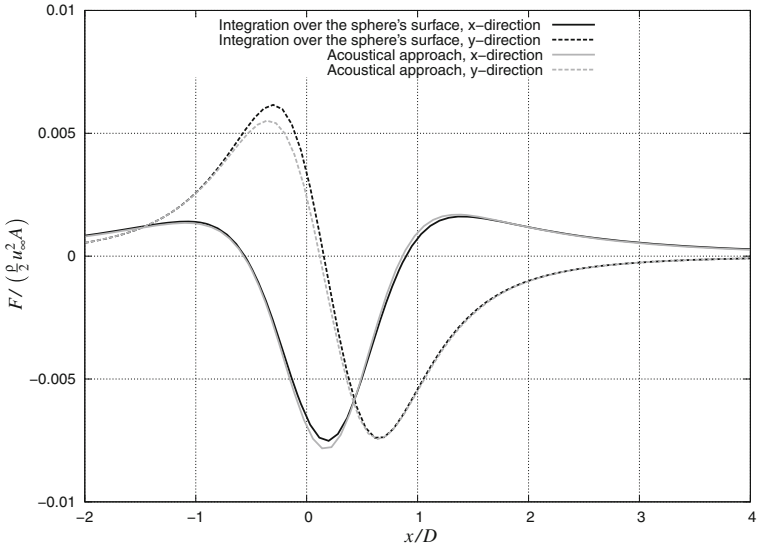

Fig. 5 Comparison of the force calculated with both theoretical models on a sphere with $R = 0.17 \cdot D$, at a track distance of $y_D = 0.83 \cdot D$ and a flow velocity of $u_\infty = 37.7$ m/s

6 Conclusion

The aerodynamic loads on a sphere induced by the head pressure pulse of a passing train were calculated using a potential flow model. The theoretical results were verified with experiments in a moving model rig. Good agreement between experimental results and the theory is obtained. The dependency of the force amplitude on the sphere radius obeys a cubic law $F \propto R^3$. It is shown that the unsteady part of the Bernoulli equation dominates the pressure load on the sphere. The situation is comparable to the scattering of an acoustic wave at the sphere at low frequencies. This leads to a simplified model where the forces are calculated neglecting nonlinear effects and the three-dimensionality of the head pressure field. Nevertheless, the results obtained with the simplified model are still in good agreement with the results of the model which uses the full potential solution and the unsteady Bernoulli equation. Since solutions exist for the scattering of waves at other object geometries, the simplified model might be used in further studies to predict the forces on different objects like for example disks.

References

1. Amtsblatt der Europäischen Union. ENTSCHEIDUNG DER KOMMISSION vom 21. Februar 2008 über die technische Spezifikation für die Interoperabilität des Teilsystems Fahrzeuge des transeuropäischen Hochgeschwindigkeitsbahnsystems (2008)
2. J. Steinheuer. Aerodynamische Wirkungen von schnellfahrenden Schienenfahrzeugen auf die Umgebung. DFVLR-Bericht IB 129–81/10, Institut für Entwurfsaerodynamik Braunschweig (1981)
3. Wieghardt, K.: Theoretische Strömungsmechanik. Universitätsverlag Göttingen (2005)
4. Deutsche Bahn AG. Faktenblatt ICE 3MF (2007)
5. Heine, D., Ehrenfried, K.: Experimental study of the compression-wave generation due to train-tunnel entry. In: Proceedings of the First International Conference on Railway Technology, ISBN 978-1-905088-53-9 doi:10.4203/ccp.98.163 (2012)
6. Wood, R.J., Cho, K.-J., Hoffman, K.: A novel multi-axis force sensor for microrobotics applications. Smart Mater Struct **18**, 125002 (2009)
7. Lord Rayleigh, F.R.S. XXXVII: On the passage of waves through apertures in plane screens, and allied problems. Phil Mag Ser 5, **43**, 263, 259–272 (1897)
8. Pierce, A.D.: Acoustics: An Introduction to its Physical Principles and Applications. Acoustical Society of America, New York (1989)

Flow-Induced Airborne and Structure-Borne Noise at a Simplified Car Model

Stefan Müller, Stefan Becker, Christoph Gabriel, Reinhard Lerch and Frank Ullrich

Abstract Experimental investigations of flow-induced noise and the resulting interior acoustics are presented. The turbulent flow field next to the side window results in sound sources and, consequently, in the radiation of sound. The combination of these sound pressure fluctuations and the hydrodynamic wall-pressure fluctuations excites the side window and results in radiation of noise into the passenger cabin. To investigate these physical effects, a simplified model of an automobile was set up. The whole model is insulated acoustically in such a way that noise radiation to the interior is limited to the side window. To modify the flow around the model, a square bar at the a-pillar or a side mirror model was mounted. A microphone at the position of the driver's ear detected the sound radiation to the interior. In order to quantify excitation of the side window, phase-resolved laser-scanning vibrometer measurements were performed. Furthermore, unsteady pressure measurements were carried out at the window surface. The investigations led to a better understanding of the physical mechanism of flow-induced sound generation and also the contribution of sound sources to the interior acoustics.

S. Müller (✉) · S. Becker
Institute of Process Machinery and Systems Engineering (iPAT),
University of Erlangen-Nuremberg, Cauerstr. 4, D-91058 Erlangen, Germany
e-mail: mue@ipat.uni-erlangen.de
http://www.ipat.uni-erlangen.de

S. Becker
e-mail: sb@ipat.uni-erlangen.de

C. Gabriel · R. Lerch
Department of Sensor Technology (LSE), University of Erlangen-Nuremberg,
Paul-Gordan-Str. 3/5, D-91052 Erlangen, Germany

F. Ullrich
BMW AG, EG-42, D-80788 Munich, Germany

A. Dillmann et al. (eds.), *New Results in Numerical and Experimental Fluid Mechanics IX*,
Notes on Numerical Fluid Mechanics and Multidisciplinary Design 124,
DOI: 10.1007/978-3-319-03158-3_36,

1 Introduction

One aim of the ongoing development of passenger cars is to predict and to optimize the interior acoustics early in the product development process. A significant noise component results from the flow phenomena in the field of the side doors. The complex turbulent flow field involves acoustic sources in the field and due to the interaction of the flow with solid surfaces. Both these sound pressure fluctuations and the hydrodynamic pressure fluctuations in the wake of the front of the vehicle, the a-pillar and the side mirrors excite the doors. These excitations cause the radiation of airborne and structure-borne noise to the interior.

In the present work, the radiation of noise via the side window to the driver's ear was studied in detail. For this purpose, a test case was developed which represents a simplified model of an automobile. A description of the test case is given in the following section.

The experiments were performed in a low-noise wind tunnel using microphone measurements and unsteady pressure measurements. Flow-induced structural vibrations were determined by a laser-scanning vibrometer. Additionally, the wavenumber spectra of the wall-pressure fluctuations were calculated. Further details of the experimental methods are given below.

For several decades, numerous investigations have been performed on the interaction of pressure fields with flexible plate structures (e.g., [6]) and the flow and sound field in the wake of vehicle components and side mirrors (e.g., [4]). Detailed investigations of the flow field, the pressure fluctuations at the surface of a flat plate or the side window and the sound radiation to a cavity or the interior have been reported recently (see, e.g., [1, 3, 7]).

2 Model Setup

The outer geometry of the car model is identical with the SAE Type 4 body (see Fig. 1) [8]. The whole model is acoustically insulated in such a way that noise radiation to the interior is limited to the side window. The streamwise and spanwise extension of the glass plate is illustrated in Fig. 1, corresponding approximately to real side windows. Sheet glass with a thickness of $h_g = 3$ mm was selected. The glass plate is fixed to a frame by means of silicone at each edge over a length of 30 mm. As frame material, a wooden sandwich element with two heavy layers was used. For the experimental investigations, there was no mechanical connection between the side window element and the complemental frame of the car model. The window element lay swimming in a bed of sealing material, and gaps between the surface of the vehicle model and the surface of the window element were sealed and closed with tape. This mounting limits the noise radiation to the interior to the free surface of the side window and prevents transmission of structure-borne sound via the frame.

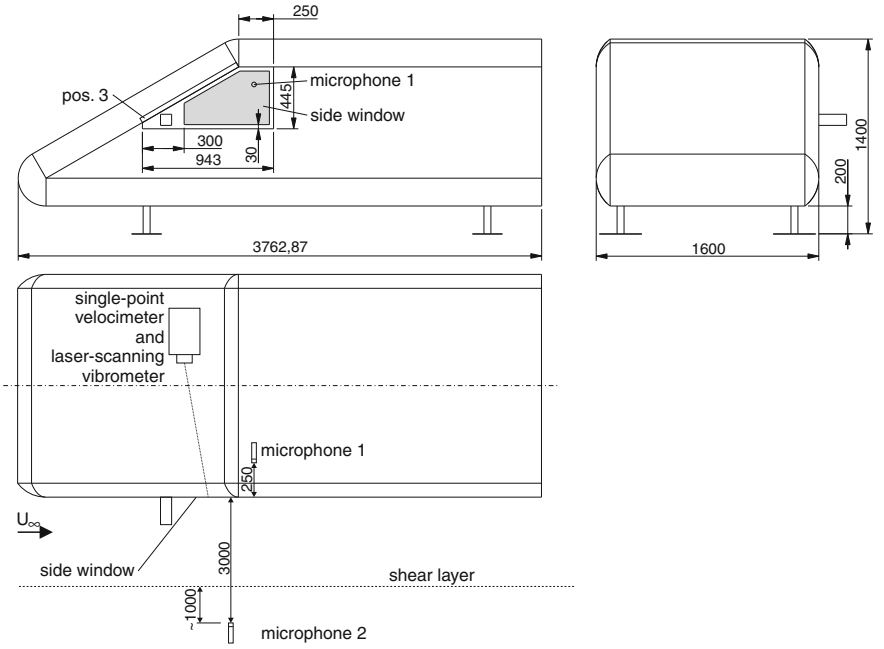

Fig. 1 Schematic drawing of the setup (units in mm)

According to regions with better absorbing characteristics in passenger cars, absorbers were attached to the walls and to the roof interior. In addition, a carpet covered the bottom interior. These absorbers are indispensable to obtain a reverberation time comparable to that in real cars [5]. The configuration with the whole driver's door fully insulated represents the reference in terms of the performance of the model setup. For the wind tunnel experiments, the model was not mounted directly to the balance of the wind tunnel; rather, there was a damper between the vehicle body and the cylindrical stilts.

In order to induce excitation of the side window, an obstacle at the a-pillar or a simplified side mirror was mounted. To induce periodic vortex shedding from the model of the side mirror, a model with square cross-sectional area was attached to the car model. The mirror model with an edge length of $D = 80$ mm had a ratio between height and edge length of $H/D = 2.5$ which is similar to that for real side mirrors. To disturb the flow around the a-pillar, a square bar with an edge length of 20 mm and an overall length of 800 mm was mounted at position no. 3 in the radius of the a-pillar (see Fig. 1). To generate a basis for comparison, additional investigations were carried out without any obstacle. A free-stream velocity of $U_\infty = 80, 100, 120, 150$ and 180 km/h was applied.

3 Experimental Method

The measurements were performed under semi free field conditions in the acoustic wind tunnel of BMW AG, Munich [8].

A 1/2-inch free field condenser microphone (B&K 4189) was employed for the sound measurements at the position of the driver's ear facing the side window at a distance of 250 mm, and another one was positioned next to the measuring section facing the side window at a distance of 3 m. There was a distance of approximately 1 m between the microphone next to the measuring section and the shear layer of the wind tunnel flow. Additionally, the outer microphone was protected by a wind screen (see Fig. 1).

Phase-resolved laser-scanning vibrometer measurements were carried out to identify the vibration modes of the side window. For this purpose, a Polytec single-point laser-Doppler velocimeter (OFV-505) was used together with a Polytec scanning vibrometer (PSV-400) to detect the vibration velocity of the side window at 1,624 uniformly distributed measuring positions. The microphone at the driver's ear acted as an additional reference for correlation measurements.

To investigate the correlation of different pressure fluctuations at the surface of the side window, correlation measurements of 39 homogeneous distributed piezoresistive pressure transducers (Kulite XCS-093-1PSID) were carried out. The pressure transducers had an diameter of 2.42 mm and were inserted into drill holes in an aluminium plate instead of the glass plate, resulting in flush surfaces between the pressure transducers and the aluminium plate.

For the microphone measurements, a standard measurement time of 60 s was used at a sample rate of 96 kHz and, for the correlation measurements, a measurement time of 180 s was used at a sample rate of 44.1 kHz. Simultaneous recording of the different signals was guaranteed by the National Instruments data acquisition system (PXIe-1082 with PXIe-4496 and PXIe-4331).

4 Results

Unless noted otherwise in the following sections, the results correspond to investigations at a free-stream velocity of $U_\infty = 150$ km/h. As mentioned in Sect. 2, "fully insulated" defines the reference case with the whole door element fully insulated; "w/o obstacle" means that neither the mirror model nor the square bar at the a-pillar was mounted, but the side window was present.

4.1 Interior Acoustics

Figure 2 (left) shows the spectra of the measurements of the sound radiation to the driver's ear for the single configurations described in Sect. 2. The spectrum of

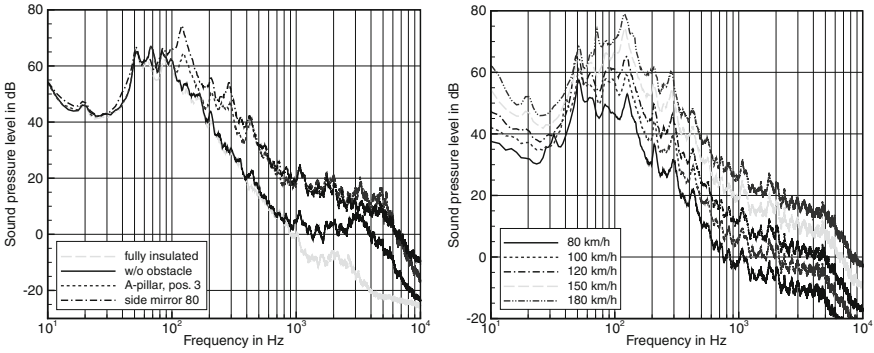

Fig. 2 Sound pressure level at the position of the driver's ear: comparison of different configurations (*left*) and free-stream velocities (*right*; case with mirror model)

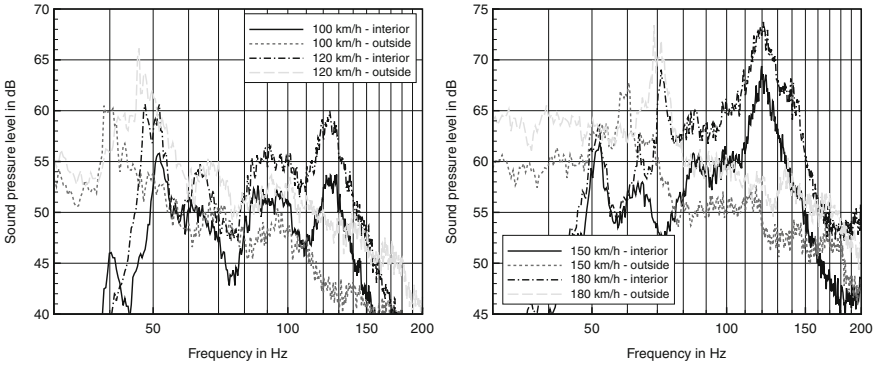

Fig. 3 Sound pressure level at the position of the driver's ear *(interior)* and at the microphone next to the measuring section *(outside)*, with different free-stream velocities; case with model of the side mirror

the case without any obstacle differs significantly from the acoustic fully insulated configuration over 1 kHz. The spectra of the cases with the model of the side mirror and the obstacle at the a-pillar have an almost constant offset from the fully insulated reference for frequencies greater than 100 Hz. With the mirror model, the tonal components between 100 and 300 Hz are more prominent, but with the square bar at the a-pillar, the broadband noise over 1 kHz is more dominant.

With increasing free-stream velocity, the amplitude of the radiated sound rises in accordance with expectation (Fig. 2 (right)). Under 100 Hz, many cavity modes are excited. Figure 3 shows the sound radiation to the interior and to the microphone next to the measuring section depending on the free-stream velocity for the frequency range from 30 to 200 Hz. The frequency resolution amounts to 0.35 Hz. Next to the measuring section, the tonal components resulting from periodic vortex shedding at the mirror model are clearly visible at approximately 40, 50, 60, 70 Hz for $U_\infty =$ 100, 120, 150, 180 km/h, respectively. However, at the driver's ear, it is difficult to

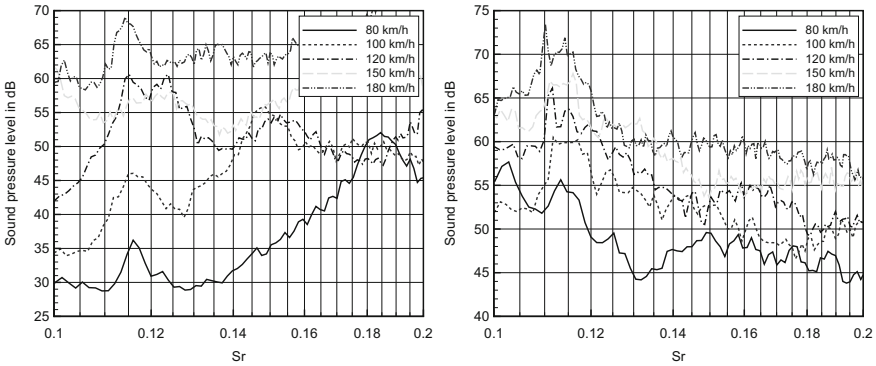

Fig. 4 Sound pressure level at the position of the driver's ear (*left*) and at the microphone next to the measuring section (*right*), with different free-stream velocities; case with model of the side mirror

identify the corresponding peaks in the spectra. Calculation of the Strouhal number $\mathrm{Sr} = f D/U_\infty$ and substitution of the frequency axis in Fig. 3 reveal tonal sound components due to periodic vortex shedding next to the measuring section and also in the interior (see Fig. 4) at about $\mathrm{Sr} = 0.115$.

4.2 Sound Radiation by the Side Window

There is a strong coherence between the measured vibration velocity at a single point of the side window surface and sound pressure fluctuations at the driver's ear at frequencies corresponding to the structural modes of the side window. The fundamental frequency of the side window is 106 Hz; further structural modes are marked with dashed lines in Fig. 5 (left). For frequencies higher than 300 Hz, a weak coherence can be found. However, the mean coherence between the surface velocity measured at 1,624 positions distributed over the whole surface and the sound pressure is significant for frequencies greater than 1 kHz. It should be emphasised that the distribution of the coherence is very similar to the distribution of the sound pressure level in Fig. 2 for higher frequencies. This clarifies the excitation of the side window by hydrodynamic and acoustic pressure fluctuations and, consequently, sound is radiated to the interior by these vibrations. Especially at higher frequencies, the modes become denser and more complex. Therefore, the mean of the coherence measured over the entire side window is larger than the coherence measured at a single point.

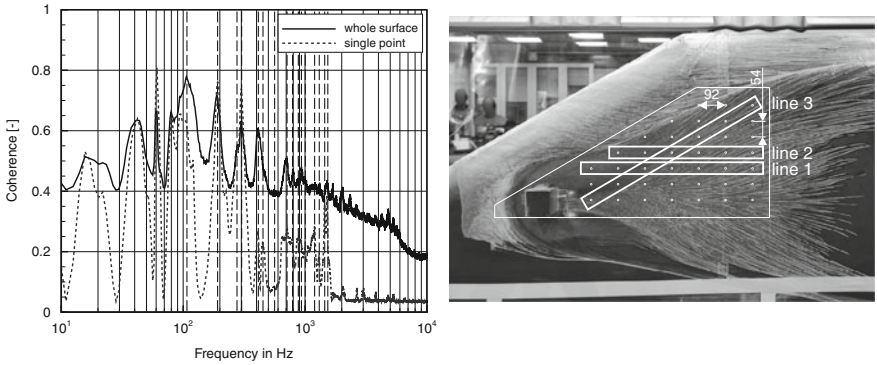

Fig. 5 Coherence between the sound pressure at the driver's ear and the vibration velocity at test points distributed over the whole window surface (mean) and at a single point (*left*); oil-flow visualization with distribution of the pressure transducers at the side window (*right*); case with model of the side mirror

4.3 Excitation of the Side Window

The results in Fig. 5 (left) do not allow for a separation of hydrodynamic and acoustic pressure fluctuations exciting the side window. In particular, separation and quantification of the acoustic part are required, e.g., regarding an improvement of results from statistical energy analysis [1]. Figure 5 (right) illustrates the distribution of 39 pressure transducers for the measurement of the wall pressure fluctuations (see Sect. 3). As a result of the minimal spacing $\Delta x = 0.092$ m in the streamwise direction, wavenumber spectra of the wall pressure fluctuations with maximum wavenumbers $k_{\max} = 1/(2\Delta x) = \pm 5.4\ \mathrm{m}^{-1}$ can be calculated without aliasing effects. The wall-pressure fluctuations sampled simultaneously at the sensors along the lines marked with the white frames in Fig. 5 (right) were used to calculate the wavenumber spectra in Fig. 6 (right) according to [1, 2]. The focus lay on the identification of tonal acoustic pressure fluctuations at the frequency of periodic vortex shedding at the mirror model. Assuming that sound propagates uniformly over the side window, the cross power spectral density can be calculated between each single sensor and the last sensor downstream and vice versa, corresponding to a virtual number of 13 sensors. The fact that only the convective transport of hydrodynamic pressure fluctuations can be identified at wavenumbers around two in Fig. 6 (right) leads to the assumption that the sound resulting from periodic vortex shedding at 71 Hz does not propagate over the whole surface of the side window. A larger number of transducers in a row improves the wavenumber resolution and could allow this assumption to be proved. In addition, Fig. 6 (left) reveals that the amplitudes of the pressure fluctuations at the window surface at 71 Hz are very large, especially in the wake of the mirror model. Hence the difference of the pressure levels might be too large for a separation by means of wavenumber filtering.

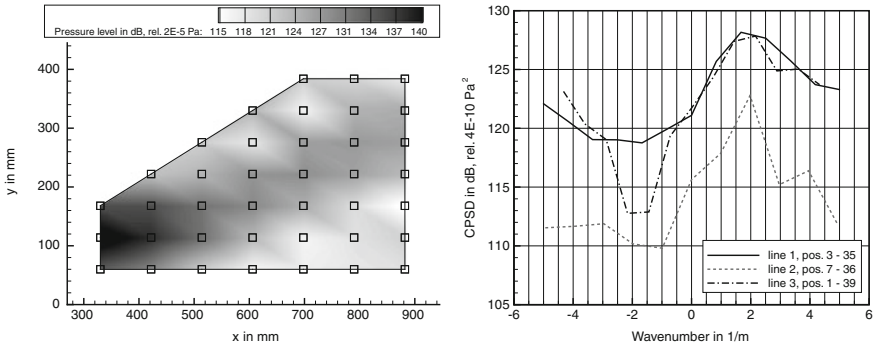

Fig. 6 Distribution of the pressure amplitude at 71 Hz (*left*) and wavenumber spectra of the wall-pressure fluctuations along the *lines* in Fig. 5 at 71 Hz (*right*), $U_\infty = 180$ km/h; case with model of the side mirror

5 Conclusion

The simplified car model presented allows for the investigation of the radiation of flow-induced sound via the side window into the passenger cabin. Both the side mirror model and the square bar at the a-pillar involve strong radiation of sound to the driver's ear. In the frequency range under 100 Hz, several cavity modes of the model are excited. However, recalculation of the sound pressure spectra with Strouhal number instead of frequency allows the identification of tonal sound resulting from periodic vortex shedding at the mirror model next to the measuring section and in the interior. The mean of the coherence between the vibration velocity at many test points distributed over the side window and the sound pressure at the driver's ear is a complement to the distribution of the sound radiation to the interior. This reveals the excitation of the side window by pressure fluctuations and the resulting sound radiation by the window modes. For tonal components in the low-frequency range, separation and quantification of hydrodynamic and acoustic pressure fluctuations by means of wavenumber filtering are not possible with the present setup. Presumably, the sensor alignment has to be modified and the amplitudes of the hydrodynamic pressure fluctuations are too large.

Acknowledgments Financial support by the Bavarian Research Foundation (BFS) is gratefully acknowledged.

References

1. Bremner, P. G.: Vibroacoustic source mechanisms under aeroacoustic loads. In: 18th AIAA/CEAS Aeroacoustics Conference, Colorado Springs (CO), USA, AIAA 2012–2206, 4–6 June 2012
2. Ehrenfried, K., Koop, L.: Experimental study of pressure fluctuations beneath a compressible turbulent boundary layer. In: 14th AIAA/CEAS Aeroacoustics Conference, Vancouver, AIAA 2008–2800, 5–7 May 2008

3. Hartmann, M. et al.: Wind noise caused by the a-pillar and the side mirror flow of a generic vehicle model. In: 18th AIAA/CEAS Aeroacoustics Conference, Colorado Springs (CO), USA, AIAA 2012–2205, 4–6 June 2012
4. Khalighi, B., Iaccarino, G., Khalighi, Y.: Automotive flow and acoustic predictions using large eddy simulations. Int. J. Fluid Mech. Res. **39**(3), 272–289 (2012)
5. Müller, S., Becker, S., Gabriel, C., Ullrich, F.: Influence of the flow-induced structure-borne noise on the interior acoustics of a simplified car model. In: European Conference on Noise Control, Prague, 10–13 June 2012
6. Rocha, J., Palumbo, D.: On the sensitivity of sound power radiated by aircraft panels to turbulent boundary layer parameters. J. Sound Vib. **331**(21), 4785–4806 (2012)
7. Schäfer, F., Müller, S., Uffinger, T., Becker, S., Grabinger, J., Kaltenbacher, M.: Fluid-structure-acoustic interaction of the flow past a thin flexible structure. J. AIAA **48**(4), 738–748 (2010)
8. Ullrich, F. et al.: Investigations of sunroof buffeting in an idealised generic vehicle model - Part I: Experimental results. In: 14th AIAA/CEAS Aeroacoustics Conference, Vancouver, Canada, AIAA 2008–2900, 5–7 May 2008

Part VIII
Aeroelasticity and Structural Dynamics

Prediction of Transonic Flutter Behavior of a Supercritical Airfoil Using Reduced Order Methods

Nagaraj K. Banavara and Diliana Dimitrov

Abstract The flutter behavior of a supercritical airfoil is investigated using a panel formulation, which solves the subsonic unsteady linearized small-disturbance integral equations. Linear aerodynamic theories provide good predictions for attached moderately subsonic and supersonic flows but break down in the transonic flow conditions due to the nonlinearities inherent in unsteady transonic flow. These nonlinearities dominate the transonic flutter behavior typically resulting in the so-called transonic dip. Time-domain aeroelastic simulations involving Computational Fluid Dynamics (CFD) are computationally very expensive and are not favored when a large number of simulations are required. It is a common practice to correct the unsteady aerodynamics calculated from linear formulations to account for the flow nonlinearities associated with unsteady transonic flows. A Reduced Order Method (ROM) is presented yielding to complex-valued aerodynamic corrections for vibration modes. This ROM is used in linear frequency-domain flutter analyses.

1 Introduction

The nonlinearities inherent in unsteady transonic flows make the characteristics of such flows distinctly different from those at low to moderate attached subsonic conditions. The classic reviews of unsteady transonic flows by Tijdeman [1] and Bendiksen [2] reveal that the steady and unsteady flow-fields are essentially coupled in transonic flow. The presence of local supersonic regions terminated by shock-waves (due to the mean steady flow-field) affect the propagation of the unsteady pressure pertur-

N. K. Banavara (✉) · D. Dimitrov
DLR Institute of Aeroelasticity, Bunsenstr.10, 37073 Göttingen, Germany
e-mail: Nagaraj.Banavara@dlr.de;
http://www.dlr.de/ae

D. Dimitrov
e-mail: Diliana.Dimitrov@dlr.de

A. Dillmann et al. (eds.), *New Results in Numerical and Experimental Fluid Mechanics IX*,
Notes on Numerical Fluid Mechanics and Multidisciplinary Design 124,
DOI: 10.1007/978-3-319-03158-3_37,

bations. This in turn affects the magnitude and phase of the unsteady pressures on the airfoil/wing. This essential coupling between the steady and unsteady flow-fields is absent in the linear aerodynamic theories. In addition, the unsteady motion of the shock wave causes a peak in the unsteady pressure distribution, which cannot be modeled by linear aerodynamic theories. The above discrepancies are due to the mathematical formulation of the linear governing equations, which assume a constant speed of propagation of the pressure disturbances equal to the free-stream speed of sound [3]. On account of these limitations, linear aerodynamic theories cannot predict unsteady transonic aerodynamic characteristics—magnitude and phase of the unsteady pressures— accurately.

Despite these limitations, linear frequency-domain unsteady aerodynamic theories such as Doublet Lattice Method (DLM) [4, 5] have been in use for decades due to their speed and efficiency. They still are the *de facto* aerospace industry standard for aeroelastic applications. An improvement in the prediction accuracy in the transonic range therefore forms an important step in the calculation of dynamic aeroelastic behavior of airfoils and wings. Several methods have been proposed over the decades. Rodden and Revell [6] used experimentally measured pressures due to steady angle of attack to derive a diagonal correction matrix that would pre-multiply the Aerodynamic Influence Coefficient (AIC) matrix. They assumed that this single matrix based on quasi-steady aerodynamics (frequency $= 0$) and a single mode (rigid pitch) would be applicable to an arbitrary vibration mode at non-zero reduced frequencies. Bergh and Zwaan [7] extended this method by deriving correction matrices for various reduced frequencies but still based on a single mode. These earliest attempts used experimental pressures as the basis for deriving aerodynamic corrections as accurate numerical predictions of nonlinear unsteady transonic flows were not available. Later on, as the emerging field of CFD matured over the years, numerical calculations were also considered for deriving these corrections. Palacios et al. [8] and Brink-Spalink et al. [9] have reviewed the various aerodynamic correction methodologies developed over the years.

In the present investigation, a CFD based Reduced Order Method (ROM) [10, 11] is presented and implemented in conjunction with a frequency-domain formulation to investigate the flutter behavior of a three degree-of-freedom NLR 7301 airfoil.

2 NLR 7301 Supercritical Airfoil

2.1 CFD Model of NLR 7301

The configuration considered in this chapter is the 2D supercritical airfoil NLR 7301 [1, 12, 13] at a Reynolds number of $1.8e6$. It is a 16% thick airfoil and reaches transonic flow conditions at around Mach 0.7. Figure 1 shows the mesh around the airfoil, which is chosen after a comprehensive grid convergence study. The farfield

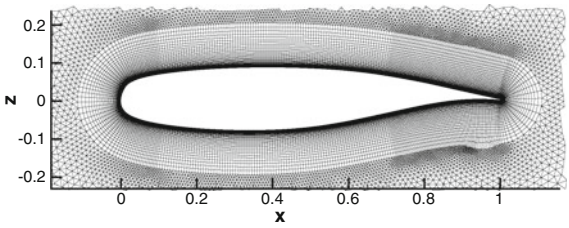

Fig. 1 NLR 7301 nearfield CFD mesh

extension amounts to 100 chords, with 102734 points in total. The y^+ value for the first cell height is kept below 1 in every case.

The CFD calculations are carried out using the TAU code [14] which is based on the Finite-Volume method and solves the time-dependent Reynolds-averaged Navier-Stokes (RANS) equations. The Menter SST [15] turbulence model is applied as well as a central scheme for the discretization of the fluxes. For the temporal discretization, a local timestepping is applied for the steady cases [16], and a dual timestepping [17] for the unsteady calculations.

2.2 ZAERO Aerodynamic Model

To demonstrate the applicability of the ROM based aerodynamic corrections, the panel formulation of ZAERO is utilized. ZONA6, the subsonic theory of ZAERO is used to generate the unsteady aerodynamic pressures. ZAERO models wing-like components using a thin sheet of unsteady vortex singularities whereas the body-like components are modeled using a sheet of constant unsteady source singularity to account for the aerodynamic perturbation created by the body volume effects [18].

A box convergence study as well as the *minimum chord length criterion* [18] indicate that 40 chord-wise boxes are sufficient for convergence.

2.3 Structural Dynamic Model

The structural dynamic model and the geometrical parameters of the NLR 7301 airfoil are illustrated in Fig. 2. The airfoil consists of three degrees of freedom: plunge (h), pitch (α), and flap (β) rotation. The structural parameters are summarized in Table 1.

It is customary to transform the structural dynamic equations of motion from time-domain to the frequency-domain, which in non-dimensional form can be represented as the following matrix equation:

$$\begin{bmatrix} \left(1-\omega_{h\alpha}^2 X\right) & \chi_\alpha & \chi_\beta \\ \chi_\alpha & r_\alpha^2\left(1-X\right) & \left(r_\beta^2+\left(c_\beta-a_h\right)\chi_\beta\right) \\ \chi_\beta & \left(r_\beta^2+\left(c_\beta-a_h\right)\chi_\beta\right) & r_\beta^2\left(1-\omega_{\beta\alpha}^2 X\right) \end{bmatrix} \begin{Bmatrix} h/b \\ \alpha \\ \beta \end{Bmatrix} = \begin{Bmatrix} 0 \\ 0 \\ 0 \end{Bmatrix} \tag{1}$$

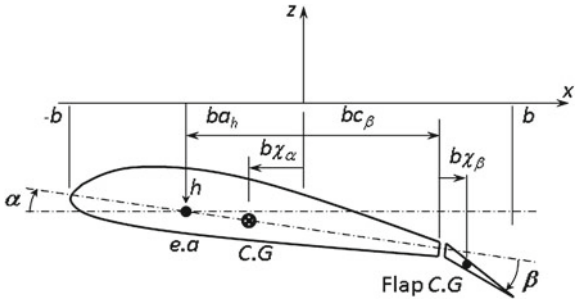

Fig. 2 Airfoil parameters

Table 1 Geometric and structural dynamic parameters [19] of NLR 7301 airfoil

Parameter	b	a_h	c_β	χ_α	χ_β	r_α	r_β	ω_h	ω_α	ω_β	μ
				$\left(\frac{S_\alpha}{mb}\right)$	$\left(\frac{S_\beta}{mb}\right)$	$\sqrt{\frac{K_\alpha}{I_\alpha}}$	$\sqrt{\frac{K_\beta}{I_\beta}}$	$\sqrt{\frac{K_h}{m}}$			$\left(\frac{m}{\pi\rho b^2}\right)$
Units	m	–	–	–	–	–	–	rad/s	rad/s	rad/s	–
Value	0.5	−0.5	0.5	0.086	0.001	0.42	0.143	105.0	140.0	230.0	350.4

where, $\omega_{h\alpha} = \frac{\omega_h}{\omega_\alpha}$; $\omega_{\beta\alpha} = \frac{\omega_\beta}{\omega_\alpha}$; $X = \frac{\omega_\alpha}{\omega}$. This is an algebraic eigenvalue problem, whose non-trivial solution yields the mode shapes q_i and natural frequencies ω_i of the airfoil, where, $i = 1, 2, 3$. The generalized mass and stiffness matrices along with the aerodynamic model described in Sect. 2.2 form the input to ZAERO.

3 Reduced Order Method for Aerodynamic Corrections

With increasing compressibility, the unsteady pressures predicted by linear theories start to depart in comparison to nonlinear formulations such as those based on RANS equations. At transonic conditions, the predictions are grossly incorrect. The purpose of the ROM presented here is to improve the accuracy of the unsteady transonic airloads for all relevant real structural modes and range of reduced frequencies deemed necessary for the flutter computations. In order to restrict the associated computational cost, this has to be done with few CFD computations at each Mach number.

3.1 ROM Description

The various steps in the ROM process are briefly outlined below. For details, refer to [10, 11].

Step 1: Define suitable synthetic modes.
Step 2: Compute unsteady pressures due to the harmonic motion of the synthetic and real modes using ZAERO.

Step 3: Compute unsteady pressures due to the harmonic motion of the synthetic modes only using CFD.

The assessment of the flutter behavior in the transonic range requires accurate description of unsteady pressures due to real modes from which the Generalized Aerodynamic Forces (GAFs) are derived. Thus, ZAERO requires a set of correction factors (CF) for each real mode (index r) and at each Mach number and reduced frequency. These correction factors are intended to capture the nonlinearities inherent in transonic flows. But, they have to be derived from the available CFD simulations, performed using synthetic modes (index s). The correction factors are obtained from the following equation:

$$CF_r = \frac{\triangle p_r^{CFD}}{\triangle p_r^{ZAERO}} = \left\{ 1 + \frac{\sum w_{rs} \left[\triangle p_s^{CFD} - \triangle p_s^{ZAERO} \right]}{\triangle p_r^{ZAERO}} \right\} \tag{2}$$

where, $\triangle p$ represents the pressure difference between the upper and lower surfaces of the airfoil. The weighting coefficients w_{rs} combine with synthetic modes as a weighted sum to approximate the real structural modes.

3.2 Selection of Synthetic Modes

The number and type of synthetic modes used in the ROM depends on the configuration being modeled. The goal is to define a small number of synthetic modes that can accurately describe as many real structural modes as are relevant for the flutter investigation. Synthetic mode sets can include a combination of rigid modes such as pitching and control surface deflection modes and 'flexible' modes such as polynomial functions, Legendre polynomials, Tschebyscheff polynomials, or trigonometric functions. Selection of synthetic modes for the NLR 7301 with three degrees of freedom is straightforward. The pure plunge, pitch, and flap deflection modes are considered as the synthetic modes. While the current set-up may seem simplistic, it serves to demonstrate the ROM procedure. However, complex configurations such as 3D swept wings with under-wing nacelles or pods require a careful choice to reduce computational effort.

3.3 Unsteady Pressures from CFD

The unsteady pressures for the corrections are obtained using the pulse technique [20]. In this way, the frequency response to each synthetic modeshape can be calculated by only one unsteady calculation. An amplitude of 0.1° for the rotational and 0.01 m for the translational modeshapes are chosen for excitation. The assumption of small perturbation around a steady-state field is still valid.

For the correction process, the corresponding unsteady pressures Δp_s^{CFD} are extracted at discrete reduced frequencies (0, 0.02, 0.04, 0.1, 0.2, 0.4, 0.6, 0.8) at

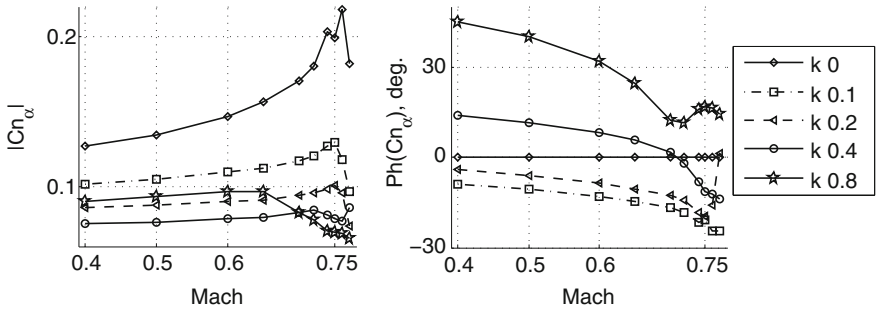

Fig. 3 Cn_α for different reduced frequencies, excitation mode: pitch

each Mach number of interest. These unsteady pressure values are then directly fed into the ROM as discussed in Sect. 3.1. The steady angle of attack is always kept at zero degree. The importance of CFD derived transonic corrections is illustrated in Fig. 3, which shows the complex derivatives of the normal force (Cn_α) over Mach number for various reduced frequencies. A pronounced nonlinear behavior is clearly exhibited at transonic conditions ($Ma > 0.7$). These trends may already give a hint to the location of the transonic dip: at a Mach number of about 0.75, the curves show local extrema in magnitude and phase and therefore indicate a high sensitivity of the pressure distribution towards angle of attack.

4 Results

The validity of the assumption of superposition of the unsteady pressures (ΔC_p) is clearly demonstrated in Fig. 4. The weighted superposition of the unsteady pressures due to synthetic modes gives the same result as the unsteady pressures directly obtained by the perturbation of the real mode.

Figure 5 compares flutter boundaries obtained from various methods. Without any corrections to account for the nonlinear transonic flow effects, ZAERO predicts a flutter boundary without any transonic dip. The reference flutter boundary computed from GAFs that are derived from CFD shows a pronounced transonic dip with a minimum flutter speed at Mach 0.75. When applied to the present configuration, corrections based on steady normal force and moment coefficients due to pitch (Cn_α and Cm_α respectively), similar to those derived by Rodden and Revell [6] are unconservative. Corrections based on unsteady Cn_α, Cm_α, similar to those derived by Bergh and Zwaan [7] are conservative. The ROM based corrections, on the other hand, provide the most accurate prediction of the flutter boundary. This implies that it is very important to correct the unsteady aerodynamic pressures of the real structural modes, at least for those relevant for the flutter computations. Corrections based on a single mode (such as pitch) or based only on integrated loads cannot accurately

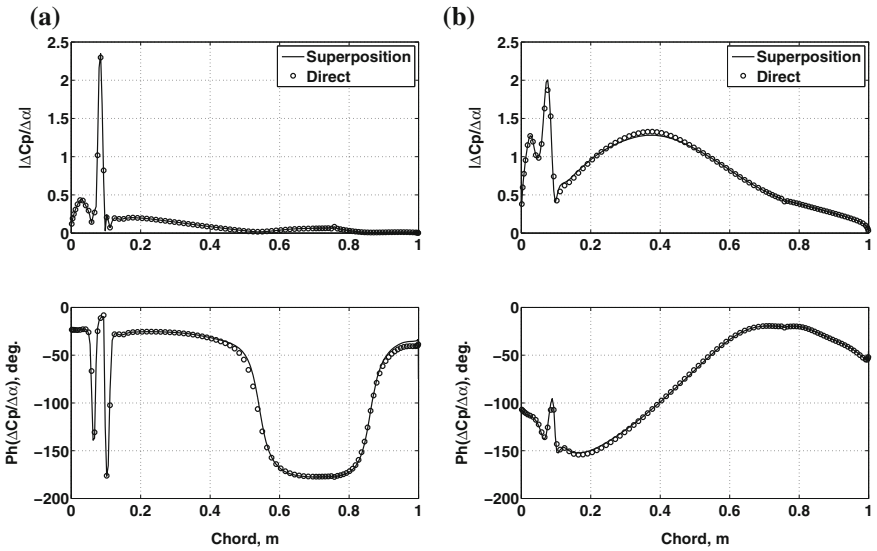

Fig. 4 Validation of superposition of unsteady pressures at Mach 0.7. **a** Reduced frequency 0.02 **b** Reduced frequency 0.8

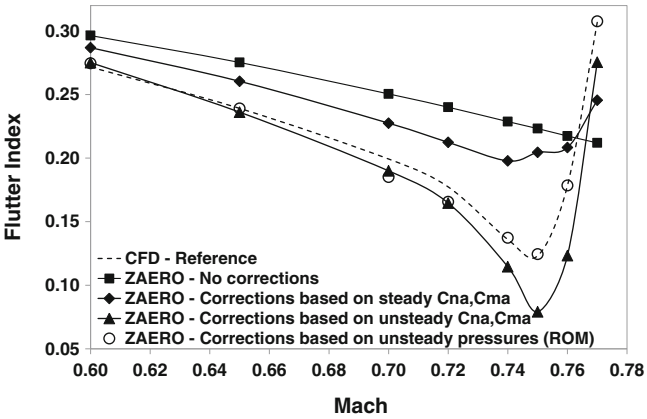

Fig. 5 Flutter boundaries of NLR 7301 airfoil

capture the phase relationship between the unsteady pressures and the underlying mode shape motion.

5 Conclusions and Future Work

A Reduced Order Method is presented and implemented on a 3 degree-of-freedom NLR 7301 airfoil. The ROM provides a means to accurately capture the unsteady aerodynamics of the real modes with the help of synthetic modes. It is important to choose the synthetic modes judiciously: smallest number of synthetic modes that can accurately describe as many real structural modes as are relevant for the flutter investigation. Depending on this number of synthetic modes compared to the real modes, the time saving factor will be different for every configuration. Moreover, unlike the case considered in this chapter, it is possible that the proposed synthetic modes (either the type or the number) may not entirely recreate the real modes, in which case, the accuracy of the flutter prediction is degraded. In the present case, the synthetic modes recreate the real modes perfectly and hence the flutter boundary with the ROM update also recreates the flutter boundary predicted by CFD almost exactly. Also, it is important to individually correct the unsteady aerodynamics (magnitude as well as phase) of each structural mode relevant for flutter. Corrections based only on rigid pitch lead to wrong result and are unconservative if only steady corrections are applied.

Future study involves the validation of the ROM on a complex configuration consisting of a fuselage, 3D swept wing with an under-wing store.

References

1. Tijdeman, H.: Investigations of the transonic flow around oscillating airfoils. Technical report NLR TR 77090 U, NLR (1977)
2. Bendiksen, O.O.: Review of unsteady transonic aerodynamics: theory and applications. Prog. Aerosp. Sci. **47**(2), 135–167 (2011)
3. Bendiksen, O.O.: Unsteady aerodynamics and flutter near Mach 1: aerodynamic and stability reversal phenomena. In: International Forum on Aeroelasticity and Structural Dynamics IFASD-2011-091 (2011)
4. Albano, E., Rodden, W.P.: A doublet-lattice method for calculating lift distributions on oscillating surfaces in subsonic flows. J. Aircr. AIAA **7**, 279–285 (1969)
5. Blair, M.: A compilation of the mathematics leading to the doublet lattice method. Technical report NASA WL-TR-95-3022 (1994)
6. Rodden, W.P., Revell, J.D.: Status of unsteady aerodynamic influence coefficients. In: Institute of the Aeronautical Sciences, 279–285 FF-33 (1962)
7. Bergh, H., Zwaan, R.J.: A method for estimating unsteady pressure distribution for arbitrary vibration modes from theory and from measured distributions for one single mode. Technical report NLR NLR-TR F.250 (1966)
8. Palacios, R., Climent, H., Karlsson, A., Winzell, B.: Assessment of strategies for correcting linear unsteady aerodynamics using CFD or test results. In: Progress in Computational Flow-Structure Interaction, pp. 209–224. Springer, Berlin (2003)
9. Brink-Spalink, J., Bruns, J.M.: Correction of unsteady aerodynamic influence coefficients using experimental or CFD data. In: International Forum on Aeroelasticity and Structural Dynamics, IFASD-2001-015 (2001)

10. Voss, R., Tichy, L., Thormann, R.: A ROM based flutter prediction process and its validation with a new reference model. In: International Forum on Aeroelasticity and Structural Dynamics, IFASD-2011-036 (2011)
11. Voss, R., Thormann, R.: Flutter computations for a generic reference aircraft adopting CFD and reduced order methods. In: 53rd Structures, Structural Dynamics and Materials Conference, AIAA-2012-1715 (2012)
12. Bland, S.R.: AGARD two-dimensional aeroelastic configurations. Technical report AGARD AGARD-AR-156 (1979)
13. Voss, R., Hippe, C.: Computation of the flutter boundary of the NLR 7301 airfoil in the transonic range. Volume 92 of Notes on Numerical Fluid Mechanics and Multidisciplinary Design. Springer, Berlin (2006)
14. Schwamborn, D., Gerhold, T., Heinrich, R.: The DLR TAU-Code: recent applications in research and industry. In: ECCOMAS 2009 (2009)
15. Menter, F. R.: Zonal two-equation k-ω turbulence models for aerodynamic flows. In: 24th Fluid Dynamics Conference AIAA-93-2906 (1993)
16. Jameson, A., Schmidt, W., Turkel, E.: Numerical solutions of the euler equations by the finite volume methods using Runge Kutta time stepping schemes. In: 14th Fluid and Plasma Dynamics Conference. AIAA-81-1259 (1981)
17. Jameson, A.: Time dependent calculations using multigrid, with applications to unsteady flows past airfoils and wings. In: 10th Computational Fluid Dynamics Conference. AIAA-91-1596 (1991)
18. ZONA Technology, Inc.: ZAERO User's Manual. 8.5 edn. June 2011
19. Theodorsen, T.: General theory of aerodynamic instability and the mechanism of Flutter. Technical report 496, NACA (1935)
20. Thormann, R., Nitzsche, J., Widhalm, M.: Time-linearized simulation of unsteady transonic flows with shock-induced separation. In: ECCOMAS 2012 (2012)

Partitioned Fluid-Structure Interaction on Solution-Adaptive Hierarchical Cartesian Grids

Gonzalo Brito Gadeschi, Matthias Meinke and Wolfgang Schröder

Abstract A solution-adaptive hierarchical Cartesian cut-cell method is validated for fluid-structure interaction problems involving rigid bodies. The response of a tandem configuration of elastically supported cylinders is then investigated.

1 Introduction

Fluid-structure interaction (FSI) phenomena play an important role in the design of many technical devices such as airplanes and bridges. In these systems, the relationship between the peak vibration amplitude and the remaining problem parameters is of high engineering interest. However, this relationship is, even for elastically-mounted cylinders, still not well understood. Numerical methods that handle multiple moving boundaries both accurately and efficiently are thus of interest. In this work, a hierarchical Cartesian cut-cell method with automatic mesh generation and adaptation is validated for Vortex-Induced Vibrations (VIV). A parameter study involving a tandem configuration of two elastically supported cylinders demonstrates the ability of the proposed approach to handle multiple bodies.

2 Mathematical Model

2.1 Unsteady Compressible Flow

Let the fluid density, pressure, velocity, and total specific energy per unit mass be denoted by ρ, p, $\mathbf{u}$, and E, respectively. The dimensionless unsteady Navier-Stokes equations for compressible flow are

G. B. Gadeschi (✉) · M. Meinke · W. Schröder
Institute of Aerodynamics, RWTH Aachen University, Wüllnerstraße 5a,
52062 Aachen, Germany
e-mail: g.brito@aia.rwth-aachen.de

A. Dillmann et al. (eds.), *New Results in Numerical and Experimental Fluid Mechanics IX*,
Notes on Numerical Fluid Mechanics and Multidisciplinary Design 124,
DOI: 10.1007/978-3-319-03158-3_38,

$$\frac{\partial \mathbf{Q}}{\partial t}+\nabla\cdot\mathbf{F}(\mathbf{Q})=0\,,\quad \mathbf{Q}=\begin{pmatrix}\rho\\ \rho\mathbf{u}\\ \rho E\end{pmatrix}\text{ and }\mathbf{F}(\mathbf{Q})=\begin{pmatrix}\rho\mathbf{u}\\ \rho\mathbf{u}\mathbf{u}+p\\ \mathbf{u}(\rho E+p)\end{pmatrix}+\frac{1}{\mathrm{Re}}\begin{pmatrix}0\\ \overline{\boldsymbol{\tau}}\\ \overline{\boldsymbol{\tau}}u+\mathbf{q}\end{pmatrix}, \tag{1}$$

where *Re* denotes the Reynolds' number. Let λ denote the heat conductivity, η the dynamic viscosity, and $\gamma = c_p/c_V$ the ratio of specific heats, where the coefficients c_p and c_V are the specific heats at constant pressure and volume, respectively. The Fourier's heat flux $\mathbf{q}$, and the stress tensor for a Newtonian fluid with zero bulk viscosity $\overline{\boldsymbol{\tau}}$ are given by

$$\mathbf{q}=-\frac{\lambda}{\mathrm{Pr}(\gamma-1)}\nabla T\,,\quad\text{and}\quad \overline{\boldsymbol{\tau}}=-\eta\left(\nabla\mathbf{u}+(\nabla\mathbf{u})^{\mathrm{T}}\right)+\frac{2}{3}\eta(\nabla\cdot\mathbf{u})\mathbf{I}\,, \tag{2}$$

respectively. Sutherland's law: $\eta(T) = (T)^{2/3}\,\frac{1+S/T_0}{T+S/T_0}$ gives an approximation for the dynamic viscosity which is valid for gases at moderate temperatures. The Sutherland's constant is $S = 111\,\mathrm{K}$, and the reference temperature is $T_0 = 273.15\,\mathrm{K}$. For constant Prandtl number flows, the heat flux $\mathbf{q}$ is computed by approximating $\lambda(T) \approx \eta(T)$. For a thermally perfect and calorically perfect gas: $p = (\gamma-1)\rho(E-\frac{1}{2}\|\mathbf{u}\|^2)$. The boundary conditions on the inflow, outflow, far-field, and adiabatic moving walls are described in [1, 2].

2.2 The Fluid-Structure Interface

The computational domain is $\Omega = \Omega_{\mathrm{f}} \cup \Omega_{\mathrm{s}}$, where the fluid and structural domains overlap only at the fluid-structure interface: $\Gamma_{\mathrm{f/s}} = \Omega_{\mathrm{f}} \cap \Omega_{\mathrm{s}}$ ensuring mass conservation. Energy and momentum conservation require the kinematic ($\mathbf{u}\big|_{\Gamma_{\mathrm{f/s}}} = \dot{\mathbf{x}}_{\mathrm{s}}\big|_{\Gamma_{\mathrm{f/s}}}$ and $\dot{\mathbf{u}}\big|_{\Gamma_{\mathrm{f/s}}} = \ddot{\mathbf{x}}_{\mathrm{s}}\big|_{\Gamma_{\mathrm{f/s}}}$) and the dynamic ($\mathbf{f}^{\mathrm{f}}_{\Gamma} = \mathbf{f}^{\mathrm{s}}_{\Gamma}$) compatibility conditions to be satisfied.

2.3 Rigid Body Dynamics

Let the reduced mass, the reduced velocity, and the undamped natural vibration frequency be denoted by $m^i_{\mathrm{red}} = \frac{m^i}{\rho l^2}$, $U_{\mathrm{red},\,i} = \frac{u_\infty}{f^i_{\mathrm{n}} l}$, and f^i_{n}, respectively. In this work, $m_{\mathrm{red}} = 2.0$. Neglecting structural damping, the evolution of the translational degrees-of-freedom $\mathbf{x}_{\mathrm{s}}$ of an elastically-supported rigid body is obtained from Newton's second law. For the i-th translational component it is given in dimensionless form by

$$\ddot{x}^i_{\mathrm{s}}+\frac{4\pi^2}{U^2_{\mathrm{red},\,i}}x^i_{\mathrm{s}}=\frac{C^i_{\mathrm{y}}(t)}{2m^i_{\mathrm{red}}}\,, \tag{3}$$

where the fluid force acting on an immersed rigid body is $2\mathbf{C}_{\mathrm{y}}(t) = \int_{\Gamma_{\mathrm{f/s}}} -p\mathbf{n} + \frac{1}{Re_0}\overline{\tau}\mathbf{n}\,dA$.

3 Numerical Method

The Generalized-α method [3] is used to integrate the system of second-order ODEs resulting from the equations of rigid body motion. The fluid equations are discretized with the hierarchical Cartesian cut-cell method of Hartmann et al. [1]. The mesh is automatically generated by fitting the domain of interest into a single square Cartesian cell of length h_0. This cell is then refined isotropically until the cell length $h_L = h_0/2^L$ is smaller than the minimum required cell length h_{req}, which occurs at level L. The cells outside the domain of interest are then deleted. Those cells intersected by the boundary are reshaped, producing a boundary conforming mesh (see Fig. 1).

The Navier-Stokes equations are integrated in time using a 5-stage second-order accurate Runge-Kutta scheme optimized for stability [4]. The Courant number $C = 1.0$ is used in this work. A consistent time-integration of the fluid forces [5] exerted on the structure is performed to ensure conservation:

$$\mathbf{f}_{\text{f}}(t^{n+1}) \approx \sum_{i=0}^{n=5} \chi_i \mathbf{f}_{\text{f}}(t^n + \chi_i \Delta t) / \sum_{i=0}^{n=5} \chi_i \ . \tag{4}$$

Here χ_i is the Runge-Kutta coefficient of the corresponding Runge-Kutta stage, and $f_{f,i} = C_{\text{y}}^i(t)/2m_{\text{red}}^i$. A second-order accurate spatial discretization is obtained with the MUSCL approach by performing a slope reconstruction using the unweighted least-squares method [1]. The inviscid flux is discretized in space with a modified version of the AUSM flux [4]. The second derivatives in the viscous terms are computed with a central-difference scheme. The level-set method is used to implicitly describe the position of moving boundaries. The level-set function $\phi(\mathbf{x}, t)$ is defined as the smallest signed Euclidean distance from the point $\mathbf{x}$ to the fluid-structure interface $\Gamma_{\text{f/s}}$; positive in the fluid domain, negative in the solid domain, and zero on the fluid-structure interface:

$$\phi(\mathbf{x}, t) = \min_{\mathbf{x}_\Gamma \in \Gamma_{\text{f/s}}} ||\mathbf{x} - \mathbf{x}_{\text{f/s}}||_2 \begin{cases} > 0 \text{ for } & \mathbf{x} \in \Omega_{\text{f}} \ , \\ = 0 \text{ for } & \mathbf{x} \in \Gamma_{\text{f/s}} \ , \\ < 0 \text{ for } & \mathbf{x} \in \Omega_{\text{s}}. \end{cases} \tag{5}$$

The extension and validation of the method for moving boundary problems is described in Schneiders et al. [2]. The adaptive mesh refinement (AMR) algorithm uses the level-set function to ensure that all cells located at a distance $\phi(\mathbf{x}_i) < \phi_{\min}$ of the moving boundary are at the required discretization level h_{mb}. At every AMR step the subset of cells $\Omega_{\phi\max} = \{\mathbf{x}_i | \mathbf{x}_i \in \Omega_{\text{f}}, |\phi(\mathbf{x}_i) - \phi_{\max}| < \epsilon_{\text{tol}} = \sqrt{2}h_{mb},\ \phi_{\max} > \phi_{\min}\}$ is registered for a fixed $\phi_{\max}$. Verifying if $\phi(\mathbf{x}_i) > \phi_{\min} \forall \mathbf{x}_i \in \Omega_{\phi_{\max}}$ at every subsequent step is very efficient because usually $|\Omega_{\phi\max}| \ll |\Omega_{\text{f}}|$ (see Fig. 1). Shear layers in the wake of moving bodies are captured using a vorticity sensor $\Lambda_\omega = |\nabla \times \text{v}| \cdot \text{h}^{3/2}$ proportional to the magnitude of the vorticity vector ω. The curl of the velocity is weighted with the length scale $\text{h}^{3/2}$, weakening the

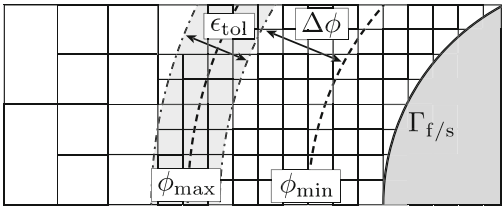

Fig. 1 Hierarchical Cartesian mesh. Cut-cells are reshaped to conform the boundary. The sub-set $\Omega_{\phi\text{max}}$ is depicted in light grey at ϕ_{max}

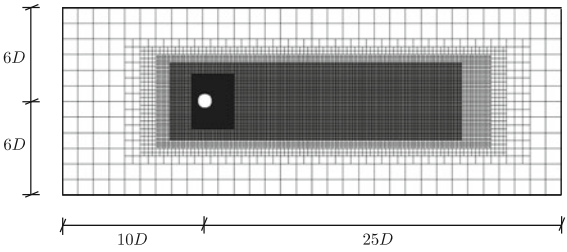

Fig. 2 The static rectangular computational domain Ω_{11} contains a cylinder of diamter D, is of dimensions $[-10D : 25D] \times [-6D : 6D]$, and cell length $h_{11} \approx 0.017D$ at the cylinder surface

strength of flow features as they are refined. The variance of the sensor distribution $\sigma_\omega = \sqrt{(\sum_{\mathbf{x}_i \in \Omega_\text{f}} \Lambda\omega, i^2)/|\Omega_\text{f}|}$ is used to compute the upper and lower sensor limits $\Lambda^u_\omega = \sigma_\omega$, and $\Lambda^l_\omega = 0.1\sigma_\omega$. Cells are refined and coarsened if $\Lambda_{\omega,i} > \Lambda^u_\omega$, or $\Lambda_{\omega,i} < \Lambda^l_\omega$, respectively. A solution-adaptive mesh using this procedure is shown in Fig. 4 for the VIV of a single elastically supported cylinder.

The dynamic compatibility condition for the fluid-structure interface is enforced iteratively with the method proposed by Küttler and Wall [6], in which the interface operators for the fluid, $\mathbf{f}^f_\Gamma = \mathbf{F}_\Gamma(\mathbf{x}_\Gamma)$, and the solid, $\mathbf{f}^s_\Gamma = \mathbf{S}_\Gamma(\mathbf{x}_\Gamma)$, are substituted into the dynamic compatibility condition. The resulting non-linear equation $\mathbf{x}_\Gamma = \mathbf{S}^{-1}_\Gamma(\mathbf{F}_\Gamma(\mathbf{x}_\Gamma))$ is solved with a fix-point iteration of the form $\mathbf{x}^{n+1}_{\Gamma,\,i+1} = \omega_i \hat{\mathbf{x}}^{n+1}_{\Gamma,\,i+1} + (1-\omega_i)\mathbf{x}^{n+1}_{\Gamma,\,i}$, and the dynamic relaxation parameter ω_i is computed with Aitken's Δ^2 method [7]. The unrelaxed structural displacements are denoted with $\hat{\mathbf{x}}$. Convergence is achieved when the L_2-Norm of the displacement residual $\|\mathbf{r}^{n+1}_{\Gamma,\,i}\|_2 < \epsilon_{\text{tol}} = 10^{-15}$ is smaller than a given tolerance ϵ_{tol}, where $\mathbf{r}^{n+1}_{\Gamma,\,i+1} = \mathbf{x}^{n+1}_{\Gamma,\,i} - \mathbf{x}^{n+1}_{\Gamma,\,i-1}$. For rigid-body motion we propose a central finite-difference predictor that results from approximating the dynamic equilibrium at the time level t^n with central differences

$$x^{n+1}_i = \left(\frac{m_i}{\Delta t^2} + \frac{c_i}{2\Delta t}\right)^{-1} \left(f^n_{f,\,i} + \left(\frac{2m_i}{\Delta t^2} - k_i\right) x^n_i + \left(\frac{c_i}{2\Delta t} - \frac{m_i}{\Delta t^2}\right) x^{n-1}_i\right), \tag{6}$$

which results in a second-order accurate predictor. The coefficients $m_i = 1$, $c_i = 0$, and $k_i = 4\pi^2/U^2_{\text{red}}$ follow from the equations of motion (3).

Table 1 Peak amplitude ratio $y_{\max}/D$ of an elastically-supported cylinder for different reduced velocities U_{red} ($m_{\text{red}} = 2.0$, $Re_{\text{D}} = 150$, $M_\infty = 0.1$)

U_{red}	3.0	4.0	5.0	6.0	7.0	8.0
Ahn et al. [8]	0.088	0.576	0.545	0.472	0.367	0.132
Borazjani et al. [9]	0.070	0.530	0.491	0.442	0.381	0.068
Present work	0.077	0.582	0.554	0.466	0.360	0.126

4 Validation

The numerical method has already been validated for stationary [1] and moving boundary problems [2]. In this section the FSI approach with AMR is validated against experimental and numerical results of VIV on elastically mounted cylinders.

The peak vibration amplitude ratios $y_{\max}/D$ predicted by the proposed approach for a single elastically supported cylinder are shown in Table 1 as the reduced velocity U_{red} is varied. A good agreement with the numerical results of Ahn et al. [8] and Borazjani et al. [9] is found. The results are shown in Fig. 3, where $f_{\text{v}}/f_{\text{n}} = St \cdot U_{\text{red}}$, $St = f_{\text{v}}/(u_\infty l)$ is the Strouhal number, and θ_{f} is the phase difference between the total lift force and the body vibration. The Strouhal number follows from assuming that the predominant vortex-shedding frequency corresponds to the frequency associated with the maximum spectral density of the fluid lift force acting on the cylinder. The maximum amplitude $y_{\max} \approx 0.6D$ occurs at $4 < U_{\text{red}} < 5$. The vortex-shedding frequency for a stationary cylinder is denoted by f_{v0}. The dashed line indicates the vortex-shedding frequency to natural vibration frequency ratio for a cylinder at rest, which clearly shows the "lock-in" phenomenon [10] within the interval $U_{\text{red}} = [5, 7]$ where $f_{\text{v}}/f_{\text{n}} \approx 1$. Outside the synchronization region $f_{\text{v}}/f_{\text{n}}$ behaves approximately as $f_{\text{v0}}/f_{\text{n}}$. Two different response branches characterized by the peak vibration amplitude are identified. In the initial response branch (for $U_{\text{red}} < 6$) the peak vibration amplitude increases with the reduced velocity. At $U_{\text{red}} \approx 6$, the transition into the lower response branch is characterized by a jump in the phase difference of the total force θ_{f} with respect to the body position of about 180°. In the lower response branch the peak vibration amplitude decreases as the reduced velocity increases. This results are in very good agreement with the experimental results shown in [10, 11].

4.1 Numerical Studies

A sequence of grids Ω_L with $L \in \{9, 11\}$ is used to study the convergence of the coupling scheme (see Table 2, Ω_{11} is illustrated in Fig. 2). A reference solution is computed on the mesh Ω_{12} with the strongly coupled algorithm. The slopes of the error reduction as the fluid time step is reduced are of $\mathcal{O}(2)$ for both the amplitude and phase errors.

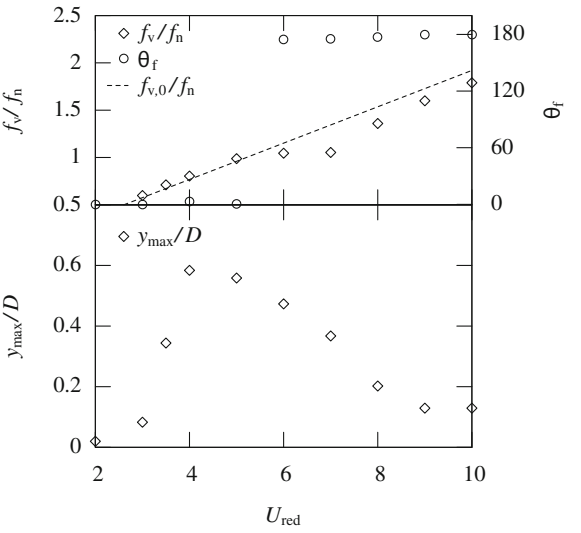

Fig. 3 System response as a function of the reduced velocity

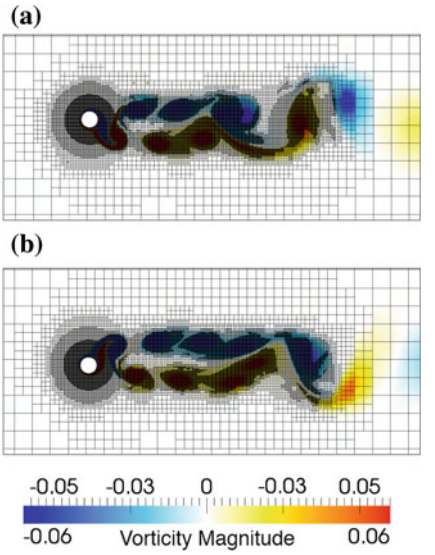

Fig. 4 The vorticity field is shown over a sequence of adaptively-generated meshes. **a** $t_h = 62.02$, **b** $t_h = 94.52$

Table 2 Convergence data of the strongly-coupled schemes as the mesh is refined

L_{min}	No. cells	$h_{min} \cdot D$	$\Delta t_{f,\,min}$	Amplitude error $\lvert y_{max,\,L} - y_{max,\,12}\rvert/D$	Phase error $\lvert\theta(y_{max,\,L}) - \theta(y_{max,\,12})\rvert$
9	36104	0.068	0.058	3.35×10^{1}	1.06×10^{2}
11	63560	0.017	0.015	1.43×10^{0}	4.09×10^{0}

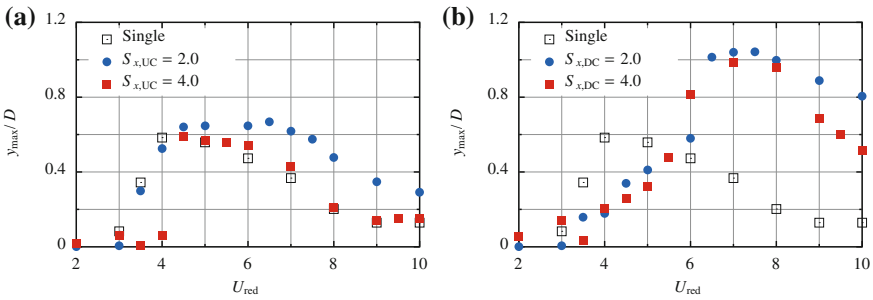

Fig. 5 Peak amplitude ratio y_{max}/D as a function of the reduced velocity U_{red} for the upstream and downstream located cylinders of a tandem cylinder configuration. The curves are an interpolation of the data points. **a** Upstream-located cylinder, **b** Downstream-located cylinder

5 Tandem Configuration of Elastically-Supported Cylinders

A parameter study of a tandem configuration of two elastically-supported cylinders is performed for two different cylinder spacings $S_x = L_x/D = \{2, 4\}$ where the cylinder spacing is defined as the distance between the centers of mass. The maximum amplitude ratio y_{max}/D is shown in Fig. 5 as a function of the reduced velocity U_{red} for both cylinders and cylinder spacings. The wake modes of the system are shown in Fig. 6. The behavior of the upstream cylinder (UC) resembles that of a single oscillating cylinder as the spacing ratio is increased; initial and lower response branches are clearly observed in both cases. The peak amplitude is located at $U_{red} = 4.5$ for $S_x = 4.0$ (i.e., the beginning of the lower response branch) and at $U_{red} = 6.5$ for $S_x = 2.0$ (i.e., in the transition between the lower branch and decoherence). As for a single vibrating cylinder, the transition between the initial and lower response branches presents hysteresis, and a phase jump in the total force phase difference of 180° is observed within the interval $U_{red} = [6, 8]$. Due to wake-interference, the response of the downstream cylinder (DC) significantly differs from the behavior of a single oscillating cylinder. In particular, the peak amplitude is of the order of one cylinder diameter in both cases, almost twice as large as that of the upstream-located cylinders. Two branches, initial and lower, are again present in the DC response showing, overall, much larger vibration amplitudes. The vortex-shedding of the DC for large spacing ratios is controlled by the vortices shed from the UC, while for closely-spaced cylinders there is a region where this is not the case. However, for $S_x = 2.0$ an abrupt transition displaying hysteresis is also observed. The initial-lower transition of the largely-spaced cylinder configuration is fairly smooth and produces a stable mode with two pairs of vortices and two single vortices per cycle (2P + 2S mode, see Fig. 6f). This mode has been observed in forced vibrations of single-cylinder configurations. However, the 2P + 2S mode does not feed enough energy into the structure to sustain itself and as such is not present in VIV (i.e., is an unstable mode) [11, 12]. Still, a stable 2P + 2S mode is observed for a two-cylinder configuration with $S_x = 4.0$ at $U_{red} = 5.5$. The UC

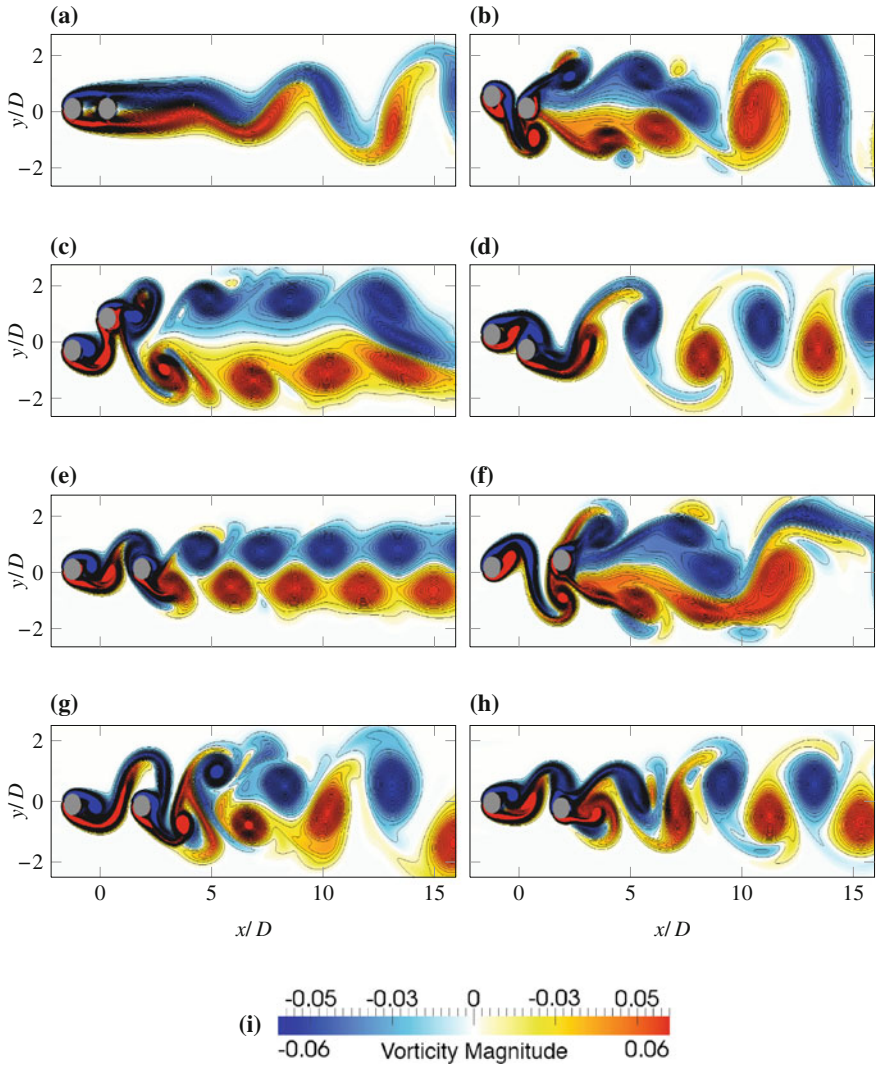

Fig. 6 The wake modes of a tandem configuration of two elastically-supported cylinders with the spacings $S_x = \{2, 4\}$ are illustrated for the reduced velocities $U_{\text{red}} = \{2, 5, 7, 11\}$ and $U_{\text{red}} = \{2, 5.5, 7, 11\}$, respectively. The interval $-0.06 \leq \omega \leq 0.06$ of the vorticity field is colored. Additionally, one-hundred equidistant iso-lines of the vorticity are graphed in the range $-0.06 \leq \omega \leq 0.06$. **a** $S_x = 2.0$, $U_{\text{red}} = 2.0$, (2S), **b** $S_x = 2.0$, $U_{\text{red}} = 5.0$, (2P), **c** $S_x = 2.0$, $U_{\text{red}} = 7.0$, (2P), **d** $S_x = 2.0$, $U_{\text{red}} = 12.0$, (2S), **e** $S_x = 4.0$, $U_{\text{red}} = 2.0$, (2P), **f** $S_x = 4.0$, $U_{\text{red}} = 5.5$, 2(P+S), **g** $S_x = 4.0$, $U_{\text{red}} = 7.0$, (2P), **h** $S_x = 4.0$, $U_{\text{red}} = 12.0$, (2S), **i** Vorticity magnitude

shows a 2S mode and the vortices produced by the UC are split by the movement of the DC. The co-rotating vortices do not merge, and a pair of co-rotating vortices with a counter-rotating vortex is produced.

6 Summary

A solution-adaptive hierarchical Cartesian cut-cell method has been validated for solving FSI problems involving multiple rigid bodies. The suitability of automatic mesh generation and adaptation for performing parameter studies has also been demonstrated. Fundamental FSI problems such as those involving VIV in simple cylinder arrangements already show very complex behavior and should be further investigated. In particular, 3D effects have not been considered here. Furthermore, the relationship between the reduced velocity, the damping ratio, the mass ratio, and the Reynolds number is of high engineering interest.

References

1. Hartmann, D., Meinke, M., Schröder, W.: A strictly conservative Cartesian cut-cell method for compressible viscous flows on adaptive grids. Comput. Methods Appl. Mech. Eng. **200**, 1038–1052 (2011)
2. Schneiders, L., Hartmann, D., Meinke, M., Schröder, W.: An accurate moving boundary formulation in cut-cell methods. J. Comput. Phys. **235**, 786–809 (2013)
3. Chung, J., Hulbert, G.M.: A time integration method for structural dynamics with improved numerical dissipation: the generalized-α method. J. Appl. Mech. **60**, 371–375 (1993)
4. Meinke, M., Schröder, W., Krause, E., Rister, T.: A comparison of second- and sixth-order methods for large-eddy simulations. Comput. Fluids **31**, 695–718 (2002)
5. Piperno, S., Farhat, C.: Partitioned procedures for the transient solution of coupled aeroelastic problems Part II: energy transfer analysis and three-dimensional applications. Comput. Methods Appl. Mech. Eng. **190**, 3147–3170 (2001)
6. Küttler, U., Wall, W.A.: Fixed-point fluid structure interaction solvers with dynamic relaxation. Comput. Mech. **43**, 61–72 (2008)
7. Irons, B., Turk, R.: A version of the Aitken accelerator for computer implementation. Int. J. Numer. Meth. Eng. **1**, 275–277 (1969)
8. Ahn, H., Kallinderis, Y.: Strongly coupled flow/structure interactions with a geometrically conservative ale scheme on general hybrid meshes. J. Comput. Phys. **219**, 671–696 (2006)
9. Borazjani, I., Ge, L., Sotiropoulos, F.: Curvilinear immersed boundary method for simulating fluid structure interaction with complex 3d rigid bodies. J. Comput. Phys. **227**, 7587–7620 (2008)
10. Govardhan, R., Williamson, C.: Modes of vortex formation and frequency response of a freely vibrating cylinder. J. Fluid Mech. **20**, 85–130 (2000)
11. Khalak, A., Williamson, C.: Motions, forces and mode transitions in vortex-induced vibrations at low mass-damping. J. Fluids Struct. **13**, 813–851 (1999)
12. Williamson, C., Govardhan, R.: Vortex-induced vibrations. Annu. Rev. Fluid Mech. **36**, 413–455 (2004)

An Assessment of the Influence of Fuselage Deformations on the Numerical Prediction of High-Lift Performance

Stefan Keye

Abstract Within the scope of the joint research project HINVA (High-Lift In-Flight Validation) a fluid-structure coupled simulation approach based on high-fidelity numerical fluid dynamics and structural analysis methods has been applied to DLR's Airbus A320-232 Advanced Technology Research Aircraft (ATRA) in landing configuration. Coupled analyses were performed using an in-house simulation procedure built around DLR's flow solver TAU and the commercial finite-element analysis code NASTRAN. In order to assess the influence of fuselage and empennage deformations in the context of high-lift aerodynamics, the existing coupling approach, which considers only the wing and high-lift system to be elastic, has been expanded to the full aircraft. Preliminary results show that fuselage bending deformations lead to a modified flow field on the wing's upper surface along the wing root and over the engine nacelle where lift breakdown and wing stall originate. It is therefore assumed that for an accurate numerical prediction of maximum lift and associated angle of attack deformations of fuselage and horizontal stabilizer should be taken into account.

1 Introduction

HINVA's main goal is the reliable and accurate prediction of maximum lift for a representative transport aircraft configuration, Fig. 1, using numerical simulation methods and cryogenic wind tunnel testing [1]. Maximum achievable lift $C_{L,max}$ and the corresponding angle of attack $\alpha(C_{L,max})$ are of particular importance for the landing configuration. The prediction accuracy of both numerical simulation and wind tunnel test with respect to flight test results strived for in HINVA is $\Delta C_{L,max} \leq 2\,\%$ for maximum lift and $\Delta\alpha(C_{L,max}) \leq 2\,\%$ for the corresponding angle of attack. A physically correct simulation of all aerodynamic effects relevant for maximum lift is essential for the trustworthiness of simulation results in general, the identification

S. Keye (✉)
Institute of Aerodynamics and Flow Technology, DLR, Braunschweig, Germany
e-mail: Stefan.Keye@dlr.de

A. Dillmann et al. (eds.), *New Results in Numerical and Experimental Fluid Mechanics IX*,
Notes on Numerical Fluid Mechanics and Multidisciplinary Design 124,
DOI: 10.1007/978-3-319-03158-3_39,

Fig. 1 DLR's Airbus A320-232 Advanced Technology Research Aircraft (ATRA)

of sources of deviations between CFD and experiment, the improvement of flight physics knowledge of high-lift configurations, and the derivation of conclusions regarding the specific future development of numerical methods.

Work presented in this article focuses on the assessment of aero-elastic effects in the context of high-lift aerodynamics and flow separation behavior. In particular, the influence of fuselage bending deformations of the fully elastic aircraft on the global pitching moment and the longitudinal trim state are investigated and compared to conventional fluid-structure coupled simulations where only the wing and high-lift devices are considered compliant.

2 Determination of Static Equilibrium

DLR's fluid-structure coupled simulation procedure, Fig. 2, is based on a direct coupling of high-fidelity CFD and computational structural mechanics (CSM) methods [2]. The simultaneous interaction of outer flow and flexible aircraft structure is modeled through alternately solving the Reynolds-averaged Navier-Stokes equations and the basic equations of structural mechanics, and the interpolation of aerodynamic forces and structural deflections over the common surface of CFD and structure. For the investigations described here, DLR's in-house flow solver TAU [3] and the structural analysis code NASTRAN [4] were used.

3 Numerical Models and Simulations

3.1 CFD Grid

The CAD geometry used in HINVA is a highly realistic representation of the A320-232 ATRA aircraft in landing configuration, including horizontal and vertical tail planes, engines, nacelle strakes, flap track fairings, slat tracks, slat horn, and

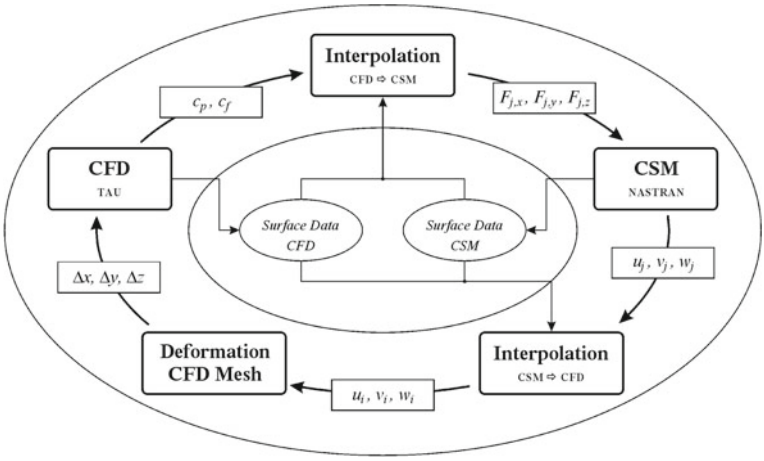

Fig. 2 Simulation approach for steady-state fluid-structure coupling

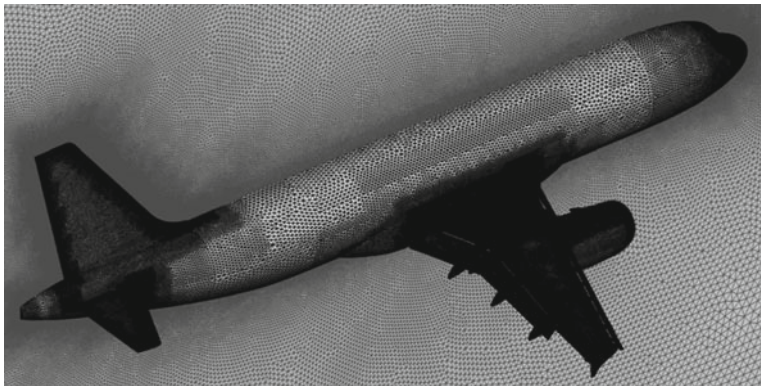

Fig. 3 A320-232 CFD surface (*black*) and symmetry plane (*grey*) meshes

de-icing pipe. In order to enable a most accurate numerical prediction of maximum lift, only minor simplifications, inevitable for successful mesh generation, were introduced [5]. The unstructured, hybrid CFD mesh was generated using the commercial grid generation software CENTAUR [6]. Particular attention was dedicated to the geometric details most relevant for high-lift performance, including slat tracks, nacelle strake, and nacelle strake vortex resolution. The final CFD mesh has 80.3 million grid points, Fig. 3.

All CFD results shown in this article were generated using a central spatial discretization scheme, Jameson-type artificial dissipation in matrix mode, LU-SGS time integration, and the Spalart-Allmaras turbulence model.

To ensure a correct distribution of aerodynamic loads on the individual aircraft components, all conventional and fully elastic fluid-structure coupled simulations are

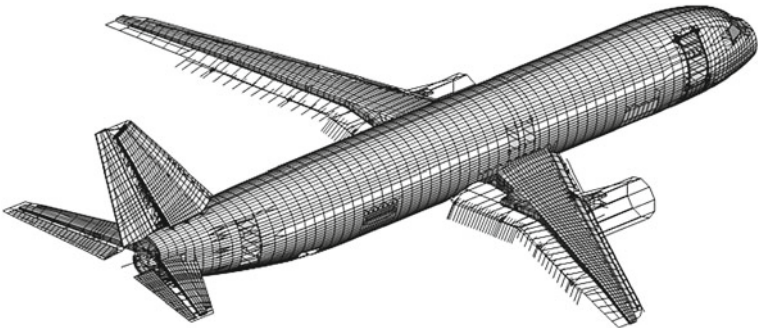

Fig. 4 A320-232 finite-element model

run at a longitudinally trimmed flight state, where pitching moment equals zero for a given center of gravity location. The required horizontal stabilizer incidence angle i_{HS} is computed from the residual pitching moment C_{My} obtained by the integration of static pressure from the previous flow solution over the CFD surface, and the known gradient $\partial i_{HS}/\partial C_{My}$. Then, the stabilizer is rotated to the new incidence angle and the surrounding volume mesh is aligned using TAU's mesh deformation algorithm. The mesh deformation approach was favored over chimera methods to avoid the gap between stabilizer and fuselage and the interpolation needed with this technique, or local re-meshing, because this would inhibit restarts.

3.2 Structural Model

A NASTRAN finite-element model of wing, fuselage, horizontal stabilizer, vertical tailplane, and engines was made available by AIRBUS Operations GmbH, Fig. 4. Contrary to the CFD analyses a full model is used to take into account structural non-symmetries. The model consists of 25,200 nodes, 58,900 elements, and 151,000 degrees of freedom and has been dynamically validated using ground vibration test data. Finite-element model updating has been restricted to an adaptation of the stiffness distribution in order to ensure accurate results for both dynamic and static loads. High-lift devices, i.e. slats, slat tracks, inner and outer flaps, and flap tracks, are represented by Timoshenko beam elements.

In the structural analyses the linear static solution sequence 'SOL 101' is applied. To accurately model free flight conditions a 'free-free' suspension is simulated using NASTRAN's 'inertia relief' option [4]. Engine thrust values are derived from the C_D computed in the CFD solution and introduced as discrete structural forces, equally distributed onto the engine pivot nodes.

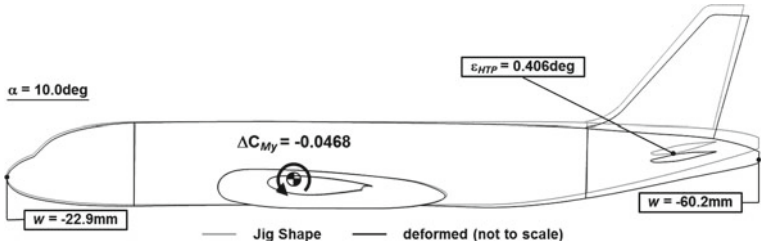

Fig. 5 Fuselage deformation

3.3 Coupling

In previous applications, coupling of aerodynamic loads and structural deflections between CFD simulation and finite-element analysis was implemented on the main wing and high-lift system only.[1] To study the aerodynamic influence of body and empennage deformations on maximum lift prediction, the existing coupling approach has been extended to fuselage, horizontal stabilizer and vertical tailplane. This allows investigating the lift and pitching moment contributions of horizontal stabilizer and fuselage to the overall lift and trim state and therefore a more accurate determination of aerodynamic loads acting on the wing.

4 Results

Figure 5 shows the longitudinal outline of the A320-232 ATRA for both the jig and deformed state as obtained from a coupled simulation of the fully elastic aircraft at $\alpha = 10.0°$, $Re = 16.9 \times 10^6$, and $Ma = 0.204$. At the aft fuselage section, i.e. in the region behind the wing, vertical deflection magnitudes are considerably larger than at the front. This is due to the combination of gravity and aerodynamic forces acting on the horizontal stabilizer, whereas the front section is mostly subjected to gravitational loads. The fuselage's bending deformation leads to a modified flow field around the fuselage tube and a change in effective incidence angle of the horizontal stabilizer. Integration of static pressure over the individual components indicates that the stabilizer generates approximately 30 % of the resulting change in overall pitching moment, while about 70 % originate from the flow around the cambered fuselage tube.

In Fig. 6 the convergence of horizontal stabilizer incidence i_{HS} and pitching moment coefficient C_{My} is plotted versus the number of iterations, showing the adjustment of incidence angle in each CFD-CSM coupling step and the approaching of the trimmed flight state.

[1] When coupling a CFD half model to a full structural model, aerodynamic loads for the structure's left hand side are mirrored from the right hand side CFD solution.

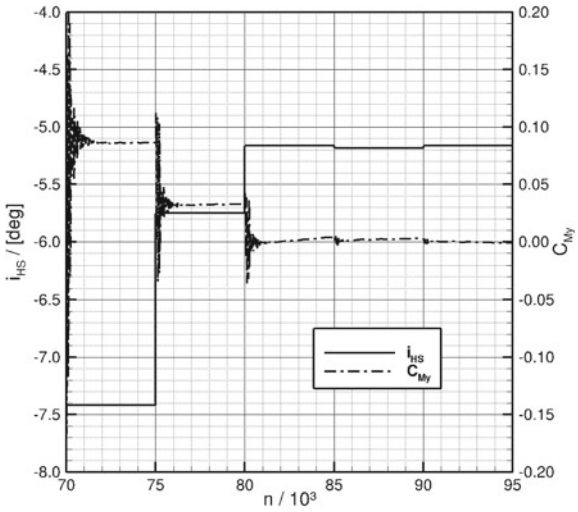

Fig. 6 Convergence of horizontal stabilizer incidence and pitching moment coefficient

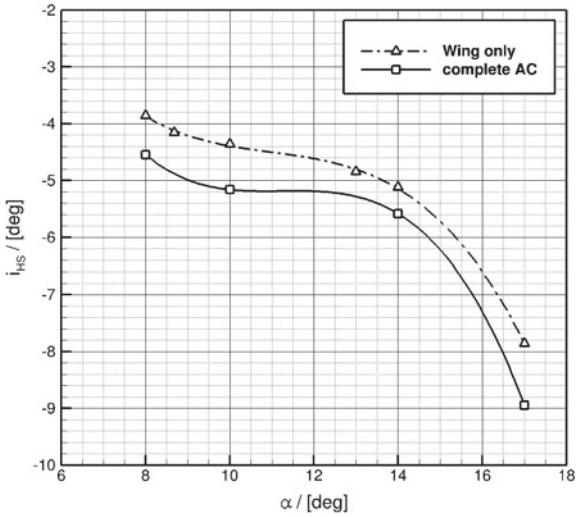

Fig. 7 Influence of fuselage deformation on horizontal stabilizer trim angle

The influence of fuselage deformation on the horizontal stabilizer angle required for trimmed flight is shown in Fig. 7 for angles of attack between $\alpha = 8.00°$ and $\alpha = 17.0°$ with each symbol representing a trimmed aero-elastic equilibrium solution. Compared to the partial coupling approach, where only the wing is assumed to be elastic, stabilizer settings for the fully coupled simulations are generally smaller by $\delta i_{HS} = -0.47°$ to $\delta i_{HS} = -1.10°$ in order to compensate for the additional nose-down pitching moment caused by the fuselage bending deformation. Owing to the moment generated by the curved fuselage, changes in i_{HS} are always larger than the geometric stabilizer rotation alone.

Fig. 8 Comparison of c_p-distribution on wing-only (*left*) and fully elastic (*right*) aircraft

Figures 8 and 9 display the static pressure coefficient distribution and surface streamlines, respectively, at $\alpha = 17.0°$, shortly before $C_{L,max}$ is reached. Results for the partial coupling approach are plotted on the aircraft's left-hand side, the fully elastic simulation results are shown on the right-hand side. Both c_p-distributions and streamline plots indicate that taking into account fuselage deformations does not only lead to a modified trim state as seen earlier, but also causes distinct differences in the flow about the wing, although both coupling approaches converge to the same spanwise twist distribution.

The most obvious dissimilarities are found on the wing's upper surface along the wing root and over the engine nacelle, which is best seen in the streamline plots in Fig 9. The delta-shaped flow pattern (shaded in grey) originating from the wing leading edge at the pylon intersection is of particular interest for maximum lift prediction as comprehensive CFD studies [5] and a preliminary analysis of flight test data have identified this area to be the location where lift breakdown triggered by a wing trailing edge separation first occurs. A correct simulation of the flow physics, in particular the complete vortex system and the interaction between the nacelle strake vortex and regions of high aerodynamic loading near the wing pylon intersection, is essential for a precise prediction of the stall scenario. With the partial coupling approach, left-hand side of Fig. 9, this flow pattern does not occur until the angle

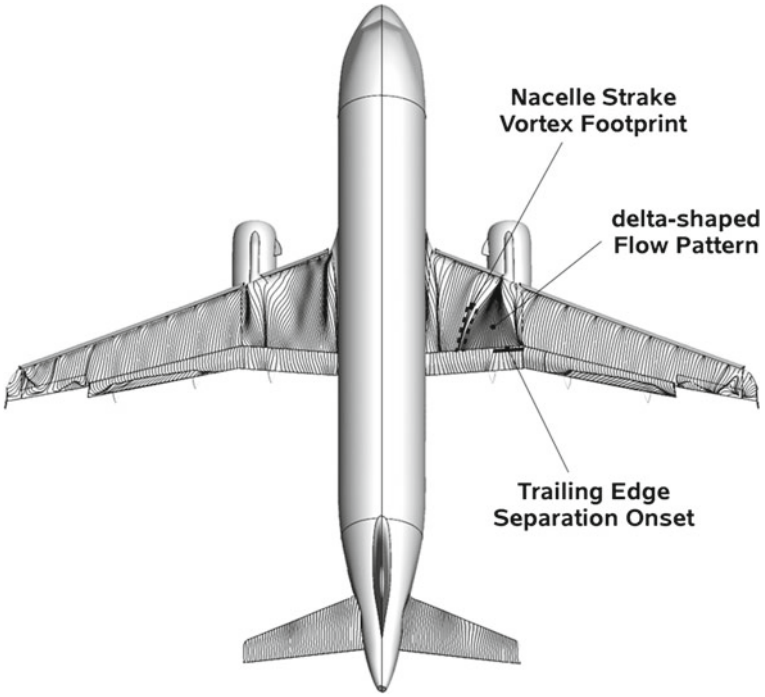

Fig. 9 Comparison of surface streamlines on wing-only (*left*) and fully elastic (*right*) aircraft

of attack is increased to approximately 18°. This suggests that the deformation of fuselage and stabilizers will have a non-negligible influence on the prediction of maximum lift and, in particular, the associated angle of attack $\alpha(C_{L,max})$.

A minor influence of fuselage and stabilizer deformations is also visible in the pressure distribution on the outboard wing, including flap and aileron, and in the wing tip separation location, although the outboard flap separation remains mostly unaffected.

On the horizontal stabilizer's lower side (not shown) a small change in pressure distribution occurs, which is due to the increased negative lift required to balance the additional nose-down pitching moment caused by the fuselage's deformation.

Although the differences between the partial and complete fluid-structure coupling approaches described here are comparatively small and of local character, and alterations with respect to the integrated aerodynamic parameters, i.e. C_L, C_D, spanwise lift distribution, or structural parameters, like wing bending and twist deformations remain marginal, the aerodynamic effects observed are still likely to have an impact on maximum lift prediction.

5 Conclusions

Aero-elastic simulations have been performed on DLR's Airbus A320-232 Advanced Technology Research Aircraft (ATRA) in landing configuration. To evaluate the impact of fuselage deformations on the numerical prediction of maximum lift and associated angle of attack, the existing in-house coupling procedure has been upgraded from a 'wing-only' approach to also include the fuselage, horizontal stabilizer, and vertical tailplane. Initial results show that fuselage deformations generate an additional nose-down pitching moment, which is caused by a change in effective horizontal stabilizer incidence angle and a modified flow field around the cambered fuselage tube. Additionally, differences in the flow field on the wing's upper surface along the wing root and over the engine nacelle were found. As lift breakdown and wing stall have been observed to originate in this region the effect is of particular interest for the high-lift aerodynamics investigations currently conducted in the HINVA project. Regarding the overall lift coefficient, including fuselage deformations and the according horizontal stabilizer deflections leads to a reduction of $\delta C_L = -0.784\,\%$ for the trimmed flight state at $\alpha = 17.0°$, close to $C_{L,max}$. While this amounts to almost half the accuracy goal of $\Delta C_{L,max} \leq 2\,\%$ set in HINVA, the extra computing time required affects the interpolation of nodal forces and surface deflections only and is negligible in comparison to generating the converged aero-elastic equilibrium solution.

The perceived differences to the partial coupling approach suggest that the deformation of fuselage and horizontal stabilizer will have a non-negligible influence on the prediction of maximum lift and associated angle of attack.

Acknowledgments The joint research project HINVA is funded by the German Federal Ministry of Economics and Technology within the fourth Aeronautical Research Program LuFo IV.

References

1. Rudnik, R., Reckzeh, D., Quest, J.: HINVA-High lift INflight VAlidation-Project Overview and Status. In: 50th AIAA Aerospace Sciences Meeting, AIAA Paper 2012–0106, Nashville, Tennessee (2012)
2. Heinrich, R., Wild, J., Streit, T., Nagel, B.: Steady fluid-structure coupling for transport aircraft. In: ODAS Symposium, Toulouse, France (2006)
3. Rossow, C.-C., Kroll, N., Schwamborn, D.: Numerical aerodynamics at DLR, East-West-High-Speed-Flow-Field Conference 2005, Beijing. China, pp. 31–49 (2005)
4. MSC Software Corporation, http://www.mscsoftware.com/Contents-/Products/CAE-Tools/MSC-Nastran.aspx
5. Bier, N., Rohlmann, D., Rudnik, R.: Numerical maximum lift predictions of a realistic commercial aircraft in landing configuration. In: 50th AIAA Aerospace Sciences Meeting, AIAA Paper 2012–0279, Nashville, Tennessee (2012)
6. CentaurSoft, http://www.centaursoft.com/

Combined Time-Resolved PIV and Structure Deformation Measurements for Aeroelastic Investigations

Hauke Ehlers, Reinhard Geisler, Sebastian Gesemann and Andreas Schröder

Abstract The aeroelastic behaviour of a thin plate has been investigated by applying two different optical measuring techniques: velocity field (PIV) and structure deformation (IPCT) measurements. The aim of the experiment is to solve Collar's triangle of forces. The focus of the present chapter is on describing the wind tunnel experiment and the measuring techniques in detail. A second key aspect is on the calculation of instantaneous pressure fields and aerodynamic forces from PIV data.

1 Introduction

The interaction of structural (elastic and inertial) as well as aerodynamic forces causes complex dynamic aeroelasticity problems. Part of this is the flutter phenomena which is potentially destructive and needs to be avoided in most cases. Great effort is made experimentally and numerically in considering flutter characteristics to avoid structural failure. This includes the safety for aeronautical light weight structures but also for buildings and for bridges.

Within the Advanced Flow Diagnostics for Aeronautical Research project (AFDAR) flutter of a thin plate in a low-speed wind tunnel has been investigated by using optical measuring techniques. The advantage is to measure contactless, non-destructive, time-resolved and with high accuracy. The acquired time-resolved data enables solving Collar's triangle of aerodynamic A, inertial I and elastic E forces (general aeroelastic stability problem: $A + I + E = 0$) and is also useful for computational code validation aiming in coupling CFD and CSM-codes in subsonic flows.

H. Ehlers (✉) · R. Geisler · S. Gesemann · A. Schröder
German Aerospace Center (DLR), Institute of Aerodynamics and Flow Technology,
Bunsenstr 10, 37073 Göttingen, Germany
e-mail: hauke.ehlers@dlr.de

A. Dillmann et al. (eds.), *New Results in Numerical and Experimental Fluid Mechanics IX*,
Notes on Numerical Fluid Mechanics and Multidisciplinary Design 124,
DOI: 10.1007/978-3-319-03158-3_40,

Recent efforts have derived pressure fields from planar velocity field data measured by Particle Image Velocimetry (PIV). The so called planar pressure imaging (PPI) is based on the momentum conservation principle and has been investigated by e.g. Bauer and Köngeter [1] and Oudheusden et al. [2] for steady flows under approximately two-dimensional (2D) flow conditions. By measuring time-resolved velocity data instantaneous pressure fields have been estimated on a square cylinder by Kurtulus et al. [3] and de Kat et al. [4].

High precision image based surface reconstruction methods are developed at DLR Göttingen. Konrath et al. [5] investigated the simultaneous measurement of forces, model position, wing deformation and flow velocity fields for plunging wing models. An approach to determine inertial forces for a harmonically oscillating stiff wing model by using an optical measuring set-up is given by Ehlers et al. [6].

The present chapter shows a generic flow-structure-interaction experiment which has been performed in a low speed wind tunnel at DLR Göttingen. The self-excited oscillation of a thin rectangular plate has been investigated by applying two optical measuring systems to synchronously measure the flow field around (high-speed PIV) and the deformation of the plate (high-speed IPCT). The PIV set-up enables for calculating time series of planar velocity vector fields. The estimation of the unsteady aerodynamic forces on the plate surfaces rely on the assumption of a 2D flow hence the thin plate is assumed to oscillate mainly in a 2D bending mode. By solving the incompressible momentum equation end spatially integrating the pressure gradients [4] for each time step and extrapolating the related pressure fields close to the plate surface along the span of the plate the time-resolved aerodynamic force distribution results. The high-speed IPCT system is applied to measure the 3D unsteady deformation of the thin plate hence this set-up is capable to detect higher modes of the bending oscillation. Inertia forces can be calculated from the acceleration of the plate surface which is achieved by differentiating the deformation with respect to the time and by using the mass distribution of the plate [6]. The elastic forces are calculated from the measured surface deflection, the plate stiffness and by using an analytical thin flat plate deformation model. As the IPCT measuring set-up provides the 3D distribution of the two different structural forces, the 3D distribution of the aerodynamic forces can be calculated, too.

The focus of the present chapter is on the detailed description of the complete experimental set-up and on the presentation of some first results of the planar pressure fields and the related aerodynamic force data. The calculation of structural forces should be considered as an outlook.

2 Experimental Set-up and Measuring Procedures

The experiment has been performed in a circular Göttingen-Type low speed wind tunnel at DLR Göttingen with a cross section of $1.0 \times 0.7\,\mathrm{m}^2$. The turbulence level for flow velocities below $20\,\mathrm{ms}^{-1}$ is less than $0.5\,\%$. A flat plate supporting base with an elliptical leading edge has been installed within the wind tunnel test section.

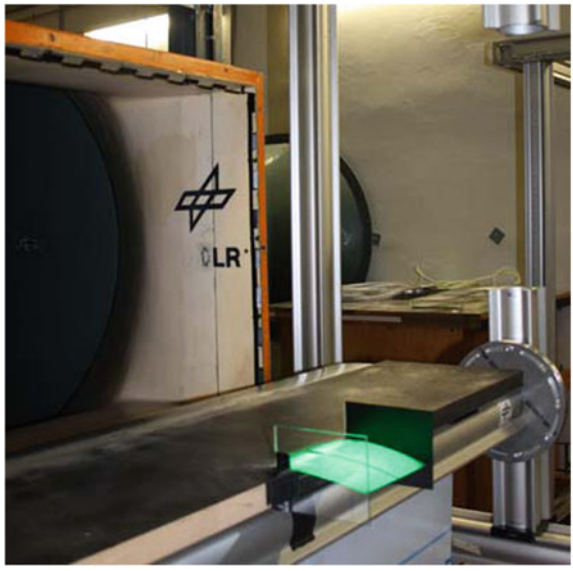

Fig. 1 Thin plate model (*green* illuminated) and glass end plates mounted downstream to the supporting plate; wind tunnel nozzle is seen in the background

A thin plate model was fixed to one side downstream to the supporting base. The other edges of the model were freely suspended. The support ensures a laminar approaching flow overflowing the upper side of the thin plate only (Fig. 1). The model has a thickness of 0.05 mm and is made of hardened carbon steel. The plate dimensions are ($b \times l$) $150 \times 75\,\text{mm}^2$. By means of a FEM model the first five eigenmodes could be detected at $f = 7.7$, 11.8, 22.4, 41.9 and 48.0 Hz. The model has been specially prepared for the optical measuring techniques. For the surface reconstruction measuring technique the surface was coated with a random white dot pattern on black background. In the central plane of the model a narrow band of high-gloss black dye was applied to optimize the PIV measurement close to the surface. Two glass plates on the lateral sides of the thin plate inhibit a 3D-flow exchange at the plate side edges. The influence of the glass end plates to the 3D characteristics of the flow is assumed to be low. The applied high-speed PIV system consists of a diode-pumped Nd:YAG Laser from Lee. Inc. (LDP-200MQG) providing 20 mJ per pulse at 5 kHz using both cavities simultaneously. The laser was guided through a set of light sheet forming lenses and a combination of mirrors enabling an illumination of a mist of 1 μm DEHS tracer particles in a central plane on the upper and lower side of the oscillating thin plate. For this purpose the light sheet was split in two by the mirror arrangement (see Fig. 2). The digital imaging system consists of a pco.dimax CMOS camera (12 bit) which has been operated at 5 kHz framing rate and a reduced resolution of 1344×688 Pixel (Pixel size: 11 μm). The camera sensor was aligned parallel to the illuminated measuring plane. A 85 mm Nikon lens at $f/\# = 2.0$ was mounted on the camera imaging a field of view of $66 \times 130\,\text{cm}^2$. The recordings are processed with a 2D cross-correlation algorithm with a final interrogation window

size of 18 × 18 pixels and an overlap of 66 %. The image magnification factor was 10.22 pixel mm which leads to a spatial resolution of 0.587 × 0.587 mm^2 for the resulting vector field. The multi-grid interrogation method was applied starting with an initial window size of 96 × 96 pixels. Assuming a precision of the determined displacements of better than 0.1 pixel, the uncertainty of the velocity vectors is less than 1 % of U_∞. An automatic mask generation tool was constructed which is able to detect the line of reflection on the model surface by digital image processing (erosion/dilatation principles). The high-speed IPCT set-up consists of two Photron SA1.1 CMOS cameras (12 bit) mounted on lens adapters allowing an adjustment of the Scheimpflug angle for oblique viewing directions. Two 60 mm Zeiss lenses have been used at $f/\# = 5.6$ to get the desired depth of field. The cameras have been operated at 2.5 kHz framing rate and a reduced resolution of 1024 × 544 Pixel (Pixel size: 20 μm). Two pulsed LED illuminators developed at DLR Göttingen have been used as light sources to illuminate the random pattern of small white paint dots on the upper side of the thin plate surface. The light pulse width was 12 μs at 2.5 kHz. The illuminated surface has been imaged by both cameras in stereo viewing. The size of the angle between the IPCT cameras was about 67°. A two-plane calibration target has been imaged within the measurement volume for calculating a function for all possible lines-of-sight of the two IPCT cameras. This function enables a local triangulation of the found dot correspondences from both camera viewings which have been estimated by using an initial mapping of the surface dot pattern image and a successive iterative 2D cross-correlation scheme (similar to a PIV evaluation). Hence the surface can be reconstructed. Before the dynamic measurements the static rest position of the model has been recorded as a reference position for later deformation calculations.

Both measuring systems have been operated simultaneously. For this purpose a controlling system was used consisting of a pulse generator as master clock (output frequency: 2.5 kHz) and two sequencers (see Fig. 3). *Sequencer 1* was triggered directly by the pulse generator and did provide the laser with a continuous output signal of 5 kHz. A second output signal of 2.5 kHz was used as input for the second sequencer. A manual switch was applied to interconnect *sequencer 2* which was programmed to control the exposure of the PIV camera (*pco*) synchronous to the laser and the IPCT measuring system (*Photron* cameras and *LED*s). The IPCT images have been recorded between two successive PIV recordings.

3 Pressure Calculation

The in-plane pressure gradients are obtained by the incompressible momentum equation. Written in conservative differential form for a fixed fluid element the equation is given as

$$\nabla p = -\rho \left[\frac{\partial \boldsymbol{u}}{\partial t} + (\boldsymbol{u} \cdot \nabla)\, \boldsymbol{u} - \nu \nabla^2 \boldsymbol{u} \right] . \tag{1}$$

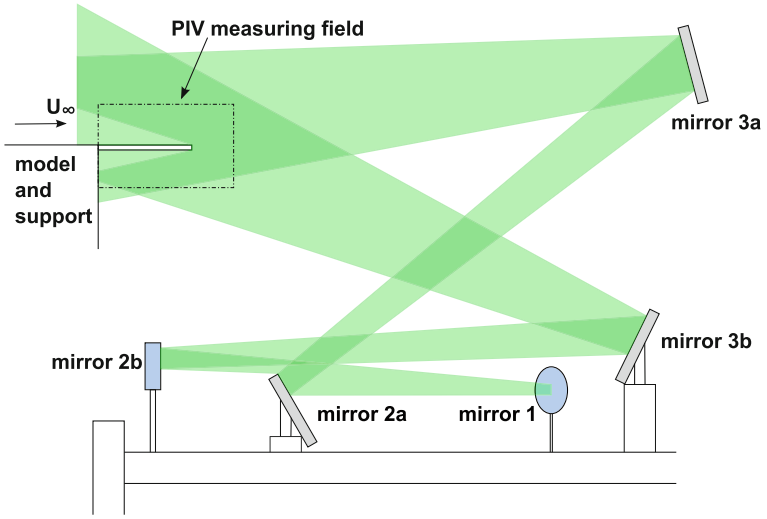

Fig. 2 Part of the optical set-up for PIV measurement; light sheet is reflected into the measuring plane by *mirror 1*; *mirror 2a* only reflects the lower part of the light sheet to illuminate the upper part of the measuring plane; *mirror 2b* is installed to illuminate the lower part of the measuring plane

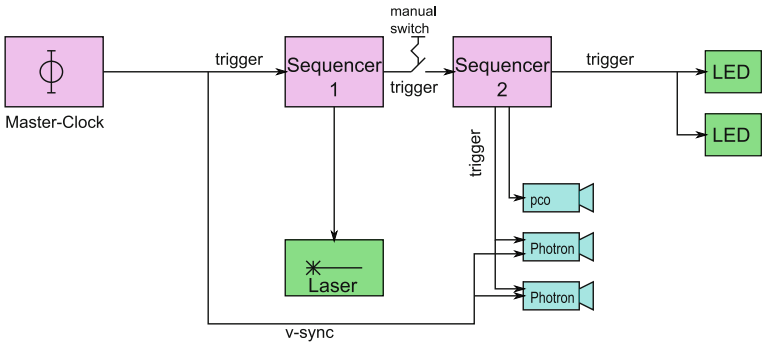

Fig. 3 Schematic of the measuring control system; the PIV system (*Laser* and *pco* camera) is operated at 5 kHz, the IPCT system (*LED*s and *Photron* cameras) is operated at 2.5 kHz

In Eq. 1 ∇p is the pressure gradient, ρ the fluid density, $\boldsymbol{u}$ the velocity vector and ν the kinetic viscosity. If the flow field under investigation is nearly two-dimensional Eq. 1 can be reduced. In Cartesian coordinates we obtain the 2D form:

$$\frac{\partial \boldsymbol{p}}{\partial x} = -\rho \left[\frac{\partial \boldsymbol{u}}{\partial t} + \boldsymbol{u}\frac{\partial \boldsymbol{u}}{\partial x} + \boldsymbol{v}\frac{\partial \boldsymbol{u}}{\partial y} - \nu \left(\frac{\partial^2 \boldsymbol{u}}{\partial x^2} + \frac{\partial^2 \boldsymbol{u}}{\partial y^2} \right) \right] , \tag{2}$$

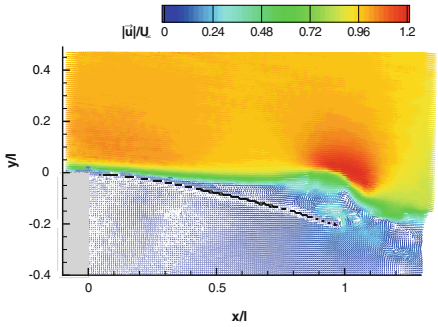

Fig. 4 PIV velocity vector field for $t/T = 0.333$

$$\frac{\partial \boldsymbol{p}}{\partial y} = -\rho \left[\frac{\partial \boldsymbol{v}}{\partial t} + \boldsymbol{u} \frac{\partial \boldsymbol{v}}{\partial x} + \boldsymbol{v} \frac{\partial \boldsymbol{v}}{\partial y} - \nu \left(\frac{\partial^2 \boldsymbol{v}}{\partial x^2} + \frac{\partial^2 \boldsymbol{v}}{\partial y^2} \right) \right] . \tag{3}$$

The terms on the right hand side of Eqs. 2 and 3 can all be obtained from time-resolved PIV measurements. For the assumption of 2D flow characteristics the 2D velocity field measured by a mono PIV set-up do suffice to determine the in-plane pressure gradients. For the derivatives with respect to the time a least squares differential operator is applied [7]. Spatial derivatives are approximated by central difference operators of fourth order.

The pressure filed is obtained by spatially integrating the pressure gradient field and using Dirichlet boundary conditions at the inflow boundary. Therefore an algorithm has been developed to solve the overdetermined system of equations ($\mathbf{M} \cdot p = \nabla p$) fast and precise. A fourth order approximation of the differentials is applied.

4 Results

For further descriptions a test case has been selected were the thin steel plate was oscillating in a steady-state flutter mode. The free stream velocity was $U_\infty = 5.5\ \mathrm{ms}^{-1}$. Figure 4 shows the measured velocity vector field for one instant of time. The model support is marked by a light grey box, the thin plate is shown as a black line. The boundary layer is clearly visible. For this instant the flow starts to follow the curvature of the plate, separates before the first third of the plate length and a vortex develops. The interaction of growing and convecting vortices leads to variations in the pressure field and stimulates the thin plate to flutter. The deformation frequency of the model is about $1/T \approx 40$ Hz. It oscillates in the fifth mode. In Fig. 5 the high resolution instantaneous pressure field calculated from PIV data by Eqs. 2 and 3 is given at six different time instants of one period of oscillation. Colour-coded is the relative pressure. The profile of the thin plate and the model support are shown in dark blue. The time series illustrates the evolution and movement of low and high

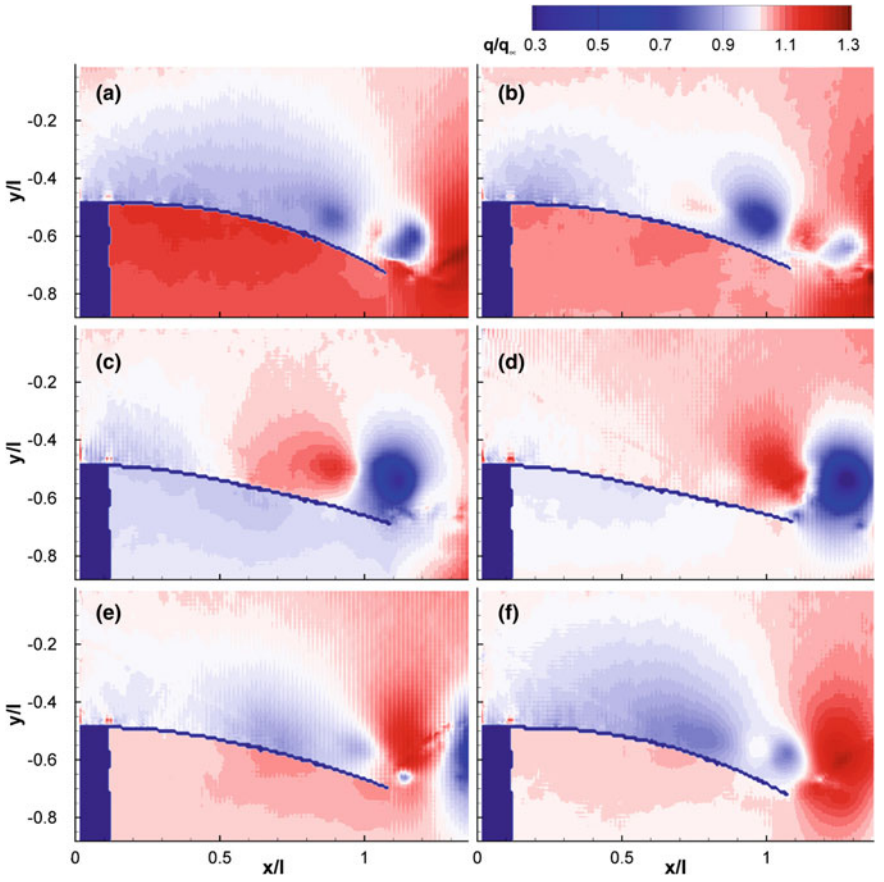

Fig. 5 Pressure results calculated from PIV data; **a** $t/T = 0$; **b** $t/T = 0.167$; **c** $t/T = 0.333$; **d** $t/T = 0.5$; **e** $t/T = 0.667$; **f** $t/T = 0.833$

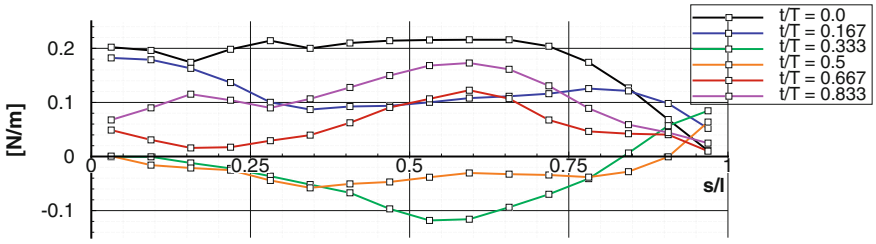

Fig. 6 Chord wise force distribution for six instants of time

pressure regions. The data sets enable for calculating the aerodynamic forces in the measuring plane acting on the model surface. Figure 6 illustrates the chord wise 2D force distribution for the six instants of time.

5 Conclusion and Outlook

A generic aeroelastic wind tunnel experiment has been carried out by means of two different optical high-speed measuring techniques. The first step of calculating instantaneous pressure fields and forces from 2D PIV data is shown above. The next step will be to evaluate the 3D approach of calculating the involved structural forces from surface deformation measurements and to compare the results of the two different measuring techniques.

References

1. Bauer, T., Köngeter, J.: PIV with high temporal resolution for the determination of local pressure reduction from coherent turbulent phenomena. In: 3rd International Workshop on PIV, pp. 671–676. Santa Barbara (1999)
2. Oudheusden, van B.W., Souverein, L.J.: Evaluation of the pressure field from PIV in a shock wave boundary layer interaction. In: 7th International Symposium on Particle Image Velocimetry, Rome, Italy (2007)
3. Kurtulus, D.F., Scarano, F., David, L.: Unsteady aerodynamic forces estimation on a square cylinder by TR-PIV. Experiments in Fluids. 42/2, pp. 185–196 (2007)
4. de Kat, R., van Oudheusden, B. W., Scarano, F.: Instantaneous planar pressure field determination around a square-section cylinder based on time-resolved stereo-PIV. In: 14th International Symposium on Application of Laser Techniques to Fluid Mechanics, Lisbon (2008)
5. Konrath, R., Schlager, B., Kirmse, T., Kompenhans, J., Möller, T.J., Wokoeck, R., Emge, M., Radespiel, R.: Simultaneous Measurements of Unsteady Aerodynamic Loads, Flow Velocity Fields, Position and Wing Deformations of MAVs in Plunging Motion. In: Dillmann, A., Heller, G., Klaas, M., Kreplin, H.-P., Nitsche, W., Schröder, W. (eds.) New Results in Numerical and Experimental Fluid Mechanics VII. NNFM, vol. 112, pp. 331–338. Springer, Heidelberg (2010)
6. Ehlers, H., Konrath, R., Agocs, J., Radespiel, R., Wokoeck, R.: Ermittlung der Massenkräfte periodisch bewegter Tragflügelmodelle unter Anwendung von optischer Messtechnik. In: Deutscher Luft- und Raumfahrtkongress 2001, Paper DLRK 2011–241269, Bremen, Germany (2011)
7. Raffel, M., Willert, C., Wereley, S., Kompenhans, J.: Particle Image Velocimetry: A Practical Guide, Springer, Berlin (2007)

Part IX
Numerical Simulation

CTAU, A Cartesian Grid Method for Accurate Simulation of Compressible Flows with Convected Vortices

Philip Kelleners and Frank Spiering

Abstract A zonal approach for simulation of compressible fluid flow is presented. Within this approach a Cartesian solver of fourth order spatial accuracy is used for simulation of convection of vortical structures over larger distances with small numerical losses.

1 Accurate Flow Simulation Using a Zonal Approach

Many present day well established aerospace numerical codes, of which the DLR TAU-code is an example, for the simulation of subsonic, transonic or supersonic flow are second order accurate in physical space. For these second order codes it has been observed that freely convecting vortices, amongst other free convected coherent structures, suffer from rapid decay on grids of practical mesh density. The computational cost of accurate simulation of freely convected vortices becomes rapidly excessive as the distances over which the vortices travel increase, for second order accurate codes. Presently designated higher-order methods, that is of spatial order higher than two, are better able to represent these free vortices on grids of moderate density, and thus potentially, could lower the computational cost. However these higher-order methods may not be well suited to simulate flows with discontinuities like strong shocks in transonic flow, or close to complex shaped solid structures embedded in the fluid. A solution is a zonal approach. Within this zonal approach, based on experience, that is best-practice, the flow domain of interest is simulated with different discretization methods each being applied in those regions where their strengths excel. In the implementation of this zonal approach developed and presented here the boundaries of the different grids overlap and the developing flow

P. Kelleners (✉) · F. Spiering
DLR, Institute of Aerodynamics and Flow Technology, Lilienthalplatz 7,
38108 Braunschweig, Germany
e-mail: Philip.Kelleners@dlr.de

A. Dillmann et al. (eds.), *New Results in Numerical and Experimental Fluid Mechanics IX*,
Notes on Numerical Fluid Mechanics and Multidisciplinary Design 124,
DOI: 10.1007/978-3-319-03158-3_41,

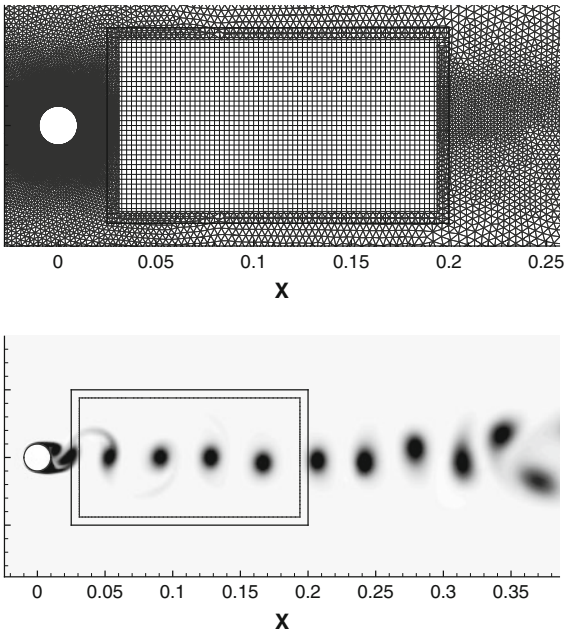

Fig. 1 The von Kármán vortex street behind a circle cylinder. A closeup of the chimera grid in the upper part, dimensionless entropy-like quantity given by the greyfilled iso-contours in the lower part

state is coupled in these overlapping regions. This procedure is called the Chimera or overset grid approach, and the overlapping grids are also referred to as Chimera grids (see [1]). This zonal approach is illustrated in Fig. 1. The DLR TAU-code, a second order accurate method is used for the regions of the flow close to the solid geometry. CTAU, the Cartesian grid higher order method presented here, is used on the portion of the grid enclosed by the two boxes. As can be seen from the thick black lines, the grids overlap at their boundaries where a code coupling module, (see [2]), performs the exchange of the fluid states and thus implements a strong volume coupling based upon the Chimera technique. The two components of this framework other than the Cartesian Solver are presented briefly below.

1.1 TAU Code

The DLR TAU-code is a fully featured package for simulation of steady and unsteady flow, of both inviscid and viscous compressible fluids, on unstructured hybrid, possibly moving, grids. It implements different turbulence models, overset grid techniques (Chimera), a large number of physical boundary conditions and can efficiently compute solutions on massive parallel computer clusters; e.g. see [3].

1.2 Code2Code Domain Coupling

The Code2Code program (see [2]) is the domain coupling tool, implementing a Chimera boundary between two possibly different CFD-codes, designated code A and code B. The domain coupling is done in three basic steps. There must be a region where the grid domain boundaries of code A and code B overlap. The coefficients for the data-exchange and interpolation for the overlapping region of grids A and B must be computed. At Run-time there must be exchange of the flow-states at the domain boundary grid overlap area at every time level or relaxation step. Code A and code B can be any different code or two instances of the same code.

2 Cartesian Solver, CTAU

The Cartesian solver prototype CTAU is a derivative of the TAU-code. It is a conventional explicit Runge–Kutta based relaxation solver for steady or unsteady flow problems. Discretization of the spatial terms in the equations of fluid flow is done using compact finite difference schemes, or Padé-type schemes, (see [4]), which formally, can be up to tenth order accuracy in space when operating on Cartesian meshes.

2.1 Padé Schemes

As a quick way to illustrate these compact finite difference schemes consider values u_i of a function given at discrete nodes on a regular equidistant one dimensional mesh. Quantities constructed from these nodal values like the derivative u'_i or interpolated values, $u_{1/2}$ inbetween the discrete nodes are computed by *implicit* operators with difference molecules of limited footprint. As an example a first derivative of fourth order accuracy is:

$$u'_{i-1} + 4u'_i + u'_{i+1} = \frac{3(u_{i+1} - u_{i-1})}{h}, \tag{1}$$

where index i designates the position on the regular mesh, u' is the first derivative of u and h is the local meshspacing. The expression for interpolation is:

$$u_{i-1/2} + 6u_{i+1/2} + u_{i+3/2} = 4(u_i + u_{i+1}), \tag{2}$$

which is also fourth order accurate. Inspect the left hand sides of (1) and (2) to check that the derivative or the interpolated values are given in implicit form. For these examples the actual values of the derived or interpolated quantities, at fourth order accuracy, comes at the price of having to solve a tridiagonal system of equations.

In the paper of [4] implicit formulations of up to tenth order accuracy of these Padé operators are given of the general form;

$$\beta u'_{i-2} + \alpha u'_{i-1} + u'_i + \alpha u'_{i+1} + \beta u'_{i+2} = a\frac{u_{i+1} - u_{i-1}}{2h} + b\frac{u_{i+2} - u_{i-2}}{4h} + c\frac{u_{i+3} - u_{i-3}}{6h}, \tag{3}$$

where the parameters α, β, a, b and c are derived by matching Taylor series coefficients of various orders. Different schemes of different order of accuracy can be derived for particular combinations of these parameters, again the reader is referred to [4].

2.2 Padé-type Operators for Finite Volume Schemes

The implicit operators introduced above are used in a finite difference context. For the simulation of fluid flow, the conservation properties of the numerical scheme used are of prime importance. Finite-volume schemes are inherently conservative whereas finite difference schemes are not. A finite-volume formulation of the Padé-type scheme, as described by Lacor et al. [5], which restores conservation of the dependent, now cell averaged, quantities is implemented in the Cartesian solver presented. The basis for the finite-volume formulation is the definition of *cell-averaged* dependent variables or quantities:

$$\bar{u}_i \equiv \frac{1}{(x_{i+1/2} - x_{i-1/2})} \int_{x_{i-1/2}}^{x_{i+1/2}} u(\xi) d\xi. \tag{4}$$

The fourth order accurate Padé-type operators used as examples before are now expressed in the cell averaged quantity $\bar{u}_i$:

$$u'_{i-1} + 4u'_i + u'_{i+1} = \frac{3(\bar{u}_{i+1} - \bar{u}_{i-1})}{h}, \tag{5}$$

for the first derivative, and:

$$u_{i-1/2} + 4u_{i+1/2} + u_{i+3/2} = 3(\bar{u}_i + \bar{u}_{i+1}), \tag{6}$$

for the interpolated values.

Notice how the stencil weights for the interpolated values have changed as a result of application of cell averaged values.

We are concerned with fluid flow. With the finite volume method we need to calculate the fluxes at the interfaces of the control volumes, hence the emphasis on the ability to calculate interpolated values. The fluxes of the Euler and Navier-Stokes equations of motion of fluid are non-linear, as illustrated by a line integral in y-direction for the mass flux in x-direction for two dimensional flow:

$$\int_a^b \rho(x, y)u(x, y)dy, \tag{7}$$

which complicates matters considerably as products of the primitive values are not readily available at the volume interfaces. A second order accurate approximation for the flux, averaged over the interface, is:

$$\frac{1}{y_b - y_a}\int_a^b \rho u dy \approx \frac{1}{y_b - y_a}\int_a^b \rho dy \; \frac{1}{y_b - y_a}\int_a^b u dy. \tag{8}$$

Additional correction terms of the form $\rho'_x u'_x \frac{\Delta x^2}{12}$ are needed to compute a fourth order accurate flux, where the first derivatives are now evaluated at the interfaces, for the details again refer to [5].

Ghost cells opposite of the domain boundary with quasi cell-averaged values prescribed by the local physical character at the boundary are needed to complete the boundary fluxes.

An implicit assumption for these Padé-type schemes is that argument values and their derivatives exist and are continuous. This is generally not true for discrete initial data, boundary conditions or when flow conditions result in flow structures like e.g. shear regions at length scales which are not resolved by the grid. As a result spurious waves will become part of the discrete solution. These spurious waves are removed effectively from the solution by high-order Padé filters, designed with similar discretization techniques as used for computation of the derivatives, to filter the solution to restore monotone solutions.

To limit the complexity of the current implementation of the Cartesian solver only the Padé-type schemes with parameter β set to zero are considered such that only tridiagonal systems of coupled equations need to be solved. As a consequence the complexity of implementation of the boundary conditions in the ghost cells is reduced.

2.3 Gust Boundary Condition

A series of boundary conditions is available in the Cartesian Solver e.g. farfield and symmetry boundary conditions as well periodic boundaries. The domain coupling interface as introduced in Sect. 1.2 is also implemented as a boundary condition.

To be able to accurate simulate aircraft response due to gust loading while there is a strong interaction between the aircraft structure, aircraft induced flow patterns and the gust itself is one of the goals of this research and development. Preferably the gust enters the flow domain at the farfield, is transported towards the aircraft, interacts with the aircraft and leaves the domain again at the farfield. The discrete gust should suffer much less from dissipation and dispersion errors as it is convected over large distance from the farfield towards the aircraft by the Cartesian solver.

A gust boundary condition at the farfield is superimposed on a non-reflecting inflow boundary condition. The gust is modeled as a velocity profile perpendicular to the undisturbed mean flow u_∞:

$$v = v(x,t) = v(x - u_\infty t), \tag{9}$$

with pressure and density, and thus internal energy as well, taken constant at inflow. This gust-model is a solution to the Euler equations as can be checked by substitution.

The non-reflecting inflow boundary condition for subsonic flow is formulated by assuming local one dimensional inviscid flow, followed by an eigenvalue-eigenvector-analysis of the Euler equations, diagonalization of the system by pre-multiplication with the left eigenvectors, and identification of the waves entering the domain. These inward running waves are then replaced with physical boundary conditions simulating constant entropy and enthalpy (refer to [6] for more details). This gives:

$$\begin{aligned} \boldsymbol{l}_i^T \left(\tfrac{\partial \phi}{\partial t} + \lambda_i \tfrac{\partial \phi}{\partial x} \right) &= -\boldsymbol{l}_i^T \boldsymbol{D}_{GH} \\ \boldsymbol{b}_j^T \frac{\partial \phi}{\partial t} &= 0, \end{aligned} \tag{10}$$

for i outward running characteristics and j inward running characteristics replaced with the boundary conditions $\boldsymbol{b}_j^T$. Notice that these boundary conditions have effective zero wave speed, $\lambda = 0$, thus are constant.

Then the actual $(1 - \cos)$-gust velocity profile superimposed at the inflow is formulated as a non-constant boundary condition:

$$\rho_\infty \frac{\partial v}{\partial t} = \rho_\infty \frac{2\pi}{L_{vg}} a_{vg} u_\infty^2 \sin\left(-\frac{2\pi}{L_{vg}} (x_\infty - x_{g0} - u_\infty t) \right), \tag{11}$$

with L_{vg} being gust length, a_{vg} the gust amplitude as dimensionless fraction of the undisturbed flow velocity u_∞, x_∞ the geometrical position of the farfield boundary and x_{g0} the initial position of the gust at time $t = 0$ beyond the farfield boundary. A result of a numerical experiment with this gust inflow boundary condition is shown in Fig. 2. Only minute spurious waves in the pressure, density were observed as the gust entered the domain. These numerical waves can be expected as the implementation of the discrete boundary condition is of a lower order of accuracy. However the typical dimensionless absolute error in the density induced by this boundary condition remained below $3 \cdot 10^{-4}$ at all simulated time.

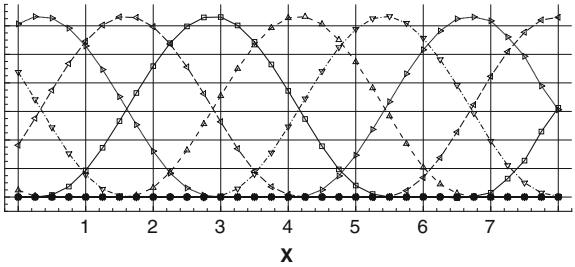

Fig. 2 Gust boundary condition; A domain of length 8, discretized with 32 cells. Flow from left to right. A (1 − cos)-gust of length 5 is fed into the domain at the left inflow boundary. Shown with different linetypes is the position of the gust at regular time intervals. Note the near-perfect conservation of amplitude and shape of the gust as it is convected through the domain by the Cartesian solver

3 Testcases

3.1 Von Kármán Vortex Street Behind Circle Cylinder

The well known von Kármán vortex street is simulated at a free-stream Mach number of 0.1 at a Reynolds-number of 1,000. Both grid and a snapshot at a point in time where the vortex street is well developed are depicted in Fig. 1, the thick black boxes indicate the boundaries of the overlapping grids. The TAU-grid is hybrid with a prismatic layer wrapped around the circle cylinder for good support of the viscous boundary layer and the flow separation at the downstream side close to the cylinder. The vortices are convected with very small losses over the full length of the Cartesian domain, whereas they are quickly dissipated upon further convection in the triangular TAU-grid.

3.2 Wake Flow Resulting from Transonic Buffet

The configuration of the two airfoils shown in Fig. 3 is a useful approximation to study the effect of the unsteady wake, resulting from transonic wing buffet, as it interacts with a horizontal tailplane. The wing is modeled with the supercritical NLR7301 airfoil of 4.47 m length at an angle of incidence of 3°. The horizontal tailplane is modeled with a NACA0012 airfoil of half the wing-chord length at 0° angle of incidence. The undisturbed flow is angled at 0.5°, freestream Mach number is 0.73 and the Reynolds number is 26 million. At these conditions shock buffet occurs over the wing airfoil and the unsteady wake influences the pressure distribution at the tailplane considerably. Development in the wake of structures of considerable size in the crossflow direction could only be observed in simulations performed with the Cartesian solver inbetween the two airfoils.

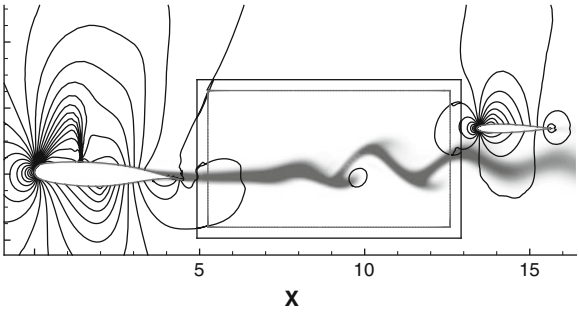

Fig. 3 A snapshot of flow at conditions of transonic buffet; the wake of the wing airfoil interacting with a tailplane airfoil. Greycolored isocontours depict a dimensionless entropy-like quantity, the static pressure is drawn with black isolines, the black boxes show the overlapping boundaries of the chimera grid parts

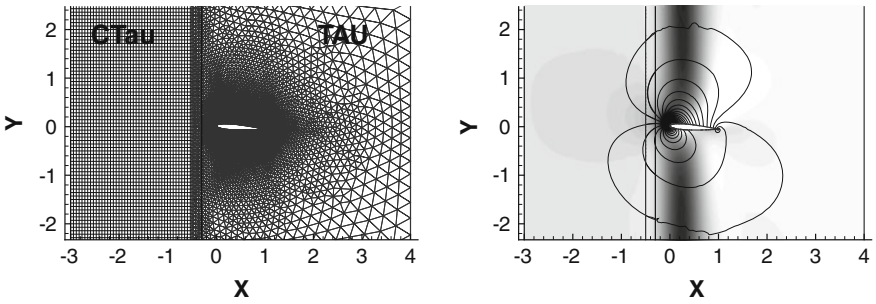

Fig. 4 Gust encounter, grid on the left, vertical velocity (isocontours) and pressure (black iso-lines) on the right at the moment in time of maximum lift during the gust encounter

3.3 Gust Encounter, NACA0012

The gust-velocity model described in Sect. 2.3 is convected in a Cartesian grid shown to the left in Fig. 4, towards a NACA0012 airfoil fixed in space at 4° angle of attack at a freestream Mach-number of 0.3. The gust length is 1.4 times the chord length of the airfoil, the gust amplitude fraction, a_{vg}, is $\frac{1}{8}$th of the undisturbed freestream velocity. The flow is inviscid. There is no noticeable decay of the gust as it is transported in the Cartesian grid and it interacts in its unaltered shape with the airfoil as intended. At the moment of maximum lift, as shown in the figure, the lift coefficient (C_l) peaks at approximately 2.5 times the value of lift generated in steady undisturbed flow. After having traversed along the fixed airfoil, the structure of the gust has changed significantly and it was observed that inside the airfoil wake the downflow induced by the airfoil is dominant. We conclude that the zonal approach enables near lossless gust convection and accurate gust-airfoil interaction.

4 Conclusions

A zonal approach for simulation of compressible fluid flow has been presented. The Padé-type scheme used in a finite volume context to simulate flow of a compressible, possibly viscous, fluid at fourth order accuracy on Cartesian grids has been introduced, as well as a gust-velocity boundary condition superimposed upon a non-reflective inflow boundary condition. Three testcases showing the effective use of the higher order Cartesian method with help of chimera-based domain coupling between two different flow solvers, illustrate the prosperous perspective of the present framework under development. Further work will include testing of the method on full three dimensional configurations and, amongst others, implementation of whirl fluxes to allow for moving meshes, as needed for simulation of rotorcraft.

References

1. Chesshire, G., Henshaw, W.D.: Composite overlapping meshes for the solution of partial differential equations. J. Comp. Phys. **90**, 1–64 (1990)
2. Spiering, F.: Coupling of TAU and TRACE for parallel accurate flow simulations. In: International Symposium "Simulation of Wing and Nacelle Stall", Braunschweig Germany, June 2012
3. Schwamborn, D., Gerhold, T., Heinrich, R.: The DLR TAU-code: recent applications in research and industry. Invited Lecture. In: Proceedings on CD of the European Conference on Computational Fluid Dynamics ECCOMAS CDF (2006).
4. Lele, S.K.: Compact finite difference schemes with spectral-like resolution. J. Comp. Phy. **103**, 16–42 (1992)
5. Lacor, C., Smirnov, S., Baelmans, M.: A finite volume formulation of compact central schemes on arbitrary structured grids. J. Comp. Phys. **198**, 535–566 (2004)
6. Kelleners, P. H.: An edge-based finite volume method for inviscid compressible flow with condensation. Ph.D. Thesis, University of Twente (2007)

Coupling of Flow Solvers with Variable Accuracy of Spatial Discretization

Frank Spiering and Philip Kelleners

Abstract In this work a coupling procedure for flow solvers of different accuracies of spatial discretizations by the Chimera technique is introduced. To adapt the coupling procedure to the properties of the incorporated flow solvers, the accuracy of different interpolation methods is investigated. The coupling module used for the data transfer between the flow solvers is extended by a high order interpolation method and two test cases are presented to illustrate the effects of the interpolation methods on the flow solution.

1 Introduction

The accurate simulation of interactions of a disturbed flow and aerodynamic bodies is a complex challenge in computational fluid dynamics. The simulation of blade-vortex-interactions on helicopter rotors or the interaction of a wing wake and the horizontal tail plane of an aircraft demand the preservation of the flow field disturbance from its origin to the body it interacts with. In common finite volume methods of second order spatial accuracy the computational grid needs to be very fine in the region where vortices have to be preserved, which results in a high computational effort.

At DLR's Institute of Aerodynamics and Flow Technology an approach of coupling two different flow solvers is developed to account for the needs in this kind of flow scenario. The efficient convection of flow disturbances in the far-field is realized by a high order accurate flow solver utilizing Cartesian grids (*CTAU*) and an

F. Spiering (✉) · P. Kelleners
German Aerospace Center, Member of the Helmholtz Association, Institute of Aerodynamics and Flow Technology, Lilienthalplatz 7, 38108 Braunschweig, Germany
e-mail: frank.spiering@dlr.de

P. Kelleners
e-mail: Philip.Kelleners@dlr.de

A. Dillmann et al. (eds.), *New Results in Numerical and Experimental Fluid Mechanics IX*, Notes on Numerical Fluid Mechanics and Multidisciplinary Design 124,
DOI: 10.1007/978-3-319-03158-3_42,

implicit PADE-scheme (see [1]) formulated in fourth order accuracy. The flow in the vicinity of the aerodynamic body is simulated with DLR's TAU code (see [2]), to allow for flexible unstructured grid generation of complex configurations. To couple both flow solvers the data is transferred with use of the Chimera technique, a bidirectional interpolation between the grids in an overlapping region (see [3]). It should be mentioned that the data transfer by interpolation is not conservative. However, if an appropriate grid overlap and resolution can be realized, the influence on the flow solution should be negligible.

The method of coupling different flow solvers in this work was originally developed to couple the flow solvers TAU and the turbomachinery code TRACE (see [4]) of the Institute of Propulsion Technology of DLR. The coupling procedure is performed by an external coupling module, which contains the necessary functionalities for the flow data interpolation and the management of the parallel flow data transfer between the flow solvers (see [5]).

2 Code Coupling Procedure

To realize a coupled simulation, the flow data has to be exchanged during the iterative time stepping process of the flow solvers. To allow for different grid topologies and discretization metrics the data is interpolated in an overlapping region of the grids of each flow solver. This approach requires a search of an appropriate donor cell as data source for each coupling boundary point on both grids. This donor cell search, which already includes the calculation of the interpolation coefficients, has to be performed only once in simulations with no relative movements of the grids. The calculated point mapping and the interpolation coefficients can then be used for the data exchange in the solution process.

To compute the coupling point mapping and the associated interpolation coefficients, both flow solvers have to send the grids of their flow domains to the coupling module. Then an appropriate donor cell for data interpolation is searched for each coupling boundary point of both grids. Finally the located donor cell, respectively the associated donor points have to be transmitted back to the flow solvers. This mapping procedure is shown in Fig. 1. Within the iterative time stepping procedure a close coupling between the flow solvers is applied. In simulations of steady flows with a local time stepping method the data can be exchanged during each time step to result in a converged flow solution with both solvers. In time-accurate simulations with dual time stepping the data can be exchanged in each pseudo time step to converge to a quasi-steady state in each physical time step. To exchange the flow data, both flow solvers send the data from the mapped donor points to the coupling module. Then the calculated interpolation coefficients are applied to compute the flow data updates for the coupling boundary points of the opposing grid. After that, both solvers perform the next iteration of the flow computation as shown in Fig. 2. All communication between the flow solvers and the coupling module is realized via socket communication to avoid any file access. The implementation of the cou-

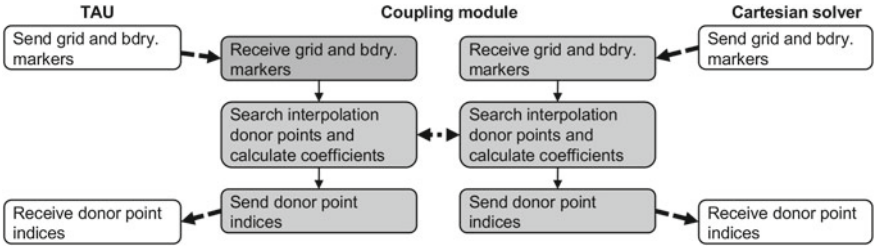

Fig. 1 Coupling point mapping and calculation of interpolation coefficients

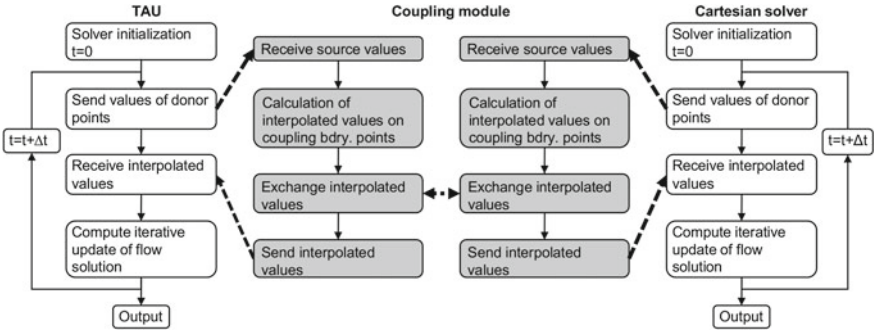

Fig. 2 Data exchange during iterative time stepping

pling method also allows for massively parallel simulations on a high performance computing (HPC) cluster.

3 Interpolation Method

The original coupling procedure followed the implementation of the internal Chimera method in the TAU code (see [6]), using a trilinear interpolation method to calculate the interpolation coefficients with respect to the cell nodes of the primary grid. This approach is suited to maintain an overall spatial discretization accuracy of second order and can be applied to both structured and unstructured grids.

The Cartesian solver uses a cell-centered discretization metric. To realize an interpolation with respect to these discretization points, a dual grid based on the cell centers is constructed which is used to calculate the interpolation coefficients. For linear interpolation the dual grid has to extend to the first layer of ghost cells around each grid block to provide valid donor cells at the boundaries of a grid block.

Compared to the fourth order accurate discretization of the flow data of the Cartesian solver, the linear interpolation leads to numerical dissipation. This may lead to a dampening of local minimum and maximum values of the data in the flow field.

Furthermore the CTAU grid is assumed to be relatively coarse to realize an efficient simulation, which also may increase the interpolation error.

For the data transfer from TAU grid to CTAU grid, the approach of linear interpolation is left unchanged, for it is assumed that the interpolation error on the finer TAU grid is not significant. Additionally the TAU code also provides only a second order accurate data discretization, so that the linear interpolation is able to capture local minimum and maximum values of the flow data.

For a more accurate data transfer from CTAU grid to TAU grid, interpolation methods have been investigated, which better approximate the data discretization of the Cartesian solver. Interpolation by cubic Hermite splines, Lagrangian polynomials and radial basis functions have been concerned.

Interpolation by cubic Hermite splines is done with the formula:

$$f(x) = h_{00}(t)f(x_i) + h_{10}(t)lf'(x_i) + h_{01}(t)f(x_{i+1}) + h_{11}(t)f'l(x_{i+1}) \qquad (1)$$

with the Hermite basis functions h and the geometrical parameters t and l depending on the location of the interpolation point. This results in a compact stencil for the interpolation itself if the gradients are known. If gradients have to be computed accurately to provide a high order of accuracy, the compactness is compromised.

The interpolation with Lagrangian polynomials on a N-point stencil is defined as:

$$f(x) = \sum_{i=1}^{N} L_i f(x_i) \quad \text{with} \quad L_i = \prod_{k=1,k\neq i}^{N} \frac{x - x_k}{x_i - x_k} \qquad (2)$$

The order of accuracy with respect to the truncation error is N. Data interpolation by Lagrange polynomials needs an extended stencil on a structured grid. Nevertheless this method can be formulated for an arbitrary order of accuracy and is fast in terms of computational time.

In the approach with radial basis functions the interpolation is performed by evaluation of a radial function as follows:

$$f(x) = \sum_{i=1}^{N} \alpha_i \Phi(\|x - x_i\|) + p(x) \quad \text{with} \quad \Phi(d) = d^2 \log(d) \qquad (3)$$

with global support of all source points. The interpolation coefficients α_i are depending on the function values at the sample points and thus would have to be recomputed for each data transfer in a flow simulation, which makes this much more expansible in terms of computational time compared to the other methods. The applicability to unstructured grid is not of importance in this work, for the CTAU grids provide a structured indexing of the grid cells.

With respect to the properties of the interpolation methods discussed above, a high order interpolation by Lagrangian polynomials has been implemented into the coupling module. For three-dimensional interpolation on a stencil of $N \times N \times N$ source

points this method can be extended straight forward to a sequential combination of three one-dimensional interpolations.

The implementation provides both fourth and sixth order accurate interpolation. To provide a valid extended stencil at the CTAU grid boundaries, the dual grid used for the interpolation is extended up to the second or third layer of ghost cells respectively. At the coupling boundary a larger grid overlap has to be generated so that the interpolation stencils do not include coupling boundary points.

4 Applications

Two different test cases are used to examine the effect of the interpolation method on the solution of a coupled flow simulation. The first test case demonstrates the transport of a vortex through a grid consisting of three blocks with different resolutions. In the second test case a gust encounter on a airfoil is simulated. In both cases a two-dimensional inviscid flow is assumed to exclude dissipation by turbulence effects.

In both cases the bidirectional data transfer at the coupling interface uses various interpolation methods for the data transfer from the CTAU grid to TAU grid, whereas the data transfer from TAU grid to CTAU grid is always performed by linear interpolation, for the TAU grid is significantly finer than the CTAU grid, so that a reasonable interpolation accuracy can be assumed.

4.1 Vortex Transport

In this test case a vortex is convected within a grid consisting of three grid blocks coupled by two overlapping regions (see Fig. 3) in a time-accurate simulation. The reference density of the flow field is set to $\rho = 1.29\,\mathrm{kg/m^3}$ and the Mach number of the flow field is set to $Ma = 0.5$. The vortex is initialized by an analytical data distribution in the first CTAU grid block with a minimum density set to $\rho_v = 1.2255\,\mathrm{kg/m^3}$. The flow in the coarse grid blocks is simulated with the Cartesian solver and the flow in the fine grid block is simulated with TAU. It should be noted that the erroneous representation of the minimum density value in the initial CTAU data (see Fig. 3) is caused by postprocessing of the flow solution of CTAU. Therefore the flow data of the coarse CTAU grid blocks is compared to the initial CTAU data, whereas the data of the fine TAU grid block is compared to the analytical density profile of the vortex.

Figure 4 shows the density profiles of the vortex core of the simulations using different interpolation methods. On the left side the analytical density profile and the initial CTAU solution is shown. In the middle and on the right side the resulting density distributions of both TAU and CTAU of the convected vortex at the first and second grid overlap are shown.

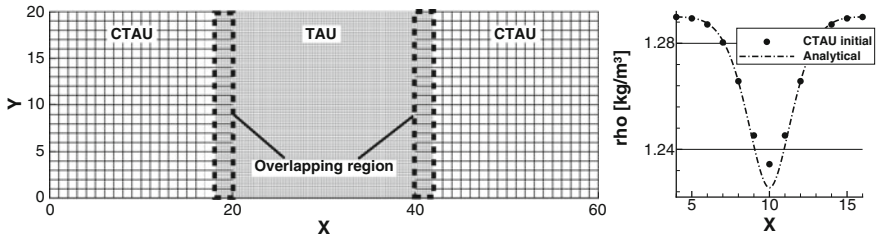

Fig. 3 *Left* Grid of vortex transport test case. *Right* Initial density distribution of vortex in CTAU grid block

At the first coupling interface the high order accurate interpolation methods are almost able to reconstruct the analytical density distribution of the vortex in the TAU grid. The density at the vortex core is about $\Delta\rho_v = 0.003\,\mathrm{kg/m^3}$ higher than the analytical minimum value. The linear interpolation results in a noticeably larger error with a difference of the minimum density of about $\Delta\rho_v = 0.008\,\mathrm{kg/m^3}$. Moreover, the bidirectional data transfer at the coupling interface causes a feedback that also disturbs the density distribution in the CTAU grid block, so that the minimum density at the vortex core is increased. This indicates the necessity of a high order accurate interpolation method for the data transfer from the coarse CTAU grid to the fine TAU grid at this coupling interface.

At the second coupling interface the density distributions in the fine TAU grid are almost similar to the first interface, which indicates a negligible numerical dissipation for the vortex convection within the fine grid. The minimum density in the CTAU grid using linear interpolation is $\Delta\rho_v = 0.008\,\mathrm{kg/m^3}$ higher compared to the initial CTAU solution (see Fig. 4), whereas using the higher order accurate interpolation methods reduce the difference of the density values to about $\Delta\rho_v = 0.002\,\mathrm{kg/m^3}$.

These differences of the minimum density at the second interface in the CTAU grid compared to the initial CTAU data resemble a similar error as the density differences between TAU data at the first coupling interface and the analytical density distribution. This indicates that the significant interpolation error occurs at the first coupling interface, where the vortex is convected from the coarse CTAU grid to the fine TAU grid. The convection of the vortex from the fine grid to the coarse grid at the second interface is less sensitive to the order of accuracy of the interpolation method.

However, using higher order accurate interpolation methods yield noticeably better results in terms of preservation of the vortex compared to linear interpolation, at which sixth order accurate interpolation shows slightly better results than fourth order accurate method.

Comparing the location of the density minimum of the different simulations to the analytical solution, the higher order accurate interpolation methods also seem to have a positive influence on dispersion properties of the flow simulation.

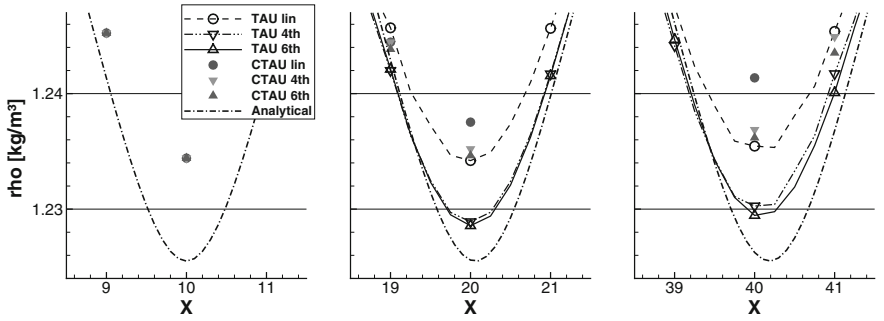

Fig. 4 Density distribution of vortex core. *Left* Analytical data and CTAU solution at initialization. *Middle* Data in grid overlap of first coupling interface. *Right* Data in grid overlap of second interface

4.2 Gust Encounter

This test case represents a gust encounter of an airfoil, where the gust is transported on coarse Cartesian grid. The unstructured grid around the airfoil extends only to a short distance upstream of the airfoil to cover as much of the flow field as possible by the Cartesian grid. The properties of the flow field are set to standard atmospheric conditions and the Mach number is $Ma = 0.3$. The '*1-cos*'-gust is initialized with a maximum vertical velocity of one fourth of the reference velocity, which results in a value of $v_g = 25.48\,\mathrm{m/s}$. During the time-accurate simulation the gust passes through the coupling region and encounters the airfoil, increasing the lift due to the increased vertical velocity.

Figure 5 on the left shows a detailed view on the coupling region in front of the airfoil and a horizontal line at which the vertical velocity of the gust is evaluated in the unstructured grid at the time the gust reaches this area. The vertical velocity distributions of simulations with coupling by linear and sixth order accurate interpolation are illustrated in Fig. 5 on the right. In the simulation using sixth order accurate interpolation the peak velocity of the gust is $\Delta v_y = 0.48\,\mathrm{m/s}$ higher than the peak value in the simulation with linear interpolation. This results in a relative difference of about 2 % in vertical velocity, but this may increase at shorter wave lengths of the gust.To examine the stability of the high order interpolation method a third simulation without gust has been performed and the vertical velocity of the undisturbed flow and the initial gust velocity is superposed at the location of the gust peak at a horizontal position of $x = -0.315$. This results in a theoretical gust velocity of $v_{y,theor.} = 27.95\,\mathrm{m/s}$, which indicates that the high order accurate interpolation method does not overpredict the values of the flow data and remains stable for this test case.

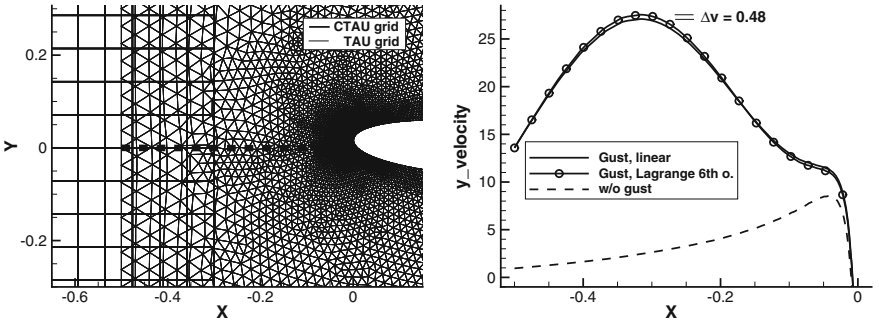

Fig. 5 *Left* Detailed view on the grid overlap at the coupling interface and velocity profile extraction line. *Right* Profile of vertical velocity at gust transport through coupling region and profile in undisturbed flow at the same time step

5 Conclusion

In the presented work the applicability of an overset grid approach has been demonstrated to couple flow solvers with discretization methods of different orders of accuracy. The encapsulated implementation of data interpolation and communication in an external coupling module was suited to realize the coupling of TAU and the Cartesian solver without effort apart from the extensions of the interpolation method. The test cases show a noticeable error for linear interpolation from the coarse CTAU grid to the fine TAU grid. Although the influence on integral coefficients might be negligible, the interpolation error might influence non-linear behavior in test cases with transonic flow. Therefore a higher order accurate interpolation should be preferred in the coupling of TAU and the Cartesian solver if the necessary size of the grid overlap can be realized.

In future work the coupling process may be extended to incorporate the flow data gradients computed by the flow solvers. This enables the use of the cubic Hermite spline interpolation without losing the compactness of the interpolation stencil by reconstructing the gradients in the coupling module, allowing for a smaller grid overlap.

Acknowledgments The development of the code coupling procedure and the implementation of the coupling module was done in the German research project FOR 1066 “Simulation des Überziehens von Tragflügeln und Triebwerksgondeln” funded by the “Deutsche Forschungsgemeinschaft DFG”.

References

1. Lele, S.K.: Compact finite difference schemes with spectral-like resolution. J. Comput. Phys. **103**, 16–42 (1992)
2. Schwamborn, D.; Gerhold, T.; Heinrich, R.: The DLR TAU-Code: recent applications in research and industry. In: Proceedings of the European Conference on Computational Fluid Dynamics (ECCOMAS CFD 2006), Delft, The Netherlands, 5–8 September 2006

3. Benek, J.; Steger, J. L.; Dougherty, F. C.: A flexible grid embedding technique with application to the Euler equations. AIAA Paper 83–1944 (1983)
4. Yang, H.., Nuernberger, D., Kersken, H.-P.: Toward excellence in turbomachinery computational fluid dynamics: a hybrid structured-unstructured Reynolds-averaged Navier-Stokes solver. J. Turbomach. Trans. ASME **128**, 390–402 (2006). Conference, Manchester, 2009
5. Spiering, F.: Coupling of TAU and TRACE for parallel accurate flow simulations. In: International Symposium "Simulation of Wing and Nacelle Stall. Braunschweig, (2012)
6. Madrane, A.; Raichle, A.; Stürmer, A.: Parallel implementation of a dynamic overset unstructured grid approach. In: ECCOMAS 2004, Jyväskylä, 24–28 July 2004

Overlapping Grids in the DLR THETA Code

Roland Kessler and Johannes Löwe

Abstract There is an increasing interest in flow simulations in configurations where parts are moving relatively to each other. A general approach to this problem is the use of overlapping grids, often called Chimera-technique. An incompressible flow solver based on a projection scheme with a fast multi-grid method for the pressure correction equation requires an implicit coupling between the grids on all levels of the multi-grid hierarchy in order to retain the good convergence properties. The efficient implementation of the overlapping grid technique in the DLR THETA code and its validation are presented in this chapter.

1 Introduction

With constantly growing compute resources the fidelity of numerical fluid simulations is also increasing. Besides the demand for higher accuracy of the physical models there is also demand for functional capabilities to simulate more complex problems. Being able to handle moving objects and boundaries is one such feature of modern CFD codes. There are different approaches to moving geometry in flow solvers based on boundary fitted grids. One possibility is to use globally conforming adapted meshes. Boundary movement then leads to mesh deformation and distortion of the mesh cells that must be addressed by updating the mesh topology or complete remeshing [8]. Another approach is to decompose the computational domain into several parts which can move independently. At the artificially introduced interior interfaces a coupling mechanism must be used to match the solutions on the individual subdomains. A method with overlapping subdomains and direct interpolation

R. Kessler (✉) · J. Löwe
German Aerospace Center (DLR), Göttingen, Germany
e-mail: roland.kessler@dlr.de

J. Löwe
e-mail: johannes.loewe@dlr.de

A. Dillmann et al. (eds.), *New Results in Numerical and Experimental Fluid Mechanics IX*,
Notes on Numerical Fluid Mechanics and Multidisciplinary Design 124,
DOI: 10.1007/978-3-319-03158-3_43,

for the coupling is often termed overset-grid method or Chimera-technique in the literature [10, 11].

The Chimera-technique addresses not only moving boundaries but can also be used to replace parts of a given grid. This can be used to locally change the shape of objects or add structural parts to objects and examine the impact onto the flow, which has the advantage that the effect due to remeshing can be minimized. Furthermore special grid types (e.g. structured hexahedral blocks) or grid parts that move with the mean fluid velocity can be employed to increase the numerical accuracy and reduce numerical dissipation and dispersion.

The Chimera-technique we use is based on the method described in [1], where it is applied to a block-structured compressible Euler-flow solver. At the German Aerospace Center (DLR) the technique was integrated into the block-structured and unstructured CFD codes for compressible flows FLOWer and TAU [2, 5]. In the literature one can also find applications of the Chimera-technique to projection methods for viscous incompressible flow on unstructured grids [9, 11]. Details of the efficient implementation in combination with a multi-grid method are not presented in these papers, where explicit iteration schemes like the additive Schwarz method are used.

2 The Numerical Method

We intend to solve the incompressible Navier-Stokes equations with variable density in conservative form (here without external forces):

$$\partial_t(\rho u) + \nabla \cdot F(\rho, u) + \nabla p = 0 \tag{1}$$

$$\partial_t \rho + \nabla \cdot (\rho u) = 0 \tag{2}$$

The velocity field u and pressure p are treated as unknown while the density ρ is considered to be known and independent of the pressure. For constant density ρ or more generally $\frac{D\rho}{Dt} = 0$ the continuity equation (2) simplifies to the incompressibility condition

$$\nabla \cdot u = 0. \tag{3}$$

The convective and diffusive fluxes F are discretized with a cell-centered Finite-Volume method on the dual topology of hybrid unstructured grids. The primal grids can contain mixed elements (tetrahedra, prisms, pyramids and hexahedra) and often feature anisotropic structured layers near solid walls. A face based representation is used to store the dual grid topology and a geometric agglomeration is performed on the dual grid to construct successively coarser grids for a multi-grid hierarchy. First and second order upwind and central schemes are available for the convective fluxes.

In the next step we apply a time discretization scheme to Eq. (1) and introduce defect equations for the velocity and pressure at time $t_{n+1} = t_n + \tau_n$ (besides the implicit Euler scheme presented here, there are also second order BDF and

Crank-Nicolson schemes available in the DLR THETA code):

$$\frac{\rho_{n+1}u_* - \rho_n u_n}{\tau_n} - \nabla \cdot F_n(\rho_{n+1}, u_*) + \nabla p_n = 0, \tag{4}$$

$$p_{n+1} = p_n + \delta p_{n+1}, \qquad u_{n+1} = u_* - \frac{\tau_n}{\rho_{n+1}} \nabla \delta p_{n+1}. \tag{5}$$

Here F_n is a linearization of F with known data from the last time-step n and u_* is an intermediate velocity that does not fulfill the continuity equation (2). Inserting the defect equations (5) into (2) and applying the divergence operator leads to the pressure correction equation

$$\nabla \cdot \nabla \delta p_{n+1} = \nabla \cdot \frac{1}{\tau_n} \left[\rho_{n+1} u_* + \frac{\rho_{n+1} - \rho_n}{\tau_n} \right]. \tag{6}$$

The linear equations (4) and (6) for the intermediate velocity u_* and pressure defect δp_{n+1} can be solved with iterative methods. For the momentum equation (4) we use the preconditioned BiCGStab method and for the elliptic pressure correction Eq. (6) a geometric multi-grid method with Jacobi-smoothing and again BiCGStab as the coarse grid solver is employed. These methods are implemented in a matrix-free way based on the matrix-vector-product operator and are parallelized using MPI.

2.1 Basic Chimera-Components

We can decompose the Chimera-method into several independent parts. The grid must be split into multiple *blocks* and a motion description hierarchy is created that describes their motion relative to each other. We restrict the motion of individual grid blocks to rigid transformations (translations and rotations). With this information the interpolation point coordinates can be transformed from one local coordinate system to another and all other motion-relevant data can be computed.

The next step is to select grid points at the non-physical interior boundaries that should be interpolated during the computation. The selection criterion depends on the spatial (and temporal) discretization scheme used. At least all points with incomplete stencil for the flux (and time derivative) computations must be interpolated. This typically leads to one or more layers of interpolation points, also called *fringe* points. The region of overlap must be large enough, such that elements from different blocks containing fringe points do not overlap. This ensures that variables used for interpolation are not itself interpolated.

The interpolation itself is split in three phases. Before the simulation starts a binary search tree with axis-aligned bounding boxes of all elements from the primal grid is constructed for each grid block. These trees are fixed during the simulation because they use the block local coordinate systems that do not change. Then for each physical time-step we compute the interpolation coefficients for all fringe points.

This is done by searching for every fringe point in the binary search trees of the other blocks for possible *donor elements* and performing a Newton-iteration to solve for the barycentric coordinates of the fringe point within the candidate elements. If the barycentric coordinates fall inside a candidate element, it is accepted as the donor and the interpolation coefficients are stored for later use. On coarse grids from the multi-grid hierarchy (where no primal grids are available) we interpolate the prolongation of the coarse grid variable to the finest grid. The interpolation residuals can later be evaluated efficiently many times per physical time-step. For the interpolation of vector quantities like the velocity field the change of coordinate system from one block to another must also be considered.

2.2 Integration of the Chimera-technique into the Flow Solver

Formulating the incompressible Navier-Stokes equations on a rigidly moving domain introduces two additional terms into Eq. (1). One term corresponds to convective transport and the other is a Coriolis force because we no longer operate in an inertial coordinate system (if rotational movement is present). These terms must be implemented into the existing flux-kernels according to the spatial discretization. The convective term based on the grid velocity should be locally mass conserving, otherwise large counteracting pressure fluctuation might accumulate.

Changing the systems of linear equations to include the Chimera-interpolation residuals requires two steps. First, we must replace all incorrectly computed fluxes (due to incomplete discretization stencils) in the matrix-vector-product operator with the interpolation residuals, which we define as the difference between the variable value at a fringe point and the interpolated value. Second, the right hand sides of the equations must be adjusted. For the intermediate velocity u_* the fringe point value should equal the interpolated value, so we set the corresponding entries to zero. For the pressure defect equation we construct right hand side values at the fringe points such that the updated pressure p_{n+1} (and not the pressure correction δp_{n+1}) satisfies the interpolation condition. The interpolation is then strongly included in the systems of linear equations and is automatically resolved when solving the equations. This approach does not introduce an additional iterative procedure to establish the interpolation conditions as for example the additive Schwarz method does.

When applying a multi-grid method to the pressure correction equation, it is important to account for the interpolation on all grid levels. Otherwise the progress of the method on the coarser levels is wasted, because it is not coupled to the other blocks. In this case the convergence reduces almost to that of the multi-grid smoother that is used on the finest grid, where the interpolation is considered.

Another important property is global mass conservation. The mass conservation is disturbed by non-conservative barycentric interpolation. There are attempts to improve the conservation properties by mass-flux based interpolation [10], but we observed that this is not neccessary. However, it is important to ensure that the right hand side of the pressure equation is in the image of the laplace operator. If this is

not already the case, we add a constant to the right hand side of (6) such that its mean value is zero. The constant is a measure for the global mass imbalance caused by non-conservative interpolation at the Chimera-boundaries. It can be reduced by increasing the numerical resolution in the overlapping regions.

3 Numerical Results

3.1 Two Dimensional Flow Around a Cylinder

The first type of problem we will consider is the flow around a circular cylinder with diameter $D = 1$, placed at the coordinate origin. The computational domain is $[-10, 20] \times [-10, 10]$ with constant inflow at $x = -10$ and symmetry boundary conditions at $y = \pm 10$. For the multi-block grid we use two blocks which overlap in a circular ring with inner radius 2.0 and outer radius 2.45 around the cylinder. The Reynolds-number $Re = \frac{UD}{\nu}$ is based on the cylinder diameter D and the constant inflow velocity U. Due to the rotational symmetry of the cylinder the following multi-block computations can be validated against single-block computations. For comparison between the single- and multi-block solutions and results from the literature we use the drag and lift coefficients C_d, C_l and for periodic solutions in time also the Strouhal-number St given by

$$C_\mathrm{d} = \frac{2F_x}{\rho U^2 D}, \qquad C_\mathrm{l} = \frac{2F_y}{\rho U^2 D} \quad \text{and} \quad St = \frac{fD}{U}, \tag{7}$$

where F_x and F_y are the horizontal and vertical components of the force acting on the surface of the cylinder and f is the vortex shedding frequency.

The computational domains are discretized with triangular and quadrilateral elements. The maximum edge length is 1.25 and quadrilaterals are only used in 4 layers around the cylinder with a surface mesh size of 0.025 and an initial layer thickness of 0.01. Furthermore the maximum edge length in the wake region of the cylinder is limited to 0.125. The overlap region is resolved with approximately 6 elements in radial direction. On these grids the Chimera-computation is about 30 % more expensive compared to the single block computation.

Non-rotating Circular Cylinder. We start with the presentation of the results for the non-rotating cylinder at Reynolds-numbers $Re = 100$ and $Re = 200$. The geometry and initial conditions are perfectly symmetric about the x-axis. But at these Reynolds numbers even the small truncation errors of finite precision arithmetics trigger unsteady vortex shedding behind the cylinder and lead to the formation of a von Kármán vortex street. This is a non-trivial test for the Chimera-implementation because the detached vortices travel across the Chimera-interfaces. Computations were done with a non-dimensional time-step size of $\tau = \frac{1}{256}$ (CFL ≈ 0.2) and central schemes were used for all fluxes.

Table 1 Drag and lift coefficients and Strouhal-number for a flow over a circular cylinder at $Re = 100$ and $Re = 200$

$\omega = 0$	$Re = 100$			$Re = 200$		
	C_d	C_l	St	C_d	C_l	St
Present: single block	1.39 ± 0.01	± 0.36	0.170	1.37 ± 0.05	± 0.72	0.200
Present: multi block	1.39 ± 0.01	± 0.36	0.169	1.38 ± 0.05	± 0.73	0.198
Zhang et al. [11]	1.36 ± 0.01	± 0.34	0.168	1.34 ± 0.03	± 0.66	0.197
Liu et al. [4]	1.36 ± 0.01	± 0.34	0.164	–	–	–
Pan and Damodaran [9]	–	–	–	1.37 ± 0.04	± 0.63	0.192

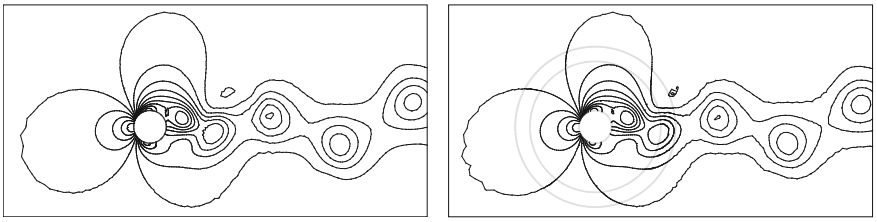

Fig. 1 Comparison of pressure isolines between single- and multi-block solutions for $\omega = 0$, $Re = 200$ when C_l is maximal (identical view and isoline spacing)

Average drag and lift coefficients together with the amplitude of their oscillation and the Strouhal-number are printed in Table 1. The difference between the single- and multi-block solutions is less than 1 %. The drag and especially the lift coefficient are predicted to be larger than the reference values from the literature (by up to 10 % for the lift coefficient at $Re = 200$).

Figure 1 shows a comparison of pressure isolines between the single- and multi-block solutions for $Re = 200$ at a discrete time step when C_l is maximal. The agreement between both solutions is very good, even downstream after the vortices crossed the Chimera-interfaces. For the multi-block solution we can observe a nice matching of the isolines in the overlap region (where two solutions were computed) and a smooth transition over the Chimera-interfaces (indicated by two circles).

Rotating Circular Cylinder. For Reynolds-number $Re = 200$ we now consider two cases with rotating cylinders at angular velocities $\omega = \pi$ and $\omega = 4$. At low tip velocity ratios $q = D\omega/2U$ the flow is periodic as in the non-rotating case. At higher values of q ($1.91 \leq q \leq 4.35$) the solution is known to be steady [7]. The two cases we consider fall into these two ranges ($q = 1.57$ and $q = 2$). In the second case the convergence to steady state is very slow, as observed in other publications [7, 11]. We compare our results for drag and lift coefficients and the Strouhal-number with values from the literature in Table 2.

The quality of the multi-block solutions show a stronger dependence on the time-step size than in the previous cases. This is caused by larger temporal splitting errors of the projection scheme. Even in the second case with $\omega = 4$ that has a stationary

Table 2 Drag and lift coefficients and Strouhal-number for a flow over a circular cylinder rotating counterclockwise at $Re = 200$ with $\omega = \pi$ and $\omega = 4$

$Re = 200$	$\omega = \pi$			$\omega = 4$	
	C_d	C_l	St	C_d	C_l
Present: single block	0.79 ± 0.25	-4.09 ± 0.66	0.191	0.34	-5.34
Present: multi block	0.83 ± 0.30	-4.20 ± 0.88	0.182	0.37	-5.61
Zhang et al. [11]	0.77	-3.98	0.191	0.39	-5.26
Maruoka [6]	0.84	-4.11	0.191	–	–
Mittal and Kumar [7]	–	–	–	0.31	-5.29

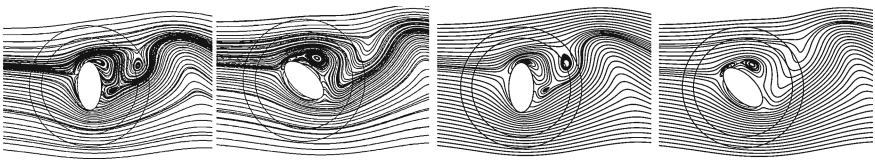

Fig. 2 Streamlines of flow around a rotating elliptical cylinder with aspect ratio 2 at $Re = 200$ and $\omega = \pi/2$ (*left* from Ref. [11], *right* present)

solution (in an inertial coordinate system) the computed solution is time-dependent in the moving coordinate system of the rotating grid block containing the cylinder.

Rotating Elliptical Cylinder. The following example shares the basic properties of the previous one, but the obstacle now is an rotating ellipse with major and minor radius of 1 and 0.5 respectively. This test case exhibits no rotational symmetry on the moving block which precludes a comparison with single block solutions. Figure 2 shows a comparison of streamlines for $Re = 200$ and $\omega = \pi/2$ with results from Ref. [11]. Drag and lift coefficients (not shown) are also in good agreement with aforementioned results.

3.2 Rotating Fan with Stationary Guiding Vanes

After the academic test cases in the previous section we will now report on a more industrial relevant case of a rotating 5-blade axial fan in a pipe with 300 mm diameter with stationary guiding vanes behind the fan (see Fig. 3). The configuration shown has a gap size of 1.5 mm between the blades and the pipe wall, a volume flux of 1,380 cfm and rotational speed of 3,000 rpm. Simulations were done on grids with 6 to 31 million grid points and on up to 144 processor cores. The parallel efficiency of the code including all Chimera-functions was about 70 % for the largest core count and the total CPU time for all Chimera-functions was less than 4 %.

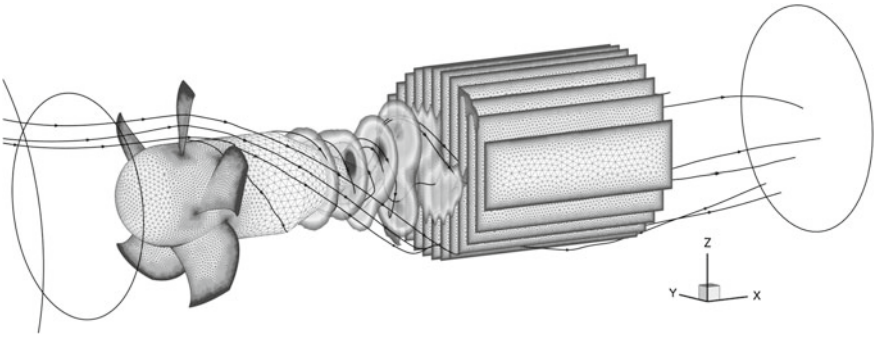

Fig. 3 Surface grids of a rotating fan in a pipe with stationary guiding vanes, streamlines and slices with pressure contours

4 Summary

We presented the implementation of the Chimera-technique in the incompressible DLR THETA code and highlighted some critical aspects of the implementation for incompressible flow solvers based on projection schemes. Numerical experiments were conducted to validate the method and demonstrate its applicability to industrial sized problems.

Acknowledgments This work was partially supported by the Forschungsvereinigung für Luft- und Trocknungstechnik e.V. (FLT). Furthermore we want to thank Dr. Markus Lambert for the preparation of the implementation of the Chimera-technique in the DLR THETA code.

References

1. Benek, J.A., Steger, J.L., Dougherly, F.C.: A flexible grid embedding technique with application to the Euler equations. AIAA paper 83–1944 (1983)
2. Heinrich, R., Kalitzin, N.: Numerical simulation of three-dimensional flows using the chimera-technique. In: New Results in Numerical and Experimental Fluid Mechanics II, volume 72 of Notes on Numerical Fluid Mechanics and Multidisciplinary Design, pp. 226–233. Springer, Berlin (1999)
3. Kessler, R., R*ü*tten, M., Pennecot, J.: Simulation of the flow in a human nose. In: New Results in Numerical and Experimental Fluid Mechanics VII, volume 112 of Notes on Numerical Fluid Mechanics and Multidisciplinary Design, pp. 521–528. Springer, Berlin (2010)
4. Liu, C., Zheng, X., Sung, C.H.: Preconditioned multigrid methods for unsteady incompressible flows. J. Comput. Phy. **139**(1), 35–57 (1998)
5. Madrane, A., Heinrich, R., Gerhold, T.: Implementation of the chimera method in the unstructured hybrid DLR finite volume TAU-Code. In: 6th Overset Grid Symposium, Ft. Walton Beach, 8–10 October 2002
6. Maruoka, A.: Finite element analysis for flow around a rotating body using chimera method. Int. J. Comput. Fluid Dyn. **17**(4), 289–297 (2003)
7. Mittal, S., Kumar, B.: Flow past a rotating cylinder. J. Fluid Mech. **476**, 303–334 (2003)

8. Muñoz, D.J., Springel, V., Marcus, R., Vogelsberger, M., Hernquist, L.: Multi-dimensional compressible viscous on a moving voronoi mesh. MNRAS, submitted 2012. http://arxiv.org/abs/1203.1037
9. Pan, H., Damodaran, M.: Parallel computation of viscous incompressible flows using Godunov-projection method on overlapping grids. Int. J. Numer. Methods Fluids **39**, 441–463 (2002)
10. Tang, H.S., Jones, S.C., Sotiropoulos, F.: An overset-grid method for 3D unsteady incompressible flows. J. Comp. Phy. **191**(2), 567–600 (2003)
11. Zhang, X., Ni, S., He, G.: A pressure-correction method and its applications on an unstructured Chimera grid. Comput. Fluids **37**(8), 993–1010 (2008)

Detached Eddy Simulation Using the Discontinuous Galerkin Method

Michael Wurst, Manuel Keßler and Ewald Krämer

Abstract In the present paper the Discontinuous Galerkin (DG) method is applied for the discretisation of the Reynolds-Averaged Navier-Stokes (RANS) equations. Turbulence modelling is done with the Detached eddy simulation (DES) model based on the Spalart-Allmaras (SA) turbulence equation. In this method a turbulent length-scale based on the cell width of the mesh is used for the filter width of the large eddy simulation (LES) region. As DG employs higher-order polynomial basis functions inside a cell an adaptation of the "cell width definition" is needed so that the turbulent viscosity is not too high in the LES region of the simulation. Hence, the cell width is adapted with the polynomial degree of the employed basis functions. Simulations of a backward facing step as well as a circular cylinder show that the adaptation is successful.

1 Introduction

There is a growing interest in higher-order methods used for CFD calculations at the moment. These methods tend to be more accurate than the standard second-order finite volume (FV) methods and it is expected that they can better predict many phenomena, either with complex physics (e.g. stall of an airfoil) or where a good vortex transport is needed (e.g. blade vortex interaction at helicopter rotors). One of the most promising methods in the context of higher-order methods is the

M. Wurst (✉) · M. Keßler · E. Krämer
Institut für Aerodynamik und Gasdynamik, Universität Stuttgart, Pfaffenwaldring 21, 70569 Stuttgart, Germany
e-mail: michael.wurst@uni-stuttgart.de

M. Keßler
e-mail: manuel.kessler@uni-stuttgart.de

E. Krämer
e-mail: ewald.kraemer@uni-stuttgart.de

A. Dillmann et al. (eds.), *New Results in Numerical and Experimental Fluid Mechanics IX*, Notes on Numerical Fluid Mechanics and Multidisciplinary Design 124,
DOI: 10.1007/978-3-319-03158-3_44,

Discontinuous Galerkin method first introduced in [1] for hyperbolic equations. It is a finite element approach with polynomial basis functions for the representation of the solution inside the cell. Furthermore, it is basically a local method which can be applied for different kinds of elements. The connection to the neighboring cells is low and no reconstruction of the flow quantities across cells has to be applied to achieve the high-order accuracy. The connection between cells is only given by the defintion of unique fluxes (as the flow variables are not unique at element faces) between them, which is usually done by Riemann solvers—as in FV codes—for inviscid fluxes and by averaging the viscous fluxes as done in [2]. As a consequence, DG methods scale very good on modern high-performance architectures [3]. First DES results using the DG method were presented by Lübon et al. [4]. Based on these results turbulence modelling was extended here by the Delayed DES (DDES) method and the higher-order representation of the solution inside a cell is considered in the calculation of the turbulent lengthscale.

2 The Discontinuous Galerkin Method for the RANS Equations

2.1 Governing Equations

In this section the Discontinuous Galerkin scheme for the discretisation of the RANS equations as employed in our solver SUNWinT [5] is described. The RANS equations using the Spalart-Allmaras (SA) turbulence [6] equation are given as

$$\frac{\partial U}{\partial t} + \nabla \cdot F_{inv}(U) - \nabla \cdot F_{vis}(U, \nabla U) = S(U, \nabla U). \tag{1}$$

The vector U is the vector of the conservative variables, $F_{inv} = (F^x_{inv}, F^y_{inv}, F^z_{inv})$ and $F_{vis} = (F^x_{vis}, F^y_{vis}, F^z_{vis})$ are the vectors of the inviscid and viscous fluxes:

$$U = \begin{pmatrix} \rho \\ \rho u_i \\ \rho E \\ \rho\tilde{\nu} \end{pmatrix}, F^j_{inv} = \begin{pmatrix} \rho u_j \\ \rho u_i u_j + p\delta_{ij} \\ u_j(\rho E + p) \\ \rho\tilde{\nu} u_j \end{pmatrix}, F^j_{vis} = \begin{pmatrix} 0 \\ \tau_{ij} \\ \tau_{ji} u_i + q_j \\ \frac{1}{\sigma}(\mu_t + \rho\tilde{\nu})\frac{\partial\tilde{\nu}}{\partial x_j} \end{pmatrix}, \tag{2}$$

where ρ is the fluid density, (u_1, u_2, u_3) the velocity vector, $\tilde{\nu}$ a viscosity like variable, p the pressure and E the specific total energy. The pressure p and the specific energy E are connected via the equation of state for an ideal gas

$$p = (\gamma - 1)(\rho E - \frac{1}{2}(u_1^2 + u_2^2 + u_3^2)), \tag{3}$$

where $\gamma = \frac{c_p}{c_v} = 1.4$ is the ratio of specific heats. The viscous stress tensor τ_{ij} and the heat flux q_j include both contributions from the Reynolds averaging via a turbulent eddy viscosity μ_t and a turbulent thermal conductivity λ_t:

$$\tau_{ij} = (\mu + \mu_t)\left(\frac{\partial u_i}{\partial x_j} + \frac{\partial u_j}{\partial x_i} - \frac{2}{3}\frac{\partial u_k}{\partial x_k}\delta_{ij}\right) - \frac{2}{3}\delta_{ij}\rho k, \tag{4}$$

$$q_j = -(\lambda + \lambda_t)\frac{\partial T}{\partial x_j}\,. \tag{5}$$

The turbulent eddy viscosity is determined from the SA-model as

$$\mu_t = \rho\tilde{\nu} f_{v1} \tag{6}$$

with a calibration function f_{v1}. The source term S in Eq. (1) is only present in the SA equation and serves as a term to model turbulent production and destruction in the RANS equations:

$$\begin{aligned} S = {} & \frac{1}{\sigma}\rho c_{b2}\frac{\partial\tilde{\nu}}{\partial x_i}\frac{\partial\tilde{\nu}}{\partial x_i} + c_{b1}(1 - f_{t2})\rho\tilde{S}\tilde{\nu} \\ & - \left(c_{w1} f_w - \frac{c_{b1}}{\kappa^2} f_{t2}\right)\frac{1}{\rho}\left(\frac{\rho\tilde{\nu}}{d}\right)^2 + \rho f_{t1}\Delta U^2. \end{aligned} \tag{7}$$

In the source term the distance to the wall d is a decisive part to model the production and destruction.

2.2 Discontinuous Galerkin Formulation

Equation (1) constitutes the strong form of the RANS equations. A weak variational formulation is derived by multiplying it with a test function V, integrating over the computational domain Ω and integrating by parts:

$$\begin{aligned} & \int_\Omega V\frac{\partial U}{\partial t}d\Omega - \int_\Omega \nabla V \cdot F_{inv}(U)d\Omega + \int_{\partial\Omega} V F_{inv}(U)\cdot n\, d\sigma \\ & + \int_\Omega \nabla V \cdot F_{vis}(U,\nabla U)d\Omega - \int_{\partial\Omega} V F_{vis}(U,\nabla U)\cdot n\, d\sigma = \int_\Omega V S(U,\nabla U). \end{aligned} \tag{8}$$

The computational domain is subdivided in to non-overlapping elements and within each element the solution U_h and the test function V_h is approximated by linear combination of n_{dof} basis function ϕ_k:

$$U_h = \sum_{k=1}^{n_{dof}} U_k(t)\phi_k(x), \quad V_h = \sum_{k=1}^{n_{dof}} V_k\phi_k(x) \tag{9}$$

We employ hierarchical and orthogonal basis functions. For the inviscid fluxes $F_{inv} \cdot n$ in the surface integral we use an approximate HLL-Riemann solver [7] to define a unique flux at the boundary between elements. The viscous fluxes depend not only on the conservative variables but also on their gradients. They are computed by solving an additional equation for the gradients [2]

$$\Theta - \nabla U = 0 \tag{10}$$

with the same Discontinuous Galerkin method and then inserting the solution Θ in the viscous fluxes.

3 Turbulence Modelling with the Detached Eddy Simulation Model

The SA turblence model can be employed as Detached Eddy Simulation (DES) [8] model by replacing the distance to the wall d by

$$l_{DES} = \min(d, C_{DES}\Delta). \tag{11}$$

Here Δ is a measure of the grid spacing (longest cell edge) and $C_{DES} = 0.65$ a constant to calibrate the model in order to operate the model in RANS mode close to the wall and in LES mode away from the wall. A disadvantage of the method is cleary that the model depends on the applied mesh, e.g. it can happen that the change from the RANS to the LES model is too early in the boundary layer. Hence, the model is not able to resolve the necessary scales of an LES. At worst, this can lead to a low turbulent viscosity and low Reynolds stresses in the boundary layer and in succession to a grid-induced separation. A possible improvement is the use of the DDES model [9], which also includes information about the flow field in the calculation of the turbulent lengthscale:

$$l_{DDES} = d - f_d \max(0, d - C_{DES}\Delta) \tag{12}$$

with

$$f_d = 1 - \tanh([8r_d]^3) \tag{13}$$

and

$$r_d = \frac{\nu_t + \nu}{\sqrt{u_{i,j}u_{i,j}}\kappa^2 d^2}\,. \tag{14}$$

Both DES models were developed for the simulation with second-order FV methods. As the DG method is normally used as a higher-order method using polynomial basis functions of order p > 1, this higher resolution inside a cell should be represented in a SA based DES model. Thus, the adaptation of the cell width Δ with the polynomial degree p seems a possible solution

$$\Delta := \frac{\text{cell width } \Delta}{\text{polynomial degree } p} . \tag{15}$$

The division by the polynomial degree p leads to a decrease of the effective cell width Δ from a polynomial degree of 2 on. That means, if $p = 1$ we still have the original DES model which is adjusted for FV methods.

4 Results

4.1 Backward Facing Step

The simulation of a backward-facing step at Re = 28,000 is used for the comparison of the DES and DDES model and as a test for the adaptation of the lengthscale with the polynomial degree. The simulation is based on the experiment by Eaton and Vogel [10], numerical reference data is available in Spalart et al. [9]. A key property for the correct simulation of this kind of simulation is the definition of an inlet profile to achieve a correct boundary layer thickness close to the step. For that reason an inlet profile based on a power-law is imposed at the domain inlet. The spanwise width of the domain is two step heights (including 20 cells) employing periodic boundary conditions. The mesh for the simulation consist of only 1,41,000 hexahedral cells, probably too small for a simulation with a FV method. As the simulation is carried out with 4th-order accurate elements consisting of 20° of freedoms (DOFs) per element, the simulation corresponds to a FV simulation with 3.82 Mio cells. However, by adjusting the cell width with the polynomial degree, it could be made sure to not achieve too high turbulent viscosity values in the LES area of the DES simulation. In Fig. 1a and b the mean friction coefficient at the lower wall behind the step is plotted in comparison to the experimental and numerical reference data. Temporal averaging was done for a period of seven flow through periods of the domain behind the step and after that the flow was also averaged in spanwise direction. It can be clearly seen that the adaptation of the cell width is successful in this case. There is some difference to the reference data, which may be due to different inlet conditions. Spalart et al. give no details about their inlet velocity profile, but results have been found to be sensitive to the given profile.

In Fig. 2a the λ_2 vortex criterion is used for the identification of the vorticies behind the step. Directly behind the step, the free shear layer begins to roll up to form essentially two dimensional vortices. After about 1 step height these vortices

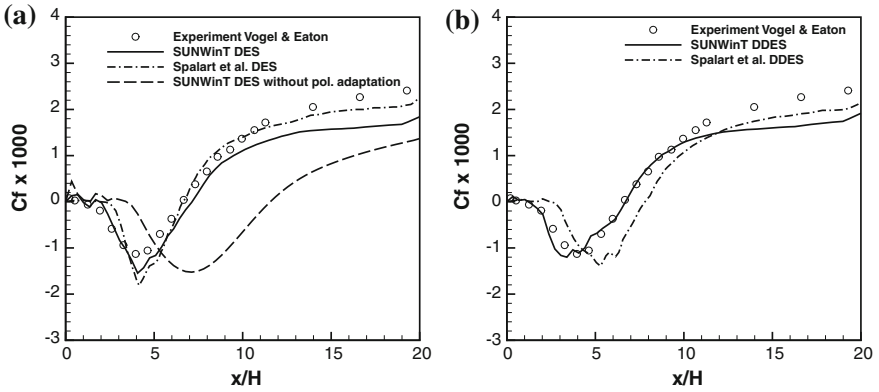

Fig. 1 Mean friction coefficient at the lower wall behind the step employing the **a** DES **b** DDES model

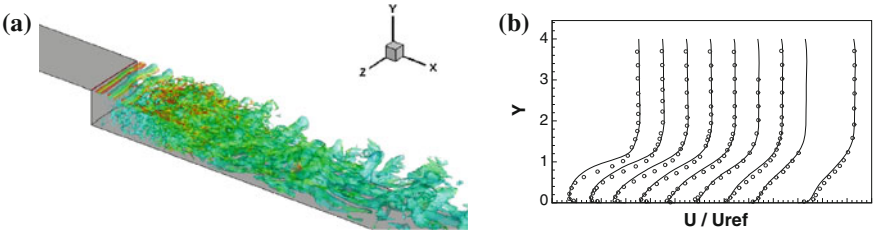

Fig. 2 **a** $\lambda_2 = -0.01$ colored with vorticity magnitude and **b** velocity profiles behind the step for the DES calculation

burst and the flow becomes three-dimensional. In the experiment the flow reattaches at 6.7 step heights behind the step. Here, the flow reattaches at 7.3 h in the DES case and at 6.8 h in the DDES case. Velocity profiles presented in Fig. 2b also show a good agreement with the experiments with only small deviations in the upper part of the profiles.

4.2 Circular Cylinder

As a second test case for the valdiation of the DES model the simulation of a circular cylinder at Re $= 1.4 \cdot 10^5$ is performed. This kind of simulation was also done by Travin et al. [11], experiments with different Reynolds numbers are also presented in [12, 13]. The mesh for the cylinder is an O-grid with a total number of 1,32,000 cells. The depth of the cylinder is two cylinder diameters (including 20 cells) with periodic boundary conditions applied in spanwise direction. As before, the RANS, DES and DDES simulations were performed with 4th-order accurate elements and adaptation

Table 1 Drag coefficient C_d, lift coefficient rms C_l', Strouhalnumber St and separation angle Θ

Model	C_d	C_l'	St	Θ
RANS	0.53	0.09	0.25	103°
DES	0.54	0.04	0.32	103°
DDES	0.54	0.05	0.32	103°
RANS Travin et al.	0.56	–	–	–
DES Travin et al.	0.59	0.06	0.31	99°

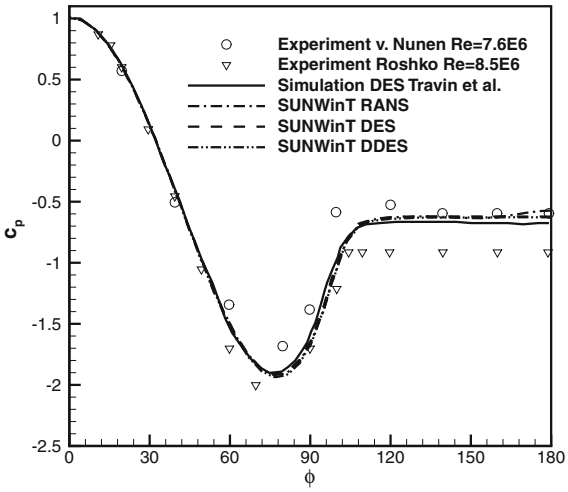

Fig. 3 Mean pressure coefficient at the upper side of the circular cylinder

of the effective cell width was applied in all simulations. Temporal averaging was performed for 70 convective times after start-up transients disappeared. Integral force values, the Strouhal number and the separation angle are presented in Table 1. In general, they agree well with the results of Travin et al.. The RANS results are comparable to DES results in drag, however, they show a higher value in the lift coefficient rms resulting in a lower shedding frequency. Almost no differences are present in the DES and DDES. This is more or less what was expected. DDES was designed to have little impact on the separated evolving shear layer in the wake of the cylinder (compare [9]). Compared to the reference data, there are slight differences in drag and lift coefficient. These are also present in the mean pressure coefficient at the upper side of the cylinder shown in Fig. 3, especially on the backside of the cylinder. A reason for that may be the different meshes used in both simulations. While here a simple O-grid was used, the mesh in the reference is finer in the wake of the cylinder.

5 Conclusion

We used the DG method for the the discretisation of the RANS equations. For turbulence modelling the DES and DDES approach based on the SA turbulence model is applied. As the DG method employs a higher-order polynomial basis function inside the cell, cell sizes are usually larger than in classical FV methods for a given accuracy. Therefore the lengthscale in the DES method is adapted with the polynomial degree of the basis function. Calculations of a backward facing step and a circular cylinder show that this approach was able to model the physical behaviour correctly. However, further studies will have to analyse the influence of the polynomial degree in conjunction with the element size inside the LES region in more detail. Afterwards a DES simulation of a spanwise extruded airfoils with a small trailing edge device defined in the LuFo3-Project FREQUENZ will be carried out and also analysed acoustically.

References

1. Reed, W., Hill, T.: Triangular mesh methods for the neutron transport equation. Technical report, Los Alamos Scientific Laboratory (1973)
2. Bassi, F., Rebay, S.: A high-order accurate discontinuous finite element method for the numerical solution of the compressible Navier-Stokes equations. J. Comput. Phys. **131**, 267–279 (1997)
3. Busch, E., Wurst, M., Keßler, M., Krämer, E.: Computational aeroacoustics with higher-order methods. In: High Performance Computing in Science and Engineering, accepted. Springer (2012)
4. Lübon, C., Kessler, M., Wagner, S.: Turbulence modeling and detached eddy simulation with a high-order unstructured discontinuous Galerkin code. In: Dillmann, A., Heller, G., Klaas, M., Kreplin, H.P., Nitsche, W., Schröder, W. (eds.) New Results in Numerical and Experimental Fluid Mechanics VII, Notes on Numerical Fluid Mechanics and Multidisciplinary Design, vol. 112, pp. 143–150. Springer, Berlin (2010)
5. Landmann, B.: A parallel discontinuous Galerkin code for the Navier-Stokes and Reynolds-averaged Navier-Stokes equations. Ph.D. thesis, Universität Stuttgart (2008)
6. Spalart, P., Allmaras, S.: A one-equation turbulence model for aerodynamic flows. La Rech. Aerospatiale **1**, 5–21 (1994)
7. Harten, A., Lax, P., Leer, B.: On upstream differencing and Godunov-type schemes for hyperbolic conservation laws. SIAM Rev. **25**(1), 35–61 (1983)
8. Spalart, P., Jou, W.H., Strelets, M., Allmaras, S.: Comments on the feasability of LES for wings, and on a hybrid RANS/LES approach. In: Advances in DNS/LES (1997)
9. Spalart, P., Deck, S., Shur, M., Squires, K., Strelets, M., Travin, A.: A new version of detached-eddy simulation, resistant to ambiguous grid densities. Theor. Comput. Fluid Dyn. **20**(3), 181–195 (2006)
10. Vogel, J., Eaton, J.: Combined heat transfer and fluid dynamic measurements downstreams of a backward facing step. J. Heat Transf. **107**, 922–929 (1985)
11. Travin, A., Shur, M., Strelets, M., Spalart, P.: Detached eddy simulations past a circular cylinder. Flow Turbul. Combust. **63**, 293–313 (2000)
12. van Nunen, J.: Pressure and florces on a circular cylinder in a cross flow at high Reynolds numbers. In: Naudascher, E. (ed.) Flow Induced Structural Vibrations, pp. 748–754. Springer, Berlin (1974)
13. Roshko, A.: Experiments on the flow past a circular cylinder at very high Reynolds number. J. Fluid Mech. **10**, 345–356 (1961)

Application of Point and Line Implicit Preconditioning Techniques to Unsteady Flow Simulations

Dian Li and Stefan Langer

Abstract To improve the efficiency for unsteady flow simulations a modification of a family of preconditioners known for steady state simulations is investigated when applied to unsteady flow simulations. The modification applied to specific—namely point and line implicit preconditioners—is implemented into an existing CFD code. For high Reynolds number turbulent flows the gain with respect to efficiency of the preconditioned methods will be demonstrated when compared with the classical solution methods, explicit Runge-Kutta with local time-stepping and matrix free LU-SGS.

1 Introduction

Because of increasing computational power unsteady simulations for high Reynolds number viscous flows reach a higher level of interest in Computational Fluid Dynamics (CFD). Unfortunately, in many existing CFD codes the simulation of such problems is still a very time consuming exercise. This is often due to the fact that the lack of reliability and efficiency which can often be observed already for the steady state solution procedures plays the role as a multiplicator in unsteady simulations. If for example for some high Reynolds number viscous flow an explicit Runge-Kutta method accelerated by local time-stepping [1] already shows a significant deterioration in the convergence rate it can not be assumed that this is an acceptable

D. Li (✉)
German Aerospace Center, Member of the Helmholtz Association, Institute of Aerodynamics and Flow Technology, Lilienthalplatz 7, 38108 Braunschweig, Germany
e-mail: dian.li@dlr.de

S. Langer
German Aerospace Center, Member of the Helmholtz Association, Institute of Aerodynamics and Flow Technology, Lilienthalplatz 7, 38108 Braunschweig, Germany
e-mail: stefan.langer@dlr.de

A. Dillmann et al. (eds.), *New Results in Numerical and Experimental Fluid Mechanics IX*, Notes on Numerical Fluid Mechanics and Multidisciplinary Design 124,
DOI: 10.1007/978-3-319-03158-3_45,

solution method for an associated unsteady flow problem. A heuristic explanation is the following: To solve the arising inner nonlinear systems the original steady state solver is used. Since due to the physical time step and the good initial guess the inner nonlinear systems are directly iterated in the asymptotic region, often no significant residual reduction can be observed and the update of the variables is questionable.

Within CFD codes it is often established to find some easy way to use the steady state solver for an unsteady simulation. This is often achieved by multistep time marching methods. These methods are well known and in CFD codes these methods have been established under the so-called dual time stepping synonym [2]. Here the unsteady residual is used in the steady state solver to find an approximate solution for the inner linear systems. Hence, efficiency improvement with respect to the steady state solver has direct impacts on the unsteady solver.

Within the literature many suggestions have been made over several years to improve established explicit Runge-Kutta methods [3–6]. Recently it has been shown that approximately all of the preconditioning techniques integrated into some explicit Runge-Kutta may be put under one umbrella. They all can be viewed as diagonal implicit Runge-Kutta methods where some approximate Jacobian is used as preconditioner and the arising linear systems are approximately solved by different algorithms [7].

To improve the existing unsteady CFD solver in the DLR TAU code in this article we consider flow problems arising from boundary movement, such as pitching airfoils. In the first part of this article we investigate the existing multistep time marching process to understand which modifications are required to carry the preconditioners presented in [7] over such that they are applicable to unsteady flow problems. Within this article we restrict ourselves to those preconditioners which arise from approximate first order Jacobians along predetermined grid anisotropies, so-called line and point implicit preconditioners. And then two numerical simulations will demonstrate the gain with respect to efficiency when the preconditioning methods are compared with classical solution procedures. Finally, some conclusions close the artical up.

2 Numerical Method

2.1 Governing Equations

To describe flow effects we consider for an open domain $\Omega \subset \mathbb{R}^3$ the Reynolds averaged Navier-Stokes equations. In time dependent form for a moving or deforming control volume $\Omega = \Omega(t)$ with boundary $\partial\Omega$ these equations read

$$\frac{d}{dt}\int_{\Omega} \mathbf{W}\,\mathrm{d}\Omega + \int_{\partial\Omega} \left(\mathbf{F}_c - V_g\mathbf{W} - \mathbf{F}_v\right)\,\mathrm{d}s = \int_{\Omega} \mathbf{Q}\,\mathrm{d}\Omega. \tag{1}$$

The conservative variables are given by $\mathbf{W} := (\rho, \rho u_1, \rho u_2, \rho u_3, \rho E, \rho\tilde{\nu})$ and the term modeling the motion is defined by $V_g := \sum_{j=1}^{3} n_j \frac{\partial x_j}{\partial t}$. Then the total convective flux is given by

$$\mathbf{F}_c - V_g\mathbf{W} = \begin{pmatrix} \rho(V - V_g) \\ \rho u_1(V - V_g) + n_1 p \\ \rho u_2(V - V_g) + n_2 p \\ \rho u_3(V - V_g) + n_3 p \\ \rho H(V - V_g) + V_g p \\ \rho\tilde{\nu}(V - V_g) \end{pmatrix}.$$

For the definition of the viscous terms $\mathbf{F}_v$ as well as the additional equation and source term $\mathbf{Q}$ arising from the Spalart-Allmaras turbulence model we refer to [8].

2.2 Discretization in Space

The work presented in this paper is integrated into the CFD solver TAU developed at the Deutsches Zentrum für Luft- und Raumfahrt e.V. (see e.g. [9]). TAU is based on a finite volume formulation where a median dual grid forms the control volumes with the unknowns in the vertices of the primary grid. An agglomeration multigrid algorithm is used to approximate a steady state solution of the governing equations. A multistage preconditioned Runge-Kutta scheme may be used as a smoother. The dual grid is created in a preprocessing step.

The discretization of the convective terms is done by a matrix dissipative scheme described in [10]. The discretization of the viscous terms is straightforward. The gradients are reconstructed using either a Green-Gauss Ansatz or a thin shear layer formulation. For more details on these topics we refer to [8].

The spatial discretization carries the continuous Eq. (1) over into a semi-discrete ordinary differential equation

$$\frac{d}{dt}\left(\mathbf{M}(t)\mathbf{W}(t)\right) = -\mathbf{R}(t, \mathbf{W}(t)), \qquad \mathbf{M}(t) := \operatorname{diag}\left(\operatorname{Vol}(\Omega_i)(t)\right), \tag{2}$$

which needs to be integrated in time.

2.3 Discretization in Time

At the outset there are in general two possibilities to integrate (2) in time:

(a) Multistep methods,
(b) one step methods such as Runge-Kutta methods.

Taking into account that (2) is in general stiff for high Reynolds number viscous flows explicit time marching methods are usually not an adequate choice. Due to stability restrictions the allowable time step size is usually not acceptable. Therefore we consider implicit time integration methods to iterate (2) in time.

With respect to one step methods so-called ESDIRK methods have been established. When compared with multistep methods their advantage is that in some general framework high-order time integration methods can be included. Moreover, exploiting embedded methods an adaptive time step can be computed with negligible computational effort. An application of such methods to flow problems can be found in [11, 12].

However, the advantages of ESDIRK methods are paid by several necessary operator evaluations. And, as presented in [11], the advantages of such methods show up when going to high order, i.e. $p \geq 4$. Having our focus on first of all improving efficiency of classical second order schemes we restrict ourselves in this article with respect to the BDF2 method. This method is widely used for its stability, moderate accuracy and computational efficiency. Then a fully discrete form of (2) is given by

$$\frac{3\mathbf{M}^{n+1}\mathbf{W}^{n+1} - 4\mathbf{M}^{n}\mathbf{W}^{n} + \mathbf{M}^{n-1}\mathbf{W}^{n-1}}{2\Delta t} = -\mathbf{R}(\mathbf{W}^{n+1}), \tag{3}$$

where the superscript denotes the time level, $\mathbf{W}^n := \mathbf{W}(t_n)$, $\mathbf{M}^n := \mathbf{M}(t_n)$ and Δt the physical time step. Equation (3) represents in general a large scale nonlinear equation which needs to be solved approximately such that the outer time iteration is not influenced by the approximation error. To solve (3) we rearrange the equation and obtain

$$\frac{3}{2\Delta t}\mathbf{M}^{n+1}\mathbf{W}^{*} = -\mathbf{R}(\mathbf{W}^{*}) + \mathbf{Z},\ \mathbf{Z} := \frac{1}{\Delta t}\left(2\mathbf{M}^{n}\mathbf{W}^{n} - \frac{1}{2}\mathbf{M}^{n-1}\mathbf{W}^{n-1}\right). \tag{4}$$

The approximate solution $\mathbf{W}^{*}_{\text{app}}$ of (4) is then our new time level $\mathbf{W}^{n+1} := \mathbf{W}^{*}_{\text{app}}$.

To apply some existent steady state solution procedure to find some approximate solution of (4) we introduce some so-called pseudo time τ. Then we may apply our existing steady solution procedure as inner iterative procedure to

$$\frac{d\mathbf{W}^{*}}{d\tau} = \mathbf{R}^{*}(\mathbf{W}^{*}), \qquad \mathbf{R}^{*}(\mathbf{W}^{*}) := \frac{3}{2\Delta t}\mathbf{W}^{*} + \left(\mathbf{M}^{n+1}\right)^{-1}\left(\mathbf{R}(\mathbf{W}^{*}) - Z\right). \tag{5}$$

Obviously, the main complexity of an unsteady flow problem arises from the solution process of the steady state solver applied to (5). The total complexity is then simply given by

$$\#\,(\text{physical time steps}) \cdot (\text{complexity of inner iterative solver})\,.$$

Hence, to improve the efficiency of an unsteady simulation our main goal is the improvement of the steady state solution procedure, which plays the role of inner iterative solver.

2.4 Preconditioned Runge-Kutta Method

Recently, a hierarchy of preconditioning technqiues for Runge-Kutta methods has been presented to find efficiently steady state solutions for high Reynolds number viscous flows [7]. Applied to (5) these methods can be written as

$$\begin{aligned}
\mathbf{W}^{(0)} &:= \mathbf{W}^n = \mathbf{W}(t_n) \\
\mathbf{W}^{(1)} &= \mathbf{W}^{(0)} - \mathrm{CFL}_{\mathrm{impl}}\alpha_{21}\Delta T\mathbf{P}_1^{-1}\mathbf{R}^*\left(\mathbf{W}^{(0)}\right) \\
&\vdots \\
\mathbf{W}^{(s)} &= \mathbf{W}^{(0)} - \mathrm{CFL}_{\mathrm{impl}}\alpha_{s+1,s}\Delta T\mathbf{P}_s^{-1}\mathbf{R}^*\left(\mathbf{W}^{(s-1)}\right) \\
\mathbf{W}(t_{n+1}) = \mathbf{W}^{n+1} &= \mathbf{W}^{(s)},
\end{aligned} \tag{6}$$

where $\Delta T := \mathrm{diag}(\Delta\tau_i)$ denotes the matrix of local pseudo time steps. The sequence of preconditioners $\mathbf{P}_j$ are given by some approximate derivative of the residual $\mathbf{R}^*$. Differentiation of (5) with respect to $\mathbf{W}^*$ yields

$$\frac{\partial \mathbf{R}^*}{\partial \mathbf{W}^*} = \frac{3}{2\Delta t}\mathbf{I} + (\mathbf{M}^{n+1})^{-1}\frac{\partial \mathbf{R}}{\partial \mathbf{W}^*}. \tag{7}$$

With respect to the analysis given in [7] we conclude that using (7) the preconditioner required to solve the inner nonlinear equations (5) is given by

$$\mathbf{P}_j := \left(\frac{1}{\mathrm{CFL}}(\Delta T)^{-1}\mathbf{M}^{n+1} + \left(\frac{3}{2\Delta t}\mathbf{I} + \frac{\partial \mathbf{R}}{\partial \mathbf{W}^*}\right)\right).$$

Hence, by a slight of modification of adding the term $\frac{3}{2\Delta t}\mathbf{I}$ to the diagonal of the preconditioners presented in [7] these techniques are applicable to unsteady flow simulations described by (1).

Finally a suitable approximation of $\frac{\partial \mathbf{R}}{\partial \mathbf{W}^*}$ is required. In this article we restrict our investigations with respect to point implicit (see also [10]) and line implicit methods [13]. For more detailed discussion concerning line identification etc. we refer to [14].

3 Results

To evaluate the efficiency of the preconditioned Runge-Kutta method (6) we consider first a 2-D pitching airfoil and second a 3-D pitching wing. As inner iteration to find some approximate solution of (5) we compare

(a) Explicit Runge-Kutta method with local time stepping,
(b) Matrix-free LU-SGS presented in [15],
(c) Point implicit Preconditioned Runge-Kutta method (6), and
(d) Line implicit Preconditioned Runge-Kutta method (6).

In all our computations a 4W multigrid cycle is applied.

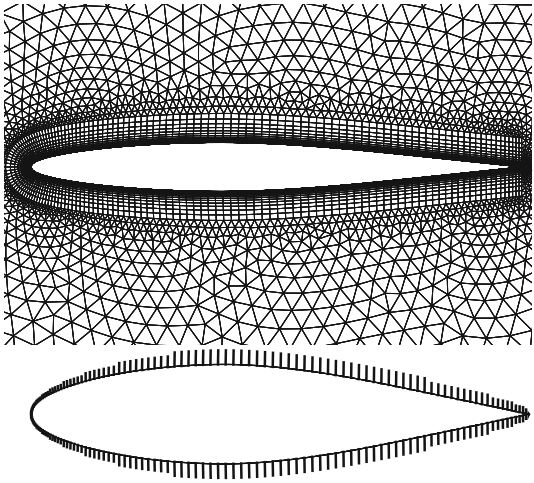

Fig. 1 Computational grid and lines for NACA64A010 simulation

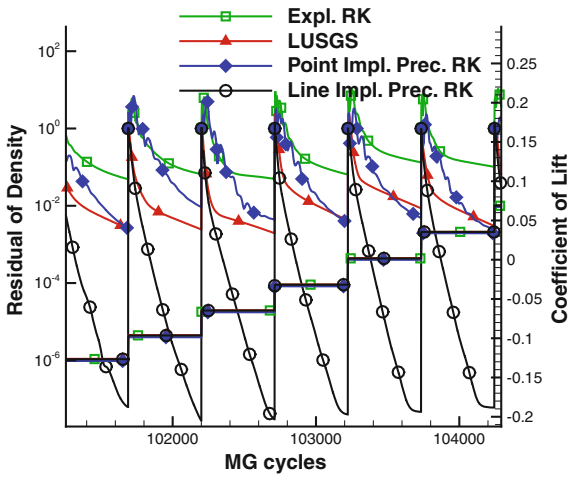

Fig. 2 Convergence histories for NACA64A010 simulation

3.1 NACA64A010 Pitching Oscillation

We first consider a NACA64A010 airfoil. The free stream Mach number is 0.8, the Reynolds number 6.2*e*6 and the angle of attack is 0° . The airfoil oscillates around the quarter chord point with an amplitude of 2° and a frequency of 0.1628. The computation comprises 5 periods and each period is divided into 50 intervals. The computational grid and the lines for constructing the line implicit preconditioner

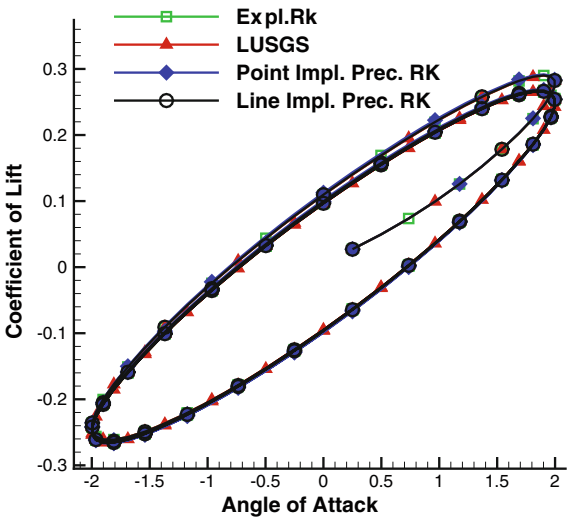

Fig. 3 Computational periodic lift coefficient of NACA64A010

Table 1 Comparisons of iteration numbers and wall clock time of NACA64A010 test case

Stopping criteria		#Iter. ratio				Wall time ratio			
		ERK	LUSGS	PIRK	LIRK	ERK	LUSGS	PIRK	LIRK
Unsteady residual of density	$1.e-01$	1	0.15	0.24	0.08	1	0.23	0.73	0.29
	$1.e-02$	1	0.2	0.18	0.06	1	0.28	0.52	0.2
	$1.e-03$	1	0.28	0.2	0.16	1	0.35	0.54	0.16
	$1.e-04$	1	0.32	0.25	0.05	1	0.38	0.67	0.16

are plotted in Fig. 1. All lines are located in the boundary layer resolving the high grid stretching. Figure 2 shows a comparison of the convergence histories of density residual and lift coefficient as a function of multigrid cycles. Here every pseudo-time marching is terminated after 500 inner iterations. Obviously, the line implicit preconditioner outperforms all other compared methods. However, to compare the efficiency of the different methods as a second criterion the inner iterations have been stopped when some certain error level is reached. Here we considered the reduction of density residual. Clearly, the improved convergence rate observed in Fig. 2 not only maintains a good accuracy, see Figs. 3 and 4 but also yields a significant speed up in computational time summarized in Table 1.

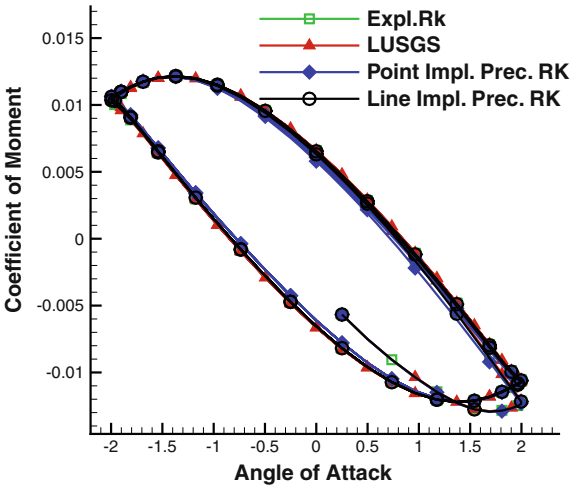

Fig. 4 Computational periodic moment coefficient of NACA64A010

Table 2 Comparisons of iteration numbers and wall clock time of LANN wing test case

Stopping criteria		#Iter. ratio			Wall time ratio		
		ERK	LUSGS	LIRK	ERK	LUSGS	LIRK
Unsteady residual of density	$1.e-01$	1	0.17	0.11	1	0.045	0.043
	$1.e-02$	1	0.27	0.19	1	0.13	0.076
	$1.e-03$	1	0.30	0.18	1	0.29	0.072

3.2 LANN Wing Pitching Oscillation

The flow conditions for the LANN wing are as follows: The free stream Mach number is 0.82 at a Reynolds number of of $7.31e6$. The angle of attack is 0.6° while the wing flaps around the axis which is perpendicular to its root slice at the 62 % of chord with an amplitude of 0.25° and a frequency of 0.204. To achieve the periodic state, 5 periods are simulated and 50 time steps per period is considered and computational efforts are compared in Table 2. Figure 5 plots the surface grid and lines for computation. The lines resolve the anisotropies in the boundary layer and wake region. From the convergence history represented in Fig. 6, it is clear that the line-implicit preconditioning technique improves the convergence rate significantly. There is a good agreement in computational coefficients when compared with the other solution methods, Figs. 7 and 8.

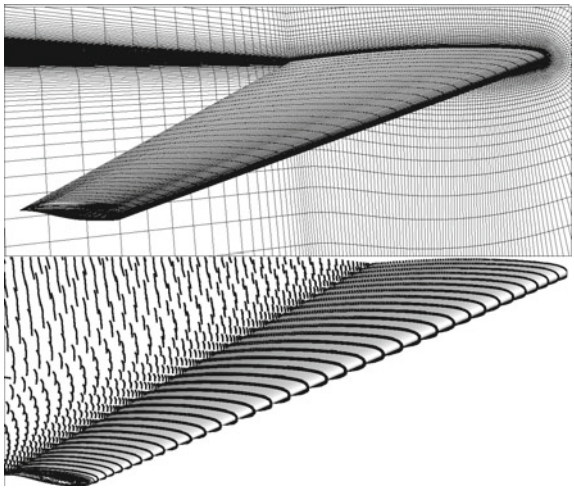

Fig. 5 Computational grid and lines for LANN wing simulation

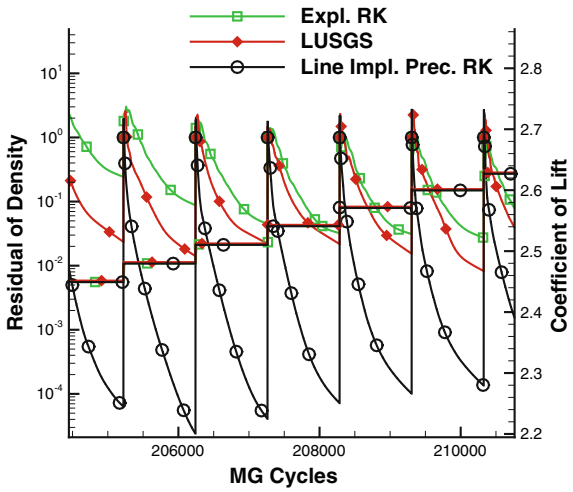

Fig. 6 Convergence histories for LANN wing simulation

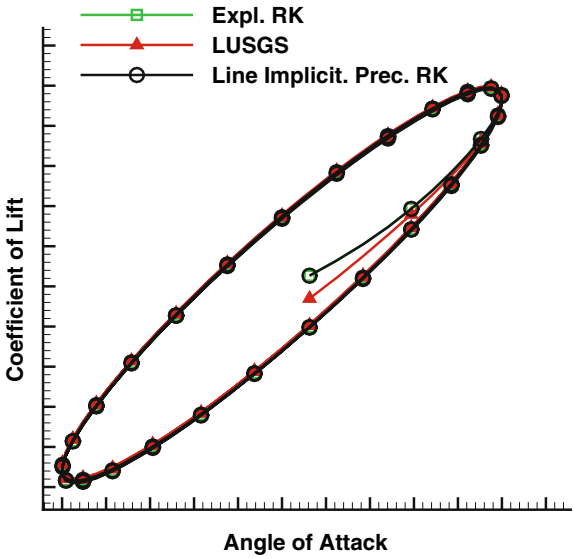

Fig. 7 Computational periodic lift coefficient of LANN wing

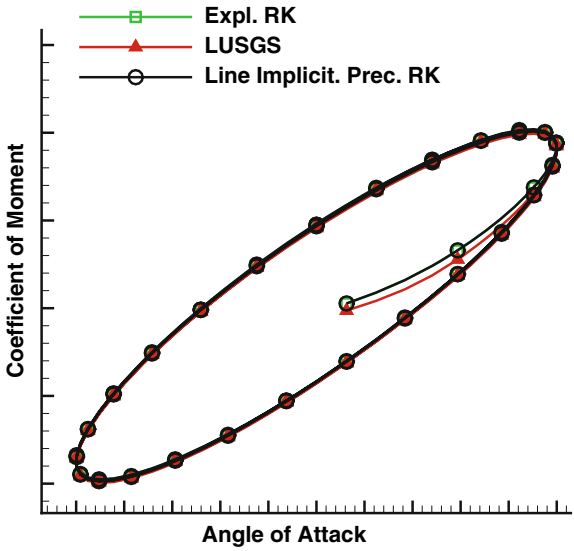

Fig. 8 Computational periodic moment coefficient of LANN wing

4 Conclusion

We have presented the extension of point and line implicit preconditioning techniques for a BDF2 scheme. It was shown that having an existing point and line implicit preconditioning for a steady state solver at hand only slight modifications are required to make the methods ready for unsteady problems. The method was applied to an oscillating NACA64A010 airfoil and an oscillating LANN wing. In comparison with the explicit Runge-Kutta scheme and the matrix free LU-SGS scheme the implicitly preconditioned Runge-Kutta method was shown to achieve a gain in both convergence rate and CPU time.

References

1. Jameson, A., Schmidt, W., Turkel, E.: Numerical solutions of the Euler equations by finite volume methods using Runge-Kutta time-stepping schemes. AIAA paper 81–1259, pp. 315–333 (1981)
2. Jameson, A.: Time dependent calculations using multigrid, with applications to unsteady flows past airfoils and wings. AIAA paper 91–1596 (1991)
3. Mavriplis, D.J.: On convergence acceleration techniques for unstructured meshes. ICASE Report No 98–44 (1998)
4. Allmaras, S.A.: Analysis of semi-implicit preconditioners for multigrid solution of the 2-d compressible Navier-Stokes equations. AIAA Paper 95–1651-CF (1995)
5. Pierce, N.A., Giles, M.B.: Preconditioned multigrid methods for compressible flow calculations on stretched meshes. J. Comput. Phy. **136**(2), 425–445 (1997)
6. Mavriplis, D.J.: Directional coarsening and smoothing for anisotropic Navier-Stokes problems. Electron. Trans. Numer. Anal. **6**, 182–197 (1997)
7. Langer, S.: Hierarchy of preconditioning techniques for the solution of the Navier-Stokes equations discretized by 2nd order unstructured finite volume methods. ECCOMAS (2012)
8. Blazek, J.: Computational fluid dynamics: principles and applications. Elsevier Science Ltd, London (2001)
9. Schwamborn, D., Gerhold, T., Heinrich, R.: The DLR TAU-Code: recent applications in research and industry. Invited Lecture in Proceedings of the European Conference on Computational Fluid Dynamics ECCOMAS CFD (2006), 2006
10. Langer, S.: Investigation and application of point implicit Runge-Kutta methods to inviscid flow problems. Int. J. Numer. methods Fluids **69**(2), 332–352 (2012)
11. Ashcroft, G., Heitkamp, K., Kügeler, E.: High-order accurate implicit Runge-Kutta schemes for the simulation of unsteady flow phenomena in turbomachinery. ECCOMAS CFD (2010)
12. Birken, P.: Numerical Methods for the Unsteady Compressible Navier-Stokes Equations. Habilitationsschrift Universität Kassel, Kassel (2012)
13. Langer, S.: Point and line implicit methods to improve the robustness and efficiency of the DLR TAU Code, 17. In: New Results in Numerical and Experimental Fluid Mechanics VIII, pp. 419–428. Springer, Berlin (2013)
14. Langer, S.: Application of a line implicit method to fully coupled system of equations for turbulent flow problems. Int. J. Comput. Fluid Dyn. **27**(3), 131–150 (2013)
15. Dwight, R.P.: Efficiency improvements of RANS-Based analysis and optmization using implicit and adjoint methods on unstructured grids. PhD Thesis, University of Manchester (2006)

Validation of a Time-Domain TAU-Flight Dynamics Coupling Based on Store Release Scenarios

Lars Reimer, Ralf Heinrich and Rosemarie Meuer

Abstract A six degrees of freedom flight dynamics module was coupled to DLR's CFD solver TAU. The algorithms implemented in the flight dynamics module for solving the 6-DoF equations of motion are explained in detail. The coupling is validated using one analytic test case and two store release experiments. The effects on the prediction accuracy of a strong coupling approach using an error-based coupling convergence criterion are compared to classical weak coupling.

1 Introduction

For more accurate and improved prediction of airframe loads appearing during gust encounter of aircraft and for the design of flight control systems enabling the alleviation of the loads by selective control surface deflections, it is expedient to couple CFD solvers based on Reynolds-averaged Navier-Stokes (RANS) equations to flight dynamics solvers—called rigid-body dynamics (RBD) solvers henceforth. Based on the aerodynamic loads computed by the CFD solver, the RBD solver can predict the translatory and rotatory motion of the aicraft—at least upon assumption of a rigid aircraft.

This chapter discribes the implemented coupled CFD-RBD solver. In Sect. 2, the applied CFD solver is explained; the properties of the implemented RBD solver

L. Reimer (✉) · R. Heinrich
C2A2S2E Department, German Aerospace Center (DLR), Institute for Aerodynamics and Flow Technology, Lilienthalplatz 7, 38108 Braunschweig, Germany
e-mail: Lars.Reimer@dlr.de

R. Heinrich
e-mail: Ralf.Heinrich@dlr.de

R. Meuer
Rheinmetall Waffe and Munition GmbH, Heinrich-Ehrhardt-Street 2, 29345 Unterlüß, Germany
e-mail: Rosemarie.Meuer@rheinmetall.com

A. Dillmann et al. (eds.), *New Results in Numerical and Experimental Fluid Mechanics IX*, Notes on Numerical Fluid Mechanics and Multidisciplinary Design 124,
DOI: 10.1007/978-3-319-03158-3_46,

and the way in which both solvers are coupled are clarified in Sects. 3 and 4. Since experimental data of aircraft gust encounters are scarce, alternatively, the behaviour of the developed coupled solver is studied in Sect. 5 based on the predicted results for a test case with an analytic solution and for two publicly available store release experiments. Special attention is paid to the comparison between results from simulations with weak and strong coupling. In addition, it is studied, how an error-based termination criterion of the corrector steps in the strong coupling, which is added to the version of the CFD-RBD solver presented in [1], affects the solvers' efficiency and accuracy.

2 CFD Solver TAU

DLR's flow solver TAU [2] solves the RANS equations with second order accurate finite volume discretization schemes on unstructured grids. For moving grids, TAU is written in an arbitrary Eulerian-Lagrangian formulation. In the present work, the central scheme with scalar dissipation according to Jameson is used to compute the convective fluxes, with one exception. For the supersonic case presented in Sect. 5.3, the AUSMDV upwind scheme is applied. For the turbulent test cases in the present work, either Spalart-Allmaras' one-equation model (Sect. 5.2) or Menter's SST two-equation model (Sect. 5.3) are used.

For unsteady simulations, the dual-time stepping method is applied. The time integration of steady-state problems, including the solution of the pseudo-time problem contained in the dual-time stepping scheme, is done by using TAU's implicit LU-SGS scheme.

3 Rigid-Body Dynamics Solver

The motion of the rigid body is computed in the RBD solver by solving Newton's second law and the Euler equation:

$$\frac{d\boldsymbol{v}_{CG}^{g}}{dt} = \frac{\boldsymbol{F}_{total}^{g}}{m_{total}}, \quad \text{with } \boldsymbol{F}_{total}^{g} = \boldsymbol{F}_{grav}^{g} + \boldsymbol{A}^{gb}\boldsymbol{F}_{aero}^{b} + \cdots \tag{1}$$

$$\frac{d\boldsymbol{\omega}^{b}}{dt} = \boldsymbol{\Theta}_{CG,b}^{-1}\left(\boldsymbol{M}_{total}^{b} - \boldsymbol{\omega}^{b} \times \left(\boldsymbol{\Theta}_{CG,b}\,\boldsymbol{\omega}^{b}\right)\right). \tag{2}$$

In (1) and (2) $\boldsymbol{v}_{CG}$ and $\boldsymbol{\omega} = (p, q, r)^T$ denote the translatory velocity vector of the body's centre of gravity and its angular velocity vector. m_{total} and $\boldsymbol{\Theta}_{CG}$ are the mass and inertia tensor relative to the centre of gravity. $\boldsymbol{F}_{total}$ and $\boldsymbol{M}_{total}$ represent the added up forces and moments acting on the body including gravitational force $\boldsymbol{F}_{grav}$ and aerodynamic force $\boldsymbol{F}_{aero}$. The superscript g indicates that the coefficients of the

respective vector are computed with respect to the geodesic frame.[1] The superscript b refers to the body-fixed frame. The following two equations are solved by the RBD solver in addition to (1) and (2):

$$\frac{d\mathbf{r}_{CG}^{g}}{dt} = \boldsymbol{v}_{CG}^{g} \quad \text{and} \quad \frac{d\mathbf{q}}{dt} = \frac{1}{2}\mathbf{B}^{T}\,\boldsymbol{\omega}^{b} \quad \text{with} \quad \mathbf{B} = \begin{pmatrix} -q_1 & -q_2 & -q_3 \\ q_0 & -q_3 & -q_2 \\ q_3 & q_0 & -q_1 \\ -q_2 & q_1 & q_0 \end{pmatrix}. \tag{3}$$

Equation (3) link the actual position $\boldsymbol{r}_{CG}$ and attitude of the rigid-body to the body's translatory and angular velocity state. Following the method described in [3], the body's attitude is expressed in the present RBD solver in terms of quaternion parameters $\boldsymbol{q} = (q_0, q_1, q_2, q_3)$. In contrast to the Euler angles, which are widely used in flight dynamics, quaternions avoid the so-called gimbal lock—a singularity at certain rotation angles. The transformation matrix $\boldsymbol{A}^{gb}$, which is used in (1) and is needed in general to transform vectors from the body-fixed frame to the geodesic frame of reference, is also formulated in the RBD solver in terms of quaternion parameters:

$$\boldsymbol{A}^{gb} = 2\begin{pmatrix} q_0^2 + q_1^2 - 1/2 & q_1q_2 - q_0q_3 & q_1q_3 + q_0q_2 \\ q_1q_2 + q_0q_3 & q_0^2 + q_2^2 - 1/2 & q_2q_3 - q_0q_1 \\ q_1q_3 - q_0q_2 & q_2q_3 + q_0q_1 & q_0^2 + q_3^2 - 1/2 \end{pmatrix}. \tag{4}$$

Note that the known drift of the quaternions is to be avoided by normalizing them at the end of every physical time step.

Equations (1)–(3) can be assembled and written in short as first order ordinary differential equation system

$$\frac{d\boldsymbol{W}}{dt} - \boldsymbol{R}\left(\boldsymbol{W}, \boldsymbol{W}_{ext}\right) = \mathbf{0}, \tag{5}$$

with the vector of unknowns $\boldsymbol{W} = \left(\boldsymbol{r}_{CG}^{g}, \boldsymbol{v}_{CG}^{g}, \boldsymbol{\omega}^{b}, \boldsymbol{q}\right)^{T}$, the vector of external loads $\boldsymbol{W}_{ext} = \left(\boldsymbol{F}_{total}^{g}, \boldsymbol{M}_{total}^{b}\right)^{T}$ and the residual vector $\boldsymbol{R}$ which subsumes the equations' right hand side terms. Implicit temporal discretization of (5) by the second order time-accurate trapezoidal scheme and subsequent application of the well-known dual-time stepping approach yields the following equation which is to be solved in the so-called pseudo-time τ for every physical time step of size Δt so that $d\boldsymbol{W}^{\nu}/d\tau \to \mathbf{0}$:

$$\frac{d\boldsymbol{W}^{\nu}}{d\tau} - \boldsymbol{R}^{*}\left(\boldsymbol{W}^{\nu}, \boldsymbol{W}_{ext}^{n}\right) = \mathbf{0} \text{ with } \boldsymbol{R}^{*} = \frac{\boldsymbol{W}^{\nu} - \boldsymbol{W}^{n}}{\Delta t} - \frac{\boldsymbol{R}^{\nu} + \boldsymbol{R}^{n}}{2}. \tag{6}$$

For the time-integration of (6), the version of the RBD solver presented in [1] uses a five-stage Runge-Kutta (RK) scheme. The RK-based approach was replaced in the course of the work at hand by solving the equation $\boldsymbol{R}^{*} = \mathbf{0}$ using Newton's method:

[1] The geodesic frame is regarded as inertial frame in the present work.

$$\frac{\partial \boldsymbol{R}^*}{\partial \boldsymbol{W}} \boldsymbol{\Delta W} = -\boldsymbol{R}^* \left(\boldsymbol{W}^{\nu}, \boldsymbol{W}^{n}_{ext} \right), \quad \frac{\partial \boldsymbol{R}^*}{\partial \boldsymbol{W}} = \left(\frac{\boldsymbol{I}}{\Delta t} - \frac{1}{2} \frac{\partial \boldsymbol{R}}{\partial \boldsymbol{W}} \right), \tag{7}$$

$$\boldsymbol{W}^{\nu+1} = \boldsymbol{W}^{\nu} + \boldsymbol{\Delta W}, \quad \nu = 1, \ldots, N_{inner,RBD}. \tag{8}$$

ν denotes the iteration counter for the pseudo-time steps and $N_{inner,RBD}$ is a user-defined maximum number of pseudo-time steps. The entries of the Jacobian $\partial \boldsymbol{R}^* / \partial \boldsymbol{W}$ are computed as algebraic expressions that can be evaluated exactly. The RK scheme needed about 10–200 iterations, depending on the test case, whereas the Newton scheme needed only 1–5 iterations to converge down to machine accuracy. Hence, the Newton scheme turned out to be faster than the RK scheme by a factor of 10–20, even though the Jacobian was updated in every iteration. Although the RBD solver consumes much less computing time than the CFD solver, the choice of the Newton scheme can reduce the total computing time spent for the RBD part in very long runs of coupled CFD-RBD simulations from several hours to a few minutes.

4 Coupling

The coupled CFD-RBD problem is solved in a partitioned manner. A so-called "strong coupling" is implemented. Strong coupling means that the coupled equations are iteratively solved within every physical time step by repeatedly solving the involved disciplines CFD and RBD separately, based on the exchanged coupling quantities; these are CFD loads and RB motion state. Strong coupling consists of one predictor step and a number of corrector steps. The corrector steps are terminated and the code continues with the next physical time step once one of the following criteria is fulfilled: (1) either a user-defined number of corrector steps k^{max}_{corr} is exceeded—in the CFD-RBD solver presented in [1] this was the only available termination criterion—or (2) the solution falls below a user-defined convergence threshold:

$$\sqrt{\left(\frac{||\boldsymbol{\Delta W}^{k_{corr}}_{ext}||}{||\boldsymbol{W}^{k_{corr}-1}_{ext}||} \right)^2 + \left(\frac{||\boldsymbol{\Delta W}^{k_{corr}}||}{||\boldsymbol{W}^{k_{corr}-1}||} \right)^2} \leq \varepsilon_{CFD/RBD}, \tag{9}$$

with $\boldsymbol{W}, \boldsymbol{W}_{ext}$ according to (5). The latter termination criterion is added to the current CFD-RBD solver for more efficient and more accurate coupling. When k^{max}_{corr} is set to zero, the strong coupling scheme turns into a weak coupling scheme.

Apart from the aforementioned aspects, the coupled computation is also influenced by the number of maximum inner CFD iterations ($N_{inner,CFD}$) and RBD iterations ($N_{inner,RBD}$) defined by the user, as well as by the convergence thresholds. The so-called Cauchy convergence criterion was used in the CFD solver TAU. The criterion claims that the relative variation of an observed quantity, e.g. the lift coefficient, must fall below a defined threshold $\varepsilon^{Cauchy}_{rel,CFD}$ for a defined number of inner iterations ($N^{eval,Cauchy}_{inner,CFD}$). In the RBD solver the inner iterations are terminated once the norm of the residual $\boldsymbol{R}^*$ drops below the user-defined threshold ε_{RBD} which is set to 10^{-12} in all test cases discussed in the present chapter.

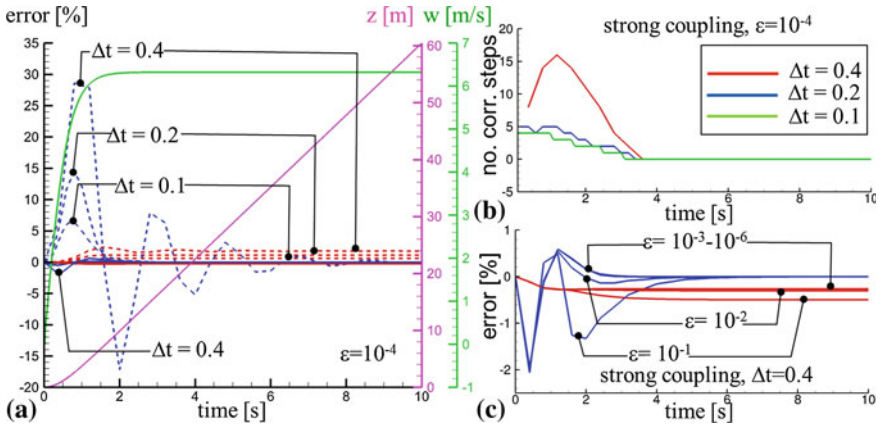

Fig. 1 **a** Error between simulation and analytic solution; *solid lines* = strong coupling; *dashed lines* = weak coupling; *red-colored lines* = error in z; *blue-colored lines* = error in w; **b** no. of correction steps needed in the strong coupling scheme to obtain $\varepsilon_{CFD/RBD} = 10^{-4}$; **c** error between the simulation with strong coupling and the analytic solution for different convergence thresholds $\varepsilon_{CFD/RBD}$

5 Results

5.1 Falling Sphere

A sphere falling in air, which is subjected to gravitational force $\boldsymbol{F}_{grav} = mg\boldsymbol{e}_z$ and aerodynamic drag force $\boldsymbol{F}_d = -1/2\ \rho c_d S||\boldsymbol{v}||^2\boldsymbol{e}_z$, is simulated. ($m = S = \rho = 1$, $c_d = 0.5$). Since TAU is not needed for this test case, it is replaced by a dummy CFD solver which evaluates the formula for the drag force in every coupling step based on the instantaneous RB motion. The analytic solution for the test case, i.e. the position z and velocity w in direction $\boldsymbol{e}_z$, is stated in [1] and plotted in Fig. 1a.

The motion of the sphere was computed by using the coupled solver in weak and strong coupling mode with three different time step sizes. The errors between numerically predicted results and the analytical solution are plotted in Fig. 1a. While the strong coupling scheme ($\varepsilon_{CFD/RBD} = 10^{-4}$) yields relatively low errors—below 2 % for the largest applied time step $\Delta t = 0.4$ s, for $\Delta t = 0.1$ s even below 0.14 %, the weak coupling scheme produces maximum errors above 25 %. Even for the lowest time step $\Delta t = 0.1$ s the maximum mismatch with the weak coupling scheme is still above 5 %. As expected, Fig. 1b demonstrates that the number of corrector steps in the strong coupling scheme increases with rising time step size. The curves in Fig. 1b apply to the case with $\varepsilon_{CFD/RBD} = 10^{-4}$. Exemplarily for $\Delta t = 0.4$ s, Fig. 1c shows the influence of $\varepsilon_{CFD/RBD}$ on the error. For $\varepsilon_{CFD/RBD} \leq 10^{-3}$ no significant improvement in the error distribution can be observed. This means, that the time step size must still be carefully chosen so that it fits to the given physical problem—even for simple test cases and even when applying strong coupling.

Put simply, even strong coupling with many corrector steps resulting from very low threshold values $\varepsilon_{CFD/RBD}$ cannot improve the results if an inappropriately large time step size is chosen. However, for identically large time step sizes, the strong coupling scheme will at least produce less mismatch than the weak coupling approach.

5.2 AFRL Store Release Experiments

The simulations of the store release experiments [4] conducted at AFRL[2] are described in the following. The test case with transonic conditions was chosen: $M = 0.95$, $Re = 4.1 \cdot 10^6$, $\alpha = 0°$. The studied configuration consists of the carrier, i.e. a generic delta wing with pylon for which an Euler CFD mesh was generated, and a store with four fins. For the store an individual Navier-Stokes CFD mesh was created. For simulating the motion of the store TAU's overset grid technique [5] was applied. Fully unsteady simulations using the strong coupling scheme were conducted with two different time steps $\Delta t = 0.005$ and 0.01 s. In the CFD solver the following coupling-relevant parameters were used: $N_{inner,CFD} = 100$, $\varepsilon_{rel,CFD}^{Cauchy} = 10^{-4}$, $N_{inner,CFD}^{eval,Cauchy} = 30$. For comparison a simulation using a quasi-steady coupling approach was also performed. In the approach the CFD operates in steady mode (here: $N_{inner,CFD} = 1,000$) while the RBD solver still runs in unsteady mode. In combination with the quasi-steady approach, weak coupling must be used. In Fig. 2 the results of the simulations are plotted. Though Fig. 2a shows differences in the number of corrector steps needed for both time steps ($\varepsilon_{CFD/RBD} = 10^{-3}$), no differences can be observed in Fig. 2b and c showing the time histories of predicted store positions and Euler angles. Thus, the larger time step is sufficient. A good agreement can be found between the results numerically predicted by the simulations with strong coupling and the measurements. Differences appear only for the roll angle. The reason for that is yet unclear. Though the store positions computed by the quasi-steady simulation differ only slightly, the Euler angles and rotation rates, which cannot be shown here due to space limitations, deviate considerably from the experimental data and the other simulation results. Particularly, the roll angle and roll rate predicted by the quasi-steady approach show a very different behaviour. The popular quasi-steady approach has thus proved to be inappropriate for simulating the present test case.

[2] Air Force Research Laboratory: www.wpafb.af.mil/AFRL.

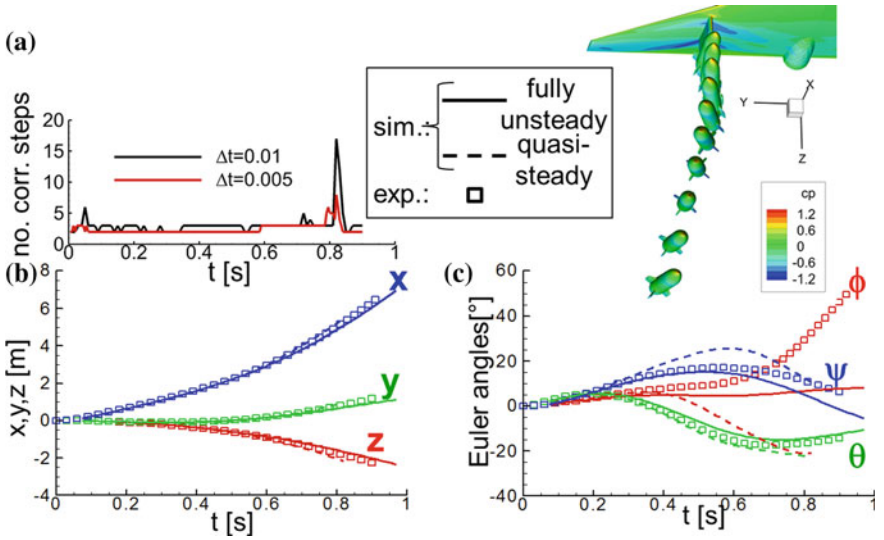

Fig. 2 **a** No. of corrector steps needed with the strong coupling approach; **b**–**d** comparison between experiment, fully unsteady coupling and quasi-steady coupling approach in terms of the store RB motion state

5.3 ISL Multi-Function Projectile Release Experiments

At ISL[3] the free flight of a multi-function projectile was investigated in shock tube experiments [6]. The initial flight conditions of the projectile were $M = 3.06$, $\Theta = 4°$. The inertia properties of the projectile are given in [6]. Preceding the coupled TAU-RBD simulation, the 3D CFD mesh provided by Rheinmetall was adapted in five stages during the steady TAU computation; cf. upper Fig. 3a. Acceptable agreement between the results of the steady simulation and corresponding wind tunnel experiments was found; cf. the Schlieren photograph and the predicted Mach number distribution in the lower Fig. 3a. Subsequent to the steady computation, a coupled TAU-RBD simulation with strong coupling and the following setting was conducted: $\varepsilon_{CFD/RBD} = 10^{-3}$, $\Delta t = 50\,\text{ms}$, $N_{inner,CFD} = 200$, $\varepsilon_{rel,CFD}^{Cauchy} = 10^{-3}$, and $N_{inner,CFD}^{eval,Cauchy} = 30$. On average the strong coupling scheme performed two corrector steps to converge down to the given $\varepsilon_{CFD/RBD}$. Figure 3b compares the time history of the pitch angle derived from video recordings of the projectile's flight in the shock tube with the prediction by the TAU-RBD solver. Excellent agreement is found.

[3] German-French Research Institute Saint-Louis: www.isl.eu.

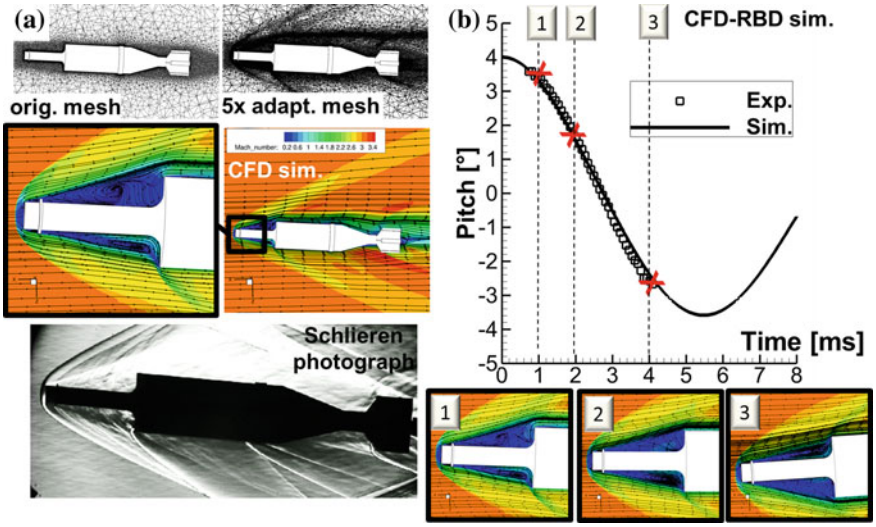

Fig. 3 **a** *Top* original and fivefold adapted CFD mesh; *bottom*; comparison between steady uncoupled CFD simulation with the adapted mesh and the Schlieren photograph from wind tunnel experiments; **b** comparison of measured pitch angle with the angle numerically predicted by the CFD-RBD solver

6 Conclusions

The ingredients of the developed CFD-flight dynamics solver and its validation are presented in this chapter. The following influences have been identified during the application of the developed coupled solver:

- The strong coupling approach with corrector step convergence thresholds $\varepsilon_{CFD/RBD}$ between 10^{-3} and 10^{-4} appears to be the best compromise between accuracy/stability and computational efficiency.
- The strong coupling approach in most cases requires much less computing time because much larger maximum inner iteration numbers, i.e. $N_{inner,CFD} > 1{,}000$, had to be chosen with the weak coupling approach. On the contrary, $N_{inner,CFD} =$ 100–200 in combination with the limitation of the number of corrector steps by $\varepsilon_{CFD/RBD}$ turned out to be the best choice with the strong coupling scheme.
- The Cauchy convergence criterion should be used to terminate the CFD solver's inner iterations. The authors recommend the following settings: $\varepsilon_{rel,CFD}^{Cauchy} = 10^{-4}$, $N_{inner,CFD}^{eval,Cauchy} = 30$.
- The popular quasi-steady coupling approach produced unsatisfactory results and needed significantly more computing time—at least for the AFRL test case studied in this chapter.

Since we find very good agreement between the measurements and the simulations of the store release experiments, the coupled CFD-flight dynamics solver can be regarded as validated. The recommendations stated above will particularly be of use in planned simulations of the gust encounter of aircraft.

References

1. Heinrich, R., Michler A.: Unsteady simulation of the encounter of a transport aircraft with a generic gust by CFD flight mechanics coupling. In: Proceedinfs of CEAS 2009 European Air and Space Conference Manchester, 26–29 Oct 2009
2. Schwamborn, D., Gerhold, T., Heinrich, R.: The DLR TAU-code: recent applications in research and industry. In: Proceedings of European Conference on Computational Fluid Dynamics EC-COMAS CFD 2006, Delft, The Netherlands (2006)
3. Murman, S. M., Aftosmis, M. J., Berger, M. J.: Simulations of a 6-DOF Motion with a cartesian method. AIAA-Paper 2003–1246 (2003)
4. Fox, J. H.: Generic Wing, Pylon, and moving Finned store. RTO Technical report 26 (RTO-TR-26)–verification and validation data for computational unsteady aerodynmamics, Chapter 23 (2000)
5. Madrane, A., Raichle, A., Stürmer, A.: A parallel implementation of a dynamic overset unstructured grid approach. In: Proceedings of European Conference on Computational Fluid Dynamics ECCOMAS CFD, Jyväskylä, 24–28 July 2004
6. Leopold, F., Seiler, S., Gauthier, Th., Bastide, M., Srulijes, J.: Instationary flow around multi-function projectiles. French-German Research Institute Saint-Louis report ISL-RV 234/2011 (2011)

Implementation of Flow Through Porous Media into a Compressible Flow Solver

Michael Mößner and Rolf Radespiel

Abstract A method for simulating turbulent compressible flow through porous material is presented. The demonstration is based on spatial and time averaging of the Navier-Stokes equations. The averaging procedure leads to additional terms which have to be modelled. The integration of the resulting theory into the flow solver DLR TAU is explained. The extended code is verified by analytical solutions which are used as reference.

1 Introduction

Airplane noise during lift off and approach is is a huge problem for the environment. This is why noise reduction gains high attention by researchers besides the other well known area of increasing efficiency. One way to make airplanes quieter is shown experimentally by Herr in [1]: A significant reduction of noise is achieved by making the trailing edges of the wing porous. As a side effect, the added porous regions can alter the flow around the wing (see Fig. 1). This chapter shows a way to integrate porous media simulation capabilities into compressible flow solvers used for aeronautical applications to enable them simulating the modified flow.

M. Mößner (✉) · R. Radespiel
Technische Universität Braunschweig, Hermann-Blenk-Straße 37, 38108 Braunschweig, German
e-mail: m.moessner@tu-bs.de

R. Radespiel
e-mail: r.radespiel@tu-bs.de

A. Dillmann et al. (eds.), *New Results in Numerical and Experimental Fluid Mechanics IX*, Notes on Numerical Fluid Mechanics and Multidisciplinary Design 124,
DOI: 10.1007/978-3-319-03158-3_47,

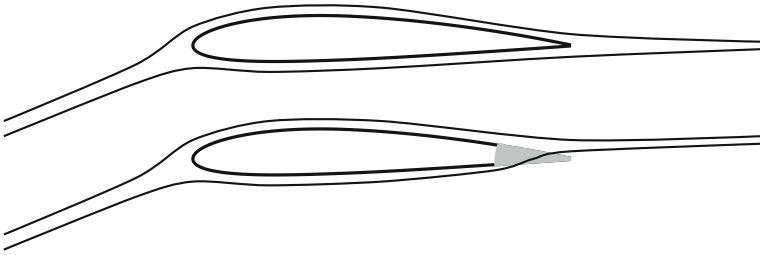

Fig. 1 *Upper* airfoil with solid trailing edge, *lower* airfoil with porous trailing edge which is permeable

2 Derivation of the Porous Transport Equations

At present, in most technical relevant simulations flow inside the single pores of a porous material cannot be resolved. This problem can be overcome by spatial averaging. Instead of simulating the flow through the pores it models the porous effect homogeneously. A similar procedure is used for turbulence. The turbulence is not resolved rather its effect is taken into account by averaging in time and modelling the Reynolds stresses. The basic strategy for spatial averaging in incompressible flow can be found in [2]. The procedure for obtaining nonporous turbulence equations is described in [3] extensively. The two principles are used in the present chapter to obtain the compressible RANS equations which are valid inside and outside porous media. To keep the equations simple density weighted averaging is used. The final equations result in

$$\frac{\partial \overline{\rho}}{\partial t} + \frac{\partial \overline{\rho}\widetilde{v}_k}{\partial x_k} = 0 \tag{1a}$$

$$\frac{\partial \overline{\rho}\widetilde{v}_i}{\partial t} + \frac{\partial \overline{\rho}\widetilde{v}_i\widetilde{v}_k}{\partial x_k} + \frac{\partial \overline{\rho}\widetilde{v_i'' v_k''}}{\partial x_k} + \frac{\partial \overline{p}}{\partial x_i} - \frac{\partial \overline{\tau_{ik}}}{\partial x_k} + \phi\frac{\mu}{\kappa}\widetilde{v}_i + \overline{\rho}\frac{c_F}{\sqrt{\kappa}}\widetilde{\sqrt{v_k v_k}}\, v_i = 0 \tag{1b}$$

$$\frac{\partial \overline{\rho e}}{\partial t} + \frac{\partial \frac{1}{2}\overline{\rho}\widetilde{v}_j\widetilde{v}_j}{\partial t} + \frac{\partial \frac{1}{2}\overline{\rho}\widetilde{v_j'' v_j''}}{\partial t} + \frac{\partial \overline{\rho}\widetilde{h}\widetilde{v}_k}{\partial x_k} + \frac{\partial \overline{\rho}\widetilde{h'' v_k''}}{\partial x_k} + \frac{\partial \frac{1}{2}\overline{\rho}\widetilde{v}_j\widetilde{v}_j\widetilde{v}_k}{\partial x_k} \tag{1c}$$
$$+ \frac{\partial \frac{1}{2}\overline{\rho}\widetilde{v}_k\widetilde{v_j'' v_j''}}{\partial x_k} + \frac{\partial \overline{\rho}\widetilde{v}_j\widetilde{v_j'' v_k''}}{\partial x_k} + \frac{\partial \frac{1}{2}\overline{\rho}\widetilde{v_j'' v_j'' v_k''}}{\partial x_k} - \frac{\partial \widetilde{v}_j\overline{\tau_{jk}}}{\partial x_k} - \frac{\partial \overline{v_j''\tau_{jk}}}{\partial x_k} - \frac{\partial \overline{k_{d,k}}}{\partial x_k} = 0$$

by using the Einstein notation. All variables are spatially averaged which is not labelled explicitly. The Favré average in time is marked with a tilde, the fluctuation with two primes: $\varphi = \widetilde{\varphi} + \varphi''$. In the equations, v is the velocity, p is the pressure, τ is the tensor of viscous stresses, e is the internal energy, h is the enthalpy, k_d is

the thermal diffusion and μ is the dynamic viscosity. The porous variables are the porosity ϕ, permeability κ and the Forchheimer coefficient c_F.

The following simplifications which were used: The correlations between spatial fluctuations are negligible [2] and the additional integrals which appear after spatial averaging can be modelled by the Darcy- and Forchheimer term. A further simplification of the energy equation is setting the thermal diffusion at the pore surfaces to zero.

The correlations in the energy Eq. (1c) are not investigated any further here. Basically, they can be modelled with a turbulent Prandtl number Pr_t and the eddy viscosity μ_t. The main difficulty to be solved is finding an approximation for the Forchheimer term $\overline{\rho}\frac{c_F}{\sqrt{\kappa}}\widetilde{\sqrt{v_k v_k}v_i}$ and the derivation of the Reynolds stresses $\widetilde{v_i'' v_k''}$.

Getachew, Minkovycz and Lage [4] use a Taylor expansion to approximate the Forchheimer term. In here, a Taylor expansion is used in a similar way but resulting from a slightly different approach ($v_i = x\widetilde{v_i}$ where x at the reference point is 0 and the deviation from the reference point is 1) the final approximation contains more terms:

$$\overline{\rho}\frac{c_F}{\sqrt{\kappa}}\widetilde{\sqrt{v_k v_k}v_i} = \overline{\rho}\frac{c_F}{\sqrt{\kappa}}\left[\sqrt{\widetilde{v_l}\widetilde{v_l}}\cdot\widetilde{v_i} + \frac{1}{2}\frac{\widetilde{v_i}}{\sqrt{\widetilde{v_l}\widetilde{v_l}}}\widetilde{v_j'' v_j''} + \frac{\widetilde{v_j}}{\sqrt{\widetilde{v_l}\widetilde{v_l}}}\widetilde{v_i'' v_j''} - \frac{1}{2}\frac{\widetilde{v_i}\widetilde{v_j}\widetilde{v_k}}{\sqrt{(\widetilde{v_l}\widetilde{v_l})^3}}\widetilde{v_j'' v_k''}\right]. \tag{2}$$

The remaining unknows are the Reynolds stresses which have to be modelled. The modelling is done by introducing Reynolds stress transport equations. Following the principle of Wilcox in [3] and taking into account the effects of porosity the resulting Reynolds stress equations are

$$\frac{\partial\overline{\rho}\widetilde{v_i'' v_j''}}{\partial t} + \frac{\partial\overline{\rho}\widetilde{v_k}\widetilde{v_i'' v_j''}}{\partial x_k} = P_{ij} + \Phi_{ij} + D_{ij} + \varepsilon_{ij} - \overline{v_j''}\frac{\partial\overline{p}}{\partial x_i} - \overline{v_i''}\frac{\partial\overline{p}}{\partial x_j} - \mathcal{D}_{\mathrm{RS}} - \mathcal{F}_{\mathrm{RS}} \tag{3}$$

where P_{ij} is the production term, Φ_{ij} is the redistribution term, ε_{ij} is the dissipation and D_{ij} stands for diffusion. These equations also show the extension due to the Darcy term

$$\mathcal{D}_{\mathrm{RS}} = \phi\frac{\mu}{\kappa}\left[\overline{v_i''}\widetilde{v_j} + \overline{v_j''}\widetilde{v_i} + 2\overline{v_i'' v_j''}\right] \tag{4}$$

and the extension caused by the Forchheimer term

$$\mathcal{F}_{\mathrm{RS}} = \frac{c_F}{\sqrt{\kappa}}\overline{\rho}\Bigg[2\widetilde{v_i'' v_j''}\sqrt{\widetilde{v_l}\widetilde{v_l}} + \frac{\widetilde{v_j}\widetilde{v_k}}{\sqrt{\widetilde{v_l}\widetilde{v_l}}}\widetilde{v_i'' v_k''} + \frac{\widetilde{v_i}\widetilde{v_k}}{\sqrt{\widetilde{v_l}\widetilde{v_l}}}\widetilde{v_j'' v_k''} + 2\frac{\widetilde{v_k}}{\sqrt{\widetilde{v_l}\widetilde{v_l}}}\widetilde{v_i'' v_j'' v_k''} + \frac{1}{2}\frac{\widetilde{v_j}}{\sqrt{\widetilde{v_l}\widetilde{v_l}}}\widetilde{v_i'' v_k'' v_k''} + \frac{1}{2}\frac{\widetilde{v_i}}{\sqrt{\widetilde{v_l}\widetilde{v_l}}}\widetilde{v_j'' v_k'' v_k''} - \frac{1}{2}\frac{\widetilde{v_j}\widetilde{v_m}\widetilde{v_k}}{\sqrt{(\widetilde{v_l}\widetilde{v_l})^3}}\widetilde{v_i'' v_m'' v_k''} - \frac{1}{2}\frac{\widetilde{v_i}\widetilde{v_m}\widetilde{v_k}}{\sqrt{(\widetilde{v_l}\widetilde{v_l})^3}}\widetilde{v_j'' v_m'' v_k''}\Bigg]. \tag{5}$$

The influence of the Forchheimer term shown here is a Taylor expansion with 2nd order accuracy.

3 Modelling of the Interface Region

The derivation of the Navier-Stokes-equations in porous materials underlies the assumption of constant porosity ϕ. This condition does not hold at the interface area between porous and nonporous flow. As a consequence, the interface region has to be modelled. For flow directions normal to the interface plane an isentropic flow change is used:

$$\text{Mass conservation:} \quad \rho_f \cdot v_{n,f} = \phi \cdot \rho_p \cdot v_{n,p} \tag{6a}$$

$$\text{Energy conservation:} \quad \frac{\gamma}{\gamma - 1}\frac{p_f}{\rho_f} + \frac{v_f^2}{2} \frac{\gamma}{\gamma - 1}\frac{p_p}{\rho_p} + \frac{v_p^2}{2} \tag{6b}$$

$$\text{Isentropic condition:} \quad \frac{p_f}{\rho_f^{\gamma}} = \frac{p_p}{\rho_p^{\gamma}} \tag{6c}$$

The index f labels the nonporous flow and p marks porous flow. v_n is the flow velocity perpendicular to the interface and γ is the isentropic exponent. The equations are solved by the Newton method.

According to literature [2] the velocities v_t tangential to the interface are related as follows:

$$v_{t,f} = v_{t,p} \cdot \phi \tag{7}$$

This relation should be proven for compressible flow but is adopted here in order to compare the solution with analytical results available.

The widely acknowledged strategy to overcome the error of the interface models is the use of a stress jump at the interface [2, 5]:

$$\mu \cdot \frac{\partial v_{t,f}}{\partial n} - \mu \cdot \frac{\partial v_{t,p}}{\partial n} = \beta\phi\frac{\mu}{\sqrt{\kappa}} v_{t,f} \tag{8}$$

with $\frac{\partial}{\partial n}$ being the derivative in interface normal direction and β as the jump coefficient of order one. The jump condition can be seen as an additional source term at the interface which corrects the Darcy term.

4 Integration into the DLR Flow Solver TAU

The DLR TAU Code [6] is an unstructured flow solver based on the finite volume method. There are three implementation issues to provide the code with porous computation capabilities. First of all, volume source terms (Darcy- and Forchheimer) are added to the residuals of porous volume cells. This has the effect of additional flow drag inside the porous region.

Computing the fluxes at the nonporous–porous interface is implemented as central scheme. To determine the flux into the porous cell the states of the contacting nonporous cell (v_f, p_f, ...) are first transformed into dummy porous cell states ($v_{f,i}$, p_{v_i},...) which are compatible with the porous states. The transformation is accomplished by Eqs. (6) and (7) (see also Fig. 2). The central scheme for computing the mass flux $\dot{m}$ into the porous cell is then

$$\dot{m}_{\text{porous}} = \frac{1}{2}\left(\rho_p \cdot v_{n,p} + \rho_{f,i} \cdot v_{n,f,i}\right) \cdot A \cdot \phi \ . \tag{9}$$

The same scheme is applied to the momentum and energy equations over the interface. The viscous forces also need a transformation of velocity gradients. They are scaled by the relation

$$\frac{\partial v_{f,i}}{\partial x_j} = \frac{v_f}{v_{f,i}} \cdot \frac{\partial v_f}{\partial x_j}. \tag{10}$$

The flux into the nonporous interface cell is determined the same way as described for the flux into the porous cells but with the porous flow conditions transformed to nonporous conditions (Fig. 2 to the bottom right).

The third step of integrating porous material into TAU is correcting the residuals of the interface cells to fulfill the jump condition (8). This is accomplished by adding an additional force as source term to both interface cells. The additional force leads to a kink in the velocity profile which is equal to a stress jump (see Fig. 3).

5 Verification Computations

As first verification experiment which can be compared easily with well known solutions serves a channel flow where the first part is nonporous and the second part is filled completely with porous material. It is clear that as long as the flow is incompressible the velocity between the pores has to increase by the factor of $\frac{1}{\phi}$ as the effective flow area decreases by the factor of ϕ. If the channel walls are

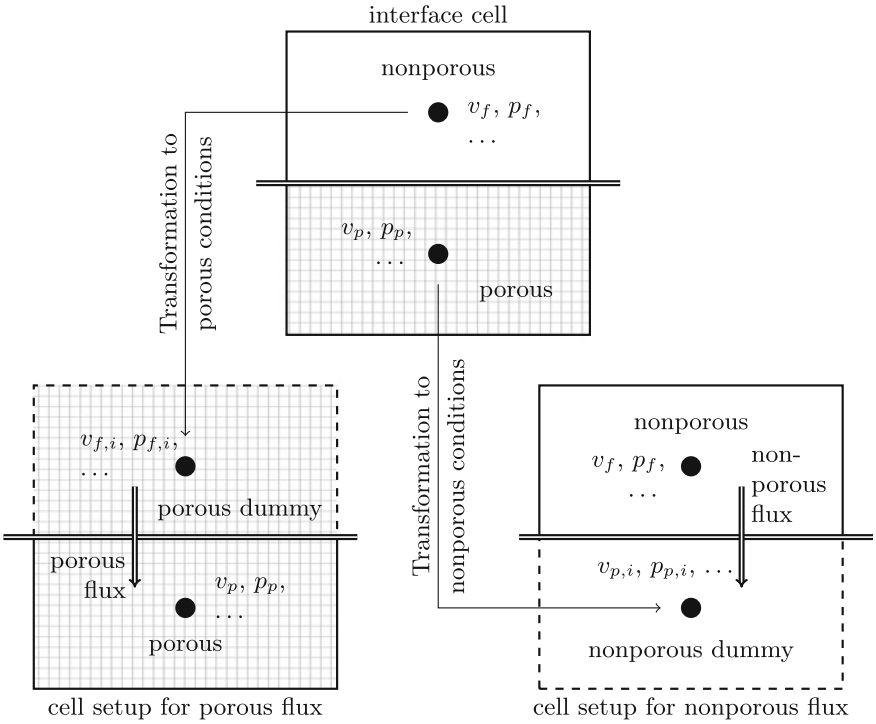

Fig. 2 Flux computation at nonporous–porous interface. Transformation to porous/nonporous conditions is based on Eqs. (6) and (7)

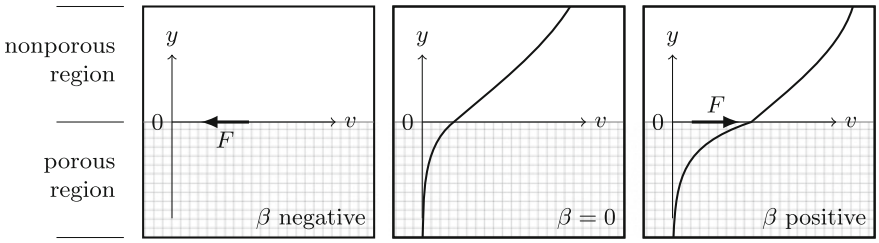

Fig. 3 Correction of boundary layer shape by additional source term to fulfil the jump condition

defined using slip wall boundary conditions pressure losses will only occur inside the porous region. The theoretical pressure decrease can be compared with the theory of Darcy. The results using the modified TAU-Code are demonstrated in Fig. 4. As the porosity ϕ is 0.5, the velocity doubles from 2.6 to 5.6 m/s at the nonporous–porous interface. There is also a small pressure jump at the interface which is hard to see due to the low kinetic energy in the flow. However, the effect of the pressure drop inside the porous region is visible very well. The theory of Darcy yields

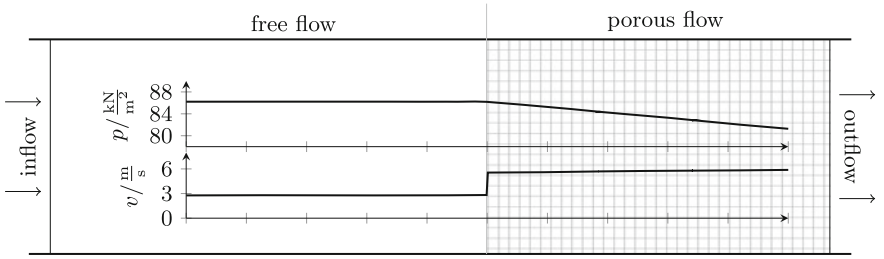

Fig. 4 Channel flow with the *right* part being filled with porous material (porosity $\phi = 0.5$). The diagrams show the pressure p and velocity v along the channel

$$\Delta p = \phi \cdot \frac{\mu}{\kappa} \cdot v_p \cdot l_{\text{channel}} = 0.5 \cdot \frac{1.74 \cdot 10^{-5}\,\text{kg s/m}}{1 \cdot 10^{-8}\,1/\text{m}^2} \cdot 5.7\,\text{m/s} \cdot 1\,\text{m} = 4959\,\text{N/m}^2. \tag{11}$$

The pressure drop on the CFD results is $4{,}947\,\text{N/m}^2$ which is almost equal. The small difference occurs as the CFD results are based on compressible equations.

An evaluation of a boundary layer flow can serve as a second verification case. Breugem [2] showed an analytical way for computing a laminar boundary layer over a porous region. His theory is based on the Blasius boundary layer with a porous wall correction. The ordinary differential equations which describe the boundary layer are

$$f_0''' + f_0 f_0'' = 0 \tag{12a}$$

$$f1''' + f_1'' f_0 + f_0' f_1' = 0 \tag{12b}$$

with the boundary conditions

$$\begin{aligned} \eta = 0: \quad & f_0' = 0 \quad & f_1' = f_0'' \\ & f_0 = 0 \quad & f_1 = 0 \\ \eta \to \infty: \quad & f_0' \to 1 \quad & f_1' \to 0 \end{aligned}$$

and are solved by a shooting method. The dimensionless variables f_0, f_1 and η define the wall distance y and flow velocity v according to

$$y = \eta \cdot \delta \qquad \text{with} \quad \delta = \sqrt{2\frac{x \cdot \mu V_\infty}{\rho}}$$

$$v_{\text{nonporous}} = V_\infty \cdot (f_0' + \kappa f_1')$$

$$v_{\text{porous}} = \frac{1}{\phi} V_\infty f_1'(0) \cdot e^{\left(\frac{\sqrt{\phi}\eta}{a \cdot b}\right)} \qquad \text{with} \quad a = \frac{1}{\sqrt{\phi}} - \beta \text{ and } b = \frac{\sqrt{K}}{a\delta}$$

A comparison of the analytical results with the TAU solutions is shown in Fig. 5. The differences between the two curves are very small demonstrating the correct TAU implementation.

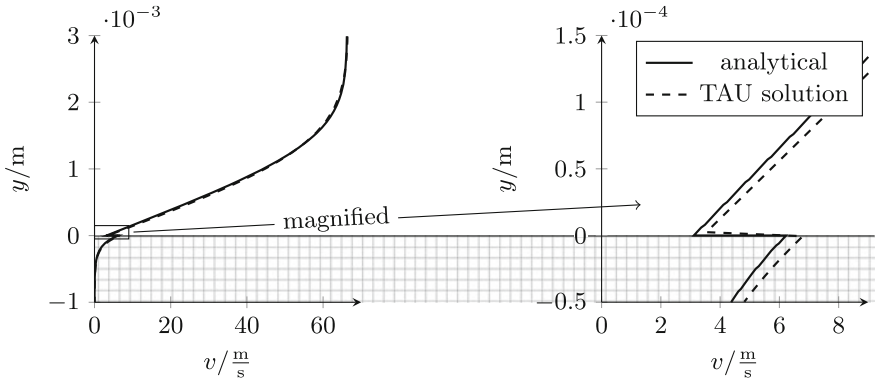

Fig. 5 Comparison of porous boundary layers at a jump coefficient $\beta = 0$

6 Conclusion

A theory to compute compressible flow through porous material has been presented. That includes the Reynolds stress equation in porous material which are needed for turbulent flows. The basic principles for the derivation of the equations are spatial and time averaging. This procedure avoids the need for resolving the porous structure and the turbulent time scales. Instead unknown terms are emerging which are modelled by the Darcy and Forchheimer term. These terms can also be found in the Reynolds stress equations which are needed for turbulence modelling.

Besides the modelling of terms inside the porous material the interface region between nonporous and porous flow has to be modelled in a suited way. This is necessary as the porosity is not constant at the interface region. The modelling strategy is the assumption of isentropic flow change over the interface area. The error which occurs through the assumptions is compensated by a stress jump condition which conforms with literature.

The theoretical derivations are followed by a description about the implementation of the equations into a flow solver. Virtual states have to be computed at the interface to determine the fluxes. The implementation is verified by channel and boundary layer flows. Therefore, reference cases can be found in the literature which show the implementation to be correct.

Further verifications will need DNS computations to prove the models used are valid. Especially, the interface conditions tangential to the wall have to be checked. Turbulent cases will also be verified in future.

The resulting extension of the TAU code will provide the ability to predict the aerodynamic behaviour of shapes like airfoils and wings with porous regions.

References

1. Herr, M.: Design criteria for low-noise trailing-edges, DLR, German aerospace Center, 38108 Braunschweig (2007)
2. Breugem, W.P.: The influence of wall permeability on laminar and turbulent flows. PhD thesis, Technische universiteit delft (2005)
3. Wilcox, D.C.: Turbulence modeling for CFD, 3rd edn. DCW industries, La Canada Flintridge (2006)
4. Getachew, D., Minkowycz, W.J., Lage, J.L.: A modified form of the $\kappa - \varepsilon$ model for turbulent flows of an incompressible fluid in porous media. Int. J. Heat Mass Transf. **43**, 2909–2915 (2000)
5. de Lemos, M.J.S., Silva, R.A.: Turbulent flow over a layer of a highly permeable medium simulated with a diffusion-jump model for the interface. Int. J. Heat Mass Transf. **49**, 546–556 (2006)
6. Schwamborn, D., Gerhold, T., Heinrich, R.: The dlr tau-code: recent applications in research and industry. In: Wesseling, P., Oñate, E., Périaux, J. (eds.) ECCOMAS CFD 06. TU Delft, Delft (2006)

Evaluation of Hybrid RANS/LES Methods for Computing Flow over a Prolate Spheroid

Sunil Lakshmipathy

Abstract The objective of the current study is towards comparative assessment of the performance of hybrid RANS/LES turbulence models in predicting flow over a 6:1 prolate spheroid. Two hybrid RANS/LES turbulence models formulated in seamless framework are assessed for their predictive capabilities in performing aerodynamic analysis of the prolate spheroid geometry at relatively low angles of attack. The turbulence models of interest in this study are the Partially-Averaged Navier Stokes (PANS) of Girimaji and Scale-Adaptive Simulations (SAS) method of Menter. PANS and SAS model computations of flow over the prolate spheroid geometry are performed at incidence angles of 10° and 20° to match the experimental flow conditions of Kreplin, and Chesnakas and Simpson, respectively. Distribution of the surface quantities at various sections are reported. The agreement between the computations and the experimental data improve for the higher incidence angle.

1 Introduction

Flow around a 6:1 prolate spheroid has been a representative geometry towards performing numerical analysis of varied engineering applications such as underwater hulls [1], missile bodies [2], and airship [3] geometries. Flow dynamics for this test case are complicated and three-dimensional. The attached laminar boundary layer on the windward side transitions to turbulence over the hull body and separates on the lee side due to azimuthal variation of the adverse pressure gradient. The separated flow rolls up to form coherent streamwise vortices on either side of the spheroid body. At higher incidences, the primary vortices drive a secondary vortex system adjacent to the wall that separate and re-attach at the top end of the spheroid. The complexity of the flow in the leeward side increases due to multiple regions of flow separation

S. Lakshmipathy (✉)
German Aerospace Center, Lilienthalplatz 7, 38108 Braunschweig, Germany
e-mail: l.sunil@gmail.com

A. Dillmann et al. (eds.), *New Results in Numerical and Experimental Fluid Mechanics IX*,
Notes on Numerical Fluid Mechanics and Multidisciplinary Design 124,
DOI: 10.1007/978-3-319-03158-3_48,

and re-attachment as the angle of attack is increased. Therefore it is critical to have a simulation methodology that is capable of predicting accurate results for a wide range of incidence angles.

Flow around prolate spheroid has been subjected to both experimental and numerical analysis for various flow conditions. Kreplin [4] reported experimental data for three flow conditions, all pertaining to fairly high Reynolds numbers based on the spheroid hull length. Studies were performed to examine the flow field and the boundary layer development for both free transition and fixed transition cases. The reported data included detailed surface pressure, skin friction coefficient measurement, and velocity field measurement at several axial stations. Chesnakas and Simpson [5], and Wetzel et al. [6] sought to characterize the three-dimensional separation on the lee side of the spheroid through experimental techniques. They noted that eddy-viscosity based models would not be suitable to compute the spheroid flow as there is very little correlation between the strain rate and the turbulent shear stress for this flow. Numerical analysis using a variety of turbulence models have been performed for the spheroid geometry. Tsai and Whitney [2] and Omari et al. [3] presented $k-\epsilon$ based RANS results for the spheroid test case. Hedin et al. [7] and Fureby et al. [8] performed both conventional large eddy simulations (LES) and monotone integrated LES (MILES) to study the feasibility of using LES and its alternatives for such flows of practical relevance. Alin et al. [1] performed computations on the spheroid geometry using very large eddy simulations (VLES) approach. The aim of the study was to validate their VLES approach for underwater hull configurations. Omari et al. [3], in addition to RANS results also reported LES results for the spheroid test case in the context of showing the necessity of computing such flows using scale-resolving methods. Spalart-Allmaras based detached eddy simulations (DES) were performed by Constantinescu et al. [9] as well as Xiao et al. [10]. They both concluded that the advantages of using DES were only apparent for higher incidence angles as at lower angles the instabilities generated on the lee side of the spheroid geometry are not too significant.

The current study is our on-going effort to develop robust simulation capabilities in performing scale resolving simulations at reasonable computational costs. We perform a comparative assessment of two seamless hybrid RANS/LES approaches, namely partially-averaged Navier Stokes (PANS) method proposed by Girimaji [11] and scale-adaptive simulations (SAS) method proposed by Menter and Egorov [12], in simulating the turbulent flow over a prolate spheroid. These models aim to resolve a fraction of the flow by reducing the modeled eddy viscosity to levels lower than that of an equivalent unsteady RANS (URANS) computation. Closure for the unresolved scales in both the turbulence models is achieved by solving the modified RANS equations [11, 12]. In PANS, the reduction in modeled eddy viscosity is achieved by modifying the dissipation rate transport equation to reduce its destruction through appropriate modification of the destruction term coefficient. In SAS, the reduction in modeled eddy viscosity is achieved by adding an additional production term to the dissipation rate transport equation. The modifications in both these methods are independent of any explicit appearance of grid scales and are very easy to implement in existing RANS solvers

2 PANS and SAS Model Formulations

Both PANS and SAS turbulence models are formulated with the capability to be used with different background RANS models and in the current study, these models are implemented into the DLR TAU code [13] with Menter SST turbulence model as the base RANS model.

The detailed formulations of the PANS and SAS turbulence models used in the current study are presented in references [12] and [14], respectively. The PANS model implementation is simplified by keeping the resolution control parameter, f_k constant throughout the flow domain. A varying f_k would necessitate solving an additional transport equation for f_k to minimize introducing commutation errors in the solution process. One of the key factors in the implementation of the SAS turbulence model is the calculation of the Von Kármán length scale which includes calculating the second velocity gradients. To compute the second velocity gradients we use a three-point stencil as suggested by Menter and Egorov [12]. The numerical settings which include coefficients for the anisotropic artificial dissipation, and the Smagorinsky coefficient (C_S) of the SAS model used to compute the spheroid test case were obtained through calibration studies performed on the decaying homogeneous isotropic (DHIT) test case as recommended by Menter and Egorov [12].

3 Results

Computations of the flow over the prolate spheroid geometry are performed using the DLR TAU code [13], an edge-based, hybrid, unstructured, compressible flow solver that has been validated extensively for aeronautical applications. The numerical settings to compute this flow include using Jameson-type central scheme with anisotropic artificial dissipation for spatial discretization of the mean flow equations. The turbulent convective fluxes are discretized using a second-order upwind scheme. Source terms in the turbulence model equations are treated implicitly. Time-stepping of the mean flow equations is performed using implicit LU-SGS scheme with dual time-stepping. Multigrid smoother is employed to accelerate the solution of the inner iterations. Two reference flow conditions have been considered in this study.

3.1 Test Case 1: $Re_\infty = 7.7 \times 10^6$, $Ma = 0.16$, $AoA = 10°$

The flow conditions for this test case are based on the experimental studies performed by Kreplin [4]. The computational domain consisted of an outer sphere of radius 20 times the major axis length with the spheroid geometry placed at the center of the sphere. A hybrid unstructured mesh generated to discretize the computational domain has about 4.3×10^6 points. The near-field mesh consists of hexahedral prismatic layers

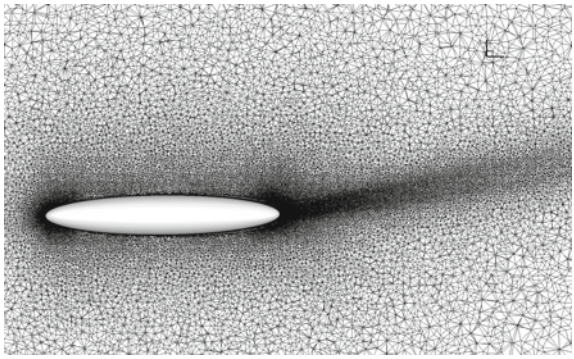

Fig. 1 Grid details on the symmetry plane

growing in the wall normal direction from the spheroid surface. The grid in the far-field consists of tetrahedral elements. Details of the mesh on the symmetry plane are presented in Fig. 1. The height of the first grid cell in the wall normal direction is sufficiently fine to resolve the laminar region of the boundary layer ($y^+ < 1$). Far-field boundary conditions are imposed on the outer sphere. The spheroid is treated as a no-slip adiabatic wall. A laminar zone is prescribed for the first 20 % of the spheroid hull.

Flow Pattern: Figure 2 shows the flow pattern on the leeward side of the spheroid as predicted by the different models. At this low incidence angle, the flow is attached over a large portion of the geometry and the primary vortex is fairly flat. PANS computations produce a stronger counter-rotating vortex pair compared to SAS and URANS predictions.

The primary vortex pair for the PANS computations detach from the spheroid body at a shallower azimuthal angle compared to SAS and URANS predictions. The primary vortex separation angle decreases further as f_k value is reduced. Also, the PANS model with $f_k = 0.4$ predicts formation of smaller secondary vortices in addition to the primary counter-rotating vorticity pair leading to a more chaotic flow downstream of the spheroid hull. SAS model prediction for the flow pattern shows a well defined primary vortex pair emanating from the leeward side of the spheroid body. The computed URANS results also show a steady primary vortex pair detaching from the leeward side of the hull and dissipating further downstream. The high unsteadiness in the PANS results is caused due to lower modeled eddy viscosity by PANS computations compared to SAS and URANS. SAS model reduces the modeled eddy viscosity as intended to resolve more scales in the separated wake region. PANS results show much lower eddy viscosity levels than the SAS model predictions as the PANS filtering parameter is active in the boundary layer region as well.

Skin Friction Coefficient: Azimuthal variation of the skin friction coefficient (C_f) at three different streamwise locations are plotted in Fig. 3. The difference between

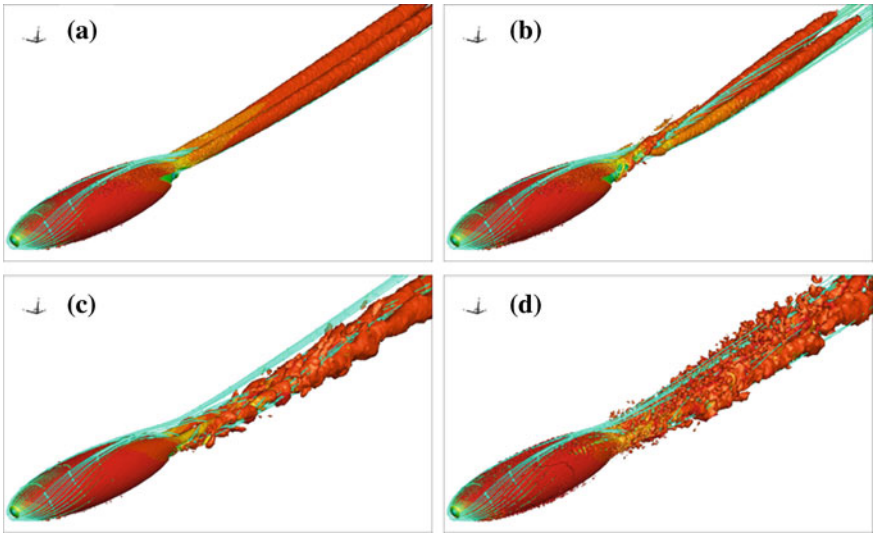

Fig. 2 Iso Q-criterion contours **a** URANS **b** SAS **c** PANS ($f_k = 0.5$) **d** PANS ($f_k = 0.4$)

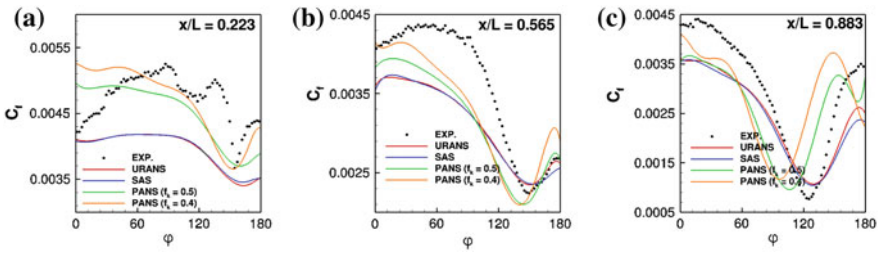

Fig. 3 Azimuthal distribution of C_f **a** $x/L = 0.223$ **b** $x/L = 0.565$ **c** $x/L = 0.883$

the URANS and SAS model predictions are minimal. At the later sections, both the URANS and SAS model predictions capture the trend as observed by the experiments in that they predict no secondary separation and re-attachment for this incidence angle. Wetzel et al. [6] note that the azimuthal separation angle is in very good correlation with the local minima of the C_f. The URANS and SAS results predict the C_f local minima in general agreement with the experimental data. However, the magnitude of C_f at low azimuthal angles (φ) is under-predicted compared to experimental data. At the fore section ($x/L = 0.223$), the PANS results are over-predicted compared to the experimental data at low azimuthal angles. However, on the upper side of the spheroid, PANS with $f_k = 0.4$ shows improved prediction. At $x/L = 0.883$, the PANS results suffer from a phase shift. They show the primary separation to occur at a much lower azimuthal angle compared to the experimental data and the compared numerical results.

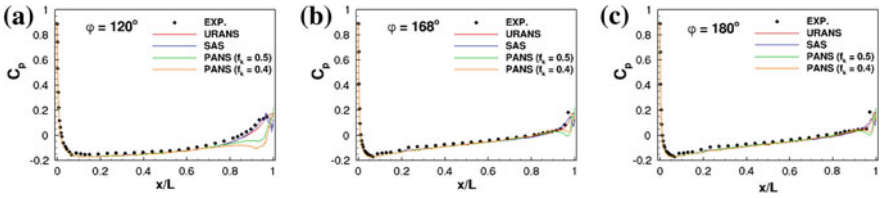

Fig. 4 C_p distribution along streamwise cuts **a** $\varphi = 120°$ **b** $\varphi = 168°$ **c** $\varphi = 180°$

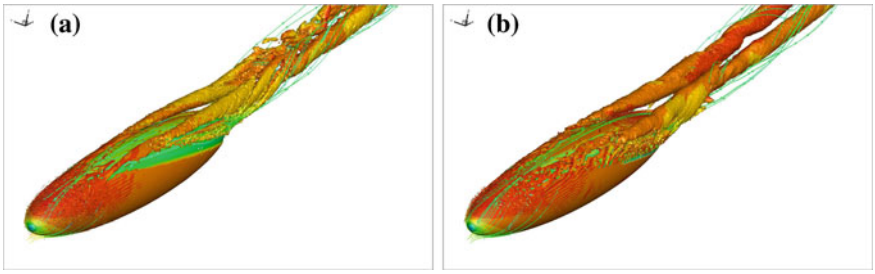

Fig. 5 Iso surface of Q-criterion **a** SAS **b** PANS

Coefficient of Pressure: Distribution of coefficient of pressure (C_p) at different streamwise cuts are presented in Fig. 4 and compared with the data of Kreplin [4]. Unlike the C_f distribution, the computational data for URANS, PANS and SAS show similarity in the C_p distribution for a major portion of the hull length. On the leeward side, the PANS model results show a deviation from the experimental data as the primary vortex is too close to the hull and separation is delayed. URANS and SAS capture the correct trend with the SAS model showing the best agreement with the experimental data for the majority of the hull length for three angles plotted.

3.2 Test Case 2: $Re_\infty = 4.2 \times 10^6$, $Ma = 0.135$, $AoA = 20°$

The second test considered in this study is at a higher angle of attack of 20°. The flow on the downstream leeward side is more complicated with the primary vortex strong enough to drive a secondary vortex pair on either side as reported in the experimental observation. The flow conditions for this test case were set-up to match the experimental condition of Chesnakas and Simpson [5]. As in test case 1, a laminar zone is prescribed for the first 20 % of the hull length in agreement with the experimental set-up. URANS results have not been reported for this test case.

Flow Pattern: The emanating counter-rotating vortices from the spheroid hull are visualized for the SAS and PANS models in Fig. 5. The SAS and PANS results predict a secondary vortex system emerging from the spheroid leeward side. SAS

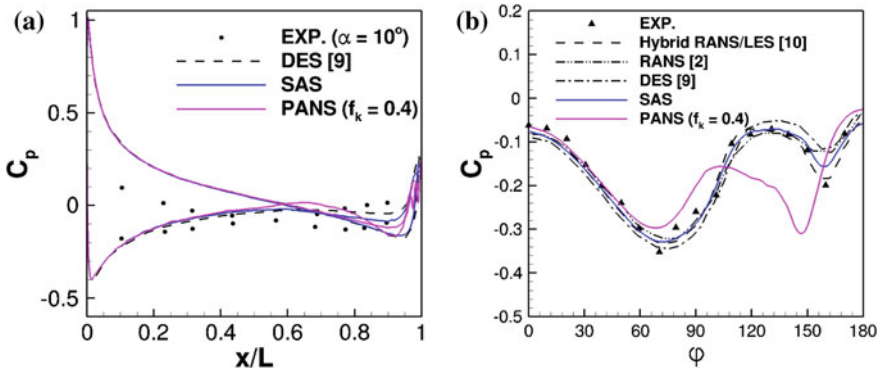

Fig. 6 C_p distribution **a** $y/L = 0$ **b** $x/L = 0.77$

shows increased turning of the primary vortices and a subsequent break-down in the wake region. The primary vortices, in the case of PANS results separate from the spheroid hull at a much sideward angle compared to the SAS results.

Coefficient of Pressure (C_P): Distribution of C_p on the symmetry plane is presented in Fig. 6a. The experimental data in this figure is from $\alpha = 10°$. Reference DES result of Constantainescu [9] who reported this data for the $\alpha = 20°$ is plotted alongside. SAS results show good agreement with the DES results on the windward side for the entire hull length whereas the PANS results plotted deviates from the SAS and DES predictions close to the downstream trailing end of the spheroid. On the leeward side, the SAS results predict higher suction pressure in comparison to reference DES results for $x/L > 0.7$. PANS results show a different trend for the C_p variation on the leeward side compared the SAS and DES results. The C_p distribution at $x/L = 0.77$ presented in Fig. 6b shows that the SAS model predictions are more accurate than the DES results plotted. Though the C_p trough at $\varphi = 150°$ is under-predicted, the SAS results agree with the experimental data for the azimuthal angle at which the dip occurs. At $x/L = 0.77$, PANS results do not capture the general trend for the C_p distribution and the suction pressure on the leeward side is over-predicted

Coefficient of Friction (C_f): Figure 7 shows plots of azimuthal variation of the skin friction distribution at two different x-planes. At $x/L = 0.6$ (Fig. 7a), the SAS results show better agreement with the experimental data than the reference RANS results of Tsai and Whitney [2] on the leeward side. The local minima is located close to the experimental observed azimuthal angle and the SAS results present a second dip in the C_f values, at about $\varphi = 150°$. PANS results capture the general trend by predicting two local minima. However, the levels of C_f predicted is off in comparisons to the SAS results and the reference data plotted. At $x/L = 0.77$ (Fig. 7b), the SAS predictions are in very good agreement with experimental data for the entire azimuthal angle variation on the leeward side. The SAS model predicts the

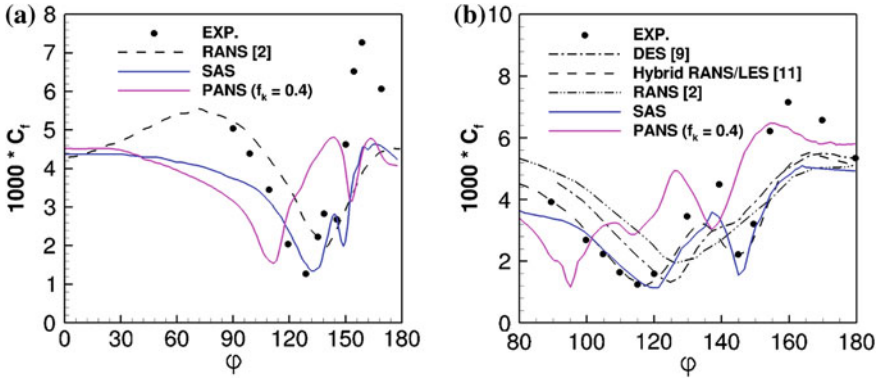

Fig. 7 C_f distribution **a** $x/L = 0.6$ **b** $x/L = 0.77$

right levels for the local C_f minima, at both the primary and secondary separation locations. The PANS results fail to capture the correct trend and phase-shift for the primary and secondary separation angles is exaggerated at this section.

4 Concluding Remarks

Flow over a prolate spheroid has been used as one of the test cases to benchmark the performance of PANS and SAS turbulence models in the DLR TAU code. Both these methods are easy to implement into existing RANS codes and require relatively less effort in performing scale resolving turbulent flow computations. The capability of both the models to scale up/scale down the physical fidelity of the computation depending on the available computational resources render these models highly favorable for industrial application.

The prolate spheroid flow computations performed at AoA of 10° show minimal improvement in the results when scale resolving turbulence models are used. Both SAS and URANS produce similar plots for the surface quantities. SAS model predictions show better agreement than URANS at the downstream region of the spheroid, where separation is a dominant flow feature. PANS, on the other hand fails to predict correct separation behavior. The eddy viscosity in the PANS boundary layer is altered as the scale resolving parameter is active in the entire domain. Computations performed at a higher AoA of 20° show the advantages of using scale-resolving models in comparison to averaging methods. SAS model provide very good prediction of the surface quantities, especially in regions of unsteadiness. The SAS model predictions for the surface quantities are on par with the reference RANS results plotted.

The relatively poor performance of the PANS computations could be attributed to the choice of performing the PANS computations with the fixed f_k for the entire domain. Although fixed f_k PANS computations have been performed with high

success in the past [15, 16], the test cases in these studies involved massive flow separation where the separation was due to a geometric singularity and the separation behavior in the wake was less influenced by the attached turbulent boundary layer on the upstream side. The spheroid test case shows the criticality of predicting the right asymptotic behavior of the turbulent quantities in the attached boundary layer which the constant f_k computations fail to predict. Recent studies [17] to implement a low Reynolds number correction model for the PANS equations have shown to be effective in improving the PANS model behavior in the boundary layer region. Future work will include testing a low Reynolds number correction to the PANS model.

SAS model results for the spheroid test case show the readiness of this model for future industrial application. The model formulation ensure that the SAS term is only activated in regions of unsteadiness and thereby provide correct wall limiting behavior for the turbulent quantities in the boundary layer.

References

1. Alin, N., Berglund, M., Fureby, C.: A VLES approach applied to flows around underwater vehicle hulls, vol. AIAA 00–0543, AIAA, Jan 2000
2. Tsai, C.Y., Whitney, A.K.: Numerical study of three-dimensional flow separation for a 6:1 ellipsoid, vol. AIAA 99–0172, AIAA, Jan 1999
3. Omari, K.E., Schall, E., Koobus, B., Dervieux, A.: Turbulence Modeling Challenges in Airship CFD Studies. Monografias del Seminario Matematico Garcia de Galdeano **31**, 545–554 (2004)
4. Kreplin, H.P.: Three dimensional boundary layer and flow field data of an inclined prolate spheroid. In: A Selection of Experimental Test Cases for the Validation of CFD Codes, vol. AR 303 of AGARD Advisory Report. AGARD Neuilly-Sur-Seine, pp. 96–97 (1994)
5. Chesnakas, C.J., Simpson, R.L.: Detailed investigation of the three-dimensional separation about a 6:1 prolate spheroid. AIAA J. **35**(6), 990–999 (1997)
6. Wetzel, T.G., Simpson, R.L., Chesnakas, C.J.: Measurement of three-dimensional crossflow separation. AIAA J. **36**(4), 557–564 (1998)
7. Hedin, P.O., Berglund, M., Alin, N., Fureby, C.: Large Eddy simulation of the flow around an inclined prolate spheroid, vol. AIAA 2001–1035, AIAA, Jan 2001
8. Fureby, C., Alin, N., Wikstrom, N., Menon, S., Svanstedt, N., Persson, L.: Large-Eddy simulation of high-Reynolds-number wall-bounded flows. AIAA J. **42**(3), 457–468 (2004)
9. Constantinescu, G.S., Pasinato, H., Wang, Y.Q., Forsythe, J.R., Squires, K.D.: Numerical investigation of flow past a prolate spheroid. J. Fluids Eng. **124**(4), 904–910 (2002)
10. Xiao, Z., Zhang, Y., Huang, J., Chen, H., Fu, S.: Prediction of separation flows around a 6:1 prolate spheroid using RANS/LES Hybrid approaches. ACTA MECHANICA SINICA **23**(4), 369–382 (2007)
11. Girimaji, S.S.: Partially-averaged Navier-Stokes model for turbulence: a Reynolds-averaged Navier-Stokes to direct numerical simulation bridging method. J. Appl. Mech. **73**(3), 413–421 (2006)
12. Menter, F., Egorov, Y.: The scale-adaptive simulation method for unsteady turbulent flow predictions. Part 1: theory and model description. Flow Turb Combust **85**, 113–138 (2010)
13. Schwamborn, D., Gerhold, T., Heinrich, R.: The DLR TAU code: recent applications in research and industry. In: Proceedings of the European Conference on Computational Fluid Dynamics, The Netherlands, ECCOMAS CFD 2006, pp. 1–25
14. Lakshmipathy, S., Togiti, V.: Assessment of alternative formulations for the specific-dissipation rate in RANS and variable-resolution turbulence models, vol. AIAA 2011–3978, AIAA, June 2011

15. Murthi, A., Reyes, D.A., Girimaji, S.S., Basara, B.: Turbulence transport modeling for PANS and other bridging closure approaches. In: V European Conference on Computational Fluid Dynamics, Portugal, ECCOMAS CFD 2010, pp. 1–20
16. Lakshmipathy, S., Girimaji, S.S.: Partially averaged Navier-Stokes (pans) method for turbulence simulations: flow past a circular cylinder. J. Fluids Eng. **132**(12), 121202 (2010)
17. Ma, J., Peng, S.H., Davidson, L., Wang, F.: A low Reynolds Number variant of partially-averaged Navier Stokes model for turbulence. Int. J. Heat Fluid Flow **32**(3), 652–669 (2011)

RANS-based Aerodynamic Drag and Pitching Moment Predictions for the Common Research Model

Olaf Brodersen and Simone Crippa

Abstract DLR TAU results of the fifth AIAA CFD Drag Prediction Workshop are presented. A focus is set on the grid convergence behaviour of full hexahedral and hybrid hexahedral-dominant grids. Calculated drag values are close to experimental data at the design point but differ at off-design. A short interpretation of the results and explanations for differences are given.

1 Introduction

The accurate prediction of aerodynamic forces and moments is of significant importance for aircraft design. Reynolds-averaged Navier-Stokes (RANS) based CFD has been developed over the last decades regarding robustness, efficiency, and accuracy [1]. Incremental values can be calculated with an acceptable reliability at transonic cruise design points for non-separated flows but full grid convergence was not achievable in the past. At off-design challenges still exist to compute incremental and absolute data as well as flow physics with the accuracy required. Pitching moments can be more difficult to predict accurately because small deviations in pressure distributions can cause large discrepancies compared to experimental data. Flow separations that start to develop at off-design conditions, e.g. in corner-flows can have a strong impact on the predictions of aerodynamic coefficients too. Due to these challenges a working group of the AIAA Applied Aerodynamics Technical Committee initiated in 2001 the CFD Drag Prediction Workshop (DPW) series resulting in five workshops that are documented in more than 120 papers [2–4]. The latest workshop DPW-5 took place in June 2012 and also was focused on the following objectives [5]:

O. Brodersen (✉) · S. Crippa
Institute of Aerodynamics and Flow Technology, DLR—German Aerospace Center,
38108 Braunschweig, Germany
e-mail: o.brodersen@dlr.de

A. Dillmann et al. (eds.), *New Results in Numerical and Experimental Fluid Mechanics IX*,
Notes on Numerical Fluid Mechanics and Multidisciplinary Design 124,
DOI: 10.1007/978-3-319-03158-3_49,

- Assess CFD methods as aerodynamic tools for the accurate prediction of forces and moments on industry-relevant aircraft configurations,
- Set up an international forum of experts from industry, research and academia for the verification and validation of RANS based CFD methods,
- Define areas for additional research needed,
- Build and maintain a public-domain database.

The DLR Institute of Aerodynamics and Flow Technology is supporting these objectives as a committee member since the second workshop and as a participant in all workshops [6]. In the first workshops the DLR F4 and F6 models have been used whereas for the fourth workshop (DPW-4) the Common Research Model (CRM) was designed and build by NASA, in collaboration with Boeing and the DPW committee [7]. In DPW-4 DLR had its focus on the assessment of turbulence models (Spalart-Allmaras, Menter kω-SST, SSG/LRR-ω) and two unstructured grid strategies. The grids were based on the resolution of the boundary layer with prismatic or hexahedral elements using Centaur^{TM} and Solar [8, 9]. The corner flow in the wing-fuselage junction became a topic of interest because of a very small separation (< 1 % chord) that can become important at off-design because it may increase towards a strong inboard separation that can trigger the lift break down [2, 6]. A correct prediction is necessary when CFD should be applied more for a reliable aerodynamic data production at borders of the flight envelope. Both grid methods have shown some shortcomings for corner flows because of the O-type grid topology leading to non-orthogonal grid lines and especially for Solar to large steps of element sizes between near-wall and tetrahedral elements. Based on these outcomes DLR put its focus in DPW-5 on the investigation of the grid convergence behaviour of the corner flow separation and the aerodynamic coefficients for the sequence of common grids provided by the workshop as well as three additional grid types generated by DLR.

2 Common Research Model—CRM

In DPW-5 the NASA Common Research Model (CRM) aircraft configuration without horizontal tail is used at cruise conditions ($M_\infty = 0.85$, $C_L = 0.5$, flight alt. 11.3 km), see Fig. 1. The wing with an aspect ratio and sweep of $\Lambda = 9.0$, $\varphi_{c/4} = 35.0°$, has a slightly stronger pressure recovery at the last 10–15 % local chord on the upper surface of the outboard wing section than a standard transonic wing. The objective is to reduce the strength of the boundary layer to provoke trailing edge separation and to amplify effects of turbulence models [7]. A cryogenic wind tunnel model was built by NASA and tested in two NASA wind tunnels [7, 10].

Fig. 1 NASA Common Research Model (CRM)

3 Cases

DPW-5 required two mandatory test cases at $M_\infty = 0.85$ and $Re = 5{\cdot}10^6$. Additional parameter, grid, and turbulence model variation studies were encouraged. Case 1 is the "Common Grid Study" using a sequence of common and optional custom grids at a constant lift of $C_L = 0.5 \pm 0.0001$. Case 2 is called "Buffet Study" in DPW because approximately for $\alpha \geq 4.5°$ unsteady effects begin to occur. Nevertheless in DPW only fully converged steady calculations are requested. For the medium (L3) common and custom grid a sequence of incidence angles has to be calculated between $\alpha = 2.5°$ and $\alpha = 4.0°$.

4 Computational Grids

4.1 Common Grids

A six level common grids family of point-matched O-O topology multi-block grids has been build by Boeing [11]. The sequence is based on an extra-fine grid (L5) with $40.9{\cdot}10^6$ hexahedral elements. To limit grid sizes a 2-to-3 cell grid generation strategy was applied. The L6 grid has been generated by refining L5 by 1.5 in each parameter direction. The coarser grids L4-L2 and L3-L1 have been defined by dividing the grids by 8 appropriate for multigrid [11]. Table 1 presents the grid sizes for a half model and the cases investigated.

4.2 DLR Custom Grids

Since DPW-3 DLR is investigating unstructured hybrid prismatic and hexahedral elements dominated grids [6, 12]. The hexahedral based approach offers potentially higher stretched elements and lower discretization errors compared to prismatic elements for high aspect ratio wings. Here it is one objective to further compare the grid convergence behaviour of the common grids with a hexahedral grid family generated with Solar. Because of difficulties of element sizes and shapes in corners with the

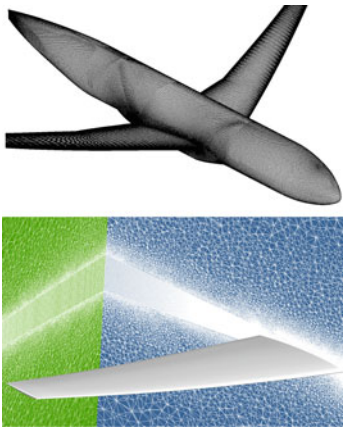

Fig. 2 Common hexahedral grid (*top*), Centaur with hexahedral wake block (*bottom*)

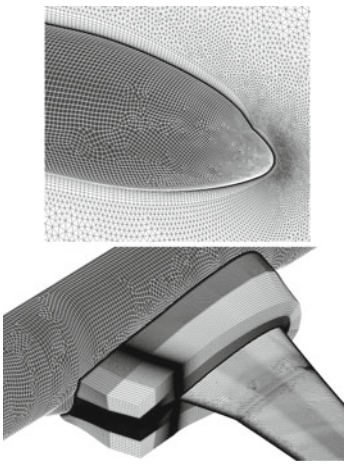

Fig. 3 Solar hex-dominant grid (*top*), Solar with hexahedral overlapping block (*bottom*)

Solar hex-dominated technique, additionally Solar plus an overlapping H-topology hexahedral grid block have been generated too. Due to the fact that Centaur^{TM} is a very mature software, that prisms dominated grids are well established at the institute, and because it offers some hexahedral element features near the walls and partly in the field another objective is to compare the results of all four grid types (common hexahedral, Solar, Solar plus overlapping hex-block, Centaur^{TM}) for Case 2. Figures 2 and 3 show the grids. Figure 4 presents the grid surface resolution in the wing fuselage junction at the trailing edge and normal to the surface. Custom grid sizes are listed in Table 1 too.

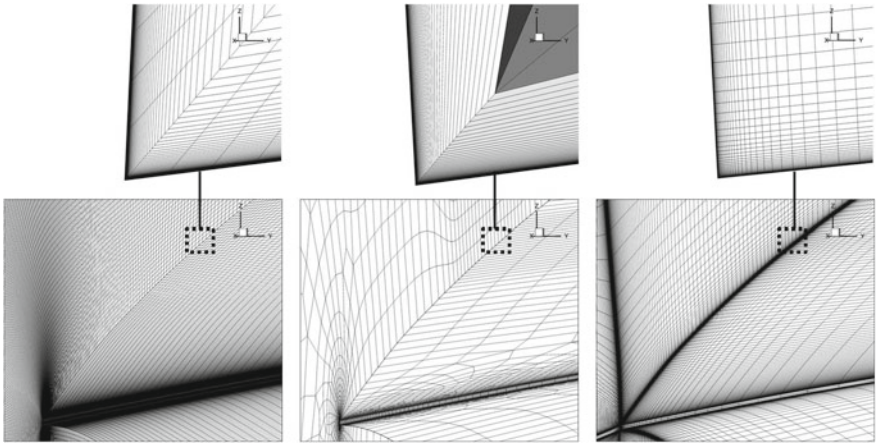

Fig. 4 Grid resolution in wing fuselage corner, common grid L6 (*left*), Solar (*middle*), and Solar plus overlapping hex block (*right*)

Table 1 Cases investigated by DLR, nodes in million (half model)

Case	Level	Common		Solar		Solar+overlapping		Centaur+hexa-wake	
		Turb	Nodes	Turb	Nodes	Turb	Nodes	Turb	Nodes
1	2	SA, $k\omega$SST	2.2	SA	3.7	SA	4.5		
	3	SA, $k\omega$SST	5.2	SA	11.0	SA	13.7	SA, $k\omega$SST	37.4
	4	SA, $k\omega$SST	17.4	SA	33.0	SA	42.2		
	5	SA, $k\omega$SST	41.2						
	6	SA, $k\omega$SST	138.8						
2	3	SA, $k\omega$SST	5.2	SA	11.0	SA	13.7	SA, $k\omega$SST	37.4

5 Reynolds-Averaged Navier-Stokes Solver TAU

Since the mid 1990s the RANS solver TAU is under development at DLR and applied by DLR, industry, and academia [13, 14]. TAU is an edge-based unstructured solver using the dual grid technique and fully exploits the advantages of hybrid grids. The numerical scheme is based on the Finite-Volume method and provides different spatial discretization schemes. Here, a central scheme of second order accuracy using the Jameson-type of artificial dissipation in scalar and matrix mode has been applied [15]. Turbulence models of different fidelity are available. The one-equation Spalart-Allmaras (SA) and the two-equations Menter $k\omega$-SST models have been applied here [16, 17]. All TAU results presented are converged to the degree required by DPW.

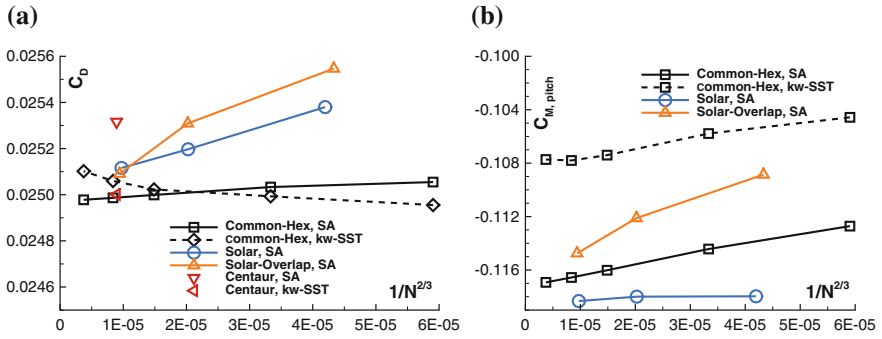

Fig. 5 Grid convergence behaviour. **a** Total drag C_D, **b** Pitching moment C_M

6 Results

6.1 Case 1

Figure 5 presents the behaviour of the drag and pitching moment coefficients for all grids including both turbulence models. Total drag shows a nearly linear behaviour for the L2 – L6 common grids. The variation is less than one drag count ($1\text{dc} = 10^{-4}$) applying the SA turbulence model. The Solar and Solar with overlapping corner grid block solutions show a larger gradient of about 2–3 dc. But all three SA solutions converge for infinite fine grids towards $C_D \approx 249.5$ dc which is close to the experimental value of the NASA NTF test ($C_D = 249$ dc). Nevertheless it has to be pointed out that the NASA Ames test resulted in $C_D = 241$ dc [18]. The solutions on the Centaur grid show a slightly higher value for the SA model of approx. 3 dc whereas with the kω-SST model the difference to the solutions on the common grid is small (<1 dc).

For the Menter kω-SST turbulence model a slightly increasing drag for finer grids is calculated for the common grids (≈1 dc) but a slightly decreasing drag on the Centaur grids (≈3 dc) compared to the SA model. The differences are caused mainly by small deviations of the pressure distributions and, to a smaller extend, by flow features, e.g. a tiny side-of-body flow separation, see Fig. 6. Figure 7 presents how the size of the tiny side-of-body separation is linked to the grid resolution and topology. The Solar grid with overlapping corner block leads to a more upstream beginning of separation whereas its size at the trailing edge is similar for the common L6 and the Solar grid with overlapping block. The calculated small differences of the flow features and of the wing pressure distributions affect the pitching moment more than the total drag, see Fig. 5. Again, the results of the Solar grid with overlapping block extrapolate to the same pitching moment as for the common grids. This stresses the fact that a good grid convergence behaviour can be achieved with this grid type.

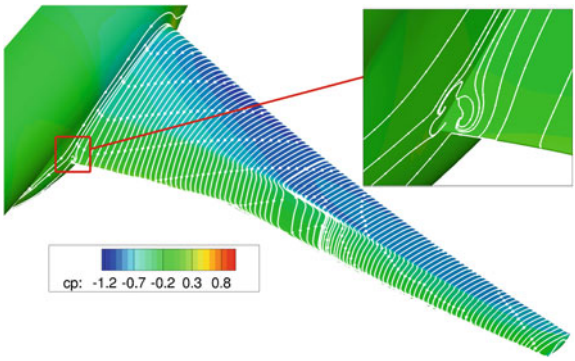

Fig. 6 Case 1: surface pressure distribution, near-wall stream lines, side-of-body flow separation

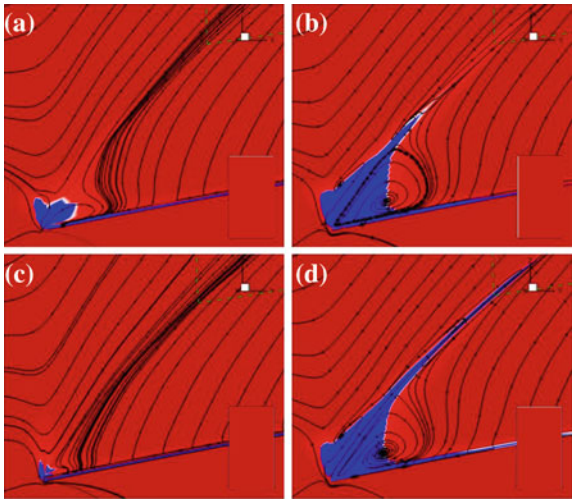

Fig. 7 Case 1: skin friction, positive (*red*), negative (*blue*), wing fuselage corner, SA model. **a** Common grid, L2, **b** Common grid, L6, **c** Solar grid, L3, **d** Solar + hex. overlap. block, L3

6.2 Case 2

Figures 8 and 9 present the lift, idealized drag, and pitching moments for all grid types and turbulence models in comparison with the NASA test data. At the design point the numerical results are close together but an offset to the experimental lift data and especially to the pitching moments can be observed. For $\alpha \geq 3.0°$ a lift break-down is calculated that starts early for fine grids or reduced numerical dissipation. Partly this is caused by the growth of the side-of-body separation. Therefore the solution on the Solar grid with corner block shows the beginning of the break-down more pronounced than the pure Solar grid. The Menter kω-SST solutions do not show this break-down at $\alpha \approx 3.0°$ but later at about $\alpha \approx 4.0°$. Nevertheless the experiments do not show any break-down at these angles. The variation of coefficients for the different grids increase at off-design ($C_L > 0.62$). It was noticed already in DPW-4

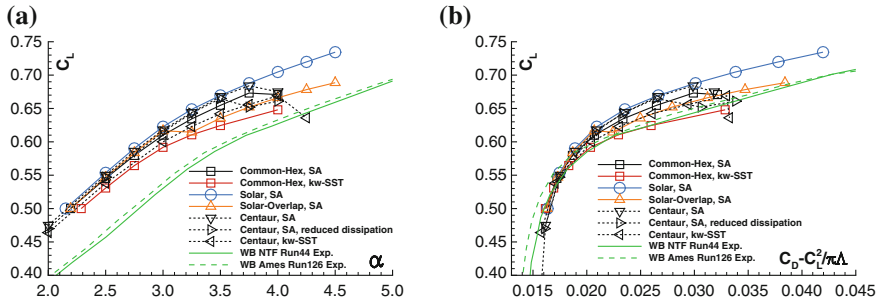

Fig. 8 Case 2: Lift and drag. **a** Lift C_L, **b** Idealized drag $C_D - C_L^2/\pi\,\Lambda$

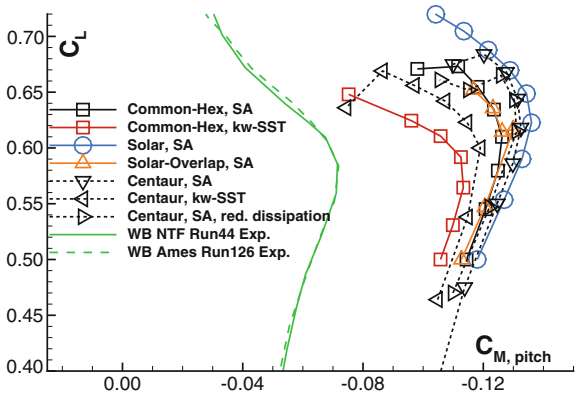

Fig. 9 Case 2: pitching moment C_M

that the trends can be computed but a significant offset exists for all participants [2]. Recent investigations by Rivers et al. have shown that this is mainly caused by the tunnel support system and a discrepancy of the experimental and CFD geometries [4].

7 Summary

The DLR objectives and results in DPW-5 to further analyse different unstructured hybrid hexahedral dominant grids regarding their grid convergence behaviour in comparison to full hexahedral element grids have been presented. In addition the focus has been set on the development of a small flow separation in the wing fuselage junction and its dependence on grid resolution and topology. The results show that the unstructured hybrid method in combination with an H-topology grid block in a corner resolves flow features in more detail and can converge towards nearly identical aerodynamic coefficients compared to a full hexahedral grid for infinite grid resolutions. At off-design conditions larger variations of the results for the different grids have been observed, basically caused by the different developments of flow

features for increasing incidence angles, e.g. side-of-body, shock-induced, and trailing edge separations. It can be concluded that further improvements of the behaviour of the turbulence models regarding early lift break-down at off-design conditions are needed.

Acknowledgments The authors would like to thank the AIAA DPW Committee for the more than 10 years of very excellent collaborations, especially the chairman J. Vassberg

References

1. Becker, K., Vassberg, J.: Numerical Aerodynamics in Transport Aircraft Design. In: Hirschel, E.-H., Krause, E. (eds.) Notes on Numerical Fluid Mechanics and Multidisciplinary Design, vol. 100, pp. 209–220. Springer (2009)
2. Vassberg, J., Tinoco, E., Mani, M., Zickuhr, T., Levy, D., Brodersen, O., Crippa, S., Wahls, R., Morrison, J., Mavriplis, D., and Murayama, M.: Summary of the fourth AIAA drag prediction workshop. AIAA Paper 2010–4547, June 2010
3. Levy, D., Laflin, K., Tinoco, E., Vassberg, J., Mani, M., Rider, B., Rumsey, C., Wahls, R., Morrison, J., Brodersen, O., Crippa, S., Mavriplis, D., and Murayama, M.: Summary of data from the fifth AIAA CFD drag prediction workshop. AIAA Paper 2013–0046, Jan 2013
4. Rivers, M., Hunter, G., Campbell, R.: Further investigation of the support system effects and wing twist on the NASA common research model. AIAA Paper 2012–3209, June 2012
5. AIAA, Drag Prediction Workshop, (online database), http://aaac.larc.nasa.gov/tsab/cfdlarc/aiaa-dpw, 2012
6. Brodersen, O., Crippa, S., Eisfeld, B., Keye, S., and Geisbauer, S.: DLR results from the fourth AIAA CFD drag prediction workshop. AIAA Paper 2010–4223, June 2010
7. Vassberg, J., DeHaan, M., Rivers, S., Wahls, R.:Development of a common research model for applied CFD validation studies. AIAA Paper 2008–6919, June 2008
8. CentaurSoft, Centaur Hybrid Grid Generation System, (online database), http://www.centaursoft.com, 2012
9. Martineau, D., Stokes, S., Munday, S., Jackson, A., Gribben, B., and Verhoeven, N.: Anisotropic hybrid mesh generation for industrial RANS applications. AIAA Paper 2006–0534, Jan 2006
10. NASA, Common Research Model, (online database), http://commonresearchmodel.larc.nasa.gov, 2012
11. Vassberg, J.: A unified baseline grid about the common research model wing-body for the fifth AIAA CFD drag prediction workshop. AIAA Paper 2011–3508, June 2011
12. Brodersen, O., Eisfeld, B., Raddatz, J., Frohnapfel, P.: DLR results from the third AIAA CFD drag prediction workshop. AIAA J. Aircr. **45**(3), 823–836 (2008)
13. Kroll, N., Rossow, C.-C., Becker, K., Thiele, F.: MEGAFLOW—A numerical flow simulation system. Aerosp. Sci. Technol. **4**, 223–237 (2000)
14. Gerhold, T., Overview of the hybrid RANS code TAU, MEGAFLOW. In: Kroll, N., Fassbender, J. (eds.) Vol. 89 of Notes on Numerical Fluid Mechanics and Multidisciplinary Design, pp. 81–92. Springer (2005)
15. Jameson, A., Schmidt, W., Turkel, E.: Numerical solution of the Euler equations by finite volume methods using Runge-Kutta time stepping schemes. AIAA Paper 81–1259, Jan 1981
16. Spalart, P., Allmaras, S.: A one-equation turbulence model for aerodynamic-flows. AIAA Paper 92–0439 (1992)
17. Menter, F.R.: Two-equation eddy-viscosity turbulence models for engineering applications. AIAA J. **32**(8), 1598–1605 (1994)
18. Rivers, M., Dittberner, A.: Experimental investigations of the NASA common research model in the NASA Langley national transonic facility and NASA ames 11-Ft transonic wind tunnel. AIAA Paper 2011–1126, Jan 2011

Aerodynamic Effects of Tip Tanks on a Swept Wing Wind-Tunnel Model

Claus-Philipp Hühne, Peter Scholz and Rolf Radespiel

Abstract This chapter discusses the effects of different wing tip devices on the aerodynamics of a swept wing. The choice of a wingtip device with a specific, required volume suited for an experimentally investigation is first discussed, followed by a detailed analysis of the wingtip flow. The flow analysis is based on numerical simulations of the RANS equations. The effects of the interaction between the wingtip and the wing on local flow separation and global aerodynamic wing loading are assessed. The results show that the design of the tip region has significant effect on the overall behavior—suited tip tanks can yield experimental configurations with useful high-lift behavior.

1 Introduction

Wing tip devices are a commonly used part of the wing in the aeronautics industry. They offer different advantages for the overall performance of an aircraft. The major benefits are increased lift and reduction or diffusion of the wing tip vortex. It appears that the effectiveness of the devices is mission and configuration dependent, thus this is still an important design field for new aircraft.

The present work is no further optimization study, which aims at finding a novel winglet geometry. Rather, the objective is to provide a suitable wing tip for high-lift wind-tunnel testing. Further the present work does not aim primarily to reduce influence on the inducted drag. Rather the geometric shape has to fulfill requirements derived from the overall objective to perform systematic tests on a swept airfoil with high-lift system with various means of flow control, including active flow control system (AFC). Previous research findings [1, 2] for the same airfoil but without sweep

C. -P. Hühne (✉) · P. Scholz · R. Radespiel
Institute of Fluid Mechanics, TU Braunschweig, Hermann-Blenk-Strae 37,
38108 Braunschweig, Germany
e-mail: c-p.huehne@tu-braunschweig.de

A. Dillmann et al. (eds.), *New Results in Numerical and Experimental Fluid Mechanics IX*,
Notes on Numerical Fluid Mechanics and Multidisciplinary Design 124,
DOI: 10.1007/978-3-319-03158-3_50,

revealed a characteristic leading edge stall. The motivation for the study presented herein is based on the approach of the accompanying experiment (see [3]). The interest is to use an existing (non-swept) airfoil model for testing of the high-lift performance of a swept airfoil. This means the experimental setup should generate "quasi-infinitely swept" conditions (so-called 2.5D setup) in the center section of the airfoil model, which is the section with pressure taps. Preliminary investigations showed that a swept wall-to-wall integration of such an airfoil is not necessarily a good configuration for 2.5D testing, because the intersection of the airfoil with the wind-tunnel wall will generate massive local separations, especially at the side where the wing appears to be forward swept (seen from the wind-tunnel wall). The integration of the model in terms of a constant-chord finite swept wing will generate the known effects of finite wings (tip vortex and thus induced flow angles), however, if the free wingtip is properly designed, local separations do not have a severe influence on the overall airfoil stall behavior. Therefore the main objective is to design a wingtip for a swept constant-chord wing that, on the one hand, gives representative 2.5D-flow in the section of the pressure taps and, on the other hand, does not feature massive local separations that might trigger premature stall. The second requirement for the wingtip results from the necessary volume at the tip, which is required to install measurement devices, such as acceleration sensors, and to enable the installation of pressure feed tubes for certain tests of the AFC system. The latter requirement can be fulfilled by a special wing tip device—a tip tank. The tip tank is commonly used in certain types of military aircraft to increase the operating range. Here, it is used to provide volume space for testing equipment.

2 Numerical Approach

The experimental and numerical investigation used as test case is the DLR-F15 two-element, high-lift airfoil with a reference chord length of $c = 600\,\text{mm}$. The wing for the wind-tunnel experiment has a sweep angle of $\Lambda = 30°$ and a half span of $S = 1800\,\text{mm}$. Previous studies show separation mechanism is strongly depend on the flap setting [1, 4] and The flap setting corresponds to Scholz et al.[1]. This caused a L/E stall at the main element, which was desired, see [3]. During the experimental work the transition was tripped by a thin $2\,\text{mm} \times 50\,\mu\text{m}$ tape to prevent laminar flow separation at the nose. Thus the simulations were run fully turbulent.

The DLR-TAU code [5] was used to perform the flow simulations. It solves the three-dimensional, compressible Reynolds-averaged Navier-Stokes (RANS) equations. For the turbulence modelling the TAU code has various options available. This work employs the one-equation Spalart Allmaras model (SA) [6]. This model was chosen due to its relatively low computational costs with good performance. Furthermore converged results can be reached in a short time. The spatial discretization in TAU can be done using different types of grids like hybrid meshes consisting of prism layers and tetrahedral mixed with hexahedral cells.

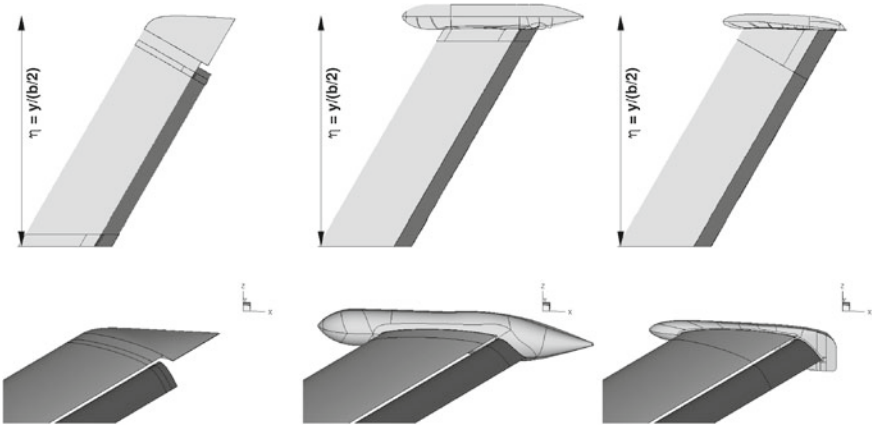

Fig. 1 Investigated wing tip geometries

Table 1 Overview of the different tip tank shapes

	Tip Tank V1	Tip Tank V2
Shape generation	Rotation about x	Individuell
Length	1500 mm	1000 mm
Thickness at wing nose	200 mm	120 mm
Thickness at flap	270 mm	225 mm

Since the results are used to compare the 3 wing tip devices, it is crucial to generate grids as similar as possible. It was ensured that a wall distance of $y+$ less than 3 is always achieved. The numerical setup used here involves the Chimera technique [7] to treat the complex geometry. The whole computational grid consists of three individual parts: wind-tunnel, wing and wing tip device. The approach has been chosen to perform the variation of the wing tip devices without a modification of the wind-tunnel and model grid. An automatic hole cut is used to insert the model grid at the desired location. In a similar way the wing tip device is attached to the model. An analysis of the interaction between the wind-tunnel wall and wing boundary layer was not intended for the current study, so that the wind-tunnel grid was fully unstructured and would be treated as Euler walls. A structured hexahedral grid resolves the region of wing boundary layer for an exact resolution of the interaction between the wing and the tip device. Furthermore the different wing tips were discretized in the same manner except the Küchemann tip. Here the near wall grid is based on an unstructured surface mesh. The number of grid points for the Chimera grid is approximately $12 \cdot 10^6$ for all configurations. The surface and boundary layer resolution depends on the results of Mahmood et al. [8], whereby it can be assumed that the results are independent from the grid.

The free-stream conditions are defined by a Reynolds number of $Re = 2.5 \cdot 10^6$ and a corresponding Mach number of $Ma = 0.18$, which corresponds to wind-tunnel testing.

3 Wing Tip Geometry

The considered wing tip devices are shown in Fig. 1. The Küchemann tip serves as a reference geometry to compare with both tip tanks. An overview of both tip tanks is given in Table 1. The first version consists of a axi-symmetric symmetric body with a local enlargement near the flap. The enlargement was defined such that a complete intersection with the fully deployed Fowler flap is possible. As a result of that, the enlargement is substantial. The second version of the tip tank is shorter and has a smaller cross section compared to the first version. The shape exhibits a an axial symmetry in the front half of the body. At the flap location it is locally constructed, such that the deployed flap intersects with the wing tip device along its whole length. Furthermore the tip is flattened at the inboard side. Thus the flap ends on a planar surface similar to an end plate.

4 Results

In order to ensure comparability with the experimental investigations, the boundary conditions of the numerical setup correspond to the experimental model. The flow behavior is evaluated at three span-wise sections which are arranged perpendicular to the leading edge. The center sections reference point is located at the span-wise position $\eta = 0.38$ at the leading edge and the outer pressure tabs reference point at row at $\eta = 0.75$ parallel to center section. The third section corresponds to the junction between the original 2D-wing-model and tip. In the further the term η is used for the position of the reference point at the leading edge

4.1 Tip Tank V1 Versus Tip Tank V2

This section discusses the difference between the two tip tank geometries. The results of both 3D cases are obtained at an angle of attack at of $\alpha = 7°$ which is around 5° below the angle of wing stall. The comparison of both geometries guides the selection of the more useful tip tank configuration. The decision is based on the requirements of the experimental investigation. Primarily the interaction between the wing and the wing tip device is an important factor, since both configurations provide sufficient space for the measurement instruments and the pressure supply. Fig. 2 illustrates the skin friction distribution at the section $\eta = 0.75$ and $\eta = 0.85$. The first version reveals flow separation at $\eta = 0.85$. This separation is triggered by the tip tank boundary layer which grows until the intersection point and strongly affects boundary layer development over the wing. Figures 2 and 3 indicate that the second version exhibits a better aerodynamic behavior. The separated flow region (grey area) close to the intersection point is reduced by approximately 75 %, due to

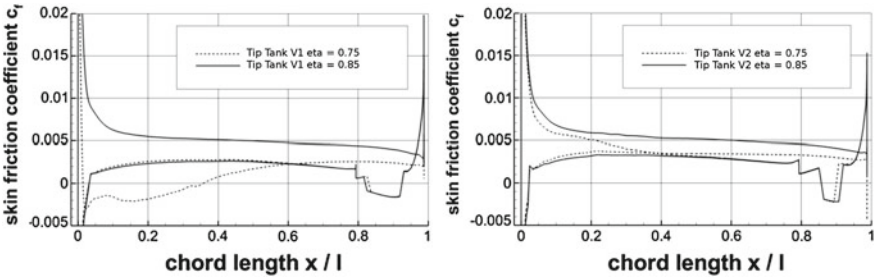

Fig. 2 Skin friction distribution for the tip tanks at two different span-wise positions, $\alpha = 7°$, $Ma = 0.18$

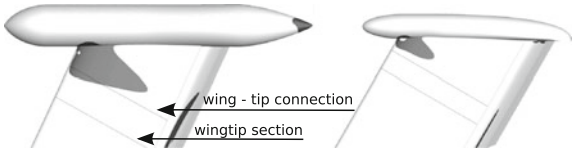

Fig. 3 Upper surface of both tip tanks, grey areas denote negative skin-friction , $\alpha = 7°$

the new shape, which has a smaller device diameter and a shorter length form the nose to the intersection point.

4.2 Aerodynamic Characteristics of the Tip Tank V2

This section provides the comparison of the tip tank V2 and the Küchemann tip. Doing so, the flow behavior at the wing tip and the effects of the tip on the stall characteristics are discussed. The center section, $\eta = 0.38$, displays a similar lift slope for both shapes in the linear regime of c_L over α, see Fig. 4, whereas the Küchemann tip is approximately $\Delta c_L = 0.15$ lower. This corresponds to a shift in the effective angle of attack of $\Delta\alpha \approx 2°$. The tip tank V2 stalls at $\alpha \approx 13°,\ 2°$ earlier then the reference tip. However, the maximum lift is for both configurations nearly equal. This suggests an effect in induced angle of attack. Inspection of the wing tip pressure section shows that the reference case separates over the whole span abruptly at the same angle of attack, as expected. This behavior is also intended for the tip tank V2. However, the distribution of the lift coefficient show that the wing tip section starts to separate earlier than the center section, as seen in Fig. 5. The lift of the reference tip increases along whole the span with increasing angle of attack. In contrast, although in the center section of the tip tank model lift increases continuously until $c_{L,\,max}$, however, a local lift decrease can already be noted at the wingtip for $\alpha \approx 12°$.

This behavior can be attributed to two effects. First the lift produced near the wing tip device is much higher at the tip tank, because the flap system is extended to the

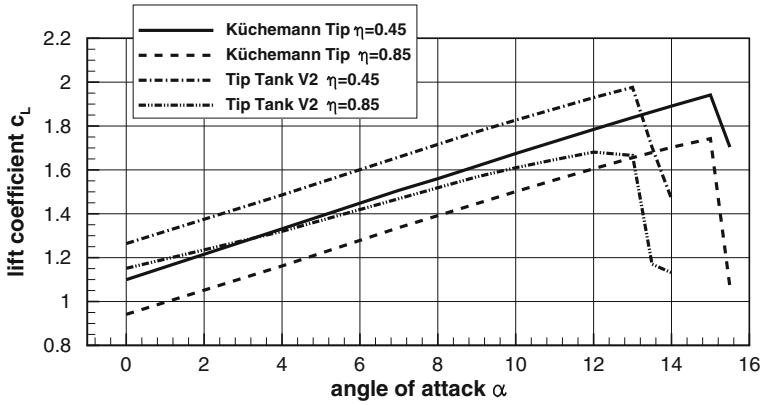

Fig. 4 Comparison of the lift coefficient between the Küchemann Tip and the tip tank V2 at center and wingtip section

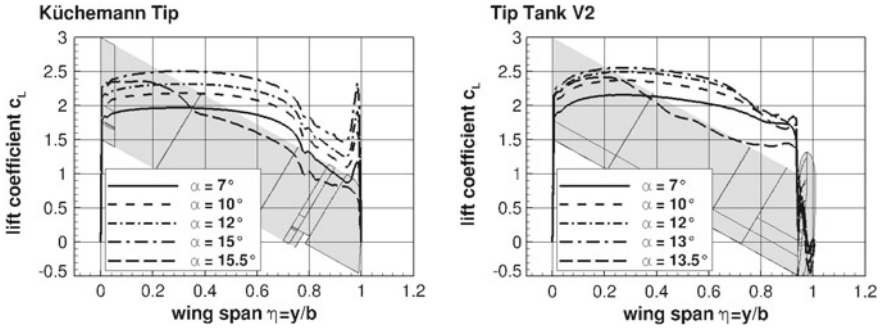

Fig. 5 Span-wise lift distribution of both wing tip devices for $\alpha = 7°$ up-to stall

tip tank. The result of this is high lift near the tip and thus a boundary layer that is subject to stronger adverse pressure gradients. Secondly the boundary layer on the wing is adversely affected by inflow of the tip tank boundary layer, which triggers the separation as mentioned in Sect. 4.1.

The question is how the tip separation affects the flow at the center section. A closer look to the lift distribution shows that the span-wise distribution is approximately equal for a range from $y/b = 0$ until $y/b = 0.6$. Both configurations reach their maximum lift of $c_L \approx 2.5$ at $y/b = 0.3$. With a further increase of the angle of attack leading edge flow separation starts and the lift distribution looks similar for both configurations. It seems that both configurations feature the intended leading edge stall at the center section. In order to confirm this findings, the pressure and skin friction distributions of the center section are shown in Fig. 6. The pressure distributions indicate a very similar flow behavior at $c_{L,max}$. The configuration incorporating the Küchemann tip shows a somewhat higher suction peak. However, the pressure gradient after reaching the minimum c_p is equal for both cases. Thus it can

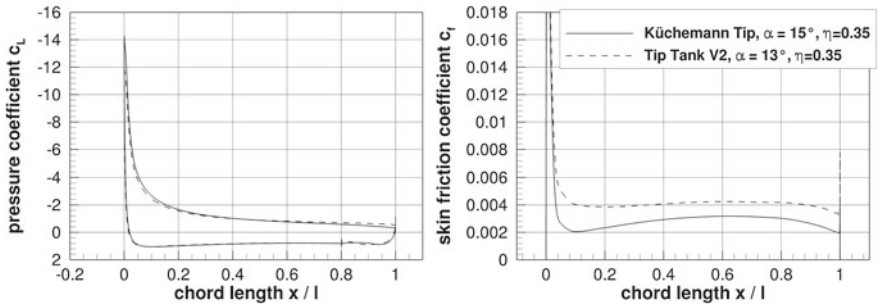

Fig. 6 Skin friction (left) and pressure (right) distribution at the center section of the Küchemann tip and tip tank at $c_{l,max}$

be assumed that both configurations stall with a leading edge separation at the center section. The same conclusion can be drawn from the skin friction distribution which is an indicator of flow separation. The shape of both curves are approximately equal with a reasonably small off-set at the nose. It must be noted that for the analysis shown in Fig. 6 one is limited to the respective AoAs that have been used in the simulations (15° for the Küchemann Tip and 13° for the Tip Tank V2, both are resolved with $\Delta - \alpha = 1°$)—thus the small offset does not mean that the aerodynamic behavior is different, but it means that the Küchemann Tip at 15° is somewhat slightly closer to stall than the Tip Tank V2 at 13°. The key statement of Fig. 6 is that both variants show a local minimum of c_f near the leading edge in the region $x/c = 0.1, \ldots 0.2$. The differences in the amount of the skin friction can be attributed to a slightly different angle of attack relative to the maximum angle of attack. This is a indicator that both are stalling with the same mechanism.

5 Conclusion

This chapter describes a numerical investigation of different wing tip devices used in 3D high lift experiments. The objective was to provide a suitable wing tip which fulfills requirements, derived from needs to perform the wind-tunnel tests. The requirements could be met by a tip tank device. For the analysis two tip tanks and a Küchemann tip were created. In comparing the two tip tanks, the aim was to identify the interaction between the tip tank and wing boundary layer at the leading edge. The first larger shape revealed flow separation at a span-wise position of $\eta = 0.85$ at $\alpha = 7°$. This separation was triggered by the tip tank inflow boundary layer. It could be shown that it is possible to reduce this separation by 75 % with a device which was smaller in diameter and less extended upstream of the leading edge. Thus, the tendency of separation of the entire model due to a wingtip induced separation can be reduced. The comparison between the smaller tip tank and the Küchemann tip was performed for a detailed analysis of the separation at intersection and the

influence of the wing tip inducted separation to the middle section. The lift slope at the center section, $\eta = 0.38$, was similar for both configurations and reached an maximum lift of $c_{L,max} \approx 1.95$. However for the reference geometry the angle of separation was shifted by $\alpha \approx 2°$ to higher angles of attack. This shift in the effective angle of attack suggests an effect of locally different induced angle of attack. Both lift slope at $\eta = 0.75$ and span-wise lift distribution of the tip tank case showed a local separation at $\alpha \approx 12°$. Thus the wingtip section stalled one degree earlier then the center section. For a range form $y/b = 0$ to $y/b = 0.6$ the span-wise distribution was approximately equal for both configurations. Furthermore the pressure distribution as well as the skin friction at $\eta = 0.38$ suggests that both configurations had the intended leading edge stall at the center section. It had been found that the tip tank triggers the separation; however, this did not affect the stall behavior at the center section.

Acknowledgments The research leading to these results has received funding from the European Community's Seventh Framework Programme (FP7/2007–2013) for the Clean Sky Joint Technology Initiative under grant agreement N 255752. The support of the Nordeutscher Verbund für Hoch- und Höchstleistungsrechnen (HLRN) by providing the computational resources is gratefully acknowledged.

References

1. Scholz, P., Kähler, C.J., Radespiel, R., Wild, J., Wichmann, G.: Active control of leading-edge separation within the German flow control network. In: 47th AIAA Aerospace Sciences Meeting (2009)
2. Casper, M., Scholz, P., Radespiel, R., Wild, J., Ciobaca, V.: Separation control on a high-lift airfoil using vortex generator jets at high Reynolds numbers. In: 41st AIAA Fluid Dynamics Conference and Exhibit (2011)
3. Hühne, C.-P., Scholz, P., Radespiel, R., Wild, J., Ciobaca, V.: Active Control of Leading Edge Flow Separation for a Swept High-Lift Airfoil, 61. Deutschen Luft- und Raumfahrtkongresses, Berlin (2012)
4. Wild, J.: Experimental investigation of Mach- and Reynolds-number dependencies of the stall behavior of 2-element and 3-element high-lift wing sections. In: 50th AIAA Aerospace Science Meeting (2012)
5. Schwamborn, D., Gerhold T., Heinrich R.: The DLR TAU-code: recent applications in research and industry. In: Wesseling, P., Oate, E., Priaux, J. (eds.) ECCOMAS CFD (2006)
6. Spalart P.R., Allmaras S.R.: A one equation turbulence model for aerodynamic flows. La Rech., Aerospatiale No.1 (1994)
7. Madrane A., Reichle A., Stuermer A.: Parallel implementation of a dynamic overset unstructured grid approach. In: ECCOMAS CFD (2004)
8. Mahmood, S., Scholz, P., Radespiel, R.: Numerical design of leading edge flow control over swept high-lift airfoil. In: 3rd CEAS Air Space Conference/21st AIDAA Congress, Venice, Italy, ID-116, 24–28 Oct 2011

Simulation of Interaction of Aircraft and Gust Using the TAU-Code

Ralf Heinrich

Abstract Two different methods for modeling of gusts have been implemented into the CFD-code TAU. The first one is the so called disturbance velocity approach, a simplified method which allows predicting the influence of a gust on the aircraft, but not the influence of the aircraft aerodynamics on the shape of the gust. Alternatively, an unsteady boundary condition has been implemented to feed in the gust into the flow field. Thereby the mutual interaction of gust and aircraft is captured. Both methods are compared in order to access the validity range of the simplified approach. A result is that for gust wavelength larger than two reference chords the agreement of the highly accurate method and simplified approach is good. For such a case the simplified approach has been used to simulate the interaction of a generic fighter aircraft with a lateral gust. Here, the reaction of the aircraft due to the additional loads has been taken into account by coupling of aerodynamics and flight-mechanics.

1 Introduction

The prediction of unsteady loads caused by atmospheric effects like gusts is essential for aircraft development. The knowledge of the additional loads arising is of importance for the design of the structure but also for the layout of the control surfaces and the Flight-Control-System (FCS). To predict these additional air-loads two different approaches for gust-modeling have been implemented in the CFD-code TAU [1].

One of these methods for modeling of gusts is the so called Disturbance Velocity Approach (DVA), see for example [2]. This method is straight forward to implement in CFD-codes and allows the usage of standard meshes, which usually are characterized by a reduced mesh resolution with growing distance from the aircraft.

R. Heinrich (✉)
$C^2A^2S^2E$ DLR, DLR Institute of Aerodynamics and Flow Technology,
Lilienthalplatz 7, 38108 Braunschweig, Germany
e-mail: ralf.heinrich@dlr.de

A. Dillmann et al. (eds.), *New Results in Numerical and Experimental Fluid Mechanics IX*,
Notes on Numerical Fluid Mechanics and Multidisciplinary Design 124,
DOI: 10.1007/978-3-319-03158-3_51,

The method captures the influence of the gust on the aircraft, but is not able to predict the feedback of the aerodynamics of the aircraft on the gust shape. Therefore, especially for gusts of short wavelength, a prediction error can be expected. To get a clearer view of the range of validity of the DVA an alternative method has been implemented in TAU: The gust can be fed into the discretized flow field using an unsteady boundary condition at the far-field boundaries. The advantage of the method is that the mutual interaction of gust and aircraft is captured, since the gust is resolved in the flow field. Therefore the abbreviation of this approach is RG in the following standing for Resolved Gust. However, a high resolution in the whole domain is required, to transport a gust from the inflow boundary to the aircraft without too much numerical losses.

In the following the DVA is described at first and, afterwards, the strategy to simulate the mutual interaction using the unsteady boundary condition. A comparison of both approaches is presented in Sect. 2.3. To demonstrate the capability of the DVA for industrial applications, the interaction of a generic fighter aircraft with a lateral gust is presented in Chap. 3. Here, this simulation the reaction of the aircraft due to the additional loads is captured by coupling of aerodynamics and flight-mechanics.

2 Gust Modeling in TAU

2.1 Disturbance Velocity Approach

To enable the simulation of an aircraft interacting with atmospheric effects, several approaches are possible. One popular method is the DVA, which has been implemented into the block structured DLR FLOWer code [3] for the simulation of the influence of wake-vortices of a large leading aircraft model on the loads of a smaller aircraft model following [2]. Good agreement to experimental data was found. Motivated by the success of this method, the DVA has now also been implemented into the hybrid TAU-code.

In this method the flux balance is slightly altered by superposition of an additional disturbance velocity field $\mathbf{v}_i$ induced by e.g. a gust. $\mathbf{v}_i$ is prescribed as a function of space and time, depending on the shape and position of the gust. The convection across the cell interface of a control volume changes from $\mathbf{v} - \mathbf{v}_b$ to $\mathbf{v} - \mathbf{v}_b - \mathbf{v}_i$. with $\mathbf{v}_b$ being the velocity of the boundary of a control volume. For example the continuity equation then changes to

$$\frac{d}{dt}\int_V \rho dV + \oint_S \rho(\mathbf{v} - \mathbf{v}_b - \mathbf{v}_i)dV = 0 \quad . \tag{1}$$

Figure 1 shows a gust with wavelength λ_{gust} moving with a speed of u_{inf} relative to an airfoil. The shape of the gust is specified as a function of the coordinate x and time t. In Fig. 1 left ($t = 0$), the gust is in front of the airfoil. The velocity $\mathbf{v}_i$ induced

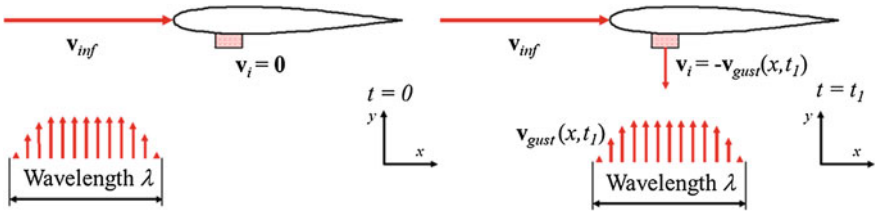

Fig. 1 Gust traveling relative to an airfoil

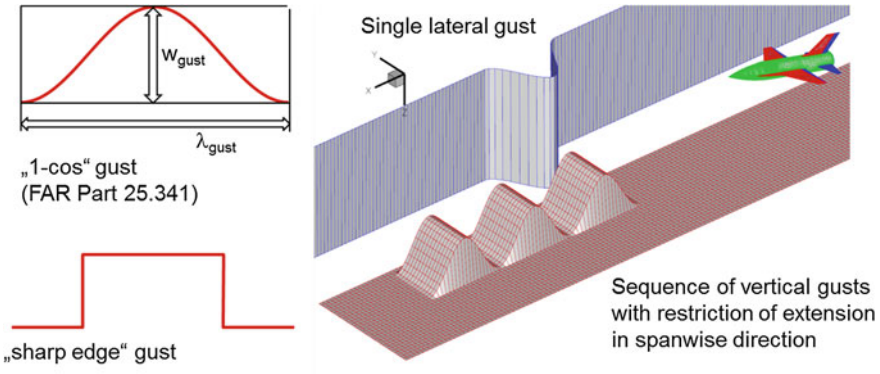

Fig. 2 *Left* Gust shapes allowed in TAU. *Right* Aircraft encountering a sequence of three vertical gusts (with restriction of the extension in spanwise direction) and a single lateral gust

by the gust at the interface of the control volume is **0**. In the right part of Fig. 1 the gust is just beneath the airfoil ($t = t_1$). The induced velocity is now equal to the amplitude of the gust. The local effect of the gust is approximately the same, as if the airfoil is moving with the negative gust vertical speed $\mathbf{v}_{gust}(x, t)$ downward. More about the motivation and verification of this method may be found in [4].

In TAU, gusts with a "1-cos" shape as described in the Federal Aviation Regulations (FAR) part 25.341 can be defined or, alternatively, sharp edge gusts, see Fig. 2 left. The amplitude of the gust w_{gust} and the wavelength λ_{gust} are input parameters. Vertical as well as lateral gusts can be specified. The user can select between isolated gusts and sequences of gusts. The extension of the gusts in spanwise direction (vertical gusts) and vertical direction (lateral gusts) can also be specified. Figure 2 right shows as example a generic fighter aircraft encountering a sequence of three vertical gusts restricted in spanwise direction and a single lateral gust.

2.2 Resolved Gust Approach

To enable the simulation of a mutual interaction of aircraft and gust, the resolution of the gust in the flow field is required. This can be realized by feeding the gust

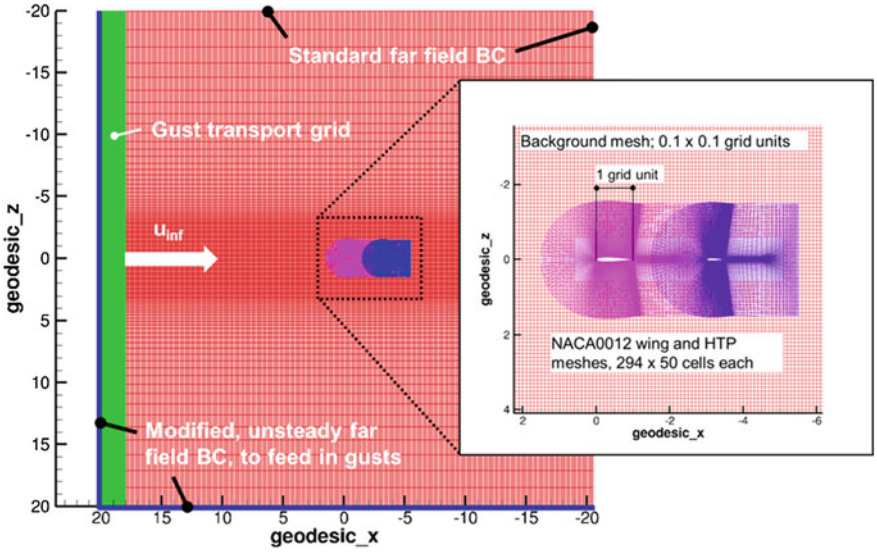

Fig. 3 Overset grid setup for simulation of interaction of wing-HTP configuration with a gust of wavelength 1 grid unit (plotted in inertial (geodesic) coordinate system)

into the flow field at the far field boundary. Therefore, in TAU, the non-reflecting far field boundary condition based on the work of Whitfield [5] has to be adapted. For this boundary condition a far field state including velocity components u_{inf}, v_{inf}, w_{inf} has to be specified at the outer side of the discretized domain. Usually these values are constant at the whole far field boundary. For gust simulations the velocity components of the far field state can now be specified as a function of space and time.

As already mentioned a disadvantage of the approach is the requirement of high spatial resolution to transport the gust without too much numerical losses, since TAU is only of 2nd order accuracy in space. To minimize the effort necessary to transport a gust through the discretized flow domain from inflow boundary to the aircraft, a technique making use of "gust-transport-meshes" has been developed. The idea behind will be described for a 2D test case, which has been set up to compare the DVA and the RG approach: The interaction of a symmetrical NACA0012 airfoil with a Horizontal Tail Plane (HTP) with a vertical gust. The reason for selection of this configuration is the expectation, that the aerodynamic of the wing will have an influence on the shape of the gust, which afterwards interacts with the HTP. This effect is not captured with the DVA, but with the RG (Resolved Gust) approach. So, if the effect is of relevance, this test case will give an answer on the magnitude of the prediction error regarding e.g. maximum loads acting on the configuration.

The grid used in this example is an overset mesh, as shown in Fig. 3. Component meshes for wing and HTP are placed into a Cartesian background mesh. The distance between inflow boundary and wing is 20 chord lengths. An additional grid (green) with a high resolution in flow direction is used for the "transport" of the gust from

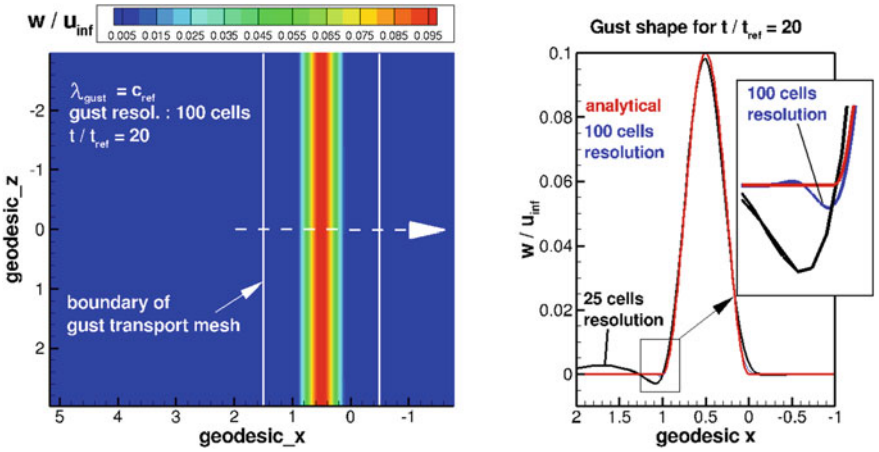

Fig. 4 *Left* Zoom-in of computed z-velocity distribution normalized with u_{inf} after gust has travelled 20 grid units. 100 cells have been used for one gust wavelength). *Right* Corresponding velocity profile for $z = 0$ for a resolution of 25 and 100 cells for one gust wavelength, compared to analytical solution (unchanged "1-cos" shape)

the far field boundary to the wing-HTP configuration. For time $t = 0$s, the gust is just in front of the computational domain. For time $t > 0$s, the gust is fed into the flow field at the left and the lower far field boundary marked blue in Fig. 3. The position of the gust transport grid is unchanged, until the gust is centered in the gust transport mesh. Afterwards the grid is starting to move with the convection velocity u_{inf} of the flow.

To find an appropriate resolution of the gust transport mesh, a grid density study has been made, using only the background grid and the gust transport grid. We assume a short gust wavelength of only one grid unit, corresponding to the reference chord length of the wing (cases with longer wavelength are less critical). As gust amplitude 10 % of the convection speed is selected. Three different resolutions in flow direction have been tested: 25, 50 and 100 cells to resolve one gust wavelength. Figure 4 left shows the z-velocity (w) distribution of a zoom-in of the flow field, after the gust has travelled already 20 chord lengths using a resolution of 100 cells for one gust wavelength. This is the travelling distance of the gust between far field and wing needed later on for comparison of DVA and RG approaches in Sect. 2.3. The contour lines are still straight lines, as could be expected for an appropriate resolution of the gust. A more detailed view of the resulting velocity profile for $z = 0$ is presented in Fig. 4 right (same z-position as of the wing-HTP configuration used in the simulations for comparison of DVA and RG approach described below). The solid red line is the analytical solution (gust shape unchanged after 20 chord lengths travelled distance). The black line shows the result using 25 cells for gust resolution. Compared to the analytical solution the amplitude of the gust is slightly reduced. Deviations from the analytical solution are especially visible left of the gust. The

Table 1 Maximum lift prediction error of DVA and RG approach

$\underline{\lambda} = \lambda / c_{ref}$	$err_{C_{L,\max}}$ [%]	
	$Ma_{inf} = 0.25$	$Ma_{inf} = 0.75$
1	1.96	10.69
2	1.17	2.72
4	0.14	0.21

blue line corresponds to the result using a resolution of 100 cells. The comparison to the analytical solution is very good (the blue line is covered almost entirely by the red line). Only minor deviations are visible at the base of the gust, see zoom-in in Fig. 4, right. For the comparison of both approaches a resolution of 100 cells is used to be on the safe side.

2.3 Comparison of Both Approaches

Computations have been made for three different gust wavelengths (1, 2 and 4 wing chord-lengths). As in the study in the previous chapter the classical "1-cos" gust shape has been selected. Two different on-flow Mach numbers are used, to allow checking the influence of compressibility. For the Mach number of $Ma_{inf} = 0.25$, we expect nearly incompressible flow, whereas compressibility effects can be expected for $Ma_{inf} = 0.75$. The gust amplitude is 10 % of the on-flow velocity. The angle of attack α is 0°. Since the airfoils of wing and HTP are symmetrical, the resulting lift is purely created by gust loading.

As measure for the prediction error of the DVA relative to the RG approach, the maximum lift found during the simulation is used:

$$err_{C_{L,\max}} = \frac{\left| C_{L,\max,RG} - C_{L,\max,DVA} \right|}{\left| C_{L,\max,RG} \right|} \tag{2}$$

The resulting errors for both Mach numbers and the three wavelengths are discussed below and summarized in Table 1. Figure 5 shows the comparison of results of the DVA (dashed lines) and the more accurate RG approach (solid line). The lift history computed for all three wavelengths is plotted versus dimensionless time. Time has been made dimensionless using the time t_{ref} of a gust needed to travel a distance of one reference chord length c_{ref} with velocity u_{inf} ($t_{ref} = c_{ref}/u_{inf}$). The agreement of the simple approach with the accurate approach predicting the mutual interaction is surprisingly good! Nearly no difference is visible for the wavelength of 4 and 2 chord length for $Ma = 0.25$. The error of the DVA for prediction of the maximum lift is only 0.14 % for $\underline{\lambda} = \lambda / c_{ref} = 4$ and 1.17 % for $\underline{\lambda} = 2$. The situation is similar for $Ma_{inf} = 0.75$, but compared to nearly incompressible flow the prediction error is higher (2.72 % for maximum lift for $\underline{\lambda} = 2$). But all in all the discrepancy between DVA and RG approach is acceptable.

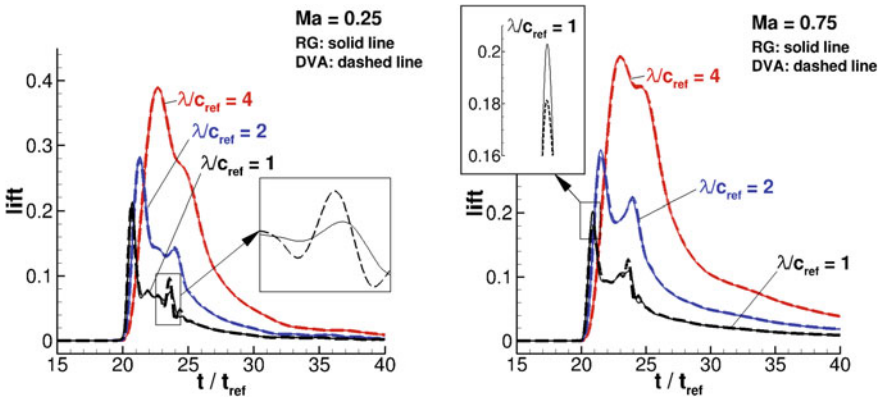

Fig. 5 Comparison of lift versus dimensionless time predicted by DVA and RG approach

A clearer difference is visible for the short wavelength of 1 chord length for dimensionless time between 23 and 25 for both Mach numbers, corresponding to the time when gust and HTP interact. The peaks are over-predicted by the DVA, since this method does not capture the effect of the wing aerodynamic on the gust shape. Additionally the maximum lift found with the DVA is under-predicted for $Ma_{inf} = 0.75$, see also zoom-in in Fig. 5 right. The error of 10.69 % is not acceptable. For the incompressible regime the error in is still below 2 %, which is acceptable.

3 Applications

3.1 Simulation of Generic Fighter Aircraft Encountering a Lateral Gust

To demonstrate the simulation of a gust encounter, as geometry the so-called SDM configuration [6] has been selected, which is a generic fighter configuration similar to an F16. We assume the aircraft is set to fly horizontally at sea level with a Mach number of $Ma_{inf} = 0.5$. We assume that the aircraft encounters a gust ("1-cos" shape) with a wavelength λ_{gust} of 30 m, which corresponds to a non-dimensional wavelength $\underline{\lambda}$ of nearly 10. In that case the DVA is a good choice for modeling the gust. The gust amplitude is $w_{gust} = 30$ m/s. To take into account the reaction of the aircraft, TAU is coupled to a six degree of freedom flight-mechanics module. For details of the coupling procedure and the flight-mechanics module, the reader is referred to [4].

Figure 6 left shows the situation when the gust is just beside the aircraft. The grey sinusoidally shaped geometry represents the position and shape of the gust relative to the aircraft. The effect of the gust is an increase of side slip angle. Therefore a lateral

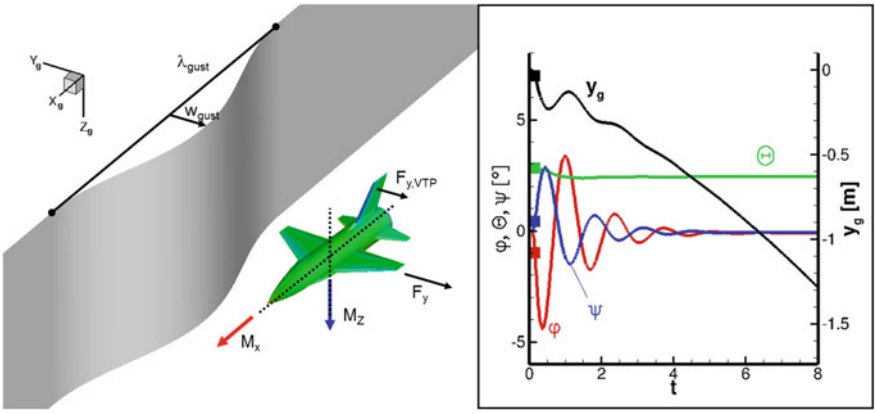

Fig. 6 Lateral gust encounter of generic fighter aircraft. *Right* History of Euler angles & lateral position of center of gravity

force F_y is created pushing the aircraft in negative y_g direction (subscript "g" stands for the geodesic inertial coordinate system). This is also a result of the simulation as can be seen in the plot of the time history in Fig. 6 right. One portion of the lateral force ($F_{y,VTP}$) is acting on the vertical tail plane, creating a rolling and a yawing moment M_x and M_z. Therefore we expect a damped yawing and rolling motion. As the gust is coming from starboard position, we do not expect a large influence on the angle of attack, the pitching moment and the pitching angle Θ. The expectations are confirmed by the computed time history of the Euler angles plotted in Fig. 6.

4 Summary and Conclusions

Two different methods for modeling of gusts have been implemented into the CFD-code TAU:

1. A simplified method called disturbance velocity approach allowing the usage of standard CFD meshes. The disadvantage is that the mutual interaction of gust and aircraft is not captured;
2. A method resolving gusts in the flow field, allowing the simulation of a mutual interaction of aircraft and gusts. They are fed into the flow field via an unsteady boundary condition. The disadvantage is that a high mesh resolution is required to resolve the gusts properly.

A comparison for a 2D wing-HTP configuration shows that the prediction quality of the simplified approach is comparable to the highly accurate method for dimensionless gust wavelengths $\lambda = \lambda/c_{ref}$ down to a value of 2. For shorter wavelengths, especially for compressible flow, the prediction error is not negligible. The applicability of the disturbance velocity approach for industrial applications has been

demonstrated for the simulation of the interaction of a generic fighter aircraft with a lateral gust. For the future it is planned to undertake a comparison of both approaches for 3D configurations with fuselage.

References

1. Schwamborn, D., Gerhold, T., Heinrich, R.: The DLR TAU-Code: recent applications in research and industry. In Proceedings of European Conference on Computational Fluid Dynamics ECCOMAS CDF 2006, Egmond aan Zee, The Netherland (2006)
2. Heinrich, R.: Numerical simulation of wake-vortex encounters using the chimera-technique. In: STAB-Symposium 2000 in Stuttgart, in New Results in Numerical and Experimental Fluid Mechanics III. Springer, Heidelberg (2002)
3. Kroll, N., Fassbender, J. K. (eds.): MEGAFLOW—Numerical Flow Simulation for Aircraft Design. Notes on Numerical Fluid Mechanics and Multidisciplinary Design (NNFM), vol. 89. Springer, Heidelberg (2005)
4. Heinrich, R., Reimer, L., Michler, A.: Multidisciplinary simulation of maneuvering aircraft interacting with atmospheric effects using the DLR TAU-code. In: RTO AVT-189 Specialists' Meeting on Assessment of Stability and Control Prediction Methods for Air and Sea Vehicles, 12–14 Oct 2011, Portsdown West, UK (2011)
5. Whitfield, D. L.: Three-dimensional unsteady Euler equation solutions using flux vector splitting, NASA contractor report NASA CR-173254 (1983)
6. S. Zan et al.: Wing and Fin Buffet on the Standard Dynamic Model, RTO Technical, Report, RTO-TR-26, pp. 361–381 (2000)

Numerical Investigation of the Magnus Effect of a Generic Projectile at Mach 3 up to 90° Angle of Attack

Daniel Klatt, Robert Hruschka and Friedrich Leopold

Abstract The subject of the present work is the investigation of the Magnus effect in the supersonic flow regime by means of 3-D Reynolds-Averaged Navier-Stokes simulations on a generic 6.37 diameter long tangential-ogive-cylinder type projectile especially for high angles of attack. The Mach number is 2.98 and the Reynolds number based on the model length is 1.09×10^7. The Magnus side force shows a nonlinear increase with the angle of attack and thus with the cross-flow Mach number before reaching a maximum value. After a slight decrease, a plateau at 10° to 30° is developed, followed by a distinct decrease of the side force for even higher angles of attack. Using numerical simulations reveals the relationship between side force and angle of attack which leads to the limiting case of a rotating cylinder in cross-flow at 90° angle of attack.

Nomenclature

A_c	Body longitudinal cross-section area, m^2
C_{y_p}	Magnus force coefficient, $F_y/q_\infty \left(\pi D^2/4\right) \overline{p}$
$C_{y_p}{}^*$	Magnus force coefficient after Eq. (1)
D	Model diameter, m
F_y	Magnus side force, N
p	Spin rate, rad/s
$\overline{p}$	Dimensionless spin rate, $pD/2U_\infty$

D. Klatt (✉) · R. Hruschka · F. Leopold
French-German Research Institute of Saint-Louis, Aerodynamic Research Group,
5 rue du General Cassagnou, BP 70034, 68301 Saint Louis Cedex, France
e-mail: daniel.klatt@isl.eu

R. Hruschka
e-mail: robert.hruschka@isl.eu

F. Leopold
e-mail: friedrich.leopold@isl.eu

A. Dillmann et al. (eds.), *New Results in Numerical and Experimental Fluid Mechanics IX*,
Notes on Numerical Fluid Mechanics and Multidisciplinary Design 124,
DOI: 10.1007/978-3-319-03158-3_52, © Springer International Publishing Switzerland 2014

P_∞	Free-stream static pressure, Pa
q_∞	Dynamic pressure, $1/2\rho\ {U_\infty}^2$
Re_D	Reynolds number based on diameter
U_∞	Free-stream velocity, m/s
α	Angle of attack, deg
ρ_∞	Free-stream density, kg/m^3

1 Introduction

Spinning slender bodies such as projectiles experience side forces and moments when exposed to cross-flow. The phenomenon is known as Magnus effect and depends on multiple parameters. These are not only spin rate and angle of attack, but also Mach and Reynolds number as well as the body shape and the surface properties. As any change of these parameters influences the state of the boundary layer, also the Magnus effect is affected. Experimental studies on free-flying [1, 2] and wind-tunnel-mounted projectiles [3–6] provide an extensive database for the validation of computational fluid dynamic (CFD) simulations [2, 7, 8] and theoretical models [4, 9] which, both aim to predict the Magnus effect.

Each approach, however, has some particular assets but also shortcomings: while wind tunnel experiments are limited in the range of accessible flow conditions, free-range tests often suffer substantial experimental uncertainty as the forces were extracted from the recorded trajectory of the projectiles and especially the side forces are small compared to other forces. Furthermore, both wind tunnel experiments and free-flight tests have their own limitations in the accessible ranges of angle of attack and spin rate. The maximum magnitudes of angle of attack investigated experimentally are around 20° [3, 6]. Using numerical simulations, angles up to 30° [8] have been investigated.

The current study is motivated by the fact that, especially during control maneuvers, guided projectiles can experience flight attitudes combining both—high angles of attack and supersonic flight Mach numbers.

Contrary to the linear dependency between incidence and Magnus effect a typical projectile shows for small angles of attack, the intermediate range between 4° and 20° is characterized by nonlinear growth up to a maximum value of the side force coefficient [3, 6].

The work presented in this paper is concentrated on numerical simulations on a generic tangential-ogive-cylinder projectile at Mach number 2.98 over the entire range of angles of attack up to 90° by means of steady-state as well as unsteady Reynolds-Averaged Navier-Stokes (RANS) simulations. The dimensionless spin rate ($\overline{p} = 0.107$) of this investigation lies within the range where Magnus effects are expected to increase linearly with the spin rate [3, 5]. While the side force coefficients for the lower angles of attack are compared to experimental wind tunnel measurements on generic projectile configurations, the range of the higher angles of attack is compared to experiments, investigating the limiting case of a cylinder in supersonic cross-flow [10] as well as to corresponding simulations.

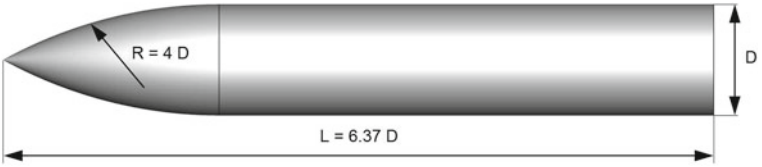

Fig. 1 Model geometry: tangential-ogive-cylinder projectile

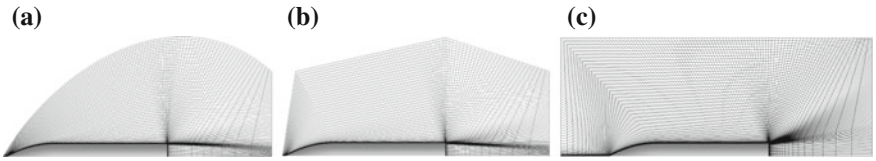

Fig. 2 Topology of the meshes used for the different ranges of angles of attack

2 Investigation Approach

The geometry of the generic tangential-ogive-cylinder type projectile under investigation (D = 30 mm) with a total length of 6.37 diameters is shown in Fig. 1. In order to evaluate three-dimensional tip and end effects for the highest angles of attack investigated, additional simulations on a cylinder in cross-flow with the same diameter are compared to the projectile simulations.

All simulations presented here were conducted at a Mach number of 2.98 with a static pressure P_∞ of 0.209 bar. A temperature T_∞ of 106 K leads to a Reynolds number $\mathrm{Re_D}$ based on the model diameter of 1.71×10^6.

2.1 Numerical Grid Generation

The 3-D hexahedral grids for the numerical simulation were created using ANSYS ICEM CFD V13. As the Magnus effect primarily occurs in the viscous boundary layer, it is modeled with taking particular care for adequate grid resolution. Therefore the dimensionless wall distance y^+ was kept smaller than unity with a wall-normal growth ratio of 1.2 for the projectile meshes. Three different mesh topologies (Fig. 2a–c) were used to fit the requirements of supersonic flow calculations for the lower, intermediate and higher range of angles of attack. A discretization of the model with 130 nodes in length, 180 nodes in circumferential and 70 nodes in radial direction results in meshes consisting of 2.090.880 elements.

For the 2-D simulations of the rotating cylinder in cross-flow, a fine mesh with 400 nodes in circumferential and 300 nodes in radial direction with a total size of 117.208 elements is used. The 3-D cylinder simulations were performed on the same mesh

topology but with 240 nodes in circumferential and 200 nodes in radial direction. In spanwise direction the cylinder extends 1.5 diameters and is discretized with 80 nodes, which leads to a total mesh size of 3.647.272 elements.

2.2 Numerical Flow Simulation

The numerical flow equations are solved with the commercial code ANSYS FLUENT V13 using the double precision density-based solver in the implicit formulation. A second order upwind scheme and the Advection Upstream Splitting Method (AUSM) were used to calculate the convective and pressure fluxes. The $k-\omega$ Shear Stress Transport (SST) two-equation eddy-viscosity model which combines the robust and accurate formulation of the $k-\omega$ model in the near-wall region with the independence from turbulent kinetic energy and dissipation rate of the $k-\varepsilon$ model in the far-field [11] was used to model the turbulence.

The boundaries of the exterior calculation domain were defined as pressure-far-field and the model wall was specified as a no-slip, adiabatic, rotating wall boundary. The model longitudinal axis was defined as axis of rotation with a rotational sense anti-clockwise when viewing the model base from the rear.

Additionally to the steady simulations, selected angles of attack have been simulated using an unsteady RANS formulation with a time discretization of second order.

3 Results and Discussion

Depending on the angle of attack, numerical simulation have been performed on the meshes shown in Fig. 2. In order to check and to avoid mesh topology influences, some angles of attack have been calculated with both meshes and have shown the same aerodynamic coefficients.

3.1 Dependence of the Magnus Side Force on the Angle of Attack

The measured as well as the simulated Magnus side force coefficients for all possible angles of attack are shown in Fig. 3. For small angles of attack up to approximately 3°, the side force starts to grow linear with incidence before a maximum value is reached by a monotonous but nonlinear increase. Between 12° and 26°, the force remains relatively constant. For even higher angles of attack, the side force suddenly decreases to a value less than half of the maximum force and only shows a slight increase towards the limiting case of 90° angle of attack.

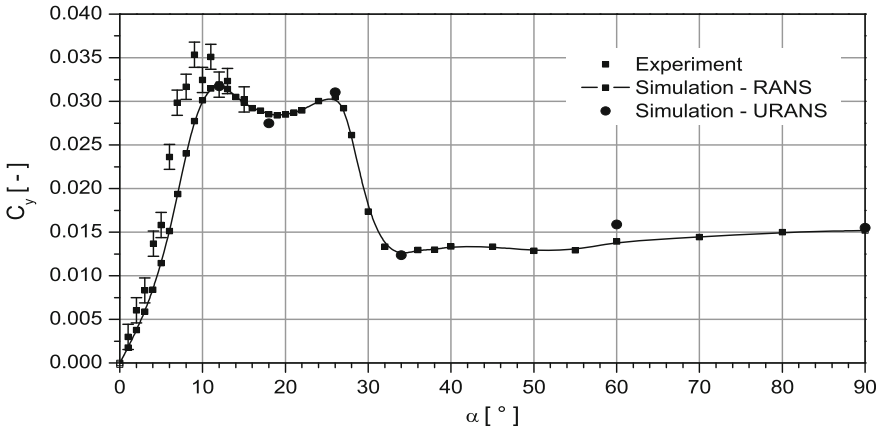

Fig. 3 Magnus side force coefficient versus angle of attack

Due to technical constrains, the experiment only covers angles of attack up to 15°, a range also relevant for many projectiles in flight. The simulations, which generally agree with the measurements within their accessible range of angles of attack, allow analyzing the structure of the flow field around the model. They indicate the existence of lee side vortices, which are mostly invariant with time for angles of attack smaller than 26°. This is supported by transient simulations also shown in Fig. 3, which allow to assess the level of unsteadiness in the flow.

3.2 Source of the Intense Decrease of the Side Force Coefficient

The contour plot in Fig. 4 visualizes the distribution of the Magnus side force coefficient on the model surface for an angle of attack of 26° and indicates that the main part of the side force is generated on the leeward side in a confined region along the axis of the model.

The side force coefficient per length also shown in Fig. 4 for 26° to 34° angles of attack, reveals the distribution of the Magnus force along the longitudinal axis of the model. The integration along the model length leads to the total side force coefficient as shown in Fig. 3.

]

Up to 26° angle of attack, the force increases mostly monotonously from tip to base, as the corresponding curve in Fig. 4 shows representatively. Moreover, this force distribution remains invariant with time.

For angels of attack higher than 26°, the total Magnus force successively decreases, as a consequence of lower local forces towards the model base. Additionally, the flow becomes increasingly unsteady, which also reflects in an unsteady force distribution along the model axis, as is demonstrated by the difference between

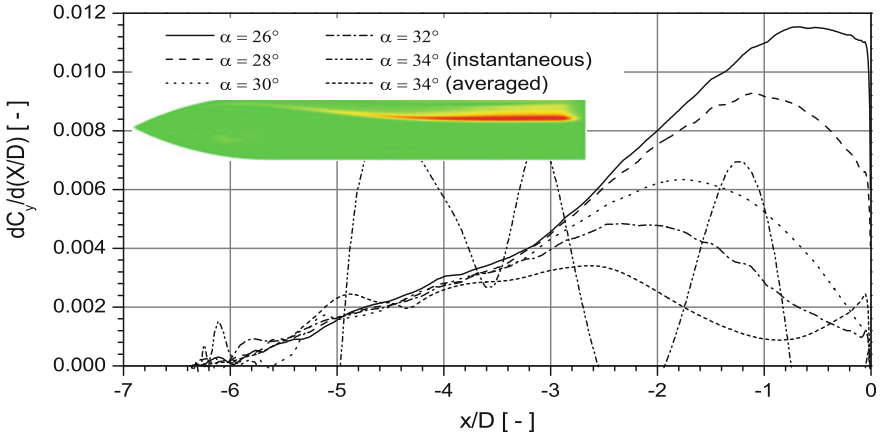

Fig. 4 Magnus side force coefficient distribution along the model longitudinal axis

the instantaneous side force distribution and the corresponding time-averaged one for 34° angle of attack in Fig. 4.

Between 34° and 90° angle of attack, the force distribution becomes increasingly flat, as expected from a supersonic cylinder in cross-flow, with some additional end effects due to the limited aspect ratio of the current model.

Figure 5 shows the distribution of the side force coefficient depending on the circumferential position. The windward stagnation point of the flow is at an position of 180°. An integration along the circumferential direction φ_k results in the total side force coefficient (Fig. 3) acting on the model.

The main part of the side force results from the leeward side of the model between 60° and 75°, the region, where cross-flow separation is expected. On the windward side, however, only a small portion of the total side force is created, resulting mainly from viscous forces.

Increasing the angle of attack shifts the cross-flow separation lines in leeward direction. Furthermore, the additional shift of the separation lines in spin direction due to the rotating model surface become less. Therefore, the differences in the position of the cross-flow separation on the left and right side of the model decreases, which leads to a smaller local magnitude of the Magnus side force coefficient.

3.3 Correlation for High Cross-Flow Mach Numbers

For a sufficiently long projectile, the side effects due to the nose and the base of the model can be neglected, so that the distribution of the side force coefficient in circumferential direction in the middle section of the cylindrical part of the spinning projectile can be compared to corresponding data of rotating cylinders in cross-flow.

Platou [4] proposed to re-compute the side force coefficients of available projectile data, taking into account the cross velocity and the body longitudinal cross-section area according to Eq. (1) and plot it versus the cross-flow Mach number.

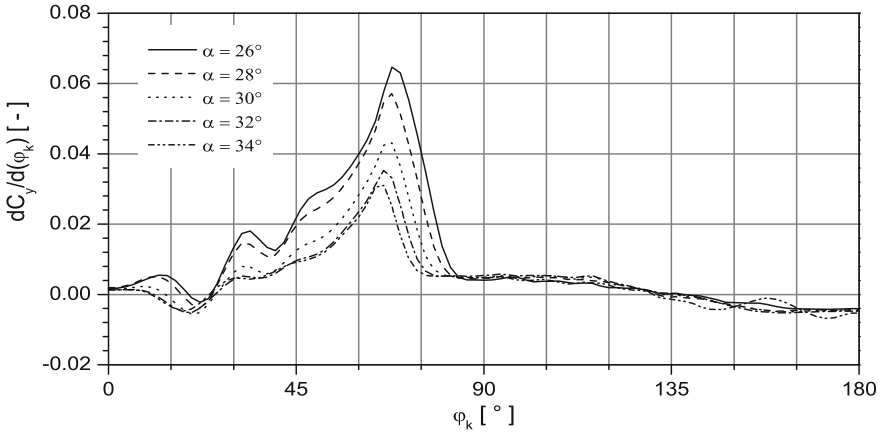

Fig. 5 Total Magnus side force coefficient distribution depending on circumferential position

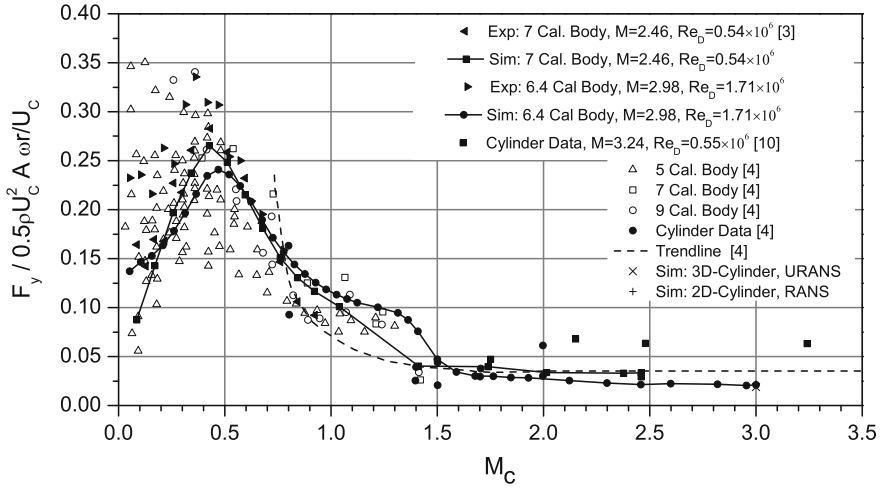

Fig. 6 Magnus side force parameter versus cross-flow Mach number

$$C_{y_p}{}^{*} = \frac{F_y}{\frac{1}{2}\rho_\infty \left(U_\infty \sin\alpha\right)^2 A_c \frac{pD}{2U_\infty \sin\alpha}} \tag{1}$$

Figure 6 shows the chart from Platou [4] completed with the data from Luchuk and Sparks [3] as well as the data from the present numerical study and the corresponding experimental investigation. The data of Luchuk and Sparks are compared to laminar flow simulations.

Additionally to the side force data resulting from projectile investigations, lift coefficients for rotating circular cylinders are shown [4, 10]. The experimental results and the numerically determined coefficients from the present study well reproduce

the trendline interpolated by Platou [4] for rotating cylinders in cross-flow. For the cylinder in cross-flow, the Magnus force is insensitive to the simulation setup, i.e. steady or transient and 2-D or 3-D.

4 Conclusion

In this paper, the Magnus effect for angles of attack up to 90° has been investigated by means of numerical simulations for a generic projectile at Mach 3. After a nonlinear increase, the side force reaches a maximum value between 10° and 26° angle of attack. It has been shown that between 26° and 32° angles of attack the Magnus side force strongly decreases. For angles higher than 32°, the side force coefficient only shows a slight increase towards the value of the limiting case of 90°. The analysis of the force distribution along the model axis indicated decreasing local forces towards the base for increasing angles of attack. This results primarily from a shift of the cross-flow separation lines in leeward direction and a decreasing influence of the rotating model surface on the separation with higher incidence. The projectile Magnus data for cross-flow Mach numbers higher than 1.5 correlate with the data from rotating cylinders in cross-flow. This validates at least the order of magnitude and the global trend of the side force coefficients above 34° angle of attack as no experimental data for projectiles is available for this range of angle of attack.

References

1. Donneaud, O., Chemière, C., Cayzac, R., Champigny, P.: Recent developments on aeroballistics of yawing and spinning projectiles. Part II. Free flight tests. In: 20th International Symposium on Ballistics, Orlando, Florida, pp. 157–164 (2002)
2. DeSpirito, J., Silton, S.I., Weinacht, P.: Navier-Stokes predictions of dynamic stability derivatives: evaluation of steady-state methods. J Spacecraft Rockets **46**(6), 1142–1154 (2009)
3. Luchuk, W., Sparks, W.: Wind-tunnel magnus characteristics of the 7-caliber army-navy spinner rocket. Technical Report NAVORD Report 3813, U. S. Naval Ordnance Laboratory, White Oak, Maryland (1954)
4. Platou, A.S.: Magnus characteristics of finned and nonfinned projectiles. AIAA J. **3**(1), 83–90 (1965)
5. Sturek, W.B.: Boundary layer studies on a spinning tangent-ogive-cylinder model. Technical Report BRL-MR-1801, USA Ballistic Research Laboratories, Aberdeen Proving Ground Maryland (1975)
6. Champigny, P., Ceroni, D., Thépot, R., Cayzac, R., Carette, E., Trouillot, C., Donneaud, O.: Recent developments on aeroballistics of yawing and spinning projectiles. Part I. Wind tunnel tests. In: 20th International Symposium on Ballistics, Orlando, Florida, pp. 203–208 (2002)
7. Cayzac, R., Carette, E., Champigny, P., Thépot, R., Donneaud, O.: Recent developments on aeroballistics of yawing and spinning projectiles. Part III. First CFD validation results. In: 20th International Symposium on Ballistics, Orlando, Florida, pp. 11–19 (2002)
8. Cayzac, R., Carette, E., Denis, P., Guillen, P.: Magnus effect: physical origins and numerical prediction. J. Appl. Mech. **78**(5), 051005 (2011)
9. Vaughn, H.R., Reis, G.E.: A magnus theory. AIAA J. **11**(10), 1396–1403 (1973)

10. Hall, R.T.: The lift and drag on a rotating cylinder in supersonic crossflow. Technical Report NAVORD Report 6039, U. S. Naval Ordnance Laboratory, White Oak, Maryland (1960)
11. Menter, F.R.: Two-equation eddy-viscosity turbulence models for engineering applications. AIAA J. **32**(8), 1598–1605 (1994)

Part X
Experimental Simulation and Test Techniques

Large Scale Tomographic Particle Image Velocimetry of Turbulent Rayleigh-Bénard Convection

Daniel Schiepel, Johannes Bosbach and Claus Wagner

Abstract A non-invasive method to simultaneously measure the three-dimensional velocity and temperature fields in thermal convection would be a very valuable tool for studying the underlying thermal transport processes, which are important in nature and in many technical applications. With our study we aim at bridging this gap in the long run by combining Tomographic Particle Image Velocimetry (Tomo-PIV) with liquid crystal thermometry. As a first step towards this goal, we applied Tomo-PIV to Rayleigh-Bénard convection (RBC) of water in a cubic sample to obtain the instantaneous three-dimensional velocity field at $\mathrm{Ra} = 1.0 \cdot 10^{10}$ and $\mathrm{Pr} = 6.9$. A comparison of the measured large-scale circulation with results from direct numerical simulations (DNS) and planar PIV measurements demonstrates the reliability of the Tomo-PIV technique. This is a prerequisite for employing Thermochromic Liquid Crystals (TLC) as tracer particles.

1 Introduction

Turbulent thermal convection occurs frequently in nature and is of utmost importance for many technical applications. Lately, these problems are often approached using Computational Fluid Dynamics (CFD), which are based on semi-empirical models to account for the effect of small-scale turbulence. To validate the predictive capabilities of such CFD-computations, experimentally obtained time-resolved and three-dimensional velocity and temperature data are needed.

D. Schiepel (✉) · J. Bosbach · C. Wagner
German Aerospace Center (DLR), Institute of Aerodynamics and Flow Technology, SCART, Bunsenstraße 10, 37073 Göttingen, Germany
e-mail: Daniel.Schiepel@dlr.de
J. Bosbach
e-mail: johannes.bosbach@dlr.de
C. Wagner
e-mail: claus.wagner@dlr.de

A. Dillmann et al. (eds.), *New Results in Numerical and Experimental Fluid Mechanics IX*, Notes on Numerical Fluid Mechanics and Multidisciplinary Design 124,
DOI: 10.1007/978-3-319-03158-3_53,

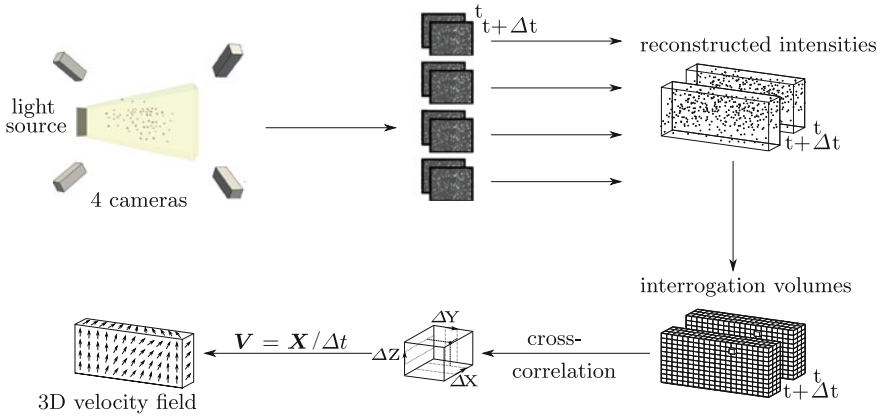

Fig. 1 The Tomo-PIV work flow

Turbulent flows are characterised by 3D structures occurring on large as well as small scales, making it necessary to capture the complete velocity field with high spatial resolution. With the introduction of Tomo-PIV, the non-invasive acquisition of all three velocity components (3C) in the measurement volume (3D), became possible [1]. In the beginning, this technique was restricted to small measurement volumes—a limitation, which was overcome recently. In [2, 3] Tomo-PIV was adapted to large scales and applied to study turbulent mixed convection in a rectangular container at $\mathrm{Pr} = 0.7$.

Besides the velocity fields, which are accessible by Tomo-PIV, the corresponding temperature fields are of equal importance for studies of thermal convection since temperature gradients are one driving force of such flows. Hence, the long term goal of this work is the simultaneous acquisition of the instantaneous three dimensional velocity and the temperature fields of the fluid. We plan to combine large-scale Tomo-PIV with Particle Image Thermometry [4] (PIT), which allows to non-invasively measure the temperature field by using TLCs as tracer particles [5]. For an extensive review on TLCs the reader maybe referred to [6].

Characterstic for turbulent thermal convection is the occurrence of large, circulating flow structures with a size comparable to the sample dimensions, which are usually termed "large scale circulation" (LSC). They are known to interact with the turbulent background and the thermal structures emitted from the thermal boundary layers ("Plumes"), which results in complex dynamics comprising rotations, cessations, reversals and re-orientations as well as twisting and sloshing modes, see e.g. [7–9]. Here we employed the LSC in a cubic RBC sample as a model system for turbulent thermal convection in order to develop our measurement technique and to apply Tomo-PIV with classical seeding particles in the first step.

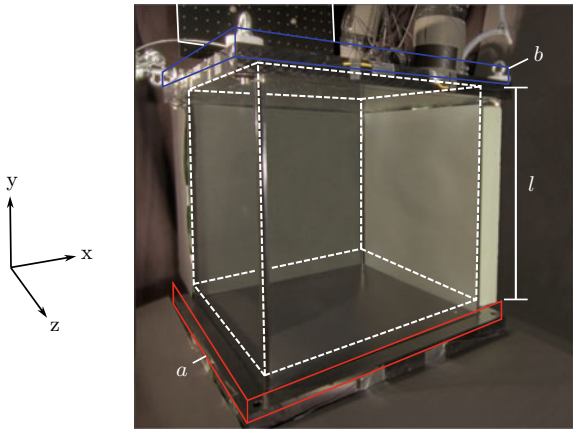

Fig. 2 Picture of the cubic RBC-convection sample. a and b indicate the heating and cooling plate, respectively and the sample height l

2 Tomographic Particle Image Velocimetry

Tomo-PIV methods, as the one applied here, follow a common procedure, see Fig. 1. The measurement volume is observed under different observation angles by several cameras, four in the given case. A calibration, using a standard calibration plate, is applied to the measurement volume, providing the translation $\boldsymbol{x} \leftrightarrow \boldsymbol{X}$ from the image planes $\boldsymbol{x}$ to the measurement volume $\boldsymbol{X}$. The fluid is seeded with tracer particles, which are illuminated by a pulsed volume light source and imaged by the cameras.

After image-processing of the particle images, the initial particle distribution in physical space $\boldsymbol{X}$ is reconstructed by a tomographic procedure based on the SMART-implementation [10]. Once those intensity maps $E(\boldsymbol{X})$ are known for two positions in time t and $t + \Delta t$, the measurement volume is divided into sub-volumes, called the interrogation volumes. The cross correlation of the intensities $E(\boldsymbol{X}, t)$ and $E(\boldsymbol{X}, t + \Delta t)$ within those volumes is calculated, resulting in a local maximum, its position corresponding to the mean particle displacement $\Delta \boldsymbol{X}(\boldsymbol{X}, t)$. The exact position of this maximum is determined using a Gaussian fit to obtain the position of the correlation maximum. Finally, the velocity is computed by $\boldsymbol{V}(\boldsymbol{X}, t) = \Delta \boldsymbol{X}/\Delta t$.

In addition to the common procedure, we apply a volume self-calibration based on [11] following the initial calibration. This provides us a higher level of accuracy for the particle detection in $\boldsymbol{x}$ and thereby for the full evaluation procedure.

3 Experimental Set-Up

A cubic RBC sample was developed, which has a side length of $l = 500\,\text{mm}$ and uses water as working fluid, see Fig. 2. The heating- and cooling plates (a and b) consist of anodised aluminium.

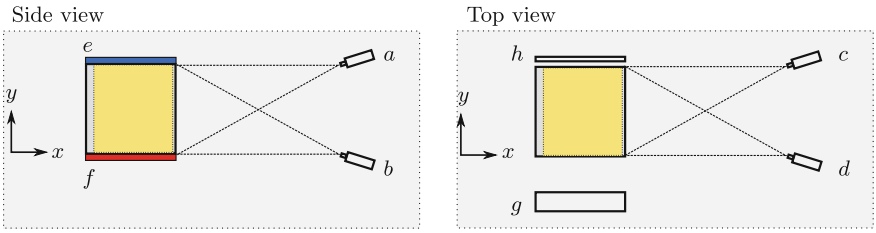

Fig. 3 Sketch of the Tomo-PIV set-up. a to d mark the cameras with their respective viewing lines. In the side view perspective, e and f mark the heating- and cooling plate. In the top view perspective, g and h indicate the light source and the mirror

To characterise the flow, two characteristic numbers are required, which are the Rayleigh number Ra and the Prandtl number Pr. They are given by $\mathrm{Ra} = \frac{g\beta}{\nu\alpha}\,\Delta T\, l^3$ and $\mathrm{Pr} = \nu/\alpha$, with the gravitational acceleration g, the heat expansion coefficient β, the kinematic viscosity ν, the thermal diffusivity α, the temperature difference ΔT between heating- and cooling plate and the characteristic length l. The experimental set-up is designed to cover a range of $\mathrm{Ra} = 0.5 - 5.0 \cdot 10^{10}$. Nearly isothermal boundary conditions are provided by the heating- and cooling plates, which are temperature controlled and aligned horizontally within 0.01°. Glass with a thickness of 10 mm is employed for the side walls, yielding optical accessibility to the flow. In order to minimise the heat loss through the side walls, the surrounding air temperature was kept at the mean sample temperature within ±0.5 K by an environmental control system. 45 Pt1000 resistance temperature detectors (RTD) were used to monitor the temperatures in the heating and cooling plates as well as in the surrounding during the experiments. 16 of these sensors were installed in each of the top and bottom plates with just 1 mm of aluminium between the fluid and the sensors.

The experiment was conducted at an average sample temperature of $\overline{\mathrm{T}} = 21\,°\mathrm{C}$, which corresponds to $\mathrm{Pr} = 6.9$ [12]. Setting $\Delta\mathrm{T}$ to 6 K, a Rayleigh number of $\mathrm{Ra} = 1.0 \cdot 10^{10}$ was realised. For this parameter combination the emerging 3D-flow fields were measured using Tomo-PIV.

A sketch of the experimental set-up is shown in Fig. 3. The measurement volume is indicated in yellow and covers the entire sample in $x - y$-direction. In z-direction it is reduced to 450 mm. The camera set-up is chosen in such a way that each camera (a to d) has two viewing lines parallel to two of the boundaries. This approach reduces the number of additional ghost particles, which are induced by mirror images of the particles from the sidewalls. Heating- and cooling-plates are indicated with e and f, respectively, in the side view perspective. The top view perspective illustrates the position of the light source g with a mirror h placed on the opposite side to reflect the light and thus increase the light intensity in the measurement volume.

As seeding particles for 3D velocity field measurements, TiO_2-coated latex particles with a mean diameter $d = 100\,\mu$m were inserted into the flow. The coating increases the light scattering efficiency, while the latex core leads to a combined density close to the one of water and therefore neutral buoyancy.

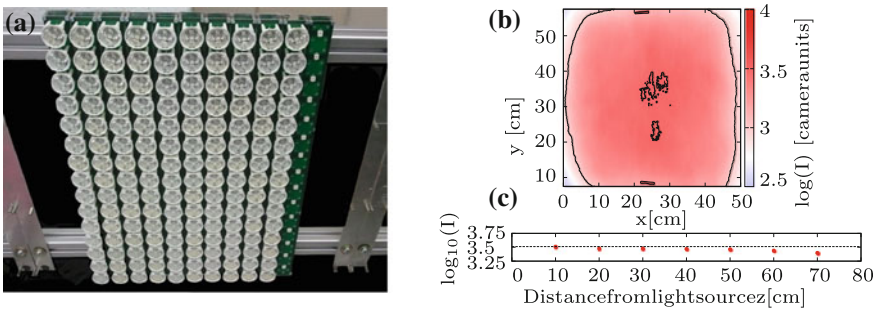

Fig. 4 The light source of the experiment. **a** shows the disassembled LED-array with one row without optics. **b** depicts the light intensity distribution in $x-y$ direction. The intensity distribution in one point along z is shown in (**c**)

Since we aim at measuring 3D temperature fields in the next step, a high intensity of the scattered light is required in order to detect the colour information in addition to the particle positions with high accuracy. In order to achieve this, the illumination intensity and the size of the tracer particles should be maximised. While the first is mainly bounded by technological restrictions, the latter is limited by the fact that the particles should be obviously smaller than the smallest coherent structures in the flow. For $\mathrm{Ra} = 1.0 \cdot 10^{10}$ the estimated Kolmogorov length [13, 14] is $\eta_K \approx 1\,\mathrm{mm}$, and therfore the TiO_2 particles are small enough to follow the flow.

The TLCs, we plan to use, have a diameter of $d = 200\,\mu\mathrm{m}$, which is also well below the Kolmogorov length. As a light source a specially built high power white-light LED-array with a broad wavelength spectrum is used. The array consists of 15×15 LEDs of the type Osram Platinum Dragon LW W5SNA, see Fig. 4a. It can be triggered by a specially developed power supply. Optics are placed in front of the LEDs to reduce the divergence of the light and thus generate a more homogeneous intensity distribution within the measurement volume. To characterise the light source, the light intensity was measured by directing the array to a faint black surface. A camera was aligned to record the $x-y$ plane and the black surface was additionally traversed in z-direction to investigate the distribution of the light intensity in depth. The obtained intensity distribution in the $x-y$-plane at $z = 40\,\mathrm{cm}$ is presented in Fig. 4b. It reveals that the intensity varies less than 10 % within the sample. In (c) the light intensity distribution at the position $(x, y) = (40\,\mathrm{cm}, 30\,\mathrm{cm})$ is shown as a function of z. The variation of the light intensity in z-direction amounts to less than 4 %. We conclude, that the LED-array provides a very homogeneous illumination of our sample and is thus suitable for the conducted Tomo-PIV measurements.

The images of the illuminated TiO_2 particles were recorded using four CCD cameras (PCO Pixelfly) at a recording rate of 5 Hz. The light pulses from the LED array have a duration of 800 μs, which is closely matched to the exposure time of the cameras of 1 ms. Each camera is equipped with a 21 mm Nikon lens and tilted into the volume according to the Scheimpflug condition. The aperture is set to $f_\sharp = 8$, giving us a calculated [15] depth of field of $0.4-0.5$ m for the spectrum of the LEDs, i.e. for wavelengths between 400 and 800 nm.

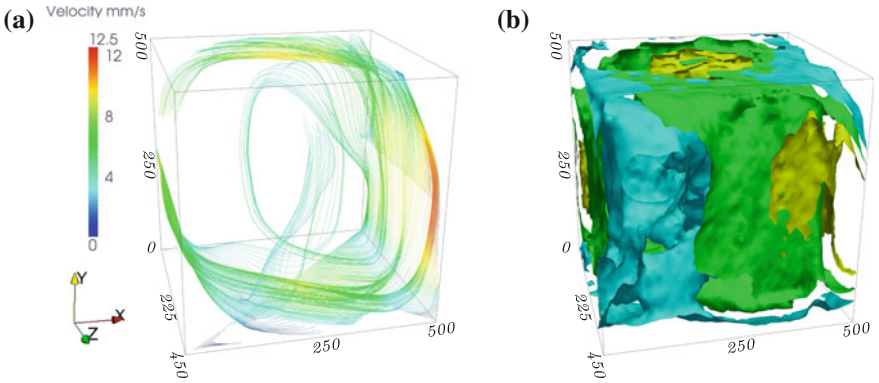

Fig. 5 Mean velocity field with colour coding according to the velocity magnitude. In **a** streamline visualisation. In **b** a isosurfaces of the velocity magnitude

4 Measured 3D Large Scale Circulation

Prior to reconstruction of the intensity distribution the self-calibration procedure was performed, which was found to converge already after 100 images. The most time consuming step of the evaluation process, the reconstruction of the 3D intensity distribution, was carried out for 500 images. The cross correlation procedure, providing $\Delta \boldsymbol{X}$, was applied using interrogation windows with a side length of $(10\,\mathrm{mm})^3$. We operated the cameras in single shutter mode at a recording rate of $f = 5\,\mathrm{Hz}$. The corresponding time difference is $\Delta t = 1/f = 0.2\,\mathrm{s}$ used for the calculation the instantaneous 3D-3C velocity fields $\mathbf{V}(\Delta \mathbf{X}, t)$. A time averaging was conducted to eliminate turbulent fluctuations. As convergence criteria we defined three points (two on opposite sites of the LSC and one in the bulk) and determined the remaining fluctuations to be within $\pm 1.2\,\mathrm{mm/s}$. This approach reduces the turbulent fluctuations but will not average over the low frequent fluctuations of the LSC, which can occur [7]. The 500 evaluated velocity fields correspond to a measurement time of 100 s and span a time for 2.5 turn-arounds of the LSC.

To see whether we can resolve the smallest structures of the flow, we use the equation for η_K [14] and apply a dimensional analysis

$$\eta_K = (\nu^3/\epsilon)^{1/4} = (\nu^3\, l/\overline{u}_{max}^3)^{1/4} = 0.74\,\mathrm{mm}$$

with the kinetic energy dissipation rate per unit mass ϵ and the obtained amplitude of the mean velocity $\overline{u}_{max}$. The smallest coherent structures have a size of $l_{\mathrm{coh}} = 10 \cdot \eta_K$ [16] which corresponds to 7.4 mm in our case. This is a length, which is just comparable to our interrogation window size of 10 mm. Consequently, we almost resolve the flow down to its smallest structures in our measurement.

The obtained time averaged velocity field is presented in Fig. 5a using streamlines colour-coded with the velocity magnitude. The LSC is oriented along the $x - y$-

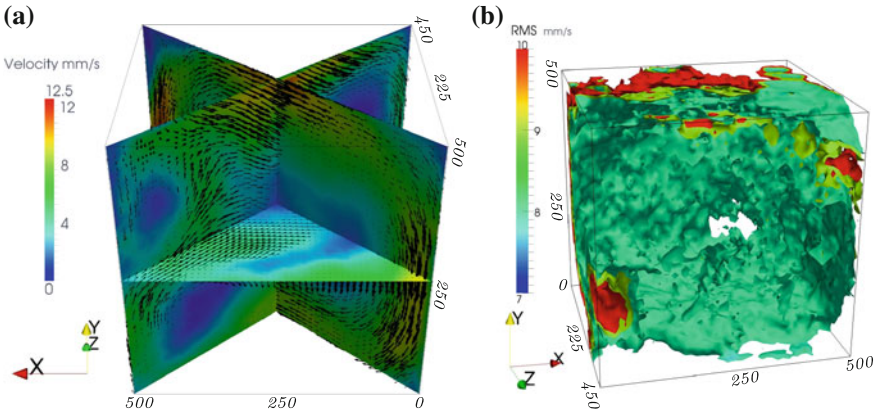

Fig. 6 Mean velocity field. In **a** slices along two diagonals of the RB sample and one horizontal slice at h/2 are shown. Colour coding is according to the velocity magnitude. The velocity is indicated with 3C vectors. **b** RMS of the velocity magnitude

diagonal of the sample. To underline that the method also allows the reconstruction of low velocity values in the corners, isosurfaces are used to visualise the velocity magnitude in Fig. 5b. The yellow isosurfaces correspond to the LSC. The green surfaces closer to the walls and even more the blue regions in the corners of the cube visualise the fluid which is significantly slower.

In order to judge on the validity of our measurement and the quality of our apparatus, Re was calculated and compared to other studies. Figure 6a shows the time averaged velocity field using a vectorial representation. We deduced a maximal time averaged velocity of 12 mm/s, yielding $\mathrm{Re} = \frac{\overline{u}_{max}\, l}{\nu} = 6275$. In [17], a scaling law for Re as a function of Ra was deduced from planar PIV measurements in a rectangular sample filled with water. Applying the reported scaling law $\mathrm{Re} = 0.0184\,\mathrm{Ra}^{0.55}$ to our Ra, we obtain Re = 5818 in good agreement with our velocity data. Extrapolating the three dimensional DNS data of RBC in water in a cubic sample [18] from $\mathrm{Ra} = 3 \cdot 10^9$ to $\mathrm{Ra} = 1.0 \cdot 10^{10}$ yields Re = 6300. This value agrees within 1 % with our result. Further, we were able to resolve two smaller, counter rotating flow structures perpendicular to the LSC, very similar to the ones reported in [18] for a lower Ra, see Fig. 6a.

In order to check the stability of our measurements, the root mean square (RMS) of the velocity magnitude fluctuations $|\boldsymbol{V}| - <|\boldsymbol{V}|>$ was computed as $\mathrm{RMS}(|\boldsymbol{V}| - <|\boldsymbol{V}|>) = \sqrt{<|\boldsymbol{V}|^2> - <|\boldsymbol{V}|>^2}$. The result is shown in Fig. 6b. It can be seen that at the front of the measurement volume, i.e. large z, the RMS values are smaller than 8 mm/s which is also true for the flow in the sample's centre. The fluctuations increase up to 10 mm/s in the sample's corners and in the back. This is most likely due to smaller viewing angles at low z and can be improved by increasing the viewing angles of the cameras, which will be considered in further studies.

5 Summary and Outlook

A pathway towards a new measurement technique for simultaneous detection of 3D velocity and temperature fields, based on combination of Tomo-PIV and TLC-PIT, was explored. As a model system for turbulent thermal convection, RBC in a cubic sample was chosen. Therefore, an RBC apparatus with high optical accessibility and a high power LED array allowing for pulsed and intense volume illumination were developed and installed. Using this set-up, we conducted Tomo-PIV in turbulent RBC and were able to measure the time-dependent 3D-3C velocity field in the complete RB sample. For $\mathrm{Ra} = 1.0 \cdot 10^{10}$ the observed large scale circulations as well as the deduced Reynolds number agree well with 2D measurements and predictions by DNS in a similar configuration.

The validity of the Tomo-PIV data encourages us to proceed to the next step and apply TLCs as seeding particles instead of the TiO_2 particles.

References

1. Elsinga, G., Scarano, F., Wieneke, B., Oudheusden, B.: Tomographic particle image velocimetry. Exp. Fluids **41**, 933–947 (2006)
2. Kühn, M., Ehrenfried, K., Bosbach, J., Wagner, C.: Large-scale Tomo PIV using helium-filled soap bubbles. Exp. Fluids **50**, 929–948 (2011)
3. Kühn, M., Ehrenfried, K., Bosbach, J., Wagner, C.: Large-scale Tomo PIV in forced and mixed convection using a parallel SMART version. Exp. Fluids **53**, 91–103 (2012)
4. Dabiri, D.: Digital particle image thermometry/velocimetry: a review. Exp. Fluids **46**, 191–241 (2009)
5. Koch, S.: Berührungslose Messung von Temperatur und Geschwindigkeit in freier Konvektion. Mitteilungen aus dem MPI für Strömungsforschung, Göttingen (1993)
6. Dabiri, D., Gharib, M.: Digital particle image thermometry: the method and implementation. Exp. Fluids **11**, 77–86 (1991)
7. Brown, E., Ahlers, G.: Rotations and cessations of the large-scale Circulation in turbulent Rayleigh-Bénard convection. J. Fluid Mech. **568**, 351–386 (2006)
8. Zhou, Q., Xi, H.D., Zhou, S.Q., Sun, C., Xia, K.Q.: Oscillations of the large-scale circulation in turbulent Rayleigh-Bénard convection: the sloshing mode and its relationship with the torsional mode. J. Fluid Mech. **630**, 367–390 (2009)
9. Sugiyama, K., Ni, R., Stevens, R.J.A.M., Chan, T.S., Zhou, S.Q., Xi, H.D., Sun, C., Grossmann, S., Xia, K.Q., Lohse, D.: Flow reversals in thermally driven turbulence. Phys. Rev. Lett. **105**, 034503 (2010)
10. Atkinson, C., Soria, J.: An efficient simultaneous reconstruction technique for tomographic particle image velocimetry. Exp. Fluids **47**, 553–568 (2009)
11. Soloff, S., Adrian, R., Liu, Z.C.: Distortion compensation for generalized stereoscopic particle image velocimetry. Meas. Sci. Technol. **8**(12), 1441 (1997)
12. VDI-Gesellschaft: VDI-Wärmeatlas. Berechnungsunterlagen für Druckverlust, Wärme- und Stoffübergang. 10 edn. Springer, Berlin (2006)
13. Bosbach, J., Weiss, S., Ahlers, G.: Plume fragmentation by bulk interactions in turbulent Rayleigh-Bénard convection. Phys. Rev. Lett. **108**, 054501 (2012)
14. Ahlers, G., Grossmann, S., Lohse, D.: Heat transfer and large scale dynamics in turbulent Rayleigh-Bénard convection. Rev. Mod. Phys. **81**, 503–537 (2009)

15. Raffel, M., Kompenhans, J., Wereley, S., Willert, C.: Particle Image Velocimetry: a Practical Guide. Springer, New York (2007)
16. Sugiyama, K., Calzavarini, E., Grossmann, S., Lohse, D.: Non-Oberbeck-Boussinesq effects in two-dimensional Rayleigh-Bénard convection in glycerol. Europhys. Lett. **80**(3), 34002 (2007)
17. Sun, C., Cheung, Y.H., Xia, K.Q.: Experimental studies of the viscous boundary layer properties in turbulent Rayleigh-Bénard convection. J. Fluid Mech. **605**, 79–113 (2008)
18. Kaczorowski, M., Shishkina, O., Shishkin, A., Wagner, C., Xia, K.Q.: Analysis of the large-scale circulation and the boundary layers in turbulent Rayleigh-Bénard convection. In: Direct and Large-Eddy Simulation VIII. Volume 15 of ERCOFTAC Series, pp. 383–388. Springer (2011)

Pressure Measurement on Rotating Propeller Blades by Means of the Pressure-Sensitive Paint Lifetime Method

C. Klein, U. Henne, W. E. Sachs, S. Hock, N. Falk, V. Ondrus, U. Beifuss and S. Schaber

Abstract The pressure distribution on the surface of a high-speed rotating propeller was measured using the Pressure-Sensitive Paint (PSP) lifetime method. This chapter describes the developed PSP formulation, the experimental setup as well as the image acquisition, processing procedure, and the data evaluation. The PSP lifetime method delivers a continuous pressure distribution, which allows even small pressure differences and aerodynamic phenomena such as vortices and flow separation to be detected. These phenomena occur often on rotating blades [1]. Based on the results from a feasibility study, a wind tunnel experiment was conducted in the low-speed wind-tunnel BLSWT of AIRBUS in Bremen at propeller rotation speeds up to 14,400 rpm.

1 Introduction

Surface pressure distributions can be determined by means of Pressure-Sensitive Paint (PSP). A specific measurement technique using PSP is the lifetime method which is based on the dependence of the lifetime of luminescence on the concentration of oxygen, and is proportional to the pressure. The PSP lifetime method has already

C. Klein (✉) · U. Henne · W. E. Sachs
Deutsches Zentrum für Luft- und Raumfahrt e.V. (DLR), Bunsenstrasse 10,
37073 Göttingen, Germany
e-mail: Christian.Klein@dlr.de

S. Hock · N. Falk
Institut für Luft- und Raumfahrt, Technische Universität Berlin, Marchstrasse 12,
10587 Berlin, Germany

V. Ondrus · U. Beifuss
Institut für Chemie, Universität Hohenheim, Garbenstr. 30 , 70599 Stuttgart, Germany

S. Schaber
AIRBUS Operations, 28199 Bremen, Germany

A. Dillmann et al. (eds.), *New Results in Numerical and Experimental Fluid Mechanics IX*,
Notes on Numerical Fluid Mechanics and Multidisciplinary Design 124,
DOI: 10.1007/978-3-319-03158-3_54,

been used in various wind tunnel tests [2–4]. The pressure distribution on a rotating propeller blade is of interest for the development of such systems. PSP is a contact-free and image-based measurement technique with which pressure gradients on a surface can be visualized. The PSP lifetime method is able to detect the expected pressure differences despite the short exposure times needed to capture the rapid decay of the fluorescence. This chapter describes in the first part a feasibility study on a high-speed rotating propeller using the PSP lifetime method. The following part describes the paint and binder as well as their relevant properties for PSP. The third section deals with the experimental setup for the feasibility study. Finally, the experiments in the low-speed wind tunnel BLSWT of AIRBUS Bremen at propeller rotation speeds up to 14,400 rpm are presented.

2 PSP Lifetime Method for Propeller Testing

The working principle of Pressure-Sensitive Paint (PSP) is based on the oxygen quenching mechanism of molecules which are embedded in the paint. These so-called luminophores are excited by incident light of a certain wavelength to an excited electronic state after which they relax back to the ground state (after some internal re-arrangement) via emission of a photon (luminescence). Since the fluorescence can be quenched by oxygen, the higher the concentration of oxygen in the surrounding air, the lower is the intensity of emission of the dye. Furthermore, the lifetime of the luminescence decreases with an increase of oxygen concentration (viz. pressure). The Stern-Volmer-equation shows this relation:

$$\frac{1}{\tau} = A\,(T) + B\,(T)\,p$$

where τ is the lifetime of the luminescence, p is the ambient pressure and A and B are specific coefficients of the paint as a function of the ambient temperature T [5].

Several PSP formulations, containing sensor dye and binder, have been evaluated in calibration tests. The ideal PSP for the propeller measurements has to fulfill the following characteristics at ambient conditions: high luminescent intensity, high pressure sensitivity, low temperature sensitivity, and magnitude of lifetime $\leq\sim 10\,\mu$s.

It was found that PtTFPP-based PSP is suitable for the propeller testing. The more relevant properties of this paint are listed in Table 1 and illustrated in the emission spectra in Fig. 1. This PSP has a sufficiently high pressure sensitivity (−0.8 %/kPa), a medium temperature sensitivity (−0.81 %/K), with a fluorescence lifetime in the required range (7.9 μs at 295.75 K and 100 kPa). The binder poly(4-tert-butylstyrene) has sufficient oxygen permeability to deliver good pressure sensitivity.

With lifetime systems, pressure is determined from the decay time of luminescence, which is based on time-resolved measurements of luminescence after the paint has been excited by a light pulse. Typically, decay times are determined from the ratio of intensities measured during at least two gates at different times after excitation [2].

Table 1 PSP formulations and characteristics

PSP formulation	
Sensor dye	PtTFPP
Binder	Poly(4-tert-butylstyrene)
PSP characteristics (297.75 K, 100 kPa)	
Excitation wavelength	405 nm
Emission peak	650 nm
Pressure sensitivity	−0.8 %/kPa
Temperature sensitivity	−0.81 %/K
Lifetime	7.9 μs

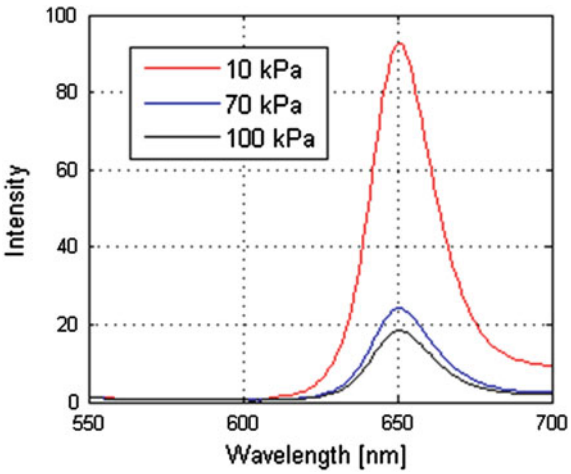

Fig. 1 Pressure sensitivity of PSP

An important advantage of this approach is that, under ideal conditions, this ratio is independent of illumination intensity and luminophore concentration, and thus it is not necessary to normalize the data by measurements acquired at a reference condition.

The principal difficulty is simultaneously measuring the intensity time histories at all points on the model at the timescales of luminescence lifetimes ($<10\,\mu s$). In this work, the so called two gated intensity method [2] is used as a method to measure luminescent lifetimes. In this method, the luminescent images are obtained by integrating the luminescent decay curve at two different gates from which the lifetime can be calculated by the intensity ratio for the images taken at these two gates. It means that the lifetime method can measure pressure using only run images. Many researchers have reported the influence of temperature and the non-uniformity of PSP thickness on the pressure results obtained by PSP [6]. Therefore, the "double-ratio" method of run- and reference images has been proposed to calculate absolute pressure values with the lifetime method.

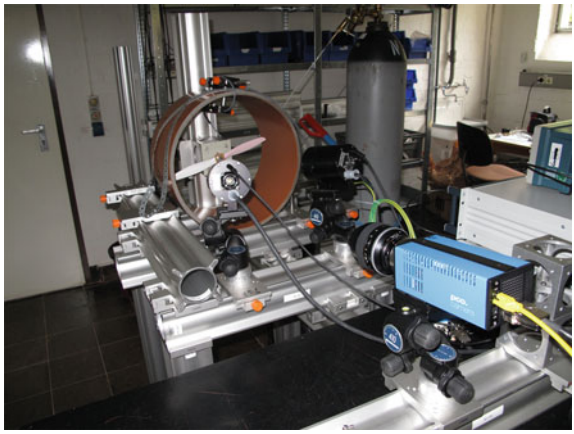

Fig. 2 A picture of the PSP testing

3 Pre-test for the Wind Tunnel Experiments

3.1 Propeller

The commercial wooden propeller EVO-RC 30–10 cm was used in this experiment. It has a diameter of 0.33 m, a mean chord length of 0.03 m and a pitch of 0.1 m. The propeller was driven by a current-controlled direct-current motor. The maximum speed is 10,800 rpm. For this speed the maximum operating time is limited to 1 min because of motor heating [7]. One blade of the propeller was coated with PSP.

3.2 Excitation Light and Camera System

A picture and schematic view of the PSP apparatus are shown in Figs. 2 and 3, respectively. The excitation light for PSP was provided by two high-power LED ULD 119 from Rapp Opto Electronic, with emission between 395 and 405 nm. The luminescent emission of PSP was captured by a 14-bit CCD camera (PCO 4000). A 650 $\pm$ 40 nm optical band-pass filter was mounted in front of the camera lens to remove excitation and emission light. To increase the Signal-to-Noise Ratio (SNR) of the obtained images, the camera was operated in 'modulation mode'. In this operational mode, the camera shutters were opened always at the same positions of the rotating propeller (same phase angle) and the small measured intensities of a single exposure were accumulated on the CCD chip. The camera exposure timing and excitation LED were controlled by an external trigger unit, as shown in Fig. 4. A photo detector generated a TTL signal when a propeller blade passed by it. This signal was the input signal for the pulse generator Model 725 by BNC, which generated two new TTL signals for the camera and the light sources. One TTL signal for the camera was generated for every second detector signal, because just one blade was coated with PSP.

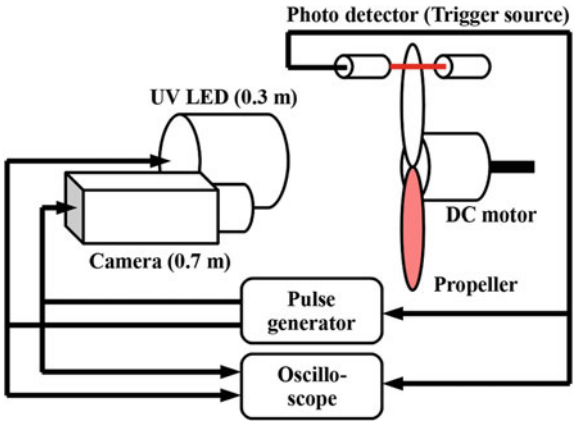

Fig. 3 A schematic view of the PSP testing

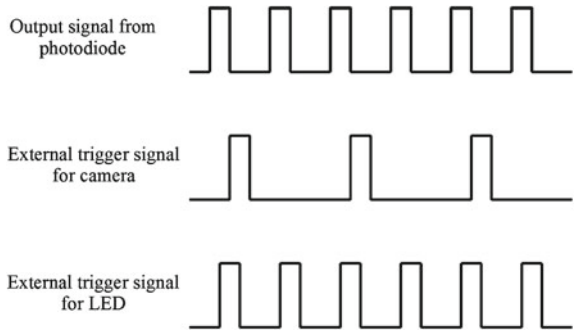

Fig. 4 Timing of camera shutter and LED control

3.3 Acquisition and Processing Procedure of PSP Lifetime Images

To measure the lifetime of the PSP luminescence, images at two different times after the excitation pulse have to be acquired. As shown in Fig. 5, this was achieved by two different delay times for the excitation light trigger, while the delay of the external camera signal was kept fixed. The delay time of the camera signal depends on the rotational speed of the propeller, the delay times of the LED signals were 7 and 15 µs shorter. The illumination time was 10 µs. A single exposure time of the camera was 5 µs, 750 single exposures were accumulated on chip to obtain the one image. The same sequence was used to acquire two reference images by using a pulse generator to trigger the individual experiment, since the propeller was not rotating and no signal from the photo detector was available. Furthermore, dark images for the run and reference cases, but without excitation light, were obtained.

With a distance between the camera lens and the propeller was 0.7 m. The resolution of the acquired images became 42 pixel per mm^2. The maximum rotational speed of the propeller during the measurements was 9,600 rpm so that with these

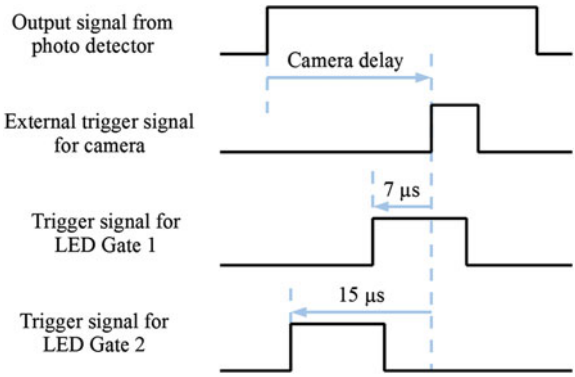

Fig. 5 Sequences for image acq. at gate 1 and 2

conditions the spatial resolution was better than 0.8 mm at all positions and at all frequencies.

A median filter was applied to the reference and run images, again to increase the SNR. The run images from gates 1 and 2 were divided to obtain an image of the change of luminescent intensity in time. The same was done with the reference images from gates 1 and 2. The gate images from run and reference were divided again to obtain the result image. The last division removed effects on the lifetime measurement due to paint non-homogeneity. Finally, four result images of distinct measurements at the same conditions were again averaged to further increase the SNR again.

3.4 Results and Discussions

Figure 6 shows the result where a nitrogen jet impinged on the stationary propeller blade. The area where the nitrogen interacts with the PSP coated propeller has a low concentration of oxygen. As expected, this area in the image ratio has a low value and hence a dark color. The smaller dark area at the trailing edge of the blade is the shadow of the nitrogen canula, the white rectangular object above. This experiment verifies the developed method, because it shows the relation between the measured result image values and the partial pressure of oxygen.

Measurements with a rotating propeller were carried out with the rotational speeds 6,000, 7,800, and 9,600 rpm [8]. For such high speeds of the propeller large thermal heating of the propeller blades occurs. The luminescence lifetime also decreases with a higher temperature because of thermal quenching, so that, to calculate the exact pressures, the temperatures on the blade at reference and run conditions must be known.

For an application of the PSP, as described in Sect. 2, on a propeller in a wind tunnel the temperature sensitivity of the paint would be still too high. Due the stronger

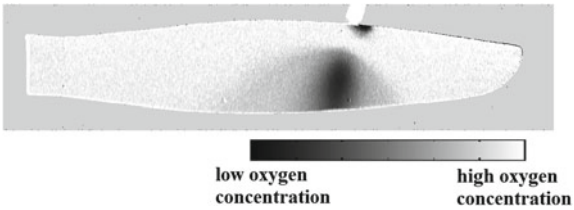

Fig. 6 Propeller blade with nitrogen jet

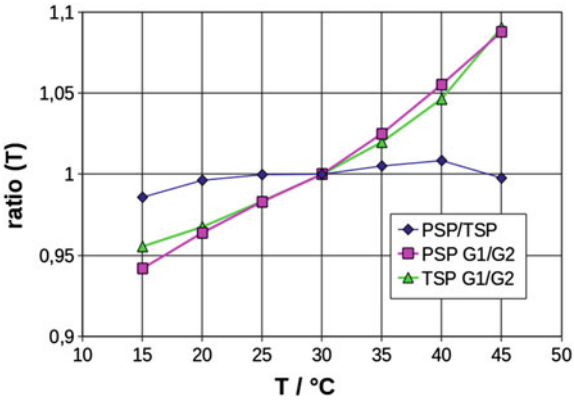

Fig. 7 Gate ratios for PSP, TSP and ratio of ratios for temperature corrected signal

heating of the tip of the blades for high rotation frequencies a temperature difference of several degrees had been observed in previous IR measurements [7], which would make precise PSP measurements with this paint impossible. To compensate for the temperature sensitivity of the PSP it is possible to use another blade with the same luminophores but incorporated into an oxygen-impermeable polyurethane-based polymer. This temperature-sensitive paint (TSP) has very much the same spectral properties as the PSP coating and its luminescence can thus be acquired with the same setup as the luminescence of the PSP. Even though the lifetime itself as well as the temperature sensitivity of the TSP will differ significantly from that of the PSP, one can find settings (delays and exposure times) for the lifetime setup with the TSP where the temperature sensitivity of the gate ratios is almost the same as that for PSP at ambient pressures. This is shown in Fig. 7, where the normalized gate ratios for PSP (delay1 $= -4\,\mu$s, delay2 $= 6\,\mu$s) and TSP (delay1 $= 6\,\mu$s, delay2 $= 18\ \mu$s) are plotted as a function of temperature. For the ratio of TSP and PSP gate ratios (double ratio) the temperature sensitivity can be reduced by a factor of 10 with, however, the drawback that the acquisition of additional two images at delays of 6 and 18 μs between end of LED pulse and start of camera exposure is required. These settings have been applied to the wind-tunnel test described in the next Sect. 4, where the double ratio method has also been used for the data analysis.

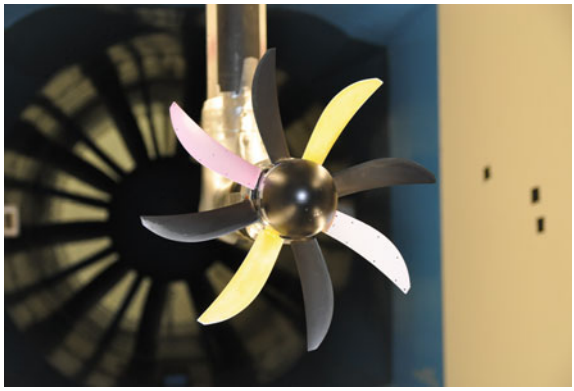

Fig. 8 Picture of the PSP/TSP coated propeller model in the test section of BLSWT

4 Wind Tunnel Experiments

Based on the results of the pre-test, a wind-tunnel experiment was conducted in the low-speed wind tunnel BLSWT of AIRBUS in Bremen. The experimental setup and wind tunnel setup are introduced here. The BLSWT is an Eiffel type wind tunnel having a test section with a cross sectional area of $2 \times 2\,m^2$. The wind speed is adjustable up to 70 m/s. The model consists of eight blades of diameter 0.3092 m, and it rotates clockwise when looking from the rear of the propeller. The pitch angle of the propeller blades can be chosen and manually adjusted. The number of revolutions per minute is adjustable between 3,000 and approximately 15,000 rpm. The propeller is driven by a pneumatic motor. PSP measurements were carried out in the low speed wind tunnel, with the propeller installed in the middle of the test section, as shown in Fig. 8. One CCD camera was installed upstream of the propeller and below the wind tunnel test-section wall. Another CCD camera was installed downstream of the propeller and in the sidewall of the wind tunnel test-section wall. The cameras were positioned behind glass windows where the high-power LED systems for excitation of the PSP were also located, see Fig. 9.

5 Results of the Wind Tunnel Test

With the above mentioned double-ratio lifetime approach for PSP and TSP quantitative pressure distributions could be measured on the fast rotating propeller. As an example for typical final results the pressure distribution on the suction side of the blade for $U_\infty = 50$ m/s and different rotational speeds of the propeller from $n = 3{,}000$ up to $n = 14{,}550$ rpm are presented in Fig. 10. In this figure one can see the growth of the low pressure area along the leading edge of the propeller blade with increasing rotational speed. For very high rotational speeds a vortex has developed along the leading edge and the corresponding low pressure regions are clearly

Fig. 9 Picture of the propeller model in the test section of BLSWT. One camera and one LED were mounted upstream the propeller

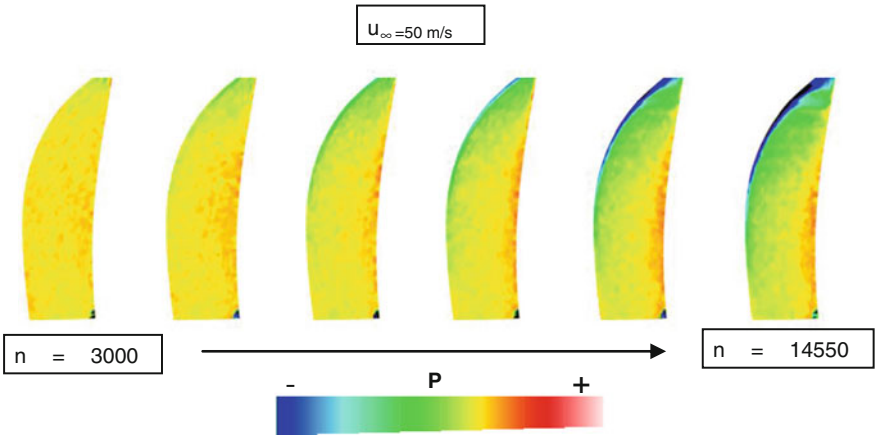

Fig. 10 PSP results of the suction side of the propeller blade

visible in the PSP result. On the trailing edge of the blade the pressure increases with increasing rotational speed and the high pressure area along the trailing edge grows with increasing rotational speed. This behaviour is in good agreement with the expected flow separation near the trailing edge on the blade [9]. From the analysis of calibration characteristics of the paint one can conclude that with the installed PSP system pressures within an accuracy of better than ± 10 mbar could be measured. Since pressures were measured on both the suction and pressure sides of the blade, force and moments can thereby also be calculated by integrating the pressure data.

6 Conclusion

Pressure measurements using the PSP lifetime method were applied to a high-speed rotating propeller. PtTFPP-based PSP was used, which shows high pressure sensitivity. Furthermore, the lifetime of the PSP is sufficiently short ($\sim$8 μs) so that feasible exposure times of the cameras can be used. In a test under controlled conditions, the ability of the experimental setup to measure pressure differences was shown using a nitrogen jet. The images from a rotating propeller blade are sharp even at very high rotational speeds. For the large temperature differences which exist on the blade, the temperature sensitivity of the PSP used here is still too high, so that a combined PSP and TSP lifetime measurement system was suggested and implemented in the wind tunnel test. With this approach quantitative pressure values could be measured on the suction and pressure side of a propeller.

References

1. Bräunling, W.: Flugzeugtriebwerke, 2nd edn. Springer, Berlin (2004)
2. Liu, T., Sullivan, J.P.: Pressure and Temperature Sensitive Paints. Springer, Berlin (2004)
3. Klein, C., Engler, R., Henne, U., et al., Application of pressure-sensitive paint for determination of models in a wind tunnel. Exp. Fluids **39**, 475–483 (2005) (DLR Göttingen)
4. Juliano, T.J., Kumar, P., Peng, D., et al.: Single-shot, lifetime-based pressure-sensitive paint for rotating blades. Meas. Sci. Technol. **22**, 085403 (2011)
5. Fey, U., Egami, Y.: Transition detection by temperature-sensitive paint. In: Tropea, C., Yarin, A., Foss, J. (eds.) Springer Handbook of Experimental Fluid Mechanics, Kap. 7.4, Springer, Berlin (2007)
6. Goss, L.P., Crafton, J.W., Jones, E.G., et al., Lifetime based pressure sensitive paint systems: issues and solutions. In: ICIASF Conference (2007)
7. Rabe, K., Rosemann, H., Schülein, E.: Transition measurements on a rotating propeller using IR thermography. DLR-IB **224–2011**, C94 (2011)
8. Hock, S.: Voruntersuchung zur Druckmessung am sich drehenden Propeller mittels der bildgebenden PSP-Lifetime-Methode. Bachelorarbeit, TU-Berlin, ILR (2012)
9. Daisuke, Y., Asai, K., Klein, C., et al., Transition detection on rotating propeller blades by means of temperature-sensitive paint. 50th AIAA Aerospace Sciences Meeting including the New Horizons Forum and Aerospace Exposition 09–12 January 2012, Nashville, Tennessee, AIAA 2012-1187 (2012)

Optical In-Flight Wing Deformation Measurements with the Image Pattern Correlation Technique

Ralf Meyer, Tania Kirmse and Fritz Boden

Abstract This chapter addresses image based deformation measurements and the development of specific optical deformation metrology for experimental flight test installations. Apart from the technical background it is a contribution to the national funded research projects FTEG-InnoLA and HINVA (LuFo IV). Based on a standard setup the measurement equipment required to perform the Image Pattern Correlation Technique (IPCT) was adapted to an application on an ultralight aircraft. In order to design the test setup a digital camera mock-up (camera DMU) was used. The analysis of selected flight test data proved the capability of the miniaturized IPCT system. A second flight test setup was developed for the DLR research aircraft Airbus A320 "ATRA" using the experience gained from the ultralight measurements. Here, the design of the IPCT components also made use of the camera DMU. Both the overall wing deformation and that of high lift devices have been measured in high-lift configuration.

1 Introduction

Optical metrologies have become more and more important for experimental flight test setups as they provide high-order position information instead of acceleration values (2nd derivative of the position vector). Also they are non-intrusive and easy to install compared to conventional approaches. Especially the "Image Pattern

R. Meyer (✉) · T. Kirmse · F. Boden
Institute of Aerodynamics and Flow Technology, German Aerospace Center DLR,
Bunsenstr. 10, 37073 Goettingen, Germany
e-mail: ralf.meyer@dlr.de

T. Kirmse
e-mail: tania.kirmse@dlr.de

F. Boden
e-mail: fritz.boden@dlr.de

A. Dillmann et al. (eds.), *New Results in Numerical and Experimental Fluid Mechanics IX*,
Notes on Numerical Fluid Mechanics and Multidisciplinary Design 124,
DOI: 10.1007/978-3-319-03158-3_55,

Correlation Technique" (IPCT) is able to deliver valuable sets of data, e.g. to investigate the wing shape of an aircraft during flight. Its spatial results can be an important input to validate numerical simulations or to improve models for wind tunnel testing.

All preparation and work on this topic was carried out at the German Aerospace Center (DLR), Institute of Aerodynamics and Flow Technology in the Department of Experimental Methods and in cooperation with several partners, e.g. the private research institute FBZ attached to the University of Applied Sciences Merseburg, Germany and Airbus Operations GmbH.

2 Principles of IPCT

The Image Pattern Correlation Technique (IPCT) is a non-intrusive, image based measurement method. It is used to virtually reconstruct spatial surface areas with an applied random dotted pattern which is recorded by at least one pair of cameras.

For post-processing the principles of stereo photogrammetry are combined with the cross correlation algorithms of Particle Image Velocimetry (PIV) to find corresponding areas in two concurrent pictures. Time-resolved evaluation of sequence recordings gives information on three dimensional deflection and deformation of the observed section via triangulation [1]. This deformation measurement technique has already been used by DLR in several on-ground and in-flight scenarios [2–4].

For all IPCT applications the measurement equipment has to be adapted to meet special requirements and restrictive boundaries. A new application for the CAD software CATIA is used to optimise the optical parameters and to design the IPCT pattern to be applied onto the measured surface. This digital camera mock-up (camera DMU) is based on data of available cameras as well as their appropriate lenses and was developed at DLR Goettingen [5]. The possibility to add components with optical features into a 3D model of the test object significantly facilitates the IPCT adaption and saves valuable time.

3 Wing Deformation Measurements with the Ultralight Aircraft UW-9 "Sprint"

A high-wing ultralight aircraft was chosen as a test platform. It had a strutted and stiffened double beam wing with a rib bearing structure and a skin of painted fabric. The wing span was 9.7 m with a sweep angle of 8°.

As can be seen in Fig. 1 the lower side of the starboard wing was measured with IPCT. The camera DMU was used to determine three main parameters: to find an optimal and feasible camera position, thereby to choose the lens and finally to design the IPCT pattern.

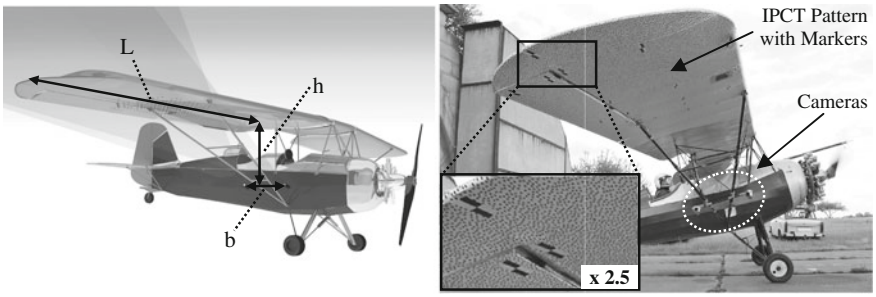

Fig. 1 *Left* CAD model of the UW-9 "Sprint" with implemented camera DMU (*b* stereoscopic base width, *h* vertical distance between cameras and wing, *L* horizontal distance of cameras to wing tip); *right* fully equipped UW-9 "Sprint" before first test flight

3.1 Experimental Setup and Test Matrix

In order to enhance the measuring accuracy and to optimize the spatial resolution the IPCT pattern should appear as homogeneously as possible in the captured images. Therefore the size, density and shape of the dots had to be modified with increasing spanwise distance from the stereoscopic camera system.

The left part of Fig. 1 shows field of view of the cameras as well as the schematic IPCT design dimensions. This includes the horizontal distance between the cameras and the wing tip of approximately 3800 mm (L), the vertical distance between the cameras and the bottom side of the wing of approximately 1000 mm (h) and the stereoscopic base width of approximately 700 mm (b). The right part of Fig. 1 shows the fully equipped test aircraft with two JAI/HS-A2 cameras mounted overhead onto a stiff CFRP pipe, the IPCT pattern with markers applied to the bottom side of the starboard wing and a miniaturized control PC in the luggage compartment (not in the picture). In this application the test pilot triggered each measurement recording sequence with a tethered remote start button.

The IPCT pattern was printed on an adhesive film which was then adhered to the fabric wing cover piece by piece. An illustration in the right part of Fig. 1 shows the camera mounting as well as the prepared measuring area. To further improve the image quality a matted but transparent adhesive film was laminated over the complete imprinted IPCT pattern prior to the application to reduce disturbing sunlight reflexions. Additionally daylight filters minimized the influence of flare light [6].

The flight test was carried out to measure the bending and twist of the wing framework. It was performed in summer 2011 and included different manoeuvres, e.g. stabilized points and a phugoid mode. This is a long-duration manoeuver induced by an elevator pulse out of a stabilized horizontal flight (damped vertical oscillation) [7]. Takeoff and landing were also recorded. With a constant frame rate of 14.5 Hz the measurement sequences had a recording length of 60 or 120 s, depending on their complexity.

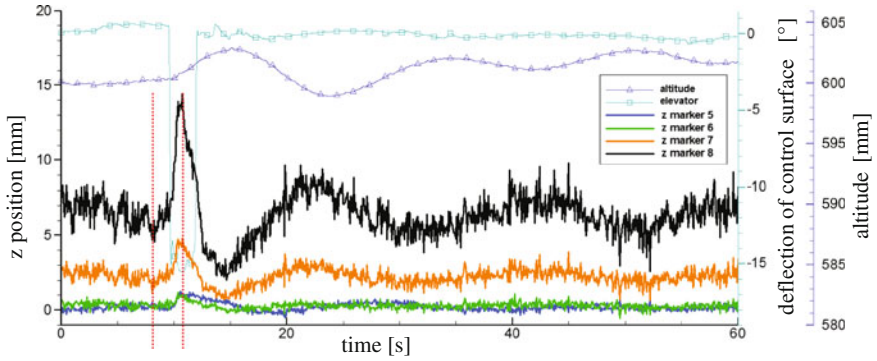

Fig. 2 Time series of marker evaluation in vertical direction (z position) including elevator pulse and flight altitude history; the *red dotted* vertical lines indicate two timestamps during stabilized flight at approx. 8.3 s and the maximum of wing deformation at approx. 10.6 s

3.2 Data Evaluation

New IPCT post-processing software has been developed at DLR Goettingen to analyse the real flight test recordings of the UW-9 "Sprint" measurements. Due to flat viewing angles and long-time sequence recordings the DaVis software used up until now was no longer suitable for these sets of experimental data.

To get a first impression of local deformations a few representative markers were evaluated. Figure 2 shows the time series analysis of the vertical deflection of four markers during a phugoid manoeuvre. The marker positions were: marker 5 at 58 %, marker 6 at 71.5 %, marker 7 at 81.5 % and marker 8 at 99 % along the half span of the rear wing beam. In this plot the oscillating wing movement caused by the vertical load factor is clearly visible. Aside from effects due to the system inertia, it is opposite in phase to the damped oscillation of the aircraft altitude.

Based on the marker evaluation an IPCT surface reconstruction was executed to obtain spatial deformation values. At any position within these surfaces discrete three dimensional data can be extracted. Further analysis was carried out for the point of maximum deformation relative to the stabilized flight case (referring timestamps are shown in Fig. 2 with red dotted lines).

As presented in Fig. 3 top right the phugoid manoeuvre caused a maximum deformation of approximately 12.2 mm at the rear wing position. Also the position of the characteristic bearing rib structure under the corrugated fabric wing cover is visible in the periodicity of the plot. A twist angle of 1.1° between front and rear spar relative to the stabilized flight case was measured as shown in Fig. 3 bottom right.

In considering the measurement accuracy, its error grows with the square of the distance to the camera system, as predicted by fundamental optics. This measurement uncertainty was determined to ±0.15 mm close to the cameras and ±0.99 mm at the wing tip for this particular measurement. The main causes for these errors are: a high

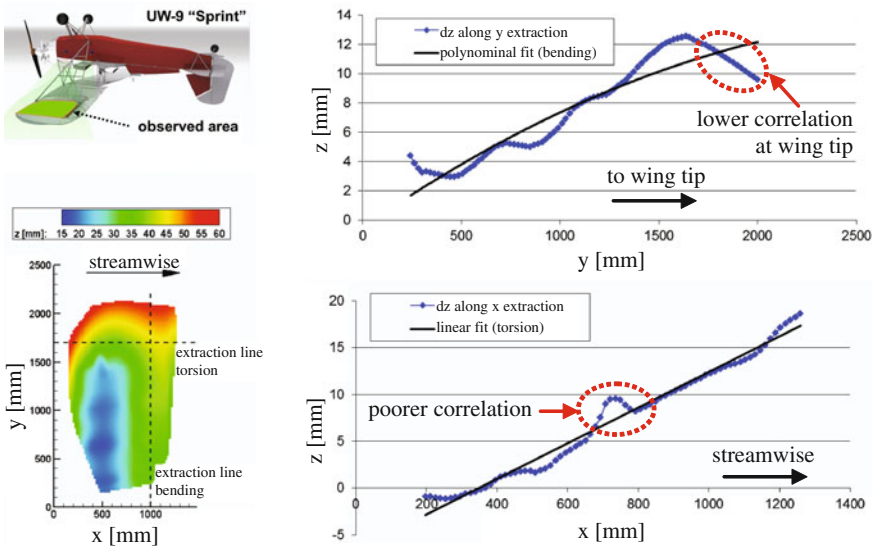

Fig. 3 *Top left* illustration of measuring area; *bottom left* IPCT surface result with extraction lines for bending and torsion analysis; *top right* bending line referred to stabilized flight; *bottom right* torsion line referred to stabilized flight

level of broadband mechanical camera vibration (induced by upstream flow and engine revolution), unsteady illumination as well as algorithmic limitations caused by image noise.

4 Wing Deformation Measurements with the Airbus A320 MSN659 "ATRA"

In summer 2012 a further flight test campaign has been performed within the framework of the LuFo IV/3 project HINVA [8] using the experience in IPCT deformation measurements gained with the ultralight aircraft UW-9 "Sprint". The Advanced Research Technology Aircraft "ATRA" of the German Aerospace Center DLR was equipped with four stereo camera systems for IPCT.

4.1 Experimental Setup and Test Matrix

The upper side of the starboard wing was divided into three main sections and equipped with IPCT pattern and markers. Figure 4 illustrates the layout of the IPCT setup including four stereo camera pairs, of which three were operated simultaneously. All cameras were mounted with stiff supports onto the cabin floor seat rails.

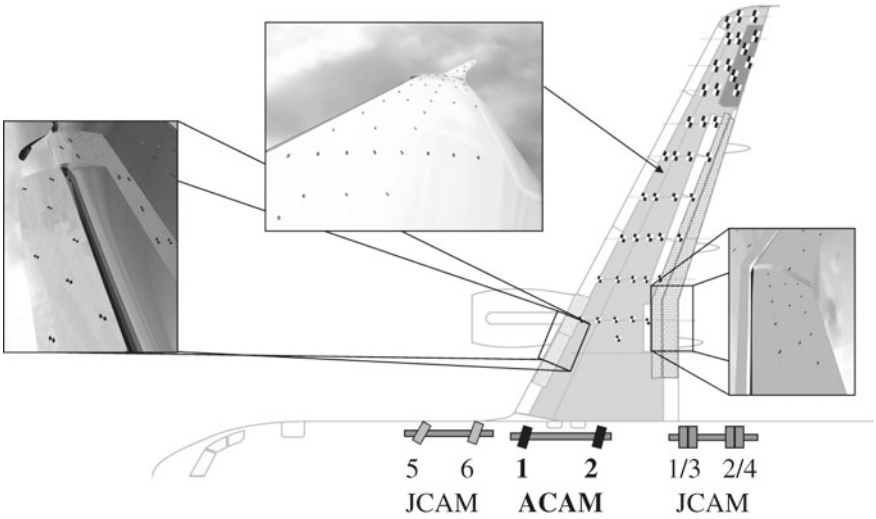

Fig. 4 Schematic layout of the IPCT setup for the HINVA flight test on the "ATRA"

With one stereo camera system ("ACAM", AVT GX3300, 8 Mpx) a grid of markers on the main wing and the inner side of the wing tip fence was observed. These high resolution cameras measured the overall deformation of the wing box. In addition another three pairs of cameras ("JCAM", JAI/HS A2, 2 Mpx) were installed to record the IPCT pattern on the flaps and on the in-board slat.

All components and parameters needed to build up the IPCT system were prepared with the camera DMU (see also Sect. 2): camera positions and their field-of-view as well as the choice of suitable objective lenses were determined. This was the first time that the complete virtual design of the IPCT pattern and markers had been carried out fully prior to the measurement. An example of a virtual and a real camera recording is presented in Fig. 5. It demonstrates the performance of the camera DMU and its close resemblance to the final marker dimensions and distribution during flight test.

With a frame rate of 10 Hz synchronized sequences were captured in landing ("full", deployed high lift devices) and in cruise configuration ("clean"). The measurements were carried out during dynamic stall manoeuvres. In addition stabilized points with a varied angle of attack up to about 18° (close to maximum lift) were recorded.

4.2 Data Evaluation and First Results

All data sets of these deformation measurements were processed with the new further-improved IPCT software (see also Sect. 3.2). In Fig. 6 the time series analysis of 41 evaluated markers illustrates the progress of the wing deformation across specific

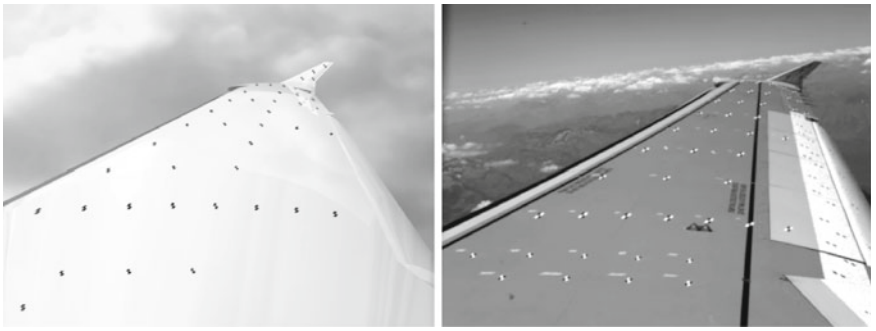

Fig. 5 *Left* virtual design of the markers and their distribution with camera DMU; *right* real camera recording of the marker grid on the starboard wing during flight test

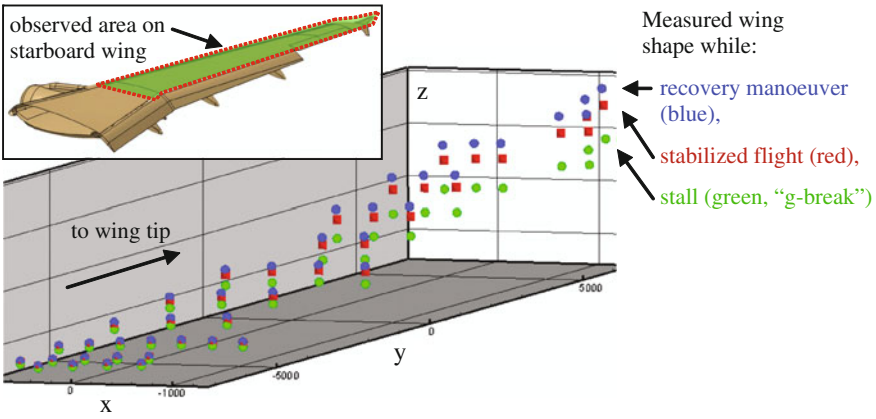

Fig. 6 Evaluation of marker grid on the starboard wing during stabilized level flight, "g-break" of stall manoeuver and recovery manoeuver after stall with maximum deformation

stages of one specific stall manoeuver with idle thrust. The high lift devices were in landing configuration.

For stabilized flight and a mean load factor n_z of 1 g the wing tip moved downwards by about 320 mm (neg. z direction) during stall. At that point the vertical load factor n_z was below 0.5 g during the loss of lift ("g-break"). The maximum upward deformation (pos. z direction) of about 200 mm was detected during the recovery manoeuver with an n_z of 1.43 g so that the measured total amplitude of the wing tip during this particular stall manoeuver was approximately 520 mm.

The accuracy for this measurement close to the cameras and at the wing tip was at the most about ± 2.8 mm and ± 4.1 mm, respectively. Flat viewing angles, large distances between the cameras and the observed area as well as poorly calibrated sections are the main influencing factors.

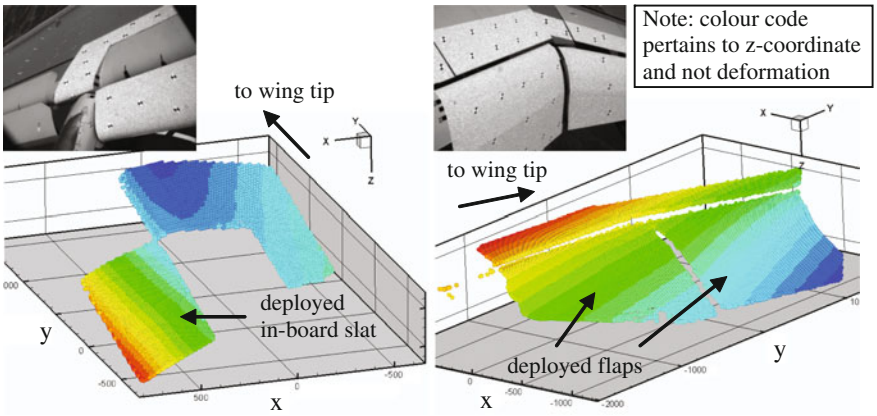

Fig. 7 *Left* IPCT surface result of in-board slat in landing configuration; *right* IPCT surface result of kink area between in-board and out-board flap in landing configuration

A first IPCT surface reconstruction of a measurement point under stabilized flight conditions with 17° angle of attack was carried out. An example of the fully deployed in-board slat and the junction of in-board and out-board flap is shown in Fig. 7 below.

Further IPCT time series analysis will concentrate on an examination of the position and shape of the high lift devices as well as their behaviour during the recorded manoeuvers.

5 Conclusion

Recent developments of the Image Pattern Correlation Technique improved its field of application. The in-flight wing deformation has been measured successfully on a small aircraft as well as on a turbo jet airliner.

In order to adapt the IPCT setup, the camera DMU was shown to be a time saving tool with good performance. For the first time the IPCT pattern and marker design was carried out completely virtually, thus demonstrating its usefulness and reliability.

The ultralight aircraft UW-9 "Sprint" has a stiff wing framework. Its largest deformation of less than 20 mm bending and about 1° twist angle at the wing tip was detected during a phugoid manoeuver. Despite influences of vibration and illumination the accuracy was better than ± 1 mm in the observed area of about 2×1 m. This miniaturized IPCT setup can easily be adapted to comparable applications on test objects such as gliders or other small aircrafts.

Multi camera deformation measurements have also been carried out on the wing of the Airbus A320 "ATRA". The aim was to investigate the deformations of the wing and its high lift devices during stall manoeuvres. First results showed wing tip amplitudes of about 500 mm from the loss of lift up to recovery. A measurement

accuracy of better than ±5 mm at the wing tip (corresponding to about 1 % of the maximum measured deformation) is a good result for a half span width of about 17 m and for the given flat viewing angles. Further IPCT time series analysis is planned to gain more information about the aircraft behaviour during stall manoeuvers. Additionally these results can be used for validation with numerical simulations.

References

1. Kompenhans, J., Schröder, A., Engler, R., Klinge, F., Stasicki, B.: Development and application of image based measurement techniques for aerodynamic investigations in wind tunnels, DLR Goettingen, conference. In: High-Speed Flow: Fundamental Problems. Zhukovsky, Russia (2004)
2. Boden, F., Kirmse, T., Weikert, T., Wolf, T., Petit, C., Jentink, H. W.: Application of a new optical measurement technique for non-intrusive wing deformation measurements on a large transport aircraft. In: DLR Goettingen, 21st SFTE (EC) Symposium, Vergiate (VA), Italia (2010)
3. Kirmse, T.: Model deformation measurements in DNW-NWB within the DLR project ForMEx. In: DLR Goettingen, 8th ONERA DLR Aerospace Symposium—ODAS (2007)
4. Boden, F., Kirmse, T., Stasicki, B., Lanari, C.: Advanced Optical In-Flight Measurements on Deformation of Wings and Propeller Blades. DLR Goettingen, Germany (2008)
5. Krombholz, C.: Benutzerhandbuch—Digital Mockup-Camera-Toolbox für CATIA V5, internal DLR report, DLR-IB 224–2010 A 41 (2010)
6. Meyer, R.: In-flight wing deformation measurements at a microlight aircraft with stereo IPCT (Image Pattern Correlation Technique), DLR Goettingen/TU Dresden, Germany, diploma thesis ILR-NWK D, 11 Feb 2011
7. Jategaonkar, R. V.: Flight Vehicle System Identification—A Time Domain Methodology. AIAA Inc., Reston, Virginia, ISBN: 1-56347-836-6 (2006)
8. Rudnik, R., Reckzeh, D., Quest, J.: HINVA - High lift INflight Validation—project overview and status. In: 50th AIAA Aerospace Science Meeting including the New Horizon Forum and Aerospace Exposition, pp. 2012–0106. Nashville, Tennessee, AIAA (2012)

Development of a Rotating Camera for In-flight Measurements of Aircraft Propeller Deformation by Means of IPCT

Fritz Boden and Boleslaw Stasicki

Abstract The efficiency of a propeller is directly affected by the shape of the propeller blades, that are deformed due to the loads during flight operation. Therefore the measurement of the real shape of the blades is of great interest. A powerful optical measuring method called Image Pattern Correlation Technique (IPCT) enables the flight test engineers to perform such measurements in a non-intrusive way. It has already been applied to in-flight investigations of aircraft wing and propeller deformations, but only for one fixed propeller phase angle. To extend the optical access to 360° a new rotating 3-D image acquisition system placed in front of the examined propeller has been designed. The measurement technique IPCT as well as the development of the rotating camera system are described in this chapter.

1 Introduction

The performance of an aircraft propeller is highly dependent on shape changes arising from in-flight deformation, the measurement of which is very demanding. Conventional methods like strain gauges and accelerometers are difficult to apply because of problems with their installation, their wiring, the data transmission, and the balancing of the propeller. Furthermore such sensors provide the data only at the location where they have been installed.

As has been demonstrated in the European Specific Targeted Research Project (STReP) AIM—Advanced In-flight Measurements Techniques [1, 2], modern optical measurement techniques like the Image Pattern Correlation Technique (IPCT) are able to deliver the in-flight shape of a deformed rotor or propeller blade in a non-intrusive way.

F. Boden (✉) · B. Stasicki
Institute of Aerodynamics and Flow Technology, DLR/German Aerospace Center, Bunsenstr. 10, 37073 Göttingen, Germany
e-mail: fritz.boden@dlr.de

A. Dillmann et al. (eds.), *New Results in Numerical and Experimental Fluid Mechanics IX*, Notes on Numerical Fluid Mechanics and Multidisciplinary Design 124,
DOI: 10.1007/978-3-319-03158-3_56, © Springer International Publishing Switzerland 2014

Within this project a stationary IPCT system measuring the deformation of the selected propeller blade has been designed and implemented [3]. Due to the limited optical access through a fuselage window only a small angle range of the blade rotation could be investigated. Moreover a very short image integration time of only 5 µs had to be applied in order to prevent pattern smearing in the images resulting from the fast rotation.

To overcome these difficulties one objective of the EC-funded follow up project AIM^2 is to develop an image-based measurement system rotating with the propeller and thus enabling blade deformation measurements over a complete revolution. In this chapter, the measurement technique IPCT, the investigated object and the first design of the new measurement system including first hardware tests are briefly presented.

2 Principle of IPCT and Example Results

According to [4], the Image Pattern Correlation Technique (IPCT) is an optical, non-intrusive measurement technique, based on photogrammetry in combination with modern correlation algorithms developed for Particle Image Velocimetry (PIV) [5]. The simplest IPCT setup consists of one monochrome camera observing an object whose surface is covered with a random dot pattern. To measure 3D coordinates directly, at least two cameras in stereoscopic arrangement are required. In that arrangement the 3-D coordinates of patterned areas identified in both camera images are directly calculated by means of central projection and triangulation. To do so, both the intrinsic (e.g. focal length, distortion, principal point) and extrinsic parameters (position and orientation) of both cameras have to be determined by a calibration of the installed stereo camera system. Figure 1 depicts the main steps of the image-based propeller deformation measurements.

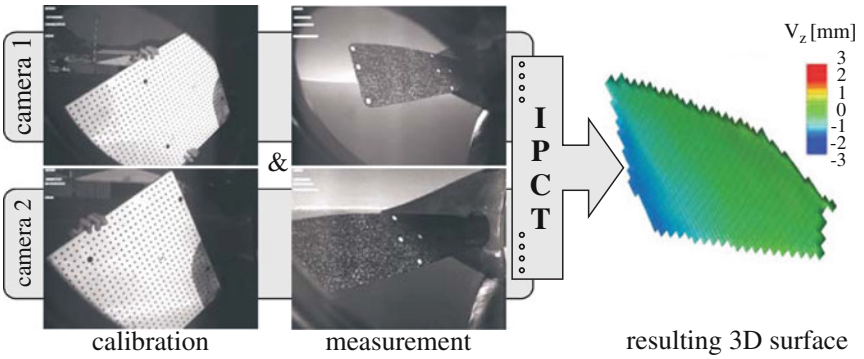

Fig. 1 Stereoscopic IPCT processing (calibration → measurement → result)

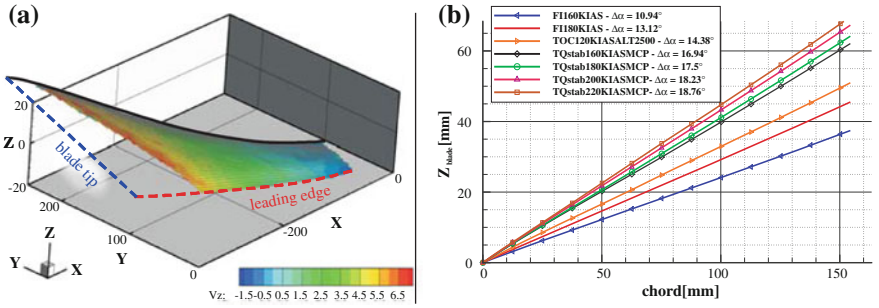

Fig. 2 Example results of IPCT propeller measurements (**a**—measured surface for one flight manoeuver, **b**—chordwise extracted *line* and local blade pitch angle for different flight manoeuvers)

Theoretically the accuracy of IPCT is of the order of 0.01 % of the observed area (e.g. 0.1 mm on 1 m), depending on the observation angle and the used optics (see [6]). Figure 2 shows some example results of the IPCT measurements performed within the EC funded project AIM. The first in-flight IPCT propeller blade measurements were conducted on a Piaggio P180 and with a stationary camera installation as described in [2]. Figure 2a depicts one in-flight measured blade surface and demonstrates the ability of the IPCT for highly accurate surface measurements in a non-intrusive way. Figure 2b shows chordwise lines extracted at the same span of the propeller blade surface but for different load cases. Out of these data, the real local pitch angle can be determined with a high accuracy.

3 The Investigated Object

Within AIM^2 it is planned to measure the deformation of a propeller blade for a complete revolution in-flight and to demonstrate the possibilities of IPCT in an industrial environment. Therefore measurements are planned on a small propeller aircraft in tractor configuration-the Evektor VUT100 Cobra (see Fig. 3). The propeller is a constant speed propeller with 3 blades having a rotation speed of 2,700 rpm and a diameter of approximately 2 m. The first tests of the system are scheduled for the end of 2012. The measurement system will be mounted on the propeller made by Avia propeller. Both ground and flight tests will be performed on the Evektor VUT100 Cobra, which will be provided by its manufacturer, the Evektor company. These are both Czech companies cooperating with DLR as members of the AIM^2 consortium. Prior to the tests at the aircraft laboratory experiments are performed using a genuine Cobra propeller hub with one blade covered with a standard stochastic dot pattern as shown in Fig. 4. However, for larger propeller diameters and/or notably flat camera position the usage of progressive dot diameter or of a cauliflower pattern according to the DLR patent DE 10 2007 056 777.6 [7] can increase a IPCT signal uniformity along the blade.

Fig. 3 Evektor VUT100 Cobra

Fig. 4 Propeller hub with one blade

4 Fast Rotating 3-D Imaging System

As mentioned above the new optical measurement system fixed onto the front of the rotating propeller hub has been designed to overcome the limitations of an installation outside the rotating frame [8]. The great advantage of this solution is an unlimited optical access to the full blade surface which allows a 360° scan to be performed. Moreover, a 10^3 times longer integration time can be chosen, since—apart from the deformation and pitch adjustment by the pilot—there is no displacement of the blade relative to the camera, i.e. no motion smearing risk. This greatly increases the light sensitivity of the cameras. The synchronized pulsed blade illumination might therefore be unnecessary. However, the design and manufacturing of this sophisticated, hitherto untried measurement system is a very demanding effort.

The described system consists of a specially designed double (stereo) camera based on two high-speed CMOS-sensors each of 1,280 × 1,024 pixel resolution, a digital phase shifter, an image acquisition board, a fast miniature computer with WLAN, a laser trigger device and a GPS receiver. All components are powered by a rechargeable lithium iron phosphate ($LiFePO_4$) battery of 13.2 V, 3.3 Ah.

The entire system shall be placed in front of the examined propeller within or instead of its spinner and will rotate together. The camera field-of-view is adjusted to observe the selected blade of the propeller. This blade is covered with the IPCT pattern. In response to each trigger pulse, which comes once per propeller revolution, an image pair will be captured simultaneously at the blade position determined by the phase lag calculated by the phase shifter. This device can be set for a constant phase shift (which does not depend on the rotation speed and its changes), in which case the blade deformation will be stroboscopically measured always in the same propeller position. Alternatively, after each image capture the phase shift can be increased or decreased by a given step, thereby enabling a scan over a full blade revolution, or, if desired, over a specified angle range.

The sequence of image pairs is acquired and transmitted over two Gig-E channels to the miniature computer and then stored on the solid-state flash drive (SSD) in

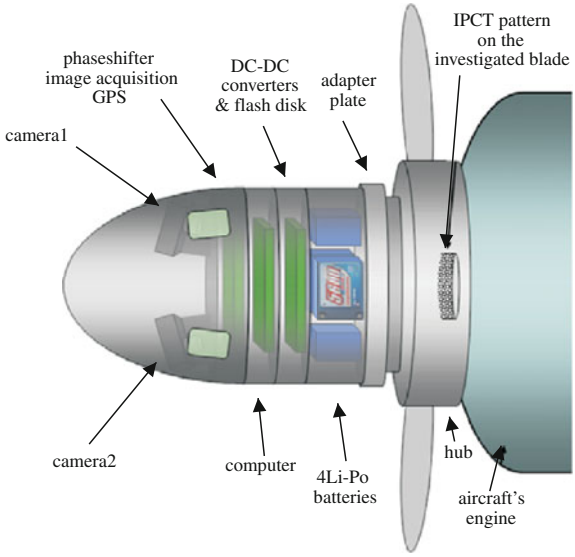

Fig. 5 Design of the imaging system

real time together with the present GPS data. Via WLAN the system can be controlled from the cabin to check the current image quality. After the test, the recorded sequences can be retrieved over WLAN, USB-connector or by removal of the SSD. The concurrent replacement of the SSD and that of the batteries is fast and is recommended when a further flight test is planned shortly after.

5 Mechanical and Optical Design Considerations

Mechanical and aerodynamic considerations dictate that the system has to be light, compact, but robust and resistant against shocks, vibrations and centrifugal forces. Therefore it is split into function blocks with smallest possible diagonal dimensions. The batteries and three printed circuit boards (PCB) are placed onto stiff metal frames, thereby reducing the risk of damage by stretching due to the centrifugal forces. These frames are stacked one upon the other, forming a cylinder fixed to the propeller's hub by means of an adapter disk (Fig. 5). This allows for easy alignment of the system when applied to measurements in other aircrafts or rotating facilities.

Rather than using two separate cameras, an optical system consisting of one double camera has been designed. The system consists of two separate CMOS sensors with light-weight microlenses having the base distance in between required for stereoscopic imaging. To endure the centrifugal forces, the cover of the camera system is made in one rigid part having the center of gravity on the rotation axis. The object plane (surface of the propeller blade) and the image plane (sensor) are not parallel. Thus, only a small region of the blade would be in focus. To ensure a sufficient focal depth, the lenses are slightly inclined to the sensors, according to the Scheimpflug principle.

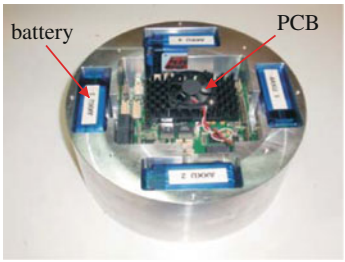

Fig. 6 Holder for the rotation test

Fig. 7 Performing the rotation test

6 The Rotation and Vibration Tests

When in rotation on the real aircraft, the whole system is exposed to extreme vibrations and high centrifugal force. According to the specifications provided by Evektor and AVIA companies, the Cobra propeller rotates at 2,700 rpm and its vibration spectrum perpendicular to the propeller axis ranges from 20 to 150 Hz and reaches load factors up to 20 g, implying an extreme load for all system components. Therefore the system components must be carefully tested before installing in the aircraft for ground and flight tests. For this testing a special metal holder has been designed (Fig. 6). The electronic boards and the $LiFePO_4$ batteries were rotated for 1 h at 3,000 rpm with the help of a digitally controlled machine (Fig. 7). Then, using a 90° holder (Fig. 8), they were vibrated by means of the programmable high-power shaker shown in Fig. 9. The specified vibration component was the vertical one I. All three components of the vibration were measured and recorded by means of an attached acceleration sensor. The system electronics were vibrated in the range from 20 up to 150 Hz/20 g at angles of 0°, 45° and 90°. Each frequency sweep of 1 octave per minute took 2 min 54 s. An example record for 0° is displayed in Fig. 10. Afterwards the system has been examined in the laboratory. No mechanical damage or electrical degradation of the component devices has been detected. After manufacturing of the final version of all components, the entire system will be tested again as described above and then installed on the Cobra propeller.

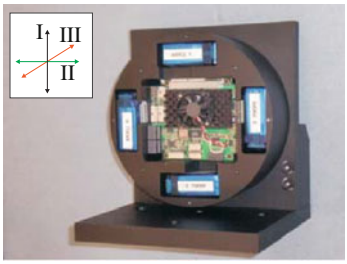

Fig. 8 Holder for the vibration test

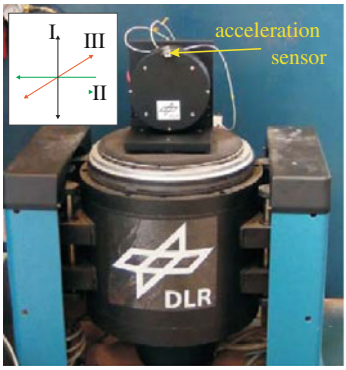

Fig. 9 Performing the vibration test

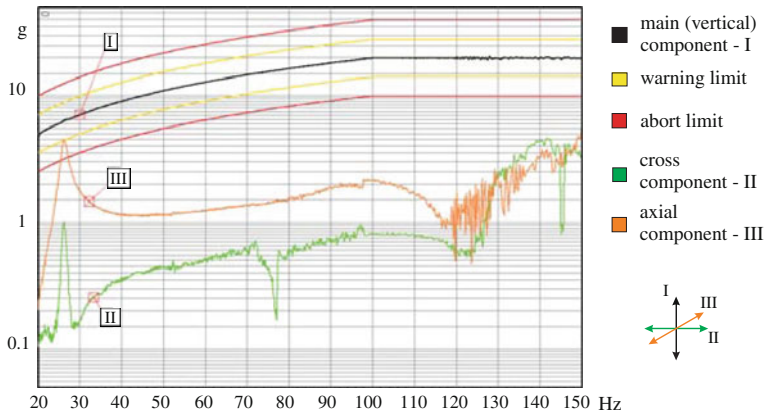

Fig. 10 Measured object acceleration for a frequency sweep from 20 to 150 Hz (shaker limits: warning limit is the acceleration limit above which the shaker gives a warning signal, abort limit means automatic abort of the test)

7 Conclusions and Next Activities

The lessons learned in the AIM project led to a new rotating camera system for 360° propeller blade deformation measurements by means of IPCT, which is now being developed within the project AIM^2. At its present status, the single components of this challenging installation have been chosen and a first prototype of the recording system has been checked for its endurance and robustness against rotational forces and vibrations. Furthermore, duration of operation over one full hour could be successfully demonstrated. From the designed recording hardware, the next step is to mount the system onto a real propeller and subsequently to build and test a first prototype. Boundary conditions of this design are the weight of the system, the ability to withstand the loads and a minimal influence to the propellers aerodynamics and balancing. Furthermore, challenges arising from the maximal frame rate as well as the design of the optics have to be dealt with. Also the handling of the overall system and the flight approval have to be taken into account.

Acknowledgments The authors would like to thank the European Commission for supporting these research activities within the 7th research framework programme. They thank also Mr. Tvrdik (AVIA Propeller) and Mr. Ružička (Evektor) for their valuable support. Furthermore they thank Dr. U. Füllekrug for his assistance in carrying out the vibration test and Mr. R. Ollech for his support in the rotation test.

References

1. Boden F., Kirmse T., Stasicki B., Lanari C.: Advanced optical in-flight measurements on deformation of wings and propeller blades. In: SFTE Symposium, Manching, 22–24 Sept 2008
2. Stasicki B., Boden F.: Application of high-speed videography for in-flight deformation measurements of aircraft propellers. In: Proceedings of 28th ICHSIP, vol. 7126. SPIE (2009)
3. Stasicki B., Boden F., Bodensiek K.: Application of image pattern correlation for non-intrusive deformation measurements of fast rotating objects on aircrafts. In: Proceedings of International Conference on Experimental Mechanics ICEM 2009, vol. 7522. SPIE (2009)
4. Kompenhans J., Schröder A., Engler R., Klinge F., Stasicki B.: Development and application of image based measurements techniques for aerodynamic investigation in wind tunnels. In: International Conference High Speed Flow. Zhukovsky, Russia, 21–24 Sept 2004
5. Raffel, M., Willert, C., Kompenhans, J.: Particle Image Velocimetry. Springer-Verlag, Berlin (1998)
6. Boden F., Torres A., Maucher C.: Advanced optical rotor blade deformation measurements on a flying helicopter. In: 35th European Rotorcraft Forum. Hamburg, Germany. ISBN 978-3-932182-65-0. ISSN 0178-6326, 22–25 Sept 2009
7. Klinge, F., Stasicki, B.: Messverfahren und messanordnung mit einem stochastischen punktemuster sowie stochastisches punktemuster zur verwendung dabei. Patent DE 10 2007 056 777.6
8. Stasicki B., Neumann B., T. Kirmse T.: Messen von Deformationen eines schnell rotierenden Objekts. Patent application DE 10 2011 001 268.0 (2011)
9. Klinge F., Schröder A., Raffel M., Binder B.: Verfahren zum Vermessen einer Oberfläche. Patent DE 103 41 959.4 (2003)

Impact of Forced High Frequency Airfoil Oscillations on the Shock Motion at Transonic Buffet Flows

Antje Feldhusen, Axel Hartmann, Michael Klaas and Wolfgang Schröder

Abstract The mechanisms of buffet are investigated by analyzing the flow over a DRA 2303 supercritical airfoil using time-resolved stereo particle-image velocimetry (TR-SPIV) in the trailing edge region and pressure measurements on the surface of the airfoil. The freestream Mach number is $M_\infty = 0.73$ and the angle of attack is $\alpha = 3.5°$ since under these conditions a distinct buffet flow occurs. To further study the influence of airfoil oscillations on the buffet flow and the occurrence of the lock-in of the buffet frequency into prescribed frequencies, the airfoil model undergoes forced oscillations near the natural buffet frequency.

1 Introduction

The flow over a supercritical airfoil under transonic conditions is characterized by the presence of a local supersonic region on the upper surface which is terminated by a shock . Complex interactions between the shock wave and the boundary layer occur that may lead to a separation of the flow downstream of the shock wave. At certain flow conditions, the so-called buffet phenomenon, i.e., a self-sustained shock wave oscillation, appears. The resulting pressure fluctuations cause unsteady loads that act on the wing structure and the aeroelastic response of the structure, known as buffeting, may lead to critical loads on the structure. Despite numerous buffet analy-

A. Feldhusen (✉) · A. Hartmann · M. Klaas · W. Schröder
Institute of Aerodynamics, RWTH Aachen University,Aachen, Germany
e-mail: a.feldhusen@aia.rwth-aachen.de

A. Hartmann
e-mail: a.hartmann@aia.rwth-aachen.de

M. Klaas
e-mail: m.klaas@aia.rwth-aachen.de

W. Schröder
e-mail: office@aia.rwth-aachen.de

A. Dillmann et al. (eds.), *New Results in Numerical and Experimental Fluid Mechanics IX*,
Notes on Numerical Fluid Mechanics and Multidisciplinary Design 124,
DOI: 10.1007/978-3-319-03158-3_57,

ses the phenomenon is not fully understood, yet. It is, however, crucial to understand this phenomenon in the context of lightweight design making further investigations necessary. Considering the buffet mechanism Lee [1] hypothesizes that the shock wave generates disturbances that travel downstream and interact with the trailing-edge. Due to this interaction, disturbances are generated at the trailing edge that travel upstream and force the shock to move into the upstream direction. The changing of the shock position modifies the separation. The separation area grows, and so the waves travelling upstream are more scattered such that they have less influence on the shock wave. As a result, the shock wave moves downstream to its former position and this marks the beginning of a new oscillation cycle. That is, the whole oscillation cycle is based on a feedback loop of upstream and downstream travelling disturbances. According to Lee's model [1] the buffet frequency is determined by the velocities of the up- and downstream travelling disturbances

$$f = \left(\frac{c - \bar{x}_{shock}}{u_d} + \frac{c - \bar{x}_{shock}}{u_u} \right)^{-1}. \tag{1}$$

The distance between the shock wave and the trailing edge is $c - \bar{x}_{shock}$ and the convection velocities of the fluctuations into the downstream and upstream direction are denoted by u_d and u_u. In recent experiments the flow over the supercritical laminar-type DRA 2303 profile has been investigated with regard to the buffet effect by means of pressure measurements and TR-PIV by Hartmann et al. [2, 3]. Using a modified formulation of Lee's equation

$$f = \left(\frac{c - \bar{x}_{shock}}{u_d} + \frac{\sqrt{(c - \bar{x}_{\mathrm{shock}})^2 + z^2_{\mathrm{shock}}}}{u_u} \right)^{-1} \tag{2}$$

the varying sound pressure level of the trailing-edge noise has been identified to be responsible for the shock movement at buffet flows. The variable z_{shock} denotes the extension of the shock. According to this approach, not the shock foot, but the upper end of the shock wave is the point where the acoustic waves do act on and force the whole shock to move into the upstream direction, since the shock is weaker and therefore more sensitive to disturbances further off the airfoil surface. The appearance of a lock-in of the buffet frequency when the airfoil undergoes forced oscillations, recently observed by Raveh et al. [4] can't yet be described by the feedback-loop model.

The objective of this investigation is to further analyze the flow above the DRA 2303 airfoil model in the region of the trailing edge by pressure measurements and TR-SPIV. The influence of prescribed airfoil oscillations is investigated to gain further insight into the buffet phenomenon and the lock-in effect. In contrast to the investigations conducted by Hartmann et al. [5], the forced oscillation amplitude is smaller, i.e., it is on the order of the magnitude of the shock wave oscillation.

2 Experimental Setup

The experiments are performed in the trisonic wind tunnel of the Institute of Aerodynamics of the RWTH Aachen University. The Reynolds number per meter ranges from $1.2 \cdot 10^7 < \mathrm{Re/m} < 1.4 \cdot 10^7$. The wind tunnel is an intermittently working vacuum storage tunnel incorporating a 0.4×0.4 m test-section with adaptive upper and lower walls to simulate unconfined flow conditions [6]. During the experiments the humidity of the air inside the tunnel is kept below 4 % and the total temperature is about 293 K such that the shock wave position remains uninfluenced by the environment [7]. The chord length of the DRA 2303 airfoil model is $c = 200$ mm and the relative thickness to chord ratio is 14 %. The laminar-turbulent transition is fixed at 5 % of the chord length. The rigid model is mounted to an elastic support consisting of two leaf springs on both sides of the model which can be independently adjusted in terms of stiffness and offset from the virtual axis of rotation located at 25 % chord in order to simulate a realistic aeroelastic damping as it occurs in swept wings due to the coupling of bending and torsion modes (see Fig. 1). The airfoil model is equipped with 43 steady pressure taps on the upper surface and 42 on the lower surface to acquire the mean pressure distribution along the chord length. Additionally, twenty Kulite XCQ-080 and two Entran EP-I sub-miniature pressure transducers are used to perform dynamic pressure measurements. The sensors are installed in a range from $x/c = 0.4 - 1.0$ on the upper surface and at $x/c = 0.3$, 0.5, and 0.7 on the lower surface. Time-resolved stereo particle-image velocimetry (TR-SPIV) is performed in the trailing edge region. DEHS droplets with a mean diameter of 0.6 μm are used as seeding. The seeding generator is positioned inside the settling chamber in order to achieve a homogeneous seeding distribution. The light for the illumination of the particles is provided by a Quantronix Darwin Duo 40M double pulsed Nd:YLF laser with a wavelength of 527 nm. The laser pulse separation time is 9 μs and the energy per laser pulse is approx. 15 mJ. The particle images are recorded by two Photon Fastcam SA–3 CMOS cameras which are mounted in Scheimpflug condition outside the tunnel on each side next to the window of the test section. Figure 1 shows a schematic drawing of the experimental setup. All PIV measurements are performed using a frame rate of 4800 Hz and a resolution of 768×512 pixels, leading to a sampling rate of 2400 Hz. The evaluation of the recorded images is done by PIVview 3C, using a multi-grid interrogation method with a final sample size of 24×24 pixels. The vector spacing is 1.36 mm/vector.

3 Results

In this study, four different cases have been investigated. First, a reference case in which the airfoil is held in a fixed position without any externally forced oscillations has been measured. This case is referred to as case I. Furthermore, three excitation

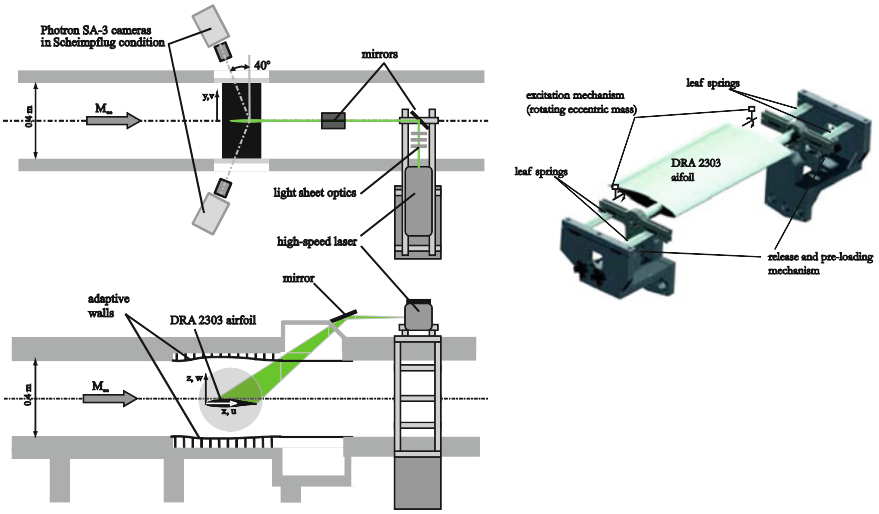

Fig. 1 TR-SPIV setup, plan view (*top*) and side view (*bottom*) and elastic model support [3]

frequencies have been chosen to generate heave/pitch model oscillation with the help of an eccentric mass added to the airfoil model at x/c = 0.675 (see Fig. 1). The reduced excitation frequencies $\omega^* = 2\pi f c/u_\infty$ based on the velocity of the incoming flow u_∞ are $\omega^* = 0.63$, referred to as case II, $\omega^* = 0.7$, referred to as case III, and $\omega^* = 0.715$, referred to as case IV. The mean pitch amplitude is about 0.02°.

3.1 Fixed Airfoil

First, the airfoil is held in a fixed position. It was shown by Hartmann et al. [2] that for an angle of attack of 3.5° and a freestream Mach number of 0.73 buffet occurs due to the natural feedback loop without any external excitation of the airfoil. The oscillating nature of the flow can be seen in Fig. 2. From the power spectral density of the pressure fluctuations it can be derived that the natural buffet frequency is $\omega^* = 2\pi\ fc/u_\infty = 0.68$ since an increased fluctuation level can be found at this value.

In the following, phase-averaged results of the flow pattern are presented. Since the flow is of an oscillating nature, the phase-averaging is done separately for the two extreme states of the flow, i.e., on the one hand when the shock is in its most upstream position and, on the other hand, when the shock is in its most downstream position. The flow angle ß between the airfoil surface and the flow just outside the separation serves as criterion to determine the shock wave position. The angle ß is

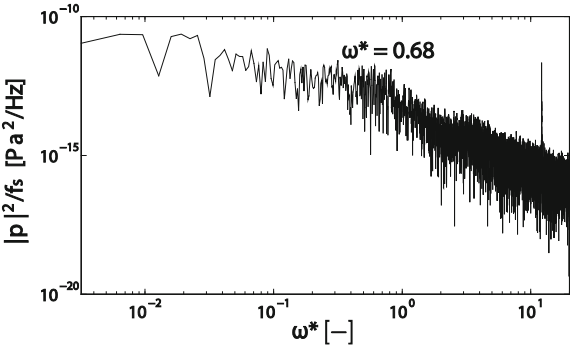

Fig. 2 Power spectral density of the pressure fluctuations at x/c = 0.5, reference case

maximum just downstream of the shock in its most upstream position and minimum when the shock is in its most downstream position [3]. Figure 3 shows the contours of the two-point correlation of the velocity field for the reference case, representing the phase-averaged vortex pattern

$$R_{x_a,z_a} = \frac{\overline{(u'w')_{x_a,z_a}.(u'w')_{x_l,z_J}}}{\sqrt{\overline{(u'w')^2_{x_l,z_J}}}}. \tag{3}$$

The correlation point is (x_a/c, z_a/c) = (1.064, 0.1617). The correlations reveal vortical structures. The mean distance between two vortices is determined to be l_v/c = 0.11. In preceding experiments Hartmann [3] determined the wave propagation speeds within the flow above the airfoil during buffet. In these experiments the downstream propagation speed of the fluctuations inside the flow was 19 m/s and the upstream propagation speed was −80 m/s. Since the vortical structures shown in Fig. 3 travel downstream at 19 m/s, sound waves at a frequency around 1000 Hz representing the upstream part of the feedback loop are emitted when the vortices pass over the trailing edge.

Figure 4 shows the correlation of the absolute velocity distribution. The time resolved velocity fluctuations along a streamline at two locations x_m/c and x_n/c and separated by the time delay τ are correlated with each other via

$$R_{nm}(x, \tau) = \frac{\overline{U'_n(t).U'_m(t+\tau)}}{\sqrt{U'^2_n.U'^2_m}}. \tag{4}$$

The chosen streamline for the correlation is located just above the separation region. The point x_n/c is constant at 0.82 and the point x_m/c varies over the whole extension of the chosen streamline in the flow direction. The time delay τ ranges from $\tau = -0.02$ to $\tau = 0.02$ s. Figure 4 evidences the correlation to change its sign in the trailing edge region. Upstream of the trailing edge (x/c = 1), the correlation

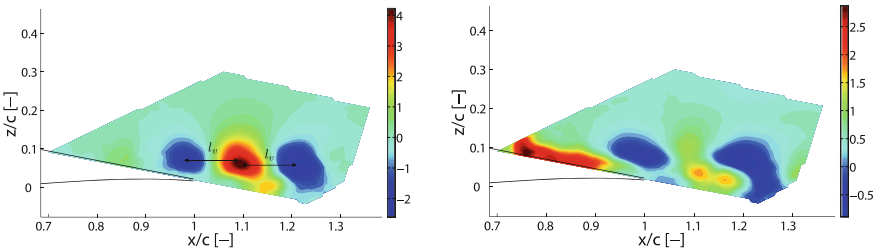

Fig. 3 Contours of the two-point correlation of the velocity fluctuation for $x_a/c = 1.064$ and $z_a/c = 0.1617$; (*left*) phase-averaged for $ß_{max}$; (*right*) phase-averaged for $ß_{min}$

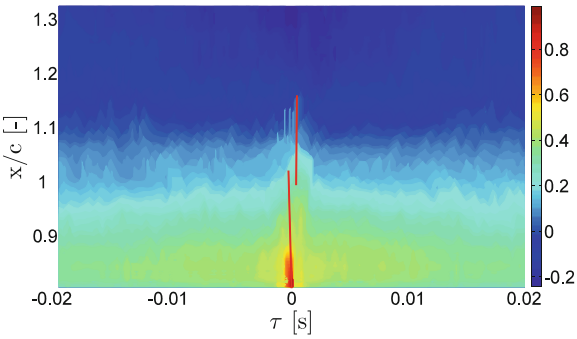

Fig. 4 Correlation of the absolute velocity fluctuation

is positive, whereas downstream of the trailing edge the correlation is negative. This indicates a phase shift of π between the flow patterns upstream and downstream of the trailing edge. The increased correlation values which can be found upstream of the trailing edge evidence upstream wave propagation at a velocity of about −80 m/s. The line with the increased correlation level downstream of x/c = 0.9 shows an even smaller slope such that a very fast propagation speed is present. This evidences that the trailing edge is the source of the noise. The noise generated at the trailing edge travels upstream with a propagation speed of −80 m/s, which corresponds approximately to the difference between the freestream flow velocity and the speed of sound. Downstream of the trailing edge, the speed of the downstream propagating noise waves interferes with the mean flow such that the resulting speed of these waves is very fast. It is assumed that the propagation downstream of the trailing edge is positive at the speed of sound which cannot be resolved by the present PIV data due to the limited recording rate of 2400 Hz. Taking into account the propagation speeds of the up- and downstream travelling disturbances and using Eq. (2), the buffet frequency is 138.6 Hz.

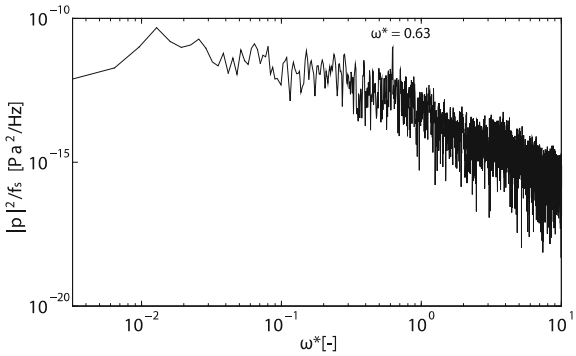

Fig. 5 Power spectral density of the pressure fluctuations at x/c = 0.5, case II

3.2 Forced Airfoil Oscillations

Figure 5 shows the power spectral density exemplarily for case II. Comparing Fig. 5 with Fig. 2, an increased fluctuation level around $\omega^* = 0.68$ is still indicated. Additionally, a peak can be found at $\omega^* = 0.63$. This evidences that the buffet frequency locks into the prescribed frequency of the airfoil oscillation, but also that the natural feedback loop still exists. Note that the $\omega^* = 0.68$ peak is more pronounced in the fft-analysis [3].

In the following, the phase-averaged correlations of the velocity fields $R_{xa,za}$ following Eq. (3) are compared. The vortex pattern still can be found as shown in Fig. 6 exemplarily for case II.

Comparing the cases shows the flow structures to stay alike and the dimensions of the structures to change only slightly. Thus, the lock-in due to forced airfoil oscillations has no influence on the flow characteristics related to the feedback loop, i.e., buffet. Fig. 7 shows a comparison of the contours of the correlation of the absolute velocity $R_{nm}(\tau)$ following Eq. (4). The phase shift of π in the trailing edge region, indicated by the change of the sign in the correlation plane, is less pronounced for the case IV than for the other cases. However, the correlation is maximum for case IV. The strong correlation marked by the black line upstream the trailing edge exceeds the correlation found for the other cases by a factor of approximately 10. Hence, the case IV can be regarded as a special case since the excitation frequency is 140 Hz ($\omega^* = 0.715$), which is close to the resulting frequency of the feedback loop with sound waves at f = 138.6 Hz ($\omega^* = 0.708$) as shown in the previous section. Therefore, the waves might interfere with each other and could be mutually amplified.

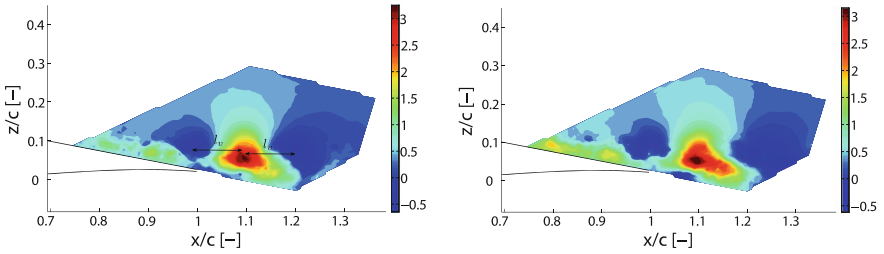

Fig. 6 Contours of the two-point correlation of the velocity fluctuation for $x_a/c = 1.064$ and $z_a/c = 0.1617$; (*left*) phase-averaged for $ß_{max}$; (*right*) phase-averaged for $ß_{min}$, case II

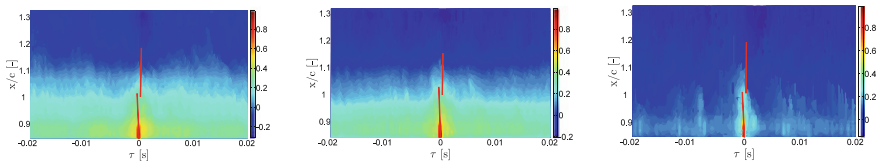

Fig. 7 Comparison of the correlation of the absolute velocity; (*left*) $\omega^* = 0.63$, (*middle*) $\omega^* = 0.7$, (*right*) $\omega^* = 0.715$

4 Conclusion

In this study, the influence of coupled heave and pitch motion with excitation frequencies in the range of the natural buffet frequency on the transonic buffet flow over a DRA 2303 supercritical airfoil model has been analyzed to get further insight into the buffet phenomenon and the lock-in reported by Raveh et al. [6]. The freestream Mach number was $M_\infty = 0.73$, the angle of attack was $\alpha = 3.5°$, and the freestream Reynolds number was $Re_\infty = 2.6 \cdot 10^6$, since under these conditions self-sustained shock wave oscillations, i.e., buffet, occurs. First of all, a reference case was investigated, where the airfoil was held in a fixed position. Then, forced heave/pitch oscillations were applied to the airfoil, exciting the airfoil at reduced frequencies of $\omega^* = 0.63$, $\omega^* = 0.7$ and $\omega^* = 0.715$. The amplitude of the forced airfoil oscillation was on the order of magnitude of the amplitude of the shock wave oscillation. To analyze the flow field steady and unsteady pressure measurements and time-resolved stereo particle-image velocimetry were performed. The natural buffet frequency was 138.6 Hz ($\omega^* = 0.708$) that is close to the measured buffet frequency of 129 Hz ($\omega^* = 0.68$) in the reference case with the airfoil held in a fixed position. When the airfoil was excited by distinct excitation frequencies which are close to the natural buffet frequency, buffet also occurred and the buffet frequency locked into the excitation frequency. The main flow characteristics and dimensions of the flow structures related to the feedback loop were hardly influenced by the airfoil motion. This leads to the conclusion that in the case of forced airfoil motions a shock oscillation rather appears due to the major changes in the flow conditions, i.e., the change of the angle of attack, and is therefore related to the frequency of the airfoil oscillation. The nat-

ural feedback loop also still exists and it is not influenced by the oscillations. At an excitation frequency of $\omega^* = 0.715$, an amplification of the oscillations within the flow was observed, when the excitation frequency is close to the frequency of the natural feedback-loop calculated by the propagation speeds. The phase-averaged flow fields show a distinct vortex structure. This results in a frequency of about 1000 Hz that should be emitted when these vortices interact with the trailing edge. The noise source is determined to be the trailing edge since the correlation of the velocity field shows a change of in this region. Furthermore, the waves that propagate at a speed of about 80 m/s can be found upstream of the trailing edge, whereas they are not found downstream of the trailing edge.

References

1. Lee, B.: Self-sustained shock oscillations on airfoils at transonic speeds. Progr. Aerosp. Sci. **37**, 147–196 (2001)
2. Hartmann, A., Klaas, M., Schröder, W.: Time-resolved stereo PIV measurements of shock-boundary layer interaction on a supercritical airfoil. Exp. Fluids. **52**, 591–604 (2011). doi:10.1007/s00348-011-1074-6
3. Hartmann, A.: Experimental Analysis of Wave Propagation at Buffet Flows. Ph.D. thesis, RWTH Aachen University, Aachen, ISBN-10: 3844009647 (2012)
4. Raveh, D.E., Dowell, E.H.: Frequency lock-in phenomenon in oscillating airfoils in buffeting transonic flows. In: International Forum on Aeroelasticity and Structural, Dynamics, IFASD-2009-135 (2009)
5. Hartmann, A., Klaas, M., Schröder, W.: Experimental investigation of coupled heave/pitch oscillations in transonic flow. In: 29th AIAA Applied Aerodynamics Conference, Paper 2011–3024, Honolulu, (2011)
6. Romberg, H.-J.: Two-dimensional wall adaption in the transonic wind tunnel of the AIA. J. Aircr. **38**(4), 177–180 (1990)
7. Binion, T.W.: Potentials for pseudo-reynolds number effects. In: Reynolds Number Effects in Transonic Flow. AGARDograph 303, Sec. 4, (1988)

Total Pressure Measurements Behind an Axial Ventilator Using a Kiel Probe Array

Till Heinemann, Claus Bakeberg, Hermann Lienhart and Stefan Becker

Abstract This work suggests a new arrangement for measuring the total pressure inside ducts or pipes with non-standard flow field distributions. The device consists of an array of 81 Kiel probes distributed over the duct's cross section. It facilitates the quick measurement of the integral total pressure e.g. behind an axial ventilator without the need to scan the duct section with a traversing or integrating additional substantial flow straightening devices. Wind tunnel tests have proven a tolerance towards deviating on-flow conditions of more than $\pm 35°$. The application of the Kiel probe array is shown in a wind tunnel fan test rig.

1 Introduction

The experimental determination of characteristic fan curves is well defined and standardized in ISO 5801. It describes the procedure of measuring flow rate and fan pressure in standard fan test rigs. In many industrial or research applications however, such a standard test rig is not available or infeasible to build due to the test site's spatial restrictions or operating environment, such as non-uniform inflow and

T. Heinemann (✉) · C. Bakeberg · S. Becker
University Erlangen-Nuremberg, Institute of Process Machinery and Systems Engineering, Cauerstraße 4, 91058 Erlangen, Germany
e-mail: hei@ipat.uni-erlangen.de

C. Bakeberg
e-mail: ba@ipat.uni-erlangen.de

S. Becker
e-mail: sb@ipat.uni-erlangen.de

H. Lienhart
University Erlangen-Nuremberg, Institute for Fluid Dynamics, Cauerstraße 4, 91058 Erlangen, Germany
e-mail: hermann.lienhart@lstm.uni-erlangen.de

A. Dillmann et al. (eds.), *New Results in Numerical and Experimental Fluid Mechanics IX*, Notes on Numerical Fluid Mechanics and Multidisciplinary Design 124,
DOI: 10.1007/978-3-319-03158-3_58,

outflow conditions. In such cases, the application of a Kiel probe array is suggested as a simple and fast substitute measurement solution to gauge fan pressure inside a duct. As an example, its application is shown within the investigation of the influence of natural wind conditions at the fan inlet.

ISO 5801 basically requires measuring the static pressure in a pipe or duct section down-flow of an axial ventilator with wall pressure tapping. Multiple measurement points in the same section are connected via a circular conduct and gauge the static pressure attached. For this method, the flow is required to be free of rotation or swirls, and the ISO standard demands substantial flow straighteners be implemented in the duct section upstream of the wall pressure tapping. In many existing measuring environments or restricted testing set-ups, there is not enough space available to do this, or the additional pressure losses are not tolerable.

A different possibility comes down to scanning the pipe cross section with multi-hole probes, which will determine total pressure and directivity of the local flow field [1]. Besides sealing problems, this method requires the possibility to reproduce exact positions inside the duct, requiring either qualified and precise manual introduction of the probe into the pipe, or a traverse. Pitot like probe heads [2] require less space and cost less than multi-hole probes, but bear the additional disadvantage that the directivity of the flow field around the probe must be known, since flow deviating from the probe axis by too large an angle will lead to incorrect measurements of the local total pressure [1, 3].

The Kiel probe array tries to overcome the major disadvantages of the aforementioned methods. The Kiel probe sensor head shape is generally known to tolerate significant deviations in on-flow conditions [3] and is comparably easy to manufacture. In a grid array, multiple Kiel type total pressure probes are realized distributed across a pipe section. The Kiel probe array does not require scanning the pipe cross section, i.e. there is no need for traversing or complicated sealing of the measurement section, and all measurement positions can be captured simultaneously.

2 Target Application and Design

2.1 Target Application Experimental Setup

The Kiel probe array was manufactured to overcome certain difficulties in measuring the fan pressure in a distinctly restricted fan test rig. To measure the influence of different outdoor on-flow conditions on axial ventilators, a fan test rig was to be realized inside a wind tunnel. Due to restrictions such as wind tunnel blockage, increasing flow losses in the duct sections, limited available space, and the target to realize different on-flow angles, standard ISO 5801 pressure measurement methods were not applicable. The test set-up is partly shown in Fig. 1.

The concept of the Kiel probe array facilitates measuring the total pressure close to the fan outlet, upstream of major and inexactly known losses due to duct

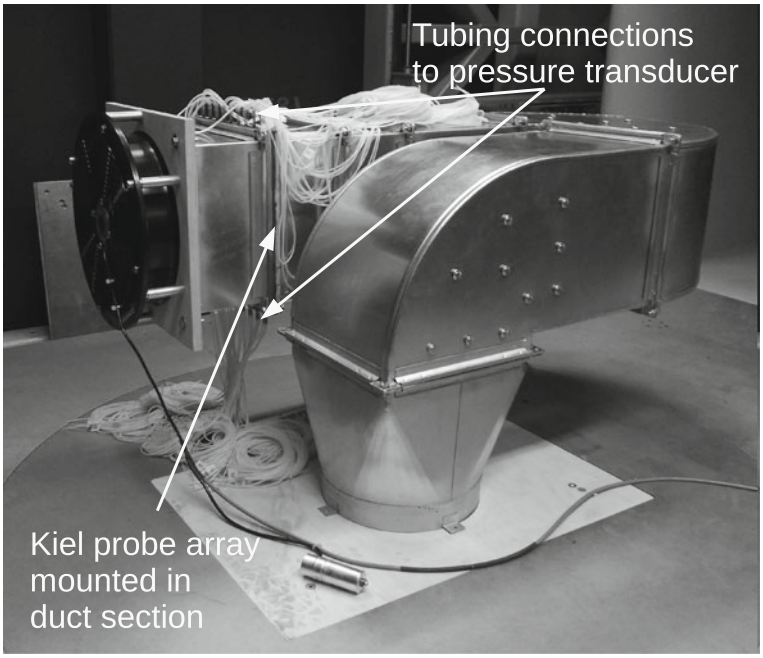

Fig. 1 Fan test rig inside wind tunnel test rig. Tubes connected to Kiel probe array located $D/2$ downstream of test fan

bends etc. The integral fan pressure computes based on the mean Kiel probe pressure $\bar{p}$ at the n equally distributed positions, and the total flow rate $\dot{V}$ measured at the test rig outlet, over cross section area $A = D \times D$,

$$p_{fan} = \sum_{i=1}^{n} p_i/n - \rho/2 \cdot \left(\dot{V}/A\right)^2 = \bar{p} - p_{dyn}\,. \tag{1}$$

2.2 Kiel Probe Array Design

A Kiel probe head basically consists of a Pitot probe wrapped by an additional larger pipe. It is supposed to focus the air flow and guide it more frontally onto the smaller Pitot pipe which is connected to the pressure measurement sensor. A sketch of the probe head manufactured at the University of Erlangen is shown in Fig. 2. The Figure also shows the entire Kiel probe array mounted in its application in the test rig mentioned in Sect. 2.1. 9×9 probes are distributed equally across the quadratic pipe cross section, mounted on a high precision laser cut steel frame.[1] Combining

[1] Duct edge length $D = 300$ mm

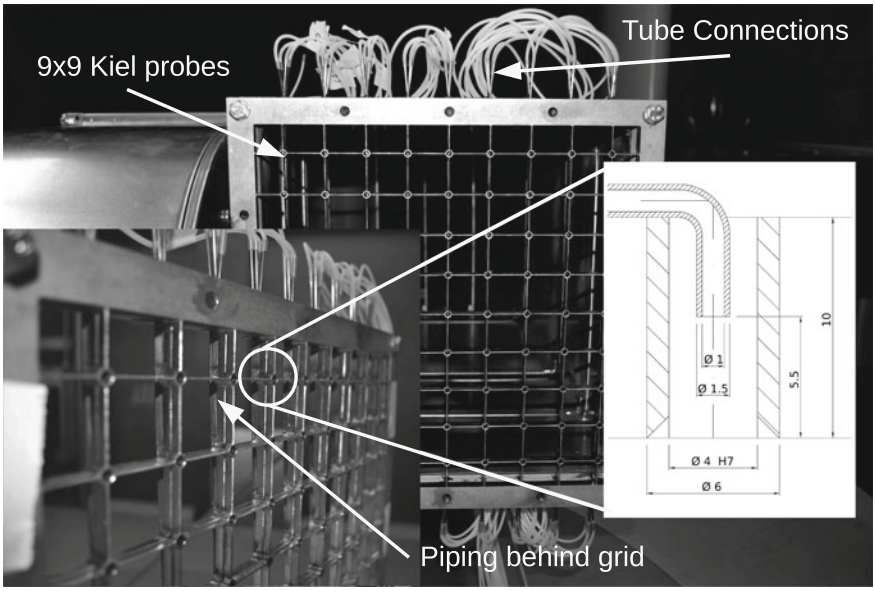

Fig. 2 Kiel probe array mounted to pipe

the cross section of the grid bars, pipes and probe heads themselves, the entity of the Kiel probe array blocks the cross section of the duct by less than 9 %. The small pressure measurement pipes are connected to tubes (and finally to pressure sensors) outside of the measurement section, which may be seen in detail on the left of Fig. 2, and in total in Fig. 1.

3 Angle Sensitivity Assessment

Previous research on the angle sensitivity of different total pressure probe head shapes suggests that the tolerated deviation angle φ_{tol} of a Kiel probe to the flow direction is about $\pm 35°$, with optimized designs up to $\pm 45°$. [2]

In order to validate this quality, the Kiel probe array was set up isolated in the test section of the wind tunnel of the University of Erlangen,[3] as shown in Fig. 3. Figure 4 shows the sensitivity of the mean measured total pressure $\bar{p}(\varphi)$ towards the on-flow conditions of the isolated Kiel probe array in the wind tunnel environment. $\bar{p}(\varphi)/\bar{p}(0°)$ is the relative mean pressure over all 81 Kiel probes plotted in circles in Fig. 4. This data set suggests that the Kiel grid provides 99 % correct $\bar{p}$ values for angles $|\varphi| \leq \varphi_{tol} \approx \pm 25°$. Still, this results is very likely to be too conservative an estimate.

[2] φ_{tol} is defined to be the maximum angle for which the measured total pressure value $p(\varphi)$ deviates by less than 1% from $p(0°)$, measured in the direct on-flow configuration.

[3] The wind velocity u_{wind} was 15 m/s during all angle sensitivity tests.

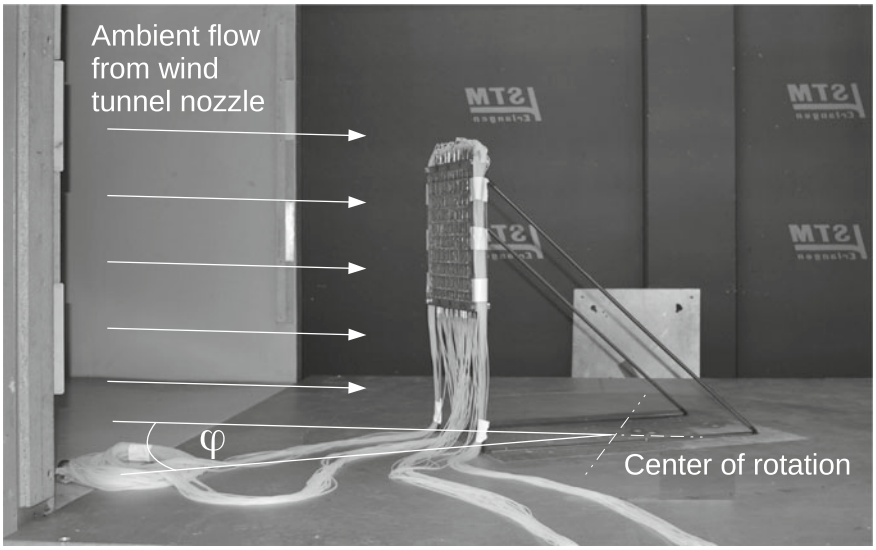

Fig. 3 Experimental set-up for angle sensitivity test inside wind tunnel test section

To explain this point, two contour plots of the total pressure distribution over the 9×9 probe positions are shown in Fig. 5. For the zero degree configuration, Fig. 5a shows $p_i(0°)$ deviating from the gauged maximum pressure $p_{max}(0°) = \max\{p_i(0°) | i = 1 \ldots 81\}$. Neglecting measurement errors, $p_{max}(0°)$ equals $p_{total} = p + \rho/2 \cdot u^2_{wind}$ generated by the uniform tunnel velocity u_{wind}.

Rotating the Kiel probe array by 30° resulted in the total pressure contour plot of Fig. 5b. Most Kiel probes deviate by comparably little from $p_{max}(30°)$, but locally distinct deviations occur. The authors explain this by locally differing on-flow conditions, caused by the outer grid frame disturbing uniform wind tunnel flow. Consequences are angles of attack $\varphi_{\text{effective}}$ different from the angle φ, here defined as the array's angle towards the wind tunnel nozzle. In Fig. 5(b), it is the right hand edge that is rotated upstream, thus being the closest point to the wind tunnel nozzle. Areas that are not affected by disturbed flow show much smaller deviation.[4]

Since the Kiel probe array has been designed to be deployed as part of a pipe section, such frame caused effects cannot occur in its measurement application. That is why another mean pressure data set is plotted in triangles Fig. 4. These data points show the mean total pressure $\bar{p}^*(\varphi)/\bar{p}^*(0°)$ values for an exemplary subset of 9 Kiel probes that were less affected by distinguished frame disturbances,[5]

[4] Pressure values were averaged over 30 s, and the same local effects could be found continuously increasing over an increasing angle of attack. Both directions of rotation showed the same effect at the respective upstream frame edge. Differences between the directions of rotation were caused by small differences in probe design caused by manufacture, and inequalities of the two frame sides

[5] In Fig. 5, the probes for $\bar{p}^*$ are located where x positions 4–6 overlap with y positions 2–4.

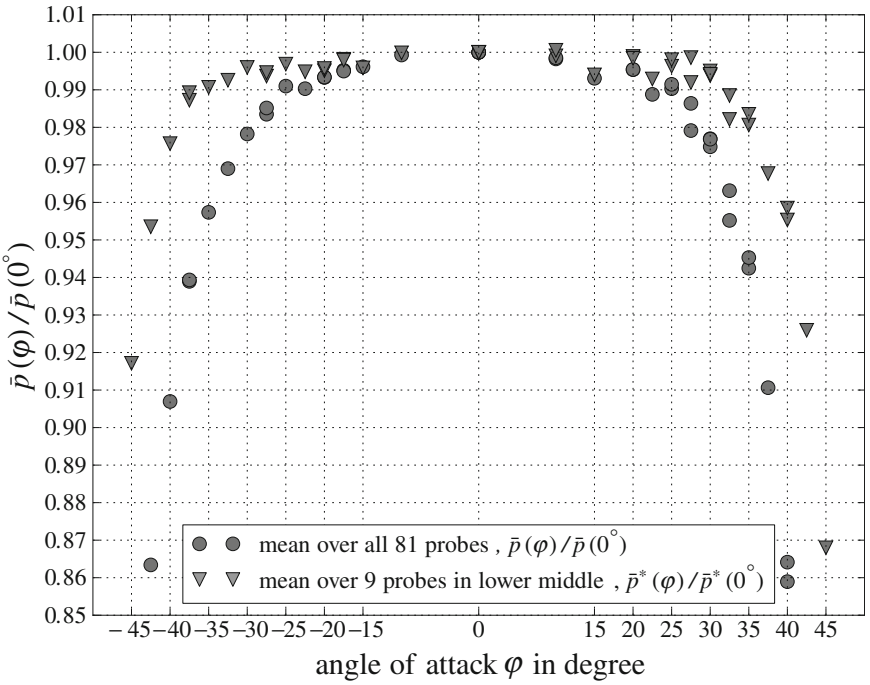

Fig. 4 Relative deviation of mean total pressure $\bar{p}(\varphi)$ compared to $\bar{p}(0°)$

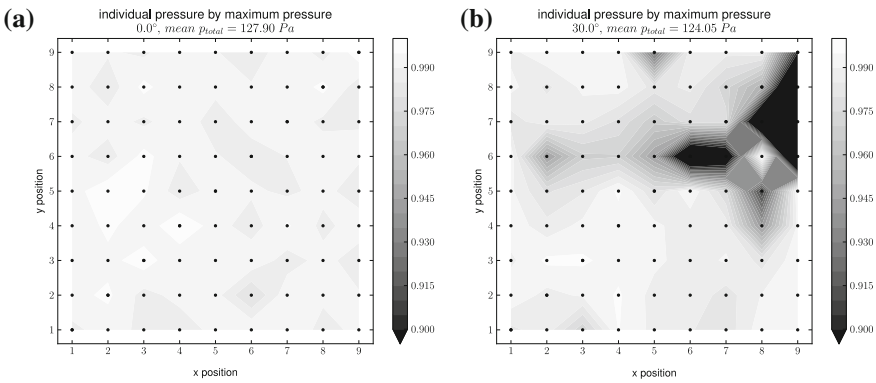

Fig. 5 Total pressure distribution $p_i(\varphi)/p_{max}(\varphi)$ over all 81 probes. **a** Perpendicular on-flow, i.e. $\varphi = 30°$. **b** $\varphi = 30°$ on-flow condition

$$\bar{p}^*(\varphi) = \sum_{j=1}^{9} p_j^*(\varphi), \quad p_j^*(\varphi) = \left\{ p_j(\varphi) \,|\, \text{x pos.} \in \{4,5,6\}\,,\ \text{y pos.} \in \{2,3,4\} \right\}. \tag{2}$$

By reducing the disturbing effects on the test result in this way, we find it much more realistic to distinguish a $\varphi_{tol} \approx \pm 35°$.

4 Application

4.1 Flow Field in Axial Ventilator Test Rig

Regarding the target application described in Sect. 2.1, the 3D velocity distribution of the flow field was measured in the Kiel probe array section at the 81 probe positions, $D/2$ downstream of the fan outlet. The Kiel probe array itself was demounted, and a glass screen section was deployed in the pipe to perform Laser Doppler Anemometry (LDA) measurements.

Figure 6a shows an exemplary measurement set of the axial ventilator blowing air into the pipe.[6] The mean meridian velocity through the pipe $\dot{V}/D^2$, scaled by the fan rotation speed $u_{bladetip} = \omega \cdot D_{fan}/2$, is $\Phi_{duct} = 0.2188$. Figure 6a contour plots the measured effective angle φ between the velocity component c_m in meridian flow direction x, and swirl components in the y, z plane, c_u. Arrows represent the direction and magnitude of the swirl component c_u.

$$\tan(\varphi) = \frac{c_u}{c_m} \tag{3}$$

Comparing the effective angles between flow velocities and Kiel probe axis with the exactness data in Fig. 4, most angles φ are within a tolerable range. Even though larger angles do appear, these are generally caused by small meridian velocity components c_m, resulting in small absolute velocities. That implies the positive effect, that those Kiel probes with the worst on-flow conditions do not distort the integral result distinctively. Even though yielding the largest relative errors, these probes gauge the smallest absolute pressures, such that larger relative deviations will still result in small absolute errors in total pressure measurement values. The flow regions with significant velocity values only show small angle deviations from 0°.

4.2 Wind Influence on Fan Performance

For the specific target fan test set-up described in Sect. 2.1, the angle distribution was considered to be satisfactory. To further decrease the deviation angles, small flow straighteners or guide vanes deployed between fan outlet and Kiel probe array have been tested to be very effective. Even though such measures require additional con-

[6] The axial ventilator is influenced by 10 m/s air approaching its inlet at an angle of 45° to its rotation axis.

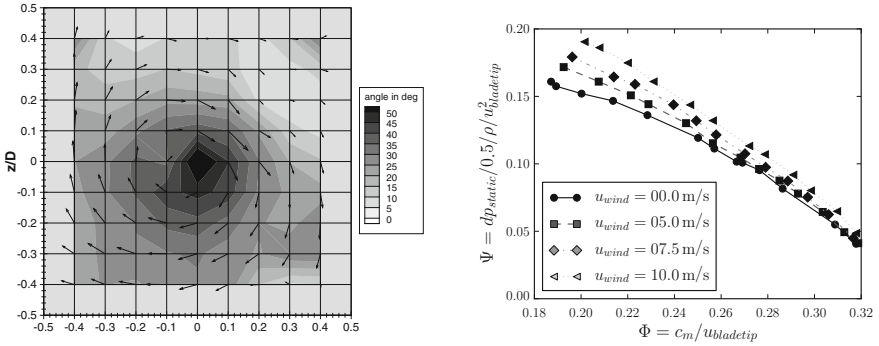

(a) **(b)**

Fig. 6 Application in study on wind influence on fan performance. **a** LDA results of φ distribution inside the void duct, at Kiel probe positions. $u_{wind} = 10\,\mathrm{m/s}$ flow approaching the fan inlet at 45°. $\Phi_{duct} = 0.2188$, **b** Characteristic curves for different wind velocities u_{wind} at 45° flow approaching fan inlet

structive changes in the test rig and cause further flow losses, these consequences can still be considered favourable compared to those invoked by alternative measurement methods described in Sect. 1.

Figure 6b shows an example of the results from measurements with the Kiel probe array in the target application. Different wind velocities are investigated in their influence on an axial ventilator's performance, approaching the fan inlet at 45°. The fan pressure Ψ is plotted over the flow number Φ for wind velocities 0–10 m/s. The results from Fig. 6 show that different wind conditions at the fan inlet influence the flow field behind the axial ventilator distinctively, leading to major effects on the characteristic fan curve.

5 Conclusions

Measuring the total pressure distribution inside a pipe with a Kiel probe array is a valid alternative to standard methods, if those cannot be applied. Fast and easily reproducible measurements are possible. Its tolerance towards deviations of the approaching flow direction from the probe axis, was determined to be approximately 35°. The successful application of the Kiel probe array has been shown in a fan test rig for investigations on the influence of different on-stream conditions on an axial ventilator.

Acknowledgments The research leading to these results has received funding from the European Union's Seventh Framework Programme (FP7/2007–2013) under grant agreement number 256797, within the "MACCSol" project.

References

1. Nitsche, W., Brunn, A.: Strömungsmesstechnik. Springer, Berlin (2006)
2. Eckelmann, H.: Einführung in die Strömungsmesstechnik. B. G. Teubner Verlag, Stuttgart (1997)
3. Chue, S.H.: Pressure probes for fluid measurement. Prog. Aerosp. Sci. **16**(2), 147–223 (1975)

Experimental Study on Wave Drag Reduction at Slender Bodies by a Self-aligning Aerospike

Oliver Wysocki, Erich Schülein and Christian Schnepf

Abstract This work describesexperimental results of a wave drag reducing device tested in the Transonic Wind Tunnel in Göttingen both under static and dynamic conditions. By means of a self-aligning aerospike, the total drag of a blunt-nosed slender body has been reduced by up to 25–30 % for Mach numbers between $M = 1.4$ and $M = 2.2$. Here, self-aligning means that the spike can pitch freely around its mounting axis and is positioned automatically in direction of the oncoming flow by means of two small vanes. Wind tunnel experiments showed that the spike was able to align with the flow direction even during a fast pitching maneuver (forced sinusoidal movement at $f \leq 7.5$ Hz and $\alpha = 0° \ldots 20°$).

1 Introduction

Similar to commercial aircraft, reducing the total drag still plays an important role when dealing with slender bodies as e.g. missiles. Therefore, it is still object of divers studies. By decreasing the drag, an air vehicle can fly longer (increased mission time), farther (increased range), faster (increased Mach number) or heavier (increased payload). By that, the efficiency can be increased.

At supersonic speeds, drag reduction devices/methods aim to decrease the wave drag of the body which can be done in different ways. One way is an optimization of the nose geometry. A pointed nose with a small semi-apex angle is often believed to be the best nose shape at supersonic speeds since producing an attached oblique shock with a relatively low wave drag but also relatively high thermal loads. Studies by several researchers (e.g. [1]) indicated that a pointed nose is not the optimum and

O. Wysocki (✉) · E. Schülein · C. Schnepf
DLR Institute of Aerodynamics and Flow Technology, Bunsenstraße 10,
37073 Goettingen, German
e-mail: Oliver.Wysocki@dlr.de

A. Dillmann et al. (eds.), *New Results in Numerical and Experimental Fluid Mechanics IX*,
Notes on Numerical Fluid Mechanics and Multidisciplinary Design 124,
DOI: 10.1007/978-3-319-03158-3_59,

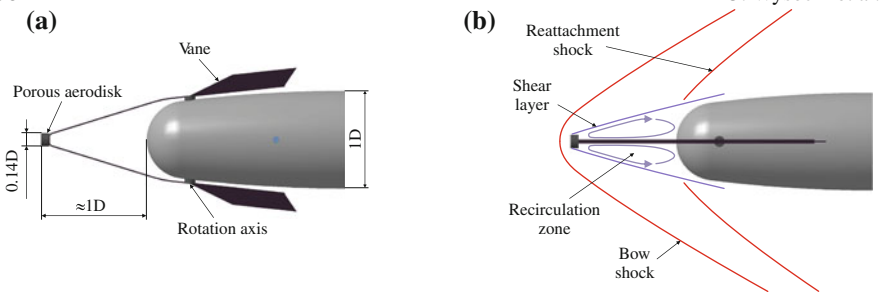

Fig. 1 Model with spike, (a) General descriptions, (b) Flowfield descriptions. **a** Top view, **b** Side view

that a certain nose bluntness has it's advantages regarding the combination of low drag and low thermal loads.

Alternatively, a drag reduction can be achieved by e.g. using spikes [2], injecting counterflow jets [3] or producing a plasma ("hot-spike") by focusing laser light [4] or creating an electric arc [5] in front of the body (cf. review paper [6]). All of these methods create a recirculation region in front of the body by inducing a separation at the spike or decreasing the total pressure by heating ("hot-spike"). Ideally, this recirculation region causes an isotropic compression and a *continuous* pressure rise (instead of an erratic pressure rise over a shock). By this gradual pressure rise, the total (wave) drag of the body is reduced.

Referring to spikes, *Ahmed et al.* [7] showed numerically that an aerodisk performs better than a pointed spike. Experimental studies by *Schülein* [8] proved that permeable shock wave generators (=porous aerodisks) of different shapes can further decrease wave drag compared to solid aerodisks by producing a thicker shear layer.

All these shock-control devices (spikes, counterflow jets, hot-spike) usually applied on the main body's axis work well at zero angle of attack but have drawbacks at higher angles of incidence which occur in maneuvers. On inclined bodies with a fixed aerospike the thermal loads at the nose can be higher than on the body without the spike (cf. [9]). Due to that, Schülein proposed a self-aligning spike and performed preliminary tests in a Ludwieg-tube facility at Mach numbers between two and five. With the self-aligning spike, drag and thermal load could be decreased for higher angles of attack in comparison to a fixed spike in front of a blunt body.

For the work presented here, the ideas of a self-aligning aerospike and a porous aerodisk were combined (see Fig. 1). The spike was mounted to a generic slender body model with a fineness ratio of $L/D = 20$. The experiments were conducted in the Transonic Wind Tunnel in Göttingen (TWG) at Mach numbers between $M = 1.4$ and $M = 2.2$ and under both static (no model motion) and dynamic (wind tunnel model undergoing forced pitching motions) conditions. In this work, the performance of the self-aligning spike is compared to this of the blunt nose without spike, for both static and dynamic conditions, by means of balance measurement results and high-speed schlieren images.

2 Experimental Setup

The experiments were done with a test rig called "maneuver simulator" which is especially made for the TWG and includes a hydraulic system to perform pitching maneuvers e.g. sinusoidal motions with a frequency of $f = 7.5\,\text{Hz}$ at an amplitude in the angle of attack (AoA) of $\Delta\alpha = \pm 10°$. The test model was mounted on an internal, cylindrical, one inch wind tunnel balance fixed to a cylindrical sting which was attached to the maneuver simulator.

The model was a generic missile model with a diameter of $D = 36\,\text{mm}$ and a length of $L = 720\,\text{mm}$ (about 1/3 of the typical original size) resulting in a fineness ratio of $L/D = 20$. It was modularly built with different configurations possible. One of them is the configuration with a self-aligning aerospike with a small porous aerodisk (Fig. 1a). The porous aerodisk had a diameter of 0.14 D and was approximately 1 D in front of the model's nose. This distance was chosen with respect to the $M = 2$ results from *Schülein* [8]. Nonetheless, the optimum of both parameters is depending on the Mach number and therefore, this combination is probably not the best which is possible. But since these tests are only a proof-of-concept, the dynamic behavior of the aerodisk is more important. In contrast to normal aerospikes, no rod was used to hold the aerodisk. Instead, a sheet metal frame with a thickness of 0.5 mm and a height of 1.5 mm connected the aerodisk with two small vanes. These vanes were located behind the axis of rotation and forced the spike to align with the oncoming flow. By the help of a screw driven break, the rotation resistance could be adjusted.

In the wind tunnel experiments, both static and dynamic tests were performed. For the pitching maneuvers, the AoA was changed between $\alpha = 0°$ and $\alpha = 20°$ using eight different sine frequencies ($f = 0.05$, 1, 2, 3, 4, 5, 6 and 7.5 Hz).

The internal balance was a six component, symmetrical balance with a maximum axial force of $F_x = 444\,\text{N}$ and maximum side and normal forces of $F_{y,z} = 3555\,\text{N}$. The total forces measured by the balance ($= F_{balance}$) are equal to the aerodynamic forces only under static conditions (no motion). Under dynamic conditions, the balance loads are a sum of the aerodynamic ($= F_{aero}$) and inertial ($= F_{inertial}$) loads acting on the model ($F_{balance} = F_{aero} + F_{inertial}$). In order to get just the aerodynamic loads from the balance data (to compare them with the static data), the model was also equipped with an internally mounted two-axis accelerometer. This was used to measure the inertial axial and normal accelerations resulting from the forced model movement. With these accelerations, the inertial forces and moments can be determined and consequently, the aerodynamic loads can be extracted for dynamic test conditions. This method is referred to as "inertial force correction" within this chapter.

Beside balance measurements, high-speed schlieren pictures have been taken. For this, a monochromatic high-speed camera of the type Photron Ultima APX-RS has been used. The maximum resolution of this camera is 1024×1024 pixels at frame rates of up to 3,000 fps. For present tests, a frame rate of 500 fps at full resolution has been used.

3 Results

As stated before, the functionality and performance of the self-aligning aerospike were tested for three different Mach numbers ($M = 1.4, 1.8, 2.2$) at a Reynolds number based on the model diameter of $Re_D \approx 3 \cdot 10^5$. Concluding from the results presented here (Figs. 2, 3), the drag of the generic slender body can be reduced by the help of the spike at all tested Mach numbers and under both static and dynamic conditions.

Figure 2a shows the drag coefficient c_d for the static, the quasistatic ($f = 0.05\,\text{Hz}$) and the dynamic cases with the highest oscillation frequency ($f = 7.5\,\text{Hz}$) at a Mach number of $M = 2.2$. The drag coefficient includes the base pressure corrected axial force coefficient. Furthermore, the results for $f = 7.5\,\text{Hz}$ are inertial force corrected (IFC) according to the method described in Sect. 2. This method proved to be better than an approach using theoretical inertial forces which neglects the natural oscillation of the model. Nonetheless, this method is also not perfect since the data obtained with the accelerometers are noisy. Furthermore, not all influencing parameters are covered by this method, e.g. the forces resulting from the spike's motion differing between the wind-off and wind-on measurements. Therefore, a certain error still remains.

Using the IFC wind-off results, this remaining error of the dynamic results for c_d is estimated to be smaller than 23 %. For this estimation, the remaining residual error from the wind-off measurements is compared with the static results. In order to further increase the accuracy, the IFC wind-off results were subtracted from the IFC data shown in Fig. 2a. Referring to Fig. 2b, this seems to be a good additional correction method.

Figure 3 presents the reduction rates obtained by the use of the self-aligning aerospike. On the left (cf. Fig. 3a), the static results of a complete "maneuver" with increasing and decreasing angles of attack are plotted demonstrating the very good reproducibility of the data. The maximum drag reduction at $M = 1.4$ ($\alpha = 0°$) is $\Delta c_{w,max} \approx 24\,\%$. This value increases with Mach number reaching $\Delta c_{w,max} \approx 30\,\%$ at $M = 2.2$ ($\alpha = 0°$). With the increase of the AoA, the beneficial drag reduction effect of the spike decreases in accordance with the increasing influence of the main body at higher angles since the spike just influences the shock systems at the nose (Fig. 3a).

On the right side (cf. Fig. 3b), the drag reduction ability of the self-aligning spike is shown for the three Mach numbers and the highest frequency of $f = 7.5\,\text{Hz}$. The effect of the spike is comparable to the static cases for AoA above $\alpha \approx 4°$ and below $\alpha \approx 20°$. Close to the turning points, the quality of the corrected data is questionable. The reason for this is probably the incorrectable influence of the spike oscillations which occur due to the fact that the center of gravity (CG) of the spike is located behind its pitch axis. In the wind-off measurements, these oscillations were suppressed by fixing the spike in a vertical position. Since the highest angular accelerations occur close to the turning points, the impact of the displacement of the spike's CG is the highest, here. Neglecting the results close to the turning points,

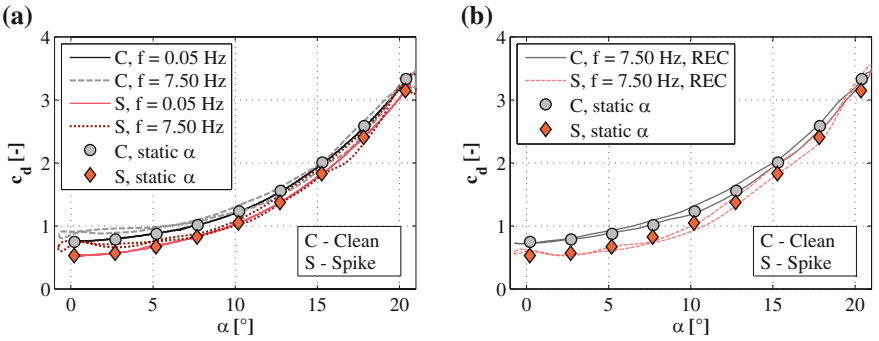

Fig. 2 Drag coefficient for $M = 2.2$, $Re_D \approx 3 \cdot 10^5$ (static and dynamic results). **a** $f = 7.5\,\text{Hz}$ with inertial force correction, **b** $f = 7.5\,\text{Hz}$ with additional residual error correction (REC)

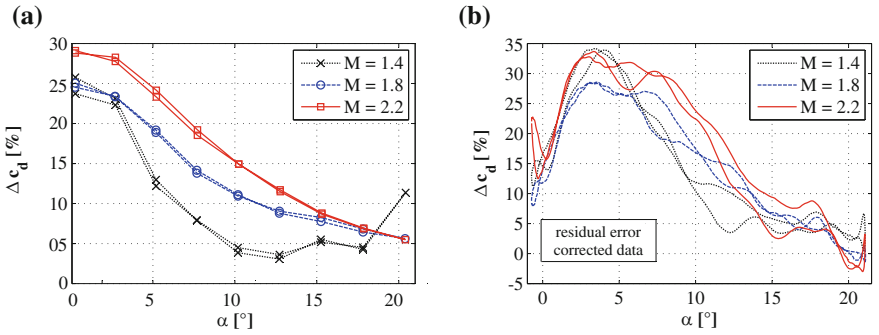

Fig. 3 Drag reduction with spike at $Re_D \approx 3 \cdot 10^5$ and different mach numbers. **a** Static results, **b** Dynamic results ($f = 7.5\,\text{Hz}$, residual error corrected)

the maximum drag reduction rates are still in the range of $\Delta c_d \approx 28, \ldots 34\,\%$. Referring to the reduction rates based on the inertial force corrected data (without residual error correction), the maximum drag reduction rates are lower, being in the range of $\Delta c_d \approx 22, \ldots 27\,\%$. Summarizing, both static and dynamic results prove the spike's ability to reduce the wave drag of a missile over a wide range of AoA. Nonetheless, the efficiency decreases with an increase of the AoA.

Despite this loss of efficiency, the self-aligning spike still has advantages at higher AoA. Heat flux measurements by *Schülein* [9] showed that at these angles, the thermal loads on a hemispherical nose with a self-aligning spike are smaller than on the same nose with a fixed spike.

Furthermore, differences between the static and dynamic results (Fig. 2) can be seen. Here, parts of this deviation come from a small residual error still left from the inertial force correction. The other portion can be explained by an increased/decreased drag due to the model movement since different flow conditions occur during the pitch-up and pitch-down part of the periodic motions resulting in a hysteresis. Nonetheless, the residual errors from the inertial force correction

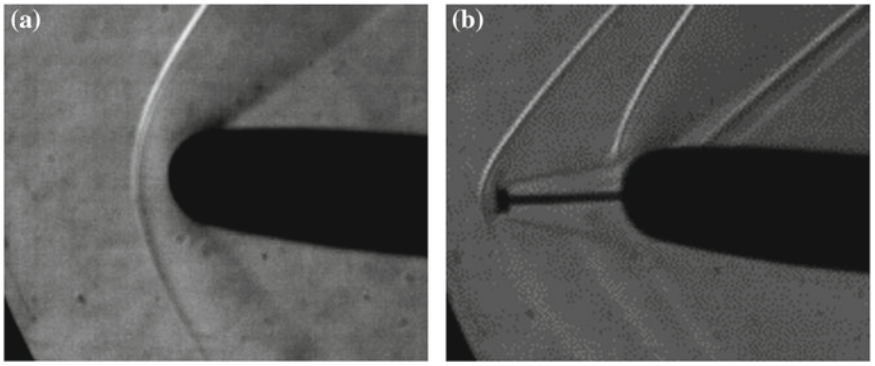

Fig. 4 Schlieren pictures at $M = 1.41$, $Re_D \approx 3 \cdot 10^5$, $\alpha \approx 5°$. **a** Clean configuration, **b** Spiked configuration

should be of approximately the same amount since the remaining errors at wind-off measurements were almost the same for both configurations (clean[1] and spiked configuration). Beside the balance measurements, also high-speed schlieren images were taken during the test. Figure 4 shows a comparison of the blunt-nosed body without spike (Fig. 4a) and the body with self-aligning spike (Fig. 4b) at $M = 1.4$ and $\alpha \approx 5°$ ($Re_D \approx 3 \cdot 10^5$). The differences between both configurations with respect to the bow shock (system) can be seen clearly. The baseline blunt nose produces a detached bow shock in front of the body. The spike produces a conical shock and a recirculation zone which is clearly visible in the schlieren images (see Fig. 4b). The latter is separated from the outer flow by a shear layer. Furthermore, a reattachment shock occurs and combines with the conical shock of the spike far away from the body. On the bottom side of the recirculation zone, an additional shock occurs which is produced due to the further compression of the flow on the windward side of the body in contrast to the expansion on the lee side. This expansion region is shifted further back for the spiked configuration.

As mentioned before, the recirculation region is responsible for the wave drag reduction effect. Because of the conical shape of the resulting shear layer, the blunt nose with aerodisk behaves more like a conical nose with a blunted tip and has consequently a lower wave drag. The boundary of the recirculation zone (shear layer) represents the edge of the effective body (displacement body) determining the wave drag (see *Moeckel* [10] and *Chang* [11]).

Schlieren images obtained also show a small misalignment of the aerospike for increasing AoA and under both static and dynamic conditions. In both cases, this misalignment results from the flow around the cylindrical body acting as an additional aerodynamic force on the vane of the spike which leads to negative spike AoA of up to $3° \ldots 4°$.

[1] clean = configuration without the spike

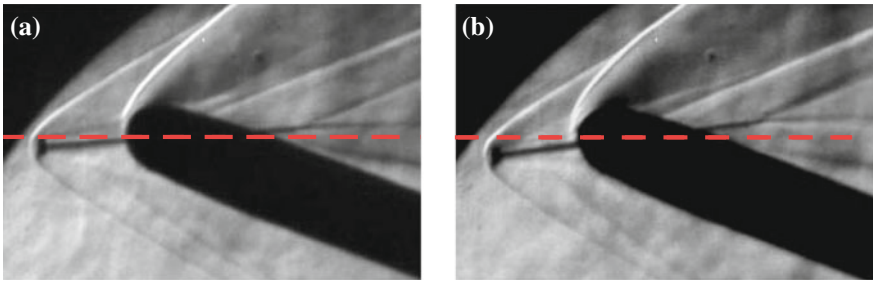

Fig. 5 Schlieren pictures showing the misalignment of the aerodisk at $\alpha \approx 20.4°$ and $M = 2.2$. **a** Static case, **b** $f_a = 7.5\,\text{Hz}$

During the sinusoidal pitching motions with frequencies of up to $f = 7.5\,\text{Hz}$, an additional factor caused a small misalignment of the spike. Due to the model motion and the induced velocity components, the effective AoA is changed compared to the static case. Moreover, there is also an influence of inertial forces due to the fact that the CG was not located exactly on the axis of rotation of the spike. Because of that, the spike's misalignment increased in the dynamic tests to $6° \ldots 7°$ (cf. Fig. 5). Furthermore, there was more variation of the misalignment over the whole AoA range. Nonetheless, Fig. 2a shows that the spike is still working well even at the maximum actuation frequency of $f = 7.5\,\text{Hz}$.

4 Conclusions

The functionality and drag reduction capability of a self-aligning aerospike in combination with a blunt-nosed slender body was experimentally examined. The results show that the aerospike effectively reduces the drag coefficient by up to $\Delta c_w \approx 30\%$ achieved at the highest Mach number $M = 2.2$ ($Re_D \approx 3 \cdot 10^5$) and zero angle of attack. As expected, the results for the two lower Mach numbers ($M = 1.4$, $M = 1.8$) show smaller drag reduction rates (see Fig. 3a). With the increase of the angle of attack, the influence of the main body increases resulting in a decrease of the drag reduction rates. Beside these static results, the graphs from the dynamic measurements show almost the same behavior (Fig. 2) with small deviations probably resulting from residual inertial force correction errors which are expected to be of approximately the same amount for both configurations.

High-speed schlieren images made clear that the self-alignment of the aerospike works well with only small misalignment angles at high angles of attack. These occurred in both static and dynamic tests and were caused by the secondary flow induced around the cylindrical main body at incidence. Furthermore, the spike showed a periodical oscillation additional to these static misalignment angles. This oscilla-

tion is caused by inertial forces since the spike's center of gravity was located behind the spike's axis of rotation.

Finally, the tests show that the self-aligning aerospike is performing well concerning wave drag reduction at low supersonic Mach numbers with the potential to perform even better at higher Mach numbers. But there is still potential for improvement by varying and optimizing parameters as e.g. disk size or spike length. The impact of a variation of the spike's center of gravity may also be studied in order to improve the dynamic behavior.

References

1. Furey, R.J.: Minimum-energy hypersonic nose and leading-edge shapes. Spacecraft and Rockets **9**(2), 107–115 (1972)
2. d'Humières, G., Stollery, J.L.: Drag reduction on a spiked body at hypersonic speeds. Aeronaut. J. **14**(1152), 113–119 (2010)
3. Venukumar, B., Jagadeesh, G., Reddy, K.P.J.: Counterflow drag reduction by supersonic jet for a blunt body in hypersonic flow. Phys. Fluids **18**, 118104 (2006)
4. Kim, J.-H., Matsuda, A., Sakai, T., Sasoh, A.: Wave drag reduction with acting spike induced by laser-pulse energy depositions. AIAA J. **49**(9), 2076–2078 (2011)
5. Schülein, E., Zheltovodov, A.: Effects of steady flow heating by arc discharge upstream of non-slender bodies. Shock Waves **21**, 383–396 (2011)
6. Bushnell, D.M.: Shock wave drag reduction. Annu. Rev. Fluid Mech. **36**, 81–96 (2004)
7. Ahmed, M.Y.M., Qin, N.: Drag reduction using aerodisks for hypersonic hemispherical bodies. J. Spacecraft and Rockets **47**(1), 62–80 (2010)
8. Schülein, E.: Shock-wave control by permeable wake generators. In: 5th Flow Control Conference, AIAA, pp. 2010–4977 (2010)
9. Schülein, E.: Wave drag reduction approach for blunt bodies at high angles of attack: proof-of-concept experiments. In: 4th Flow Control Conference, AIAA, pp. 2008–4000 (2008)
10. Moeckel, W.E.: Flow separation ahead of blunt bodies at supersonic speeds. NACA TN 2418 (1951)
11. Chang, P.K.: Separation of flow. Pergamon Press, Oxford (1970)

Part XI
Aeroacoustics

Aeroacoustic and Aerodynamic Importance of Unequal Rotor Rotation Speeds of a CROR

R. A. D. Akkermans, J. W. Delfs, C. O. Márquez, A. Stuermer, C. Richter, C. Clemen, B. Caruelle and M. Omais

Abstract In this contribution, we answer the question of aeroacoustic and aerodynamic importance of the non-periodic nature of a Contra Rotating Open Rotor (CROR) for those specific cases in which the front and the aft rotor rotate with slightly different rotational speeds. A concept to handle the non-periodicity is concisely presented based on a simultaneous least-square minimalisation approach. The results show a minor influence of the non-periodicity on the aerodynamics of the CROR. As opposed to this, a significant influence is observed for the aeroacoustics. Based on an actual non-periodic CROR, differences between corrected and uncorrected signals exceeding 10 dB in amplitude are observed in the propeller plane for frequencies below the 4th harmonic of the front rotor blade passing frequency (BPF). For upstream microphone positions, even the 1st rear BPF is highly affected by the correction procedure. Experimental validation confirms the non-periodic correction method which has been applied to the numerics. Furthermore, it reveals that ignoring the non-periodicity leads to a completely opposite conclusion regarding installation effects for the considered configurations.

1 Introduction

In recent years, Contra Rotating Open Rotors (CROR) have received considerable attention as this concept promises a considerable reduction of fuel consumption over conventional ducted turbofan engines, mainly due to their ultra-high by-pass ratio [1].

R. A. D. Akkermans (✉) · J. W. Delfs · C. O. Márquez · A. Stuermer
DLR Institute of Aerodynamics and Flow Technology, Braunschweig, Germany
e-mail: rinie.akkermans@dlr.de

C. Richter · C. Clemen
Rolls-Royce Deutschland Ltd. & Co. KG, Dahlewitz, Germany

B. Caruelle · M. Omais
AIRBUS Operation S.A.S., Toulouse, France

A. Dillmann et al. (eds.), *New Results in Numerical and Experimental Fluid Mechanics IX*,
Notes on Numerical Fluid Mechanics and Multidisciplinary Design 124,
DOI: 10.1007/978-3-319-03158-3_60,

However, the biggest challenges for the realisation of a commercially viable engine relate to the issues of noise emissions due to the absence of a duct, and installation effects of the rotors with the airframe (see, e.g. [2]).

A process chain for a coupled aerodynamic-aeroacoustic analysis has been established at the German Aerospace Center (DLR). This process chain utilizes the DLR TAU-Code for the unsteady Reynolds-Averaged Navier-Stokes (uRANS) Computational Fluid Dynamics computations and the DLR Ffowcs Williams/Hawkings (FWH) Code APSIM+ for the subsequent computation of the noise emissions (see, e.g. [3]). Often the front and aft rotor of the CROR have the same rotation speed, meaning that the problem is periodic within, or exactly at one rotor revolution (depending on the number of blades of the front and rear rotor). The CROR exhibits a dominant tonal noise emission corresponding to the rotor-alone tones and its interaction tones.

Within the framework of the German BMWi LuFo project "OPERO" together with Rolls-Royce Deutschland and the Airbus funded TOP-CROR project, isolated and semi-installed CROR propulsion systems are studied at high-speed and model-scale conditions. The specific CROR that is investigated is the Rolls-Royce RIG145 open rotor configuration. The front and rear row rotational speeds are completely independent creating a non-periodic behaviour in time after one rotation of the reference rotor. When the difference in rotational speeds is small, the case becomes periodic only after many rotor revolutions. Since the uRANS CFD computations are relatively expensive, only one or several revolutions of the rotors can be calculated.

In this contribution, we address the aeroacoustic and aerodynamic importance of the non-periodic nature of a CROR for those specific cases in which the front and the aft rotor rotate with slightly different rotational speeds. Firstly, an aerodynamic analysis of the effects of unequal rotor rotation speeds as well as the installation effects produced by the pylon is presented. Hereafter, the aeroacoustic importance of a non-periodic CROR is studied on the basis of appropriate unsteady CFD simulations in combination with a permeable FWH-solver for the extrapolation of the sound into the far field. The concept to handle the non-periodicity is concisely presented based on a simultaneous least-square minimalisation approach.

This chapter is organised as follows. In Sect. 2 the method to account for the non-periodicity is illustrated. Hereafter, the considered CROR geometry is presented as well as a short description of the prediction concept. In Sect. 4 results are presented on the effect of installation and unequal rotor speeds on the aerodynamics. Section 5 presents the effect of the non-periodic correction method on the aeroacoustics is presented. Finally, a summary is given in Sect. 6.

2 Simultaneously Least-Square Minimalisation

The concept to handle non-periodic signals uses the fact that the important CROR frequencies are known beforehand, the information of which may explicitly be used in a least-square minimalisation, i.e.

$$S = \int_0^T [s(t) - \sum_{k=0}^{N} A_k \cos(\omega_k t) + B_k \sin(\omega_k t)]^2 dt \stackrel{!}{=} \min \ . \tag{1}$$

Here $s(t)$ is the original signal and A_k and B_k are the Fourier coefficients, with which the non-periodic signal $s(t)$ is approximated in a least-square sense. Equation (1) can be rewritten as

$$\mathbf{C}_{lk} \begin{pmatrix} A_k \\ B_k \end{pmatrix} = \begin{pmatrix} \frac{2}{T} \int_0^T s(t) \cos(\omega_l t) dt \\ \frac{2}{T} \int_0^T s(t) \sin(\omega_l t) dt \end{pmatrix} , \tag{2}$$

where $\mathbf{C}_{lk}$, here referred to as the "correction matrix", equals

$$\mathbf{C}_{lk} = \begin{pmatrix} \frac{\sin(\omega_k - \omega_l)T}{(\omega_k - \omega_l)T} + \frac{\sin(\omega_k + \omega_l)T}{(\omega_k + \omega_l)T} & \frac{1 - \cos(\omega_k + \omega_l)T}{(\omega_k + \omega_l)T} + \frac{1 - \cos(\omega_k - \omega_l)T}{(\omega_k - \omega_l)T} \\ \frac{1 - \cos(\omega_k + \omega_l)T}{(\omega_k + \omega_l)T} - \frac{1 - \cos(\omega_k - \omega_l)T}{(\omega_k - \omega_l)T} & \frac{\sin(\omega_k - \omega_l)T}{(\omega_k - \omega_l)T} - \frac{\sin(\omega_k + \omega_l)T}{(\omega_k + \omega_l)T} \end{pmatrix} . \tag{3}$$

For a detailed analysis, the interested reader is referred to Akkermans et al. [4]. For time signal length $T \to \infty$, $\mathbf{C}_{lk}$ reduces to the identity matrix $\mathbf{I}$ and the standard Fourier transform is recovered in (2). For small (finite) T, the r.h.s. of (2) amounts to the discrete Fourier transform (DFT) for non-periodic frequencies. One can think of the function of $\mathbf{C}_{lk}^{-1}$ as to correct for the non-orthogonality of the used basis in this DFT. Note that matrix $\mathbf{C}_{lk}$ is not dependent on the spatial position, therefore the inverse of matrix $\mathbf{C}_{lk}$ is only computed once for all source points on the FHW-surface. Once amplitude and phase are known through the DFT coefficients, the signal is known "forever" without extrapolation.

3 Geometry and Prediction Concept

The non-periodic RIG145 CROR stems from the European project FP7-DREAM, for which aeroacoustic and aerodynamic measurements were carried out on a model scale (1:6) CROR rig. This RIG145 has 12 blades at the front rotor and 9 at the back (latter blade diameter slightly cropped). Most importantly, the front and rear rotor have slightly different rotational speeds leading to the non-periodicity. For this RIG145, uRANS simulations were performed as part of the OPERO project (see [5] for more details regarding the uRANS simulations), which are used as input for the acoustic propagation. Two geometries are considered: an isolated and a semi-installed one. In the latter configuration, a pylon is present which distorts the inflow at the front rotor plane (i.e. pusher configuration, envisioned to be mounted at rear fuselage).

A schematic of the prediction concept is depicted in Fig. 1 and consists of uRANS simulations which are used as input for the FWH propagation (in frequency domain). The correction procedure consists of a preprocessing step in the process chain, just

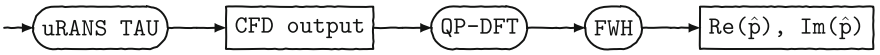

Fig. 1 Schematic of prediction concept in frequency domain with quasi-periodic correction on DFT (QP-DFT). Final output are real and imaginary part of complex pressure

before the FHW propagation. When dealing with periodic input data from CFD, one applies a DFT to transform the signal to Fourier space (i.e. (2) with $\mathbf{C}_{lk} = \mathbf{I}$). For non-periodic CROR data the Quasi-Periodic DFT is used, meaning that correction matrix $\mathbf{C}_{lk}$ is computed with (3).

4 Aerodynamic Results

The aerodynamic forces developed by the rotor blades are influenced by the local flow conditions during the rotation, mainly caused by local deviations of the flow direction and velocity magnitude (i.e. the local incidence angle at the blade). For a CROR in pusher configuration, perturbances on the blade forces are produced by different effects such as angle of attack, blade-blade interactions during the blade passings, down-wash flow or velocity deficit in the wake produced by the mounting system, and possible interactions of the blades with the fuselage boundary layer (see, e.g. [1]). For the isolated case, the blade force developments are mainly affected by the blade-blade interactions. The front blades react to the upstream potential effect induced by the aft blades; the aft blades react correspondingly to potential flow effects from the front rotor, but also to the front blade wakes and the deviations of the flow induced by the swirl flow in the front rotor wake. In addition, the installed case demonstrates the impact of the pylon on the blade force development by an abrupt change of the blade forces when the blade passes through the pylon wake.

The frequencies and amplitudes of the oscillations of the blade force development are extracted from two representative rotations of the respective rotors and plotted as the spectrum in Fig. 2a. Here, frequencies are plotted for the isolated and semi-installed case. Due to the non-periodic behaviour of the blade force time histories, they are multiplied with a Hanning window function to assure periodicity of the signal. It has been checked that this does not lead to qualitatively different results with respect to the aerodynamic analysis presented here. The front blade force development of the isolated case shows the first frequency at $n = 1$ which corresponds to the shaft rotational speed. This is produced by the non-uniform flow direction at the rotor plane induced by the potential flow around the non-axisymmetric sting [5]. The dominant frequencies are located at about two times the aft blade passing frequencies ($n = 18$) and its higher harmonics because during only about half a revolution a front blade sensor measures the interaction with all 9 aft rotor blades. The aft blade load history shows the sting effect ($n = 1$) as well and the representative frequencies at twice the front blade passing frequencies ($n = 24, 48$). The installed case on the other hand shows the dominant frequency at the rotational speed ($n = 1$).

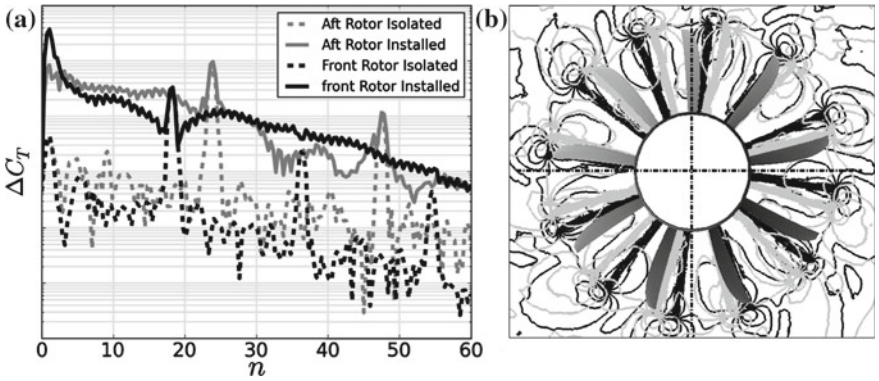

Fig. 2 **a** Spectrum of the unsteady blade load ΔC_T versus shaft order n. **b** Front rotor wake (axial velocity) at start (*black*) and end (*grey*) of one rotor revolution

This corresponds to the sting effect added to the blade passing through the pylon wake. The impingement of the pylon wake on the blades is observed for both rotors, however, this effect is reduced on the aft blade force development. Comparing the isolated to the installed case, the amplitudes of the oscillations resulting from blade-blade interactions of the installed case are slightly higher than the isolated case. This is caused by the aerodynamic interaction of the front blades with the aft blades during their interaction with the pylon wake. When the front blades pass through the pylon wake, the blade loading is increased producing with that a change in the blade wake which impinges at the same time on the aft blades.

With unequal rotor rotation speeds, the interactions of the front blade wakes with the aft blades are shifted to avoid that they always occur at the same circumferential position within several rotations. This can be observed in Fig. 2b, where the wake produced by the front blades is plotted on a plane between the two rotors for two positions during one reference rotation of the aft rotor. The rotation begins at the position where the reference blades of the respective rotors point upwards. The wake at the initial rotor position is plotted in black, whereas grey isocontours show the flow features at the end of the rotor rotation. The frequency and amplitude of the aerodynamic load changes produced by the impingement of the blade wakes with the aft blade remain constant. A shift of the location of the interactions during the next rotation is observed [cf. black and grey isocontours in Fig. 2b], however, the aerodynamic performance of the open rotor is not affected by the non-periodicity.

5 Aeroacoustic Results

The simultaneous least-square minimalisation method is first tested with artificial signals representative of a non-periodic CROR. In Fig. 3a the original artificial signal is depicted in black, the reconstructed signal without correction method in grey.

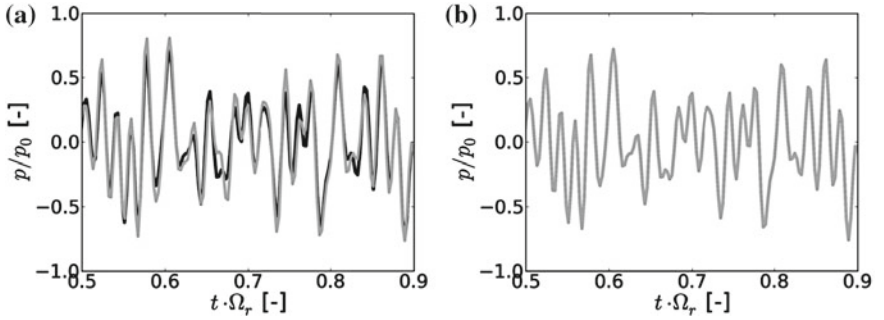

Fig. 3 **a** Reconstruction of original artificial signal (*black*) and without correction method (*grey*). **b** Same as **a** but now with non-periodic correction method applied (note that the reconstructed signal overlaps the original signal)

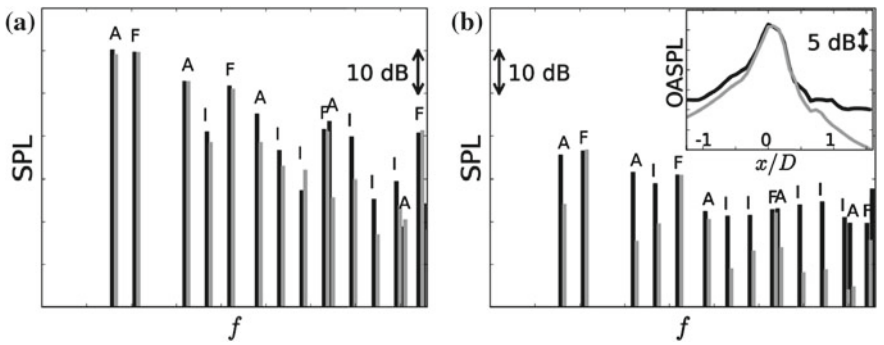

Fig. 4 Spectrum of corrected (*grey*) and uncorrected (*black*) isolated RIG145 data in **a** propeller plane at $x/D \approx 0$ and **b** for upstream position at $x/D \approx -1.1$ (both for 3.5 m from rotor axes). In these figures, 'F', 'A', and 'I' indicate front rotor, aft rotor, and interaction tones, respectively. *Inset* shows the OASPL in streamwise direction

Uncorrected means, here and in the remainder, that the non-periodicity has been ignored and a DFT has been applied. One clearly sees differences between the original and reconstructed signal in Fig. 3a. When the quasi-periodic reconstruction is used with the correction matrix, the reconstructed signal coincides with the original signal [see Fig. 3b]. This latter result illustrates that non-periodic signals can be accurately reconstructed with the method described in Sect. 2. When defining an error ϵ as $|p - p_{\text{recon}}|$, it follows that ϵ remains below 2.5×10^{-13}. This value is comparable to machine accuracy illustrating that indeed the signal is very accurately reconstructed.

In Fig. 4, spectra of the non-periodic RIG145 are depicted for two positions, i.e. (a) in the propeller plane and (b) for an upstream position. Already for frequencies below 4th harmonic of BPF_f, one observes differences up to approximately 10 dB between the corrected and uncorrected signals. As opposed to the spectrum in the propeller plane, a 12 dB correction is already observed for the amplitude of the first rear BPF for the microphone located upstream of the CROR. For the other frequencies, a similar

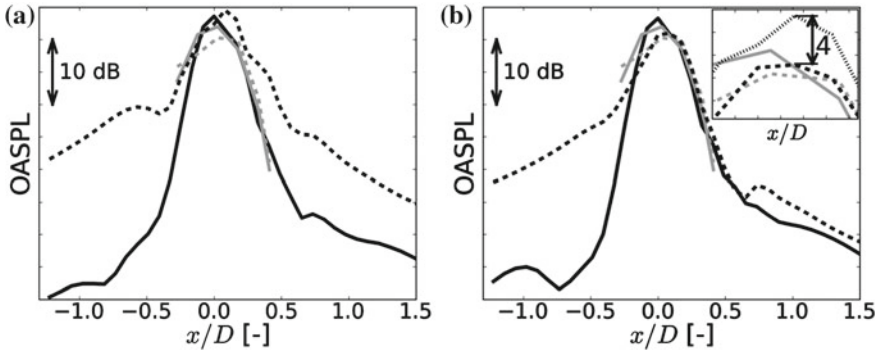

Fig. 5 Overall sound pressure level (OASPL) in streamwise direction (x/D) for 3.5 m from rotor axes. Comparison between experiments and **a** uncorrected numerical and **b** corrected numerical results. *Solid lines* represent isolated RIG145 data and dashed corresponds to the semi-installed one. *Black* and *grey* colours indicate numerical and experimental results, respectively. The *inset* displays a zoom-in around the peak, with meaning of colours and line types as in Fig. 5b, except the *dotted line* which is the installed numerical computation without correction method applied [from Fig. 5a]

behaviour is seen with slightly larger differences between corrected and uncorrected amplitudes. The impact of the quasi-periodic reconstruction on the over all sound pressure level (OASPL) is illustrated in the inset of Fig. 4b. For the OASPL, all frequencies up to $5BPF_f$ are considered. Around the rotor plane small differences are seen between the OASPL of the corrected and uncorrected signal, as already suggested in Fig. 4a. However, upstream and downstream differences exceeding 3 dB in OASPL indicate a significant correction [cf. Figs. 4a and b].

In Fig. 5, the comparison between the numerical and experimental data is presented. The experimental data is taken from tests performed in the ARA wind-tunnel in Bedford (UK) within the frame of the EU DREAM project. Note that the azimuthal angle of the polar OASPL in Fig. 5 is different than the one of the inset of Fig. 4b. When considering the uncorrected numerical results [see Fig. 5a], a good agreement is seen between experiments and numerics for the isolated case (solid black and solid grey lines, respectively). As opposed to this, a large difference is observed for the installed case (dashed lines). In Fig. 5b, the numerical result is depicted where the non-periodic correction method has been applied. Hardly any influence is seen for the isolated case (solid lines), however, for the installed case now a good agreement is seen between numerics and experiment (dashed lines). The experimental data therefore confirms the correctness of the here applied non-periodic correction method [cf. dashed lines in Fig. 5b]. The inset of Fig. 5b shows the region around the peak values in more detail, however, the dotted line is the numerical result of the installed case without correction [dashed black line in Fig. 5a]. Clearly seen is a significant correction of about 4 dB for the installed numerical simulation. Furthermore, for the considered azimuthal angle, one ends up with a completely

different conclusion when not correctly accounting for the non-periodicity, i.e. the semi-installed case is louder (dotted black line) than the isolated one instead of quieter (dashed black line) when properly taking the non-periodicity into account.

6 Conclusions

Nonequal rotation speeds of CROR rotors lead to non-periodic dataset. A way to handle such non-periodic signals was presented and tested with artificial signals. With artificial signals it is demonstrated that the correction method can accurately reconstruct a quasi-periodic signal. The results on an actual non-periodic CROR showed a minor influence of the non-periodicity on the aerodynamic performance of the CROR. As opposed to the minor importance of the non-periodicity for the aerodynamics, a significant influence is observed for the aeroacoustics. Based on the isolated CROR case, differences between corrected and uncorrected signals exceeding 10 dB in amplitude are observed in the propeller plane for frequencies below the 4th harmonic of the front rotor BPF. For upstream microphone positions, even the 1st rear BPF is highly affected by the correction procedure. Comparison of the isolated and installed CROR cases reveal that ignoring the non-periodicity leads to a complete opposite conclusion for the influence of installation effects. The experimental validation confirms the non-periodic correction method.

Acknowledgments Airbus and Rolls-Royce are acknowledged for allowing publication of the RIG145 data. Anthony Parry (Rolls-Royce UK) is acknowledged for comments regarding this proceeding. The remaining errors are solely ours.

References

1. Mann, S.A.E., Stewart, C.A.: Advanced propulsion through the 1990s : an airframer's view. In: 21st SAE, ASME and ASEE, Joint Propulsion Conference, AIAA-1985-1192, Monterey, CA, USA (1985)
2. Peake, N., Parry, A.B.: Modern challenges facing turbomachinery aeroacoustics. Annu. Rev. Fluid Mech. **44**, 227–248 (2012)
3. Stuermer, A., Yin, J.: Low-speed aerodynamics and aeroacoustics of CROR propulsion systems. In: 15th AIAA/CEAS Aeroacoustics Conference, AIAA-2009-3134, Miami, FL, USA (2009)
4. Akkermans, R.A.D., Delfs, J.W., Lummer, M., Siefert, M., Caruelle, B., Tiedemann, C.: Handling of non-periodic contra rotating open rotor data. In: 18th AIAA/CEAS Aeroacoustics Conference, AIAA-2012-2262, Colorado Springs, CO, USA (2012)
5. Márquez, C., Stuermer, A., Clemen, C.: Validation of actuator disk simulations of CROR propulsion systems at low-speed flight conditions. In: AIAA-2012-2787, New Orleans, LA, USA (2012)

Computational Aeroacoustics of a Counter-Rotating Open Rotor at Different Angles of Attack

Eirene Rebecca Busch, Manuel Keßler and Ewald Krämer

Abstract The noise emission of a 9×7 counter-rotating open rotor is examined at different angles of attack. Numerical simulations with acoustic post-processing were carried out with a finite volume code and a Ffowcs Williams and Hawkings tool. The aerodynamic analysis showed a variation of the flow field depending on the angle of attack, leading to additional forces and moments and also an altered noise emission. For the single rotor tones a shift of the emission within the rotor plane is observed, when the flow is attached to the blades. This leads to a higher emission towards the ground and a lower emission towards the sky with positive angles of attack. The trend of the polar emission is qualitatively the same. With flow separation at high angles of attack the polar directivity shows a higher emission in diagonal and x-direction. The noise emission shows a variation of the noise level and the location of the maxima for the interaction tones depending on the blade-wake and blade-vortex interaction which changes with the spanwise position of the vortex impact.

1 Introduction

Counter-rotating open rotors (CRORs) are a promising engine concept to meet the ACARE Vision 2020 goals in relation to pollutant emission. With the very high bypass ratio and two rotors rotating in opposite direction, which lead to a reduction of

E. R. Busch (✉) · M. Keßler · E. Krämer
Institut für Aerodynamik und Gasdynamik, Universität Stuttgart,
Pfaffenwaldring 21, 70569 Stuttgart, Germany
e-mail: busch@iag.uni-stuttgart.de
http://www.iag.uni-stuttgart.de

M. Keßler
e-mail: kessler@iag.uni-stuttgart.de

E. Krämer
e-mail: kraemer@iag.uni-stuttgart.de

A. Dillmann et al. (eds.), *New Results in Numerical and Experimental Fluid Mechanics IX*,
Notes on Numerical Fluid Mechanics and Multidisciplinary Design 124,
DOI: 10.1007/978-3-319-03158-3_61,

swirl in the wake, they have a great potential for fuel saving. The combination of high single rotor noise caused by transonic blade tip Mach numbers and interaction noise leads to an elevated noise level compared to conventional jet engines. The interaction noise is generated by the front rotor (FR) wake and blade tip vortices impinging on the rear rotor (RR) as well as the interaction of their potential fields. Another challenge of the CROR is the integration with current low-wing aircraft designs, as the traditional under-wing installation is not possible. A tractor-CROR type integration on a high-wing configuration causes very high inflow angles for the rotors, while installation in a pusher configuration on the aft fuselage may provoke additional rotor inflow perturbations due to the presence of a pylon. In this chapter the noise emission of a 9×7 CROR at different angles of attack is evaluated with an existing numerical process chain [1]. As only noise generated by the rotors is of interest here, the nacelle is simplified by a circular cylinder.

2 Computational Modeling

Unsteady CFD simulations of a full annulus CROR setup were carried out for 8 rotor revolutions with a resolution of 360 timesteps per revolution. Flow field data was extracted over the last rotor revolution and afterwards used for the acoustic analysis. The CROR operates at take-off conditions with both rotors at equal rotational speed n. For all cases identical blade pitch angles were used. The total setup consisted of roughly 49 million cells, which includes 1.5 million cells for each of the 16 blade meshes and 25 million for the background grid. A Navier-Stokes boundary condition was used for the blade surfaces while an Euler boundary condition was applied for the nacelle in the background grid. The same grids were already used for a comparison of take-off and cruise noise in [1].

2.1 Flow Solver

For aerodynamic modeling the CFD Code FLOWer developed by the German Aerospace Center DLR was used [6]. It is a block-structured code that solves the 3D compressible unsteady Reynolds averaged Navier-Stokes equations (RANS). Spatial discretization is carried out with a second-order accurate cell-centered finite volume scheme using central differencing. The time integration is done by the dual-time stepping method developed by Jameson [3, 4]. For turbulence modeling Wilcox' k-ω model is applied. A Chimera algorithm is implemented so a complex geometry and moving structures can be modeled [7]. In this chapter moving blade grids were introduced into a background grid at rest by cutting holes, that for each timestep move with the same rotational speed as the rotor blades, with interpolating in the overlapping areas. Grid movement is accomplished by transforming the RANS equations into a relative frame of reference, which is fixed to the moving body depending on the prescribed grid movement.

2.2 Acoustic Solver

The Institute of Aerodynamics and Gas Dynamics tool ACCO is used for acoustic evaluation. It is a C++ code that determines the noise emission at a distant observer with the Ffowcs Williams and Hawkings (FWH) analogy. The FWH equation is defined by

$$\frac{\overline{\partial}^2\overline{\rho}'}{\partial t^2} - c^2\overline{\nabla}^2\overline{\rho}' = \frac{\partial^2}{\partial x_i \partial x_j}\left[T_{ij}H\left(f_S\right)\right] - \frac{\partial}{\partial x_i}\left[\left(p'n_i + \rho u_i\left(u_n - v_n\right)\right)\delta\left(f_S\right)\right] + \frac{\partial}{\partial t}\left[\left(\rho_0 v_n + \rho\left(u_n - v_n\right)\right)\delta\left(f_S\right)\right]$$

where $\overline{\rho}'$ denotes the density distribution, c the speed of sound, p' the pressure fluctuation, n_i the normal vector, u_n the normal component of the velocity, v_n the surface normal speed and $\delta(f)$ the Dirac delta function on the integration surface [2, 5]. The right hand side stands for the acoustic source terms and the left hand side is the wave equation. The source terms are monopoles modeling thickness noise, dipoles modeling loading noise and quadrupoles which model turbulent and jet noise. In this chapter acoustic noise is calculated by using penetrable integration surfaces which include a limited source region. The surfaces enclose the blades and a defined volume of intense quadrupoles while assuming uniform flow outside this region.

3 Results

The simulations included nine different angles of attack α defined as the angle around the z-axis, see Fig. 1. For aerodynamic analysis integrated forces and moments of the blades only as well as the flow field will be shown. The noise emission is evaluated in azimuthal direction in the y-z-plane as well as in polar direction in the x-y-plane at a radius of $r/R = 3.5$.

3.1 Aerodynamics

The angle of attack causes a vertical flow component which is positive with positive α. This leads to a sinusoidal distribution of inflow over the rotor plane. For a positive angle of attack the resulting inflow velocity on the blades of the front rotor will be higher in negative z-direction and leads to an increased local angle of attack α_{local}, which may even cause local separation. For the front rotor the income flow caused by the rotational velocity $v_{rot} = -2\pi nr$, which increases with the radius r, and the vertical component of the freestream velocity $v_{y,\infty} = v_\infty \sin\alpha$ sum up in negative z-direction. This causes a higher local thrust, whereas in positive z-direction they point in opposite directions leading to a lower local thrust. This provokes a yawing

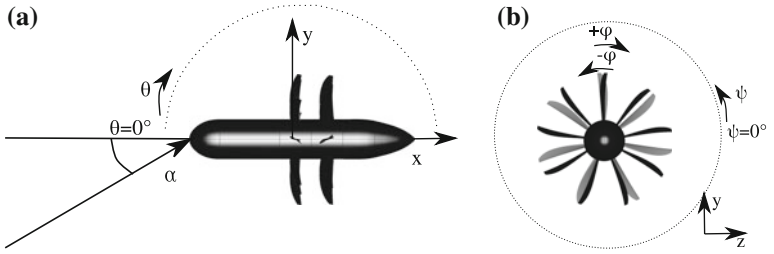

Fig. 1 Observer positions, **a** x-y plane, **b** y-z plane

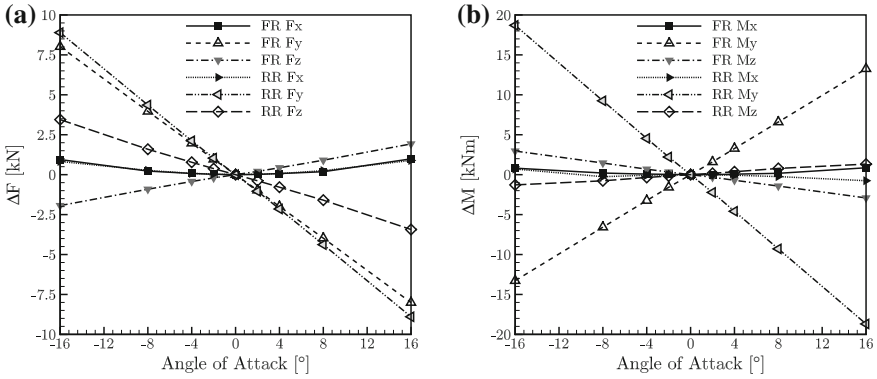

Fig. 2 Increments over the axial flow case as a function of CROR angle of attack. **a** Force increments. **b** Moment increments

moment that increases with a higher absolute value of α, see Fig. 2. On the rear rotor the velocity vectors will sum up reversed due to the opposite direction of rotation. This effect causes a non-uniform pressure distribution along both front and rear rotor planes leading to vertical and lateral forces, with a change of sign for the latter between front and rear rotor due to the reversed direction of rotation, see Fig. 3d–i. In the wake of the rotors the flow is nearly parallel to the x-axis independent of α, see Fig. 3a–c. This redirection of flow causes a force in negative y-direction with positive α and also a pitching moment. However, this pitching moment is much smaller than the yawing moment. The vertical flow component additionally causes a shift of the blade tip vortices. For positive α the blade tip vortices of the front rotor are shifted in positive y-direction, see Fig. 3a–c. Furthermore the variation of the blade loading entails blade tip vortices of different strength. As seen in Fig. 3d–i the pressure distribution varies strongly over the front and rear rotor plane. Hence the flow field is strongly instationary over a rotor revolution, which causes a high fluctuation in the thrust and also a higher acoustic emission. The wake of the CROR evens out relatively fast in x-direction with $\alpha = 0°$, whereas with $|\alpha| > 0°$ the pressure distribution shows significant differences in radial as well as circumferential direction, see Fig. 3j–l.

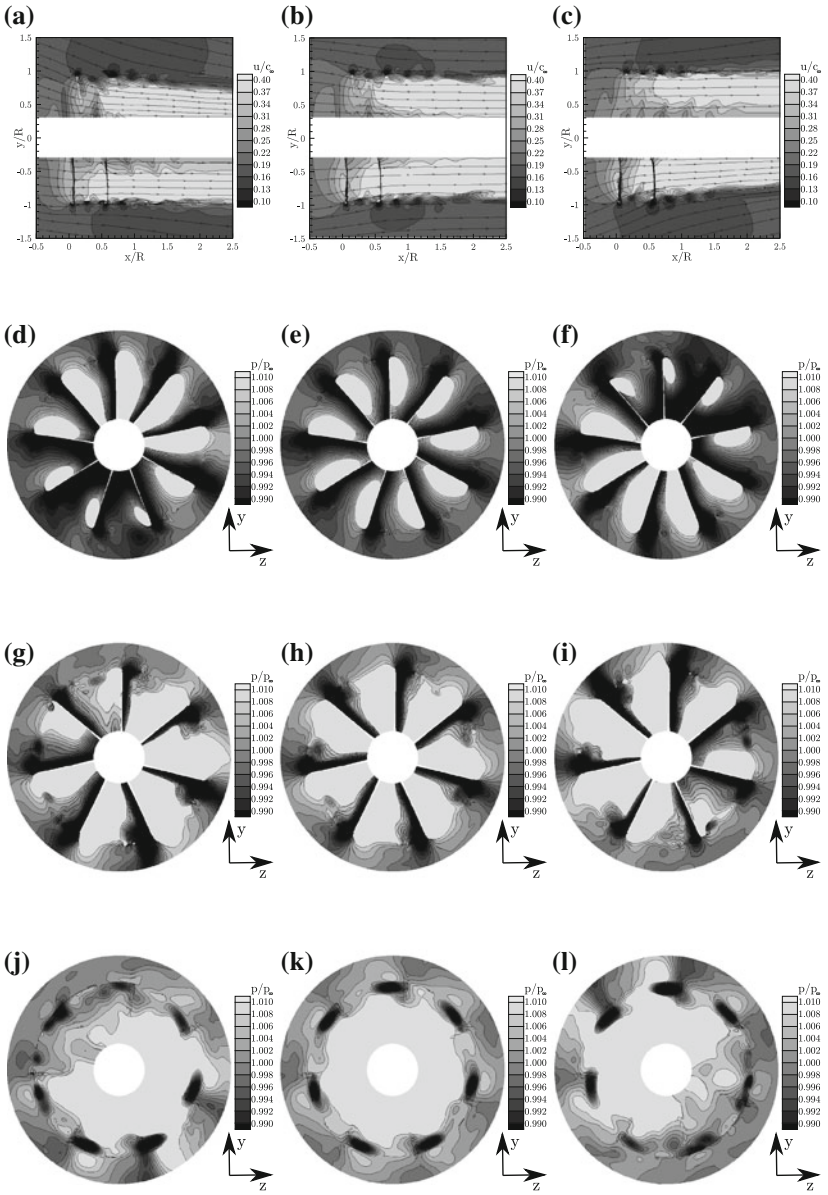

Fig. 3 Distribution of velocity component in x-direction u, non-dimensionalized with speed of sound c_∞, (**a–c**) and pressure p, non-dimensionalized with farfield pressure p_∞ (**d–l**), for different angles of attack. **a** $\alpha = -16°$, u/c_∞ in x-y-plane. **b** $\alpha = 0°$, u/c_∞ in x-y-plane, **c** $\alpha = +16°$, u/c_∞ in x-y-plane, **d** $\alpha = -16°$, p/p_∞ in FR plane ($x/R = 0$), **e** $\alpha = 0°$, p/p_∞ in FR plane ($x/R = 0$), **f** $\alpha = +16°$, p/p_∞ in FR plane ($x/R = 0$), **g** $\alpha = -16°$, p/p_∞ in RR plane ($x/R = 0.5$), **h** $\alpha = 0°$, p/p_∞ in RR plane ($x/R = 0.5$), **i** $\alpha = +16°$, p/p_∞ in RR plane ($x/R = 0.5$), **j** $\alpha = -16°$, p/p_∞ in CROR wake ($x/R = 1.0$), **k** $\alpha = 0°$, p/p_∞ in CROR wake ($x/R = 1.0$), **l** $\alpha = +16°$, p/p_∞ in CROR wake ($x/R = 1.0$)

3.2 Acoustics

Single Rotor Noise. For an inflow without an angle of attack ($\alpha = 0°$) the azimuthal directivity of single rotor noise is constant for all angles ψ, see Figs. 4a and 5a, as it is to be expected. The single rotor emission is built up by displacement noise (monopole noise) and loading noise such as thrust (dipole noise). While the monopole noise is fairly constant, the dipole noise changes due to the non-uniform thrust production in the rotor plane with $\alpha \neq 0$, cf. Fig. 3. This leads to a displacement of the azimuthal directivity depending on both the sign of α and its absolute value, see Figs. 4a and 5b. In addition to the constant loading noise emitted by each blade the sinusoidal loading causes a variation of the dipole noise over the rotor plane. As this happens for all blades it occurs with the blade passing frequency for the observer. This effect can be seen for both front and rear rotor. For the rear rotor (see Fig. 5a) the circular emission additionally shows a slight distortion which is caused by the non-uniform wake of the front rotor. The comparison of the cases $+4°$ and $-4°$ reveals a symmetric behavior depending on the direction of rotation, see Figs. 4a and 5a. Furthermore with higher angles of attack (see Fig. 4a $+16°$) a fluctuation of approximately 5 dB between $\psi = 65°$ and $\psi = 180°$ can be seen in the azimuthal directivity of the front rotor, indicating flow separation on some parts of the blades. This was also seen in the pressure distributions on the blade surfaces. The seperation phenomena are stronger on the front rotor than on the rear rotor where the fluctuations occur at $\psi = 30°$ to $\psi = 120°$ with an amplitude of 2 dB, cf. Fig. 5a. The inflow is already redirected by the front rotor causing a lower inflow angle on the rear rotor. The separation was observed over several rotor revolutions and is periodic from one rotor revolution to the next. It occurs only at high local angles of attack on each blade at the same ϕ causing the oscillation of the sound pressure level over ψ, hence the acoustic effects can be observed at blade passing frequency. In polar direction the single rotor noise shows a displacement of the maximum at $\theta = 90°$ and $\theta = 270°$ to the pressure side, that is again depending on the absolute value of α, see Figs. 4b and 5b. The emission in diagonal direction and along the x-axis for $+16°$ increases with higher absolute α, which is a clear sign of increasing flow separation due to higher α_{local}. Again a symmetry can be observed for positive and negative angles of attack as the curves for $+4°$ and $-4°$ show, see Figs. 4b and 5b. The effects observed in azimuthal as well as polar direction for the $+16°$-case can also be seen for $-16°$ with a symmetrical displacement.

Interaction Noise. The first interaction frequency shows a clear influence of α in the azimuthal directivity, but a distinct tendency cannot be observed, see Fig. 6a. For $\alpha = 0°$ the noise levels are fairly constant, while for $|\alpha| > 0°$ the interaction noise apparently varies randomly with an amplitude of 20 dB. As this noise is generated by the interaction of the blade tip vortices and blade wakes with the rear rotor blades, it is depending on the spanwise position of the collision of vortex and blade and also on the decay of the wake in x-direction. Generally, the further inward in the rotor plane the vortex collides with the rear rotor blade, the higher the noise generated and the higher the variation of sound pressure level over ψ. The combination of flow

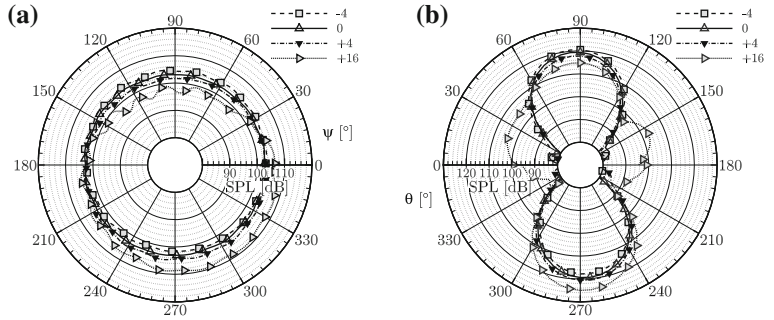

Fig. 4 Front rotor blade passing frequency $f_{BPF1} = 9n$. **a** Azimuthal directivity. **b** Polar directivity

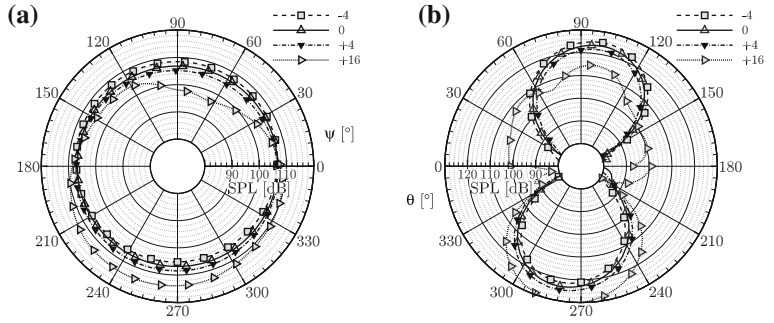

Fig. 5 Rear rotor blade passing frequency $f_{BPF2} = 7n$. **a** Azimuthal directivity. **b** Polar directivity

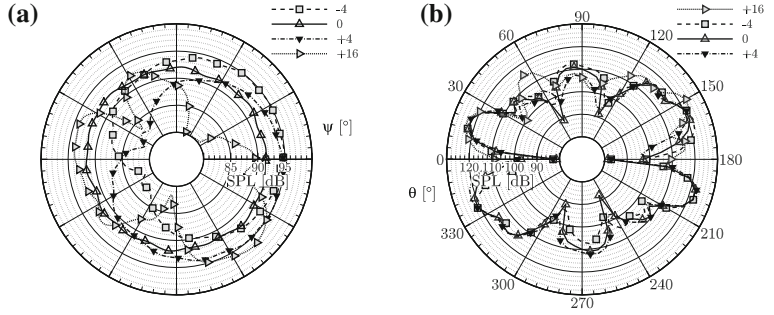

Fig. 6 First interaction frequency $f_{BPF12} = (9+7)n$. **a** Azimuthal directivity. **b** Polar directivity

redirection and displacement of the vortices in y-direction, as well as the variation of blade loading over the rotor plane leading to different vortex strengths provoke this apparent chaotic behavior. The polar emission (Fig. 6b) shows a smaller interaction noise with $\alpha = 0°$ than with $|\alpha| > 0°$, yet this is not the case for all angles θ. The interaction noise shows several peaks over the polar direction and the levels vary up

to 30 dB for all α. For higher absolute α the sound pressure levels in polar direction are overall higher but show roughly the same variation as for $\alpha = 0°$. However, they may be displaced in θ. The same symmetry effects for positive and negative α can be observed as for single rotor noise.

4 Conclusion

CFD simulations of a CROR at different angles of attack were performed with a second order accurate finite volume scheme applying the Chimera method to integrate rotating blade meshes into a background grid. The following acoustic evaluation was carried out with a FWH code. Aerodynamic results showed a significant change of the flow field with varying angles of attack. The redirection of the flow and the non-uniform blade loading over a rotor revolution in azimuthal direction cause forces and moments on the engine and also have an influence on the acoustic emission. While the single rotor noise is mainly displaced in space for varying angles of attack and shows signs of separation for very high α, the interaction noise increases due to the modified blade vortex interaction and the variation in vortex strength as well as wake strength in azimuthal direction. The results presented show a good qualitative agreement with wind tunnel experiments carried out by Woodward [8]. Further work will include CFD simulations with adapted blade shape and reduced diameter of the rear rotor.

Acknowledgments The authors would like to thank MTU Aero Engines for its support. We also thank the members of the Helicopters and Aeroacoustics group at the IAG for their input and experience.

References

1. Busch, E.R., Keßler, M., Krämer, E.: Numerical investigation of a counter-rotating open rotor noise emission in different flight conditions. In: ASME Turbo Expo. Number GT2012-68625, Copenhagen, Denmark (2012)
2. Ffowcs Williams, J.E., Hawkings, D.L.: Sound generation by turbulence and surfaces in arbitrary motion. Philos. Trans. R. Soc. A **264**(1151), 321–342 (1969)
3. Jameson, A.: Time dependent calculations using multigrid, with applications to unsteady flows past airfoils and wings. In: AIAA 10th Computational Fluid Dynamics Conference, Honolulu, Hawaii, USA (1991) 1591–1596
4. Jameson, A., Schmidt, W., Turkel, W.: Numerical solution of the euler equations by finite volume methods using Runge-Kutta time-stepping schemes. In: AIAA 14th Fluid and Plasma Dynamic Conference, Palo Alto, California, USA (1981) 15
5. Keßler, M., Wagner, S.: Source-time dominant aeroacoustics. Comput. Fluids **33**, 791–800 (2004)
6. Kroll, N., Eisfeld, B., Bleecke, H.: Flower. Notes Numer. Fluid Mech. **71**, 58–68 (1999)
7. Schwarz, T.: Ein blockstrukturiertes Verfahren zur Simulation der Umströmung komplexer Konfigurationen. PhD thesis, Universität Braunschweig (2005)
8. Woodward, R.: Noise of two high-speed model counter-rotation propellers at takeoff/approach conditions. J. Aircr. **29**(4), 679–685 (1992)

Assessment of Front Rotor Trailing Edge Blowing for the Reduction of Open Rotor Interaction Noise

A. Stuermer, R. A. D. Akkermans and J. W. Delfs

Abstract Contra-Rotating Open Rotor (CROR) propulsion systems show promise as a highly economic and environmentally friendly powerplant for future transport aircraft. One major challenge to overcome relates to the noise emissions of this type of engine, which is driven in large part by the complex mutual interactions between the two rotors of the CROR. In the present study, a coupled aerodynamic and aeroacoustic analysis using the DLR numerical methods TAU and APSIM+ is performed to assess the potential of front rotor trailing edge blowing (TEB) to achieve a reduction of interaction tone noise emissions of CROR propulsion systems. A successful alleviation of the front rotor's blade wakes could be achieved, which led to a clear reduction in local aft blade unsteady loadings for much of their spanwise extent. However, the specific CROR configuration under study here still has significant impingement of the front blade's tip vortices on the aft rotor due to an insufficient reduction of the aft rotor diameter with respect to that of the front rotor. In terms of overall aerodynamic performance, no notable difference is found between the two configurations under study. On the aeroacoustics side, interaction tones are most affected showing the expected decrease in sound pressure level near the rotor planes. Upstream of the rotors, increased levels are seen resulting from the aforementioned tip-vortex impingement on the aft rotor blades.

A. Stuermer (✉), R.A.D. Akkermans · J.W. Delfs
German Aerospace Center (DLR), Institute of Aerodynamics and Flow Technology,
Lilienthalplatz 7, 38108 Braunschweig, Germany
e-mail: arne.stuermer@dlr.de

R.A.D. Akkermans
e-mail: rinie.akkermans@dlr.de

J.W. Delfs
e-mail: jan.delfs@dlr.de

A. Dillmann et al. (eds.), *New Results in Numerical and Experimental Fluid Mechanics IX*,
Notes on Numerical Fluid Mechanics and Multidisciplinary Design 124,
DOI: 10.1007/978-3-319-03158-3_62,

1 Introduction

Increasing environmental and economic pressures have renewed interest in Contra-Rotating Open Rotor (CROR) propulsion systems as a powerplant for commercial transport aircraft, as they promise a step change in efficiency due to their ultra-high bypass ratio. The primary challenges for the realization of a commercially viable CROR engine relate to the issues of noise emissions and installation effects with the airframe. In the frame of the 7th Framework EU Joint Technology Initiative Smart Fixed Wing Aircraft project (JTI SFWA) [1], DLR is investigating the general efficacy of applying front rotor trailing edge blowing (TEB) for the reduction of interaction tone noise emissions of CROR propulsion systems. Trailing edge blowing reduces the wake momentum deficit behind the front rotor [5, 13] and therefore its wake interaction with the aft rotor. The investigation is conducted using a coupled CFD-CAA process chain based on unsteady Reynolds-Averaged Navier-Stokes (uRANS) simulations with the DLR TAU-Code [8, 12] and a subsequent noise emission analysis using the DLR Ffowcs Williams/Hawkings (FWH) Code APSIM+ [2].

2 Geometry and Test Case Definition

The investigation is performed for the Airbus-designed generic AI-PX7 CROR configuration, an 11×9-bladed design featuring an aft rotor diameter reduction of 10 % with respect to the front rotor. To study the principal efficacy of front-rotor TEB for the reduction of interaction tone noise emissions, each blade of the AI-PX7 CROR's front rotor was modified to include a slot just upstream of the trailing edge on the blade suction side for much of the blade span, as shown in Fig. 1. For both the baseline CROR as well as the powerplant with front rotor TEB, uRANS simulations are performed to assess the detailed impact of this novel active flow control approach on the aerodynamic performance of the engine as well as to provide the input data for the FWH analysis of the noise emissions. As interaction-tone noise plays a dominant role in the overall CROR noise signature as relevant for flyover noise certification purposes at take-off conditions [12], the investigations are focused on the isolated CROR at typical low-speed $M = 0.23$, high-thrust conditions. Through a parametric study of the blowing pressure ratios for each of the four spanwise slot segments, an operating point was selected that minimizes the front rotor blade wake deficit in the plane of the aft rotor.

3 Simulation Approach

A coupled simulation utilizing the DLR TAU-Code for the uRANS CFD computations and the DLR FWH-Code APSIM+ for the subsequent noise computation was performed, a process chain that has already been successfully applied to a number

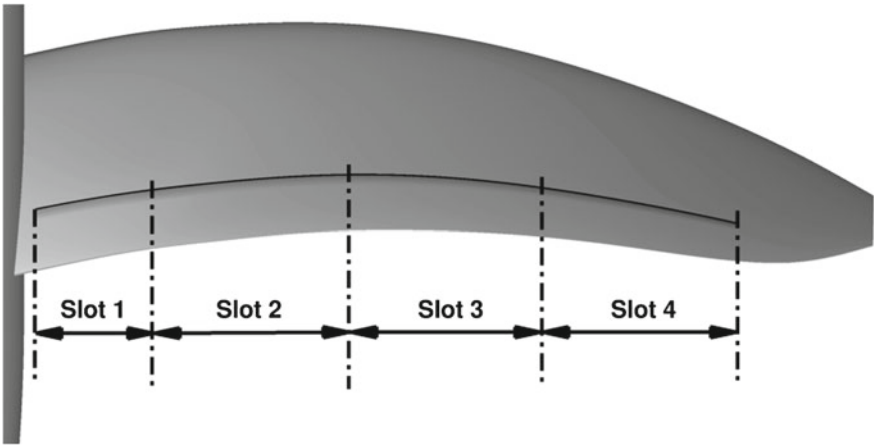

Fig. 1 CROR front rotor blade slot geometry

of propeller investigations [11, 14]. The DLR TAU-Code is an unstructured finite-volume vertex-based CFD solver. For the simulation described here, spatial discretization of the convective fluxes is done using a second order central differencing scheme with scalar dissipation while the viscous fluxes are discretized with central differences. Turbulence is modeled with the 1-equation Spalart-Allmaras model [10]. The dual time approach is used in the DLR TAU-code to compute unsteady flows with a temporal resolution set to equate to a rotor rotation of $\Delta\Psi = 0.25°$ per physical time-step [7]. For the application of TEB in the simulation, use is made of the TAU-Code's engine boundary condition. It allows for the setting of the cold, continuous jets in each slot through the specification of appropriate pressure and temperature ratios at the slot outlets. In order to simulate the relative motion of the rotors, use is made of the code's Chimera capability as well as the implemented motion libraries [9]. The meshes for the CROR configuration were generated using both the CentaurSoft Centaur and the ANSYS ICEM CFD mesh generation software and drew on grid resolution requirement experienced gained in past work on propeller and CROR simulations [11, 12]. The farfield boundaries are located at a distance of 20 times the front rotor diameter D from the engine axis and front rotor center, eliminating any adverse impact of this boundary condition on the flow solution. In addition to ensuring an adequate resolution of boundary layers (including the laminar sublayer) on all surfaces of the CROR, a particular focus of the mesh generation was the requirement to adequately resolve the aeroacoustic pressures in the rotor mesh blocks during the CFD simulation in order to use the nacelle Chimera boundary as the input permeable surface for the APSIM+ analysis. Therefore the mesh density of the front and aft rotor grids was dictated by the need to resolve all relevant sound pressures through the 5th harmonic of the front rotor blade passing frequency. Common aft rotor and nacelle meshes were used in the simulations and only the front rotor mesh was adapted to the baseline configurations unmodified or

the blowing cases slotted blade geometries. The complete 3-block Chimera meshes for the uRANS computations consists of $55 \cdot 10^6$ nodes for the baseline configuration and $62 \cdot 10^6$ points for the case with front rotor blowing. The simulations were run using 360 processors of the DLR $C^2A^2S^2E$-cluster, resulting in computation times of around 2 weeks per case.

The Aeroacoustic Prediction System based on Integral Method, APSIM+, was developed at the DLR Institute of Aerodynamics and Flow Technology for the prediction of rotor or propeller noise radiated in the free farfield. As mentioned, in the current applications the unsteady CFD data on the Chimera boundary surfaces surrounding the propellers is used for an aeroacoustic analysis based on the permeable surface Ffowcs-Williams/Hawkings (FWH) approach [3, 4, 6]. This choice was made out of practical considerations, since this boundary represents an already existing closed surface which fully encloses the relevant noise sources of the geometry, i.e. the rotors. The surface is a non-rotating cylindrical shape aligned with the rotational axis of the rotors [2, 14]. It should be noted that the final 3D surface is not closed at its two end caps because of the penetration of the nacelle. The noise contribution of the nacelle, which lies outside of the permeable surface, is not considered in the present APSIM+ computations. The calculations, performed in the frequency domain, deliver pressure amplitude and phase information at any desired observer location, which is further analyzed to derive acoustic spectrum data. For the overall sound pressure level (OASPL), all frequencies up to 5 times the front rotor blade passing frequency ($5 \cdot \mathrm{BPF_F}$) are considered.

4 Aerodynamic Analysis

The challenge of CROR front rotor TEB application lies in the close coupling of the rotors. Thus the mixing length, during which the injected air can serve to fill the front blades wake deficit is limited, and the full alleviation of the adverse impact of the wake on the aft rotor is non trivial. Figure 2 compares the front blade wakes at an axial position of $x/D = 0.08$ downstream of the front rotor in terms of the instantaneous dynamic pressure profiles at a radial positions of 80 % span of the front blade. The injection of air near the trailing edge along the front blade span serves to significantly reduce the wake deficit. In this initial assessment of this technology, the primary aim was to demonstrate the potential of front rotor blowing for CROR interaction tone noise emissions. Thus, a wake filling was targeted for the entire aft blade span, resulting in a relatively large air massflow. This air requirement is most likely prohibitive but could be reduced through a more aeroacoustically optimized application, i.e. focusing mainly on the outer portions of the front blade. The success of the reduction in front blade wake strength as shown in Fig. 2 can be seen in the reduced local loading fluctuations at a corresponding spanwise position of the aft blade, as plotted in Fig. 3. In comparison to the baseline case, the blowing configuration shows a significant reduction of the local loading oscillation (plotted as the non-dimensional coefficient of total blade loading).

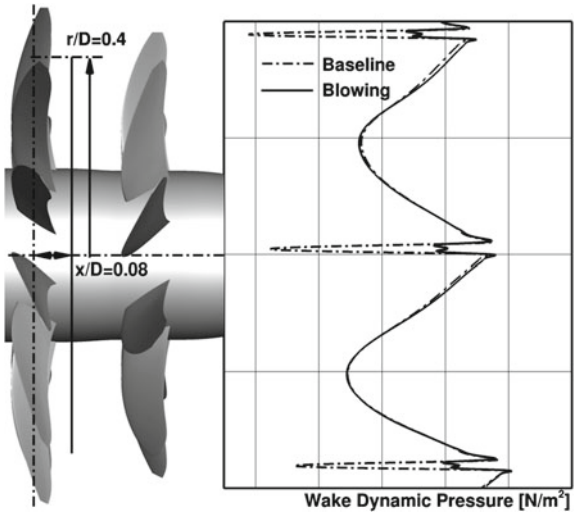

Fig. 2 Dynamic pressure profiles at $x/D = 0.08$ aft of the front rotor for a spanwise position of $r/D = 0.4$

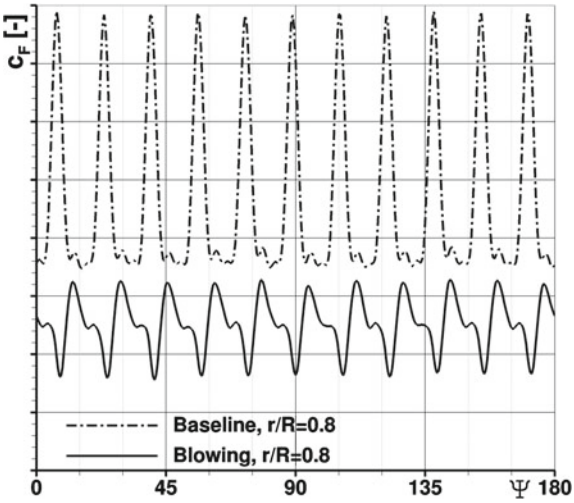

Fig. 3 Impact of TEB on the local aft blade loading development at 90 % aft blade span

Figure 4 shows a comparison of the integrated complete aft blade loading coefficient development during the relevant period of one half of the rotor rotation for the baseline and the blowing case. In both cases, the aft blade experiences an unsteady loading due to the interaction with the front rotor blades tip vortex and/or wakes. This causes a 22-cycle oscillation of the blade loading during one full rotor rotation. Surprisingly, an aft blade of the case featuring front rotor TEB shows a larger amplitude

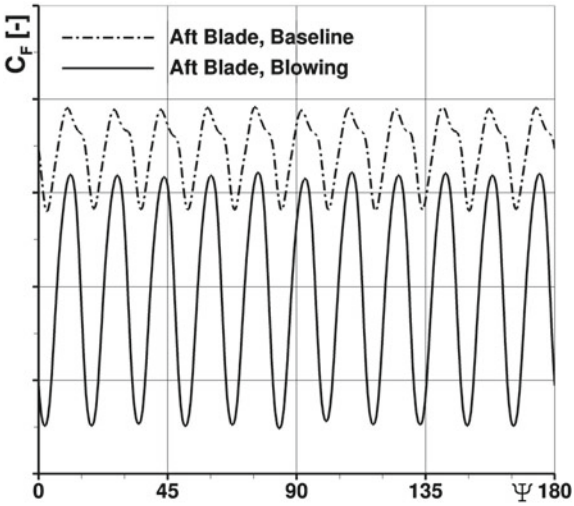

Fig. 4 Impact of TEB on total aft blade loading development

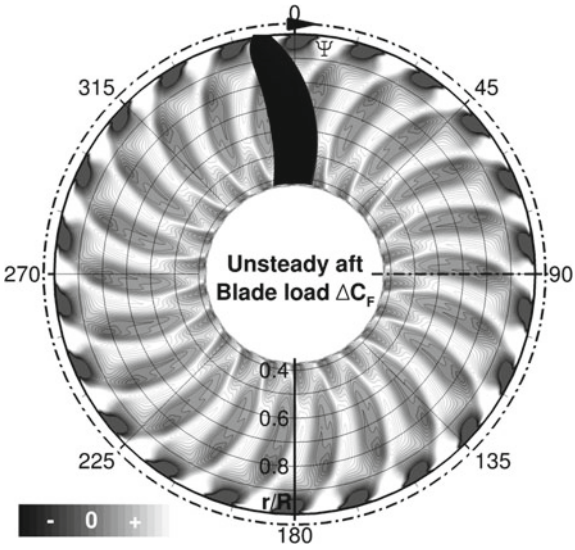

Fig. 5 Baseline configuration aft blade unsteady loading development

fluctuation than does the baseline case. This unexpected result can be traced to the interaction of the front rotor's tip vortices with the aft blades. As shown in the contour plot of the aft blade unsteady loading versus azimuth for the baseline configuration in Fig. 5, the aft rotor diameter reduction of 10 % versus the front rotor is insufficient to avoid impingement of the front blades tip vortices at this high thrust conditions, which show the dominance of this effect on the unsteady loading for roughly the

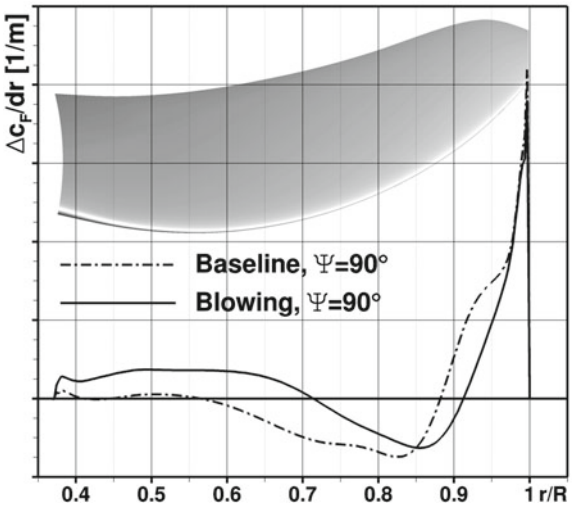

Fig. 6 Comparison of the aft blade unsteady loading for an azimuthal position of $\Psi = 90°$

outer 10 % of the aft blade span. Selecting an arbitrary azimuthal position of the aft blade, for example $\Psi = 90°$, it can be seen in the figure, that the largest increase in aft blade tip blade loading due to front rotor tip vortex impingement coincides with a strong reduction in local loading across mid portions of the aft blade due to the interaction with the front blade wakes. This phase shift between tip vortex and blade wake impingement is a result of the aft blades leading edge sweep. An analysis of the unsteady component of the aft blade loading for the azimuthal position of $\Psi = 90°$ in more detail is plotted in Fig. 6. While the baseline case shows the previously described change in sign of the unsteady loading between mid-span and the blade tip regions, the reduction of the front blade wakes through the application of TEB leads to the tip vortex impingement becoming almost the sole cause for the aft blade unsteady loading fluctuations, which thus also dominate the complete aft blade loading development as shown in Fig. 4. Therefore, while front rotor TEB seems to be quite successful in reducing the aft blade unsteady loadings due to blade wake impingement, this particular CROR configuration still suffers from a significant impact of the front blade's tip vortices on the aft rotor, which will be shown to also penalize the aeroacoustic benefit of this active flow control technology. In terms of overall performance, no notable difference is found between the two configurations. Front rotor thrust shows a small increase of 1.3 %, while aft rotor thrust decreases by 0.7 % for the blowing case in comparison with the baseline configuration, with a similar impact seen in the rotor power coefficients.

5 Aeroacoustic Analysis

Figure 7 shows noise directivities as computed by APSIM+ for a microphone array on the ground which is aligned with the rotor axis at a constant distance of $46m$. The OASPL of the baseline (black) and TEB (gray) configurations are depicted in Fig. 7a, with the inset displaying the A-weighted OASPLs. The OASPL shows a negligible decrease in OASPL for the TEB case around the front rotor plane ($x/D = 0$), with alternating regions of decrease and increase levels downstream (flow is from left to right). However, in the upstream direction, increased levels of up to 5 dB are seen. When considering the A-weighted OASPL [see inset of Fig. 7a], a small reduction of 1 dBA in maximum OASPL value is achieved for the TEB blowing case. In up- and downstream directions, qualitatively similar behavior to the unweighted OASPL is seen. The decomposition of the OASPL into its front rotor-alone tones and interaction tones is depicted in Fig. 7b. The front rotor tones, comprising the rotor fundamental tone and its' higher harmonics through $5 \cdot \mathrm{BPF_F}$, radiate mainly in the rotor plane, with a negligible decrease of the rotor alone tones when TEB is active (the black and gray solid lines almost completely overlap). This behavior illustrates that TEB is not an additional sound source (i.e. a rotating mass source) for the considered configurations. Aft rotor tones show qualitatively the same behavior as the front rotor tones (not shown). From the dashed lines it becomes clear that the interaction tones, including all interaction associated tones up to a frequency of $5 \cdot \mathrm{BPF_F}$, are responsible for the increased radiation in the upstream direction when TEB is active. A small decrease of these interaction tones (max. 4 dB) is observed around the rotor plane. It has been checked that the sound radiation in azimuthal direction is uniform (as expected for this 11×9-bladed isolated CROR at $\alpha = 0$), therefore the analysis presented here is confined to a ground-plane microphone array parallel to the engine axis.

When considering the spectrum at the upstream position $x/D = -0.77$ [see Fig. 8a], one clearly sees that the interaction tones are responsible for the increased OASPL in flight direction when TEB is active. More specificly, the first interaction tone (1,1) is the main cause for this. A possible explanation is that although the front rotor blade wakes are reduced, the tip vortices of the front rotor still impinge on the aft rotor, dominating the interaction noise. The spectrum in the front rotor plane at $x/D = 0$ is presented in Fig. 8b. Negligible TEB influence on the front and aft rotor-alone tones are observed, while the first (1,1) and third (2,1) interaction tones are reduced. Here it also becomes clear that the previously observed A-weighted OASPL decrease in the rotor plane mainly stems from the downweighting of the first two frequencies in favor of the first interaction tone [cf. Figs. 8b and inset of 7a].

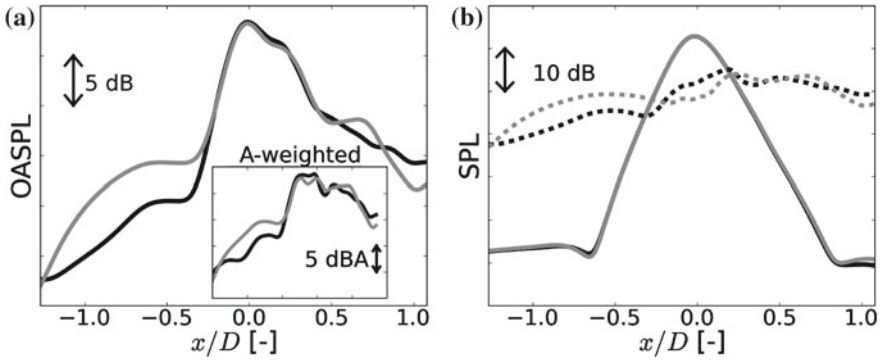

Fig. 7 **a** Overall sound pressure level (OASPL) in streamwise direction (x/D) for baseline (*black*) and blowing (*gray*) case, with inset displaying A-weighted OASPL. **b** Front rotor tones (*solid lines*) and interaction tones (*dashed lines*). Coloring as in left figure

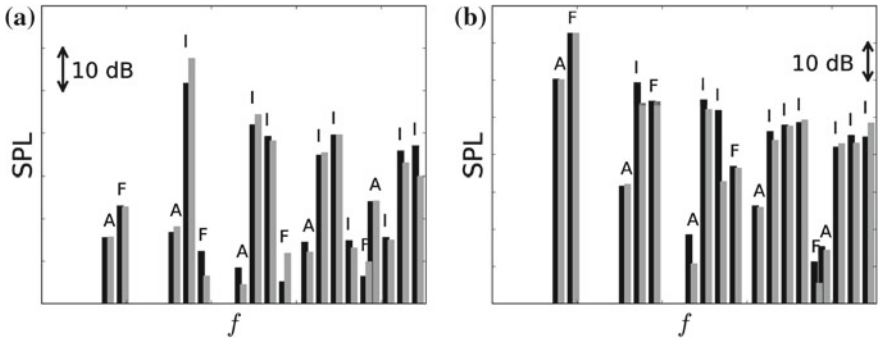

Fig. 8 Comparison between baseline (*black*) and blowing (*gray*) configuration spectra for **a** upstream direction $x/D = -0.77$ and **b** front rotor plane $x/D = 0$. '*F*', '*A*', and '*I*' indicate front rotor, aft rotor, and interaction tones, respectively. Line coloring as in Fig. 7

6 Conclusion and Outlook

In the frame of the 7th Framework EU Joint Technology Initiative Smart Fixed Wing Aircraft project, the principal aerodynamic and aeroacoustic benefit of employing blowing at the trailing edge of the front rotor of a CROR propulsion system was studied at low-speed take-off conditions. The challenging aspect of the application of this technology to this type of engine is the close coupling of the rotors, leading to a short mixing length for the achievement of full front blade wake alleviation. A successful reduction of the front rotor's blade wake deficit could be achieved, leading to a clear reduction in local aft blade unsteady loadings for much of the span. However, the specific CROR configuration under study here still has significant impingement of the front blades tip vortices on the aft rotor due to an insufficient reduction of the aft rotor diameter with respect to that of the front rotor. Thus, while many of

the interaction tones could be shown to be reduced notably by the reduction in front blade wake deficit, the first interaction tone in particular was seen to radiate much more strongly in the direction of flight. This is thought to be caused primarily by the dominance of the front rotor tip vortex induced unsteady loading of the aft blades. Future research would aim to avoid the interaction of the front rotor tip vortex with the aft blades to more clearly isolate the benefit of front blade wake reductions on interaction tone noise emissions. A study of optimizing the strength and extent of the blowing on the front rotor trailing edge to reduce the air massflow requirements of this active flow control technology is also a promising avenue of research.

Acknowledgments Airbus is greatly acknowledged for a fruitful collaboration in the JTI SFWA project and for permitting publication of this work.

References

1. http://www.cleansky.eu/content/page/sfwa-0
2. Akkermans, R.A.D. et al.: Handling of non-periodic contra rotating open rotor data. In: AIAA 2012–2262; 18th AIAA Aeroacoustics Conference. Colorado Springs, CO (2012)
3. Brentner, K., Farassat, F.: An analytical comparison of the acoustic analogy and Kirchoff formulation for moving surfaces. AIAA J. **36**(8), 1379–1386 (1998)
4. Williams, J.F., Hawkings, D.: Sound generation by turbulence and surfaces in arbitrary motion. Phil. Trans. R. Soc. Lond. **264**(1151), 321–342 (1969)
5. Fite, E., Woodward, R., Podboy, G.: Effect of trailing edge flow injection on fan noise and aerodynamic performance. In: AIAA-2006-2844, 3rd AIAA Flow Control Conference, San Francisco (2006)
6. Di Francescantonio, M., Giles, M.: A new boundary integral formulation for the prediction of sound radiation. J. Sound Vib. **202**(4), 491–509 (1997)
7. Jameson, A.: Time dependent calculations using multigrid, with applications to unsteady flows past airfoils and wings. In: 10th AIAA Computational Fluid Dynamics Conference, Honolulu, (1991)
8. Kroll, N., Fassbender, J.K.: MEGAFLOW—numerical flow simulation for aircraft design. Notes Numer. Fluid Dyn. Multi Design **89**, 81–92 (2005)
9. Madrane, A., Raichle, A., Stuermer, A.: Parallel implementation of a dynamic unstructured chimera method in the DLR finite volume TAU-code. In: 12th Annual Conference of the CFD Society of Canada; Ottawa, Ontario, Canada, 524–534 (2004)
10. Spalart, P.R., Allmaras, S.R.:A one-equation turbulence model for aerodynamic flows. In: AIAA paper 1992–0439 (1992)
11. Stuermer, A., Yin, J.: Aerodynamic and aeroacoustic analysis of contra-rotating open rotor propulsion systems at low-speed flight conditions. New results in numerical and experimental fluid mechanics VII. Notes Numer. Fluid Mech. Multi. Design **112** (2010)
12. Stuermer, A., Yin, J.: The case for counter-rotation of installed contra-rotating open rotor propulsion systems. In: AIAA2012-2785; 30th AIAA Applied Aerodynamics Conference. New Orleans (2012)
13. Woodward, R.P. et al.: Noise benefits of rotor trailing edge blowing for a model turbo-fan. In: AIAA 2007–1241; 45th Aerospace Sciences Meeting and Exhibit. Reno, (2007)
14. Yin, J., Stuermer, A., Aversano, M.: Coupled uRANS and FW-H analysis of installed pusher propeller aircraft configurations. In: AIAA 2009–3332; 15th AIAA/CEAS Aeroacoustics Conference. Miami (2009)

Examination of the Influence of Flow Speed on the Coherence Lengths in Turbulent Boundary Layers at High Subsonic Mach Numbers

Stefan Haxter, Klaus Ehrenfried and Stefan Kröber

Abstract Wind tunnel measurements of wall pressure fluctuation were conducted at high subsonic Mach number. The data was analyzed in order to calculate the spatial decay of coherence of turbulent structures in the turbulent boundary layer as a function of the Strouhal number. The decay parameter determined from the measurements was compared with the predictions from the coherence length model of Efimtsov. The Mach number was varied in order to investigate the influence of a change in flow speed on the decay parameter for various Strouhal numbers.

1 Introduction

In the past, several models for the prediction of the spatial decay of coherence in the turbulent boundary layer have been set up to describe empirically the excitation of a surface—like an aircraft fuselage—by the flow [1, 2]. These models can be used to predict the excitation and noise radiation into the cabin from fuselage panels [3]. A model for the input is, for instance, the Efimtsov model [2]. It describes the loss of coherence over distance as exponential functions in flow and cross-flow direction. The decay factors are also predicted by the model. By transforming the model into the wavenumber domain, it can be used for the prediction of modal excitation of plate-structures. The Efimtsov model was derived from sub- and supersonic flight test data. It is therefore considered to be applicable for the prediction of aircraft hull excitation. Although considered applicable, the Efimtsov model documentation gives no information about the flight conditions at which the measurements were taken, nor about the positioning of transducers on the aircraft. Therefore, the influence of each of these parameters on the decay of coherence in the turbulent boundary layer,

S. Haxter (✉) · K. Ehrenfried · S. Kröber
German Aerospace Center (DLR), Bunsenstr, 10, 37073 Göttingen, Germany
e-mail: stefan.haxter@dlr.de

A. Dillmann et al. (eds.), *New Results in Numerical and Experimental Fluid Mechanics IX*,
Notes on Numerical Fluid Mechanics and Multidisciplinary Design 124,
DOI: 10.1007/978-3-319-03158-3_63,

Table 1 Overview of the measurement conditions

Case	Mach number	u_∞ [m/s]	Reynolds number Re_x	Boundary layer thickness δ [mm]
1	0.5	166	$1.07 \cdot 10^7$	≈ 25
2	0.65	215	$1.39 \cdot 10^7$	≈ 25
3	0.8	265	$1.71 \cdot 10^7$	≈ 25

shall be investigated separately, starting with the variation of Mach number in this paper. Data from high subsonic wind tunnel measurements are used for investigation.

2 Measurement Setup

Data was acquired in the Transonic Wind tunnel Göttingen (TWG) at high subsonic Mach numbers with a total pressure of $p_0 = 50\,\text{kPa}$. The setup consisted of a long rigid plate with a run length of approximately 2 m in front of a pressure transducer array at the end of the plate. The wind tunnel was equipped with flexible walls that could be adjusted to adapt the pressure gradient in the test section . The pressure transducer array consisted of 48 Kulite sensors that were pinhole mounted over an area of $0.6 \times 0.6\,\text{m}$. A quasi-randomized transducer distribution was chosen and resulted in an optimized pattern with maximal spacing number. The effect of a pinhole mounting had already been considered in reference [4] where the measurement was described in detail. Up to a frequency of $f = 10\,\text{kHz}$, there was no difference in the auto spectra of a pinhole-mounted sensor compared with a flush-mounted sensor. Data was acquired at a sampling frequency of $f_s = 120\,\text{kHz}$. Three flow speeds, as shown in Table 1, were chosen for the evaluation. The pressure gradient in the measurements was approximately zero for the two lower speeds. At the highest speed, the adaptive wall was not able to compensate for the flow acceleration in the test section, leading ot a difference in the pressure coefficient at the beginning to the end of the measurement area of $\Delta c_p \approx 0.035$. Table 1 shows also the Reynolds number, which is dependent on flow speed and run length. The boundary layer had a thickness of approximately 25 mm. The local friction coefficient was estimated by [5]

$$c_f = 0.0576 \cdot Re_x^{-0.2}. \tag{1}$$

This estimation was applied here even though the Reynolds numbers lay slightly outside the range used in deriving Eq. 1.

3 Data Processing

The time-domain data from each sensor pair was transformed into the frequency domain by using a Fast Fourier transform routine with 2^{14} sample points. The resulting spectra had a frequency resolution of 7.3 Hz and were combined and then

averaged to provide the mean cross spectrum of the pairing. In order to obtain the cross correlation coefficient of the sensor pairs, the absolute values of the cross spectra were normalized with the auto spectra of the involved transducer signals (Eq. 2).

$$\Gamma_{nm}(f) = \frac{|R_{nm}(f)|}{\sqrt{R_{nn}(f) \cdot R_{mm}(f)}} \tag{2}$$

Here, Γ is the cross-correlation coefficient, n and m are transducer indices, and R is the cross spectral density at the frequency f. A double index nn or mm indicates the auto power spectral density at transducer n, or m respectively. The cross correlation coefficient is the degree of linear dependence of two transducer signals, shown here in the frequency domain.

Each transducer pairing has a unique spacing between the transducer positions. The spacings are defined as follows:

$$\xi_{nm} = x_n - x_m \tag{3}$$

$$\eta_{nm} = y_n - y_m \tag{4}$$

where x is the transducer position in flow direction (designated "longitudinal"), and y the position in cross-flow direction ("lateral"). It is obvious that a combination of a transducer with itself (i.e. nn or mm) results in a spacing of zero for all the auto spectra and therefore a cross-correlation coefficient value of 1 at zero spacing.

The resulting cross correlation coefficient is shown for a single frequency of $f = 1{,}001$ Hz over the spacing domain in Fig. 1. An exponential fit can be applied to the experimental data points in order to determine the spatial decay of the coherence in the flow. This had already been done separately by Palumbo for the decay in the in-flow (ξ) and cross-flow directions (η) using flight test data [6]. As suggested by Corcos [1], an exponential trial function was used for the fit (Eq. 5). The exponential fit yields a decay coefficient which can be used to describe the decay of coherence. With the array used in this investigation, two-dimensional cross-correlation data are available. In this way, the direction at which the coherent structures are convected the furthest can be determined and taken as the predominant flow direction. For this, a singular value decomposition using all transducer spacings with a cross-correlation coefficient value above a threshold of $\exp(-1)$ was applied. For frequencies above 2,500 Hz, this threshold was lowered to $\exp(-2)$ to avoid an error resulting from the limited spatial array resolution. The two-dimensional distribution of cross-correlation data can be used together with the flow direction to apply a two-dimensional fit to the cross-correlation data points (Eq. 6).

$$\Gamma(f) = \exp\left(-\frac{\xi}{l_x(f)}\right) \tag{5}$$

$$\Gamma(f) = \exp\left(-\frac{\xi}{l_x(f)}\right) \cdot \exp\left(-\frac{\eta}{l_y(f)}\right) \tag{6}$$

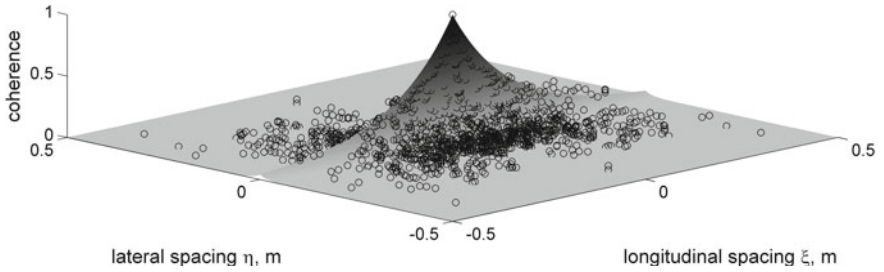

Fig. 1 Measured cross-correlation coefficient with two-dimensional fit

A fit error (or residuum) results from subtracting the fitted curve from the data points at the data point locations. For evaluation of the goodness of the fit in only the longitudinal direction, the error on the whole two-dimensional spacing area was weighted with the fitted cross-correlation coefficient in cross-flow direction. This way, the error from spacings lying very close to the line of the in-flow direction were weighted more than spacings lying far away from it.

The fits can be applied to the cross-correlation coefficient at all frequencies provided by the Fourier Transform, resulting in a longitudinal coherence length for each frequency. These resulting experimental data points can be approximated by Efimtsov's model function (Eq. 7) versus the Strouhal number formed with the flow velocity u_∞ and the boundary layer thickness.

$$l_x\left(S_{u_\infty}\right) = \delta \cdot \left[\left(\frac{S_{u_\infty} \cdot a_1}{0.82} \right)^2 + \frac{a_2^2}{\left(\frac{S_{u_\infty} \cdot Re^{0.1}}{0.1924} \right)^2 + (a_2/a_3)^2} \right]^{-\frac{1}{2}} \tag{7}$$

The convective velocity, u_c is taken as constant over frequency with a value of $u_c = 0.82 u_\infty$ [4]. The variables a_1, a_2, and a_3 are the parameters determining the decay of the coherence and the limitation of the boundary layer thickness. Efimtsov found values of $a_1 = 0.1; a_2 = 72.8; a_3 = 1.54$ for these parameters. For a frequency of $f = 0$ Hz Eq. 7 returns a coherence length value which is shorter than the boundary layer thickness. This might seem odd at a first view, since one would think that a coherence length of at least the boundary layer thickness would be present. However, according to the Efimtsov-model at low frequencies, the limitation due to boundary layer thickness seems to supress the appearance of coherent structrures that would produce a coherent signal over a reasonable distance.

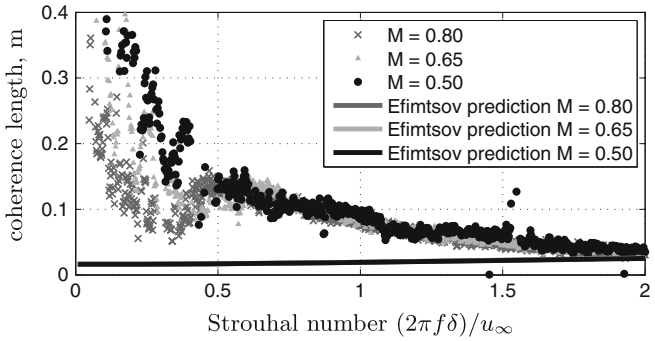

Fig. 2 Coherence lengths from one-dimensional fit

4 Results

First, the one-dimensional fit was applied to the cross-correlation-coefficient data for the three flow speeds. Secondly, the two-dimensional fit was applied to the same data for comparison and proof of applicability of this method. Thirdly, the fit error used to investigate the decay characteristic at low Strouhal numbers was determined. The coherence length is plotted versus the Strouhal number using the free-stream flow speed as the characteristic velocity, S_{u_∞}. This resulted in the best collapse of the curves at high strouhal number.

4.1 One-Dimensional Fit

Coherence lengths determined with the one-dimensional fit are shown in Fig. 2 for the three flow speeds.

Looking at the figure, the course of the coherence length can be divided into three regions from high to low Strouhal number: the high-Strouhal number decay, the kink that describes the limitation of coherence length due to boundary layer thickness, and the disperse region below the kink. For the decay at high-Strouhal numbers, a reasonable match exists between the curves at different speeds. The curve for $M = 0.5$ is bumpy and shows a disturbance at $S \approx 1.5$ which can be attributed to a tonal noise present in the wind tunnel at that speed. At the position of the kink, it is difficult to distinguish between the single measurements since the data points from evaluation start to disperse a little. A maximum coherence length of 0.15 m is extracted from the data for all three speeds. The kink position seems to first increase with speed from $M = 0.5$ to $M = 0.65$ and then decrease again considerably from $M = 0.65$ to $M = 0.8$. In the disperse region below the kink, the determined coherence length rises considerably with lower Strouhal number and disperses further. Nevertheless, the three speeds are clearly distinguishable in this

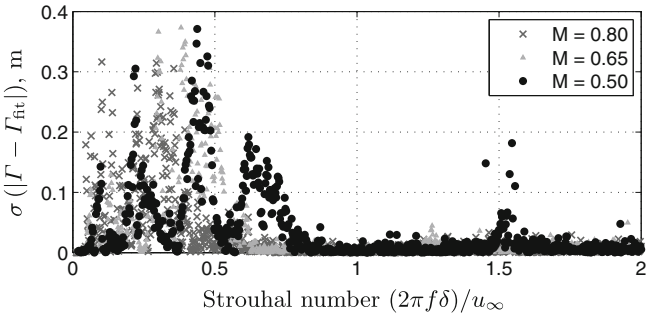

Fig. 3 Error from the one-dimensional fitting in x-direction

area. The highest coherence length at low Strouhal number is obtained for $M = 0.5$. In this region, the coherence length drops with speed.

A look at the fit error in Fig. 3 shows that the deviations are largest at low-Strouhal numbers. For the highest speed, this deviation occurs at a Strouhal number below the kink position and shows that the one-dimensional exponential fit does not correctly describe the decay of coherence in this region. The same applies for the fit deviation for $M = 0.65$. Since the kink position is located at a higher Strouhal number, this region of high error extends up to this higher Strouhal number, but does not extend beyond the kink position. At the lowest speed measured, the region with an increased fit deviation extends well into the area of the kink position. This is either a hint for a change in the characteristics of the coherent structures in the boundary layer, or that the one-dimensional fit does not resolve the decay properly. Again, the disturbance at $S_{u_\infty} \approx 1.5$ is visible.

4.2 Two-Dimensional Fit

The coherence lengths determined by using the two-dimensional fit are depicted in Fig. 4. Using this 2D-fit function for evaluation results in a smooth course of coherence length versus the Strouhal number. The curves coincide very well at $S > 0.75$, which can be attributed to the consideration of flow direction in the 2D treatment, which leads to the small deviations (as shown by Haxter and Spehr [7]). The tonal disturbance present in the wind tunnel is again visible at $S \approx 1.5$. The evaluation shows that the kink caused by the coherent structure size limitation due to boundary layer thickness changes its position and height with different speeds. This applies to all the speeds considered: The two lower speeds at which there was no pressure gradient present in the measurement area, and for the highest speed, at which the pressure gradient in the measurement area was non-zero. The higher the speed, the lower the Strouhal number at which the maximum of the kink is reached. The maximum value reaches 0.16 m at the highest speed and drops to 0.14 m at the lowest

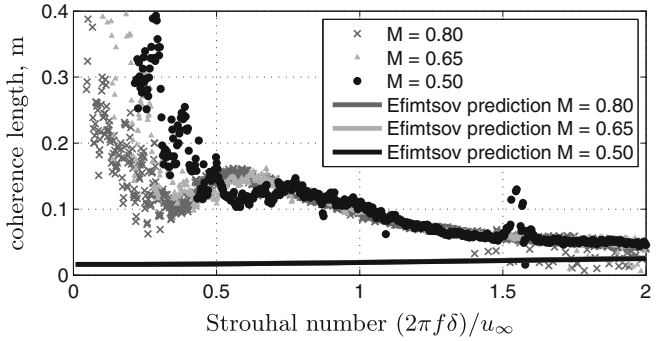

Fig. 4 Coherence lengths from two-dimensional fit

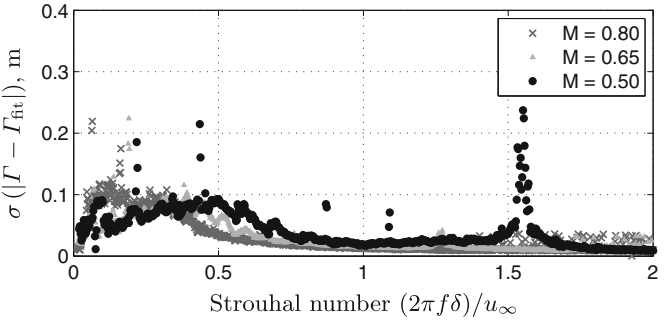

Fig. 5 Error from the two-dimensional fitting; separated x-direction

speed. At Strouhal numbers below the kink position, the coherence length rises again, but appears very disperse. The Strouhal number below which the coherence length starts to disperse is dependent on the kink position and therefore dependent on the speed. The coherence lengths at different speeds are still clearly distinguishable in this low-Strouhal number region.

The coherence lengths predicted by the Efimtsov model for this experiment are also shown in Fig. 4. The predicted values are well below the measured points for the coherence length, which can be accounted for by the limitation of coherent structure size by the boundary layer thickness, which is too pronounced in the model for this case. The different flow cased do not show a considerable difference in model behavior. The governing parameter showing a difference between the measurements is the Reynolds Number, which is taken to the power of 0.1. This leaves very little difference in the prediction. The predicted curves therefore seem to coincide.

The fit error of the two-dimensional evaluation is depicted in Fig. 5. Again, there is an increase in the error level visible in the low-Strouhal number region, the exact position of the region being dependent on the flow speed. For each speed, the increase of error level occurs just below the Strouhal number, at which the maximum of the kink is positioned. This includes the lowest speed $u_\infty = 166\,\mathrm{ms}^{-}1$, for which the

one-dimensional fit resulted in an increased error level well above the kink position. Again, one can conclude that the decay of coherence of structures in the turbulent boundary layer is disturbed in the region where the size of such structures is limited due to the boundary layer thickness.

5 Conclusion

Wind tunnel measurements at different high-subsonic Mach numbers were evaluated in order to investigate the influence of speed on the decay of coherence of turbulent structures in a turbulent boundary layer. For this, one-dimensional and two-dimensional fits were applied to the cross-correlation coefficients of transducer pairings at different transducer spacings. The two-dimensional fit took the flow direction into account, which resulted in a better determination of the coherence length. The position of the maximum of the kink in the plot of the coherence length versus Strouhal number was found to change its position towards a lower Strouhal number with increasing flow speed. Also, a higher maximum level for the kink value was found with increasing speed. This was not predicted by the Efimtsov model which was shown to describe quite poorly the decay of coherence in the present wind tunnel experiment. The reason for this is thought to be the small value for the boundary layer thickness, which is a limiting factor for the coherence length in the model. Another coherence decay model derived from low Mach number measurements (Corcos) shows a similar behavior at high frequencies. However, the boundary layer limitation had not been considered in this model, so no comparison can be made at this point. From the increased error level of the fit at low Strouhal number just below the kink position, it is concluded that the decay of coherence of turbulent structures—if present at this Strouhal number—deviates from single exponential behavior. The two-dimensional fit was shown to be a good method to extract coherence lengths and take the flow direction into account. As a next step, the evaluation can be applied to other measurement conditions and flight test data to further examine the characteristics of coherence decay in turbulent boundary layers.

References

1. Corcos, G.M.: Resolution of pressure in turbulence. J. Acoust. Soc. Am. **35**(2), 192–199 (1963)
2. Efimtsov, M.: Characteristics of the field of turbulent pressures at the wall of a boundary layer. Sov. Phys. Acoust. **28**(4), 289–292 (1982)
3. Graham, W.: A comparison of models for the wavenumber-frequency spectrum of turbulent boundary layer pressures. J. Sound Vib. **206**(4), 541–565 (1997)
4. Ehrenfried, K., Koop, L.: Experimental study of pressure fluctuation beneath a compressible turbulent boundary layer. In: Proceedings of the 14th AIAA/CEAS Aeroacoustics Conference, Vancouver, British Columbia, Canada, AIAA, May 2008
5. Thirumaleshwar, M.: Fundamentals of Heat and Mass Transfer, second impression edn. Dorling Kindersley, New York (2009)

6. Palumbo, D.: Determining correlation and coherence lengths in turbulent boundary layer flight data. J. Sound Vib. **331**(16), 3721–3737 (2012)
7. Haxter, S., Spehr, C.: Two-Dimensional evaluation of turbulent boundary layer pressure fluctuations at cruise flight condition. In: Proceedings of the 18th AIAA/CEAS Aeroacoustics Conference, Colorado Springs, Colorado, AIAA, June 2012

Sound Generation by Low Mach Number Flow Through Pipes with Diaphragm Orifices

Frank Obermeier, Mikhail Konstantinov, Andrei Shishkin and Claus Wagner

Abstract Aerodynamic noise generated by low Mach number flow through a pipe with two differently sized diaphragm orifices is investigated both theoretically as well as numerically. Such a flow may be considered as a simple model of an aircraft climate control system. The theory is based on an acoustic analogy introduced by Möhring and Obermeier in the seventies. They identified by means of the so-called Green's vector function acoustic sources in unsteady flows as the unsteady motion of vorticity "*vortices are the voice of flows*". In addition, the unsteady flow through the pipe, the aerodynamic sources, and the spectra of sound are evaluated numerically. Here effects of different numerical algorithms (PISO—PIMPLE) and of different numerical boundary conditions at the outlet of the pipe (advective, convective—wave transmissive) are identified and discussed.

1 Introduction

Aerodynamic sound generation in the interior of pipes with complex obstacles like the interior of jet engines or pipes of aircraft climate control systems is still an only partly solved problem. Therefore, to improve the understanding of the mechanisms of sound generation in the interior of pipes and to test possibilities of its numerical simulation it seems to be helpful to study more elementary problems first. The present investigation has been motivated by former work of two of the authors, Konstantinov and Wagner [1].

F. Obermeier (✉)
Institut für Mechanik und Fluiddynamik, TU Bergakademie Freiberg, Freiberg, Germany
e-mail: frank.obermeier@imfd.tu-freiberg.de

M. Konstantinov · A. Shishkin · C. Wagner
Institut für Aerodynamik und Strömungstechnik, Göttingen, Germany

A. Dillmann et al. (eds.), *New Results in Numerical and Experimental Fluid Mechanics IX*,
Notes on Numerical Fluid Mechanics and Multidisciplinary Design 124,
DOI: 10.1007/978-3-319-03158-3_64,

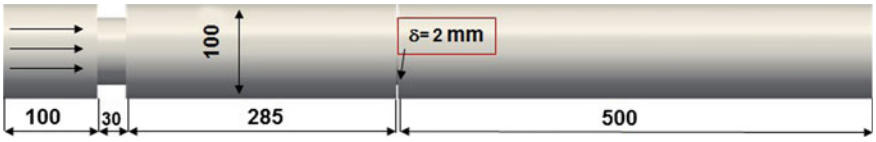

Fig. 1 Geometry of the pipe with diaphragm orifices, the inlet velocity is $10\,\mathrm{ms}^{-1}$

The purpose of the present work is twofold. First, we want to present a theoretical formulation of the mechanisms of sound generation by low Mach number flow through an axisymmetric pipe with differently sized diaphragm orifices, Fig. 1. The diaphragms cause flow separation which implies sound generation.

Second, we want to determine the time dependent pipe flow numerically in order to use the results to identify the locations of sound sources in the interior of the pipe. In addition, the sound signals and their corresponding spectra are presented.

2 Theory

The total flow within the pipe can be separated into an inner domain, where vorticity dominates and which is described approximately by an incompressible approach, and into an outer domain, where the sound dominates and which is described approximately by a homogeneous wave equation, provided the flow Mach number is small and typical flow lengths are small compared with the wave lengths of the generated sound, Obermeier [2]. In addition, it is assumed that there is no feed-back between the generated sound and the flow separation at the diaphragms. Based on the acoustical analogy suggested by Powell [3] in 1964 one gets for the inner domain

$$\Delta\left(\frac{p}{\rho_0}+\frac{|\underline{u}|^2}{2}\right)=\nabla\cdot\left(\underline{u}\times(\nabla\times\underline{u})\right)+O(M^2)\quad\text{and}\quad\nabla\cdot\underline{u}=O(M^2)\tag{1}$$

and for the outer domain

$$\left(\frac{\partial}{\partial t}+U_0\frac{\partial}{\partial x_1}\right)^2 p-a_0^2\frac{\partial^2 p}{\partial x_1^2}=O(M^2)\tag{2}$$

with p pressure, ρ density, T temperature, $\underline{u}$ velocity, $M=\frac{U_0}{a_0}$ a typical Mach number, and a_0 speed of sound.

Now, these two equations have to be solved. Free integration constants and free functions obtained for each of the two flow domains must be determined by a matching procedure. Without going into the algebraic details, which can be found elsewhere

(e.g. Obermeier [4]), we want to emphasize that one only needs to evaluate the far field approximation of the inner solution of the pipe flow to get the outer sound field.

When a feed-back between the sound field and the vortical flow does exist the calculations of the inner flow have to account additionally for compressibility effects. Nevertheless, the matching procedure will not be affected.

Inner flow field. Equation (1) can formally be integrated by means of a Green's function G. When this function is especially tailored to the geometry of the pipe, i. e. the Green's function fulfills the boundary condition $\left(\frac{\partial G}{\partial n}\right)_{wall} = 0$, one obtains only a volume integral

$$\frac{p}{\rho_0} + \frac{|\underline{u}|^2}{2} = -\int \nabla_y G\left(\underline{x}, \underline{y}\right) \cdot \left(\underline{u} \times (\nabla \times \underline{u})\right) dV. \tag{3}$$

An explicit solution for this special Green's function in the case of a wave function has been given by Howe [4], the corresponding solution for the Laplace equation is

$$\lim_{x_1 \to \infty} G\left(\underline{x}, \underline{y}\right) = \frac{1}{2\pi R_0^2} \phi\left(\underline{y}\right) \tag{4}$$

which does not depend on the observation point $\underline{x}$. ϕ describes the potential of a fictitious, non-viscous flow through the pipe. In cylindrical coordinates this potential depends only on the radial coordinate $r = \sqrt{y_2^2 + y_3^2}$ and the longitudinal coordinate y_1, but not on the azimuthal coordinate φ.

In a next step the ordinary Green's function G is replaced by a so-called Green's vector function $\underline{G}$ (Möhring [5], Obermeier [2, 6]) to be determined by the condition

$$\nabla \times \underline{G} = \nabla G. \tag{5}$$

For observation points outside the source region this condition is fulfilled by

$$\underline{G} = \left\{G_{y_1}, G_r, G_\varphi\right\} = \frac{1}{2\pi R_0^2} \left\{0, 0, -\frac{1}{r}\psi(y_1, r)\right\}, \tag{6}$$

where ψ is the axisymmetric stream function corresponding to the potential ϕ. Introducing this result into Eq. (3) and accounting for the Helmholtz equation

$$\frac{\partial}{\partial t} \nabla \times \underline{u} = \nabla \times \left(\underline{u} \times \left(\nabla \times \underline{u}\right)\right)$$

one finally obtains by partial integration

$$\lim_{x_1 \to \infty} \left(\frac{p}{\rho_0} + \frac{|\underline{u}|^2}{2}\right) = \frac{1}{2\pi R_0^2} \int \frac{\partial}{\partial t} \left(\nabla \times \underline{u}\right)_\varphi \psi\left(y_1, r\right) dy_1\, dr\, d\varphi. \tag{7}$$

As the stream function ψ does not depend on the azimuthal angle φ, the φ-integration can formally be performed, which yields

$$\lim_{x_1\to\infty}\left(\frac{p}{\rho_0}+\frac{|\underline{u}|^2}{2}\right)=\frac{1}{R_0^2}\int\frac{\partial}{\partial t}\overline{(\nabla\times\underline{u})}_{\varphi}\,\psi\,(y_1,r)\,dy_1\,dr. \tag{8}$$

This result implies that the far field of the total pressure in the inner flow region is fixed by the time dependent part of the azimuthal component of the vorticity averaged over φ, weighted with the stream function ψ over the radius r, and integrated along the y_1-axis when $\overline{(\nabla\times\underline{u})}_{\varphi}\neq 0$. As it is shown later on, this vorticity is produced predominately by the separation of vortex sheets and their subsequent disintegration into eddies behind the diaphragm orifices.

Outer flow field. Without going into any details the actual sound field up- and downstream in the pipe is obtained from the total pressure, Eq. (8), which depends on the time only, by replacing the ordinary time t by the retarded time $t'=t-(1-M)\,\frac{x_1}{a_0}$. It means that plane sound waves propagate up- ($x_1<0$) and downstream ($x_1>0$) the pipe.

3 Numerical Flow Simulations

The numerical simulation of aerodynamic sound generation usually faces two main problems: (i) Flow quantities are much larger than sound quantities generated by the flow. This difficulty is avoided by our approach. Here, the flow quantities, like velocity and vorticity, are evaluated first, then the sound field is determined by means of the method of matched asymptotic expansions in a second step. (ii) By using Computational Fluid Dynamics (CFD), e.g. by DES or LES, the flow field can be evaluated approximately only for realistic Reynolds numbers. Therefore, numerical errors could be larger than the sound quantities of interest. But again, due to our approach we hope to get round the problem. Nevertheless, the flow velocities $\underline{u}(y_1, r, \varphi; t)$ obtained numerically are slightly inaccurate. Therefore, the actual source term $\frac{\partial}{\partial t}\nabla\times\underline{u}$ could be even more inaccurate due to its twofold numerical differentiation with respect to time and space. This expectation has been confirmed when simulations were performed with two different algorithms to realize velocity-pressure coupling (PISO and PIMPLE). The sound fields and the corresponding spectra differ at least quantitatively even though the velocity fields seem to agree quite well.

In the following, the stream function ψ is determined for the given pipe geometry first. In a next step the velocity field is predicted with the code "OpenFOAM" in Cartesian coordinates. From these data the azimuthal component of the unsteady vorticity distribution and its time derivative are determined in cylindrical coordinates. Finally, these results are introduced into the integral, Eq. (7), which yields the time dependence of the total pressure and, hence, the corresponding spectra.

3.1 Incompressible Approach for the Inner Flow Domain

In a first attempt the total pressure, Eq. (7), has been evaluated by an incompressible approach in accordance with the method of matched asymptotic expansions. For the numerical simulations with the code OpenFOAM, a velocity of $U_0 = 10\,\mathrm{ms}^{-1}$ and an intensity of turbulence of 0.01 is assumed; the number of grid cells was of the order of 6 millions. The numerical simulations confirm that the two main source regions of aero-dynamic sound generation are located slightly downstream of the two diaphragms. Here the vorticity sheets separate from the diaphragms, disintegrate randomly into vortex rings, and finally decay into eddies. The signal, Eq. (7), to be matched to the sound field shows a continuous spectrum without a tonality. Contrary, results obtained in computations by Konstantinov and Wagner [1] with the commercial code STAR-CCM+, which includes the Ffowcs Williams-Hawkings-equation, show spectra with peaks. This outcome strongly indicates that compressibility and, hence, the feed-back mechanisms between the disintegration of vortex sheets and the generated sound field are not completely negligible.

3.2 Compressible Approach for the Inner Flow Domain

Sound waves generated downstream to the diaphragms and travelling upstream and downstream in the pipe are partly reflected at the exit and/or at the other diaphragm. Hence, for *right* frequencies these waves may turn into standing waves which on their parts could trigger the disintegration of the vortex sheets into vortex rings and into eddies. These mechanisms should be responsible for a tonality of the spectra. In the following numerical simulations were performed by the PISO and the PIMPLE algorithm, respectively, and in doing so both were combined either with advective or with admissive pressure conditions at the outlet of the pipe.

PISO with wave transmissive vis-à-vis-a advective pressure conditions at the outlet. In a first step results obtained by the PISO algorithm with the two different pressure conditions at the outlet of the pipe are compared. The advective condition implies that the pressure fluctuations at the exit are convected with the local velocity, while the wave transmissive condition implies that the pressure fluctuations propagate with the speed of sound out of the pipe. Obviously, both conditions do not really describe the physics correctly. The results obtained for the velocity fields (not be shown here) and the results for the azimuthal components of the vorticity averaged over the angle φ, Fig. 2, look in both cases similar. Here and in the following the amplitudes are normalized.

Contrary, the corresponding spectra are different, Fig. 3. They both show peaks but at different frequencies. In the case of the transmissive condition the main peak at 550 Hz agrees with the one obtained in [1]. It correlates well with a standing wave between the two diaphragms. In the case of the advective condition the main peak

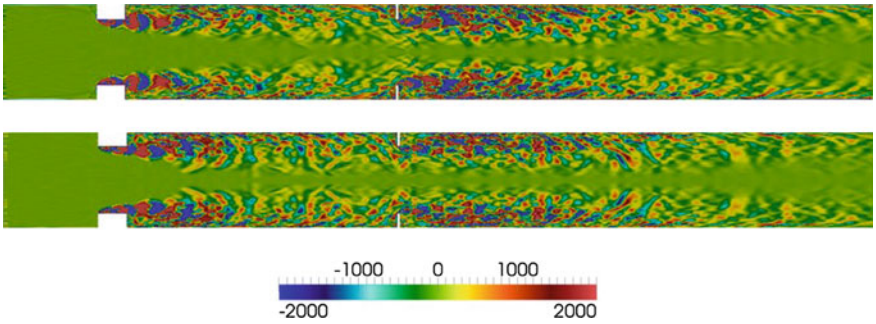

Fig. 2 $\frac{\partial}{\partial t}\overline{(\nabla \times \underline{u})}_{\varphi}$-distribution obtained by the PISO algorithm for wave transmissive (*above*) and advective (*below*) outlet conditions

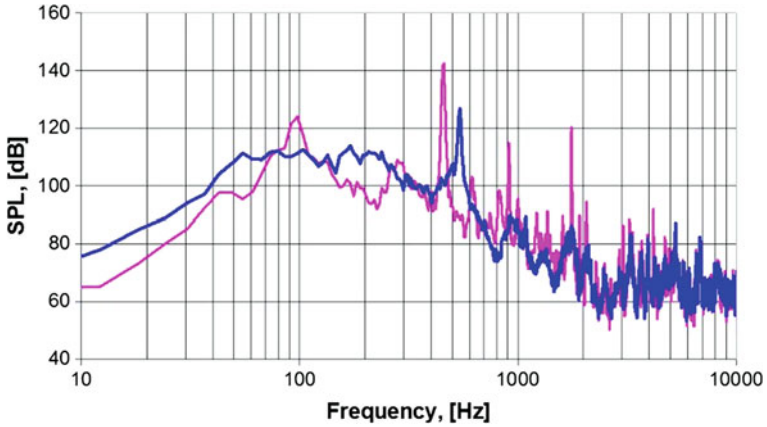

Fig. 3 Spectra obtained by the PISO algorithm for wave transmissive (*blue*) and for advective (*pink*) outlet conditions

occurs at 450 Hz, a correlation with any of the characteristic lengths within the pipe is not discernible.

PISO vis-à-vis PIMPLE with the wave transmissive condition at the outlet. Also in these simulations the velocity fields (not be shown here) look very much the same. However, there are very obvious differences between the azimuthal components of the averaged vortices. In the case of the PIMPLE algorithm the characteristic length scales of the turbulence are much smaller than the ones obtained with the PISO algorithm, Fig. 4. Furthermore, very weak disturbances are visible slightly upstream of the first diaphragm, a convincing explanation does not seem to be known, probably the differences are the result of intrinsic characteristics of the PIMPLE algorithm. Surprisingly, the corresponding spectra agree very well, Fig. 5.

Pipe with an added enlargement. Currently nobody really knows the "correct" formulation of the boundary conditions at the outlet. Therefore, to identify ambigui-

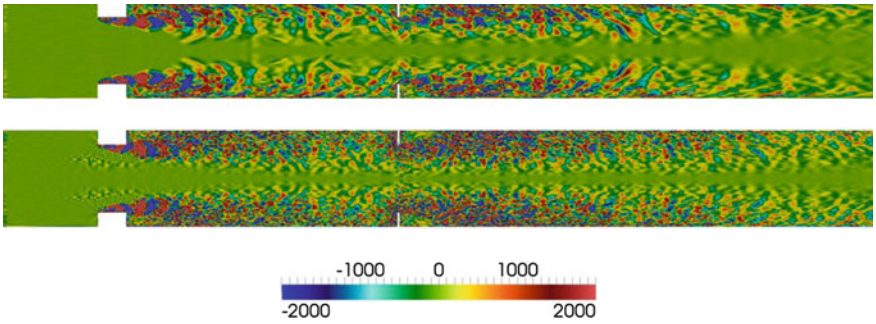

Fig. 4 $\frac{\partial}{\partial t}\overline{(\nabla \times \underline{u})}_{\varphi}$-distribution obtained by the PISO algorithm (*above*) and the PIMPLE algorithm (*below*) for wave transmissive outlet conditions

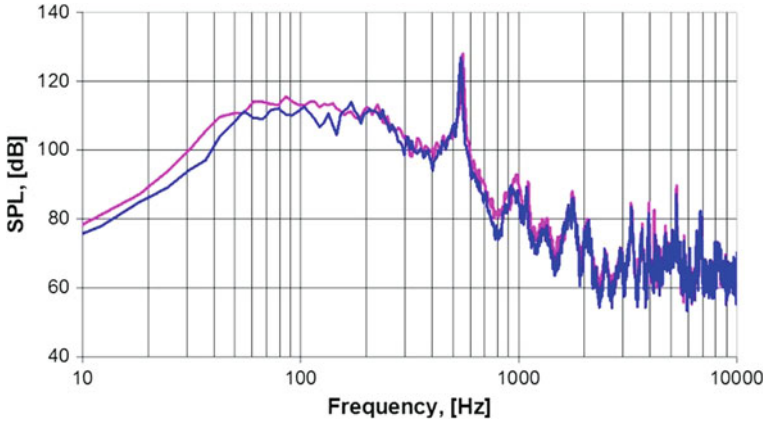

Fig. 5 Spectra resulting in the PISO algorithm (*blue*) and the PIMPLE algorithm (*pink*)

ties in numerical simulations due to alternative boundary conditions at the outlet of a flow region, it is common praxis to extend the initial flow region. In the present flow an enlarged section with a diameter of 300 mm and a length of 500 mm is mounted to the original pipe, Fig. 6. Boundary conditions imposed at the outlet of the enlarged pipe section are supposed to have only a minor influence on the flow details inside the initial pipe. Simulations were performed for wave transmissive, convective, and constant pressure conditions at the outlet.

Two spectra of the total pressure are shown in Fig. 7, where the additional sound generation behind the unsteady transition between the initial pipe and the enlarged section has not been accounted for. Important to realize, the main peak at 440 Hz, which has also been found in the case of the wave transmissive condition, agrees well with the tonality obtained for the initial pipe in the case the advective pressure condition at the outlet of the pipe. Unfortunately, there are also differences between the spectra shown here and those obtained for other outlet conditions. For instance,

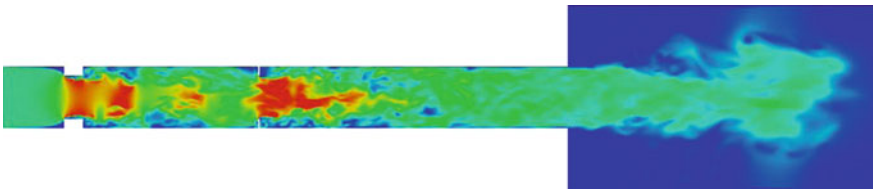

Fig. 6 Velocity amplitude in the cross section of a pipe with a mounted enlargement

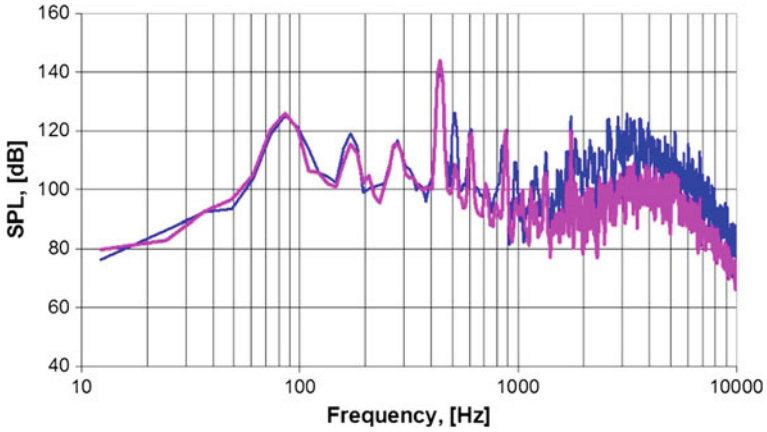

Fig. 7 Spectra for convective (*blue*) and constant (*pink*) pressure conditions

the second peak at 180 Hz, Fig. 7, does not occur in the case of the wave transmissive condition at the outlet of the enlarged section.

Finally, we were only partly successful to assign the acoustic wave lengths, which correspond to the frequencies of the peaks of the spectra obtained for the different numerical simulations, to characteristic length scales of the pipe.

4 Conclusions

The work presented demonstrates clearly that sources of sound generation are located slightly behind the diaphragm orifices; the generated sound is completely determined by the azimuthal component of the unsteady vorticity distribution of the flow.

Numerical simulations indicate that feedback mechanisms between the vortex separation and the generated sound waves are not negligible and that compressibility effects in the source region have to be accounted for. The problem why different numerical approaches and different boundary conditions at the outlet of the pipe result into partly different data for the vorticity and for the spectra of the total pressure remains largely unresolved. The time dependent data for the total pressure determine

the sound field radiated from the outlet (and from the inlet) of the pipe, details have not been discussed in the chapter. Experimental data by other authors, e.g. Spehr et al. [7], are not really applicable to open questions pointed out in the present chapter.

References

1. Konstantinov, M., Wagner, C.: Numerische Simulation der Strömung und Schallausbreitung in einem Rohr mit zwei Blenden. 15. STAB-Workshop, DLR Göttingen (2011)
2. Obermeier, F.: On a new representation of aeroacoustic source distribution. I: General theory. Acustica **42**, 56–61 (1979)
3. Powell, A.: Theory of vortex sound. J. Acoust. Soc. Am. **36**, 177–195 (1964)
4. Howe, M.S.: Contributions to the theory of aerodynamic sound, with application to excess jet noise and the theory of a flute. J. Fluid Mech. **71**, 625–673 (1975)
5. Möhring, W.: On vortex sound at low Mach number. J. Fluid Mech. **85**, 685–695 (1978)
6. Obermeier, F.: Low Mach-number noise generated by an unsteady flow through a pipe with variable cross section. MPI für Strömungsforschung, Bericht 111/1982 (1982)
7. Spehr, C., Delfs, J., Kornow, O., Krenkel, L., Wagner, C., Bouhaj, M. Gommet, A.: Simulation of flow-induced noise generation on orifice plates in air-conditioning ducts. American Institute of Aeronautics and Astronautics, 092407 (2008)

A Separated Flow Model for Semi-Empirical Prediction of Trailing Edge Noise

Chan Yong Schuele and Karl-Stéphane Rossignol

Abstract An accurate description of the mean flow, the rms values, and spectral distributions of the separated boundary layer fluctuating velocities plays an important role in predicting trailing edge far field noise. A possible method for describing the mean and rms quantities based on a modification of Coles' law of the wake and Prandtl's mixing length theory is presented. The model is validated against related experiments from literature and new measurements conducted at DLR Braunschweig. Additionally, a comparison between the von Kármán spectrum for isotropic turbulence and the measured spectra inside the separated boundary layer is given. The results strongly suggest that the spectra as well as the mean and rms values of the separated flow can be modeled with the proposed approaches.

1 Introduction

The prediction of aerodynamically generated sound e.g. on wind turbine rotor blades is essential to the economical feasibility of new wind turbine designs which are limited by stringent communal immission regulations. Several noise prediction schemes exist to predict the sound generated on the suction and pressure side of an airfoil trailing edge with an attached turbulent boundary layer [1, 2]. Nonetheless, no scheme exists currently that describe the aeroacoustic effect of mildly separated turbulent boundary layers on sharp trailing edges based on a physical description of the trailing edge flow field. Hence the framework for a semi-empirical model based on the structure of the separated flow zone for incompressible low Mach and high Reynolds numbers is briefly introduced. The focus of this work will then be the modeling of

C.Y. Schuele (✉) · K.-S. Rossignol
German Aerospace Center e.V. (DLR), Institute of Aerodynamics and Flow Technology, Lilienthalplatz 7, 38108 Braunschweig, Germany
e-mail: chan.schuele@dlr.de

A. Dillmann et al. (eds.), *New Results in Numerical and Experimental Fluid Mechanics IX*, Notes on Numerical Fluid Mechanics and Multidisciplinary Design 124,
DOI: 10.1007/978-3-319-03158-3_65,

the separated flow field in terms of mean and rms-quantities as well as the turbulence velocity spectra. These quantities are essential for the correct prediction of the separated flow noise.

1.1 Far Field Noise Prediction Scheme

The trailing edge enhancement of sound can be described e.g. by the plane wave scattering described by Chase/Chandiramani [3] for a non-compact chord length half-plane and depends on the wavenumber frequency spectrum of the fluctuating surface pressure field at the trailing edge. Surface pressure wavenumber spectra can be calculated through the following solution of the Navier - Stokes and continuity equation [4] with[1] $k >> k_0$ and $k > \delta^{-1}$ and further simplifications such as the assumption of plane waves and a linearization in u_i':

$$P(\boldsymbol{k},\omega) = \rho^2 k_1^2/k^2 \ldots$$
$$\ldots \iint dy_2 dy_2' e^{-(y_2+y_2')k} \partial_2 U(y_2) \partial_2 U(y_2') u'_{2rms}(y_2) u'_{2rms}(y_2') \Phi_{22}(\boldsymbol{k}, y_2, y_2', \omega) \tag{1}$$

with[2] $\Phi_{22}(\boldsymbol{k}, y_2, y_2', \omega) = \widetilde{u'}_2(\boldsymbol{k}, y_2, \omega)\widetilde{u'}_2(\boldsymbol{k}, y_2', \omega)/u'_{2rms}(y_2)^2$. In case of attached turbulent flow, the wave number frequency spectrum can be modeled e.g. through separation of variables[3]:

$$\begin{aligned} \Phi_{22}(\boldsymbol{k}, y_2, y_2', \omega) &= R_{22}(y_2, y_2')\Phi_{22}(k, y, \omega) \\ &= l_2 \delta(y_2 - y_2')\Phi_{22}(k, y_2)\Phi_m(\omega - U_c(y_2)k_1) \end{aligned} \tag{2}$$

with R_{22} as spatial correlation of u_2', l_2 as vertical correlation length scale, Φ_{22} as the wavenumber spectrum of u_2', and Φ_m as moving spectrum modeling the decay of correlation with downstream convection.

A very similar approach is sought for the trailing edge separated flow. Correlations between surface pressure fluctuations in the region of the trailing edge separated flow and the velocity fluctuations above indicate that the dominant sources are spatially coinciding with the maximum mean shear stress, therefore permitting the conclusion that the recirculation zone with its back flow might be negligible as source region and the dominant source term is again of convective nature [5]. Henceforth the linearized mean-shear turbulence interaction term from Eq. 1 shall suffice for the far field sound prediction scheme.

---

[1] k norm of the wavenumber, $k_0 = \omega/c$ with c speed of sound, and ω circular frequency, δ boundary layer thickness

[2] $\boldsymbol{k} = (k_1, k_2, k_3)$ wave numbers in i-direction, U mean flow in 1-direction; $\widetilde{}$ denotes a Fourier transformed quantity, y_2, y_2' wall normal coordinate

[3] U_c convection velocity

1.2 Scope of the Work

All terms except for the moving axis spectrum in Eq. 2 will be assessed in terms of modeling with semi-empirical descriptions. At first, a modified form of Coles' law of the wake is introduced and validated against several data sets from multiple authors. From this the mean flow and gradients of the boundary layer profiles can be described. rms values are then calculated from Prandtl's mixing length theory. Again, the validity of assumed dependencies is tested for data from this and other authors. Finally, the wavenumber spectrum of the vertical fluctuating velocities is compared to the isotropic von Kármán turbulence spectrum. This also allows the validation of the chosen model for the correlation length scales of the vertical velocity fluctuations. This is one of the key quantities of the modeling scheme, since it also scales the moving axis spectrum which is not further investigated within the scope of this work.

2 Modification of Coles' Law of the Wake

Coles' law of the wake is a description of the outer (wake) portion of an equilibrium turbulent boundary layer. It is added through a wake function f to the description of the inner and overlap layers and allows a complete description of the entire boundary layer based on outer variables (Eq. 3) [6]

$$u^+ \approx \frac{1}{\kappa} ln(y^+) + B + \frac{2\hat{\Pi}}{\kappa} f\left(\frac{y_2}{\delta}\right) \tag{3}$$

with $\hat{\eta} = \frac{y_2}{\delta}$, u^+ mean velocity normalized with friction velocity, κ von Kármán constant, $\hat{\Pi}$ Coles' wake parameter, B a constant, and

$$f(\hat{\eta}) \approx \sin^2\left(\frac{\pi}{2}\hat{\eta}\right) \approx 3\hat{\eta}^2 - 2\hat{\eta}^3 \tag{4}$$

The separated boundary layer is now assumed to behave rather like the wake part of the boundary layer since the viscous effect of the wall has been removed when separating from the surface. Therefore, a new wall normal coordinate η is introduced with

$$\eta = \frac{y - y_0}{\delta - y_0} \tag{5}$$

This corresponds to $\hat{\eta}$ based on an equivalent boundary layer thickness equal to the distance between the upper limit of the recirculation zone y_0 where $U(y_0) = 0$ and the boundary layer height δ where $U(\delta) = 0.99U \approx U_{edge}$. Since $\frac{df(\hat{\eta}=0)}{d\eta} = 0$, the appropriate velocity gradient at $\eta = 0$ needs to be imposed on the wake function $f(\eta)$. For this purpose, a function $g(\eta)$ composed of four linearly independent terms is created with

$$g(\eta) = a_0 + a_1\eta + a_2\eta^2 + a_3\cos\left(\frac{\pi}{2}\eta\right) \tag{6}$$

This function fulfills the following four boundary conditions

$$\begin{array}{ll} g(\eta = 0) = 0 & dg(\eta = 0)/d\eta = U_0'(\delta - y_0)/U_{edge} \\ g(\eta = 1) = 0 & dg(\eta = 1)/d\eta = 0 \end{array} \tag{7}$$

with

$$\begin{array}{ll} a_0 = -a_3 & a_2 = -\frac{U_0'}{U_{edge}}(\delta - y_0) + a_3 \\ a_1 = \frac{U_0'}{U_{edge}}(\delta - y_0) & a_3 = -\frac{2U_0'(\delta - y_0)}{U_{edge}(\pi - 4)} \end{array} \tag{8}$$

The modified Coles' law of the wake is then finalized by adding a parameter Π that corresponds to Coles' wake parameter $\hat{\Pi}$:

$$U(\eta)/U_{edge} = \Pi f(\eta) + g(\eta) + h(\eta, \Pi) \tag{9}$$

Again, $h(\eta, \Pi)$ is necessary to guarantee the desired boundary conditions after adding the wake parameter Π and results in

$$h(\eta, \Pi) = \frac{1 - \Pi}{2}(\tanh(\alpha\eta - \beta) + 1) \tag{10}$$

The hyperbolic tangens function was chosen based on the boundary conditions given in Eq. 7 since these have to be also valid for the composed modified law of the wake. Additionally, this function qualitatively fits the data to be approximated best. The hyperbolic function does not exactly fulfill the boundary conditions in a mathematical sense but fulfills it within the necessary accuracy. Best agreement was found when the constants α and β were set to $\alpha \approx 12.5$ and $\beta \approx 9.5$.

3 Experiments and Validations

Measurements were conducted in the Acoustic Wind Tunnel Braunschweig (AWB). The AWB is an open jet closed circuit wind tunnel with a rectangular nozzle cross section of 800×1200 mm. Two airfoil models with 800 mm span and 300 mm chord were tested between 40 and 60 m/s and several angles of attack which provided trailing edge separation. Both sides of the airfoils were tripped with zigzag turbulator strips close to the leading edge. Flow field measurements were performed with a 7-hole probe and cross hot wires. Chord normal velocity profiles were taken at 101 % chord for several spanwise positions.

3.1 Validation of the Modified Coles' Law of the Wake and Rms Modeling

In order to validate the suggested modification of Coles' law of the wake, several measurements from other authors as stated in Fig. 1 were fitted with U_{edge}, η, $dU_0/d\eta$, and Π and then plotted against (the original) Coles' law of the wake in terms of $U_{fit} = (U/U_{edge} - g(\eta) - h(\eta, \Pi))/\Pi = f(\eta)$. The quoted data was taken either with (flying) hot wires or LDVs and corresponds to separated flow on airfoil models [7, 8], a flap model [9], and an adverse pressure gradient plate model [10] at multiple streamwise locations in the separated flow within the separated flow region. For the present study, 7-hole probe as well as hot wire data are shown. Both, hot wire and 7-hole probe data were fitted against exactly the same scaling parameters when corresponding to the same location and flow conditions at the airfoil model.

Although the data from all authors were taken on different geometries and at different free stream velocities, the proposed modification of Coles' law of the wake leads to a good collapse of the analyzed data. One exception is the present hot wire data. Some significant deviation can be seen for small η. This height in the separated boundary layer corresponds to a region with turbulence intensities $> 30\,\%$ and leads to unreliable data. Therefore, any hot wire data for $\eta < 0.35$ are not further discussed.

The corresponding chord normal mean flow gradients are presented on the right hand side of Fig. 1. There is some scatter around the modeled $dU_{fit}/d\eta$ which is somewhat expected for the calculation of a gradient based on discrete data points from experiments.

In order to obtain rms values from the mean flow quantities, Prandtl's mixing length theory is used.

Prandtl's mixing length can be defined as $l_{mix}(y_2) = \sqrt{-\overline{uv}}/\partial_2 U(y_2)$ [6]. Therefore the x-hot wire data is used to calculated the normalized mixing length $l = l_{mix}/(\delta - y_0)$ as shown in Fig.2. Alongside are two data sets from Fig. 1.

The data seem to follow (with some scatter) a straight line with $l \approx -0.04\eta + 0.075$ for $0 < \eta < 0.8$.

Finally, the rms values can be extracted from Prandtl's mixing length theory, if the ratio between $-\overline{uv}/v_{rms}^2 = \nu \approx const.$ is known. With knowledge of ν, $v_{rms}(y_2) \approx l_{mix}(y_2)\partial_2 U(y_2)/\sqrt{\nu}$. For this purpose, Fig.3 shows ν on the left-hand side and the ratio u_{rms}/v_{rms} on the right-hand side. Interestingly, the previously pretty well matching Prandtl mixing lengths do not show agreement when relating the uv-correlation to the rms quantities. However, the overall character stays the same, namely the somewhat constant ratio ν for $0.3 < \eta < 0.75$. The discrepancy in the absolute value of ν to the reference data sets might be caused by the different ratios between u_{rms} and v_{rms}. These indicate a slightly larger degree of anisotropy for $0.3 < \eta < 0.75$ (rhs of Fig. 3) that converges to ≈ 1.15 and reaches therefore almost isotropic conditions at the edge of the separated boundary layer. The discrepancy could also have been caused by the w-component of the velocity fluctuations that were indirectly added to the u and v velocity components due to the cross wire arrangement.

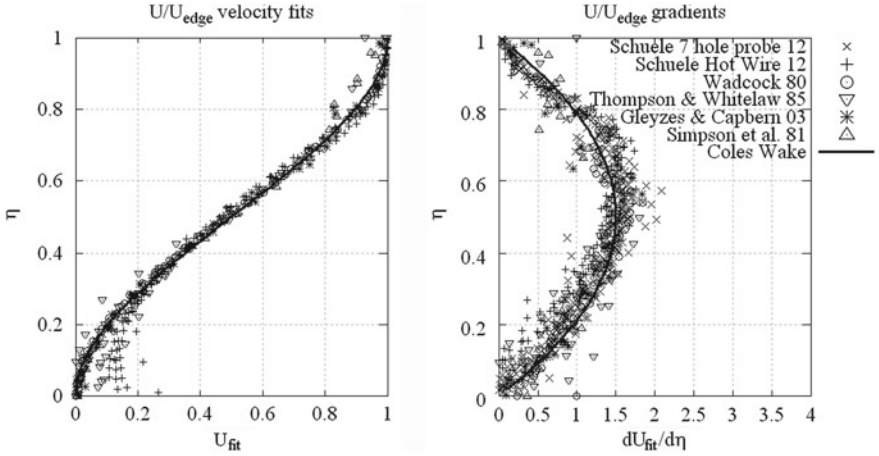

Fig. 1 Fitting of various data sets to $U_{fit} = (U/U_{edge} - g(\eta) - h(\eta, \Pi))/\Pi = f(\eta)$

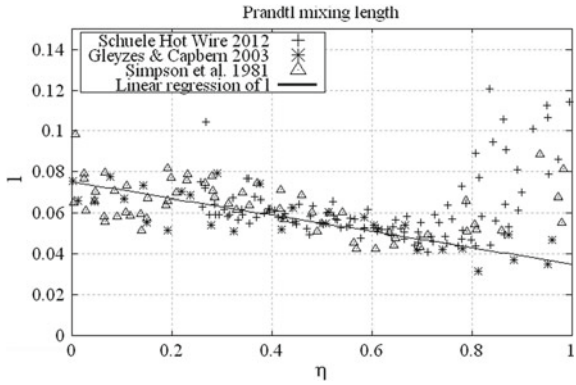

Fig. 2 Normalized Prandtl mixing length

3.2 Spectral Shape Modeling and Length Scales

The spectra of u_2' or v from the author's hot wire data is presented for 3 different angles of attack at $\eta \approx 0.4$ in Fig. 4. The original spectrum is a point frequency spectrum which was then transformed into a wavenumber spectrum by using Taylor's hypothesis: $k_1 = \omega/U_c(y_2)$. k_1 has units of $[\frac{rad}{m}]$ with $U_c(y_2) = U(y_2)$. Although not shown, the spectral shapes do not vary significantly for $\eta < 1$. All four spectra are multiplied by powers of 10 for better readablity of the diagram.

In order to model the spectral shape of the vertical velocity fluctuations, the von Kármán turbulence spectrum for isotropic turbulence was chosen [11]. Its low wave number form is

$$\Phi_{22} = \frac{4}{3}\frac{\Lambda_2}{\pi}(1 + (k_1/k_e)^2)^{-5/6+\mu/2} \tag{11}$$

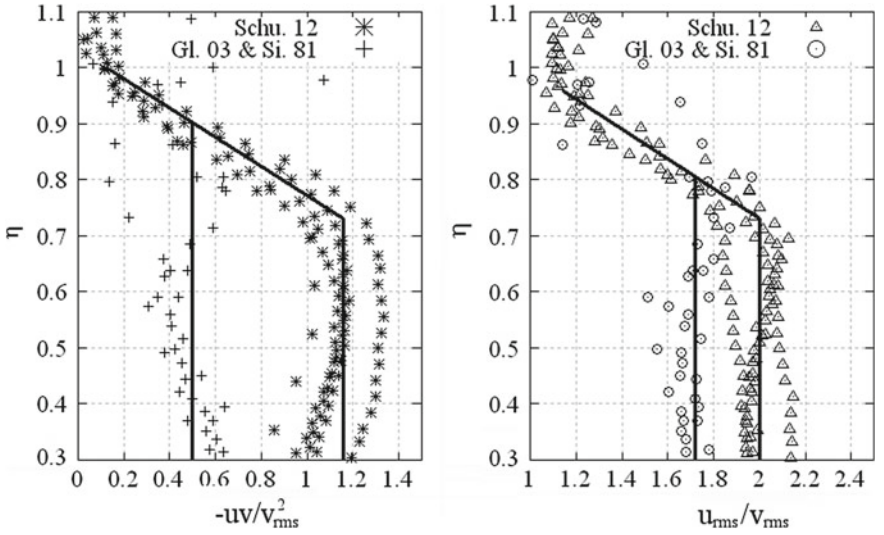

Fig. 3 $-\overline{uv}/u_{rms}$ and u_{rms}/v_{rms}

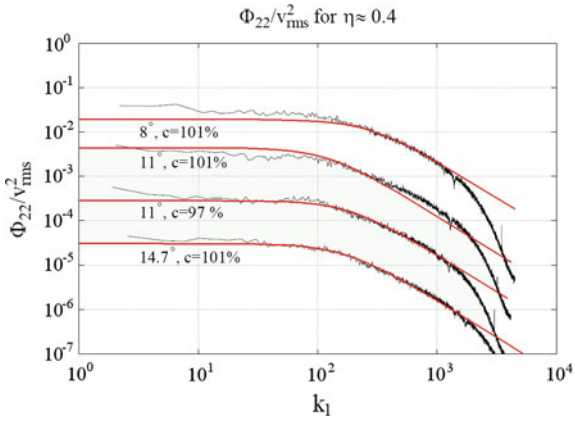

Fig. 4 Turbulence power spectral densities for several angles of attack. Comparison with the isotropic von Kármán spectral model. Absolute spectral values shifted by constant values for better visibility

with

$$k_e = \sqrt{\pi}\Gamma(\frac{5}{6} - \frac{\mu}{2})/(\Lambda_2\Gamma(\frac{1}{3} - \frac{\mu}{2})) \tag{12}$$

which corresponds to a normalization factor relating k_1 to the maximum wave number of the energy carrying eddies. In order to take the anisotropic behavior (see Fig. 3) into account, a factor $\gamma = 5/3$ was multiplied with the modeled Φ_{22}. This factor guarantees for the present anisotropy that $\int \Phi_{22}(k_1)dk_1 \approx 1$. More details on the effect of anisotropy can be found in [12]. Parchen [13] suggested Λ_2 to be $\Lambda_2 = l_{mix}/\kappa$ with κ=0.41 (van Kármán constant) since the mixing length is representative of the size of the turbulent eddies in the boundary layer. The resulting modeled

spectra for the infinite Reynolds number limit ($\mu = 0$) are shown as red lines in Fig. 4. The spectral decay $k_1^{-5/3}$ matches very well the acquired hot wire data. This also includes the beginning of the decay which was correctly predicted by Parchen's definition for Λ_2. As expected, the high wave number part with a larger rate of decay is not correctly modeled. A corrected model would include the product of the low and high frequency spectrum. This is not further pursued here.

4 Conclusion

Measurements of the mean flow velocities, rms quantities and spectra were presented for model airfoils with trailing edge separated flow. A modification of Coles' law of the wake was proposed for the description of the separated boundary layer and resulted in a good collapse of all considered data. Based on a comparison with data from literature, the modified Coles' law of the wake as well as the Prandtl mixing length seem to be of almost universal character, considering the differences in e.g. Reynolds number, surface curvature, and pressure gradient of the reference cases. The main difference in modeling the rms quantities was introduced through the anisotropy of the specific model case. It varied from $u_{rms}/v_{rms} \approx 1.7$ to 2 and resulted in $-\overline{uv}/v_{rms}^2 \approx 0.5$ to 1.1. The shapes of turbulence spectra were well predicted by using the low wave number van Kármán spectrum and defining the vertical correlation length scale as $\Lambda_2 \approx l_{mix}/\kappa$. Henceforth a semi-empirical description of the key parameters for the Blake-TNO trailing edge noise prediction scheme was identified and validated for trailing edge separated flows.

Acknowledgments The author would like to gratefully acknowledge the sponsorship through GE Wind Energy GmbH.

References

1. Brooks, T.F., Pope, D.S., Marcolini, M.A.: Airfoil Self-Noise and Prediction p. 1218. NASA Reference, Publication, NASA (1989)
2. NWTC Design Codes (NAFNoise by Pat Moriaty). http://wind.nrel.gov/DesignCodes/simulators/NAFNoise/.. Accessed 04 Dec 2006
3. Chase, D.M.: Noise radiated from an edge in turbulent flow. AIAA J. **13**(8), 1041 (1975)
4. Blake, W.K.: Mechanics of Flow-Induced Sound and Vibration, vol. I+II, Applied Mathematics and Mechanics, vol. 17(1). Academic Press, Inc., New York (1986)
5. Blake, W.K.: David Taylor Naval Ship Research and Development Center, Report 4241 (1975)
6. White, E.B.: Viscous Fluid Flow. McGraw Hill, New York (2002)
7. Wadcock, A.J.: NASA contractor report 3283 (1980)
8. Gleyzes, C., Capbern, P.: Experimental study of two AIRBUS/ONERA airfoils in near stall conditions Part I: Boundary layers. Aerosp. Sci. Technol. **7**, 439–449 (2003)
9. Thompson, B.E., Whitelaw, J.H.: Characteristics of a trailing-edge flow with turbulent boundary layer separation. J. Fluid Mech. **157**, 305–326 (1985)

10. Simpson, R.L., Chew, Y.-T., Shivaprasad, B.G.: The structure of a separating turbulent boundary layer. Part 1. Mean flow and Reynolds stresses. J. Fluid Mech. **113**, 23–51 (1981)
11. Gamard, S.: A new similarity analysis of the turbulence energy spectrum. Master Thesis Department of Mechanical and Aerospace Engineering, Graduate School of the State University of New York, Buffalo (1999)
12. Kamruzzaman, M., Lutz, T., Herrig, A., Kraemer, E.: Semi-empirical modeling of turbulence anisotropy for airfoil self-noise predictions. AIAA J. **50**(1), (2012)
13. Parchen, R.: Progress report DRAW: a prediction scheme for trailing-edge noise based on detailed boundary-layer characteristics. TNO Report HAG-RPT-980023, TNO Institute of Applied Physics, The Netherlands (1998)

Part XII
Biofluid Mechanics

Computational Analysis of a Three-dimensional Flapping Wing

Nadine Buchmann, Rolf Radespiel and Ralf Heinrich

Abstract Unsteady Reynolds-averaged Navier-Stokes simulations are presented in which two-dimensional airfoil motion parameters have been extended to three-dimensional wing motion. The motion parameters have been redefined including induced angles of attack which have been identified using a panel method based on Prandtl's wing theory. The numerical simulation approach includes a mesh deformation tool to perform the wing's movement. The resulting thrust and propulsive efficiency on wing sections are compared to equivalent two-dimensional simulations.

1 Introduction

Two-dimensional analysis of moving airfoils has created significant knowledge about the generation of thrust at high propulsive efficiency by airfoil motion. Previous works have established an appropriate definition of propulsive efficiency and favorable motion parameters for unsteady moving airfoils [1–3].

A comprehensive overview of works on flapping flight analysis gives PLATZER [4]. He referred to works of ISOGAI and TUNCER [5, 6] whose studies on pitch-plunge-oscillating NACA 0012 airfoils revealed a favourable operating range for high propulsive efficiency. Furthermore the complex unsteady wake is evident in experimental results.

This work investigates design aspects of three-dimensional flapping wings. The wing geometry in planform and airfoil sections has been inspired by measurements on live hawks [7]. The vital questioning of the present work is totransfer results of

N. Buchmann (✉) · R. Radespiel
TU Braunschweig, 38108 Braunschweig, Germany
e-mail: n.buchmann@tu-braunschweig.de

R. Heinrich
DLR, Braunschweig, Germany

A. Dillmann et al. (eds.), *New Results in Numerical and Experimental Fluid Mechanics IX*,
Notes on Numerical Fluid Mechanics and Multidisciplinary Design 124,
DOI: 10.1007/978-3-319-03158-3_66,

two-dimensional airfoil motion to a three-dimensional wing. The three-dimensional effects have to be identified and compensated in the motion description. Therefore Prandtl's airfoil theory has been adapted in an appropriate way.

2 Numerical Methods

The analysis of flapping wings shown in this work was carried out using the DLR-TAU Code [8], solving the RANS equations on hybrid unstructured grids with second order accuracy in space and time. The implemented numerical scheme is based on a Finite Volume method and the present computations apply a central discretization with fourth order dissipation. A dual time stepping approach, preconditioning for low Mach number range and multigrid operations are used to accelerate the computation.

A second-order accurate implicit Backward Euler dual time stepping scheme is used for time-accurate computations. The Menter two-layer $k-\epsilon$ -model [9] is chosen for the turbulence modeling.

For simulating a three-dimensional flapping wing, the TAU mesh deformation tool using Radial Basis Functions (RBF) is applied [10]. These functions are topology independent functions, whose values only depend on the distance from their origin. RBF are well suited for interpolation of scattered data like in our TAU simulation case with hybrid meshes.

Despite anticipated laminar regions the simulations have been performed with fully turbulent flow in order to establish the newly developed methodology for a moving wing.

3 Kinematics

The kinematics of a flapping wing is based on the parameters of a two-dimensional airfoil motion where a section $y1$ of the wing represents the airfoil. The two-dimensional motion of an airfoil at $y1$ is defined as a combined plunging $z\,(t)$ and a $\varphi = \pi/2$ phase shifted pitching motion $\alpha\,(t)$ around the quarter chord for one flapping period T:

$$\alpha_{y1}\,(t) = \alpha_m + \alpha_1 \cos\left(2\pi t/T + \varphi\right) = \alpha_m - \alpha_1 \sin\left(2\pi t/T\right) \tag{1}$$

$$z_{y1}\,(t) = z_1 \cos\left(2\pi t/T\right) \tag{2}$$

Figure 1 shows a three-dimensional motion of the wing spanwise sections, which fulfills the two-dimensional motion parameters.

Both of these motions cause changes of the effective angle of attack α_e during a flapping period. The change of α_e caused by plunging motion $\zeta\,(t)$ is described by

$$\zeta\,(t) = \zeta_1 \sin\left(2\pi t/T\right) = 2k\frac{z_1}{c} \sin\left(2\pi t/T\right). \tag{3}$$

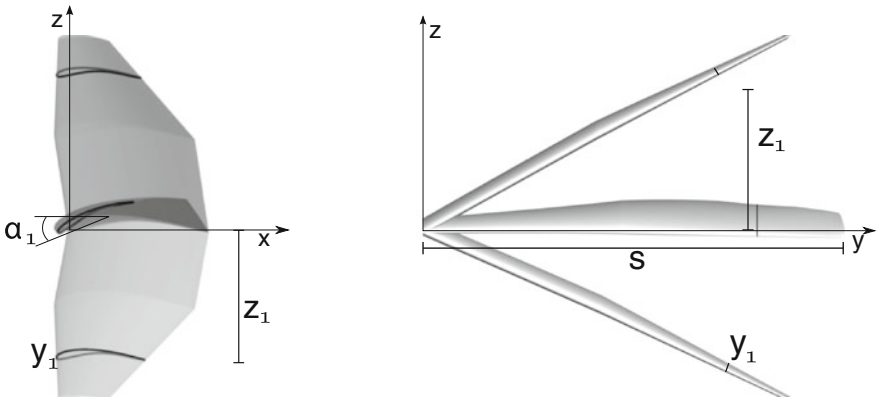

Fig. 1 Wing deformation: side (*left*) and front view (*right*) of the left wing part at top dead center, mid-downstroke and bottom dead center with design point $\eta = \frac{y1}{s} = 0.8$

With $k = \frac{\pi f c}{U_\infty}$ as reduced frequency where $f = 1/T$. The effective angle of attack during a flapping period is then

$$\alpha_e = \alpha_m + \Delta\alpha_e \sin(2\pi t/T) \tag{4}$$

$$\text{with} \quad \Delta\alpha_e = \zeta_1 - \alpha_1. \tag{5}$$

The pitch/plunge motion may be extended by superimposed gliding motion:

$$x_{y1}(t) = \Delta x \cdot z_1 \cos(2\pi t/T) \tag{6}$$

A slight forward gliding motion during downstroke had been found to affect favourably both thrust c_T and propulsive efficiency η_P [11].

A superimposition of plunging, pitching and gliding motion generates thrust over a flapping period.

$$c_T = -c_d + c_{d,stat}(\alpha_m) \tag{7}$$

$$\eta_P = \frac{(1/TU_\infty)\int_0^T c_T U_\infty dt}{(1/TU_\infty)\int_0^T (c_d\dot{x}_1 + c_l\dot{z}_1 + c_m\dot{\alpha}c)\,dt} = \frac{c^*_{\pi,out}}{c_{\pi,in}} \tag{8}$$

A suited calculation of the resulting propulsive efficiency of an active motion requires the steady drag of the airfoil at mean angle of attack to be taken into account, as the steady drag has to be overcome for every point in time of a flapping period to ensure propulsion. This steady-state correction is used to decouple thrust and drag and to allow a comparison between flapping-wing and propeller-driven propulsion. Note that our definition of thrust coefficient with subtracted steady drag differ from the one of ISOGAI, PLATZER and TUNCER [4–6].

4 Vortex Model

The calculation and interpretation of the vortex system which occurs on a flapping wing has been discussed extensively by NEEF [2]. Lifting vortices are located on the wing perpendicular to the oncoming flow. In consequence the circulation increases from the non-deformed wing root along the wingspan until it sharply decreases to zero at the wing tip. Note that lifting vortices leave the wing at the trailing edge as free vortices. Starting and stopping vortices appear in regions of large vertical deflections whereas longitudinal vortices appear particularly at maximum wing torsion.

Longitudinal vortices of a finite wing induce a downwash causing the induced angle of attack, which reduces the effective angle of attack. To determine this induced angle of attack a method based on Prandtl's wing theory is used here. The identified induced angles are taken into account when defining the wing's motion parameters.

Potential flow wing analysis methods can be divided into unsteady and steady methods. Unsteady methods include changing flow conditions into the calculation of aerodynamic forces and wake. However, unsteady methods are often based on the assumption of small perturbations and infinitely thin, plane wings [12].

Steady methods assume constant flow over a wing. Particularly panel methods allow including camber and thickness of airfoils into the calculation of lift and induced angle of attack distributions [13, 14]. A panel method is used in this work. In *xflr5* [15], a panel method coupled with integral boundary layer methods is implemented. A distribution of doublets and sources on each quadrilateral panel is calculated from a Dirichlet formulation of the kinematic flow condition. In our applications the shape of the longitudinal vortices downstream of the trailing edge is held fixed by assuming straight lines in the direction of the oncoming flow.

The induced angle of attack is calculated iteratively by determining the coefficients of a Fourier series which represents the distribution of the lift coefficient along the wingspan.

5 Airfoil and Wing Geometry

The hawk airfoil F0808 forms the basis of a birdlike shaped double tapered wing with aspect ratio $\Lambda = 6.89$ [16] that is used for three-dimensional simulations in this work, Fig. 2.

The drag polar of the F0808 is shown along with another bird airfoil, SG04 [1], in Fig. 3. These were computed with the open source software *XFOIL*. The e^N-method is used for transition prediction with the critical N-factor of 10.

Compared to the SG04, the F0808 shows increased lift and significantly larger drag coefficients. This is due to high camber and thickness of 8 % compared to only 4 % camber and thickness of the SG04. The maximum thickness of F0808 is located rather close to the leading edge. According to the large nose radius there is a large range of angles of attack for which the hawk airfoil does perform well, particularly at

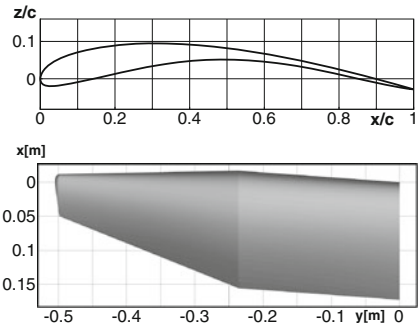

Fig. 2 Airfoil F0808 (*top*) and birdlike double tapered wing (*bottom*)

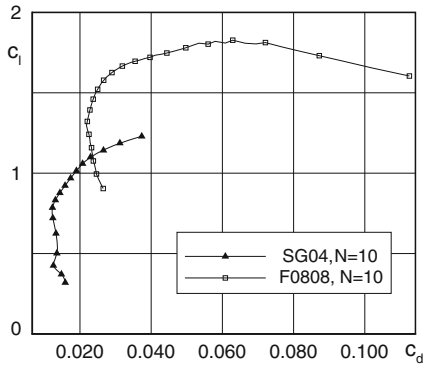

Fig. 3 Drag polar of the F0808 airfoil compared to the SG04 airfoil

high angles of attack, see also the polar in Fig. 3. High velocity on the suction surface and large thickening of the boundary layer towards the trailing edge due to adverse pressure gradients lead to a higher drag coefficient. Pitching and plunging motions of this airfoil were performed by using suited kinematics for high propulsive efficiency from Refs. [3, 11]. These kinematics constitute the 2D design point as given in Chap. 7. This airfoil performance in thrust and propulsive efficiency constitutes the reference for the wing performance in three-dimensional flapping motion.

6 Three-Dimensional Flapping Wing

A finite wing geometry causes an induced angle of attack, which requires a redefinition of the effective angle of attack for three-dimensional wings along the wingspan

$$\alpha_e(\eta, t) = \alpha_m + (\zeta_1(\eta) - \alpha_1(\eta)) \sin(2\pi t/T) - \alpha_i(\eta, t). \tag{9}$$

Pitching and plunging amplitudes depend on the spanwise position η as for the motion increases in proportion to the wingspan. The design point pitching amplitude holds then

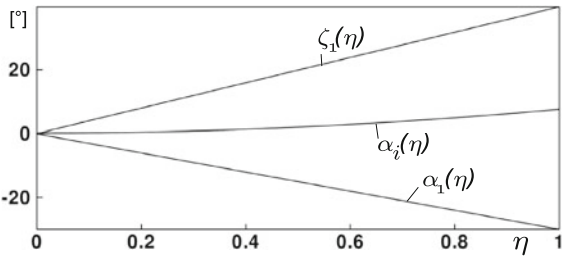

Fig. 4 Spanwise distribution of the angles of attack caused by pitch and plunge motion $\alpha_1(\eta)$ and $\zeta_1(\eta)$ and the induced angle of attack $\alpha_i(\eta)$ at mid-downstroke

$$\alpha(\eta_1, t) = \alpha_m - \alpha_1(\eta_1)\sin(2\pi t/T) - \alpha_i(\eta_1)\sin(2\pi t/T). \tag{10}$$

The deformation of the three-dimensional wing in time t is defined as a wingspan dependant function. The torsion angle along the wingspan η for one instant in flapping period t/T is defined as

$$\alpha(\eta, t) = \left(\alpha_{m_{2D}} + \alpha_i(\eta = 0)\right) - \alpha_1(\eta)\sin(2\pi t/T) - \alpha_i(\eta)\sin(2\pi t/T). \tag{11}$$

Figure 4 shows the distribution of the angles of attack caused by pitch and plunge motion $\alpha_1(\eta)$, $\zeta_1(\eta)$ and the induced angle of attack α_i calculated using *xflr5* along the wingspan for a typical downstroke.

The increasing amount of the plunge and pitch parameters ζ_1, α_1 along the wingspan according to equation [11] can be carried out with the mesh deformation tool. The distribution of the induced angle of attack has been approximated by a linear distribution passing through the design point $\eta = 0.8$.

7 Results

The determined induced angles of attack using *xflr5* have been considered in the calculation of the mean angle of attack α_m and the resulting pitching amplitude $\alpha_1 + \alpha_i$. In this manner five cases with the design point at 80 % of wingspan, $\eta = 0.8$ were calculated using the DLR TAU Code. Effective angles of attack amplitude $\Delta\alpha_e = 6°$, $\lambda = 0.8$ and superimposed gliding motions $\Delta x = -0.25, -0.125, 0, 0.125, 0.25$ were analysed, results on thrust and propulsive efficiency of these computations are shown in Fig. 6. The F0808 airfoil shows a favorable operating range at angle of attack, $\alpha = 7°$, as can be seen in the polar shown in Fig. 3. Therefore simulations have been conducted with a mean angle of attack $\alpha_m = 7°$.

Figure 5 shows lift and drag coefficients over one flapping period. The coefficients at wing sections of $\eta = 0.8, 0.9$ are compared to the ones of two-dimensional airfoil simulations calculated with equivalent parameters to demonstrate the effect of the newly defined motion, Eq. (11). The three-dimensional motion increases in proportion to the wingspan, so that at the design point $\eta = 0.8$ the parameters

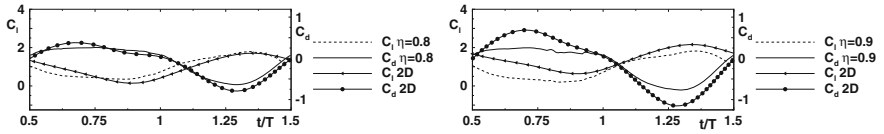

Fig. 5 Comparison of lift and drag coefficients of the three-dimensional simulation in spanwise positions $\eta = 0.8, 0.9$ according to airfoil simulations of the case $\Delta\alpha_e = 6°,\ k = 0.2$

$\alpha_1 = 24°,\ z_1 = 1.44 \cdot c_\eta$, with c_η airfoil chord at $\eta = 0.8$, $k = 0.2,\ U_\infty = 14.5$ m/s are satisfied.

Figure 5 shows a good agreement of the two-dimensional airfoil coefficients and the results of the 3D wing simulation in the design point at $\eta = 0.8$ as compared to the larger deviation in the aerodynamic coefficients at $\eta = 0.9$, close to the wing tip. There are two main reasons for this. On the one hand the induced angle of attack distribution has an increasing gradient near to the wing tip, whereas the motion parameters that take into account the induced angles of attack have been defined as a linearly increasing function. Therefore the induced angle of attack is not completely compensated in the wing tip region by the 3D motion parameters.

On the other hand the determination of the induced angle of attack is done with a steady method. This kind of method presumes free, non-lifting vortices to be constant from the trailing edge, neglecting the unsteady wake. Moreover the wake roll up is not taken into account. Note that the *xflr5* method uses Prandtl's wing theory to compute the induced angle of attack which is a rough approximation close to the wing tip. Hence we conclude that physical flow conditions are only approximately modelled close to the wing tip.

8 Propulsive Efficiency of the Flapping Wing

The propulsive efficiency of the five simulated cases was also calculated. The calculation was carried out for the design point $\eta = 0.8$ and for the entire wing. Figure 6 shows a good agreement between the values of thrust and propulsive efficiency of the wing design section and equivalent two-dimensional airfoil results.

The propulsive efficiency of the entire wing differs only slightly from that of the wing section, since the motion was carried out with the same ratio of pitch and plunge amplitude, $\lambda = 0.8$, along the wingspan. It has been observed that a superimposed slight forward gliding motion during downstroke improved both thrust and propulsive efficiency (see Fig. 6). This increase in thrust for large forward gliding motion, $\Delta x < 0.125$, but affects propulsive efficiency adversely, like earlier two-dimensional analysis already discovered [1].

We are surprised that the propulsive efficiency of the 3D wing is only slightly below the 2D result. This indicates that the free longitudinal wake vortices due to flapping motion are rather weak in the time mean and they result in a loss in η_P of around 4 % only.

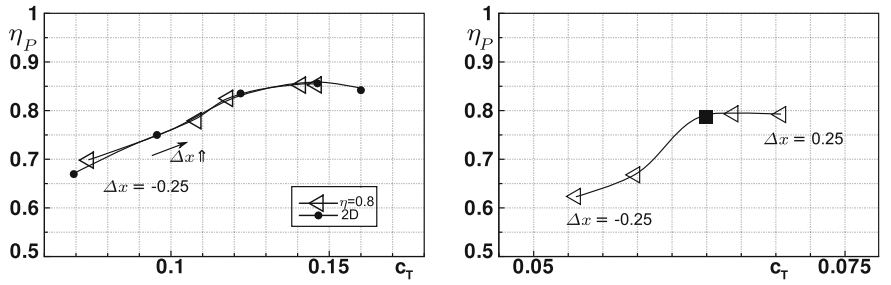

Fig. 6 Propulsive Efficiency at spanwise section $\eta = 0.8$ (*left*) and of the entire wing (*right*)

9 Conclusion

Well analysed two-dimensional airfoil kinematics was extended to three-dimensional flapping wings. The induced angles of attack on finite wings were identified with a steady vortex system method and taken into to account by defining the wing torsional flapping motion. The results in thrust and propulsive efficiency of the wing's design section $\eta = 0.8$ of a specific case with high propulsive efficiency show good agreement compared with equivalent two-dimensional values. Note that the total thrust generated by flapping is still relatively low. This is due to the constraint that the motion increases in proportion to the wingspan. Near to the wing root, where little motion is performed, only little thrust is generated. Further simulations should be carried out with an increased flapping motion in order to generate higher values of thrust.

References

1. Bansmer, S.: Strömungsanalyse an einem zwei- und dreidimensional schlagenden Flügelsegment. Dissertation, Technische Universität Braunschweig (2010). ISBN 978-3-832298-92-0
2. Neef, M.: Analyse des Schlagfluges durch numerische Strömungsberechnung. Dissertation, Technische Universität Braunschweig (2002). ISBN 978-3-928628-45-7
3. Windte, J., Radespiel, J.: Propulsive efficiency of a moving airfoil at transitional low reynolds numbers. AIAA J. **46**(9), 2165–2177 (2008)
4. Platzer, M.F., Jones, K.D., Young, J., Lai, J.C.S.: Flapping wing aerodynamics: progress and challenges. AIAA J. **46**(9), 2136–2149 (2008)
5. Isogai, K., Shinmoto, Y., Watanabe, Y.: Effects of dynamic stall on propulsive efficiency and thrust of flapping airfoil. AIAA J. **37**(10), 1145–1151 (1999)
6. Tuncer, I.H., Walz, R., Platzer, M.F.: A computational study on the dynamic stall of a flapping airfoil. AIAA Paper 98–2519, June 1998
7. Friedl, A., Kähler, C.J.: Shape and deformation measurement of naturally textured surfaces using optical flow, 17. DGLR / STAB Fach-Symposium zur Strmungsmechanik, Berlin, 9–10 November 2010
8. Kroll, N., Rossow, C.-C., Schwamborn, D.: The MEGAFLOW-project—numerical flow simulation for aircraft. In: Progress in Industrial Mathematics at ECMI 2004, pp. 81–125. Springer, Berlin (2005)

9. Menter, F.R.: Two-equation eddy-viscosity turbulence models for engineering applications. AIAA J. **32**(8), 1598–1605 (1994)
10. Gerhold, T., Neumann, J.: The Parallel Mesh Deformation of the DLR TAU-Code, New Results in Numerical and Experimental Fluid Mechanics VI, Notes on Numerical Fluid Mechanics and Multidisciplinary Design, 96, pp. 162–169. Springer, Berlin (2008)
11. Bansmer, S., Radespiel, R.: Flapping flight: high thrust and propulsive efficiency due to forward gliding oscillations. AIAA J. **50**(12), 2937–2941 (2012)
12. Laschka, B.: Zur Theorie der harmonisch schwingenden tragenden Fläche bei Unterschallanströmung. ZFW **11**, 265–292 (1963)
13. Maskew, B.: A Computer Program for Calculation Nonlinear Aerodynamic Characteristics of Arbitrary Configurations, NASA Contractor Report 4023, Analytical Methods Inc. (1987)
14. Sivells, J.C., Neely, R.H.: Method For Calculating Wing Characteristics By Lifting-Line Theory Using Nonlinear Section Lift Data. National Advisory Committee For Aeronautics, 865 Langley Memorial Aeronautical Laboratory Langley Field (1947)
15. Deperrois, A.: Guidelines for XFLR5 v6.03, URL:https://engineering.purdue.edu/∼aerodyn/AAE333/FALL11/Homeworks/HW10/xflr5-6.04-beta-win32/xflr5-6.04-beta-win32/Guidelines.pdf
16. Bansmer, S., Buchmann, N., Radespiel, R., Unger, R., Haupt, M., Horst, P., Heinrich, R.: Aerodynamics and Structural Mechanics of Flapping Flight with Elastic and Stiff Wings, Nature-Inspired Fluid Mechanics, Notes on Numerical Fluid Mechanics and Multidisciplinary Design, 119, pp. 331–354. Springer, Berlin (2012)

Combined Flow and Shape Measurements of the Flapping Flight of Freely Flying Barn Owls

Thomas Doster, Thomas Wolf and Robert Konrath

Abstract The underlying physics of the flight of birds is still not fully understood, in part due to the very complex wing movement and a lack of appropriate measurement techniques. Modern measurement technologies for fluid flows are often not suited for experiments with living animals, since these techniques may potentially harm the animal (e.g. lasers). The objective of this project was to modify the established technology *Particle Image Velocimetry* (PIV) to measure the flow around trained barn owls with the least possible hazard to the health of the animals. Furthermore, the shape of the wings was measured simultaneously using *Projected Pattern Correlation Technique* (PROPAC) to correlate the flow with the shape and movement of the wings. Results of the measurements of gliding and flapping flight are presented in this chapter.

1 Introduction

The study of gliding and particularly flapping flight of birds has a long tradition, but has been disregarded by aviation research for almost a century. With the increasing importance of Micro Air Vehicles (MAV), flapping flight came back into focus as a possibly quieter and more efficient alternative to other existing propulsion systems. However, the flow physics of the flapping flight of animals is still not completely

T. Doster (✉) · T. Wolf · R. Konrath
Department of Experimental Methods, German Aerospace Center,
Institute of Aerodynamics and Flow Technology, Göttingen, Germany
e-mail: tomdoster@gmail.com
http://www.dlr.de

T. Wolf
e-mail: thomas.wolf@dlr.de

R. Konrath
e-mail: robert.konrath@dlr.de

A. Dillmann et al. (eds.), *New Results in Numerical and Experimental Fluid Mechanics IX*,
Notes on Numerical Fluid Mechanics and Multidisciplinary Design 124,
DOI: 10.1007/978-3-319-03158-3_67,

understood. This is due to the complexity of the wing motion together with the three-dimensionality and the unsteadiness of the flow. However, the evolution over millions of years of birds leads to an enhanced flapping flight approach, so that detailed measurements of their biomechanics and the fluid flow around their bodies and wings could help in gaining more knowledge that can be used to develop flapping flight mechanisms for MAVs.

Measurement technology for fluid flows has developed rapidly over the last two decades, leading to a better understanding of transient phenomena in fluid flows. Unfortunately, most of these technologies are not suited for experiments with living animals, since they can potentially harm the animal (e.g. use of lasers). Hence, most of the PIV measurements on birds were focused on the wake behind the bird (Spedding [1, 2], Hedenström [3], Rosen [4]). Flow effects around the wings of birds especially for the flapping flight mode have rarely been explored, even though they potentially play an important role in generating lift and thrust. Measurements on bats [5] and humming birds [6] show that both create leading edge vortices to increase the lift. On larger birds such measurements have not yet been conducted.

Therefore the objective of this project was to develop a measurement setup which is capable of measuring the flow field around owls. For this purpose, the measurement technique PIV needs to be adapted so that it does not harm the animals. In order to correlate the flow field information with the movement and shape of the bird wing, the measurement technique PROPAC was also applied. This technique is used to measure a wing shape in high resolution and in a non-intrusive manner, as described in [7, 8]. Both measurement techniques were applied simultaneously. Therefore the resulting wing shapes can be correlated with the flow field obtained by PIV. The position of the light sheet on the wing as well as the kinematics of the bird movement can also be calculated by combining the methods.

2 Experimental Methods

In contrast to conventional wind tunnel experiments, another approach was applied. The birds were trained to fly a defined flight path. For the measurements the experimental setup was placed around the flight path, so that the birds themselves were able to choose their flight speed and mode (flapping, gliding). Advantages of this setup are the capability of observing manoeuvres, the steady non turbulent air flow and the possibility to measure the wake for a long time. The main disadvantage compared to wind tunnel tests is that the bird only stays within the measurements zone for a short time, which leads also to a short measurement time.

The whole measuring equipment was attached to an aluminium frame (see Fig. 1, right). The flight passage through the frame was about 1.8×1.8 m. The frame was placed in the middle of a more than 30 m long and about 5 m wide hall, where the experimental flights were carried out. At the one end of the hall the bird sat on a perch and started its flight through the measurement zone when the trainer on the other side of the hall called it by whistling.

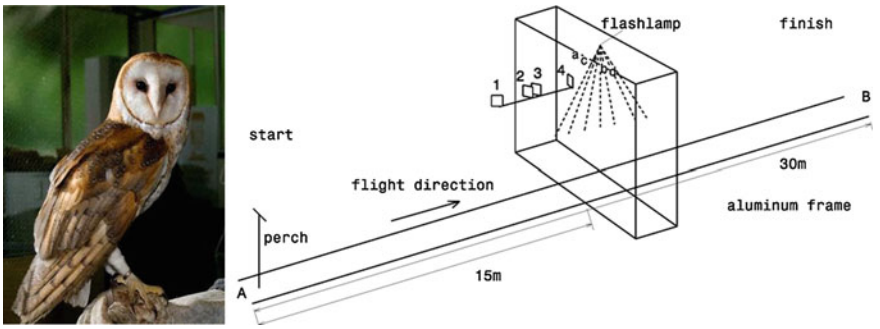

Fig. 1 *Left* Barn Owl; *Right* Sketch of the setting 1-4 PIV Cameras, (**a**, **b**) Led-Illuminator; (**c**, **d**) PROPAC Cameras

Two Barn Owls (*tyto alba*), one male and one female (see Fig. 1, left side) of RWTH Aachen University were used for the experiments. These owls are specially trained birds which had already been used for other flight experiments (see [7, 8]). Therefore the birds were well adapted to these kinds of setups and it was possible to perform the measurements without the need for extensive bird training.

Barn Owls are crepuscular predators, so they are agile and accustomed to low light conditions, which is very helpful due to the sensitivity of the measurement technique to ambient light. With a wing span of around 90 cm and an average chord length of 15 cm, Barn Owls have relatively large wings compared to their weight of 460–530 g. The flight speed in the experiments varied between 4.5 and 7 m/s. The resulting Reynolds number is $Re \sim 60{,}000$ and the reduced frequency $k \sim 0{,}275$ (calculated with an average flapping frequency $f \sim 3.5$ Hz). For comparison, typical parameters of other species are given by Herzog [9] or Hubbel [10].

2.1 Stereo PIV

PIV is a well-developed technique, which has been refined and improved over the last two decades and already adapted to measurements of many fluid problems and phenomena. For the experiments a Stereo PIV approach was applied. This allows the calculation of three dimensional velocity vectors within the measurement area. A detailed description of the principles, variations and common elements of PIV and Stereo PIV can be found in Adrian [11] and Raffel [12].

The challenge in this project is to make the technology suitable for experiments on freely flying birds without harming the animals. The use of high energy lasers poses the highest hazard to the animal, so that either the light intensity has to be reduced considerably or an alternative non-hazardous light source has to be used. In the present experiments Xenon flashlamps were applied as light source. The advantage of this light source is the harmlessness. Main disadvantages are the non-coherent

radiation characteristic, the low light source intensity (when compared with that of a laser) and the light pulse length. The radiation characteristic of the light source, i.e. emitting non-monochromatic light with low spatial coherence, caused a minimum light sheet thickness of 10 mm for the used setup. The pulse length of the applied flash lamps was 30 µs.

As tracer particles, Microsphere® expanded plastic spheres were used. These particles (*Expancel DET 80 d25*) have a density of 25 kg/m^3 and a diameter of 60 – 90 µm. They are solid particles and have no deleterious effects for the birds; for example, they do not adhere to their feathers. The particles restricted the maximum resolvable flow frequency to ~2,000 Hz, but they also have good reflection behaviour. Therefore, together with the applied high-sensitivity cameras (*PCO Dimax*) a sufficient signal to noise ratio was achieved.

The positioning of the cameras needs to be well thought out. To obtain optimal results of the fluid flow close to the surface of the wing and body, the cameras need to view parallel to the surface, so that the illuminated feathers are not visible and do not disturb the results. But there is also always the risk that parts of wing block the field of view and no results can be obtained. Also the position and shape of the bird flying through the frame varies greatly. Therefore four cameras were positioned on the side of the frame to view with different angles on the light sheet (1–4 in Fig. 1). The images of any two of these cameras could be combined to get stereoscopic results. The results of all camera pairs were merged to one result. The merged measuring field had a size of 450 × 500 mm and the images had a resolution of 7 Pixel/mm.

After the owl crossed the light barrier placed in front of the measurement volume, 100 double images with a frequency of 100 Hz were recorded. The time between the double images was $\delta t = 1.25$ ms. To identify the particle movement, a multipass cross-correlation algorithm from the program *PIVView* was applied. The adopted interrogation window size was in most cases 48 pixels with an overlap of 16 pixels, leading to a distance between two calculated vectors of 16 Pixel, or ~2.3 mm.

2.2 PROPAC

The determination of shape and position of the bird was carried out with the same system as already used for bird wing shape measurements by Wolf et al [8]. The basic principle of the measurement technique is the combination of photogrammetry with cross-correlation algorithms, as used in PIV [11, 12]. By use of the cross-correlation algorithms, corresponding patterns can be identified in the stereo images. After identification of the corresponding image sections, a stereographic reconstruction is used for the calculation of the exact three-dimensional position of the sections. For a unique identification a random distributed dot pattern is projected onto the surface of interest.

Therefore the applied setup consists of image acquisition and projection parts. For image acquisition a two camera setup, consisting of two *Phantom v12.1* high-

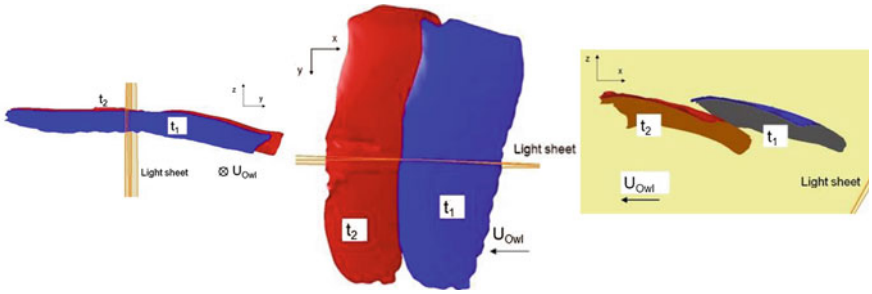

Fig. 2 Measured wing shape at two different time steps together with the PIV light sheet

speed cameras (c, d in Fig. 1), was used. Both cameras were positioned above the measurement volume, thus providing an observation of the upper wing surface.

For the optical projection of the dot pattern a specially developed projection device using LED light sources was used. The main feature of this device is the homogenous projection of patterns with high contrast and good depth-of-field. Furthermore, the light source is can be pulsed. with which it was possible to prevent that the PROPAC measurements interfere with the flow measurements; i.e. the light pattern is triggered just after the exposure times of the PIV cameras The exposure of the PROPAC cameras is triggered such that they capture the projected dot pattern and a bright line produced by the light sheet on the wing, so that the position of the PIV plane can be determined on the wing. An example of the resulting wing shape is shown in Fig. 2.

3 Results

In five days of experiments it was possible to record more than 200 flights. Not all of those flights were suitable for analysis, because the owls did not always fly at the optimal position.

Below, the results of some recorded flights are shown and discussed. The collected PIV data is displayed together with the upper wing shape at certain time steps. The position of the light sheet with respect to the wing is also given.

3.1 Gliding Flight

The first case shows gliding flight of a barn owl with a flight speed of 6.3 m/s. The three-dimensional PROPAC result for two time steps and the PIV light sheet are shown in Fig. 2. It can be seen that the wing shape does not change significantly for the displayed time steps, which is a characteristic of gliding flight.

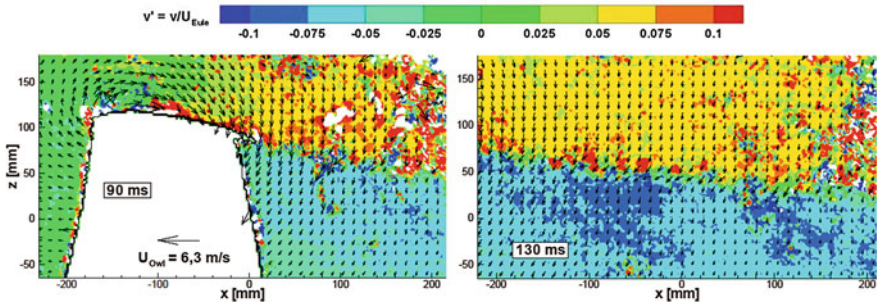

Fig. 3 PIV-results of a gliding flight at two time steps (every 5th vector shown)

The position of the light sheet and therefore the flow measurement was at 53 % of the wingspan. The result of the fluid flow measurement of the flight is shown in Fig. 3. The vectors in the images represent the velocity of the air in the measurement plane, while the colour represents the out-of-plane velocity normalized to the flight speed. The first image shows the results of flow measurements at 90 ms after entering the measurement volume, where the wing of the owl can also be seen. Around the wing there are indications of a circulation and behind it a strong downwash is visible.

The colours in the image show that the out-of-plane velocity increases over the wing continuously, starting from the leading edge, where it is close to zero, to the trailing edge, where it reaches almost 10 % of the flight speed in direction of the body. In the second time step, 130 ms after entering the volume, a thin shear layer has developed between the upper part of the flow with a positive out-of-plane velocity and the lower part with a negative out-of-plane velocity. The in plane velocity field still shows the downwash. While the vectors mainly point downwards, the main direction in the shear layer is in the flight direction, indicating the wake depression caused by the boundary layer of the wing [13].

3.2 Flapping Flight

An example of the shape measurements of a flapping flight is given in Fig. 4. Each of the three images of this figure shows one perspective of the position and shape of the wing at three different time steps. The owl was recorded during an upstroke and a flight speed of 7.1 m/s was calculated. The position of the light sheet was between the middle of the wing and the wing tip.

A result of the fluid flow measurement of this flight is shown in Fig. 5 on the left. The shear layer which divides the upper and lower parts of the flow (positive and negative out-of-plane velocities, respectively) can clearly be seen and gives an indication of the path of the wing in the measurement plane. The flow field shows a velocity from the wing tip in a direction towards the body in the area over the

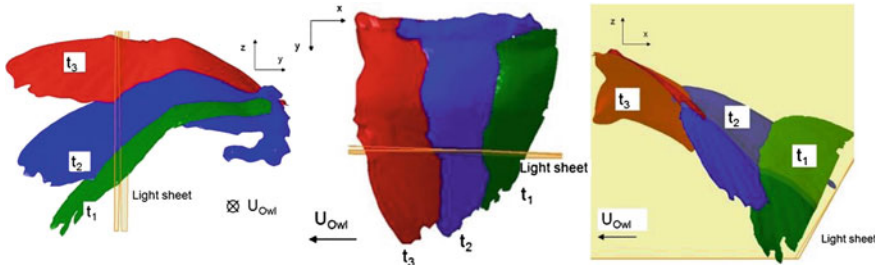

Fig. 4 Results of the geometry measurements during an upstroke at tree time steps

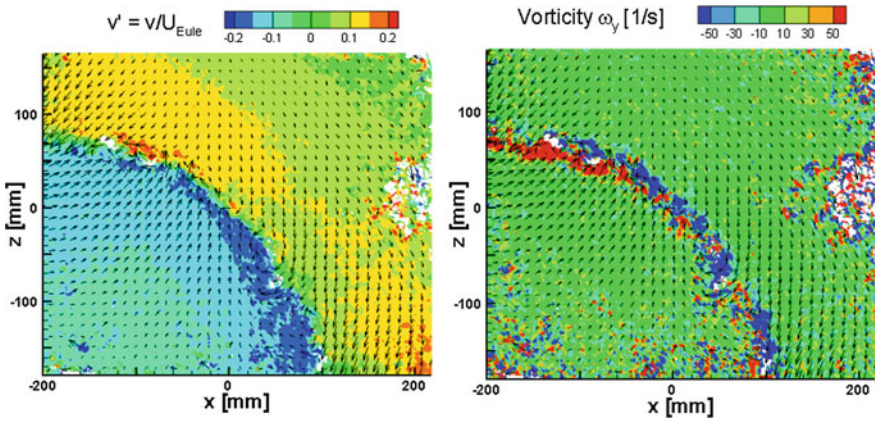

Fig. 5 The colourmap in the image on the left shows the out-of-plane velocity, the colourmap in the image on the right show the vorticity (every 5th vector shown)

shear layer, and vice versa below, similar to the gliding flight results. In Fig. 5 on the right the colour represents the vorticity in y direction. It can be seen that during the upstroke negative vortices develop in the y direction. At the end of the upstroke this changes and positive vortices emerge as shown in Fig. 5 on the right. This indicates that the lift is alternating during the upstroke, leading to the development of start and stop vortices and to a compensation for the change in vorticity around the wing that is according to the wake vortex models of [1] and [14] for flapping flight.

Another flapping flight case where the bird was recorded during down stroke is shown in Fig. 6. The speed of the owl was only 4.8 m/s during this flight.

The obtained velocity fields for the time steps t_2 and t_4 are shown in Fig. 7. The coordinate system is now fixed to the wing, which means we add the vector of the current wing movement to the measured flow field. The blank area in the wake of the wing without velocity results is caused by a lack of particles. This area is enlarged when the bird beats its wings downward ($t = t_2$) and becomes smaller as the bird reaches the end of its down stroke ($t = t_4$). One reason for that might be the occurrence of a flow separation.

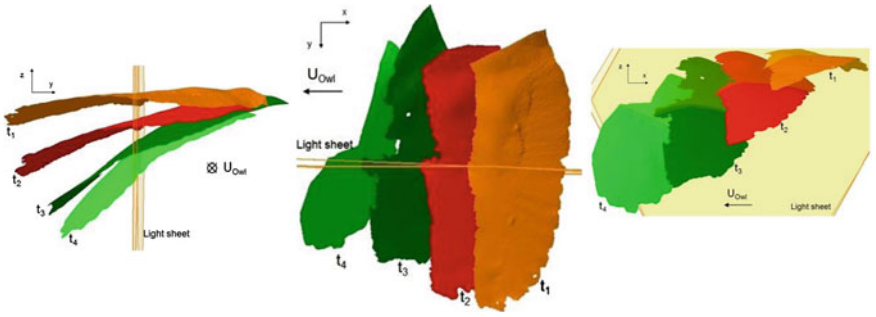

Fig. 6 PROPAC results during a down stroke at four time steps, $\Delta t = 20$ms

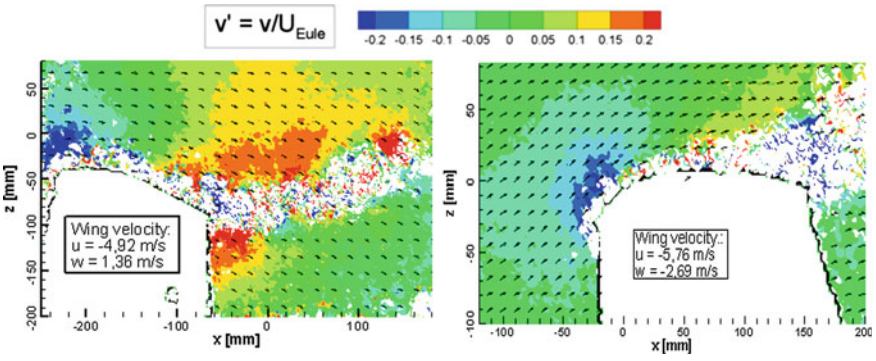

Fig. 7 Velocity results for two time steps, t_2 and t_4 (every 5th vector shown)

4 Conclusion and Outlook

The measurement technique PIV was successfully modified for the application to free-flying birds. By the use of flashlamps for the generation of a light sheet, it was possible to build a non-harmful PIV setup which is able to capture the velocity field over the wing of the bird. A suitable seeding technique using solid particles which do not adhere to the bird was also applied. It was proven during the tests that, providing sufficient training time has been given, the influence of the seeding and the setup on the flight behaviour can be neglected. For the current tests, velocity fields for 50 flights were obtained. Within these flights, it was possible to collect data from 2 birds at several positions on the wing and wing beat phases. Together with the PIV measurements a non-intrusive surface measurement system was applied simultaneously, this enabling the correlation of the flow field information with the wing shape and kinematics of the bird flight.

The obtained results show some interesting flow effects particularly for the flapping flight, which occur above the wing and in the wake where a complex vortex system develops and that should be investigated in more detail. For this the

seeding generation should be optimized getting higher spatial resolutions. Also tomographic PIV approaches can be applied to gather more information about the three-dimensional, unsteady flow fields.

References

1. Spedding, G.R., Rosen, M., Hedenström, A.: A family of vortex wakes generated by a thrush nightingale in free flight in a wind tunnel over its entire natural range of flight speeds. J. Exp. Biol. **206**(14), 2313–2344 (2003)
2. Speeding, G.R.: The wake of a kestrel (falco tinnunculus) in gliding flight. J. Exp. Biol. **127**, 45–57 (1987)
3. Hedenström, A., Rosen, M., Spedding, G.R.: Vortex wakes generated by robins Erithacus rubecula during free flight in a wind tunnel. J. Roy. Soc. Interface **3**(7), 263–276 (2006)
4. Rosén, M., Spedding, G.R., Hedenström, A.: Wake structure and wingbeat kinematics of a house-martin Delichon urbica. J. Roy. Soc. Interface **4**(15), 659–668 (2007)
5. Muijres, F.T., Bowlin, M.S., Johansson, C., Hedenström, A.: Vortex wake, downwash distribution, aerodynamic performance and wingbeat kinematics in slow-flying pied flycatchers. J. Roy. Soc. Interface **9** (2012)
6. Warrick, D.R., Tobalsk, B.W., Powers, D.R.: Lift production in the hovering hummingbird. Proc. Roy. Soc. Bio. Sci. **276**(1674), 3747–3752 (2009)
7. Wolf, T., Konrath, R., Kirmse, T., Erlinghagen, T.: Measuring shape of bird wings during flight. In: 14th International Symposium on Flow Visualization—ISFV14, Daegu, 21–24.06.2010 (2010)
8. Wolf, T., Konrath, R., Erlinghagen, T., Wagner, H.: Shape and deformation measurement of free flying birds in flapping flight. Notes on Numerical Fluid Mechanics and Multidisciplinary Design, Heidelberg (2012)
9. Adrian, R.J. Westerweel, J.: Particle Image Velocimetry. Cambridge Aerospace Series. Cambridge University Press, Cambridge (2010)
10. Raffel, M., Willert, C.E. Kompenhans, J.: Particle Image Velocimetry: A Practical Guide, Experimental Fluid Mechanics. Springer, Berlin (1998)
11. Schlichting, H. Gersten, K.: Boundary Layer Theory. Springer, Berlin (2000)
12. Pennycuick, C.: Modelling the Flying Bird. Academic Press, Bristol (2008)
13. Herzog, K.: Anatomie und Flugbiologie der Vögel. Gustav Fischer Verlag, Stuttgart (1968)
14. Hubbel, T.: Untersuchungen zur instationären Aerodynamik an einem vogelähnlichen Flügelschlagmodell. Dissertation, Fachbereich Biologie der Technischen Hochschule Darmstadt, Darmstadt (2006)

Numerical Investigation of the Aerodynamic Forces Induced by the Flow around Free Flying Fruit Fly

Andrei Shishkin and Claus Wagner

Abstract Direct Numerical Simulation (DNS) of free-flight maneuvers of a fruit fly (*Drosophila melanogaster*) is performed using the open source CFD code OpenFOAM . The fruit fly's geometry and the kinematics are generated according to experimental studies by P. Schützner and F.-O. Lehmann in which the time series of spatial coordinates of the markers on the *Drosophila*'s body, head and wings were recorded. Based on the calculated velocity and pressure fields, we evaluated the vorticity and the forces acting on the wings. The analysis of the results obtained in the simulations confirms some experimentally observed lift enhancing mechanisms such as the leading edge vortex and rotational circulation. The wing-wake inetraction is also discussed.

1 Introduction

In the past a number of the rigorous theoretical and experimental investigations were devoted to the mechanisms of force production in insect flight. The revealing lift enhancing mechanisms such as leading edge vortex (LEV) lift, rotational circulation and wake capture [1, 2] uncover the physical principles of insect flight. Though, the most of these researches dealt with robotic wing experiments and hovering flight conditions, while comparatively few studies relate to the field of numerical simulation of free flight maneuvers. This situation is due to the exceptional complexity of insect free flight kinematics for measurements as well as for numerical simulation. Considering the physical side of the problem of a freely flying animal, the aerodynamic forces are caused by the production of vorticity and the shedding of vortical structures in each stroke cycle. Moreover, a number of additional factors such as

A. Shishkin (✉) · C. Wagner
German Aerospace Center (DLR), Institute of Aerodynamics and Flow Technology, Göttingen, Germany
e-mail: Andrei.Shishkin@DLR.de

A. Dillmann et al. (eds.), *New Results in Numerical and Experimental Fluid Mechanics IX*, Notes on Numerical Fluid Mechanics and Multidisciplinary Design 124,
DOI: 10.1007/978-3-319-03158-3_68,

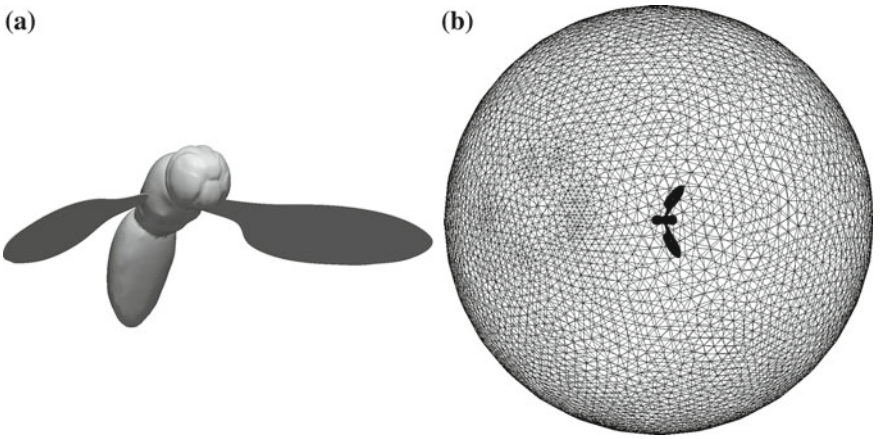

Fig. 1 Fruit fly model (**a**) and surface mesh of the computational domain (**b**)

wake components from a previous stroke, an impact of body motion, and external disturbances in surrounding air need to be accounted for in investigations of force generation mechanisms. All this indicates the challenge for numerical simulations of insect free-flight maneuvers as well as for the further analysis and interpretation of results. Detailed reviews of the current state of numerical and experimental investigations in this area can be found in [2] and [3].

For the presented study, we conducted Direct Numerical Simulations (DNS) of the flow around freely flying fruit fly (*Drosophila melanogaster*) using the kinematics measured by Schützner and Lehmann in their experiments [4]. The geometry model of the fruit fly (Fig. 1a) consisting of three solid body parts was also constructed from the experimental data. The method and the code used in the simulations were developed on the basis of the Arbitrary Lagrangian Eulerian (ALE) approach and the finite volume method [5] implemented in the open source toolkit OpenFOAM [6]. More precisely, our contribution to the method was the development of some advanced boundary conditions for the mesh motion solver based on the real flight kinematics. We evaluated the aerodynamic forces acting on the fruit fly using velocity and pressure fields calculated in DNS as well as the vorticity and some other important characteristics. Some early results of the simulations are reported in [4]. In this work, we present an advanced analysis of the aerodynamic forces induced by the flow around the fruit fly. The experimental hypothesis of lift enhancing mechanisms found their confirmation in DNS. In the first instance, it applies to LEV and rotational circulation mechanisms. Additionally, the results of the DNS indicate indirectly a contribution of the wing-wake interaction to the resulting forces. The qualitative characteristics of each of the listed phenomena need to be investigated in more detail in the future.

2 Computational Setup

For the simulations we applied the finite volume method in the computational domains with the moving boundaries [5, 6]. The governing equations are the incompressible Navier-Stokes equations which in dimensionless form read:

$$\frac{\partial \mathbf{u}}{\partial t} + (\mathbf{u} \cdot \nabla)\mathbf{u} = \frac{1}{Re}\nabla^2 \mathbf{u} - \nabla p, \quad \nabla \cdot \mathbf{u} = 0, \tag{1}$$

where $\mathbf{u}$ and p are the velocity and pressure fields, respectively, and Re is the Reynolds number which in our simulations equals $Re \approx 150$. For each time step Eq. (1) are solved but in a changed computational domain. The main idea of the method is to use a topologically equivalent mesh for each time step. More precisely, for each time step the mesh is obtained from the previous one by continuous deformation which is determined from the solution of the Laplace equation with the boundary conditions predefined by the data of the kinematics.

The computational domain (Fig. 1b) is bounded by the sphere of diameter 30mm with the center moving according to the measured motion of the center of gravity of the *Drosophila*. The fruit fly model (Fig. 1a) of the size ≈ 2.5 mm is located in the center of the computational domain. It consists of three independently moving parts—the body and the two wings. Together this results in 18 degrees of freedom in the most complicated case. Note, that the used method has the natural restriction: there exists no continuous domain deformation changing the domain's connectivity. Hence, it is impossible to simulate clapping wings or the wings touching the body. As a consequence, only a half stroke can be simulated using the model containing the body, while the simplified bodiless two-wings model allows for simulations over two full strokes of the given kinematics. Due to this, the results and the discussion concern only the two-wings model.

The measured kinematics by Schützner and Lehmann (chapters 1–3 in [4]) were presented in the form of time series of the coordinates of the markers on the body and the wings of the fruit fly. For simplicity, the data were orthogonally transformed such that the z-axis remains directed opposite to the gravity force, while the center of gravity of the fruit fly is initially placed at the origin of the coordinate system. Thus, during the simulated flight, the center of gravity moves forward-and-down along the xz-plane with small fluctuations in y-direction as illustrated in Fig. 2a. The other parameters presented in Fig. 2 are the azimuth, i.e. the angle between the projection of wing base-tip vector on the (horizontal) xy-plane and the positive x-direction, the elevation (reflecting the angle between the base-tip vector and the xy-plane) and the angle of attack, which is the angle between the wing plane and xy-plane.

The kinematics can be described shortly as follows. The insect wing motion consists of the regularly repeated cycles of up- and downstrokes. Each half stroke is divided into translational and rotational phases. The latter take place at the beginning and the end of a half stroke and contain the wing reversal. Since the force producing mechanisms depend strongly on the phase of the wing cycles, it is impor-

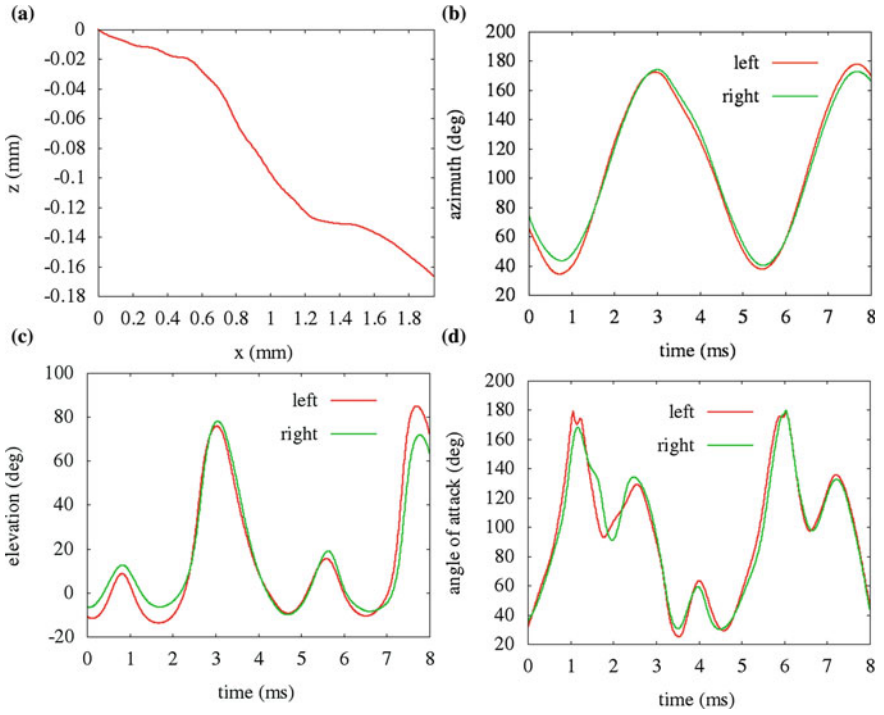

Fig. 2 Kinematics used in the numerical simulations. **a** The trace of the center of gravity of a fruit fly in xz-plane. **b** Azimuth, **c** elevation and **d** angles of attack of the two wings

tant to divide the given data into the following phases: the time segment 0 to 1 ms corresponds to the downstroke, 1–3 ms—to the upstroke, 3–5.5 ms—to the downstroke and 5.5–7.5 ms—to the upstroke again. Further, in Sect. 3 we consider also alternating translational and rotational phases in the discussion of forces.

3 Generation of Aerodynamics Forces

In this section we focus on the mechanisms which are responsible for the generation of the aerodynamic forces during *Drosophila's* free flight. The aerodynamic forces **F** acting on the wings can be split into the pressure and viscous components as follows:

$$\mathbf{F} = \underbrace{-\rho \iint_S p\mathbf{n}\mathrm{d}\mathbf{S}}_{\text{pressure component}} + \underbrace{\iint_S \mu[\nabla\mathbf{u} + (\nabla\mathbf{u})^{\mathbf{T}}] \cdot \mathbf{n}\mathrm{d}\mathbf{S}}_{\text{viscous component}}, \tag{2}$$

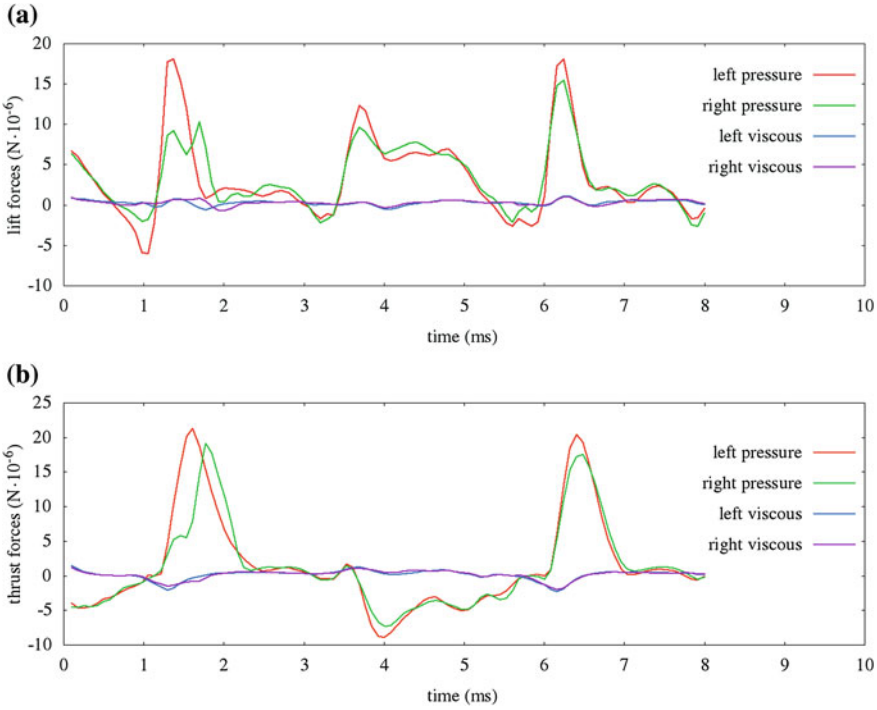

Fig. 3 Aerodynamic forces acting on the fruit fly's wings. **a** lift and **b** thrust forces

where S denotes the wing's surface with normal $\mathbf{n}$, and ρ and μ are the density and the dynamic viscosity of air, respectively. The pressure force component is directed orthogonal to the wings plane, while the viscous component acts tangentially. Further, each force component is decomposed by projection on the vertical (z), forward (x) and side (y) directions to determine the lift, thrust and lateral forces, respectively. The force components obtained in the DNS are depicted in Fig. 3.

It was found theoretically and experimentally (see [2, 3] and the literature cited there) that, depending on the phase of the wing cycle, significant forces are generated by the leading edge vorticies (LEV) during translational phase and the rotational circulation and wake capture (wing-wake interaction) during the rotation phase. These mechanisms are the subject of our discussion.

The leading edge vorticies remain attached to the wing during the whole translational phase of a half stroke. The LEV forces are generated due to the lower pressure region above the wing created by LEV (Fig. 4). In order to visualize the vorticies needed to highlight the LEV obtained in DNS, the *Q-criterion* of Hunt et al. [7] is used. The quantity Q is defined by the following equation:

$$Q = \frac{1}{2}\left(|\mathbf{\Omega}|^2 - |\mathbf{S}|^2\right), \tag{3}$$

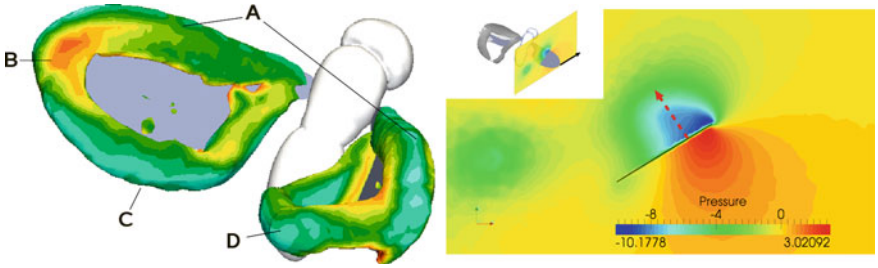

Fig. 4 *Left*: typical vortical structure of the flow around a flapping wing during translational phase. The Q-isosurfaces ($Q = 10^7$) obtained in DNS of a freely flying *Drosophila* at $t = 4$ ms are depicted. Here **A** denotes the Leading Edge Vortex (LEV), **B**—tip vortex, **C** and **D** point to trailing edge vorticies, and the latter are shedding visibly. *Right*: LEV lift enhancing mechanism. The leading edge vortex creates a region of a lower pressure above the wing. The pressure difference on the both sides of the wing produces the force (*red arrow*). The wing moving direction is shown with the black arrow

where $\mathbf{S} = \frac{1}{2}[\nabla\mathbf{u} + (\nabla\mathbf{u})^T]$ is the rate-of-strain tensor and $\mathbf{\Omega} = \frac{1}{2}[\nabla\mathbf{u} - (\nabla\mathbf{u})^T]$ is the vorticity tensor. The criterion states that in a vortical flow region the norm of the vorticity tensor $\mathbf{\Omega}$ is greater than the norm of the rate-of-strain tensor S, so $Q > 0$, and highly vortical flows are characterized by larger Q values.

The visualization of the DNS results, confirming the LEV lift enhancing mechanism, is shown in Fig. 5. The presented results obtained in the translational phase of down- (from $t = 4$ ms to $t = 5$ ms) and upstroke (from $t = 6.2$ ms to $t = 7.2$ ms) reveal that the LEV remain attached to the wings while trailing edge and tip vortices are shed.

Considering the rotational phase, the generated forces are studied experimentally and theoretically in [1]. The numerical confirmation of the force generating mechanisms is more complicated and requires a series of numerical simulations under varying conditions aiming to separate the contributions of the different force mechanisms. Nevertheless, the results obtained in our simulation allow to provide indirect confirmation of the contributions of both, rotational circulation and wake capture, to aerodynamic forces. The wing kinematics and evaluated forces acting on the wing are depicted in Fig. 6. The varying velocity fields around the right wing during the wing reversal are shown in Fig. 7. In the considered period the wing kinematics are determined mostly by the angle of attack (AoA) and azimuth. The angle of attack increases up to 90° at $t = 5.5$ ms during supination which results in the shedding of the LEV (not shown here) and the local maximum of total force. Then the supination is continued up to $t = 6.04$ ms, when it is changed by pronation. In spite of the change in wing rotation, the lift increases smoothly reaching the maximum at $t = 6.2$ ms and the total pressure force remains extremely high from $t = 6.2$ to $t = 6.5$ ms with the peak at $t = 6.3$ ms. Simultaneously at $t = 5.5$ ms, as follows from the azimuth plot, the wing begins the inverse translational motion interacting with the flow in the

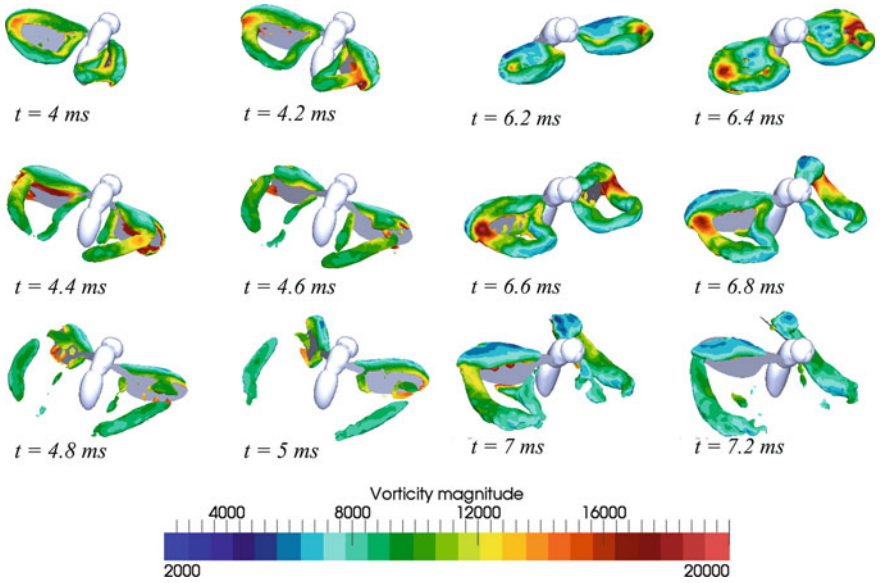

Fig. 5 Q-isosurfaces coloured with vorticity magnitude. **a**: the results obtained in the translational phase of the downstroke. **b**: the results obtained in the translational phase of the ustroke. LEV remain attached to the wings during the translational phase

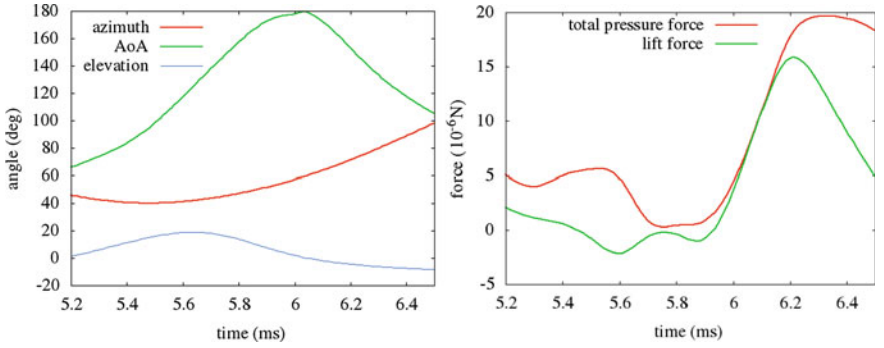

Fig. 6 Kinematics (*left*) and evaluated aerodynamic forces (*right*) during rotational phase of the right wing

near-wake region of the preceding half stroke. This suggests that the force generation in the reversal period is hard to explain sufficiently by only rotational circulation mechanism, but it is reasonable to consider the force production as a result of more complicated mechanism which includes possibly also wing-wake interaction.

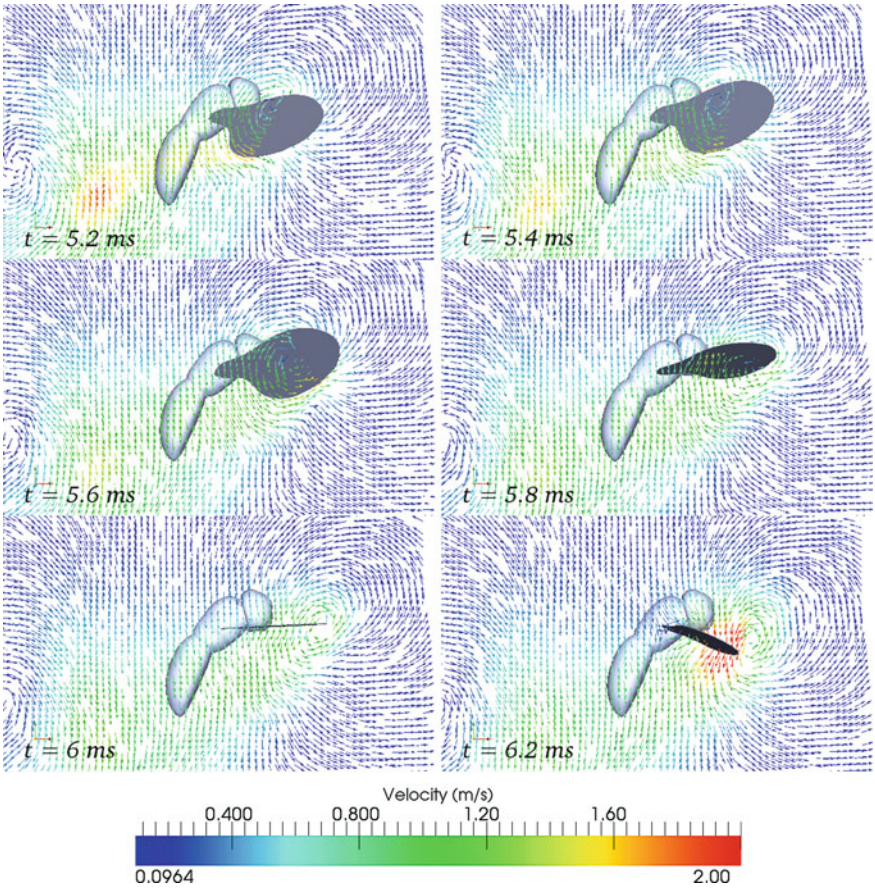

Fig. 7 Calculated velocity field around the right wing during the rotational phase of the flapping cycle

4 Conclusions

Our three-dimensional numerical simulations of the flow around the wings of freely flying fruit flies demonstrate highly dynamic and complex vortical flow structures in insects. A detailed analysis of pressure and viscous forces suggests that the leading edge vortex, rotational circulation and possibly wake capture contribute to aerodynamic force production. The action of the latter is not yet enough studied in non-hovering insect flight. A comprehensive and comparative numerical analysis on the contribution of different force enhancing mechanisms is still under investigation including an analysis on the impact of wing elasticity on forces and moments.

The authors are grateful to Dr. F.-O. Lehmann and P. Schützner for providing the experimental data and for useful discussions and acknowledge financial support by the Deutsche Forschungsgemeinschaft (DFG) under the grant WA1510/13-2.

References

1. Dickinson, M., Lehmann, F.O., Sane, S.: Wing rotation and the aerodynamic basis of insect flight. Science **284**, 1954–1960 (1999)
2. Lehmann, F.: When wings touch wakes: understanding locomotor force control by wake wing interference in insect wings. J. Exp. Biol. **211**(Pt 2), 224–233 (2008)
3. Shyy, W., Aono, H., Chimakurthi, S., Trizila, P., Kang, C., Cesnik, C., Liu, H.: Recent progress in flapping wing aerodynamics and aeroelasticity. Prog. Aerosp. Sci. **46**(7), 284–327 (2010)
4. Shishkin, A., Schützner, P., Wagner, C., Lehmann, F.O.: Experimental quantification and numerical simulation of unsteady flow conditions during free flight maneuvers of insects. In: Nature-Inspired Fluid Mechanics Notes on Numerical Fluid Mechanics and Multidisciplinary Design, vol. 119, pp. 81–99. Springer, Berlin (2012)
5. Ferziger, J., Peric, M.: Computational Methods for Fluid Dynamics, 3rd edn. Springer, Berlin (2002)
6. Jasak, H., Tuković, Z.: Dynamic mesh handling in OpenFOAM applied to fluid-structure interaction simulations. In: Pereira, J.C.F., Sequeira, A. (eds), V European Conference on Computational Fluid Dynamics, ECCOMAS CFD 2010, Portugal, 14–17 June 2010
7. Hunt, J., Wray, A., Moin, P.: Eddies, stream, and convergence zones in turbulent flows. Technical Report CTR-S88, Center for Turbulence (1988)

Author Index

A. Dillmann et al. (eds.), *New Results in Numerical and Experimental Fluid Mechanics IX*,
Notes on Numerical Fluid Mechanics and Multidisciplinary Design 124,
DOI: 10.1007/978-3-319-03158-3, © Springer International Publishing Switzerland 2014